

Understanding the Relationship between Structural Changes and the Optical Properties in Lead Halide Perovskite to Elucidate their Film Formation

Von der Universität Bayreuth
zur Erlangung des Grades eines
Doktors der Naturwissenschaften (Dr. rer. nat.)
genehmigte Abhandlung

von
Konstantin Schötz

aus Naila, Deutschland

Erste Gutachterin: Prof. Dr. Anna Köhler
Zweiter Gutachter: Prof. Dr. Markus Lippitz

Tag der Einreichung: 20.12.2021
Tag des Kolloquiums: 24.05.2022

Naja...

R.K.
sehr oft.

Deutsche Zusammenfassung

Eine der vielversprechendsten aufstrebenden neuen Halbleiterklassen ist die Klasse der Metall-Halogen-Perowskite. Solarzellen mit solchen Perowskiten als aktive Schicht stehen kurz vor der Kommerzialisierung. Aber auch in anderen optoelektronischen Bauteilen, wie lichtemittierenden Dioden (LEDs) oder Röntgendetektoren zeigen Perowskite vielversprechende Eigenschaften, beispielsweise eine hohe Detektionssensitivität für Röntgenstrahlen.

Ein Grund für die schnelle Entwicklung und Verbesserung solcher perowskitbasierter Bauteile war die Erkenntnis, dass die Struktur des Perowskiten und der Perowskitschicht großen Einfluss auf dessen optoelektronische Eigenschaften und damit auf die Funktionalität der entsprechenden Bauteile hat. Durch Optimierung der Perowskit-Kristallisation, welche wiederum Auswirkungen auf die finalen Perowskit-Filmeigenschaften hat, konnten so Bauteileffizienzen für bestimmte Herstellungsmethoden und Materialsysteme kontinuierlich verbessert werden. Meistens fanden diese Optimierungsansätze durch praktisches Herumprobieren statt, und nur die finalen Filmeigenschaften wurden untersucht. Da die Perowskitkristallisation aber sehr sensitiv von den genauen Umgebungsbedingungen sowie dem verwendeten Materialsystem abhängt, sind die gefundenen Optimierungsstrategien nur begrenzt auf andere Herstellungsmethoden und Materialsysteme, und sogar auf andere Labore mit anderen Umgebungsbedingungen, übertragbar. Um einen derartigen Transfer zu ermöglichen, muss zunächst die Perowskitkristallisation während der Filmbildung besser verstanden werden.

Eine Methode, mit der die Filmbildung untersucht werden kann und die zunehmend populärer wird, ist optische *in situ* Spektroskopie. Bei dieser Methode kann die Perowskitbildung indirekt über die Änderung der optischen Eigenschaften des Perowskiten verfolgt werden, da die optischen Eigenschaften des Perowskiten stark von dessen Struktur beeinflusst werden. Um aus den während der Filmbildung aufgenommenen Spektren die relevanten Informationen über die Filmbildung extrahieren zu können, ist daher ein präzises Verständnis des Zusammenhangs der optischen Eigenschaften des Perowskiten und dessen Struktur notwendig. Hierbei sind einige Aspekte der optischen Eigenschaften von Perowskiten, wie beispielsweise der Ursprung mancher Lumineszenz-Banden oder der Einfluss struktureller Inhomogenitäten, noch nicht gänzlich geklärt.

Aus diesem Grund wird in dieser Arbeit zunächst ein besseres Verständnis über den Zusammenhang struktureller Änderungen im Perowskiten mit dessen optischen Eigenschaften erarbeitet. Dieses Verständnis wird anschließend verwendet, um mittels optischer *in situ*

Spektroskopie die Filmbildung des Perowskiten zu untersuchen und besser zu verstehen.

Kapitel 8-10 befassen sich mit den optischen Eigenschaften und deren Zusammenhang mit der Struktur des Perowskiten. In Kapitel 8 und 9 habe ich dafür Perowskit-Einkristalle mittels Photolumineszenz-(PL-)Spektroskopie untersucht. Dabei war in Kapitel 8 das primäre Ziel, den Ursprung einer zusätzlichen PL-Bande zu klären. Mittels verschiedener PL-Messungen konnte ich verschiedene in der Fachwelt vorgeschlagene Ursachen für diese PL-Bande ausschließen. Gestützt durch optische Modellierung konnte ich schließlich zeigen, dass jene PL-Bande durch interne Reflexion und Selbstabsorption der PL zustande kommt.

Mit der Kenntnis des Effekts von Selbstabsorption auf die PL-Spektren war es mir nun möglich, in Kapitel 9 den strukturellen Phasenübergang von MAPbI₃-Einkristallen mittels temperaturabhängigen PL-Messungen detailliert zu untersuchen. Hier konnte ich mittels des optischen Modells aus Kapitel 8 die optische Signatur von strukturell verzerrten Einschlüssen der Raumtemperatur-Phase innerhalb der Tieftemperatur-Phase bis weit unterhalb der Temperatur des Phasenübergangs identifizieren.

In Kapitel 10 habe ich die optischen Eigenschaften von Perowskit-Pulvern mittels PL- und Reflexionsmessungen untersucht. Hintergrund war hier die Frage, ob sich die optischen Eigenschaften von Perowskit-Pulvern von jenen ihrer Dünnschicht- und Einkristall-Gegenständen unterscheiden. Im Zuge dessen konnte ich zeigen, dass sich mittels Änderung der Stöchiometrie des Perowskiten die Energie der Bandlücke gezielt verändern lässt, wie es auch für Dünnschichten bekannt ist. Weiter konnte ich das erste Mal zeigen, dass eine für Dünnschichten etablierte Passivierungsmethode ebenfalls auf Perowskit-Pulver anwendbar ist.

Kapitel 11 ist ein Überblicksartikel, in dem ich zunächst die wichtigsten optischen Eigenschaften von Metall Halogen Perowskiten und deren Beeinflussung durch strukturelle Änderung zusammengefasst habe. Hierbei sind einige meiner Erkenntnisse aus Kapiteln 8-10 eingeflossen. Anschließend behandelt das Kapitel, wie dieser Zusammenhang zwischen optischen Eigenschaften und Struktur bisher genutzt wurde, um mittels optischer *in situ* Spektroskopie die Filmbildung von Perowskit-Dünnschichten zu untersuchen.

In den Kapiteln 12-14 wird nun das in den vorangehenden Kapiteln generierte Wissen über den Zusammenhang zwischen strukturellen Änderungen im Perowskiten und dessen optischen Eigenschaften genutzt, um mittels optischer *in situ* Spektroskopie die Perowskit-Schichtbildung bei verschiedenen Prozessierungsmethoden besser zu verstehen.

Kapitel 12 untersucht dazu die Bildung von MAPbI₃ Dünnschichten mittels der sogenannten Two-Step-Methode. Hier konnte ich mittels des Modells aus Kapitel 8 den Einfluss von Selbstabsorption auf die PL-Spektren klar identifizieren. Dies erlaubte die Identifikation eines Auflösungs-Rekristallisations-Prozesses, welcher eine wichtige Rolle für die Filmbildung spielt. In Kapitel 13 wird nun die Filmbildung von MAPbI₃ mittels der sogenannten One-Step-Methode unter Verwendung der im Labor meistverwendeten Rotationsbeschichtung und der industrierelevanten Spritzdüsenbeschichtung untersucht. Mittels optischer *in situ* Spektroskopie

konnten wir zeigen, dass prozessbedingte Unterschiede in der Struktur der Lösungsmittelkomplex-Phase dazu führen, dass sich das Perowskit-Wachstum bei der Rotationsbeschichtung sowohl quantitativ als auch qualitativ von der bei der Spritzdüsenbeschichtung auftretenden Perowskit-Kristallisation unterscheidet.

In Kapitel 14 wird schließlich die Bildung eines Perowskiten mit unterschiedlichen Haliden mittels der Solvent-Engineering-Methode betrachtet, wobei der Einfluss der Temperatur des Anti-Lösungsmittels auf die Perowskit-Bildung und auf fertige Perowskit-Solarzellen untersucht wird. Hier konnte ich zeigen, dass für kälteres Anti-Lösungsmittel die Perowskit-Bildung langsamer und die resultierende Perowskit-Schicht dünner ist. Weiter ergaben meine Analysen, dass sich während der Filmbildung das Halid-Verhältnis im Perowskiten kontinuierlich ändert. Darüber hinaus konnte gezeigt werden, dass die mit kälterem Anti-Lösungsmittel prozessierten Filme eine reduzierte Dichte von Defektzuständen aufweisen, was auf eine bessere Relaxation von mechanischen Spannungen in den entsprechenden Perovskitschichten zurückgeführt wurde.

English Abstract

One of the most promising new classes of semiconductors is the class of metal halogen perovskites. Solar cells with such perovskites as active layer are close to commercialization. But perovskites also show promising properties in other optoelectronic devices, such as light-emitting diodes (LEDs) or X-ray detectors, for example a high detection sensitivity for X-rays, enabling lower X-ray doses for imaging.

One reason for the rapid development and improvement of such perovskite-based devices was the awareness that the structure of the perovskite and the perovskite film have a major influence on the optoelectronic properties of the perovskite and thus on the functionality of corresponding devices. Accordingly, by optimizing the perovskite crystallization, which in turn affects the final perovskite film properties, device efficiencies for specific fabrication methods and material systems could be continuously improved. Mostly, these optimization approaches took place through hands-on trial and error, and only the final film properties were investigated. However, since the perovskite crystallization depends very sensitively on the exact environmental conditions as well as the material system used, such optimization strategies are only very limitedly transferable to other fabrication methods and material systems, or even to other laboratories with different environmental conditions. To enable a better transfer, the perovskite crystallization during film formation must be better understood. One method that can be used to study film formation and that is becoming increasingly popular is optical *in situ* spectroscopy. With this method, the perovskite formation can be indirectly followed by changes in the optical properties of the perovskite, which in turn are strongly influenced by its structure. In order to extract the relevant information about the film formation from the *in situ* optical spectra, a precise understanding of the relationship between the optical properties of the perovskite and its structure is necessary. Here, some aspects of the optical properties of perovskites, such as the origin of some luminescence bands or the influence of structural inhomogeneities, are not yet fully understood.

For this reason, this thesis will first develop a better understanding of the relationship of structural changes of the perovskite and its optical properties. This understanding will then be used to investigate and better understand the film formation of the perovskite using optical *in situ* spectroscopy.

Chapters 8-10 deal with the optical properties and their relation to the structure of the perovskite. In Chapters 8 and 9, I studied perovskite single crystals by photoluminescence

(PL) spectroscopy. In Chapter 8 the primary goal was to clarify the origin of an additional PL band. Using various PL measurements, I was able to rule out several origins for this PL band which are proposed in the literature. Supported by optical modeling I could finally show that the additional PL band is caused by internal reflection of the PL and self-absorption effects.

With the knowledge of the effect of self-absorption on the PL spectra, I was now able to study the structural phase transition of MAPbI₃ single crystals in detail using temperature-dependent PL measurements in Chapter 9. Using the optical model from Chapter 8, I was able to identify the optical signature of structurally distorted inclusions of the room-temperature phase within the low-temperature phase well below the temperature of the phase transition. In Chapter 10 I investigated the optical properties of perovskite powders using PL and reflectance measurements. I was interested in whether the optical properties of perovskite powders are different compared to the ones of thin films and single crystals. In this study, I could show that by changing the stoichiometry of the perovskite powders, the energy of the band gap can be changed in a targeted way, as it is also known for thin films. Furthermore, I was able to show for the first time that a passivation method that is established for thin films can also be applied to perovskite powders.

Chapter 11 is a perspective article in which I first summarized the most important optical properties of metal halide perovskites and how they are affected by structural changes. In this article, some of my findings from Chapters 8-10 are included. The article then discusses how this relationship between optical properties and structure has previously been used to study the film formation of perovskite thin films using optical *in situ* spectroscopy.

In Chapters 12-14, the knowledge generated in the previous chapters about the relationship between structural changes in perovskite and its optical properties is now used to better understand perovskite film formation under different processing methods using optical *in situ* spectroscopy.

To this end, Chapter 12 investigates the formation of MAPbI₃ thin films using the so-called two-step method. Using the model from Chapter 8, I was able to clearly identify the influence of self-absorption on the PL spectra. This allowed the identification of a dissolution-recrystallization process, which plays an important role for the film formation.

Chapter 13 deals with the film formation of MAPbI₃ using the so-called one-step method using spin coating, which is most commonly used in the laboratory, and industrially relevant slot-die coating. Using optical *in situ* spectroscopy, we were able to show that process-related differences in the structure of the solvent complex phase caused the perovskite growth during spin coating to differ both quantitatively and qualitatively from the perovskite crystallization that occurs during slot-die coating.

Finally, in Chapter 14, the formation of a perovskite with mixed halides is investigated using the solvent-engineering method, where the influence of the temperature of the antisolvent

on the perovskite formation and on finished perovskite solar cells is considered. I was able to show that for colder antisolvent, the perovskite formation is slower and the resulting perovskite layer is thinner. Further, my analyses revealed that during film formation the halide ratio in the perovskite changes continuously. In addition, it was shown that the films processed with colder antisolvent have a reduced density of defect states, which was attributed to enhanced strain-relaxation in the corresponding perovskite films.

Contents

Deutsche Zusammenfassung	v
English Abstract	ix
I Extended Abstract	1
1 Motivation	3
2 Brief History of Metal Halide Perovskites	7
3 Optical Properties of Lead Halide Perovskites	9
3.1 The Absorption of Lead Halide Perovskites	9
3.2 Photoluminescence of Lead Halide Perovskites	14
3.3 Influence of Stoichiometry	18
3.4 Comparison of the Optical Properties of Single Crystals and Thin Films	20
4 Perovskite Processing Methods	23
4.1 Solution processing methods	23
4.2 Mechanochemical Synthesis of Perovskite Powders	25
References	27
II Overview of the Thesis	47
5 Summary	49
6 Content of the Individual Publications	55
6.1 Double Peak Emission in Lead Halide Perovskites by Self-absorption	55
6.2 Investigating the Tetragonal-to-Orthorhombic Phase Transition of Methylammonium Lead Iodide Single Crystals by Detailed Photoluminescence Analysis	58
6.3 High Versatility and Stability of Mechanochemically Synthesized Halide Perovskite Powders for Optoelectronic Devices	60
6.4 Using <i>In Situ</i> Optical Spectroscopy to Elucidate Film Formation of Metal Halide Perovskites	62

6.5	Investigating two-step MAPbI ₃ Thin Film Formation during Spin Coating by Simultaneous <i>In Situ</i> Absorption and Photoluminescence Spectroscopy	63
6.6	Understanding Differences in Crystallization Kinetics Between Slot-Die Coating and Spin Coating of MAPbI ₃ Using Multimodal <i>In Situ</i> Optical Spectroscopy	65
6.7	How Antisolvent Miscibility Affects Perovskite Film Wrinkling and Photovoltaic Properties	70
6.8	Authors' Contribution	72
7	Conclusion and Outlook	77
III	Publications	79
8	Double Peak Emission in Lead Halide Perovskites by Self-absorption	81
9	Investigating the Tetragonal-to-Orthorhombic Phase Transition of Methylammonium Lead Iodide Single Crystals by Detailed Photoluminescence Analysis	103
10	High Versatility and Stability of Mechanochemically Synthesized Halide Perovskite Powders for Optoelectronic Devices	129
11	Using <i>In Situ</i> Optical Spectroscopy to Elucidate Film Formation of Metal Halide Perovskites	161
12	Investigating Two-Step MAPbI₃ Thin Film Formation During Spin Coating by Simultaneous <i>In Situ</i> Absorption and Photoluminescence Spectroscopy	179
13	Understanding Differences in the Crystallization Kinetics between Slot-die Coating and Spin Coating of MAPbI₃ Using Multimodal <i>In Situ</i> Optical Spectroscopy	207
14	How Antisolvent Miscibility Affects Perovskite Film Wrinkling and Photovoltaic Properties	243
15	Full list of Publications	281
	Appendix	287
	Acknowledgements	287
	Erklärung und eidesstattliche Versicherung	289

Part I

Extended Abstract

1 Motivation

In view of advancing global warming, the need for renewable energies is growing. In this context, solar cells have emerged as an important contributor to the world's electricity supply.^{1,2} By now, most of the solar cell panels consist of silicon as the active layer.^{1,3} With an energy pay-back time (EPBT) of about one year,^{1,3} and an energy return on energy invested (EROI) over 10,³ silicon based solar cells already perform acceptably well.

However, in order to further increase the attractiveness of solar cells, there is an ongoing urge for higher power conversion efficiencies (PCE) of such cells, e.g. in a tandem-cell configuration. In such a tandem-cell, two solar cells with different band gaps are stacked on each other, and thus the light in the blue and green spectral range can be used more effectively.^{4,5} For such a device to be attractive, the band gap of the additional active layer has to be tuned to an optimum, which in turn depends on the band gap of the first active layer (e.g. silicon).^{4,6} Additionally, the processing of the second layer should not introduce much additional energy and additional costs into the production process, in order to keep the device economically worthwhile.⁶

One class of material which fulfills these requirements (i.e., a tuneable band gap and energetically cheap processing) are metal halide perovskites (MHP). In tandem devices in combination with silicon, MHPs have recently boosted the PCE above 29 %.⁷ But also in single-junction solar cells, MHPs perform impressively well. Starting with a PCE of 3.8 % when first used in a solar cell in 2009,⁸ perovskite solar cells now reached a PCE of 25.5 % today, outperforming today's most widely used polycrystalline silicon solar cell technology.⁹ Moreover, perovskite solar cells can be made very thin and can be processed on flexible substrates, which extends the scope of application of such devices, e.g. towards flexible electronics or their usage in aerospace.^{10,11}

Apart from solar cells, MHPs have also demonstrated good performance in LEDs¹²⁻¹⁴ or X-ray detectors.¹⁵⁻¹⁷ Especially for the latter, the use of perovskites allowed to significantly improve device sensitivities compared to existing technologies,¹⁵⁻¹⁷ which in turn allows for lower doses in any X-ray based imaging.

A key to the fast development of perovskite-based devices, especially in the case of solar cells, was the awareness that the structure of the perovskite strongly influences its optoelectronic properties.¹⁸⁻²² Thus, the perovskite film quality and structure was steadily improved by optimizing the perovskite processing, which in turn improved the optoelectronic properties of

the perovskite layer.^{21,22} This optimization of the perovskite processing was often performed in an trial-and-error approach.²³ Such an approach is problematic, since the perovskite crystallization depends on many different parameters, e.g. the precise stoichiometry.²⁴ That implies that tedious optimization has to be performed for every material system. Additionally, the influence of some parameters, such as solvent quality or the temperature of the solvent, are often not considered in such optimization approaches, causing a significant variation of perovskite layer properties from lab to lab.²⁵

In order to move from such a labor-intensive trial-and-error optimization approach to a more systematic optimization of the film properties, it is essential to study and to better understand the perovskite film formation itself. Such an understanding would enable a targeted control of the crystallization of the perovskite and the associated film formation.

One suitable method for investigating the perovskite formation during processing, which recently became more popular in the field, is optical *in situ* spectroscopy.²⁶ This method benefits from the fact that the optoelectronic properties of the perovskite are strongly influenced by the structure of the perovskite.¹⁸⁻²² Accordingly, basis for a correct interpretation of the evolution of the optical properties during film formation is a detailed knowledge of the relationship between structural changes and the optical properties of lead halide perovskites. Despite the rapid development and intense research in the field of perovskite and perovskite solar cells, this relationship between the optoelectronic properties and the perovskite structure is not entirely clear. Even some of the basic optical properties of neat perovskite samples, such as the nature of the band gap or the origin of several photoluminescence (PL) peaks, are still under debate.²⁷⁻⁴⁰

From these considerations, it becomes obvious that it is highly desirable to better understand the relationship between structural changes and the optoelectronic properties of halide perovskites, and to elucidate the perovskite film formation based on this understanding. Both aspects are therefore focus of this thesis.

To contribute to understanding the relationship between the optoelectronic properties and structural changes in lead halide perovskites, I investigated the optical properties of lead halide perovskite single crystals with different experiments based on linear and non-linear PL spectroscopy, in combination with optical modeling. I focused on the origin of the additional PL peaks mentioned above. In order to associate the insights gained from these PL experiments with structural changes, I conducted temperature-dependent PL measurements on a methylammonium lead iodide ($\text{CH}_3\text{NH}_3\text{PbI}_3$ or MAPbI_3) single crystal. MAPbI_3 is the probably best investigated lead-based halide perovskite and it has been shown that its crystal structure changes with temperature.^{18,19,41-43} Further, I investigated the optical properties of mechanochemically synthesized perovskite powders to see if they show special optical properties compared to their single crystal and thin film counterparts. Based on the knowledge about the relationship between structural changes and the optoelectronic

properties of lead halide perovskites that I gained in the previous studies, I investigated the perovskite film formation using optical *in situ* spectroscopy. These studies consider different synthesis routes, compare different processing routes for different solvent evaporation rates systematically, and investigate the influence of the temperature of the antisolvent.

The thesis is structured in three parts. Part I gives an introduction to lead halide perovskites, in which Chapter 2 describes briefly the history of metal halide perovskites, while Chapter 3 describes the current state of the field concerning the optical properties of lead halide perovskites and their relationship to the perovskite structure. Chapter 4 then presents different perovskite processing methods. Part II gives a more detailed overview of the individual publications forming the thesis. Chapter 5 outlines the interconnection of my publications, and Chapter 6 summarizes the content of each publication, and contains a subchapter about the author contributions to each publication. Chapter 7 draws an overall conclusion of the thesis. The publications are then reprinted in Part III, which also contains a full list of my publications.

2

Brief History of Metal Halide Perovskites

The term perovskite generally refers to materials with a ABX_3 crystal structure, like it is shown in Figure 2.1. It is derived from the name of the Russian mineralogist Lev Perovski.⁴⁴ While there exist several types of materials with such a crystal structure,^{45–47} the term perovskite is often used synonymously to MHPs within the research field of MHPs, and likewise within this thesis, if not stated otherwise.

In the case of MHPs, the A-side is a cation (e.g. MA^+), the B-side is a metal (e.g. Pb^{2+}) and the X-side is a halide anion (e.g. I^-). If the A-cation is an organic molecule, the perovskite is said to be a hybrid organic-inorganic perovskite (HOIP). Such perovskites were first investigated in 1978^{49,50} and investigated in more detail in the following years.^{51–54} The first solar cell with a HOIP as active layer was reported in 2009.⁸ In the following year, the research field of MHPs increased remarkably, and solar cells now reach record power conversion efficiencies of more than 25%.⁹ In addition to solar cells, MHPs have also found application in other devices such as X-ray detectors^{15–17} and LEDs,^{12–14} showing promising performance.

One reason for this rapid development is the relatively easy synthesis and processing of MHPs, which does not require complex or expensive equipment.⁵⁵ This renders the study of MHPs available for a large number of research groups. Another reason is that the optical properties of MHPs can be tuned to match the desired application, as outlined in Chapter 3.3. These two facts made MHPs a very appealing research field for many groups with different backgrounds, and the research field and the number of related publications grew immensely in the last decade.⁵⁶

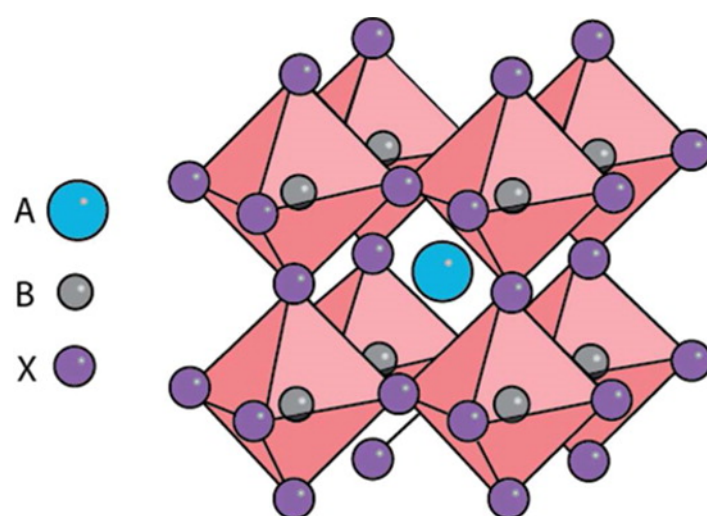


Figure 2.1: Perovskite crystal structure. In the case of MHPs, A is a cation, such as methyl ammonium, B is a metal, e.g. lead, and X is a halide, e.g. iodide. Reprinted with permission from Green et al. [48] Copyright 2015 American Chemical Society

3

Optical Properties of Lead Halide Perovskites

The basic optical properties of lead halide perovskites can be well described in the framework of solid state physics, and their characteristics are in many cases similar to such of conventional inorganic semiconductors such as gallium arsenide (GaAs).^{57,58} However, lead halide perovskites differ from conventional inorganic semiconductors insofar that they are soft ionic crystals,^{59–61} which incorporate the heavy lead atom. This leads to slight differences in the electrical and optical properties of lead halide perovskites compared to conventional inorganic semiconductors, of which some aspects remain unclear to date.⁶²

The optical properties and their relations to material properties which are relevant for this thesis are depicted in more detail in the following chapters.

3.1 The Absorption of Lead Halide Perovskites

The optical absorption of inorganic semiconductors, and likewise lead halide perovskites, is dominated by a band-to-band transition from the valence band maximum (VBM) to the conduction band minimum (CBM). If this transition is vertical, i.e. if VBM and CBM are at the same position in reciprocal space, the band gap is direct. In contrast, if they are at different positions, the band gap is indirect.⁶³ For an indirect band gap, the transition from VBM to CBM is assisted by phonons, which provide the necessary change in momentum of the excited charge carrier. Since this indirect transition is a two-particle process, the probability of this transition is lower than for a direct transition and additionally, it depends on the phonon population. Therefore, the associated absorption of the indirect transition is weaker and the absorption strength is temperature dependent.⁶³ It can be calculated that in the approximation of parabolic bands (near the extrema), the absorption coefficient is proportional to $\sqrt{E - E_g}$ for the direct band gap, and proportional to $(E - E_g \pm E_{ph})^2$ for the indirect band gap, with E_g being the energy of the band gap and E_{ph} the energy of phonons participating in the indirect transition.⁶⁴

In the case of lead halide perovskites, both conduction and valence band consist of orbitals of the lead and the halide, which thus define the width of the band gap.^{65–68} There has been an extensive discussion on whether the band gap of the most prominent halide perovskites

- MAPbI₃ and MAPbBr₃ - is direct or indirect.^{27–30,69} Some optical properties, especially long PL lifetimes and additional PL features, seemed to be in contrast to a direct band gap.^{27,28,70,71} The presence of an indirect band gap was additionally supported by theoretical prediction and experimental finding of strong spin orbit coupling and an associated Rashba effect, which leads to a splitting and shift of the conduction band in reciprocal space.^{72–74} Yet, other properties such as large absorption coefficients and sharp optical absorption edges are in contrast to an indirect band gap,^{75–78} and recent studies showed that both absorption and PL - including the long PL lifetimes - can be well explained assuming only a direct band gap.^{57,69,79}

One aspect that contributed to the uncertainty of the nature of the band gap was the use of Tauc plots for determining the band gap energy.^{80–84} In a Tauc plot, either the square of the measured absorption in the case of a direct band gap, or its root in case of an indirect band gap is plotted versus energy resulting in a straight line for the absorption near the band gap E_g . In an ideal case, a Tauc plot can therefore be used to distinguish between a direct and an indirect band gap. The band gap energy E_g can then be extracted by the crossing point of a straight line fitted to the absorption with the energy axis. However, this method fails as soon as there is some contribution of excitonic effects to the absorption spectrum^{48,57} (see below) and seemingly straight lines can be seen in both implementations of the Tauc plot (i.e., plotting the square or the square root of the absorption).^{83,84} In this case, the determination of the band gap using a Tauc plot becomes to a certain degree arbitrary.

As mentioned above, excitonic effects change the spectral shape of the absorption from the simple $\sqrt{E - E_g}$ or $(E - E_g \pm E_{ph})^2$ dependence. In general, an exciton is an excited electron bound to a hole via Coulomb interaction.⁸⁵ In inorganic semiconductors and MHPs, this is from a quantum-mechanical point of view similar to the hydrogen atom. Likewise, the Coulomb interaction results in a Rydberg series of bound states below the CBM, with the exciton binding energy E_B , and additional continuum states of unbound but correlated electron-hole pairs. These additional absorbing states superimpose with the pure band-to-band transition, as can be seen in Figure 3.1.⁸⁶ The resulting absorption spectrum can be described by Elliot's theory.⁸⁷ Since the exciton binding energy of MAPbI₃ is small compared to thermal energy at room temperature, the majority of excited charge carriers is expected to dissociate into free charges very quickly at ambient temperatures, in agreement with experimental results from, e.g., photocurrent spectroscopy and transient PL measurements.^{42,88–91} For the sake of completeness, it should be noted that the fraction of excitons over the total excitation density depends on the available thermal energy and the overall excitation density.^{42,92,93}

Another feature of the absorption of not only lead halide perovskites but a wide range of solid state materials is the presence of additional absorbing states below the band gap, so-called tail state absorption.^{94–96} If the spectral dependence of the absorption coefficient below the

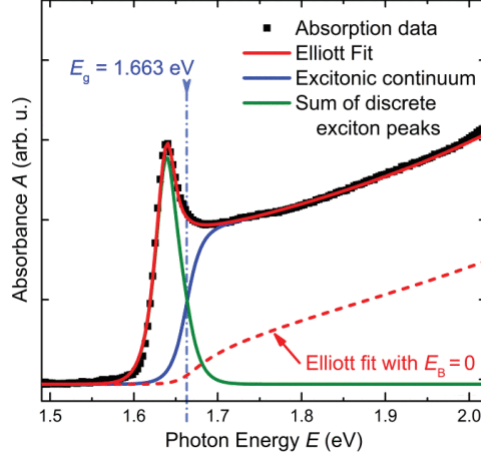


Figure 3.1: Decomposition of the absorption of a MAPbI₃ film at low temperatures into the contributions of the discrete exciton peaks (green), of the exciton continuum state (blue) and of the band-to-band absorption without excitonic effects (red dashed) according to Elliot's theory.⁸⁷ Reprinted with permission from Ruf et al. [86], Copyright 2018 IEEE.

band gap is of the form

$$\alpha(E) = \alpha_0 \exp\left(\frac{\sigma(E - E_0)}{k_B T}\right) = \alpha_0 \exp\left(\frac{E - E_0}{E_U}\right) \quad (3.1)$$

over a wide range of α -values, these tail states are called Urbach tail with the steepness parameter σ , the Boltzmann constant k_B , the absolute temperature T , the Urbach energy $E_u = \frac{\sigma}{k_B T}$, and α_0 and E_0 being constants.⁹⁷ This Urbach tail absorption is caused by electron-phonon or exciton-phonon interaction as well as thermal and structural disorder.^{94,96,98} Investigating the Urbach tail absorption of a sample and its temperature dependence thus reveals insights into the disorder and the electron-phonon interaction in the perovskite sample. While there exist different theories about the exact mechanism that lead to Urbach tail absorption,^{95,96,99–102} it is common to separate the Urbach energy into contributions from thermal disorder and static/structural disorder, i.e.

$$E_U(T, X) = K[\langle U^2 \rangle_T + \langle U^2 \rangle_X], \quad (3.2)$$

where K is a constant, $\langle U^2 \rangle_T$ is the contribution of thermal disorder to the average square displacement of the atom positions from their equilibrium position and $\langle U^2 \rangle_X$ represents the contribution of structural disorder to the average square displacement.^{99,103} For alloys, it was also found necessary to include a contribution due to compositional disorder, $\langle U^2 \rangle_C$.¹⁰⁴ Cody and coworkers introduced a widely used analytic expression for Equation 3.2 by approximating

the phonon spectrum by an Einstein oscillator model with temperature Θ , yielding

$$E_U(T, X) = \frac{\Theta}{\sigma_0} \left[\frac{1 + X}{2} + \frac{1}{\exp(\Theta/T) - 1} \right]. \quad (3.3)$$

Here, X is the mean square displacement of the atoms due to structural disorder, normalized to the zero-point uncertainty, i.e. $X = \frac{\langle U^2 \rangle_X}{\langle U^2 \rangle_0}$ and σ_0 is the so-called Urbach edge parameter.¹⁰³ Equation 3.3 was found to describe the temperature dependence of the Urbach energy of MAPbI₃ satisfactorily.¹⁰⁵

The fact that α_0 and E_0 in Equation 3.1 are temperature-independent constants has two consequences: the first is that the Urbach tails of a sample measured at different temperatures form a bundle, i.e. their interpolations intersect all in one point, that is at α_0 and E_0 , the so-called Urbach focus point. This is shown in Figure 3.2a for GaAs.¹⁰⁶ The second consequence is that if a Urbach focus point exists, the band gap energy and the steepness of the Urbach tail in one system depend on each other,¹⁰³ as illustrated for GaAs and indium phosphide (InP) in the inset of Figure 3.2b.¹⁰⁷

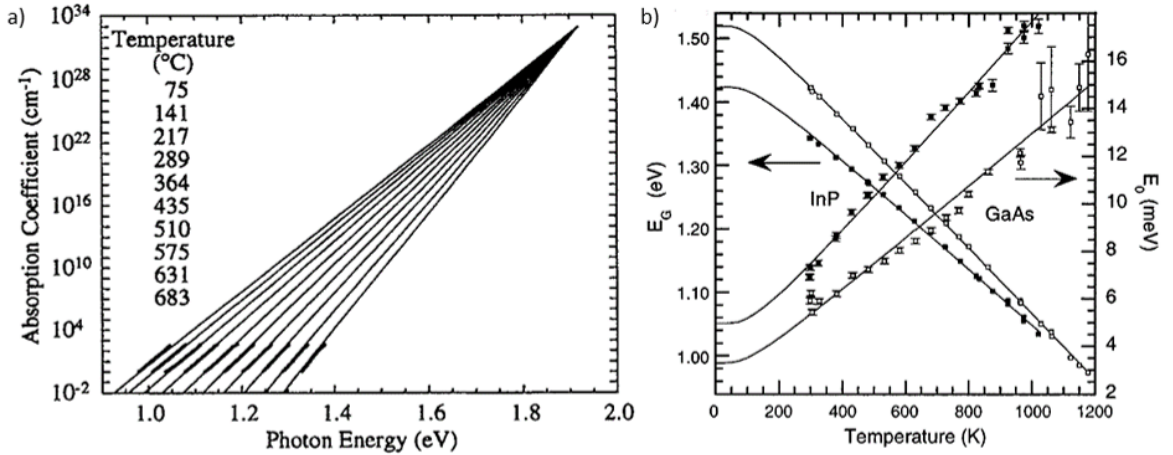


Figure 3.2: a) The logarithm of the absorption coefficient α (thick solid lines) for GaAs in the temperature range from 75 °C to 683 °C, together with exponential fits to the absorption (thin solid lines). Reprinted with permission from Johnson and Tiedje [106] with the permission of AIP Publishing. b) Optical band gap E_G and Urbach energy E_U , herein referred to as Urbach slope parameter E_0 , as a function of temperature for GaAs (solid symbols) and InP (open symbols). Solid lines represent fits obtained by the so-called Einstein model (see Equation 3.3 for the case of Urbach energies). Adapted with permission from Beaudoin et al. [107] with the permission of AIP Publishing.

After considering the basic features of light absorption in semiconductors, the following part describes the temperature-dependence of the absorption of the prototypical lead halide perovskite MAPbI₃. The temperature-dependent absorption of MAPbI₃ was already reported and described by several groups^{19,42,43} and shows the behavior depicted in Figure 3.3. Upon

cooling from 300 K to 150 K, where MAPbI₃ is in its tetragonal phase,⁵¹ the absorption onset shifts to lower energies and becomes steeper. Additionally, the peak at the absorption onset becomes more visible. Between 150 K and 120 K, the absorption around 1.6 eV decreases and a new peak around 1.7 eV appears. Upon further cooling to 5 K, this new peak shifts to lower energies and increases in intensity until around 40 K, and decreases slightly for lower temperatures.

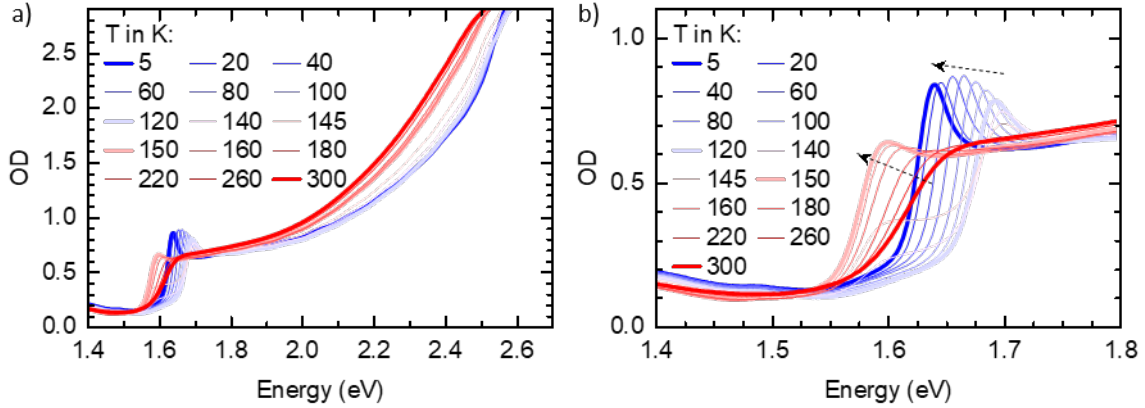


Figure 3.3: a) Absorption of a MAPbI₃ thin film in the temperature range from 300 K to 5 K. b) Spectral zoom on the region of the band edge absorption. Own unpublished data.

As mentioned above, the distinct peak at the absorption onset is associated with excitonic absorption.^{42,108} This peak becomes more distinct upon cooling, as the exciton binding energy increases.^{57,89} The changes in absorption between 150 K and 120 K are indicative for the structural phase transition from the tetragonal to the low temperature orthorhombic phase. In the case of thin films, both phases coexist in a certain temperature range.⁴²

The decrease of the band gap with decreasing temperature is special about lead halide perovskite, since most semiconductors show the opposite behavior.^{103,109–111} In general, the change of the band gap with temperature depends on the electron-phonon-coupling, which leads to an increase of the band gap with decreasing temperature, and on the lattice dilatation, which leads to a decrease of the band gap with decreasing temperature.^{18,103,109} As MAPbI₃ has a comparatively high thermal expansion coefficient, the lattice dilatation contributes dominantly to the temperature dependence of the band gap.¹⁸ In contrast, the electron-phonon-coupling dominates the temperature dependence of the band gap for most conventional inorganic semiconductors.¹⁰⁹ A direct consequence of the decreasing band gap with decreasing temperature and the presence of Urbach tail absorption is, that the Urbach focus point is at lower energies than the band gap,^{18,105} and accordingly a minimum band gap in the absence of any disorder can be estimated.

3.2 Photoluminescence of Lead Halide Perovskites

In general, there are different transitions that can lead to photoluminescence (PL) after photoexcitation. One of them is the recombination of free electrons in the conduction band with free holes in the valence band, which is also referred to as band-to-band recombination or bimolecular recombination.⁸⁵ Since this process depends on the excess concentration of free electrons n and holes p , e.g., induced by photoexcitation, the probability of recombination is proportional to the product of both concentrations. Assuming the concentration of excess electrons and holes to be equal, one can express the change in excess charge carrier density by bimolecular recombination as

$$\left(\frac{dn}{dt}\right)_{bi} = -k_2 n^2, \quad (3.4)$$

where k_2 is the rate constant for bimolecular recombination.^{85,112} This rate constant is an intrinsic material property and it is related to the absorption coefficient by the so-called van Roosbroeck-Shockley relation.¹¹³ This relation is based on the principle of detailed balance, which states that in thermal equilibrium, the rate of radiative recombination at a certain frequency is equal to the generation of electron-hole-pairs by thermal radiation at the same frequency. Also based on the principle of detailed balance, the spectral shape of the PL resulting from a band-to-band transition can be related to the absorption of a material as following:^{114,115}

$$PL(E) \propto \frac{A(E)E^2}{\exp[(E - \Delta\mu)/k_B T] - 1}, \quad (3.5)$$

where $A(E)$ is the absorptance of the sample, T is the absolute temperature, k_B is the Boltzmann constant and $\Delta\mu$ is the quasi-Fermi level splitting.^{116,117} $\Delta\mu$ denotes the splitting of the Fermi-levels of the electrons in the conduction band and of the electrons in the valence band when both populations are treated individually. Since $\Delta\mu$ is typically smaller than the photon energies of the PL, Equation 3.5 can be simplified to

$$PL(E) \propto A(E)E^2 \exp\left(\frac{E}{k_B T}\right) \exp\left(\frac{\Delta\mu}{k_B T}\right), \quad (3.6)$$

where $\Delta\mu$ only determines the intensity of the PL, but not the shape.¹¹⁷ Equation 3.6 implies that the shape of the absorption of a material, especially the sub band gap absorption, can be determined based on its PL spectrum^{105,116,117} and vice versa.

Another transition that can contribute to the PL spectrum is the luminescent recombination of excitons. As briefly described in Section 3.1, an exciton is an electron bound to a hole by Coulomb interaction. Based on the spatial extent of the exciton - or how strongly electron and hole are bound - excitons can be grouped into Frenkel-excitons (small spatial extent,

occur e.g. in organic semiconductors¹¹⁸) and Wannier-excitons (large spatial extent, occur in inorganic semiconductors and lead halide perovskites).^{85,119} Another necessary distinction is between free excitons (FE) and bound excitons (BE). The term free exciton refers to an electron-hole pair that can move freely through the material.⁸⁵ Free excitons can either recombine resonantly or under emission of phonons. While the PL features for the different free exciton recombinations show different lineshapes, they all have in common that their intensity scales linearly within a wide range of excitation densities, i.e., over a wide range of the charge carrier density.⁸⁵ A bound exciton is an exciton which is bound to a defect or impurity in the material. Because of the additional binding energy, its luminescence in general appears at lower energy compared to its free counterpart.⁸⁵ Bound excitons typically have a significantly higher oscillator strength than free excitons^{120,121,122} and due to the large spatial extend of free Wannier excitons, the excitons can be trapped efficiently to impurities or defects. Therefore, the PL of bound excitons is typically significantly stronger than the one of free excitons.⁸⁵

Aside from the band-to-band transition and from excitonic transitions, also defect-related emission can contribute to the PL of a semiconductor. Such defects are e.g. point defects such as impurity atoms, vacancy sites or interstitial sites. Commonly, The related PL spectra are significantly broader than the PL spectra of excitons, due to a stronger electron-phonon coupling at the defect sites.¹²³ The intensity of defect-related PL obviously depends on the concentration of available defects, and its contribution to the overall PL spectrum typically decreases with increasing excitation density.¹²⁴⁻¹²⁶ Additionally, the intensity of defect-related PL is strongly dependent on temperature, because its internal quantum efficiency decreases exponentially above a critical temperature T_0 and is fairly constant below.¹²³ This temperature-dependence can be e.g. explained either by the so-called Seitz-Mott mechanism,^{127,128} where defects change from a radiative to a non-radiative state by overcoming a potential barrier between ground and excited state, or by the Schön-Klasens mechanism,^{129,130} where different radiative and non-radiative recombinations compete.¹²³

The different dependency of the radiative and non-radiative recombination processes on the charge carrier density has some important implications, not only for the shape of the PL spectrum, but also for the transient PL and the PL quantum efficiency (PLQE). For example, if we consider the PL of MAPbI₃ around room temperature, which is due to bimolecular recombination, the decay of the charge carrier density in the neat material can be described by

$$\frac{dn}{dt} = -k_1n - k_2n^2 - k_3n^3, \quad (3.7)$$

where k_1 is the rate constant of defect-related Shockley-Read-Hall (SRH) recombination, which is non-radiative at room temperature, and k_3 is the rate constant of the non-radiative Auger-recombination.¹¹² While k_2 and k_3 are material-specific, k_1 depends on the defect

density and is thus a measure for the sample quality. For high charge carrier densities (i.e. in the case of transient PL shortly after sufficiently strong excitation), the decay of n is dominated by Auger- or bimolecular recombination and the corresponding PL decay is non-exponential. For lower charge carrier densities (long delay times), the decay is dominated by k_1 and the PL decay becomes approximately mono-exponential with the time constant $\tau \approx 1/(2k_1)$.^{117,131} The situation is similar for the PLQE. With the bimolecular recombination being the radiative transition, the PLQE η is given by

$$\eta = \frac{k_2 n}{k_1 + k_2 n + k_3 n^2}. \quad (3.8)$$

From Equation 3.8 it can be seen that for small n , η approaches zero. Likewise, for high n , η approaches zero as Auger-recombination, which is expressed in Equation 3.8 by the term $k_3 n^2$, becomes dominant. In between, η reaches a maximum value depending on the exact values of k_1 , k_2 and k_3 .¹³² From these considerations it becomes clear that the specification of a PLQE without an exact value of the charge carrier density can only be seen as a lower limit for the maximum PLQE. The exact charge carrier density is in turn hard to determine, since diffusion of charge carriers can be significant, as stated in Section 3.4. Additionally to charge carrier diffusion, effects such as photon recycling, which depend on light outcoupling and thus on surface roughness and used substrate, can alter the PLQE as well as the transient PL signal.^{117,133–137} Therefore, even when measured under similar experimental conditions, the comparison of the PLQY of different samples needs careful considerations.

For the sake of completeness it shall be noted that in Equation 3.7 the association of k_1 , k_2 and k_3 with SRH, bimolecular and Auger recombination, respectively, is only correct since for lead halide perovskites, $n = p$ is a valid approximation at typical excitation intensities. This does not hold true in the case of strongly doped semiconductors, where it becomes important to distinguish between low and high injection levels. Here, the approximation $n = p$ is valid at high injection levels.¹³¹

In the following, the temperature-dependent photoluminescence of MAPbI₃ is described. Figure 3.4 depicts examples for the temperature-dependent PL of a MAPbI₃ thin film (Figure 3.4a) and a MAPbI₃ single crystal (Figure 3.4b).^{88,124} At room temperature, the PL usually consists of one distinct peak around 1.6 eV (775 nm). This PL is associated with bimolecular band-to-band recombination of free carriers^{78,112,124,138,139} and can be well described within the framework of the van Roosbroeck-Shockley relation.⁵⁷ Upon cooling to the onset of the tetragonal to orthorhombic phase transition (around 160 K), the PL shifts to lower energies, in accordance with the spectral shift of the band-gap upon cooling (see Chapter 3.1). Additionally, the PL peak becomes narrower and more intense. The increasing intensity is also caused by an increase of the bimolecular recombination rate k_2

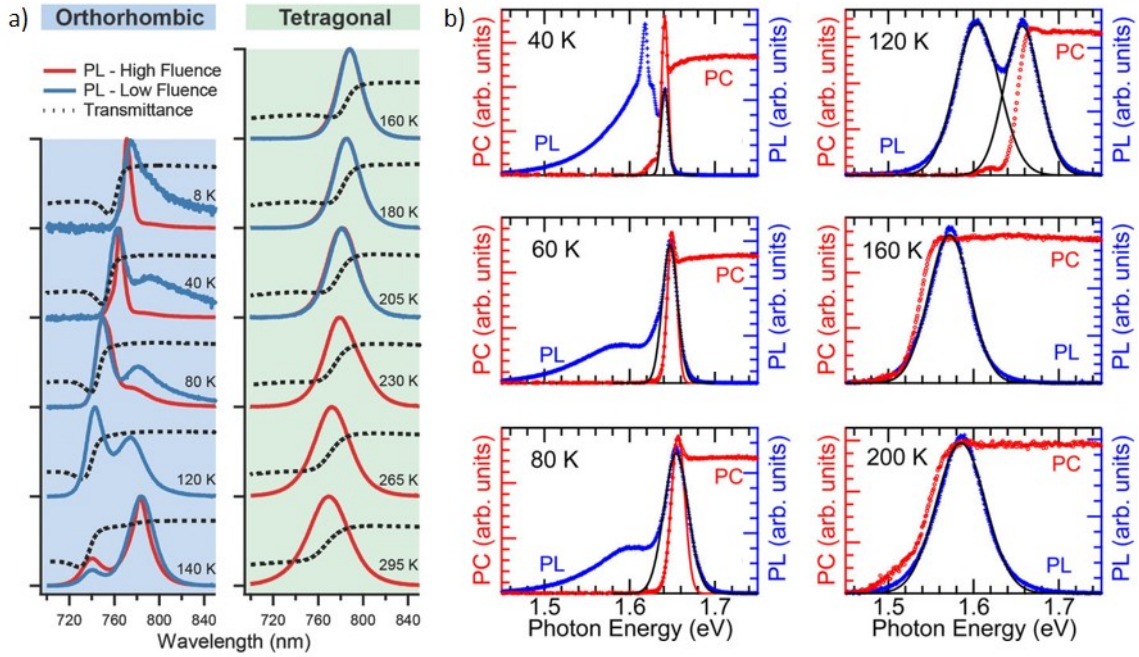


Figure 3.4: a) PL of a MAPbI₃ thin film between 295 K and 8 K at high (red line) and low fluence (blue line). Also shown is the transmittance (black dashed line) indicating the absorption onset. Adapted with permission from Milot et al. [124], Copyright 2015 The Authors. b) PL (blue line) and photocurrent (PC, red line) of a MAPbI₃ single crystal in the temperature range from 200 K to 40 K. Printed with permission from Phuong et al. [88], Copyright 2016 American Chemical Society.

with decreasing temperature.⁵⁷ Sometimes, an additional peak or shoulder at lower energies can be observed in the PL of the tetragonal phase, and at the beginning of this thesis, there was still no consensus of what causes its appearance.^{29,30,32,33,35,37–39,140} Therefore, Chapter 8 carefully addresses the origin of this additional peak.

Upon and below the phase transition, the PL spectrum heavily depends on the sample quality, e.g. defect density, and experimental conditions, such as laser fluence and associated charge carrier density (Figure 3.4a, left column), and reported spectra differ from group to group.^{88,124,141,142} During the phase transition, where tetragonal and orthorhombic phase can coexist, it is possible to observe two PL peaks (Figure 3.4b, 120 K). The one at higher energy is close to the band edge of the orthorhombic phase and is thus associated with PL from the orthorhombic phase. The one at lower energy lies close to the PL of the tetragonal phase. It is thus either attributed to PL from residual tetragonal phase or to defect related PL.^{88,125,143}

At lower temperatures and sufficient high fluences, a narrow peak in resonance with the excitonic absorption can be observed (Figure 3.4b, 40 K). This peak was identified as PL from free excitons.^{88,141} Additionally, there are two slightly broader peaks about 10-20 meV below the FE peak, which significantly gain intensity upon cooling. These peaks have been

attributed to PL from bound excitons.^{88,141} At even lower energies, i.e. below 1.6 eV, there is a broad PL feature which is associated with defect-related PL, e.g. PL from donor-acceptor pairs.^{141,143} Due to the limited number of available defect states, the intensity of this PL feature saturates with increasing excitation density (Figure 3.4a, 40 K).¹⁴³ As stated above, the relative intensity of the different spectral features, as well as how distinct they appear in the PL spectra, depends on the nature and quality of the sample and on the experimental conditions.^{88,124,141,142}

3.3 Influence of Stoichiometry

A very attractive property of halide perovskites is that their optoelectronic properties can be tuned by varying the constituents and by mixing e.g. different halogens with different stoichiometry.^{144–148} Especially the possibility to tune the band gap is beneficial for the use of halide perovskites in applications such as photo-detectors, lasers or solar cells.^{146,147,149–152} However, the choice of constituents is not arbitrary, but is constrained by their size. This is expressed by the so-called Goldschmidt rule, which states that

$$\alpha = \frac{r_A + r_X}{\sqrt{2}(r_B + r_X)}, \quad (3.9)$$

with r_i being the ionic radii for the A-, B- and X-side ions, respectively. α is the so-called Goldschmidt tolerance factor (also often labeled as t), which exhibits values between 0.8 and 1.0 for stable perovskite structures.⁴⁵ Additionally, the overall electric charge of the unit cell must be neutral. For lead-based perovskites, the commonly used constituents that fulfill both criteria are chloride (Cl^-), bromide (Br^-) and iodide (I^-) as X-side ions, and methylammonium ($[\text{CH}_3\text{NH}_3]^+$, MA), formamidinium ($[\text{NH}_2(\text{CH})\text{NH}_2]^+$, FA) and cesium (Cs^+) as A-side ions.¹⁵³

As stated in Chapter 3.1, the halide and the lead contribute most strongly to the conduction and valence band^{65–68} and are thus the obvious choice to change the electronic properties of the material. At room temperature, the band gap of MAPbI_3 is around 1.55 eV.^{145,154,155} Exchanging the iodide with bromide, the band gap increases significantly to about 2.35 eV.^{156–158} By substituting bromide with chloride, the band gap increases further to around 3.15 eV, i.e. into the ultraviolet spectral region.^{156,159,160} This increase of the band gap is associated with decreasing lattice constants upon exchanging iodide with bromide and bromide with chloride as halide anions.^{65,161} Remarkably, by using a mixture of iodide and bromide for the X-side ion, the band gap can be tuned nearly continuously from around 1.55 eV to around 2.30 eV,^{145,146,162} and from there onward to around 3.15 eV upon mixing bromide

and chloride.^{146–148,162} This is depicted in Figure 3.5 for $\text{MAPb}(\text{Br}_{1-x}\text{Cl}_x)_3$, i.e. a mixture of bromide and chloride as X-side ion. Note that the reported values of the band gap energies can vary several tens of meV from group to group, also depending on how the band gap is estimated.^{147,159} A problem of mixed-halide perovskites is that they tend to suffer from phase segregation under illumination.¹⁶³

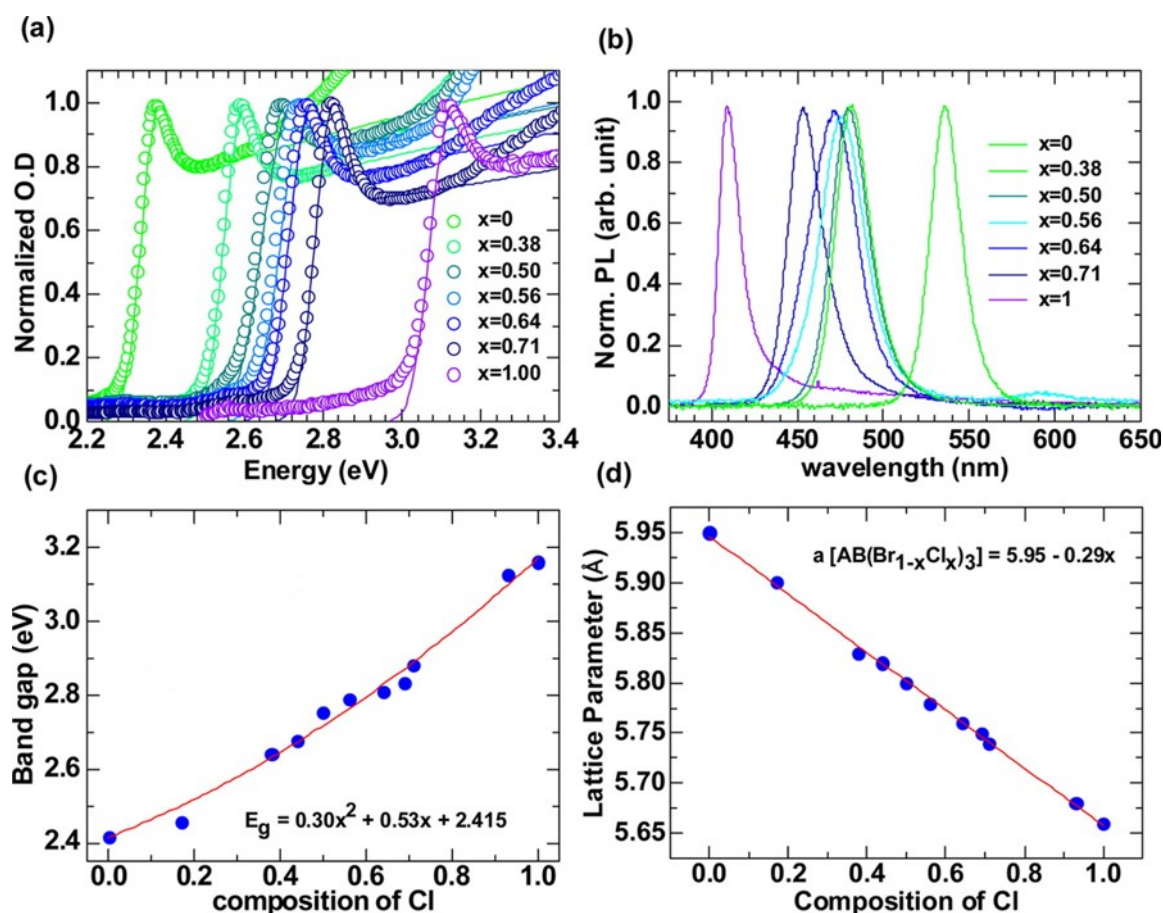


Figure 3.5: a) Absorption of $\text{MAPb}(\text{Br}_{1-x}\text{Cl}_x)_3$ thin films as a function of chlorine content x , normalized to the excitonic absorption peak. b) Normalized PL, c) band gap energy (determined applying Elliot's theory) and (d) lattice parameter of $\text{MAPb}(\text{Br}_{1-x}\text{Cl}_x)_3$ as a function of chlorine content. Adapted with permission from Kumawat et al. [147], Copyright 2015 American Chemical Society.

Despite not directly contributing to the valence and conduction band,^{65–68} the exchange of the A-side ion also impacts the optoelectronic properties of lead halide perovskites. This can be understood in terms of different tilting angles between the BX_6 octahedrons and resulting different bond lengths, depending on the choice of the A-side ion.^{161,164,165} E.g., replacing MA with FA in MAPbI_3 leads to a band gap narrowing to approximately 1.5 eV,¹⁴⁹ whereas the usage of Cs increases the band gap to more than 1.7 eV.¹⁴⁹ Besides the band gap tuning, the choice of the A-side ion can also effect the stability of the material, where mixtures of

FA, MA and Cs are particularly promising for e.g. stabilizing the perovskite structure at room temperature or for preventing halide segregation.^{151,166–169}

It becomes obvious that a huge variety of lead halide perovskites can be synthesized with different optical properties and stability. Out of this variety, mixed-cation mixed-halide perovskites have emerged as most successful material systems for highly efficient and stable perovskite solar cells.^{151,170,171}

Also lead-free halide perovskites for opto-electronic devices are a growing topic of research, where promising materials are e.g. tin-based perovskites.^{172–174} However, despite being favourable over lead-based perovskites because of the reduced toxicity, lead-free perovskites are up to today by far outplayed in terms of solar cell efficiency by their lead-containing counterparts,^{175–177} with a current record efficiency of tin based perovskite solar cells of 14.6 %.¹⁷⁸

3.4 Comparison of the Optical Properties of Single Crystals and Thin Films

Although consisting of the same material system, the reported optical properties of halide perovskites depend on the nature of the sample, i.e. if it is a polycrystalline thin film or if it is a single crystal. Many of these differences can be associated with the difference in crystallinity, sample structure and the influence of the substrate on which the thin films are processed onto.

The most obvious difference between single crystals and thin films is the defect density. Due to the slow and more controlled single crystal growth, the density of bulk defects is significantly lower for single crystals than for solution-processed thin films.^{146,179–181} Additionally, the interface-to-bulk ratio is much smaller for single crystals than for polycrystalline thin films. Since interfaces such as grain boundaries or the sample surface contribute strongly to the defect density,^{146,182} the defect density of single crystals is additionally lowered. This lower defect density is in turn reflected in longer excited state lifetimes and enhanced PLQEs, as becomes clear from Equations 3.7 and 3.8.

Another difference between singly crystals and thin films is the influence of the diffusion of charge carriers on the optical properties. The diffusion of charge carriers in single crystals was reported to be on the length scale of several μm ,^{179,183–185} i.e. significantly larger than the absorption length of above band gap excitation (around 100 nm). That implies that after (pulsed) excitation, a certain amount of charge carriers diffuses into the bulk, where they recombine. As the PL has to travel several μm through the material prior to detection, the high energy part of the PL is re-absorbed by the perovskite. Since the defect density in the

bulk is typically lower than in the near surface region, the lifetime of the charge carriers in the bulk is longer than near the surface, and a dynamic red-shift of the PL of some tens of meV on the time scale of hundreds of nanoseconds can be observed in transient PL measurements.⁷⁸ In thin films, this effect is nearly absent, since typical film-thicknesses are on the length scale of the excitation depth and the pathway that light has to travel through the material is significantly shorter.⁷⁸ As a consequence, also time-integrated PL measurements of single crystals can show a red-shifted PL compared to the PL of thin films.

One difference between single crystals and thin films that is frequently suggested is that single crystals seem to have a smaller band gap than their thin film counter parts.^{186–189} This statement is commonly based on transmission measurements of thick single crystals (in the range of mm). The resulting absorption spectrum then shows a transparent region without any detectable absorption at low photon energies, a steep rise of the absorption which then flattens out to a more or less constant absorption value. However, the latter typically reflects the sensitivity limit of the setup in use (i.e. the highest detectable optical density, limited e.g. by the dark current of the detector), and thus this region of the spectrum does not contain any meaningful information about the probed sample. The seemingly red-shifted band gap of the single crystal is then concluded either from a comparison of the normalized absorption spectrum with an absorption spectrum of a thin film,¹⁸⁹ or by use of a tauc plot.^{186–188} It should become clear from Section 3.1 that this conclusion is incorrect. Since the absorption spectrum of a single crystal by transmission can only probe very small values of the absorption coefficient due to the large thickness of the sample, the observed absorption onset is due to tail state absorption, i.e. due to Urbach tail absorption and it contains no information about the band gap. In contrast to the reports about red-shifted band gaps of single crystals based on transmission measurements mentioned above, ellipsometry measurements and the identical spectral position of the (self-absorption corrected) PL of single crystals and thin films suggest that the band gaps of single crystals and thin films are identical.^{158,190–193} However, it must be pointed out that one recent study by Schuster et al. suggests a slightly lower band gap in the bulk compared to the surface of a MAPbI₃ single crystal by comparing results of bulk-sensitive two photon induced photocurrent measurements and surface-sensitive transient magneto-optical Kerr effect measurements.¹⁴⁰

Finally, also structural phase transitions and their optical signatures are influenced by the nature of the sample, i.e. differ between thin films and single crystals. For example, for MAPbI₃ thin films, the tetragonal to orthorhombic phase transition takes place in a temperature window of several tens of Kelvin,^{19,42,125,143,194} whereas for powders, the transition was found to be significantly sharper^{194,195} and for single crystal, it was found to be quasi abrupt.^{196,197} The reason for this is that for polycrystalline samples such as thin films and powders, each crystal has its individual phase transition temperature, which is influenced by factors such as the defect density¹⁹⁸ or stress, e.g. induced by the substrate in

case of a thin film.¹⁹⁴ A further consequence of the influence of strain and defect density on the phase transition is that also the main part of the phase transition of a sample can take place at different temperatures depending on the nature of the sample. For example, the critical temperature of the tetragonal to orthorhombic phase transition of MAPbI₃ thin films can be below 140 K,^{199,200} whereas for single crystals it was determined to be at 163 K.^{51,201}

4 Perovskite Processing Methods

Driven by the goal of achieving ever better device efficiencies, many different perovskite processing methods have been investigated and optimized.^{55,202} The most relevant methods today include solution-based thin film processing methods such as spin-coating or printing,^{202–206} thermal evaporation,^{207–210} and perovskite powder synthesis.^{211–213} While spin-coating or thermal evaporation are particularly suitable for achieving high quality thin films, e.g. for solar cells,^{203,206,210} the processing of perovskite powders are interesting for devices where thick active layers are needed, such as X-ray detectors.^{15–17}

A key-role for the optimization of the different processing methods is the optical characterization of the perovskite, either *in situ* during the processing or *ex situ* after the processing. The following two sections discuss shortly the processing methods that were investigated in the framework of this thesis, namely solution-based processing of thin films and ball milling as a synthesis route for perovskite powders.

4.1 Solution processing methods

For the solution processing methods, the final film quality depends on many parameters, such as environmental conditions, processing temperature and the precursor solution.^{214–219} The optimization of processing has lead to a variety of perovskite processing protocols, in part due to slightly differing environmental conditions from lab to lab. While these processing protocols differ in detail, they can be classified into three types of methods, that are the two-step method, the one-step method, and the so-called solvent engineering method. These three methods are illustrated in Figure 4.1.⁵⁵

In the two-step method (Figure 4.1, middle), the precursor salts (e.g. MAI and PbI_2 in case of a MAPbI_3 synthesis) are deposited in two separate processing steps.^{204,218} Typically, in the first step, the lead salt (BX_2 , e.g. PbI_2) is applied onto a substrate, e.g. by spin-coating. Depending on the desired solar cell architecture, this can be done onto a flat substrate or on a mesoporous layer.^{204,220} In the second step, the AX salt (e.g. MAI) is brought onto the sample. This can be done either by dripping a MAI solution onto the sample or by dipping the sample into a MAI solution.^{204,205,218,220} While a significant amount of the lead salt can already be converted to the final perovskite during this second step, the sample is annealed afterwards in order to ensure full synthesis.^{204,220} The time at which the second step, i.e. the

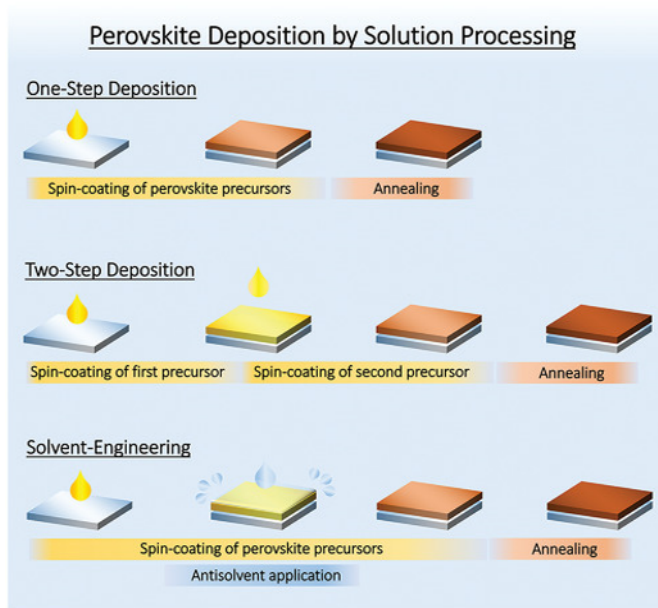


Figure 4.1: Schematic illustration of the different solution processing methods for lead halide perovskite thin films: the one-step method (top), the two-step method (middle), and the solvent engineering method (bottom). Adapted with permission from Vaynzof [55], Copyright 2020 The Authors.

AX solution, is applied and the duration of MAI exposure of the sample are important for a good film quality.^{204,218–220} For example, Barrit et al. showed that PbI_2 forms three different solvate phases prior to forming a dry film.²²⁰ They investigated the influence of the state of the PbI_2 film at the time of the addition of MAI on the perovskite formation and on resulting device efficiencies. In their work, solar cells where MAI was applied during the latest solvate phase but prior to the final PbI_2 film showed the highest power conversion efficiencies.²²⁰ In addition, the final film quality also depends on how MAI is applied onto the PbI_2 precursor film, i.e. whether the PbI_2 sample is dipped into the MAI solution or the MAI solution is applied onto the sample by spin coating.²²¹

A major conceptual drawback of the two-step method is that it is not possible to produce perovskites with mixed stoichiometry, e.g. mixed halide or mixed cation perovskites.⁵⁵ However, this is well possible with the one-step and the solvent engineering method,^{55,206,222} where the latter is a further development of the one-step method. In the one-step method (Figure 4.1, top), a single solution containing all precursors in the desired stoichiometry is brought onto a substrate in one step, e.g. by spin-coating.^{223,224} Without further treatment, the precursors often form a crystalline solvent complex phase, which can show poor substrate coverage.^{225,226} This structure is then also preserved in the perovskite phase, which forms from the solvent complex phase upon annealing.^{225,227} To overcome this problem, many different attempts were investigated to optimize the crystallization behavior and final film

morphology, such as the use of different lead salts,¹⁴⁴ different solvent mixtures²²⁸ or the use of additives.²²⁹ Depending on the details of the processing route, an annealing step can be necessary to induce or complete the perovskite formation, where again annealing time and temperature influence the final perovskite film quality.²¹⁴

An important modification of the one-step method is the so-called solvent engineering method (Figure 4.1, bottom).^{55,206} Here, similar to the one-step method, the precursors are brought onto the substrate in one single solution upon spin coating. After a certain time, a solidification process is induced by the addition of an antisolvent, i.e., a solvent in which the precursors are not soluble.^{55,206} Likewise to the other methods, the majority of the perovskite formation takes place upon a subsequent thermal annealing step. For the solvent engineering method, the time of antisolvent dripping plays a crucial role for the quality of the final perovskite film, where late as well as too early dripping times were found to lead to poorer film quality.²³⁰ The optimum dripping time as well as the choice of a suitable antisolvent depends on the perovskite stoichiometry and the solvents in use.^{219,231} Up to date, the solvent engineering method is the most commonly used solution processing method for halide perovskite thin films on a lab scale, as with this methods, the highest solar cell efficiencies can be achieved.^{55,170,232} The solution processing methods described above are insofar appealing as they do not require complex and expensive equipment, and are thus easily accessible for many groups. A drawback that is common for all three methods is that the perovskite formation is inevitably linked to the film formation, i.e. it is not possible to optimize the perovskite formation and the film structure separately.

4.2 Mechanochemical Synthesis of Perovskite Powders

An alternative processing approach is the synthesis of perovskite powder, which decouples the perovskite formation and the perovskite layer formation. There exist several different methods for the synthesis of perovskite powders, including mechanochemical synthesis,^{212,213} thermal annealing,^{233,234} precipitation reactions^{235,236} and ultrasonic synthesis.^{237,238} The following paragraph introduces one implementation of the mechanochemical synthesis, that is perovskite powder synthesis by ball milling, which is also subject of Chapter 10.

Figure 4.2 shows an illustration of the ball milling process. For this process, the precursor powders (e.g. MAI and PbI_2) in the desired stoichiometry are placed in a milling jar, together with milling balls (see Figure 4.2a). This milling jar is then closed and put into the milling machine (e.g., a planetary ball mill). In a planetary ball mill, the jar is mounted on a rotating disc and additionally, the jar rotates around its own axis. By these movements, the milling balls and the precursor powders toss against each other, which delivers enough energy for the conversion of the precursor powders to the perovskite phase (indicated in Figure 4.2b).

The synthesis of perovskite powders and their processing have gained more attention in

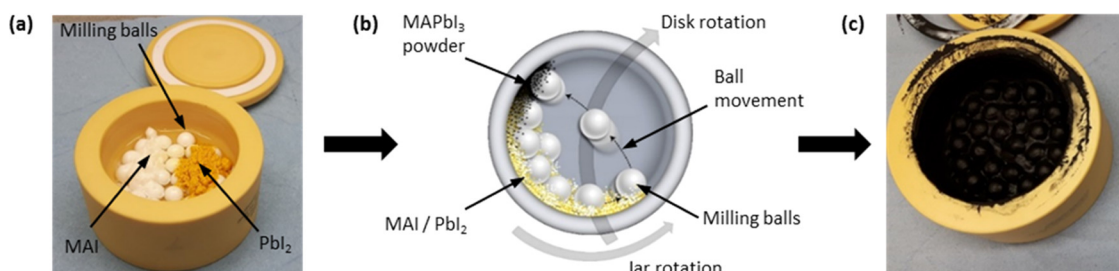


Figure 4.2: Illustration of the ball milling process using a planetary ball mill. (a) The precursor powders (MAI, white, and PbI_2 , yellowish) together with the milling balls in a milling jar. (b) Sketch of the milling process. The thick grey arrows indicate the movement of the milling jar. (c) Milling jar with perovskite powder after the milling process. Reproduced from Chapter 10.

the last few years, due to several advantages over solution processing of perovskites.^{239,240} For example, by the mechanochemical synthesis, limitations in perovskite stoichiometry due to limited solubility of the precursors can be overcome.²⁴⁰ Additionally, large amounts of perovskite in the range of kilograms can be synthesized within several hours, depending on the size of the planetary mill.²⁴¹

References

- [1] Fraunhofer ISE. *Recent Facts about Photovoltaics in Germany; version of November 25, 2020*. last accessed: 18.12.2020.
- [2] D. Jones, E. Graham, and P. Tunbridge (2020). *Global Half-Year Electricity Analysis*. last accessed: 18.12.2020.
- [3] K. P. Bhandari, J. M. Collier, R. J. Ellingson, and D. S. Apul (2015). Energy payback time (EPBT) and energy return on energy invested (EROI) of solar photovoltaic systems: A systematic review and meta-analysis. *Renewable and Sustainable Energy Reviews* **47**, 133–141.
- [4] H. Li and W. Zhang (2020). Perovskite Tandem Solar Cells: From Fundamentals to Commercial Deployment. *Chemical Reviews* **120** (18), 9835–9950.
- [5] N. N. Lal, Y. Dkhissi, W. Li, Q. Hou, Y.-B. Cheng, and U. Bach (2017). Perovskite Tandem Solar Cells. *Advanced Energy Materials* **7** (18), 1602761.
- [6] C. D. Bailie and M. D. McGehee (2015). High-efficiency tandem perovskite solar cells. *MRS Bulletin* **40** (8), 681–686.
- [7] A. Al-Ashouri, E. Köhnen, B. Li, A. Magomedov, H. Hempel, P. Caprioglio, J. A. Márquez, A. B. Morales Vilches, E. Kasparavicius, J. A. Smith, N. Phung, D. Menzel, M. Grischek, L. Kegelmann, D. Skroblin, C. Gollwitzer, T. Malinauskas, M. Jošt, G. Matič, B. Rech, R. Schlatmann, M. Topič, L. Korte, A. Abate, B. Stannowski, D. Neher, M. Stollerfoht, T. Unold, V. Getautis, and S. Albrecht (2020). Monolithic perovskite/silicon tandem solar cell with 29% efficiency by enhanced hole extraction. *Science* **370** (6522), 1300–1309.
- [8] A. Kojima, K. Teshima, Y. Shirai, and T. Miyasaka (2009). Organometal Halide Perovskites as Visible-Light Sensitizers for Photovoltaic Cells. *Journal of the American Chemical Society* **131** (17), 6050–6051.
- [9] National Renewable Energy Laboratory (NREL). *Best Research-Cell Efficiency Chart*. last accessed: 18.12.2020.
- [10] S. Kang, J. Jeong, S. Cho, Y. J. Yoon, S. Park, S. Lim, J. Y. Kim, and H. Ko (2019). Ultrathin, lightweight and flexible perovskite solar cells with an excellent power-per-weight performance. *Journal of Materials Chemistry A* **7**, 1107–1114.
- [11] M. Kaltenbrunner, G. Adam, E. D. Głowacki, M. Drack, R. Schwödiauer, L. Leonat, D. H. Apaydin, H. Groiss, M. C. Scharber, M. S. White, N. S. Sariciftci, and S. Bauer (2015). Flexible high power-per-weight perovskite solar cells with chromium oxide–metal contacts for improved stability in air. *Nature Materials* **14** (10), 1032–1039.

- [12] S. Adjokatse, H.-H. Fang, and M. A. Loi (2017). Broadly tunable metal halide perovskites for solid-state light-emission applications. *Materials Today* **20** (8), 413–424.
- [13] N. K. Kumawat, X.-K. Liu, D. Kabra, and F. Gao (2019). Blue perovskite light-emitting diodes: progress, challenges and future directions. *Nanoscale* **11**, 2109–2120.
- [14] P. Du, L. Gao, and J. Tang (2020). Focus on performance of perovskite light-emitting diodes. *Frontiers of Optoelectronics* **13**, 235–245.
- [15] L. Gao and Q. Yan (2020). Recent Advances in Lead Halide Perovskites for Radiation Detectors. *Solar RRL* **4** (2), 1900210.
- [16] H. Wei and J. Huang (2019). Halide lead perovskites for ionizing radiation detection. *Nature Communications* **10**, 1066.
- [17] M. Sytnyk, S. Deumel, S. F. Tedde, G. J. Matt, and W. Heiss (2019). A perspective on the bright future of metal halide perovskites for X-ray detection. *Applied Physics Letters* **115** (19), 190501.
- [18] S. Singh, C. Li, F. Panzer, K. L. Narasimhan, A. Graeser, T. P. Gujar, A. Köhler, M. Thelakkat, S. Huettner, and D. Kabra (2016). Effect of Thermal and Structural Disorder on the Electronic Structure of Hybrid Perovskite Semiconductor $\text{CH}_3\text{NH}_3\text{PbI}_3$. *The Journal of Physical Chemistry Letters* **7** (15), 3014–3021.
- [19] F. Panzer, C. Li, T. Meier, A. Köhler, and S. Huettner (2017). Impact of Structural Dynamics on the Optical Properties of Methylammonium Lead Iodide Perovskites. *Advanced Energy Materials* **7** (16), 1700286.
- [20] A. Merdasa, A. Kiligaridis, C. Rehermann, M. Abdi-Jalebi, J. Stöber, B. Louis, M. Gerhard, S. D. Stranks, E. L. Unger, and I. G. Scheblykin (2019). Impact of Excess Lead Iodide on the Recombination Kinetics in Metal Halide Perovskites. *ACS Energy Letters* **4** (6), 1370–1378.
- [21] T. Salim, S. Sun, Y. Abe, A. Krishna, A. C. Grimsdale, and Y. M. Lam (2015). Perovskite-based solar cells: impact of morphology and device architecture on device performance. *Journal of Materials Chemistry A* **3**, 8943–8969.
- [22] N. K. Tailor, M. Abdi-Jalebi, V. Gupta, H. Hu, M. I. Dar, G. Li, and S. Satapathi (2020). Recent progress in morphology optimization in perovskite solar cell. *Journal of Materials Chemistry A* **8**, 21356–21386.
- [23] J. Li, B. Pradhan, S. Gaur, and J. Thomas (2019). Predictions and Strategies Learned from Machine Learning to Develop High-Performing Perovskite Solar Cells. *Advanced Energy Materials* **9** (46), 1901891.
- [24] C. Rehermann, A. Merdasa, K. Suchan, V. Schröder, F. Mathies, and E. L. Unger (2020). Origin of Ionic Inhomogeneity in $\text{MAPb}(\text{I}_x\text{Br}_{1-x})_3$ Perovskite Thin Films Revealed by In-Situ Spectroscopy during Spin Coating and Annealing. *ACS Applied Materials & Interfaces* **12** (27), 30343–30352.
- [25] M. Saliba, J.-P. Correa-Baena, C. M. Wolff, M. Stollerfoht, N. Phung, S. Albrecht, D. Neher, and A. Abate (2018). How to Make over 20% Efficient Perovskite Solar Cells in Regular (n-i-p) and Inverted (p-i-n) Architectures. *Chemistry of Materials* **30** (13), 4193–4201.

- [26] F. Babbe and C. M. Sutter-Fella (2020). Optical Absorption-Based In Situ Characterization of Halide Perovskites. *Advanced Energy Materials* **10** (26), 1903587.
- [27] E. M. Hutter, M. C. Gelvez-Rueda, A. Osherov, V. Bulovic, F. C. Grozema, S. D. Stranks, and T. J. Savenije (2017). Direct-indirect character of the bandgap in methylammonium lead iodide perovskite. *Nature Materials* **16** (1), 115–120.
- [28] T. Wang, B. Daiber, J. M. Frost, S. A. Mann, E. C. Garnett, A. Walsh, and B. Ehrler (2017). Indirect to direct bandgap transition in methylammonium lead halide perovskite. *Energy & Environmental Science* **10**, 509–515.
- [29] B. Wu, H. Yuan, Q. Xu, J. A. Steele, D. Giovanni, P. Puech, J. Fu, Y. F. Ng, N. F. Jamaludin, A. Solanki, S. Mhaisalkar, N. Mathews, M. B. Roeffaers, M. Grätzel, J. Hofkens, and T. C. Sum (2019). Indirect tail states formation by thermal-induced polar fluctuations in halide perovskites. *Nature Communications* **10**, 484.
- [30] J. A. Steele, P. Puech, B. Monserrat, R. X. Y. Bo Wu, T. Kirchartz, H. Yuan, G. Fleury, D. Giovanni, E. Fron, M. Keshavarz, E. D. G. Zhou, T. C. Sum, A. Walsh, J. Hofkens, and M. B. J. Roeffaers (2019). Role of Electron–Phonon Coupling in the Thermal Evolution of Bulk Rashba-Like Spin-Split Lead Halide Perovskites Exhibiting Dual-Band Photoluminescence. *ACS Energy Letters* **4**, 2205–2212.
- [31] J. Fu, N. F. Jamaludin, B. Wu, M. Li, A. Solanki, Y. F. Ng, S. Mhaisalkar, C. H. A. Huan, and T. C. Sum (2019). Localized Traps Limited Recombination in Lead Bromide Perovskites. *Advanced Energy Materials* **9** (12), 1803119.
- [32] X. Chi, K. Leng, B. Wu, D. Shi, Y. Choy, Z. Chen, Z. Chen, X. Yu, P. Yang, Q.-H. Xu, T. C. Sum, A. Ruydy, and K. P. Loh (2018). Elucidating Surface and Bulk Emission in 3D Hybrid Organic–Inorganic Lead Bromide Perovskites. *Advanced Optical Materials* **6** (15), 1800470.
- [33] J. Shi, H. Zhang, Y. Li, J. J. Jasieniak, Y. Li, H. Wu, Y. Luo, D. Li, and Q. Meng (2018). Identification of high-temperature exciton states and their phase-dependent trapping behaviour in lead halide perovskites. *Energy & Environmental Science* **11**, 1460–1469.
- [34] D. Niesner, O. Schuster, M. Wilhelm, I. Levchuk, A. Osvet, S. Shrestha, M. Batentschuk, C. Brabec, and T. Fauster (2017). Temperature-dependent optical spectra of single-crystal $(\text{CH}_3\text{NH}_3)\text{PbBr}_3$ cleaved in ultrahigh vacuum. *Physical Review B* **95**, 075207.
- [35] B. Murali, E. Yengel, C. Yang, W. Peng, E. Alarousu, O. M. Bakr, and O. F. Mohammed (2017). The Surface of Hybrid Perovskite Crystals: A Boon or Bane. *ACS Energy Letters* **2** (4), 846–856.
- [36] S. T. Birkhold, E. Zimmermann, T. Kollek, D. Wurmbrand, S. Polarz, and L. Schmidt-Mende (2017). Impact of Crystal Surface on Photoexcited States in Organic–Inorganic Perovskites. *Advanced Functional Materials* **27** (6), 1604995.
- [37] F. Chen, C. Zhu, C. Xu, P. Fan, F. Qin, A. Gowri Manohari, J. Lu, Z. Shi, Q. Xu, and A. Pan (2017). Crystal structure and electron transition underlying photoluminescence of methylammonium lead bromide perovskites. *Journal of Materials Chemistry C* **5**, 7739–7745.

- [38] L. M. Pazos-Outón, M. Szumilo, R. Lamboll, J. M. Richter, M. Crespo-Quesada, M. Abdi-Jalebi, H. J. Beeson, M. Vrućinić, M. Alsari, H. J. Snaith, B. Ehrler, R. H. Friend, and F. Deschler (2016). Photon recycling in lead iodide perovskite solar cells. *Science* **351** (6280), 1430–1433.
- [39] Y. Fang, H. Wei, Q. Dong, and J. Huang (2017). Quantification of re-absorption and re-emission processes to determine photon recycling efficiency in perovskite single crystals. *Nature Communications* **8**, 14417.
- [40] Y. Yamada, T. Yamada, L. Q. Phuong, N. Maruyama, H. Nishimura, A. Wakamiya, Y. Murata, and Y. Kanemitsu (2015). Dynamic Optical Properties of $\text{CH}_3\text{NH}_3\text{PbI}_3$ Single Crystals As Revealed by One- and Two-Photon Excited Photoluminescence Measurements. *Journal of the American Chemical Society* **137** (33), 10456–10459.
- [41] T. Baikie, Y. Fang, J. M. Kadro, M. Schreyer, F. Wei, S. G. Mhaisalkar, M. Graetzel, and T. J. White (2013). Synthesis and crystal chemistry of the hybrid perovskite $(\text{CH}_3\text{NH}_3)\text{PbI}_3$ for solid-state sensitised solar cell applications. *Journal of Materials Chemistry A* **1**, 5628–5641.
- [42] V. D’Innocenzo, G. Grancini, M. J. P. Alcocer, A. R. S. Kandada, S. D. Stranks, M. M. Lee, G. Lanzani, H. J. Snaith, and A. Petrozza (2014). Excitons versus free charges in organo-lead tri-halide perovskites. *Nature Communications* **5**, 3586.
- [43] A. M. Soufiani, F. Huang, P. Reece, R. Sheng, A. Ho-Baillie, and M. A. Green (2015). Polaronic exciton binding energy in iodide and bromide organic-inorganic lead halide perovskites. *Applied Physics Letters* **107** (23), 231902.
- [44] G. Rose (1840). Über einige neue Mineralien des Urals. *Journal für Praktische Chemie* **19** (1), 459–468.
- [45] V. Goldschmidt (1926). Die Gesetze der Krystallochemie. *Naturwissenschaften* **4**, 477–485.
- [46] A. M. Glazer (1972). The classification of tilted octahedra in perovskites. *Acta Crystallographica Section B* **28** (11), 3384–3392.
- [47] M. A. Peña and J. L. G. Fierro (2001). Chemical Structures and Performance of Perovskite Oxides. *Chemical Reviews* **101** (7), 1981–2018.
- [48] M. A. Green, Y. Jiang, A. M. Soufiani, and A. Ho-Baillie (2015). Optical Properties of Photovoltaic Organic–Inorganic Lead Halide Perovskites. *The Journal of Physical Chemistry Letters* **6** (23), 4774–4785.
- [49] D. Weber (1978). $\text{CH}_3\text{NH}_3\text{SnBr}_x\text{I}_{3-x}$ ($x = 0-3$), ein Sn(II)-System mit kubischer Perowskitstruktur. *Zeitschrift für Naturforschung B* **33** (8), 862–865.
- [50] D. Weber (1978). $\text{CH}_3\text{NH}_3\text{PbX}_3$, ein Pb(II)-System mit kubischer Perowskitstruktur. *Zeitschrift für Naturforschung B* **33** (12), 1443–1445.
- [51] A. Poglitsch and D. Weber (1987). Dynamic disorder in methylammoniumtrihalogenoplumbates (II) observed by millimeter-wave spectroscopy. *The Journal of Chemical Physics* **87** (11), 6373–6378.
- [52] D. B. Mitzi, C. A. Feild, W. T. A. Harrison, and A. M. Guloa (1994). Conducting tin halides with a layered organic-based perovskite structure. *Nature* **369**, 467–469.

-
- [53] D. B. Mitzi, C. A. Feild, R. Schlesinger, and R. B. Laibowitz (1995). Transport, Optical, and Magnetic Properties of the Conducting Halide Perovskite $\text{CH}_3\text{NH}_3\text{SnI}_3$. *Journal of Solid State Chemistry* **114** (1), 159–163.
- [54] C. R. Kagan, D. B. Mitzi, and C. D. Dimitrakopoulos (1999). Organic-Inorganic Hybrid Materials as Semiconducting Channels in Thin-Film Field-Effect Transistors. *Science* **286** (5441), 945–947.
- [55] Y. Vaynzof (2020). The Future of Perovskite Photovoltaics—Thermal Evaporation or Solution Processing? *Advanced Energy Materials* **10** (48), 2003073.
- [56] A. S. Shikoh and A. Polyakov (2020). A Quantitative Analysis of the Research Trends in Perovskite Solar Cells in 2009–2019. *Physica Status Solidi A* **217** (23), 2000441.
- [57] C. L. Davies, M. R. Filip, J. B. Patel, T. W. Crothers, C. Verdi, A. D. Wright, R. L. Milot, F. Giustino, M. B. Johnston, and L. M. Herz (2018). Bimolecular recombination in methylammoniumlead triiodide perovskite is an inverse absorption process. *Nature Communications* **9**, 293.
- [58] L. M. Herz (2017). Charge-Carrier Mobilities in Metal Halide Perovskites: Fundamental Mechanisms and Limits. *ACS Energy Letters* **2** (7), 1539–1548.
- [59] H. Beck, C. Gehrman, and D. A. Egger (2019). Structure and binding in halide perovskites: Analysis of static and dynamic effects from dispersion-corrected density functional theory. *APL Materials* **7** (2), 021108.
- [60] Y. Rakita, S. R. Cohen, N. K. Kedem, G. Hodes, and D. Cahen (2015). Mechanical properties of APbX_3 ($A = \text{Cs}$ or CH_3NH_3 ; $X = \text{I}$ or Br) perovskite single crystals. *MRS Communications* **5** (4), 623–629.
- [61] A. Jaffe, Y. Lin, C. M. Beavers, J. Voss, W. L. Mao, and H. I. Karunadasa (2016). High-Pressure Single-Crystal Structures of 3D Lead-Halide Hybrid Perovskites and Pressure Effects on their Electronic and Optical Properties. *ACS Central Science* **2** (4), 201–209.
- [62] D. A. Egger, A. Bera, D. Cahen, G. Hodes, T. Kirchartz, L. Kronik, R. Lovrincic, A. M. Rappe, D. R. Reichman, and O. Yaffe (2018). What Remains Unexplained about the Properties of Halide Perovskites? *Advanced Materials* **30** (20), 1800691.
- [63] R. Gross and A. Marx (2012). *Festkörperphysik*. 1st ed. Chapter 10. München: Oldenbourg Verlag, 493.
- [64] J. I. Pankove (1975). *Optical Processes in Semiconductors*. Chapter 3. Dover Publications Inc.
- [65] E. Mosconi, A. Amat, M. K. Nazeeruddin, M. Grätzel, and F. De Angelis (2013). First-Principles Modeling of Mixed Halide Organometal Perovskites for Photovoltaic Applications. *The Journal of Physical Chemistry C* **117** (27), 13902–13913.
- [66] F. Brivio, A. B. Walker, and A. Walsh (2013). Structural and electronic properties of hybrid perovskites for high-efficiency thin-film photovoltaics from first-principles. *APL Materials* **1** (4), 042111.
- [67] X. Zhu, H. Su, R. A. Marcus, and M. E. Michel-Beyerle (2014). Computed and Experimental Absorption Spectra of the Perovskite $\text{CH}_3\text{NH}_3\text{PbI}_3$. *The Journal of Physical Chemistry Letters* **5** (17), 3061–3065.

- [68] L. Lang, J.-H. Yang, H.-R. Liu, H. Xiang, and X. Gong (2014). First-principles study on the electronic and optical properties of cubic ABX_3 halide perovskites. *Physics Letters A* **378** (3), 290–293.
- [69] J. M. Richter, K. Chen, A. Sadhanala, J. Butkus, J. P. H. Rivett, R. H. Friend, B. Monserrat, J. M. Hodgkiss, and F. Deschler (2018). Direct Bandgap Behavior in Rashba-Type Metal Halide Perovskites. *Advanced Materials* **30** (52), 1803379.
- [70] T. Kirchartz and U. Rau (2017). Decreasing Radiative Recombination Coefficients via an Indirect Band Gap in Lead Halide Perovskites. *Journal of Physical Chemistry Letters* **8**, 1265–1271.
- [71] F. Zheng, L. Z. Tan, S. Liu, and A. M. Rappe (2015). Rashba Spin–Orbit Coupling Enhanced Carrier Lifetime in $CH_3NH_3PbI_3$. *Nano Letters* **15** (12), 7794–7800.
- [72] D. Niesner, M. Wilhelm, I. Levchuk, A. Osvet, S. Shrestha, M. Batentschuk, C. Brabec, and T. Fauster (2016). Giant Rashba Splitting in $CH_3NH_3PbBr_3$ Organic-Inorganic Perovskite. *Physical Review Letters* **117** (12).
- [73] L. Leppert, S. E. Reyes-Lillo, and J. B. Neaton (2016). Electric Field- and Strain-Induced Rashba Effect in Hybrid Halide Perovskites. *Journal of Physical Chemistry Letters* **7**, 3683–3689.
- [74] D. Niesner, M. Hauck, S. Shrestha, I. Levchuk, G. J. Matt, A. Osvet, M. Batentschuk, C. Brabec, H. B. Weber, and T. Fauster (2018). Structural fluctuations cause spin-split states in tetragonal $(CH_3NH_3)PbI_3$ as evidenced by the circular photogalvanic effect. *Proceedings of the National Academy of Sciences* **115** (38), 9509–9514.
- [75] Y. Yamada, T. Nakamura, M. Endo, A. Wakamiya, and Y. Kanemitsu (2014). Near-band-edge optical responses of solution-processed organic–inorganic hybrid perovskite $CH_3NH_3PbI_3$ on mesoporous TiO_2 electrodes. *Applied Physics Express* **7** (3), 032302.
- [76] S. De Wolf, J. Holovsky, S.-J. Moon, P. Löper, B. Niesen, M. Ledinsky, F.-J. Haug, J.-H. Yum, and C. Ballif (2014). Organometallic Halide Perovskites: Sharp Optical Absorption Edge and Its Relation to Photovoltaic Performance. *The Journal of Physical Chemistry Letters* **5** (6), 1035–1039.
- [77] J. Even, L. Pedesseau, C. Katan, M. Kepenekian, J.-S. Lauret, D. Saponi, and E. Deleporte (2015). Solid-State Physics Perspective on Hybrid Perovskite Semiconductors. *The Journal of Physical Chemistry C* **119** (19), 10161–10177.
- [78] Y. Kanemitsu (2017). Luminescence spectroscopy of lead-halide perovskites: materials properties and application as photovoltaic devices. *Journal of Materials Chemistry C* **5**, 3427–3437.
- [79] T. Kirchartz, T. Markvart, U. Rau, and D. A. Egger (2018). Impact of Small Phonon Energies on the Charge-Carrier Lifetimes in Metal-Halide Perovskites. *The Journal of Physical Chemistry Letters* **9** (5), 939–946.
- [80] M. I. Saidaminov, A. L. Abdelhady, B. Murali, E. Alarousu, V. M. Burlakov, W. Peng, I. Dursun, L. Wang, Y. He, G. Maculan, A. Goriely, T. Wu, O. F. Mohammed, and O. M. Bakr (2015). High-quality bulk hybrid perovskite single crystals within minutes by inverse temperature crystallization. *Nature Communications* **6**, 7586.

-
- [81] T. M. Koh, K. Fu, Y. Fang, S. Chen, T. C. Sum, N. Mathews, S. G. Mhaisalkar, P. P. Boix, and T. Baikie (2014). Formamidinium-Containing Metal-Halide: An Alternative Material for Near-IR Absorption Perovskite Solar Cells. *The Journal of Physical Chemistry C* **118** (30), 16458–16462.
- [82] Y. Kumar, E. Regalado-Pérez, A. M. Ayala, N. Mathews, and X. Mathew (2016). Effect of heat treatment on the electrical properties of perovskite solar cells. *Solar Energy Materials and Solar Cells* **157**, 10–17.
- [83] C. McDonald, C. Ni, V. Švrček, M. Lozac’h, P. A. Connor, P. Maguire, J. T. S. Irvine, and D. Mariotti (2017). Zero-dimensional methylammonium iodo bismuthate solar cells and synergistic interactions with silicon nanocrystals. *Nanoscale* **9**, 18759–18771.
- [84] Z. Xiao, W. Meng, B. Saparov, H.-S. Duan, C. Wang, C. Feng, W. Liao, W. Ke, D. Zhao, J. Wang, D. B. Mitzi, and Y. Yan (2016). Photovoltaic Properties of Two-Dimensional $(\text{CH}_3\text{NH}_3)_2\text{Pb}(\text{SCN})_2\text{I}_2$ Perovskite: A Combined Experimental and Density Functional Theory Study. *The Journal of Physical Chemistry Letters* **7** (7), 1213–1218.
- [85] I. Pelant and J. Valenta (2012). *Luminescence Spectroscopy of Semiconductors*. Chapter 7. Oxford University Press.
- [86] F. Ruf, A. Magin, M. Schultes, M. F. Aygüler, P. Docampo, E. Ahlswede, H. Kalt, and M. Hetterich (2018). Temperature-Dependent Electromodulation Spectroscopy of Excitons in Perovskite Solar Cells. In: *2018 IEEE 7th World Conference on Photovoltaic Energy Conversion (WCPEC) (A Joint Conference of 45th IEEE PVSC, 28th PVSEC 34th EU PVSEC)*, 1550–1554.
- [87] R. J. Elliott (1957). Intensity of Optical Absorption by Excitons. *Physical Review* **108**, 1384–1389.
- [88] L. Q. Phuong, Y. Nakaike, A. Wakamiya, and Y. Kanemitsu (2016). Free Excitons and Exciton-Phonon Coupling in $\text{CH}_3\text{NH}_3\text{PbI}_3$ Single Crystals Revealed by Photocurrent and Photoluminescence Measurements at Low Temperatures. *The Journal of Physical Chemistry Letters* **7** (23), 4905–4910.
- [89] Y. Yamada, T. Nakamura, M. Endo, A. Wakamiya, and Y. Kanemitsu (2015). Photoelectronic Responses in Solution-Processed Perovskite $\text{CH}_3\text{NH}_3\text{PbI}_3$ Solar Cells Studied by Photoluminescence and Photoabsorption Spectroscopy. *IEEE Journal of Photovoltaics* **5** (1), 401–405.
- [90] A. Miyata, A. Mitioglu, P. Plochocka, O. Portugall, J. T.-W. Wang, S. D. Stranks, H. J. Snaith, and R. J. Nicholas (2015). Direct measurement of the exciton binding energy and effective masses for charge carriers in organic-inorganic tri-halide perovskites. *Nature Physics* **11**, 582–587.
- [91] Y. Yamada, T. Nakamura, M. Endo, A. Wakamiya, and Y. Kanemitsu (2014). Photocarrier Recombination Dynamics in Perovskite $\text{CH}_3\text{NH}_3\text{PbI}_3$ for Solar Cell Applications. *Journal of the American Chemical Society* **136** (33), 11610–11613.
- [92] M. N. Saha and A. Fowler (1921). On a physical theory of stellar spectra. *Proceedings of the Royal Society of London A* **99** (697), 135–153.

- [93] R. Cingolani, L. Calcagnile, G. Colí, R. Rinaldi, M. Lomoscolo, M. DiDio, A. Franciosi, L. Vanzetti, G. C. LaRocca, and D. Campi (1996). Radiative recombination processes in wide-band-gap II-VI quantum wells: the interplay between excitons and free carriers. *Journal of the Optical Society of America B* **13** (6), 1268–1277.
- [94] M. V. Kurik (1971). Urbach rule. *physica status solidi (a)* **8** (1), 9–45.
- [95] T. Skettrup (1978). Urbach’s rule derived from thermal fluctuations in the band-gap energy. *Physical Review B* **18**, 2622–2631.
- [96] I. Studenyak, M. Kranjcec, and M. Kurik (2014). Urbach Rule in Solid State Physics. *International Journal of Optics and Applications* **4**, 76–83.
- [97] F. Urbach (1953). The Long-Wavelength Edge of Photographic Sensitivity and of the Electronic Absorption of Solids. *Physical Review* **92**, 1324–1324.
- [98] S. R. Johnson and T. Tiedje (1995). Temperature dependence of the Urbach edge in GaAs. *Journal of Applied Physics* **78** (9), 5609–5613.
- [99] H. Sumi and Y. Toyozawa (1971). Urbach-Martienssen Rule and Exciton Trapped Momentarily by Lattice Vibrations. *Journal of the Physical Society of Japan* **31** (2), 342–358.
- [100] J. D. Dow and D. Redfield (1972). Toward a Unified Theory of Urbach’s Rule and Exponential Absorption Edges. *Physical Review B* **5**, 594–610.
- [101] J. Liebler, S. Schmitt-Rink, and H. Haug (1985). Theory of the absorption tail of wannier excitons in polar semiconductors. *Journal of Luminescence* **34** (1), 1–7.
- [102] C. H. Grein and S. John (1989). Temperature dependence of the Urbach optical absorption edge: A theory of multiple phonon absorption and emission sidebands. *Physical Review B* **39**, 1140–1151.
- [103] G. D. Cody, T. Tiedje, B. Abeles, B. Brooks, and Y. Goldstein (1981). Disorder and the Optical-Absorption Edge of Hydrogenated Amorphous Silicon. *Physical Review Letters* **47**, 1480–1483.
- [104] A. Skumanich, A. Frova, and N. Amer (1985). Urbach tail and gap states in hydrogenated a-SiC and a-SiGe alloys. *Solid State Communications* **54** (7), 597–601.
- [105] M. Ledinsky, T. Schönfeldová, J. Holovský, E. Aydin, Z. Hájková, L. Landová, N. Neyková, A. Fejfar, and S. De Wolf (2019). Temperature Dependence of the Urbach Energy in Lead Iodide Perovskites. *The Journal of Physical Chemistry Letters* **10** (6), 1368–1373.
- [106] S. R. Johnson and T. Tiedje (1995). Temperature dependence of the Urbach edge in GaAs. *Journal of Applied Physics* **78** (9), 5609–5613.
- [107] M. Beaudoin, A. J. G. DeVries, S. R. Johnson, H. Laman, and T. Tiedje (1997). Optical absorption edge of semi-insulating GaAs and InP at high temperatures. *Applied Physics Letters* **70** (26), 3540–3542.
- [108] M. Hirasawa, T. Ishihara, and T. Goto (1994). Exciton Features in 0-, 2-, and 3-Dimensional Networks of $[\text{PbI}_6]^{4-}$ Octahedra. *Journal of the Physical Society of Japan* **63** (10), 3870–3879.

-
- [109] Y. Varshni (1967). Temperature dependence of the energy gap in semiconductors. *Physica* **34** (1), 149–154.
- [110] Y. Yin, D. Yan, F. H. Pollak, M. S. Hybertsen, J. M. Vandenberg, and J. C. Bean (1995). Temperature dependence of the fundamental direct transitions of bulk Ge and two Ge/SiGe multiple-quantum-well structures. *Physical Review B* **52**, 8951–8958.
- [111] D. Lürßen, R. Bleher, and H. Kalt (2000). High-precision determination of the temperature-dependent band-gap shrinkage due to the electron-phonon interaction in GaAs. *Physical Review B* **61**, 15812–15816.
- [112] L. M. Herz (2016). Charge-Carrier Dynamics in Organic-Inorganic Metal Halide Perovskites. *Annual Review of Physical Chemistry* **67** (1), 65–89.
- [113] W. VAN Roosbroeck and W. Shockley (1954). Photon-Radiative Recombination of Electrons and Holes in Germanium. *Physical Review* **94**, 1558–1560.
- [114] P. Würfel (1982). The chemical potential of radiation. *Journal of Physics C: Solid State Physics* **15** (18), 3967–3985.
- [115] G. Lasher and F. Stern (1964). Spontaneous and Stimulated Recombination Radiation in Semiconductors. *Physical Review* **133**, A553–A563.
- [116] E. Daub and P. Würfel (1995). Ultralow Values of the Absorption Coefficient of Si Obtained from Luminescence. *Physical Review Letters* **74**, 1020–1023.
- [117] F. Staub, H. Hempel, J.-C. Hebig, J. Mock, U. W. Paetzold, U. Rau, T. Unold, and T. Kirchartz (2016). Beyond Bulk Lifetimes: Insights into Lead Halide Perovskite Films from Time-Resolved Photoluminescence. *Physical Review Applied* **6**, 044017.
- [118] A. Köhler and H. Bässler (2015). *Electronic Processes in Organic Semiconductors*. John Wiley & Sons, Ltd, 87–191.
- [119] J. Tilchin, D. N. Dirin, G. I. Maikov, A. Sashchiuk, M. V. Kovalenko, and E. Lifshitz (2016). Hydrogen-like Wannier–Mott Excitons in Single Crystal of Methylammonium Lead Bromide Perovskite. *ACS Nano* **10** (6), 6363–6371.
- [120] E. I. Rashba and G. E. Gurgenishvili (1962). On the theory of edge absorption in semiconductors. *Soviet Physics - Solid State* **4**, 759.
- [121] C. H. Henry and K. Nassau (1970). Lifetimes of Bound Excitons in CdS. *Physical Review B* **1**, 1628–1634.
- [122] Y. Toyozawa (2003). *Optical Processes in Solids*. Cambridge University Press.
- [123] M. A. Reshchikov (2014). Temperature dependence of defect-related photoluminescence in III-V and II-VI semiconductors. *Journal of Applied Physics* **115** (1), 012010.
- [124] R. L. Milot, G. E. Eperon, H. J. Snaith, M. B. Johnston, and L. M. Herz (2015). Temperature-Dependent Charge-Carrier Dynamics in CH₃NH₃PbI₃ Perovskite Thin Films. *Advanced Functional Materials* **25** (39), 6218–6227.
- [125] C. Wehrenfennig, M. Liu, H. J. Snaith, M. B. Johnston, and L. M. Herz (2014). Charge carrier recombination channels in the low-temperature phase of organic-inorganic lead halide perovskite thin films. *APL Materials* **2** (8), 081513.

- [126] M. A. Reshchikov and R. Y. Korotkov (2001). Analysis of the temperature and excitation intensity dependencies of photoluminescence in undoped GaN films. *Physical Review B* **64**, 115205.
- [127] F. Seitz (1939). An interpretation of crystal luminescence. *Transactions of the Faraday Society* **35**, 74–85.
- [128] R. W. Gurney and N. F. Mott (1939). Luminescence in solids. *Transactions of the Faraday Society* **35**, 69–73.
- [129] M. Schön (1942). Zum Leuchtmechanismus der Kristallphosphore. *Zeitschrift für Physik* **119**, 463–471.
- [130] H. Klasens (1946). Transfer of Energy Between Centres in Zinc Sulphide Phosphors. *Nature* **158**, 306–307.
- [131] T. Kirchartz, J. A. Márquez, M. Stolterfoht, and T. Unold (2020). Photoluminescence-Based Characterization of Halide Perovskites for Photovoltaics. *Advanced Energy Materials* **10** (26), 1904134.
- [132] M. B. Johnston and L. M. Herz (2016). Hybrid Perovskites for Photovoltaics: Charge-Carrier Recombination, Diffusion, and Radiative Efficiencies. *Accounts of Chemical Research* **49** (1), 146–154.
- [133] P. Asbeck (1977). Self-absorption effects on the radiative lifetime in GaAs-GaAlAs double heterostructures. *Journal of Applied Physics* **48** (2), 820–822.
- [134] T. W. Crothers, R. L. Milot, J. B. Patel, E. S. Parrott, J. Schlipf, P. Müller-Buschbaum, M. B. Johnston, and L. M. Herz (2017). Photon Reabsorption Masks Intrinsic Bi-molecular Charge-Carrier Recombination in CH₃NH₃PbI₃ Perovskite. *Nano Letters* **17** (9), 5782–5789.
- [135] C. J. Hwang (1972). Quantum Efficiency and Radiative Lifetime of the Band-to-Band Recombination in Heavily Doped *n*-Type GaAs. *Physical Review B* **6**, 1355–1359.
- [136] D. E. Hill (1965). Internal Quantum Efficiency of GaAs Electroluminescent Diodes. *Journal of Applied Physics* **36** (11), 3405–3409.
- [137] T. Kuriyama, T. Kamiya, and H. Yanai (1977). Effect of Photon Recycling on Diffusion Length and Internal Quantum Efficiency in Al_{*x*}Ga_{1-*x*}As-GaAs Heterostructures. *Japanese Journal of Applied Physics* **16** (3), 465–477.
- [138] C. S. Ponseca, T. J. Savenije, M. Abdellah, K. Zheng, A. Yartsev, T. Pascher, T. Harlang, P. Chabera, T. Pullerits, A. Stepanov, J.-P. Wolf, and V. Sundström (2014). Organometal Halide Perovskite Solar Cell Materials Rationalized: Ultrafast Charge Generation, High and Microsecond-Long Balanced Mobilities, and Slow Recombination. *Journal of the American Chemical Society* **136** (14), 5189–5192.
- [139] C. Wehrenfennig, G. E. Eperon, M. B. Johnston, H. J. Snaith, and L. M. Herz (2014). High Charge Carrier Mobilities and Lifetimes in Organolead Trihalide Perovskites. *Advanced Materials* **26** (10), 1584–1589.
- [140] O. Schuster, P. Wientjes, S. Shrestha, I. Levchuk, M. Sytnyk, G. J. Matt, A. Osvet, M. Batentschuk, W. Heiss, C. J. Brabec, T. Fauster, and D. Niesner (2020). Looking beyond the Surface: The Band Gap of Bulk Methylammonium Lead Iodide. *Nano Letters* **20** (5), 3090–3097.

- [141] H. Diab, G. Trippé-Allard, F. Lédée, K. Jemli, C. Vilar, G. Bouchez, V. L. Jacques, A. Tejada, J. Even, J.-S. Lauret, E. Deleporte, and D. Garrot (2016). Narrow Linewidth Excitonic Emission in Organic–Inorganic Lead Iodide Perovskite Single Crystals. *The Journal of Physical Chemistry Letters* **7** (24), 5093–5100.
- [142] F. Panzer, S. Baderschneider, T. P. Gujar, T. Unger, S. Bagnich, M. Jakoby, H. Bässler, S. Hüttner, J. Köhler, R. Moos, M. Thelakkat, R. Hildner, and A. Köhler (2016). Reversible Laser-Induced Amplified Spontaneous Emission from Coexisting Tetragonal and Orthorhombic Phases in Hybrid Lead Halide Perovskites. *Advanced Optical Materials* **4** (6), 917–928.
- [143] W. Kong, Z. Ye, Z. Qi, B. Zhang, M. Wang, A. Rahimi-Iman, and H. Wu (2015). Characterization of an abnormal photoluminescence behavior upon crystal-phase transition of perovskite $\text{CH}_3\text{NH}_3\text{PbI}_3$. *Physical Chemistry Chemical Physics* **17**, 16405–16411.
- [144] S. D. Stranks, G. E. Eperon, G. Grancini, C. Menelaou, M. J. P. Alcocer, T. Leijtens, L. M. Herz, A. Petrozza, and H. J. Snaith (2013). Electron-Hole Diffusion Lengths Exceeding 1 Micrometer in an Organometal Trihalide Perovskite Absorber. *Science* **342** (6156), 341–344.
- [145] J. H. Noh, S. H. Im, J. H. Heo, T. N. Mandal, and S. I. Seok (2013). Chemical Management for Colorful, Efficient, and Stable Inorganic–Organic Hybrid Nanostructured Solar Cells. *Nano Letters* **13** (4), 1764–1769.
- [146] G. Xing, N. Mathews, S. S. Lim, N. Yantara, X. Liu, D. Sabba, M. Grätzel, S. Mhaisalkar, and T. C. Sum (2014). Low-temperature solution-processed wavelength-tunable perovskites for lasing. *Nature Materials* **13**, 476–480.
- [147] N. K. Kumawat, A. Dey, A. Kumar, S. P. Gopinathan, K. L. Narasimhan, and D. Kabra (2015). Band Gap Tuning of $\text{CH}_3\text{NH}_3\text{Pb}(\text{Br}_{1-x}\text{Cl}_x)_3$ Hybrid Perovskite for Blue Electroluminescence. *ACS Applied Materials & Interfaces* **7** (24), 13119–13124.
- [148] N. Kitazawa, Y. Watanabe, and Y. Nakamura (2002). Optical Properties of $\text{CH}_3\text{NH}_3\text{PbX}_3$ (X = halogen) and their mixed crystals. *Journal of Materials Science* **37**, 3585–3587.
- [149] G. E. Eperon, S. D. Stranks, C. Menelaou, M. B. Johnston, L. M. Herz, and H. J. Snaith (2014). Formamidinium lead trihalide: a broadly tunable perovskite for efficient planar heterojunction solar cells. *Energy & Environmental Science* **7**, 982–988.
- [150] N. Pellet, P. Gao, G. Gregori, T.-Y. Yang, M. K. Nazeeruddin, J. Maier, and M. Grätzel (2014). Mixed-Organic-Cation Perovskite Photovoltaics for Enhanced Solar-Light Harvesting. *Angewandte Chemie International Edition* **53** (12), 3151–3157.
- [151] D. P. McMeekin, G. Sadoughi, W. Rehman, G. E. Eperon, M. Saliba, M. T. Hörantner, A. Haghighirad, N. Sakai, L. Korte, B. Rech, M. B. Johnston, L. M. Herz, and H. J. Snaith (2016). A mixed-cation lead mixed-halide perovskite absorber for tandem solar cells. *Science* **351** (6269), 151–155.
- [152] M. I. Saidaminov, M. A. Haque, M. Savoie, A. L. Abdelhady, N. Cho, I. Dursun, U. Buttner, E. Alarousu, T. Wu, and O. M. Bakr (2016). Perovskite Photodetectors Operating in Both Narrowband and Broadband Regimes. *Advanced Materials* **28** (37), 8144–8149.

- [153] B. Saparov and D. B. Mitzi (2016). Organic–Inorganic Perovskites: Structural Versatility for Functional Materials Design. *Chemical Reviews* **116** (7), 4558–4596.
- [154] B. Slimi, M. Mollar, I. B. Assaker, I. Kriaa, R. Chtourou, and B. Marí (2016). Perovskite $\text{FA}_{1-x}\text{MA}_x\text{PbI}_3$ for solar cells: films formation and properties. *Energy Procedia* **102**, 87–95.
- [155] H.-S. Kim, C.-R. Lee, J.-H. Im, K.-B. Lee, T. Moehl, A. Marchioro, S.-J. Moon, R. Humphry-Baker, J.-H. Yum, J. E. Moser, M. Grätzel, and N.-G. Park (2012). Lead Iodide Perovskite Sensitized All-Solid-State Submicron Thin Film Mesoscopic Solar Cell with Efficiency Exceeding 9%. *Scientific Reports* **2**, 591.
- [156] G. Papavassiliou and I. Koutselas (1995). Structural, optical and related properties of some natural three- and lower-dimensional semiconductor systems. *Synthetic Metals* **71** (1), 1713–1714.
- [157] Y. Yang, M. Yang, Z. Li, R. Crisp, K. Zhu, and M. C. Beard (2015). Comparison of Recombination Dynamics in $\text{CH}_3\text{NH}_3\text{PbBr}_3$ and $\text{CH}_3\text{NH}_3\text{PbI}_3$ Perovskite Films: Influence of Exciton Binding Energy. *The Journal of Physical Chemistry Letters* **6** (23), 4688–4692.
- [158] G. Mannino, I. Deretzis, E. Smecca, A. La Magna, A. Alberti, D. Ceratti, and D. Cahen (2020). Temperature-Dependent Optical Band Gap in CsPbBr_3 , MAPbBr_3 , and FAPbBr_3 Single Crystals. *The Journal of Physical Chemistry Letters* **11** (7), 2490–2496.
- [159] A. M. A. Leguy, P. Azarhoosh, M. I. Alonso, M. Campoy-Quiles, O. J. Weber, J. Yao, D. Bryant, M. T. Weller, J. Nelson, A. Walsh, M. VAN Schilfgaarde, and P. R. F. Barnes (2016). Experimental and theoretical optical properties of methylammonium lead halide perovskites. *Nanoscale* **8**, 6317–6327.
- [160] R. Saxena, J. Kangsabanik, A. Kumar, A. Shahee, S. Singh, N. Jain, S. Ghorui, V. Kumar, A. V. Mahajan, A. Alam, and D. Kabra (2020). Contrasting temperature dependence of the band gap in $\text{CH}_3\text{NH}_3\text{PbX}_3$ ($X = \text{I}, \text{Br}, \text{Cl}$): Insight from lattice dilation and electron-phonon coupling. *Physical Review B* **102**, 081201.
- [161] A. Buin, R. Comin, J. Xu, A. H. Ip, and E. H. Sargent (2015). Halide-Dependent Electronic Structure of Organolead Perovskite Materials. *Chemistry of Materials* **27** (12), 4405–4412.
- [162] D. M. Jang, K. Park, D. H. Kim, J. Park, F. Shojaei, H. S. Kang, J.-P. Ahn, J. W. Lee, and J. K. Song (2015). Reversible Halide Exchange Reaction of Organometal Trihalide Perovskite Colloidal Nanocrystals for Full-Range Band Gap Tuning. *Nano Letters* **15** (8), 5191–5199.
- [163] E. T. Hoke, D. J. Slotcavage, E. R. Dohner, A. R. Bowring, H. I. Karunadasa, and M. D. McGehee (2015). Reversible photo-induced trap formation in mixed-halide hybrid perovskites for photovoltaics. *Chemical Science* **6**, 613–617.
- [164] A. Amat, E. Mosconi, E. Ronca, C. Quarti, P. Umari, M. K. Nazeeruddin, M. Grätzel, and F. De Angelis (2014). Cation-Induced Band-Gap Tuning in Organohalide Perovskites: Interplay of Spin–Orbit Coupling and Octahedra Tilting. *Nano Letters* **14** (6), 3608–3616.

- [165] G. Giorgi, J.-I. Fujisawa, H. Segawa, and K. Yamashita (2014). Cation Role in Structural and Electronic Properties of 3D Organic–Inorganic Halide Perovskites: A DFT Analysis. *The Journal of Physical Chemistry C* **118** (23), 12176–12183.
- [166] C. Yi, J. Luo, S. Meloni, A. Boziki, N. Ashari-Astani, C. Grätzel, S. M. Zakeeruddin, U. Röhrlisberger, and M. Grätzel (2016). Entropic stabilization of mixed A-cation ABX₃ metal halide perovskites for high performance perovskite solar cells. *Energy & Environmental Science* **9**, 656–662.
- [167] J.-W. Lee, D.-H. Kim, H.-S. Kim, S.-W. Seo, S. M. Cho, and N.-G. Park (2015). Formamidinium and Cesium Hybridization for Photo- and Moisture-Stable Perovskite Solar Cell. *Advanced Energy Materials* **5** (20), 1501310.
- [168] Z. Li, M. Yang, J.-S. Park, S.-H. Wei, J. J. Berry, and K. Zhu (2016). Stabilizing Perovskite Structures by Tuning Tolerance Factor: Formation of Formamidinium and Cesium Lead Iodide Solid-State Alloys. *Chemistry of Materials* **28** (1), 284–292.
- [169] W. Rehman, D. P. McMeekin, J. B. Patel, R. L. Milot, M. B. Johnston, H. J. Snaith, and L. M. Herz (2017). Photovoltaic mixed-cation lead mixed-halide perovskites: links between crystallinity, photo-stability and electronic properties. *Energy & Environmental Science* **10**, 361–369.
- [170] J. Y. Kim, J.-W. Lee, H. S. Jung, H. Shin, and N.-G. Park (2020). High-Efficiency Perovskite Solar Cells. *Chemical Reviews* **120** (15), 7867–7918.
- [171] M. Saliba, T. Matsui, J.-Y. Seo, K. Domanski, J.-P. Correa-Baena, M. K. Nazeeruddin, S. M. Zakeeruddin, W. Tress, A. Abate, A. Hagfeldt, and M. Grätzel (2016). Cesium-containing triple cation perovskite solar cells: improved stability, reproducibility and high efficiency. *Energy & Environmental Science* **9**, 1989–1997.
- [172] E. Jokar, C.-H. Chien, C.-M. Tsai, A. Fathi, and E. W.-G. Diau (2019). Robust Tin-Based Perovskite Solar Cells with Hybrid Organic Cations to Attain Efficiency Approaching 10%. *Advanced Materials* **31** (2), 1804835.
- [173] L.-J. Chen, C.-R. Lee, Y.-J. Chuang, Z.-H. Wu, and C. Chen (2016). Synthesis and Optical Properties of Lead-Free Cesium Tin Halide Perovskite Quantum Rods with High-Performance Solar Cell Application. *The Journal of Physical Chemistry Letters* **7** (24), 5028–5035.
- [174] S. Shao, J. Liu, G. Portale, H.-H. Fang, G. R. Blake, G. H. Ten Brink, L. J. A. Koster, and M. A. Loi (2018). Highly Reproducible Sn-Based Hybrid Perovskite Solar Cells with 9% Efficiency. *Advanced Energy Materials* **8** (4), 1702019.
- [175] W. Kim and M. G. Kanatzidis (2019). Prospects for low-toxicity lead-free perovskite solar cells. *Nature Communications* **10**, 965.
- [176] P. V. Kamat, J. Bisquert, and J. Buriak (2017). Lead-Free Perovskite Solar Cells. *ACS Energy Letters* **2** (4), 904–905.
- [177] T. Miyasaka, A. Kulkarni, G. M. Kim, S. Öz, and A. K. Jena (2020). Perovskite Solar Cells: Can We Go Organic-Free, Lead-Free, and Dopant-Free? *Advanced Energy Materials* **10** (13), 1902500.

- [178] X. Jiang, H. Li, Q. Zhou, Q. Wei, M. Wei, L. Jiang, Z. Wang, Z. Peng, F. Wang, Z. Zang, K. Xu, Y. Hou, S. Teale, W. Zhou, R. Si, X. Gao, E. H. Sargent, and Z. Ning (2021). One-Step Synthesis of $\text{SnI}_2 \cdot (\text{DMSO})_x$ Adducts for High-Performance Tin Perovskite Solar Cells. *Journal of the American Chemical Society* **143** (29), 10970–10976.
- [179] D. Shi, V. Adinolfi, R. Comin, M. Yuan, E. Alarousu, A. Buin, Y. Chen, S. Hoogland, A. Rothenberger, K. Katsiev, Y. Losovyj, X. Zhang, P. A. Dowben, O. F. Mohammed, E. H. Sargent, and O. M. Bakr (2015). Low trap-state density and long carrier diffusion in organolead trihalide perovskite single crystals. *Science* **347** (6221), 519–522.
- [180] A. Kalam, R. Runjhun, A. Mahapatra, M. M. Tavakoli, S. Trivedi, H. Tavakoli Dastjerdi, P. Kumar, J. Lewiński, M. Pandey, D. Prochowicz, and P. Yadav (2020). Interpretation of Resistance, Capacitance, Defect Density, and Activation Energy Levels in Single-Crystalline MAPbI_3 . *The Journal of Physical Chemistry C* **124** (6), 3496–3502.
- [181] S. D. Stranks, V. M. Burlakov, T. Leijtens, J. M. Ball, A. Goriely, and H. J. Snaith (2014). Recombination Kinetics in Organic-Inorganic Perovskites: Excitons, Free Charge, and Subgap States. *Physical Review Applied* **2**, 034007.
- [182] D. W. DE Quilettes, S. M. Vorpahl, S. D. Stranks, H. Nagaoka, G. E. Eperon, M. E. Ziffer, H. J. Snaith, and D. S. Ginger (2015). Impact of microstructure on local carrier lifetime in perovskite solar cells. *Science* **348** (6235), 683–686.
- [183] X. Gong, Z. Huang, R. Sabatini, S.-S. Tan, G. Bappi, G. Walters, A. Proppe, M. I. Saidaminov, O. Voznyy, S. O. Kelley, and E. H. Sargent (2019). Contactless measurements of photocarrier transport properties in perovskite single crystals. *Nature Communications* **10**, 1591.
- [184] Q. Dong, Y. Fang, Y. Shao, P. Mulligan, J. Qiu, L. Cao, and J. Huang (2015). Electron-hole diffusion lengths $> 175 \mu\text{m}$ in solution-grown $\text{CH}_3\text{NH}_3\text{PbI}_3$ single crystals. *Science* **347** (6225), 967–970.
- [185] Z. Liao, Z. Xiao, M. Yang, M. Zhang, Y. Zhang, H. Gu, X. Jiang, Q. Wang, and J. Li (2019). Direct imaging of carrier diffusion length in organic-inorganic perovskites. *Applied Physics Letters* **115** (24), 242104.
- [186] J. Ding, S. Du, Y. Zhao, X. Zhang, H. Cui, X. Zhan, Y. Gu, and H. Sun (2017). High-quality inorganic–organic perovskite $\text{CH}_3\text{NH}_3\text{PbI}_3$ single crystals for photo-detector applications. *Journal of Materials Science* **52**, 2017.
- [187] Y. Dang, Y. Liu, Y. Sun, D. Yuan, X. Liu, W. Lu, G. Liu, H. Xia, and X. Tao (2015). Bulk crystal growth of hybrid perovskite material $\text{CH}_3\text{NH}_3\text{PbI}_3$. *CrystEngComm* **17**, 665–670.
- [188] K.-H. Wang, L.-C. Li, M. Shellaiah, and K. W. Sun (2017). Structural and Photophysical Properties of Methylammonium Lead Tribromide (MAPbBr_3) Single Crystals. *Scientific Reports* **7**, 13643.
- [189] B. Murali, S. Dey, A. L. Abdelhady, W. Peng, E. Alarousu, A. R. Kirmani, N. Cho, S. P. Sarmah, M. R. Parida, M. I. Saidaminov, A. A. Zhumeckenov, J. Sun, M. S. Alias, E. Yengel, B. S. Ooi, A. Amassian, O. M. Bakr, and O. F. Mohammed (2016). Surface Restructuring of Hybrid Perovskite Crystals. *ACS Energy Letters* **1** (6), 1119–1126.

- [190] M. S. Alias, I. Dursun, M. I. Saidaminov, E. M. Diallo, P. Mishra, T. K. Ng, O. M. Bakr, and B. S. Ooi (2016). Optical constants of $\text{CH}_3\text{NH}_3\text{PbBr}_3$ perovskite thin films measured by spectroscopic ellipsometry. *Optics Express* **24** (15), 16586–16594.
- [191] J.-S. Park, S. Choi, Y. Yan, Y. Yang, J. M. Luther, S.-H. Wei, P. Parilla, and K. Zhu (2015). Electronic Structure and Optical Properties of α - $\text{CH}_3\text{NH}_3\text{PbBr}_3$ Perovskite Single Crystal. *The Journal of Physical Chemistry Letters* **6** (21), 4304–4308.
- [192] M. I. Alonso, B. Charles, A. Francisco-López, M. Garriga, M. T. Weller, and A. R. Goñi (2019). Spectroscopic ellipsometry study of $\text{FA}_x\text{MA}_{1-x}\text{PbI}_3$ hybrid perovskite single crystals. *Journal of Vacuum Science & Technology B* **37** (6), 062901.
- [193] X. Wang, J. Gong, X. Shan, M. Zhang, Z. Xu, R. Dai, Z. Wang, S. Wang, X. Fang, and Z. Zhang (2019). In Situ Monitoring of Thermal Degradation of $\text{CH}_3\text{NH}_3\text{PbI}_3$ Films by Spectroscopic Ellipsometry. *The Journal of Physical Chemistry C* **123** (2), 1362–1369.
- [194] A. Osherov, E. M. Hutter, K. Galkowski, R. Brenes, D. K. Maude, R. J. Nicholas, P. Plochocka, V. Bulović, T. J. Savenije, and S. D. Stranks (2016). The Impact of Phase Retention on the Structural and Optoelectronic Properties of Metal Halide Perovskites. *Advanced Materials* **28** (48), 10757–10763.
- [195] P. S. Whitfield, N. Herron, W. E. Guise, K. Page, Y. Q. Cheng, I. Milas, and M. K. Crawford (2016). Phase Transitions and Tricritical Behavior of the Hybrid Perovskite Methyl Ammonium Lead Iodide. *Scientific Reports* **6**, 35685.
- [196] G. Schuck, D. M. Töbrens, M. Koch-Müller, I. Efthimiopoulos, and S. Schorr (2018). Infrared Spectroscopic Study of Vibrational Modes across the Orthorhombic–Tetragonal Phase Transition in Methylammonium Lead Halide Single Crystals. *The Journal of Physical Chemistry C* **122** (10), 5227–5237.
- [197] H.-H. Fang, R. Raissa, M. Abdu-Aguye, S. Adjokatse, G. R. Blake, J. Even, and M. A. Loi (2015). Photophysics of Organic–Inorganic Hybrid Lead Iodide Perovskite Single Crystals. *Advanced Functional Materials* **25** (16), 2378–2385.
- [198] A. Dobrovolsky, A. Merdasa, E. L. Unger, A. Yartsev, and I. G. Scheblykin (2017). Defect-induced local variation of crystal phase transition temperature in metal-halide perovskites. *Nature Communications* **8**.
- [199] H. Tahara, M. Endo, A. Wakamiya, and Y. Kanemitsu (2016). Experimental Evidence of Localized Shallow States in Orthorhombic Phase of $\text{CH}_3\text{NH}_3\text{PbI}_3$ Perovskite Thin Films Revealed by Photocurrent Beat Spectroscopy. *The Journal of Physical Chemistry C* **120** (10), 5347–5352.
- [200] T. Meier, T. P. Gujar, A. Schönleber, S. Olthof, K. Meerholz, S. VAN Smaalen, F. Panzer, M. Thelakkat, and A. Köhler (2018). Impact of excess PbI_2 on the structure and the temperature dependent optical properties of methylammonium lead iodide perovskites. *Journal of Materials Chemistry C* **6**, 7512–7519.
- [201] R. Wasylishen, O. Knop, and J. Macdonald (1985). Cation rotation in methylammonium lead halides. *Solid State Communications* **56** (7), 581–582.

- [202] R. Swartwout, M. T. Hoerantner, and V. Bulović (2019). Scalable Deposition Methods for Large-area Production of Perovskite Thin Films. *Energy & Environmental Materials* **2** (2), 119–145.
- [203] C. Liu, Y. Yang, O. A. Syzgantseva, Y. Ding, M. A. Syzgantseva, X. Zhang, A. M. Asiri, S. Dai, and M. K. Nazeeruddin (2020). α -CsPbI₃ Bilayers via One-Step Deposition for Efficient and Stable All-Inorganic Perovskite Solar Cells. *Advanced Materials* **32** (32), 2002632.
- [204] J. Burschka, N. Pellet, S.-J. Moon, Humphry-Baker, P. Gao, M. K. Nazeeruddin, and M. Grätzel (2013). Sequential deposition as a route to high-performance perovskite-sensitized solar cells. *Nature* **499**, 316–319.
- [205] J.-H. Im, I.-H. Jang, N. Pellet, M. Grätzel, and N.-G. Park (2014). Growth of CH₃NH₃PbI₃ cuboids with controlled size for high-efficiency perovskite solar cells. *Nature Technology* **9**, 927–932.
- [206] N. J. Jeon, J. H. Noh, Y. C. Kim, W. S. Yang, S. Ryu, and S. I. Seok (2014). Solvent engineering for high-performance inorganic–organic hybrid perovskite solar cells. *Nature Materials* **13** (9), 897–903.
- [207] J. Li, R. Gao, F. Gao, J. Lei, H. Wang, X. Wu, J. Li, H. Liu, X. Hua, and S. (Liu (2020). Fabrication of efficient CsPbBr₃ perovskite solar cells by single-source thermal evaporation. *Journal of Alloys and Compounds* **818**, 152903.
- [208] T. Zhang, N. Guo, G. Li, X. Qian, L. Li, and Y. Zhao (2016). A general non-CH₃NH₃X (X = I, Br) one-step deposition of CH₃NH₃PbX₃ perovskite for high performance solar cells. *J. Mater. Chem. A* **4**, 3245–3248.
- [209] A. Ng, Z. Ren, Q. Shen, S. H. Cheung, H. C. Gokkaya, G. Bai, J. Wang, L. Yang, S. K. So, A. B. Djurišić, W. W.-f. Leung, J. Hao, W. K. Chan, and C. Surya (2015). Efficiency enhancement by defect engineering in perovskite photovoltaic cells prepared using evaporated PbI₂/CH₃NH₃I multilayers. *Journal of Materials Chemistry A* **3**, 9223–9231.
- [210] D. Zhao, W. Ke, C. R. Grice, A. J. Cimaroli, X. Tan, M. Yang, R. W. Collins, H. Zhang, K. Zhu, and Y. Yan (2016). Annealing-free efficient vacuum-deposited planar perovskite solar cells with evaporated fullerenes as electron-selective layers. *Nano Energy* **19**, 88–97.
- [211] F. Palazon, Y. El Ajjouri, P. Sebastia-Luna, S. Lauciello, L. Manna, and H. J. Bolink (2019). Mechanochemical synthesis of inorganic halide perovskites: evolution of phase-purity, morphology, and photoluminescence. *Journal of Materials Chemistry C* **7**, 11406–11410.
- [212] D. Prochowicz, P. Yadav, M. Saliba, M. Sasaki, S. M. Zakeeruddin, J. Lewiński, and M. Grätzel (2017). Mechanochemical synthesis of pure phase mixed-cation MA_xFA_{1-x}PbI₃ hybrid perovskites: photovoltaic performance and electrochemical properties. *Sustainable Energy Fuels* **1**, 689–693.
- [213] A. D. Jodlowski, A. Yépez, R. Luque, L. Camacho, and G. de Miguel (2016). Benign-by-Design Solventless Mechanochemical Synthesis of Three-, Two-, and One-Dimensional Hybrid Perovskites. *Angewandte Chemie International Edition* **55** (48), 14972–14977.

- [214] J. J. VAN Franeker, K. H. Hendriks, B. J. Bruijnaers, M. W. G. M. Verhoeven, M. M. Wienk, and R. A. J. Janssen (2017). Monitoring Thermal Annealing of Perovskite Solar Cells with In Situ Photoluminescence. *Advanced Energy Materials* **7** (7), 1601822.
- [215] W. Nie, H. Tsai, R. Asadpour, J.-C. Blancon, A. J. Neukirch, G. Gupta, J. J. Crochet, M. Chhowalla, S. Tretiak, M. A. Alam, H.-L. Wang, and A. D. Mohite (2015). High-efficiency solution-processed perovskite solar cells with millimeter-scale grains. *Science* **347** (6221), 522–525.
- [216] H. Tsai, W. Nie, Y.-H. Lin, J. C. Blancon, S. Tretiak, J. Even, G. Gupta, P. M. Ajayan, and A. D. Mohite (2017). Effect of Precursor Solution Aging on the Crystallinity and Photovoltaic Performance of Perovskite Solar Cells. *Advanced Energy Materials* **7** (11), 1602159.
- [217] H. Yu, X. Liu, Y. Xia, Q. Dong, K. Zhang, Z. Wang, Y. Zhou, B. Song, and Y. Li (2016). Room-temperature mixed-solvent-vapor annealing for high performance perovskite solar cells. *Journal of Materials Chemistry A* **4**, 321–326.
- [218] B.-E. Cohen, S. Gamliel, and L. Etgar (2014). Parameters influencing the deposition of methylammonium lead halide iodide in hole conductor free perovskite-based solar cells. *APL Materials* **2** (8), 081502.
- [219] A. Dubey, N. Adhikari, S. Mabrouk, F. Wu, K. Chen, S. Yang, and Q. Qiao (2018). A strategic review on processing routes towards highly efficient perovskite solar cells. *Journal of Materials Chemistry A* **6**, 2406–2431.
- [220] D. Barrit, P. Cheng, M.-C. Tang, K. Wang, H. Dang, D.-M. Smilgies, S. (Liu, T. D. Anthopoulos, K. Zhao, and A. Amassian (2019). Impact of the Solvation State of Lead Iodide on Its Two-Step Conversion to MAPbI₃: An In Situ Investigation. *Advanced Functional Materials* **29** (47), 1807544.
- [221] M. R. Ahmadian-Yazdi, F. Zabihi, M. Habibi, and M. Eslamian (2016). Effects of Process Parameters on the Characteristics of Mixed-Halide Perovskite Solar Cells Fabricated by One-Step and Two-Step Sequential Coating. *Nanoscale Research Letters* **11**, 408.
- [222] W. Rehman, R. L. Milot, G. E. Eperon, C. Wehrenfennig, J. L. Boland, H. J. Snaith, M. B. Johnston, and L. M. Herz (2015). Charge-Carrier Dynamics and Mobilities in Formamidinium Lead Mixed-Halide Perovskites. *Advanced Materials* **27** (48), 7938–7944.
- [223] J.-H. Im, C.-R. Lee, J.-W. Lee, S.-W. Park, and N.-G. Park (2011). 6.5% efficient perovskite quantum-dot-sensitized solar cell. *Nanoscale* **3**, 4088–4093.
- [224] G. E. Eperon, V. M. Burlakov, P. Docampo, A. Goriely, and H. J. Snaith (2014). Morphological Control for High Performance, Solution-Processed Planar Heterojunction Perovskite Solar Cells. *Advanced Functional Materials* **24** (1), 151–157.
- [225] A. A. Petrov, I. P. Sokolova, N. A. Belich, G. S. Peters, P. V. Dorovatovskii, Y. V. Zubavichus, V. N. Khrustalev, A. V. Petrov, M. Grätzel, E. A. Goodilin, and A. B. Tarasov (2017). Crystal Structure of DMF-Intermediate Phases Uncovers the Link Between CH₃NH₃PbI₃ Morphology and Precursor Stoichiometry. *The Journal of Physical Chemistry C* **121** (38), 20739–20743.

- [226] Y. Tian and I. G. Scheblykin (2015). Artifacts in Absorption Measurements of Organometal Halide Perovskite Materials: What Are the Real Spectra? *The Journal of Physical Chemistry Letters* **6** (17), 3466–3470.
- [227] Y. Zhong, R. Munir, J. Li, M.-C. Tang, M. R. Niazi, D.-M. Smilgies, K. Zhao, and A. Amassian (2018). Blade-Coated Hybrid Perovskite Solar Cells with Efficiency > 17%: An In Situ Investigation. *ACS Energy Letters* **3** (5), 1078–1085.
- [228] H.-B. Kim, H. Choi, J. Jeong, S. Kim, B. Walker, S. Song, and J. Y. Kim (2014). Mixed solvents for the optimization of morphology in solution-processed, inverted-type perovskite/fullerene hybrid solar cells. *Nanoscale* **6**, 6679–6683.
- [229] S. Lee, M.-C. Tang, R. Munir, D. Barrit, Y.-J. Kim, R. Kang, J.-M. Yun, D.-M. Smilgies, A. Amassian, and D.-Y. Kim (2020). In situ study of the film formation mechanism of organic–inorganic hybrid perovskite solar cells: controlling the solvate phase using an additive system. *Journal of Materials Chemistry A* **8**, 7695–7703.
- [230] X. Zheng, B. Chen, C. Wu, and S. Priya (2015). Room temperature fabrication of $\text{CH}_3\text{NH}_3\text{PbBr}_3$ by anti-solvent assisted crystallization approach for perovskite solar cells with fast response and small J–V hysteresis. *Nano Energy* **17**, 269–278.
- [231] M.-C. Tang, D. Barrit, R. Munir, R. Li, J. M. Barbé, D.-M. Smilgies, S. Del Gobbo, T. D. Anthopoulos, and A. Amassian (2019). Bismuth-Based Perovskite-Inspired Solar Cells: In Situ Diagnostics Reveal Similarities and Differences in the Film Formation of Bismuth- and Lead-Based Films. *Solar RRL* **3** (7), 1800305.
- [232] M. Yavari, M. Mazloum-Ardakani, S. Gholipour, M. M. Tavakoli, S.-H. Turren-Cruz, N. Taghavinia, M. Grätzel, A. Hagfeldt, and M. Saliba (2018). Greener, Nonhalogenated Solvent Systems for Highly Efficient Perovskite Solar Cells. *Advanced Energy Materials* **8** (21), 1800177.
- [233] B. A. Rosales, L. Men, S. D. Cady, M. P. Hanrahan, A. J. Rossini, and J. Vela (2016). Persistent Dopants and Phase Segregation in Organolead Mixed-Halide Perovskites. *Chemistry of Materials* **28** (19), 6848–6859.
- [234] B. A. Rosales, L. Wei, and J. Vela (2019). Synthesis and mixing of complex halide perovskites by solvent-free solid-state methods. *Journal of Solid State Chemistry* **271**, 206–215.
- [235] F. Zhu, L. Men, Y. Guo, Q. Zhu, U. Bhattacharjee, P. M. Goodwin, J. W. Petrich, E. A. Smith, and J. Vela (2015). Shape Evolution and Single Particle Luminescence of Organometal Halide Perovskite Nanocrystals. *ACS Nano* **9** (3), 2948–2959.
- [236] S. Shrestha, R. Fischer, G. J. Matt, P. Feldner, A. O. Thilo Michel, I. Levchuk, B. Merle, S. Golkar, H. Chen, O. S. Sandro F. Tedde, R. Hock, M. Rührig, M. Göken, W. Heiss, G. Anton, and C. J. Brabec (2017). High-performance direct conversion X-ray detectors based on sintered hybrid lead triiodide perovskite wafers. *Nature Photonics* **11**, 436–440.
- [237] X. Jia, Z. Hu, Y. Zhu, T. Weng, J. Wang, J. Zhang, and Y. Zhu (2017). Facile synthesis of organic–inorganic hybrid perovskite $\text{CH}_3\text{NH}_3\text{PbI}_3$ microcrystals. *Journal of Alloys and Compounds* **725**, 270–274.

-
- [238] V. Bhooshan Kumar, L. Gouda, Z. Porat, and A. Gedanken (2016). Sonochemical synthesis of $\text{CH}_3\text{NH}_3\text{PbI}_3$ perovskite ultrafine nanocrystal sensitizers for solar energy applications. *Ultrasonics Sonochemistry* **32**, 54–59.
- [239] D. Prochowicz, M. Saski, P. Yadav, M. Grätzel, and J. Lewiński (2019). Mechanoperovskites for Photovoltaic Applications: Preparation, Characterization, and Device Fabrication. *Accounts of Chemical Research* **52** (11), 3233–3243.
- [240] F. Palazon, Y. El Ajjouri, and H. J. Bolink (2020). Making by Grinding: Mechanochemistry Boosts the Development of Halide Perovskites and Other Multinary Metal Halides. *Advanced Energy Materials* **10** (13), 1902499.
- [241] Z. Hong, D. Tan, R. A. John, Y. K. E. Tay, Y. K. T. Ho, X. Zhao, T. C. Sum, N. Mathews, F. García, and H. S. Soo (2019). Completely Solvent-free Protocols to Access Phase-Pure, Metastable Metal Halide Perovskites and Functional Photodetectors from the Precursor Salts. *iScience* **16**, 312–325.

Part II

Overview of the Thesis

5

Summary

The main aim of this thesis is to understand the relationship between structural changes and the optical properties of lead halide perovskites, and how to use this understanding to elucidate the perovskite film formation. The thesis addresses this issue in seven chapters, which can be grouped into two main parts. The structure of the thesis is shown in Figure 5.1. The first part deals with how structural changes influence the optical properties of lead halide perovskites and consists of three research articles, which are presented in Chapters 8-10. In Chapter 8, I investigated the optical properties of lead halide perovskite single crystals as a model system. I used the knowledge gained in this work also for understanding the optical properties of MAPbI₃ single crystals in Chapter 9, where I systematically induced structural changes by varying the temperature across the tetragonal to orthorhombic phase transition. I then turned to polycrystalline samples in Chapter 10, where I investigated whether perovskite powders show different optical properties compared to single crystals or perovskite thin films. Chapter 11 builds the transition from the first part about the relationship between structural changes and the optical properties of lead halide perovskites, to the second part, which is about using this insight to elucidate the perovskite film formation. Chapter 11 is a perspective article, which first summarizes optical properties of halide perovskites, including knowledge I gained in Chapters 8-10. Analysis approaches that have been shown to be relevant in the context of *in situ* optical properties during the thin film formation are presented. The article then summarizes how *in situ* optical spectroscopy was used in recent works to monitor and to understand the film formation of halide perovskites, building a thematic introduction to Chapters 12-14. Additionally, perspectives on how *in situ* optical spectroscopy can be used in the future to better understand the perovskite film formation and processing are elucidated. In the three chapters forming the second part, the knowledge gained from the previous works is extended and applied to the *in situ* optical properties of lead halide perovskites during film formation for different synthesis approaches. Chapter 12 focuses on the film formation of MAPbI₃ *via* spin-coating using a two-step approach, i.e., by applying a MAI-solution to a PbI₂-coated substrate. In Chapter 13, one-step spin-coating of MAPbI₃ is compared with industrially relevant slot-die coating, where the evaporation rate of the solvent was systematically varied. In Chapter 14, the film formation of a perovskite with mixed stoichiometry using the solvent engineering method is investigated, focusing on the influence of the temperature of the anti-solvent on the film formation process and the final film properties.

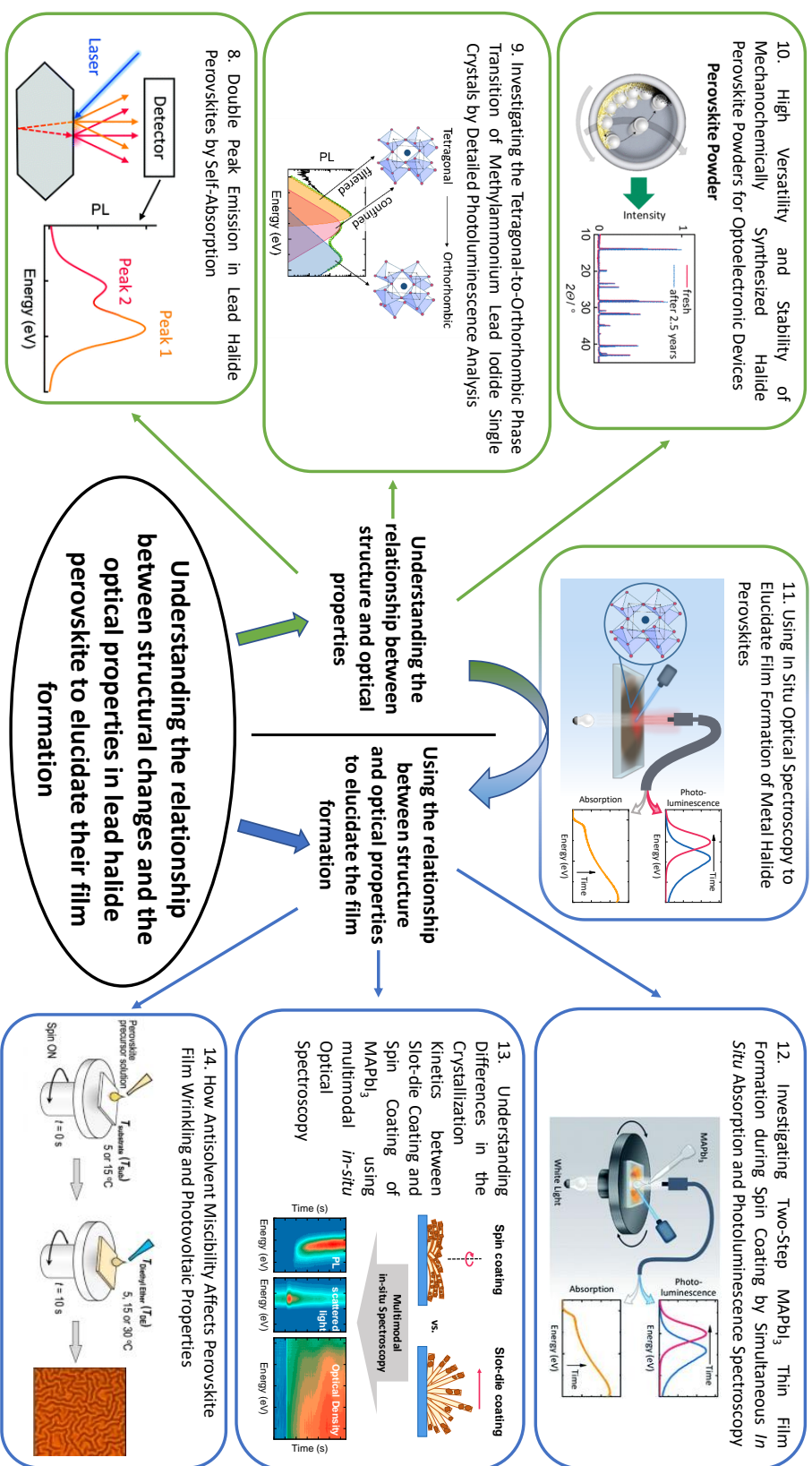


Figure 5.1: Overview of the structure of the thesis consisting of the individual publications.

The following gives a brief summary of the content of the individual chapters forming this thesis. A more detailed description is given in Chapter 6. In Chapter 8, I measured PL of lead halide perovskite single crystals of different stoichiometry. For all samples, I observed an additional PL peak at lower energies compared to the main PL peak in the tetragonal phase and a similar feature in a small temperature window in the orthorhombic phase. As this additional PL peak is controversially attributed to different origins, I addressed the origin of this PL feature in detail. As a representative material system, I focused on MAPbI₃ single crystals for further analyses. Using a combination of further optical spectroscopy, e.g. temperature-dependent two-photon induced PL, and optical modeling, I addressed the different origins for this PL peak that were suggested in literature. By doing so, I was able to elaborate that self-absorption enhanced by internal reflection of the PL - i.e., an optical filter effect - causes the additional PL feature.

With the understanding of the effect of self-absorption on the PL spectra, I was now able to investigate in detail the structural phase transition of MAPbI₃ single crystals using PL measurements, as presented in Chapter 9. I induced the tetragonal to orthorhombic phase transition in MAPbI₃ single crystals by changing the temperature between 200 K and 100 K. During the phase transition, several PL peaks appear and disappear so that the PL spectra become complex, and the origin of the individual peaks is not always clear. By performing PL measurements during the phase transition in different setup geometries, I identified two of the PL features to result from self-absorption, similar to the additional PL peak in the pure tetragonal and orthorhombic phases (see Chapter 8). By modifying the optical model that I developed in Chapter 8 so that it allowed to consider two coexisting crystal phases, I was able to characterize the phase transition of the MAPbI₃ single crystal in detail. I found that tetragonal and orthorhombic phase coexist in a temperature window of at least 40 K, despite the sample being a nominal single crystal. Further, the tetragonal inclusions below the main phase transition temperature are structurally distorted and their PL exhibits signatures of quantum confinement, and act as efficient traps for the charge carriers in the orthorhombic phase.

Motivated by the knowledge about the role of the structure on the optical properties, which I gained in Chapters 8 and 9, I aimed to answer the question whether the optical properties of perovskite powders deviate from their single crystal and thin film counter parts. Perovskite powders are insofar interesting as they are needed for the fabrication of thick film devices such as X-ray detectors, and their synthesis is easily upscalable. In Chapter 10, I investigated the optical properties of perovskite powders with different stoichiometry, which were produced by a mechanochemical synthesis approach *via* ball milling. I characterized the synthesized powders using reflection and PL spectroscopy. With that, I was able to show that the band gap of the perovskite powders can be tuned by changing the halide of the perovskite, in

agreement with reported results about mixed halide perovskite thin films. Further, I was able to demonstrate for the first time the successful defect passivation of perovskite powders by adding potassium iodide to the educts. The successful passivation was manifested in a significantly enhanced PL intensity and a slight shift of the band gap.

Forming a transition to the next part of the thesis, which is about using the optical properties to elucidate the film formation, Chapter 11 summarizes the most important optical properties of halide perovskites. I discuss related analyses and possible pitfalls in the context of *in situ* optical spectroscopy during the film formation. After summarizing technical approaches to *in situ* spectroscopy, the chapter continues with an overview of recent works, where *in situ* optical spectroscopy was performed during the film formations. It is distinguished between works, where the spectroscopy serves for the determination of timings during the film formation, and works, where the spectroscopy is used in a more elaborated way to understand the perovskite formation. Furthermore, perspectives on what should be addressed in future works are given. For example, not only the film formation of MAPbI₃, but also of perovskite with mixed stoichiometry, which are more relevant for solar cell application, should be addressed. Additionally, the role of intermediate solvent complex phases on the perovskite film formation should be investigated.

With the knowledge from Chapters 8-10 on the relationship of structural changes and the optical properties of halide properties, which is in part also summarized in Chapter 11, I investigated the film formation of halide perovskite thin films by measuring and understanding the *in situ* optical properties during the film processing. In Chapter 12, the synthesis of MAPbI₃ thin films using a two-step approach was monitored by optical *in situ* spectroscopy. In this study, it was possible to divide the film formation into five time ranges I-V based on the observed dynamics in PL and absorption. I analyzed the PL in range III and IV in terms of self-absorption, using the optical model that I derived in Chapter 8. I was able to show that in range III, the observed spectral changes can not be explained by self-absorption. This enabled the association of the narrowing of the PL with a dissolution of small perovskite grains showing quantum confinement, which in turn was explained by the formation and dissolution of a perovskite capping layer. In range IV, the observed spectral changes in the PL spectra could be indeed explained by self-absorption, and the film thickness extracted from my analysis matched well with the one extracted from absorption. Thus, my analysis was an important building block for the understanding of the film formation process.

While the synthesis of perovskite thin films using two-step spin coating is highly attractive on a lab scale to obtain high quality thin films reproducibly, the applicability of this method to upscalable techniques is limited. Therefore, Chapter 13 compares the one-step synthesis of MAPbI₃ thin films using spin and slot-die coating with the help of optical *in situ* spectroscopy. By varying the rotation speed of the spin coater for the case of spin coating, and the air pressure at an air knife installed next to the slot-die coater, the evaporation rate of the solvent

was systematically changed. By doing so, we achieved comparable durations of the film formation for both processing methods. Based on detailed analyses of the optical properties, we were able to identify that the main perovskite formation is significantly slowed down and delayed during spin coating as compared to slot-die coating. Additionally, the PL of the perovskite in the spin coated samples showed signatures of quantum confinement during the whole processing, which shows that the perovskite growth is spatially confined. We were able to associate these differences to different solvent complex structures, where the solvent complexes in the spin-coated samples showed very small crystal structures.

On a lab scale, the most relevant processing method to obtain high quality halide perovskite films leading to high efficiency solar cells is the solvent engineering method. The formation of a mixed stoichiometry perovskite using the solvent engineering method is investigated in Chapter 14. In this study, the temperature of the anti solvent was varied in order to control the wrinkling of the final perovskite film. Based on the optical *in situ* properties, I found that with higher temperature of the anti solvent, the perovskite layer formation happened faster, also resulting in thicker perovskite layers prior to annealing. Additionally, I was able to identify a change of the halide ratio during the film growth. By considering the PL peak shape, I was further able to distinguish the effect of changing halide ratio from the quantum confinement effect occurring at the beginning of the film formation.

To conclude, in this thesis, I investigated the relation between structural changes and the optical properties of halide perovskites in Chapters 8-10. I then used the gained knowledge to successfully elucidate the perovskite film formation for different relevant solution processing methods using *in situ* optical spectroscopy in Chapters 12-14.

6 Content of the Individual Publications

6.1 Double Peak Emission in Lead Halide Perovskites by Self-absorption

Chapter 8 deals with the origin of an additional PL feature (herein referred to as Peak 2) at lower energies compared to the commonly observed PL peak of lead halide perovskites (referred to as Peak 1). At the beginning of this work, the origin of this additional PL feature was under debate, as elaborated in more detail in Chapter 8. I measured the temperature-dependent PL of perovskite crystals with different stoichiometry. Figure 6.1a shows the PL of the different single crystals and of a MAPbI₃ thin film at 200 K. All samples showed double peak emission, which demonstrates that the appearance of Peak 2 is a general feature and not limited to MAPbI₃ or single crystals. However, for thin films, the additional feature is less pronounced and less separated from Peak 1. The temperature dependent PL of a MAPbI₃ single crystal is shown in Figure 6.1b. Both peaks became narrower and more intense upon cooling. Peak 1 shifted to lower energies, in accordance with the reported behavior of the band-gap upon cooling. In contrast, Peak 2 shifted in the opposite direction, i.e., to higher energies. The other samples showed a similar behavior. Apart from that, I noticed that the intensity of Peak 2 relative to the one of Peak 1 depends on the measurement geometry, such as on the alignment of the laser or on the position of the sample.

To investigate the origin of Peak 2 further, I systematically addressed the effects which were discussed in literature to cause Peak 2 by a combination of different optical experiments and optical modeling. I focused on single crystals of the well-studied material system MAPbI₃, if not stated otherwise.

One explanation of the origin of Peak 2 is that it is due to an indirect band-to-band transition coexisting with a direct transition, where the latter causes Peak 1. If an indirect band gap existed below the direct band gap, cooling would favor trapping of the charge carriers in the energetically lower valley of the conduction band, leading to an increase of the relative contribution of Peak 2 to the PL spectra. Additionally, the intensity of the PL with an indirect character, which is phonon-assisted should decrease at lower temperatures due to a thermal decrease of the phonon population. I was able to rule out an indirect band-gap as a cause for Peak 2 already from the temperature-dependent PL intensity, since the identical

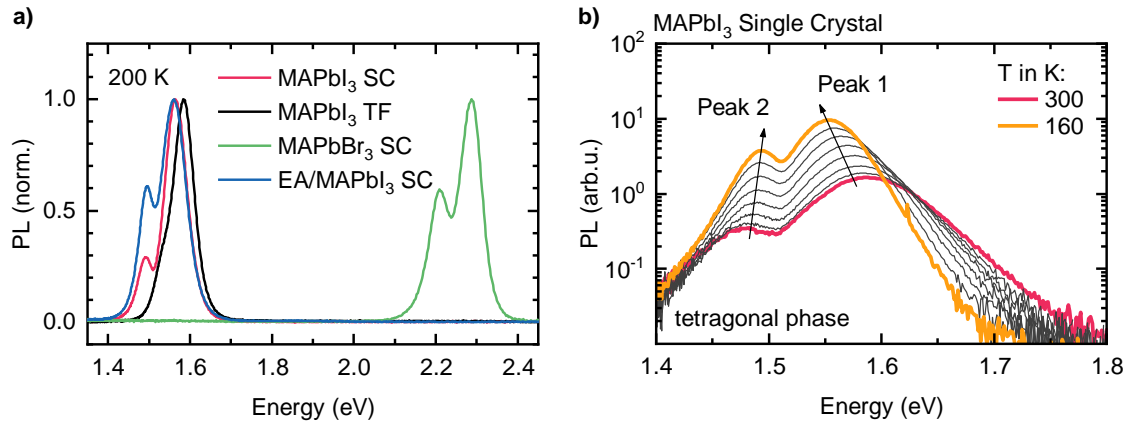


Figure 6.1: a) Normalized PL spectra of four different lead halide perovskite samples showing double peak emission. b) Temperature-dependent PL of a MAPbI₃ single crystal between 300 K (red) and 160 K (orange). Reproduced from Chapter 8.

increase of the PL intensity of Peak 1 and Peak 2 upon cooling is at variance with the expectation for an indirect transition competing with a direct transition.

As a next step, I addressed the role of defect states on causing Peak 2 with different experiments. I considered surface defects by measuring the PL before and after surface passivation of the single crystals with an electron donor (monothiophene) or an electron acceptor (benzothiadiazole). If Peak 2 was due to surface defects, it should vanish upon successful passivation. While the passivation with the acceptor had little effect on the PL, passivation with the electron donor led to a strong increase of Peak 1 and a slight increase of Peak 2. Thus, I excluded surface defects as a cause for Peak 2. Further, I considered defects in the bulk, which can be induced by strain, by comparing the evolution of the temperature-dependent PL of a MAPbI₃ thin film on a glass substrate with the one of a film on a PET substrate. Due to the difference in thermal expansion coefficient of MAPbI₃, glass and PET, cooling should induce larger strain in the glass sample than in the PET sample. Larger strain in the glass samples is underpinned by the tetragonal to orthorhombic phase transition being at lower temperatures and in a broader temperature range, in addition to a smaller shift of the PL peak upon cooling. I decomposed the PL spectra and considered the intensity of Peak 2 relative to Peak 1. Since the relative intensity evolves similarly with temperature for both samples, I excluded strain-induced defects as cause for Peak 2. I also addressed strain-independent defects in the bulk by fluence-dependent PL measurements of a MAPbI₃ single crystal. With increasing excitation fluence, defect-related PL intensity should saturate, i.e., its relative contribution to the overall PL should become less. As I observed the opposite behavior, I could also exclude strain-independent defects as cause for Peak 2.

Next, I investigated the influence of possible differences between surface and bulk. To do so, I performed 2-photon-induced (2PI) PL measurements, where I set the focus of the excitation

laser beam into the bulk of the perovskite crystal. By doing so, I excited only a volume in the bulk of the crystal and could obtain the PL from the bulk. By comparison with 1-photon-induced (1PI) PL, I realized that the 2PI-PL was nearly identical to Peak 2 of the 1PI-PL measurements concerning spectral position and shape. To answer if this similarity is due to differences in the electronic structure between surface and bulk or rather due to self-absorption, I measured temperature-dependent absorption of the single crystals. Due to the thickness of the samples, only a very small range of the absorption could be resolved within the limitations of the setup. Notably, this onset of absorption coincided with the dip between Peak 1 and Peak 2 in the PL spectra. Additionally, the temperature-evolution of the absorption revealed a shift to higher energies upon cooling, likewise the PL peak shift of Peak 2. By comparison with literature, it could be rationalized that the resolved absorption is far in the Urbach tail, even below the Urbach focus point. All together, this is a strong hint that Peak 2 is caused by self-absorption, and that optical path lengths in the material must be on the length scale of the sample size, i.e., on a mm-range.

Such long path length even in 1PI-PL are only possible if PL is internally reflected at the backside of the crystal. To investigate this hypothesis, I developed an optical model, which considers self-absorption of PL and multiple internal reflections. The reflection probability was estimated based on the refractive index of MAPbI_3 and the surrounding medium, that is air or helium. Within this model, I could reproduce the measured PL very well. Finally, I tested this hypothesis by another PL experiment: I added a drop of glycerin to the back of a single crystal. Since glycerin has a significantly higher refractive index than air, the reflection probability at this interface decreases significantly, which should therefore also decrease the contribution of Peak 2 in the PL. I measured PL before and after addition of glycerin and indeed observed a drop of the intensity of Peak 2. Finally, I also considered the change of reflection probability at the backside of the crystal by the addition of glycerin in my optical model, which reproduced the resulting PL spectrum very well. This is shown in Figure 6.2a. Based on all of my results, I concluded that Peak 2 is filtered PL, caused by self-absorption and strong internal reflections of the PL. Accordingly, the observed PL spectrum is a superposition of direct PL (Peak 1) and filtered PL (Peak 2), as shown in Figure 6.2b.

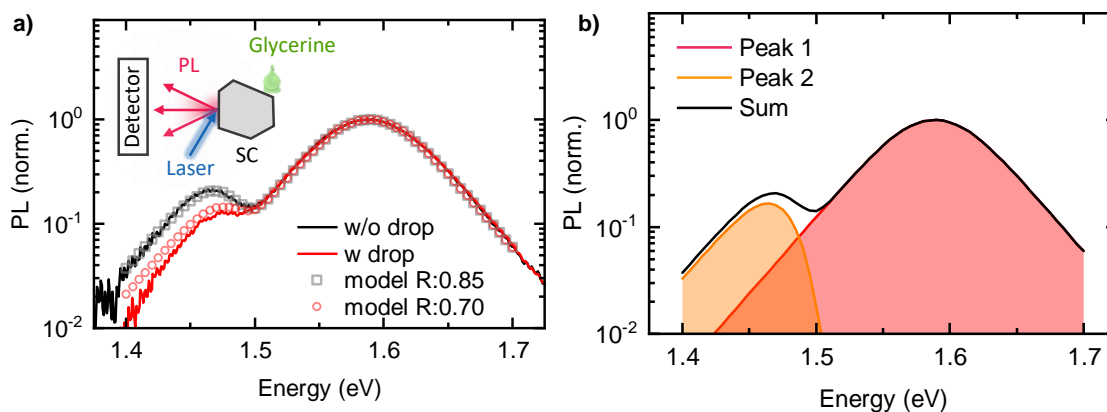


Figure 6.2: a) PL spectrum of a MAPbI₃ single crystal in air at room temperature (black solid line) together with the modeled PL considering perovskite air interfaces (black open squares). Also shown is the PL spectrum of the same crystal with a drop of glycerin at the back (red line), together with the modeled PL considering the perovskite glycerin interface at the back of the crystal (red open circles). b) Decomposition of the modeled PL into the contribution of the direct PL from the surface of the crystal and the filtered PL after self-absorption. Reproduced from Chapter 8.

6.2 Investigating the Tetragonal-to-Orthorhombic Phase Transition of Methylammonium Lead Iodide Single Crystals by Detailed Photoluminescence Analysis

Based on the knowledge gained in Chapter 8, I was now able to investigate structural phase transitions of perovskite single crystals in detail using PL measurements. In Chapter 9, I therefore induced structural changes in MAPbI₃ single crystals by changing the temperature from 200 K to 100 K, i.e., around the tetragonal to orthorhombic phase transition temperature. I measured PL in this temperature range and analyzed the PL with a modified version of the optical model from Chapter 8.

The PL during the phase transition can be complex as multiple emission peaks can occur, and the peak assignment is not always clear. In my PL measurements, I observed four different PL peaks in this temperature range, where one could be unambiguously identified as the PL of the orthorhombic phase, based on published studies on the PL of MAPbI₃. With the knowledge that I gained in Chapter 8, I was able to identify the contribution of filtered PL (i.e., an additional PL peak caused by self-absorption) experimentally. As I realized in my previous work that the relative contribution of the filtered PL to the PL spectrum depends on the setup geometry, e.g. on the laser spot position or on the angle of the sample with respect to the detection system, I recorded the PL during the phase transition in two geometries: one with pronounced filtered PL and one with strongly suppressed filtered PL in the tetragonal phase. Likewise the filtered PL in the tetragonal phase, two of the peaks during the phase

transition were strongly suppressed in the geometry with suppressed filtered PL. Thus, I tentatively associated these two PL peaks with filtered PL. Figure 6.3 shows the PL in the two geometries as well as their spectral difference for a) 160 K and b) 100 K.

To gain more insight, I modeled the PL spectra in the whole temperature range of the phase transition. To do so, I modified the optical model which I derived in Chapter 8 insofar that it can account for the coexistence of two different emitting species (e.g., co-existing tetragonal and orthorhombic phase). With that model, I was able to identify the four peaks to be tetragonal and orthorhombic PL, together with the filtered PL contributions of each phase. By using Equation 3.5 for the line shape of the PL instead of an empiric lineshape function, I was further able to extract the Urbach energies from fitting the PL data.

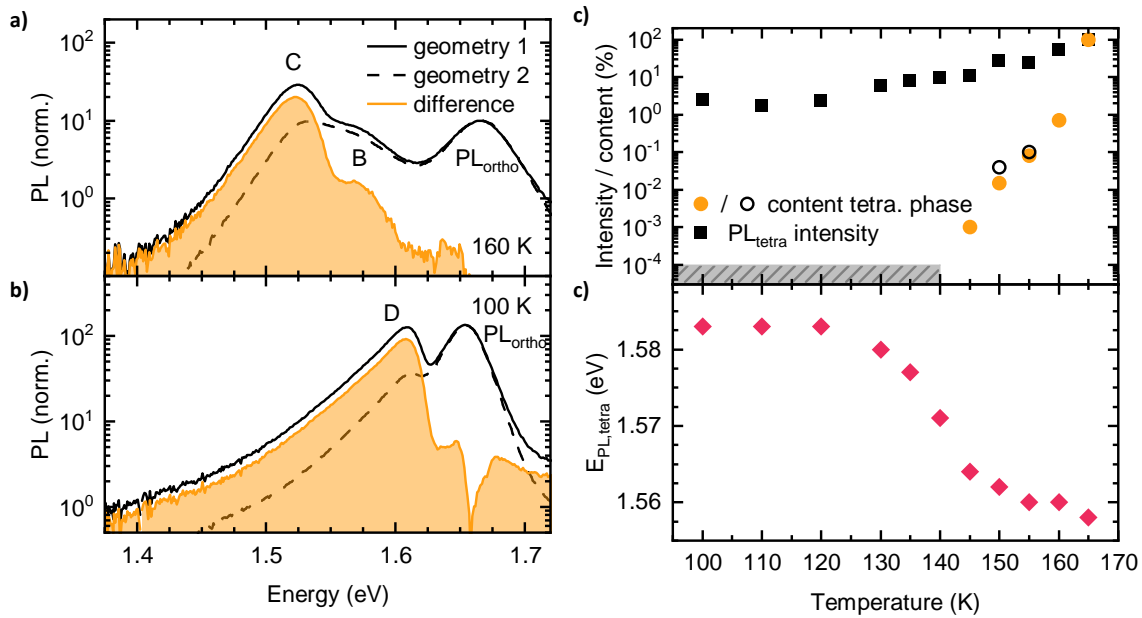


Figure 6.3: a,b) PL of a MAPbI₃ single crystal in a geometry with strongly (black solid) and weakly pronounced (black dashed) self-absorption effect, as well as the difference (orange) between both spectra at a) 160 K and b) 100 K. c) Intensity of the tetragonal PL normalized to the value at 165 K (black squares) together with the content of tetragonal phase in the crystal (orange circles) as a function of temperature. The content of tetragonal phase at 155 K and 150 K as extracted from transmission measurements on similar MAPbI₃ single crystals from Chapter 8 is also shown (open black circles). The grey shaded area indicates the upper limit of the content of tetragonal phase below 140 K. d) Temperature-dependence of the tetragonal PL peak position. Reproduced from Chapter 9.

One remarkable result of the fitting is that it strongly suggests that orthorhombic and tetragonal phase coexist down to about 120 K, although the sample is a (nominal) single crystal. The co-existence of tetragonal and orthorhombic phase is known for perovskite thin films, whereas the phase transition of single crystals was often assumed to be abrupt. Another result is that, while the content of tetragonal PL decreases by about five orders of

magnitude until 150 K, the relative tetragonal PL intensity only drops by about one order of magnitude until 150 K, and another order of magnitude until 120 K (see Figure 6.3c). This overproportionally strong tetragonal PL signal indicates an efficient energy transfer from the orthorhombic phase to the tetragonal inclusions. Thus, the latter can be seen as highly efficient traps for the charge carriers in the orthorhombic phase. The shift of the tetragonal PL peak position to higher energies between 150 K and 120 K (see Figure 6.3d) can be interpreted in the framework of quantum confinement. From doing so, it follows that the size of the tetragonal inclusions is below the confinement limit, i.e., around 7-15 nm. In combination with the obtained content of tetragonal phase and under the assumption that the tetragonal inclusions are evenly distributed throughout the bulk, I estimated the density of tetragonal inclusions to be about $3 \cdot 10^{12} \text{ cm}^{-3}$ at 145 K. By considering the extracted Urbach energies, I observed that while the contribution of thermal disorder to the Urbach energy seems to be identical for the orthorhombic and the pure tetragonal phase, the tetragonal inclusions show an enhanced Urbach energy at temperatures below the phase transition temperature. This indicates that the tetragonal inclusions are structurally distorted by the orthorhombic lattice.

With the understanding of the effect of self-absorption on the PL and associated optical modeling, I was able to investigate the tetragonal to orthorhombic phase transition in great detail. The coexistence of structurally different phases and the efficient trapping of charge carriers by such structurally different inclusions is also a relevant aspect for perovskites with mixed stoichiometries. In such systems, the role of structural homogeneity and its influence on the optoelectronic properties is not completely clear.

6.3 High Versatility and Stability of Mechanochemically Synthesized Halide Perovskite Powders for Optoelectronic Devices

With the knowledge of the relationship of structural changes and optical properties of perovskite single crystals that I gained in Chapters 8 and 9, I investigated perovskite powders in Chapter 10. I was interested in whether the optical properties of perovskite powders deviate from their single crystal and thin film counterparts. Perovskite powders are interesting since their synthesis is easily upscalable, and they are used for thick layer applications, such as X-ray detectors. Since for the application as X-ray detector, a low defect density of the perovskite is desirable, I also wanted to investigate whether defect passivation strategies for perovskite thin films can be adapted to perovskite powders.

The perovskite powders for Chapter 10 were synthesized by ball milling and characterized by XRD and SEM measurements. The influence of milling time and educt grain size were

investigated. A smaller reagent grain size lead to a shorter minimum milling time for a complete conversion to the perovskite phase. Longer milling times lead to smaller agglomerate sizes as well as smaller primary particle sizes. MAPbI₃ powder was stored for two and a half years in a dry and inert atmosphere, without showing any signs of degradation, demonstrating intrinsic stability of the material.

The versatility of the mechanochemical synthesis was demonstrated by synthesizing perovskites with mixed stoichiometry. I characterized the powders with optical spectroscopy. Since it is not trivial to obtain dense layers of perovskite powders, that are thin enough for measuring absorption in a light transmission setup, I chose to measure the diffuse reflectance of the perovskite powders. From the reflection data, I calculated the Kubelka-Munk function $F(R) = (1 - R)^2/2R$ with R being the reflectance. For comparison with reported band gap energies, I estimated the band gap energy of the powders by a tauc plot, where $\sqrt{F(R)E}$ is plotted against the photon energy. Although the use of a tauc plot neglects the influence of excitonic contributions to the absorption spectrum (see Chapter 3.1), it is sufficient for a comparison with reported band gap energies, if those energies were also estimated using tauc plots. Additionally to the reflectance measurements and band gap extraction, I also measured the PL of the powders. Since measured and reported band gap energies and PL peak positions match nicely for all investigated stoichiometries, I was able to show that the band gap of perovskite powders can be tuned by changing the feed in ratio of the educts in the ball milling process.

I also wanted to test whether it is possible to passivate the powders during the synthesis. For that purpose and inspired by a recent report, potassium iodide (KI) was added to the reactants for the synthesis of (FAPbI₃)_{0.85}(MAPbBr₃)_{0.15} and (Cs_{0.05}FA_{0.95}PbI₃)_{0.85}(MAPbBr₃)_{0.15}. With the knowledge that I gained in my passivation experiments in Chapter 8, I associated the significantly increased PL intensity of the perovskite powders containing KI with a successful defect passivation (see Figure 6.4). This was the first demonstration of the possibility to passivate perovskite powders that are produced by mechanochemistry.

To test the applicability of perovskite powders in opto-electronic devices, different powders were pressed to pellets and photo-current measurements were conducted, where all samples showed a clear photo-response. Additionally, for the use in perovskite solar cells, mechanochemically synthesized powders were dissolved for solution-processing of perovskite thin films by spin-coating. By this, highly uniform films were obtained, and the effect of KI passivation was also seen in improved solar cell performances and a reduced hysteresis effect.

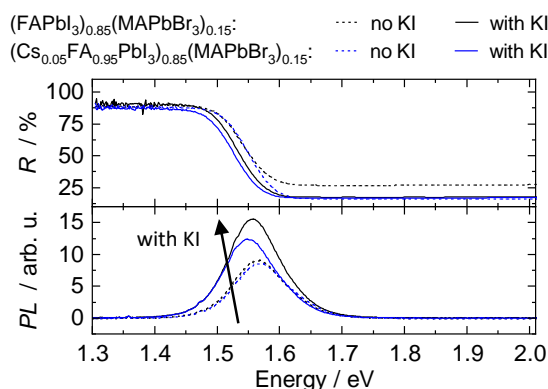


Figure 6.4: Reflectance (top) and PL spectra (bottom) of the pure (dashed line) and KI passivated perovskite powders (solid line). Reproduced from Chapter 10.

6.4 Using *In Situ* Optical Spectroscopy to Elucidate Film Formation of Metal Halide Perovskites

Optical spectroscopy is a very useful tool to study and to understand the thin film formation of halide perovskites. However, to gain proper insights into the film formation from *in situ* optical spectroscopy, a detailed knowledge of the relationship of optical properties and structural changes in the perovskite, like the one I gained in Chapters 8-10, is crucial. Therefore, Chapter 11 deals with how *in situ* optical spectroscopy can be used and was used so far to investigate the film formation of metal halide perovskites.

First, I summarized the optical properties of halide perovskite, which are relevant for the *in situ* optical spectroscopy and set them in context with the film formation. Here, I also included some of my results and much of the knowledge I gained from Chapters 8-10. The section starts with the spectral shape of absorption and PL, and continues with the relation of the quasi-Fermi-level splitting and the PL quantum efficiency (PLQY). I briefly addressed the importance of the knowledge of the charge carrier density when measuring and comparing PLQY of different samples. After discussing the material-specific optical properties, I focus on optical properties that depend on the structure of the sample. These contain the signature of white light interference, e.g., at a thin solvent layer, in the absorption spectra, the influence of incomplete substrate coverage on the absorption spectra, the influence of self-absorption on PL as observed in Chapter 8 and 9, and the effect of quantum confinement on the PL, as also observed in Chapter 9. Additionally, I briefly discuss the effect of stoichiometry on the band gap of the perovskite, as also observed in Chapter 10

The chapter continues with a section on the technical approaches for performing *in situ* optical spectroscopy. This section also considers the detection and excitation system used in Chapters 12-14. Limitations of the different approaches, related to the temporal resolution that is required to monitor the film formation, are also discussed.

In the next section of Chapter 11, a summary of how *in situ* optical spectroscopy is used to track and understand the film formation of halide perovskites is presented. This summary is grouped in works where the *in situ* spectroscopy is used to determine timings in the film formation, e.g. an optimum annealing time, and works where one or more optical properties are monitored and analyzed to gain deeper insight into the film formation. Here, also some of the optical properties and related analyses that are discussed in the beginning of Chapter 11 are used, and Chapter 12 is included in the summary of recent works as well.

After presenting the state of the art of the usage of *in situ* optical spectroscopy to study the film formation, the chapter closes with giving some future prospects, i.e., aspects that should be addressed in the future. These contain the investigation of more complex material systems, i.e., systems with complex stoichiometry, and the consideration of the role of solvent complex phases on the perovskite formation. The film formation of a perovskite with complex stoichiometry is investigated using *in situ* optical spectroscopy in Chapter 14, and Chapter 13 addresses the role of the solvent complex phase on the perovskite formation in spin and slot-die coating.

6.5 Investigating two-step MAPbI₃ Thin Film Formation during Spin Coating by Simultaneous *In Situ* Absorption and Photoluminescence Spectroscopy

Having understood the steady state optical properties of different perovskite samples in Chapters 8-10, I now used this knowledge for investigating the film formation of halide perovskites by *in situ* optical spectroscopy. A method for reliably obtaining perovskite films of good quality is the two-step method (cf. Chapter 4.1). Therefore, the film formation of MAPbI₃ upon spin-coating using the two-step method is investigated by *in situ* optical spectroscopy in Chapter 12.

In this work, the two-step method was realized by dropping a MAI solution onto an annealed PbI₂ layer. PL and absorption spectra were recorded quasi-simultaneously with the home-built setup that is also described in Chapter 11, with a frequency of 11 Hz, ensuring a sufficient temporal resolution to monitor the film formation. Based on the evolution of PL, which is shown in Figure 6.5, and absorption during the spin-coating process, five different time ranges were identified.

In time range I (Figure 6.5, top panel), that is within the first 1.4 seconds after addition of the MAI solution, there was already PL of the MAPbI₃ phase detectable, but at higher energies than expected for the bulk PL and additionally, the PL peak was asymmetrically broadened. The PL peak quickly shifted to lower energies during range I. No signatures of absorption of MAPbI₃ were visible in this time range. The fast shift of the PL during range I

was associated with a decreasing quantum confinement effect due to the growth of small perovskite crystallites. In this framework, also the evolution of the crystal size and a crystal growth rate could be calculated. The determined crystal size at the end of time range I nicely connects to the one extracted from the OD in the next time range. This indicates the formation of a dense perovskite layer which is monocrystalline in the vertical direction.

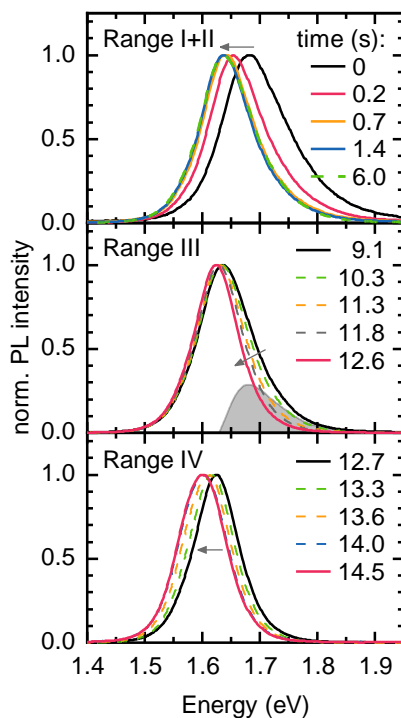


Figure 6.5: Evolution of PL during two-step spin coating. Top: normalized PL within the first 1.4 s (range I) and at 6.0 s (during range II). Middle: normalized PL from 9.1 s (black line) to 12.6 s (red line) (range III). The difference between the spectra at 9.1 s and 12.6 s is shown in grey. Bottom: normalized PL from 12.7 s to 14.5 s (range IV). Reproduced from Chapter 12.

During the following time range II, which extends to about 9 seconds after the addition of MAI, the PL and absorption remained constant. This is a result of the formation of the thin MAPbI_3 capping layer on top of the PbI_2 layer in time range I, hindering the MAI solution to penetrate the PbI_2 layer and thus suppressing further perovskite formation during range II. In range III (Figure 6.5, middle panel), ending at about 12 seconds, the PL became narrower on the high energy edge, while peak position and low energy edge remained constant. Since the high energy edge of the PL overlaps spectrally with the absorption spectrum, such a change of the spectral shape of the PL could in principle be caused by self-absorption. To test this hypothesis, I applied the optical model that I developed in Chapter 8 to the experimental data. Since the qualitative behavior of the PL spectra could not be reproduced assuming self-absorption effects, I was able to show that the observed PL behavior during range III

was not caused by self-absorption. This suggested that the changes in PL line shape were due to a decreasing number of quantum-confined grains. Since the difference spectra, i.e., the spectral difference between PL during range III and at the end of range III, did not change their shape, it was inferred that the MAPbI₃ capping layer dissolved during this time range. In range IV (Figure 6.5, bottom panel), the absorption of the perovskite increased drastically, and concomitantly, the PL shifted to lower energies and the relative PLQY decreased, both following nicely the increase in absorption. Using my model from Chapter 8, I was able to associate this peak shift to a self-absorption effect. By fitting the modeled PL to the experimental PL data, I extracted the evolution of the perovskite layer thickness. The resulting values agreed nicely with the film thickness extracted from the optical density. Based on the increase of the absorption, a fast perovskite growth rate of 445 nm s⁻¹ was estimated.

After about 15 seconds (start of range V), the film formation appeared to be finished, as no further changes in the optical properties occur. In this study, the simultaneous consideration of PL and absorption, in combination with detailed analyses, enabled the development of a complete and detailed picture of the film formation processes.

6.6 Understanding Differences in Crystallization Kinetics Between Slot-Die Coating and Spin Coating of MAPbI₃ Using Multimodal *In Situ* Optical Spectroscopy

The two-step method investigated in Chapter 12 offers good control over the perovskite film formation and is well suited for obtaining high quality thin films on a laboratory scale. However, for large scale fabrication of perovskite thin films, e.g., with roll-to-roll printing techniques, the conceptionally more simple one-step processing is more relevant. Therefore, I now wanted to investigate the perovskite formation upon one-step processing. Additionally, large-scale processing is not possible using spin coating but using printing techniques such as slot-die coating. It is generally observed that devices processed with printing techniques tend to show a lower device efficiency than comparable spin coated devices. This efficiency loss is associated with differences in the final perovskite layer properties. However, the reason for these differences is not completely understood by now.

To contribute to this understanding, we used *in situ* optical spectroscopy for investigating and comparing the formation of MAPbI₃ thin films in an one-step synthesis using spin coating and slot-die coating in Chapter 13. To obtain comparable duration of the film formation for both processes, we varied the evaporation rate of the solvent by changing the rotation speed of the spin-coater and the air-pressure at an air knife next to the slot-die coater.

In this study, we were also interested in the role of the solvent complex phase in the film

formation, which often forms prior to the perovskite phase during one-step processing, thereby addressing one of the future prospects elaborated in Chapter 11. These solvent complexes, from which the perovskite phase forms by removal of the solvent molecules, are optically inactive. However, since they form crystalline structures on a length scale of several nanometer to micrometer, they scatter light. Accordingly, for monitoring the complex phase formation, we also recorded the light of an external LED (referred to as scatter-LED), that is scattered at the sample in the case of spin coating. For slot-die coating, the room light was used instead of the scatter-LED due to practical reasons.

In the first part of Chapter 13, the recorded *in situ* data during spin coating are presented and our analysis approaches are explained. We extracted the temporal evolution of the PL peak position, as well as the PL peak width, the OD at 1.8 eV (i.e., above the band gap of MAPbI₃; referred to as OD_{1.8 eV}) and the integrated intensity of the scatter-LED ($I_{Scatter}$). To separate the contributions of scattering and absorption to the OD_{1.8 eV}, I subtracted the OD at 1.575 eV, which is below the band gap of MAPbI₃ and thus only contains contributions from light scattering, from OD_{1.8 eV}. This difference is referred to as ΔOD and it is a measure for the absorption of the perovskite. The time evolution of these parameters is shown for selected spin speeds in Figure 6.6a-d.

Based on the temporal evolution of these optical properties, which is qualitatively identical for all rotation speeds, we identified three formation phases. First, the solvent complex phase forms, which is followed by a first, short perovskite crystallization (referred to as $pero_1$), and a second, slower perovskite crystallization ($pero_2$). For describing the phase formations in a quantitative manner, I extracted critical times and temporal widths of the different phase formations from the temporal evolution of the different optical properties, similar to the approach in Chapter 12. This is also shown for the spin speed of 2000 rpm in Figure 6.6f-h. To gain more details about the perovskite crystallization kinetics, I calculated average grain sizes of the perovskite grains from the PL peak position and estimated perovskite growth rates based on my experiences with quantum confinement from Chapters 9-12. The evolution of the calculated average grain size is shown in Figure 6.6e. Here, I found a significant reduction of the growth rate at the transition from the $pero_1$ to the $pero_2$ formation. This indicates that during the $pero_2$ formation, the perovskite growth is slowed down in at least one spatial direction before outgrowing the quantum confinement limit of about 20 nm.

As a function of spin speed, we found that critical times and width of the individual transitions decrease and the determined perovskite growth rates increase with increasing spin speed.

To investigate possible spatial limitations for the growth of the complex phase, I calculated the thickness of the solvent layer based on the spectral signatures of white light interference, which we observed in the OD prior to the complex phase formation. There, I found that the solvent layer thickness decreases rapidly to about 1 μm just before the formation of the complex phase.

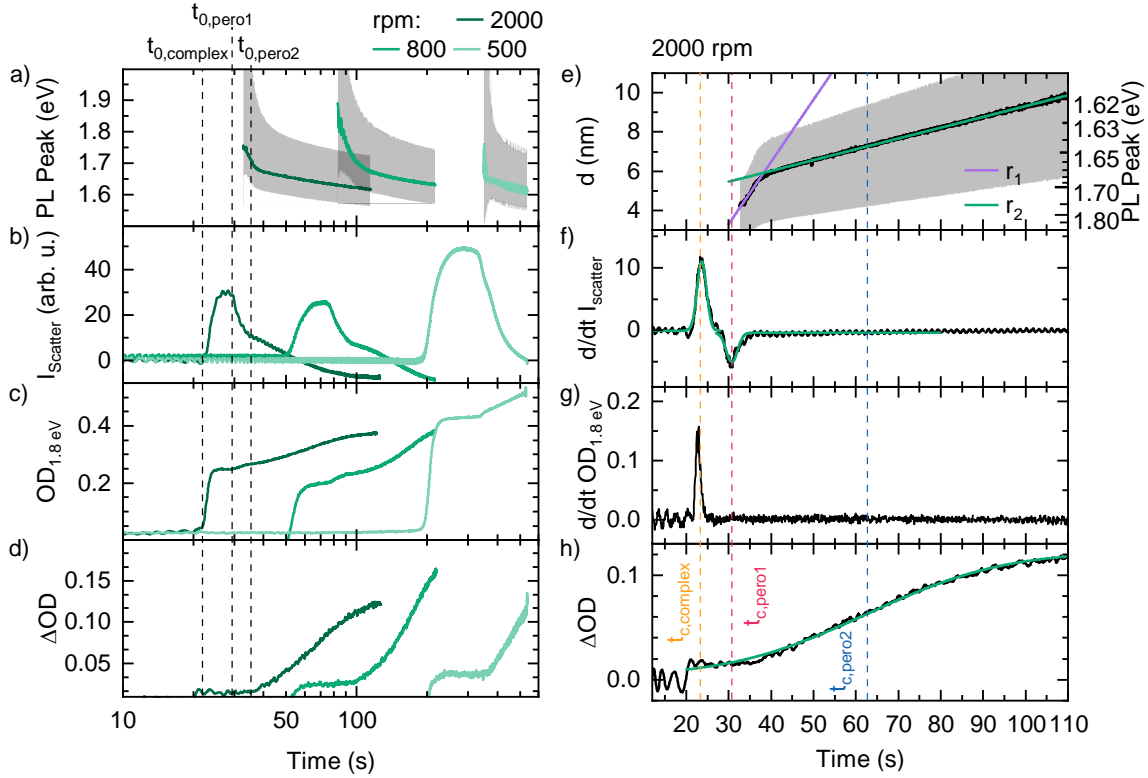


Figure 6.6: a-d) Time evolution of different optical parameters for spin coating with spin speeds of 2000 rpm (dark green), 800 rpm (green) and 500 rpm (light green). a) PL peak position, with the grey shaded area indicating the spectral range where the PL intensity is above 1/e of the peak intensity. b) Integrated intensity of the Scatter-LED, $I_{Scatter}$. c) OD at 1.8 eV. d) ΔOD , i.e. the difference of the OD at 1.8 eV and at 1.575 eV. Vertical dashed lines indicate the onsets t_0 of the different crystallization processes. e-h) analyses of the optical parameters for spin coating at 2000 rpm. e) Average crystallite size determined from the PL peak position. f) The derivative of $I_{Scatter}$. g) The derivative of $OD_{1.8eV}$ and h) ΔOD together with fits (green lines) as for extracting critical times and temporal widths. Dashed vertical lines indicate the critical times t_c of the different crystallization processes. Reproduced from Chapter 13.

In the next part of Chapter 13, we present and analyze the *in situ* optical properties of the MAPbI₃ films slot-die coated with different air pressures at the air knife analogously to the data of the spin coated films. In contrast to spin coating, we did not observe any signatures of white light interference in the spectra taken during slot-die coating, indicating that the solvent layer is significantly thicker prior to the solvent complex phase formation. Additionally, we observe only one perovskite formation, and the PL peak position saturates quickly at the PL peak position of bulk MAPbI₃, indicating that the perovskite domains outgrow the confinement limit fast. With increasing air pressure at the air knife, we found that critical times and widths decrease, while the growth rate determined from the PL peak shift increases.

A challenging step was now to compare the film formation dynamics for both processing

methods in a quantitative way. After careful consideration of the different extracted quantities, we found that it is most suitable to display the film formation kinetics as a function of the temporal width of the complex phase formation $w_{complex}$. Considering Δt_c , which is the difference of the critical times t_c of the perovskite formation and the solvent complex phase formation, and the temporal width of the perovskite formation w_{pero} as a function of $w_{complex}$, we found that the perovskite formation observed during slot-die coating behaves similar to the $pero_1$ formation during spin coating. Additionally, the perovskite growth rates extracted from the PL peak shift during the $pero_1$ formation and at the beginning of the perovskite formation upon slot-die coating match nicely for similar $w_{complex}$. In contrast, the $pero_2$ formation occurs significantly delayed and slower, as inferred from Δt_c , w_{pero2} and the extracted growth rates.

All the results indicate that the $pero_1$ crystallization is similar to the perovskite crystallization during slot-die coating, while the $pero_2$ formation is spatially restricted and slowed down. To find the cause for the hindered $pero_2$ formation, we recorded optical microscopy and SEM images of different films. Microscopy images of as cast films with similar $w_{complex}$ show a flatter morphology in the case of spin coating than for slot-die coating. SEM images further revealed that the solvent complex structures of spin coated films show many small grains on the scale of tens of nanometer, while naturally dried films showed solvent complex structures with crystal sizes in the micrometer range.

Based on our results, we could propose the following processes during film formation, which are also sketched in Figure 6.7. The complex phase formation starts identically for both processing methods. However, due to the lower solvent level in case of spin coating, the complex phase is spatially confined to a flat morphology, as evidenced by microscopy images. This leads to overall smaller grain sizes on the scale of the quantum confinement limit of $MAPbI_3$, as can be seen from SEM images. In case of slot-die coating (with the conditions used in our experiments), the complex phase is not limited significantly by the solvent level, resulting in larger grains. When the perovskite phase starts to form in the complex phase, it can initially grow freely for both processing methods. However, in case of spin coating, as soon as the perovskite phase reaches a grain boundary of the complex phase, the perovskite growth is significantly slowed down in this spatial direction. This can be seen from the persisting quantum confinement effect in the PL spectra, the reduced growth rate and the larger width of the $pero_2$ formation.

In summary, based on the detailed analyses of the multimodal optical *in situ* spectroscopy, we were able to draw a complete picture on the different crystallization behaviors during spin and slot-die coating.

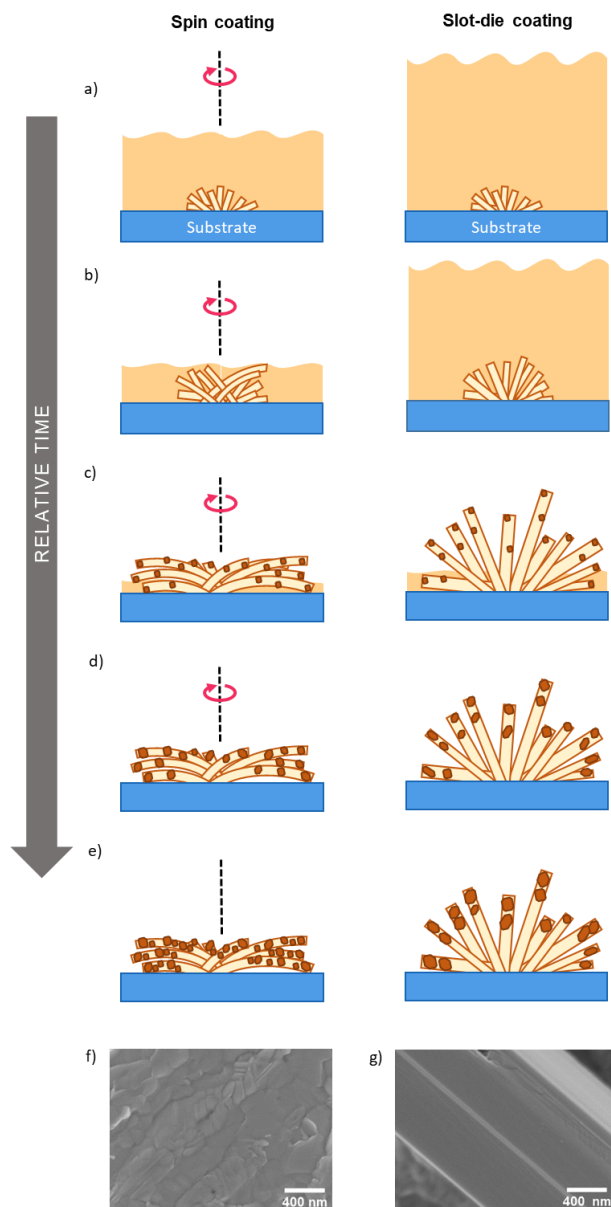


Figure 6.7: a–e) Illustration of the crystallization processes occurring during spin coating (left) and slot-die coating (right) on a relative time axis, which is normalized to the duration of the complex phase formation. Precursor solution is depicted in yellow, solvent-complexes in beige and perovskite nuclei in brown. f,g) SEM images f) of a spin-coated MAPbI₃ thin film and g) of a film obtained by drop casting. Reproduced from Chapter 13.

6.7 How Antisolvent Miscibility Affects Perovskite Film Wrinkling and Photovoltaic Properties

In Chapter 12 and 13, the film formation of the model system MAPbI_3 with the very controllable two-step method and with the upscalable one-step method was investigated. However, on a lab-scale, record efficiencies of perovskite solar cells are achieved when the perovskite films are fabricated using the solvent engineering method. Additionally, for such record efficiencies, typically perovskites with mixed stoichiometry, such as $(\text{FAPbI}_3)_{0.875}(\text{CsPbBr}_3)_{0.125}$, are used. Such perovskite films sometimes show a wrinkled morphology, where the cause and the role of this wrinkled surface structure for the optoelectronic properties of the perovskite is not clear. Additionally, the influence of the mixed stoichiometry on the film formation dynamics have rarely been investigated, as stated in Chapter 11. Therefore, the film formation of $(\text{FAPbI}_3)_{0.875}(\text{CsPbBr}_3)_{0.125}$ using the solvent engineering method is investigated by *in situ* optical spectroscopy in Chapter 14.

To study the film wrinkling in detail, the chapter starts with a systematic investigation of the influence of the temperature of the substrate, the temperature of the anti solvent and the stoichiometry of the perovskite on the film morphology after spin coating. It was found that amplitude and characteristic periodicity of the wrinkling depend on the combination of these parameters, where some combinations do not lead to a wrinkled morphology at all. The film wrinkling was explained in terms of stress relaxation in a bi-layer system, which forms due to the limited miscibility and different density of the solvent and the anti solvent. The bi-layer system comprises an elastic perovskite top layer, which forms upon addition of the anti solvent. This top layer caps a viscoelastic bottom layer consisting mainly of the solvent and perovskite precursors.

The formation and the influence of the wrinkling on the optoelectronic properties were investigated in more detail for $(\text{FAPbI}_3)_{0.875}(\text{CsPbBr}_3)_{0.125}$ and a substrate temperature of 15 °C. The film formation during spin coating was monitored using *in situ* PL and absorption measurements for different temperatures of the anti solvent. The evolution of the perovskite layer thickness during spin coating (see Figure 6.8a) calculated on the basis of the *in situ* absorption data revealed that with decreasing temperature of the anti solvent, the perovskite layer growth became slower and the layer thickness after spin coating became smaller. Based on the PL peak shift, the PL peak width and the shift of the absorption during the perovskite growth (see Figure 6.8b for the temperature of the anti solvent of 30 °C), I identified that at the beginning of the film formation, small perovskite crystallites formed, which show signatures of quantum confinement, similar to the results in Chapter 12 and 13. For later times of the spin coating, I found that the stoichiometry changed during the film formation, where the ratio of incorporated bromine to iodine decreased, i.e., iodine tended to be incorporated more slowly into the perovskite than bromine. Based on my experience with perovskites

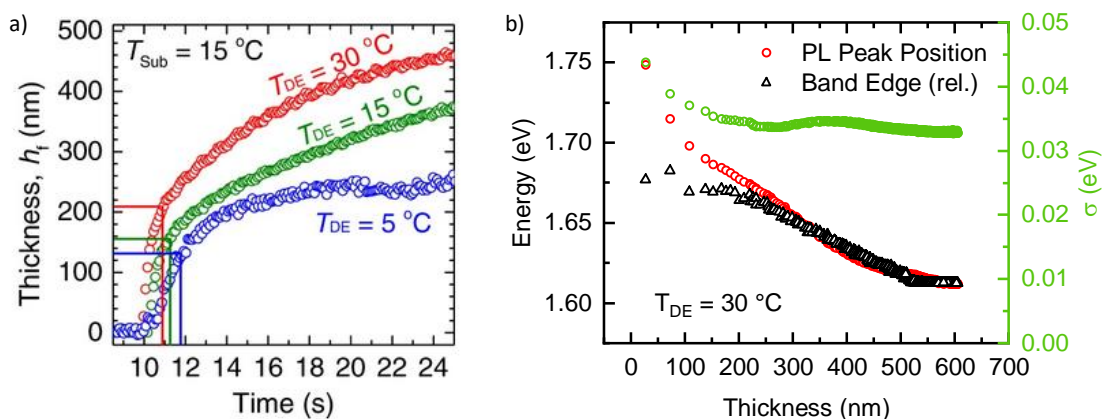


Figure 6.8: a) The evolution of the perovskite layer thickness during spin coating, calculated from the measured absorption data. b) PL peak position (red circles), PL peak width σ (green circles), and band edge energy (black triangles) as a function of perovskite layer thickness during spin coating for a temperature of 30°C of the anti solvent. For comparison, the evolution of the band edge energy was shifted in energy to match the final PL peak position. Reproduced from Chapter 14.

with mixed stoichiometry from Chapter 10, I was able to quantify this change of the halide ratio. Likewise the evolution of the film thickness, the observed dynamics of the quantum confinement and the change in stoichiometry became slower with decreasing temperature of the anti solvent.

As a next step, the role of the wrinkling on solar cell performance was investigated, where it was found that more pronounced wrinkling lead to enhanced V_{OC} and fill factor (FF). To understand the improvement of the device performance, photocurrent atomic force microscopy (pc-AFM) were measured. In the wrinkle morphology, hill sides exhibited higher photo current than valley sides and than the flat morphology. Since it could be excluded that the higher photo current was due to a higher film thickness, the increased photocurrent was explained by improved charge carrier transport, i.e., an increased charge carrier diffusion length. In search of the origin of this improvement, spatially resolved and time resolved PL was measured on hill and valley sides of perovskite films on a glass substrate. I supported the analysis of the time resolved PL data in terms of discussing the theoretical background of the transient PL in halide perovskites, and contributed to the interpretation of the results. We found that at the top of the layer, hill sides exhibited longer monomolecular lifetimes than valley sides, and that lifetimes increased with increasing wrinkling. Additionally, the change of average carrier lifetime between hill and valley for the different temperatures of the anti solvent matched nicely the corresponding observed change in photo current. Overall, this indicates that the hill sides show less defect density than valley sides and that the overall defect density decreases with increased wrinkling. The reduced defect density is consistent with the proposed stress relaxation upon film wrinkling.

6.8 Authors' Contribution

Double Peak Emission in Lead Halide Perovskites by Self-absorption

This work is published in *Journal of Materials Chemistry C*, **2020**, 8 (7), 2289-2300 and reprinted in Chapter 8. The authors are:

Konstantin Schötz, Abdelrahman M. Askar, Wei Peng, Dominik Seeberger, Tanaji P. Gujar, Mukundan Thelakkat, Anna Köhler, Sven Huettner, Osman M. Bakr, Karthik Shankar and Fabian Panzer.

FP initiated, and planned the project. KoS performed all optical characterizations and derived the optical model. FP, AK and KoS discussed the project. AMA synthesized the MAPbI₃ single crystals under supervision of KaS. WP synthesized the EAMAPbI₃ single crystals under supervision of OMB. DS synthesized the MAPbBr₃ single crystals under supervision of SH. TG produced the MAPbI₃ thin films under the supervision of MT. FP and KoS wrote the manuscript which was revised by all authors. FP supervised the project.

Investigating the Tetragonal-to-Orthorhombic Phase Transition of Methylammonium Lead Iodide Single Crystals by Detailed Photoluminescence Analysis

This work is published in *Advanced Optical Materials*, **2020**, 8 (17), 2000455 and reprinted in Chapter 9. The authors are:

Konstantin Schötz, Abdelrahman M. Askar, Anna Köhler, Karthik Shankar, Fabian Panzer.

I performed and analyzed all experiments, interpreted the data, refined the optical model and performed the optical modelling. Abdelrahman M. Askar synthesized the single crystals under the supervision of Karthik Shankar. Fabian Panzer, Anna Köhler and I discussed the results. Fabian Panzer and I wrote the manuscript. Anna Köhler edited the manuscript. All authors critically read the manuscript. Fabian Panzer supervised the project.

High Versatility and Stability of Mechanochemically Synthesized Halide Perovskite Powders for Optoelectronic Devices

This work is published in *ACS Applied Materials & Interfaces*, **2019**, 11 (33), 30259-30268 and reprinted in Chapter 10. The authors are:

Nico Leupold, **Konstantin Schötz**, Stefania Cacovich, Irene Bauer, Maximilian Schultz, Monika Daubinger, Leah Kaiser, Amelle Rebai, Jean Rousset, Anna Köhler, Philip Schulz, Ralf Moos, Fabian Panzer.

Fabian Panzer initiated, discussed and planned the experiments and project. Nico Leupold, Monika Daubinger and Leah Kaiser performed the mechanochemical synthesis of the powders under supervision of Ralf Moos. Nico Leupold and Leah Kaiser characterized the powders. Irene Bauer synthesized and characterized the organic precursors. Nico Leupold and Maximilian Schulz pressed the pellets from the powders and measured the photoresponse. I conducted the optical characterizations of the powders. Stefania Cacovich, Amelle Rebai and Jean Rousset fabricated and characterized the solar cell devices under the supervision of Philip Schulz. Nico Leupold, Fabian Panzer, Philip Schulz and I wrote the manuscript, which was revised by all authors. Anna Köhler edited the manuscript. Fabian Panzer supervised the project.

Using *In Situ* Optical Spectroscopy to Elucidate Film Formation of Metal Halide Perovskites

This perspective article is published in *Journal of Physical Chemistry A*, **2021**, 125 (11), 2209-2225 and reprinted in Chapter 11. The authors are:

Konstantin Schötz, Fabian Panzer

Fabian Panzer initiated and outlined the perspective article. We searched and discussed the literature together. I wrote Section 2, Section 4.1 and the first half of Section 4.3. I elucidated the connections between the different works and elaborated some of the future prospects for the field of *in situ* spectroscopy outlined in Section 5. Fabian Panzer wrote Section 3, Section 4.2 and the second half of Section 4.3. We worked together on Sections 1 and 5. We discussed and revised the manuscript together.

Investigating Two-Step MAPbI₃ Thin Film Formation during Spin Coating by Simultaneous *in situ* Absorption and Photoluminescence Spectroscopy

This work is published in *The Journal of Materials Chemistry A*, **2020**, 8 (10), 5086-5094 and reprinted in Chapter 12. The authors are:

Mihirsingh Chauhan[#], Yu Zhong[#], **Konstantin Schötz**, Brijesh Tripathi, Anna Köhler, Sven Hüttner, Fabian Panzer. [#] Authors contributed equally.

Yu Zhong and Mihirsinh Chauhan prepared the samples and performed the in-situ measurements. Mihirsingh Chauhan defined the different time ranges supervised by Fabian Panzer, and analyzed absorption data and the confinement effect in the PL spectra. Yu Zhong analyzed the absorption data in range III and performed SEM and XRD analysis of the samples. I investigated the influence of self-absorption on the PL spectra in range III and IV, and fitted the PL in range IV by optical modelling. Mihirsingh Chauhan, Yu Zhong, Fabian Panzer and I wrote the manuscript. Brijesh Tripathi, Anna Köhler and Sven Huettner critically read and edited the manuscript. Fabian Panzer supervised the project.

Understanding Differences in Crystallization Kinetics Between Slot-Die Coating and Spin Coating of MAPbI₃ using multimodal *in situ* Optical Spectroscopy

This work is submitted to *Advanced Optical Materials* and reprinted in Chapter 13. The authors are:

Konstantin Schötz[#], Christopher Greve[#], Arjan Langen, Harrie Gorter, Ilker Dogan, Yulia Galagan, Albert J.J.M. Breemen, Germin H. Gelinck, Eva M. Herzig, Fabian Panzer. [#] Authors contributed equally.

Christopher Greve and I recorded the in situ optical properties during spin coating. Fabian Panzer and Arjan Langen performed the slot-die coating experiments. Harrie Gorter and Ilker Dogan prepared the stock solutions for the slot-die coating. Christopher Greve performed one part of the analyses of the optical data, that is: fitting of the PL, extraction of $I_{Scatter}$, fitting of the interference pattern in the absorption spectra. I extracted the temporal evolution of the $OD_{1.8eV}$ and calculated the ΔOD . I characterized the phase formations and extracted the corresponding critical times and widths, and I analyzed the PL fits in the framework of quantum confinement. Christopher Greve performed and analyzed the microscopy and SEM

measurements, as well as profilometry measurements. Christopher Greve, Fabian Panzer and I discussed and developed the concept of comparing the film formation dynamics of spin coating and slot-die coating with respect to the temporal width of the complex phase formation. Albert van Breemen, Gerwin Gelinck, Yulia Galagan, Ilker Dogan and Eva M. Herzig discussed the results. Christopher Greve, Fabian Panzer, Eva M. Herzig and I wrote the manuscript. All authors discussed and revised the manuscript. Fabian Panzer supervised the project.

How Antisolvent Miscibility Affects Perovskite Film Wrinkling and Photovoltaic Properties

This work is published in *Nature Communications*, **2021**, 12, 1554 and reprinted in Chapter 14. The authors are:

Seul-Gi Kim, Jeong-Hyeon Kim, Philipp Ramming, Yu Zhong, **Konstantin Schötz**, Seok Joon Kwon, Sven Huettner, Fabian Panzer, Nam-Gyu Park.

N.-G.P., F.P., and S.H. supervised the research; S.-G.K. designed and conducted experiments and measurements; J.-H.K. conducted experiments and measurements; Y.Z., S.-G.K., and K.S. measured and analyzed in situ PL and absorbance measurements. P.R. and S.-G.K. measured and analyzed FLIM and TCSPC. S.J.K. conducted simulation study of bilayer wrinkle system. S.-G.K. and N.-G.P. wrote manuscript; and all authors discussed the results and revised the manuscript.

7 Conclusion and Outlook

The work presented in this thesis shows (i) how strongly the the opto-electronic properties of metal halide perovskites depend on their microscopic and macroscopic structure. It further shows (ii) how the opto-electronic properties of these semiconductors can be tuned by modifying the microscopic and macroscopic structure through external stimuli and suitable processing.

From the work in Chapters 8, 9 and 10 I can conclude that it is not sufficient to consider merely the crystal structure in order to correctly assign the features in the photoluminescence and absorption spectra. Rather, a correct interpretation requires consideration of the macroscopic sample structure as well. This is because, as I could demonstrate, the degree of self-absorption differs significantly between samples that consist of a single crystal, a polycrystalline thin film or a powder. I presented a model to quantitatively account for the effects of self-absorption. This allowed excluding features such as bound excitons, an indirect band gap, defect sites and local band gap variations as origin for additional photoluminescence features, and it allowed a detailed identification of the phase transition behaviour.

The work in Chapter 11, 12, 13 and 14 indicates how control over processing can be employed to tune the electronic structure of the resulting metal halide perovskites. This control is achieved by monitoring the formation process of the crystals *in situ*, i.e., during the drying process. I could show that it is essential to consider both, absorption and photoluminescence, as a function of drying time, to fully understand the kinetics of the film formation and I applied this approach to the two-step method, the one-step method and the solvent engineering method. Thus I pioneered the elucidation on the evolution of the opto-electronic properties of the perovskite for the major solution-based processing methods currently in use. In these works I demonstrated that even though the resulting samples are always thin films, it is important to consider both microscopic and macroscopic structure in order to interpret the optical spectra correctly. Especially, disentangling quantum confinement effects due to crystallite size, self-absorption effects through crystallite thickness and changes in crystal stoichiometry needs careful considerations.

Overall, this thesis contributes to the understanding of the relationship between the structure and the optical properties of lead halide perovskites, and it demonstrates how this understanding can be used to elucidate the perovskite film formation. Based on these results, I suggest that future studies should employ *in situ* absorption and photoluminescence spectroscopy to

address some of the most urgent questions about the perovskite film formation. For example, the role of solvate states on the perovskite crystallization could possibly be elucidated by extending the spectral range of the *in situ* absorption measurements to the UV-range, i.e., to the spectral range where such solvate states absorb. Also, for many additives such as surfactants or passivating agents, only the impact on final film properties for films processed under identical conditions are reported. *In situ* spectroscopy could shed light on the influence of such additives on the dynamics on the film formation, which could reveal that adaptation of the processing protocols for the treated samples are needed to enable an accurate comparison of treated and reference samples.

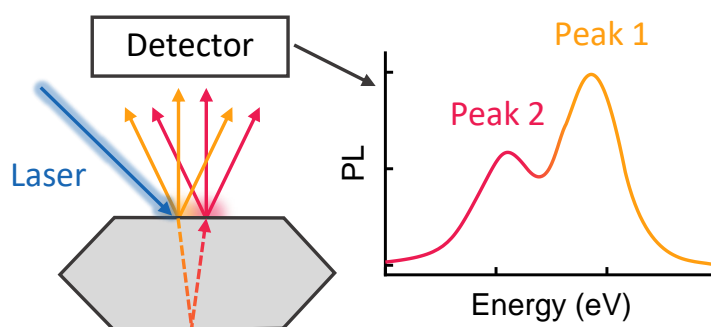
Finally, fine control over the resulting electronic structure of perovskite films could be obtained when the *in situ* optical spectroscopy was used for inline processing control. By monitoring and evaluating the optical spectra in real-time, and then reacting to changes in the optical spectra, one could optimize processing parameters such as evaporation rate, substrate temperature or timing of antisolvent addition during processing. This implies a change from timing-based processing protocol (e.g. adding antisolvent after ten seconds) to a results-based processing protocol (e.g. adding antisolvent when specific spectral signatures are observed). Such a change would make perovskite processing more robust against environmental conditions, and allow for reproducible sample preparation. In fact, the sample-to-sample variation is still a challenge for comparison of results between different scientific labs as well as for industrial fabrication. Overcoming this hurdle would push perovskite-based opto-electronic devices further towards commercialization.

Part III

Publications

8

Double Peak Emission in Lead Halide Perovskites by Self-absorption



Konstantin Schötz, Abdelrahman M Askar, Wei Peng, Dominik Seeberger, Tanaji P Gujar, Mukundan Thelakkat, Anna Köhler, Sven Huettner, Osman M Bakr, Karthik Shankar, Fabian Panzer.

Published in
The Journal of Physical Chemistry C, **2020**, 8, 7, 2289-2300
(DOI: 10.1039/C9TC06251C)

Reprinted with permission from the American Chemical Society
Copyright (2020) American Chemical Society

Double peak emission in lead halide perovskites
by self-absorption†Cite this: *J. Mater. Chem. C*, 2020,
8, 2289Konstantin Schötz,^a Abdelrahman M. Askar,^{ib} Wei Peng,^c Dominik Seeberger,^d
Tanaji P. Gujar,[‡] Mukundan Thelakkat,^{ib} Anna Köhler,^{ib}ae Sven Huettner,^d
Osman M. Bakr,^c Karthik Shankar^{ib} and Fabian Panzer^{ib}*a

Despite the rapidly increasing efficiencies of perovskite solar cells, the optoelectronic properties of this material class are not completely understood. Especially when measured photoluminescence (PL) spectra consist of multiple peaks, their origin is still debated. In this work, we investigate in detail double peak PL spectra of halide perovskite thin films and single crystals with different material compositions. By different optical spectroscopic approaches and quantitative models, we demonstrate that the additional PL peak results from an extensive self-absorption effect, whose impact is intensified by strong internal reflections. This self-absorption accounts for the unusual temperature dependence of the additional PL peak and it implies that absorption until far into the perovskite's Urbach tail is important. The internal reflections entail that even for thin films self-absorption can have a significant contribution to the PL spectrum. Our results allow for a clear assignment of the PL peaks by differentiating between optical effects and electronic transitions, which is a necessary requirement for understanding the optoelectronic properties of halide perovskites.

Received 14th November 2019,
Accepted 5th January 2020

DOI: 10.1039/c9tc06251c

rsc.li/materials-c

1. Introduction

Halide perovskites, and optoelectronic devices based on them such as solar cells, LEDs, lasers or detectors, have undergone a tremendous development in the last few years. For this, their optical properties, in particular the absorption and photoluminescence (PL) spectra, play an important role when investigating the perovskite materials such as to derive conclusions about their electronic structure.^{1,2} For example, phase transitions and different structural states can be identified by the associated optical spectra, which are experimentally easily accessible. Furthermore, from the analysis of the spectra, important material parameters can be determined, such as electron phonon coupling constants or dynamic and static disorder (in particular by temperature-dependent investigations).^{3–8} PL signatures of different defect states both at higher and especially at lowest

temperatures were identified,^{6,9,10} and the interaction of the perovskite with its environment (solvent, humidity or atmosphere) was investigated using PL measurements.^{11–13} More recently, spatially resolved PL investigations allowed to associate the occurrence of defect assisted, non-radiative decay channels with the grain boundaries of the perovskite.¹⁴ This has facilitated the development of appropriate passivation strategies, which in turn have led to the last significant increases in efficiencies of perovskite solar cells.^{15–17}

However, although PL spectroscopy has been used intensively and versatilely in the past, it is still common for PL spectra measured under nominally identical conditions to differ from work to work or from group to group, and in many cases to exhibit several peaks within a PL band. Hence, there is still an intense discussion and disagreement about the origin of these multiple PL features, and a variety of interpretations exists. Some suggest the additional PL features to stem from the coexistence of a direct and an indirect bandgap,^{18–22} defect induced recombination of (bound) excitons,^{21,23–25} different electronic structure between the bulk and the surface,^{26–28} coexistence of different crystalline phases^{10,29} and to self-absorption effects.^{30–33} Evidently, clarification on the origin of the multiple peak structure is urgently needed to allow for further understanding of the optoelectronic structure of lead halide perovskites.

In this work, we demonstrate that the occurrence of double peak structure is a general phenomenon in lead halide perovskites and not limited to single crystals or a specific material composition. We systematically address the different existing

^a *Soft Matter Optoelectronics, University of Bayreuth, 95440 Bayreuth, Germany.*E-mail: fabian.panzer@uni-bayreuth.de^b *Department of Electrical and Computer Engineering, University of Alberta, Edmonton, AB T6G 1H9, Canada*^c *King Abdullah University of Science and Technology (KAUST), Division of Physical Sciences and Engineering, Thuwal 23955-6900, Kingdom of Saudi Arabia*^d *Department of Chemistry, University of Bayreuth, 95440 Bayreuth, Germany*^e *Bayreuth Institute of Macromolecular Research (BIMF) and Bavarian Polymer Institute (BPI), University of Bayreuth, 95440 Bayreuth, Germany*

† Electronic supplementary information (ESI) available. See DOI: 10.1039/c9tc06251c

‡ Current address: Shardabai Pawar Mahila College, Shardanagar, Baramati, Pune-413115 (MS), India.

interpretations and show that neither the recombination *via* different types of defects, or different electronic states between the bulk and the surface can account for the double peak structure. Instead, from temperature dependent one-photon-induced and two-photon-induced PL measurements, optical modelling, and a systematic change of measurement geometry, we conclude that the additional PL feature is due to a surprisingly extensive self-absorption effect, significantly amplified by internal reflections of PL. Finally, we show that by changing the refractive index of the perovskite environment, and thus the internal reflectivity, the relative intensity of the two peaks can be modified, further underpinning our approach.

2. Results and discussion

2.1 The double-peak structure

Fig. 1a shows the room temperature photoluminescence (PL) of four different lead halide perovskites used in this study, namely a MAPbI₃ thin film, a MAPbI₃ single crystal, a single crystal with a different halide, MAPbBr₃, and a single crystal with a different organic cation, EA_{0.17}MA_{0.83}PbI₃. For all samples, we observe the emission to be structured, *i.e.* to consist of a dominant higher energy peak that we will refer to as “Peak 1” and of a weaker lower energy peak or shoulder, henceforth called “Peak 2”. This emission structure occurs independently of chemical composition and film structure for our four model samples, stressing the general nature of the phenomenon. The energy of

the emission band varies with sample composition. For the iodide perovskites, Peak 1 is located at 1.56 eV in the case of the single crystals, and at 1.58 eV for the thin film. While for the single crystals, Peak 2 appears as distinct peak at 1.48 eV, in the case of the thin film Peak 2 is located at 1.53 eV, *i.e.* less separated from corresponding Peak 1 and it is thus observed as a shoulder. For clarity, an alternative version of Fig. 1a with a logarithmic PL scale can be found in the ESI† (Fig. S1). For MAPbBr₃, Peak 1 and Peak 2 are located at 2.29 eV and 2.21 eV respectively. The relative PL intensity of Peak 2 compared to Peak 1 is in the range between 30 to 60% for all samples, depending on the position of excitation and detection spot and the angle of detection (see Fig. S2, ESI†).

To further investigate the two PL peaks, we performed temperature dependent PL measurements on all samples. Exemplarily, the results for the MAPbI₃ single crystal are shown in Fig. 1b (see Fig. S3 (ESI†) for the results of the other compounds). Upon cooling from 300 K to 160 K (Fig. 1b), where MAPbI₃ is in the tetragonal phase, the PL intensities of both peaks increase by an order of magnitude. Even without further analysis, it is evident that Peak 1 shifts to lower energies upon cooling, while the opposite is the case for Peak 2. Separating the spectra into the contributions of two individual peaks (see Fig. S4, ESI†) shows that Peak 1 shifts continuously to lower energies by 32 meV upon cooling, while Peak 2 shifts to higher energies by 10 meV until 240 K and then stays energetically constant (Fig. 1c).

Upon cooling below 160 K, MAPbI₃ undergoes a phase transition from a tetragonal to an orthorhombic crystal structure,³⁴

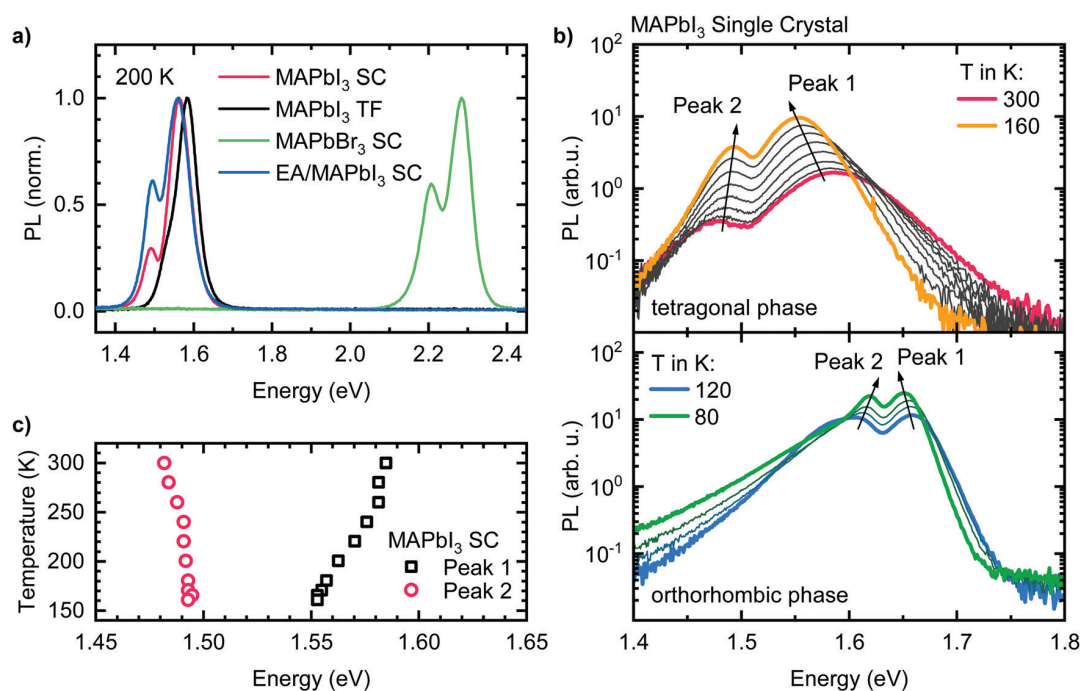


Fig. 1 (a) Normalized PL spectra of four different lead halide perovskite samples showing double peak emission. (b) Temperature-dependent PL of a MAPbI₃ single crystal between 300 K (red) and 160 K (orange), *i.e.* tetragonal phase in steps of 20 K (top) and in the orthorhombic phase between 120 K (blue) and 80 K (green). (c) Temperature-dependent peak position of Peak 1 and Peak 2 from the PL shown in (b) after spectral decomposition.

which is accompanied by an 100 meV increase of the band gap, directly impacting on the absorption and PL properties.^{35–37} Until 120 K a transition region exists in which the different phases coexist leading to PL spectra with more than two PL features (Fig. S5, ESI†). Between 120 K and 80 K we again observe two PL-Peaks, which exhibit the same spectral temperature dependence as Peak 1 and Peak 2 in the tetragonal phase (*i.e.* shift to lower (higher) energies of Peak 1 (Peak 2) with decreasing temperature). Below 80 K additional PL features appear, leading to relatively complex PL spectra at lowest temperatures (Fig. S6, ESI†). It becomes obvious that additional well-resolved/distinct PL bands can be observed over the entire investigated temperature range, *i.e.* also over different crystal phases.

2.2 Investigating possible structural origins for the double peak

Several interpretations have been proposed to account for the structure in the emission bands. We shall evaluate whether these interpretations are consistent with our data one by one.

2.2.1 Coexistence of radiative direct and indirect transitions.

Several works associated additional PL bands with the coexistence of a direct and an indirect band gap in halide perovskites.^{19,20} Indeed, Rashba splitting in halide perovskites, from which an indirect band gap character follows, has been shown.^{38–41} However, its extent and impact on the excited state properties of the perovskites is debated^{18,40–48} and some more recent publications suggest an insignificant impact of the Rashba splitting on the optical properties of the perovskite.^{42,49} Theoretical works suggested that an impact of the Rashba splitting on the perovskite PL disappears at higher excitation densities, namely around 10^{18} cm^{-3} .⁵⁰ The PL spectra in Fig. 1 were measured with an excitation density of $n = 4.8 \times 10^{18} \text{ cm}^{-3}$ (see ESI† for details), so that we do not expect the Rashba splitting to play a significant role in the PL. Furthermore, Peak 2 is clearly present even at higher excitation densities (*vide infra*), which indicates that Rashba splitting does not cause the appearance of Peak 2. Moreover, the coexistence of a radiative direct and indirect transition would imply a competition between both pathways, as it is *e.g.* reported for $\text{Ge}_{1-x}\text{Sn}_x$ alloys.^{51,52} Regarding the temperature dependence, cooling should favor electron trapping in the energetically lower indirect bandgap valley, resulting in a decreased relative contribution of the higher energy direct bandgap transitions. Concomitantly, the PL intensity should drop for an indirect character of the PL, as the phonon-assisted radiative recombination is less efficient at lower temperatures.^{51–54} This is at variance with the experimental observation shown in Fig. 1. Thus, we can exclude the double peak emission to be associated with the coexistence of an indirect and direct band gap.

2.2.2 Strain-induced defects in the bulk. Recently, the significance of strain-induced defects and their impact on the excited state recombination properties of halide perovskites were reported.^{55,56} To probe whether recombination at strain-induced defects may be at the origin of the double-peak structure, we measured the PL of perovskite thin films that were deposited either on glass, or on polyethylene terephthalate

(PET). These substrate materials exhibit different thermal expansion coefficients in the order of 10^{-5} K^{-1} (PET),^{57,58} and 10^{-6} K^{-1} (glass),⁵⁹ respectively. With the thermal expansion coefficient of MAPbI_3 being in the range of $(1.6 \times 10^{-4} - 3.8 \times 10^{-4}) \text{ K}^{-1}$,^{60,61} we expect a larger build-up of strain upon cooling for the $\text{MAPbI}_3/\text{glass}$ sample compared to the $\text{MAPbI}_3/\text{PET}$ sample.⁶² The degree of strain in a sample can be correlated to the temperature at which the tetragonal to orthorhombic phase transition occurs upon cooling.^{3,63} We identify the critical temperature T_c and the width of the tetragonal to orthorhombic phase transition from temperature dependent absorption measurements following the same approach as in previous works (also see Fig. S7, ESI†).^{3,64} We find a lower T_c and an increased width of the transition for the $\text{MAPbI}_3/\text{glass}$ sample ($T_{c,\text{Glass}} = 145.9 \pm 0.3 \text{ K}$, $\text{FWHM}_{\text{Glass}} = 10.1 \pm 0.7 \text{ K}$) compared to $\text{MAPbI}_3/\text{PET}$ ($T_{c,\text{PET}} = 147.2 \pm 0.2 \text{ K}$, $\text{FWHM}_{\text{PET}} = 8.8 \pm 0.6 \text{ K}$). Furthermore, we analyzed the temperature dependence of the PL peak positions of the two samples, where we find a shift of 0.25 meV K^{-1} for the sample on the glass substrate and a shift of 0.28 meV K^{-1} for the sample on the PET substrate. Both, the decrease in T_c and the reduced temperature dependence of the PL peak position in the $\text{MAPbI}_3/\text{glass}$ sample imply that there is indeed more strain in the $\text{MAPbI}_3/\text{glass}$ sample. Fig. 2a shows the normalized PL spectra of the $\text{MAPbI}_3/\text{glass}$ and $\text{MAPbI}_3/\text{PET}$ samples at 170 K. This is the temperature where we expect the highest strain to have built up upon cooling, without already inducing the tetragonal–orthorhombic phase transition. For both thin film samples, Peak 2 appears as shoulder, similar to the thin film sample in Fig. 1. A decomposition of the spectrum into two peaks shows that Peak 2 is about 10–15% more intense in the $\text{MAPbI}_3/\text{glass}$ sample (see Fig. S8, ESI†). Upon cooling, the intensity of Peak 2 relative to Peak 1 increases continuously and, importantly, in the same manner for both samples (Fig. 2b). If Peak 2 was related to strain-induced defects, it should evolve differently with temperature in the sample with the larger strain. This is at variance with the observation of an identical temperature-evolution for both samples, and thus implies that strain-induced defects are not the cause for the double-peak structure.

2.2.3 Surface defect states. To address whether surface defect states, and the associated recombination *via* bound excitons, may be responsible for the occurrence of Peak 2, we passivated the surface of MAPbI_3 single crystals. We used either a cyclohexane solution of the electron-accepting benzothiadiazole or the electron-donating, liquid mono-thiophene to selectively passivate negatively and positively charged surface defects, respectively.^{16,65} We measured the PL directly before and after dropping the respective liquids onto the single crystals (Fig. 2c and d), ensuring that the crystals, the laser and the detector did not move during this process. When dropping benzothiadiazole onto the single crystals, both, Peak 1 and Peak 2 remain nearly unchanged in their energy and intensity (Fig. 2c). This suggests that negatively charged surface defects are either not present or do not affect the spectral shape of the PL. In the case of thiophene, the energetic position and the intensity of Peak 2 hardly changes. However, the intensity of Peak 1 more

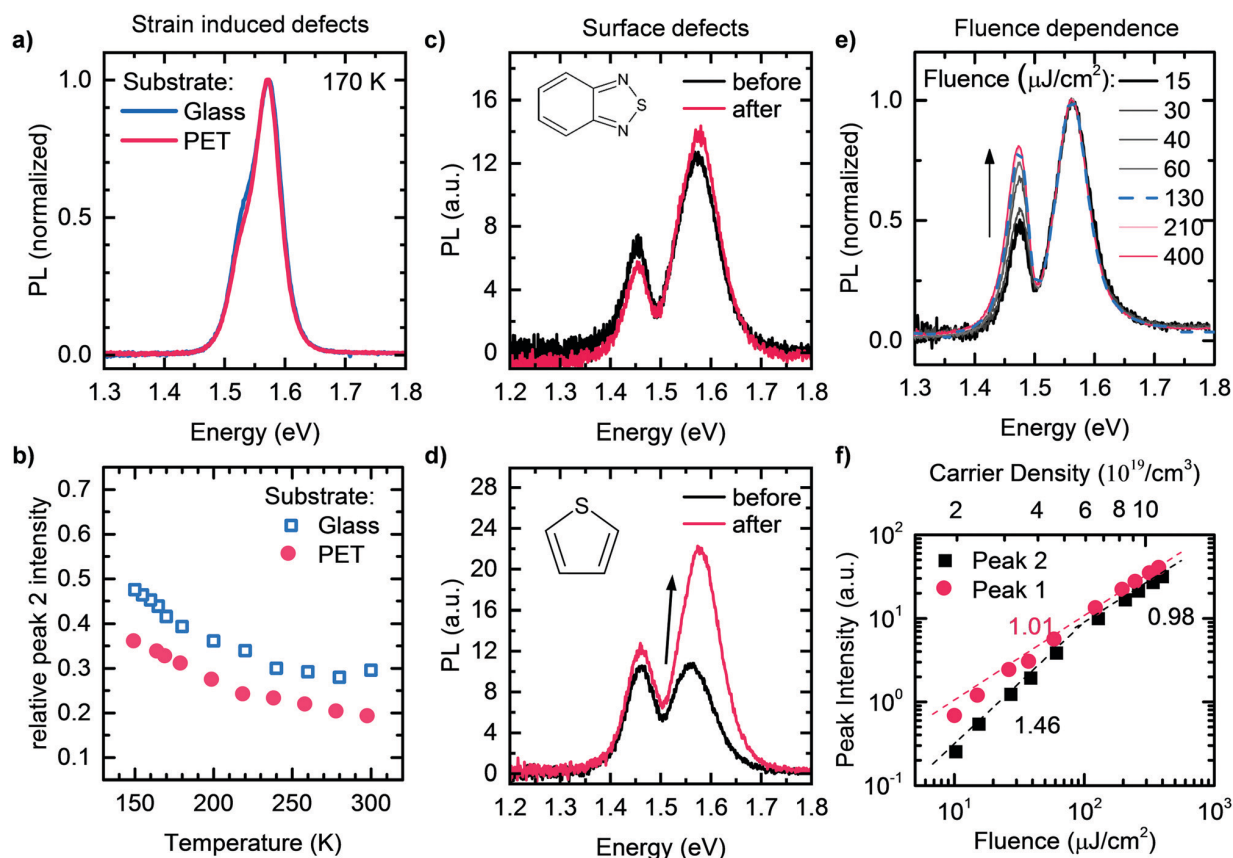


Fig. 2 (a) PL of MAPbI₃ thin films at 170 K processed on glass (blue) and on PET (red). (b) Temperature dependence of the PL Peak 2 intensity relative to Peak 1 intensity of the two thin films processed on glass (blue squares) and PET (red dots). (c and d) Room temperature PL of a MAPbI₃ single crystal before (black) and after (red) surface passivation with (c) benzothiadiazole dissolved in cyclohexane and (d) mono-thiophene. (e) Fluence dependent PL (normalized) of a MAPbI₃ single crystal at 200 K and (f) corresponding peak intensities as a function of laser fluence, plotted on a double logarithmic scale. The dashed lines represent fits with slope values as indicated.

than doubles, and the peak position shifts by about 15 meV to higher energies (Fig. 2d), as expected for a successful surface passivation (see Fig. S9 (ESI[†])) for a discussion on the observed blue shift of Peak 1. Evidently, emission from Peak 1 is affected by positively charged defects on the surface of the MAPbI₃ single crystals, most likely due to iodine vacancies as proposed in the past,¹⁶ while emission from Peak 2 is hardly affected. From this passivation experiment, we can deduce that the higher-energy Peak 1 is associated with emission near the crystal surface, while the lower-energy Peak 2 may be associated with emission that is predominantly from the bulk of the crystal. However, it is not clear, whether only the spatial origin of the emission differs for the two peaks, or whether they also result from actual different electronic states, as has been suggested in the past.^{28,66}

2.2.4 Surface versus bulk emission. To follow up the question whether the two peaks may originate from emission near the surface and in the bulk, we performed temperature dependent two-photon-induced photoluminescence (2PI-PL) measurements and compared them with the results from one-photon-induced photoluminescence (1PI-PL) experiments. In the more common 1PI-PL experiments, a sample volume near the surface is excited, determined by the exponential fall-off in

the absorbed light well known as Lambert-Beer's law. In contrast, for a 2PI-PL experiment, a high excitation intensity is required, which is typically achieved by focusing of a laser beam. Thus, only a small, well-defined spot in the sample bulk is excited.⁶⁷ Even though the two processes follow different selection rules and thus excite different transitions, in either case, electrons and holes are generated that thermalize in the band and subsequently recombine *via* the same radiative transition.^{68,69} The results of the temperature dependent 2PI-PL-experiment are shown exemplarily for the tetragonal phase at 200 K and for the orthorhombic phase at 80 K together with the corresponding scaled 1PI-PL spectra in Fig. 3a and b respectively. The peak position of the 2PI-PL resembles very well Peak 2 from the 1PI-PL at both temperatures (*i.e.* both crystal phases). This demonstrates that Peak 2 is associated with the bulk. However, from these results it is still not distinguishable whether Peak 2 results from different distinct transitions occurring at the bulk and the surface, or to which extend self-absorption effects modulate the PL spectra, contributing to the observation of Peak 2.

2.2.5 Strain-independent defects in the bulk. To address, whether Peak 2 may be caused by recombination at defects in

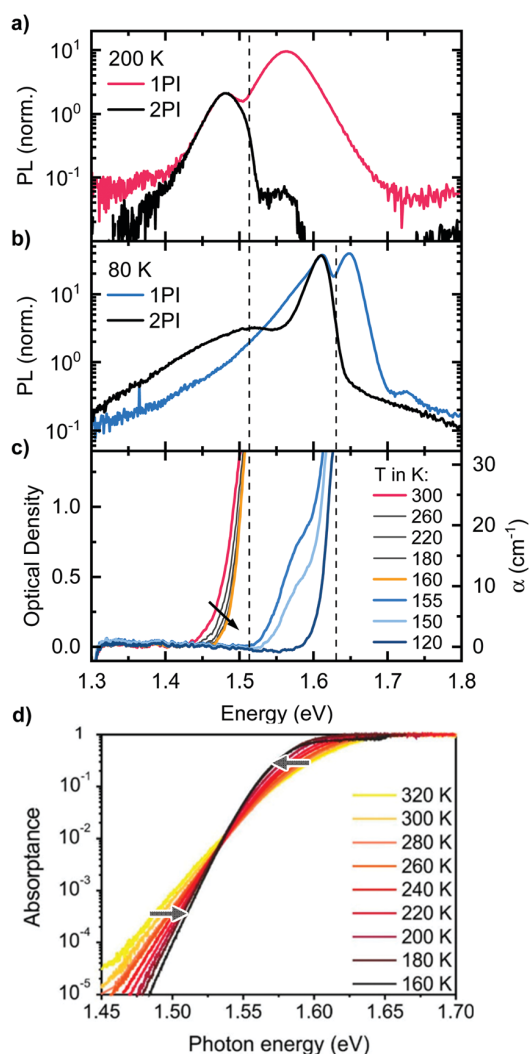


Fig. 3 One-photon-induced (1PI) and two-photon-induced (2PI) PL of a MAPbI₃ single crystal, (a) at 200 K (tetragonal phase) and (b) at 80 K (orthorhombic phase). (c) Optical density of a MAPbI₃ single crystal in the temperature range from 300 K to 120 K. The arrow indicates reducing temperature. (d) Temperature-dependence of the Urbach-tail absorption. Reprinted with permission from Ledinsky *et al.*⁷⁴ Copyright 2019 American Chemical Society.

the bulk that are independent of any mechanical strain, we recorded the PL at 200 K as a function of laser fluence (Fig. 2e) and analyzed the corresponding PL intensities of Peak 1 and Peak 2. This is shown in Fig. 2f on a double logarithmic scale. For laser fluences up to 120 $\mu\text{J cm}^{-2}$, Peak 2 grows with a slope of 1.46, while the intensity of Peak 1 increases with a slope of 1.01. For higher fluences, both peaks grow with a slope of about 1. Usually, when an emission feature results from recombination at defect sites, its relative contribution to the overall PL decreases with increasing laser fluence as such traps are filled up.^{6,10} This would result in a sublinear slope for the defect-based emission, at variance with our experiment, where we observe a superlinear slope. This speaks against assigning the origin of Peak 2 to recombination at defects in the bulk.

2.3 Addressing optical effects as possible origin for the double-peak structure

So far, we could establish that Peak 2 results from the bulk while Peak 1 is associated with PL near the surface. We did not find any structural causes in the bulk that could account for Peak 2. We therefore consider whether self-absorption may be associated with the occurrence of the double peak structure. For this, it is obviously useful to consider the absorption of the perovskite crystals. Thus, we determined the temperature-dependent optical density of the MAPbI₃ single crystal by transmission measurements (Fig. 3c). With our experimental setup, we can reliably determine optical densities (OD) in the range from about 0.1 to 1.5. This corresponds to absorption coefficients α in the range of 1 to 30 cm^{-1} , considering a thickness of 1 mm, which is typical for the single crystals we used. Such low α -values occur in the Urbach tail of MAPbI₃, which has been characterized in the past using photothermal deflection spectroscopy (PDS) or external quantum efficiency (EQE) measurements.^{70–72} At 300 K, detectable absorption for our setup starts at 1.44 eV and rises steeply to an OD of 1.5 at 1.5 eV. Importantly, upon cooling, the detectable absorption shifts to higher energies and the absorption edge becomes steeper. Below 160 K, the absorption jumps to 1.63 eV, indicating the transition to the orthorhombic phase.^{34,35} This is accompanied by an additional well-resolved shoulder at 1.58 eV that matches the energy for absorption of the tetragonal phase of thin films at this temperature.^{4,73} Evidently, some small residues of tetragonal phase still prevail at 155 K and 150 K. An estimation considering a crystal thickness of 1 mm and the absorption coefficient of MAPbI₃ as reported by Crothers *et al.*⁷⁰ implies that approximately 0.1% of tetragonal phase are still present at 155 K. The shift of the measured absorption of the single crystal to higher energies upon cooling from 300 K to 160 K is opposite to the trend observed for the absorption edge of thin films. However, it can be understood when considering which part of the absorption spectrum we probe with our transmission measurement: both the estimated values of the absorption coefficient and the energetic position of the absorption edge indicate that we measure Urbach tail absorption below the so called Urbach focus point, which was found for MAPbI₃ to be around 1.54 eV, where the absorption coefficient takes a value of $\alpha = 500 \text{ cm}^{-1}$.^{60,74} For absorption coefficients below this point, the temperature-dependence of the absorption is inverted, *i.e.* the absorption edge shifts to higher energies upon cooling, in accordance with our results. For clarification, the temperature-dependence of the Urbach-tail, including the Urbach focus point, is displayed in Fig. 3d, taken from Ledinsky *et al.*⁷⁴ The arrows indicate the temperature-evolution above and below the Urbach focus point. We also would like to emphasize that the measured absorption edge of the single crystal only represents a small part of the Urbach tail and cannot be used to determine the optical band gap of the material and thus does not imply a red shifted band gap of the single crystal compared to thin films.

The temperature dependent absorption spectra reveal two important facts: first, significant absorption, which reduces the transmission of photons generated deep in the crystal bulk to less

than 10%, occurs in the same energetic range as the high energy edge of the 2PI-PL, both for the tetragonal (1.51 eV) and the orthorhombic phase (1.63 eV) as indicated by dashed lines in Fig. 3. This is essentially the position of the minimum between Peak 1 and 2. A similar observation was reported for MAPbBr₃ single crystals by Yamada *et al.* comparing transmission with 2PI-PL measurements.³³ Second, the shift of the absorption to higher energies upon cooling from 300 K to 160 K, matches well with the temperature dependence of the energetic position of Peak 2 in Fig. 1c. These two observations are a strong indication that the occurrence of Peak 2 is correlated to a self-absorption effect.

To test the plausibility of self-absorption as origin of Peak 2, we modelled our 1PI-PL by explicitly considering the effect that self-absorption will have on emission generated throughout the crystal as illustrated in Fig. 4. To do so, we calculated the one-dimensional charge carrier distribution $n(x)$ that results from laser excitation. For this, we considered the absorption coefficient of MAPbI₃ at 337 nm, which can be found *e.g.* in Crothers *et al.*,⁷⁰ and the Beer–Lambert-law. This charge carrier distribution leads to photoluminescence *via* bimolecular recombination. The PL generated by recombination at a site x' can then travel towards either to front or the backside of the crystal, which are taken to be 1 mm apart. This is about the size of the single crystals examined in this study. On the way through the crystal, the perovskite absorbs part of the PL, thus attenuating it. At the interface between perovskite and surrounding media, the PL is either transmitted or reflected with a certain probability. A key feature of our model is that we allow for multiple inner reflections. The PL that is detected at the front surface is then a superposition of the PL that leaves the crystal at the front without internal reflections, $PL_{\text{direct}}(E)$, and the PL that leaves the crystal after (multiple) internal reflections, $PL_{\text{filtered}}(E)$.

$$PL_{\text{detected}}(E) = C \cdot PL_{\text{direct}}(E) + PL_{\text{filtered}}(E). \quad (1)$$

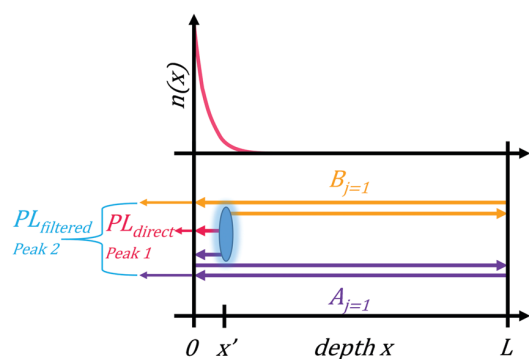


Fig. 4 Illustration of the optical paths considered in the optical modeling. From a certain depth in the crystal x' , the PL can either hit the front surface and escape with a certain probability (red), contributing to Peak 1 (PL_{direct}), or can be reflected and travel towards the back surface. There it is reflected with a certain probability and travels back to the front surface, where it is either transmitted (purple) and contributes to Peak 2 (PL_{filtered}), or reflected again. Alternatively, the PL originating from x' can travel to the back, being reflected and traveling to the front, where it likewise can either escape (orange), contributing to Peak 2, or be reflected. On its way through the crystal, the PL is filtered by the absorption of the perovskite.

The constant C was found necessary to allow for a mismatch between excitation spot and detection spot. $PL_{\text{direct}}(E)$ and $PL_{\text{filtered}}(E)$ are calculated according to the Beer–Lambert law,

$$PL_{\text{direct}}(E) = \int_0^L PL_{\text{int}}(E) \cdot n(x)^2 \cdot (1 - r_f) \cdot \exp[-\alpha(E) \cdot x] dx \quad (2)$$

$$PL_{\text{filtered}}(E) = \int_0^L \sum_{j=1}^L PL_{\text{int}}(E) \cdot n(x)^2 \cdot (1 - r_f) \cdot \{A_j + B_j\} dx, \quad (3)$$

where $A_j = r_f^j \cdot r_b^{j-1} \cdot \exp[-\alpha(E) \cdot (2jL + x)]$ considers the part of the PL that propagates from the site of generation, x' , towards the front surface. Propagation towards the back surface is considered by $B_j = r_f^{j-1} \cdot r_b^j \cdot \exp[-\alpha(E) \cdot ((2j - 1)L + (L - x))]$. Here, $\alpha(E)$ denotes the absorption coefficient of the material, r_f and r_b are the reflection probabilities at the front and back interface, respectively, and L denotes the length of the crystal. j denotes the number of reflections at the back interface. For the intrinsic PL lineshape $PL_{\text{int}}(E)$, we assume a hyperbolic secant fitted to Peak 1, see Fig. S4 (ESI[†]). Even though there is no immediate physical meaning to this lineshape, this phenomenological approach reproduced the spectral shape better than a Gaussian, Lorentzian or Voigt lineshape function. For the absorption spectrum $\alpha(E)$, we took the spectrum, especially of the Urbach tail, reported by Ledinsky *et al.*⁷⁴ and normalized it to the absolute values from Crothers *et al.*,⁷⁰ which are not available in the region of Urbach absorption. The average reflection probabilities r_f and r_b were calculated *via* the Fresnel equations with a refractive index of 2.5 for MAPbI₃ in the relevant energy range,⁷⁵ and of 1 for air. Averaging over all angles of incidence, we obtain a reflection probability of 0.85 for the perovskite–air interface. This high reflection probability demonstrates the importance of considering multiple inner reflections, where up to $j_{\text{max}} = 10$, an increase of Peak 2 can be observed. However, for our calculation, we considered $j = 20$ reflections to be well above j_{max} . We note that this approximation does not consider that PL reaching the interface with a larger angle also travelled a larger distance through the material. However a slightly bigger (smaller) reflection probability can be easily compensated by a slightly smaller (bigger) crystal to obtain a similar result. For comparison with experimental PL spectra, the calculated spectrum $PL_{\text{detected}}(E)$ is finally normalized to the experimental data. We note that for infinitely large, perfect and parallel front and back surfaces, photons that hit the surface outside the escape cone would not be able to leave the sample. In reality however, when hitting irregularities, such as grain boundaries in the case of thin films, or when reaching the edges or side surfaces of single crystals, the photons can escape the perovskite even after multiple inner reflections.

The comparison between the PL spectrum calculated using our model (with a value of $C = 0.66$) and the experimental PL spectrum of the MAPbI₃ single crystal at room temperature is shown by the black squares and the black line in Fig. 5a. The excellent agreement for this simple model – which only uses a

single “fitting” factor in the form of C – clearly demonstrates the significant importance of self-absorption. Fig. 5b indicates which part of the PL results from the directly transmitted PL, $PL_{\text{direct}}(E)$, and from PL that suffered internal reflections and self-absorption, $PL_{\text{filtered}}(E)$. We stress again here the key role of considering multiple reflections. Effects that are neglected in our model are carrier diffusion, photon recycling and internal scattering. Carrier diffusion and photon recycling both have similar effects insofar that they can generate PL at a site that is different from the original absorption. While photon recycling can have significant impact on the PL properties^{76,77} and should, together with carrier diffusion, enhance the intensity of Peak 2, we found it was not necessary to include photon recycling explicitly to model our measured spectra.

To further test whether self-absorption, magnified by reflection at the crystal back surface, is indeed causing the double peak structure, we repeated the room temperature 1PI-PL of the same MAPbI₃ single crystal while modifying the outcoupling, and thus the reflection, at the back surface. For this, we placed a drop of glycerin at the backside of the crystal, while we excited the sample and detected resulting PL at the front side, identical to the previous measurement. This measurement was performed directly after the one without glycerin drop without moving the crystal or detection, to exclude any influence of a changed measurement geometry. The refractive index of glycerin is 1.47,⁷⁸ *i.e.* higher than the one of air, which reduces the reflection probability at the backside of the crystal from 0.85 to 0.70. According to our model, this should lead to a decreased intensity of Peak 2, accompanied by a spectral shift to higher energies. The obtained experimental data and the model data (keeping all parameters identical to before, except of the reflection probability), are shown as red line and dots in Fig. 5a. We find the intensity of Peak 2 to reduce to half the previous value and to shift to the blue by 10 meV. This observation is excellently captured by our model.

These findings represent compelling evidence that Peak 2 originates from an extreme self-absorption effect, which is

caused by significant internal reflections in the temperature ranges investigated in this study. We stress that below about 80 K, the temperature-dependence of Peak 2 changes, probably due to an increasing contribution of PL of bound exciton states,⁷⁹ which becomes increasingly efficient at lower temperatures. In passing we mention that changes in reflectivity for example due to the addition of thiophene or benzothiadiazole, or due to different substrates such as Glass and PET can easily account for the slightly different intensities of Peak 2 that we observed in Fig. 2a and b.

With the insight provided by our results on the different origin of Peak 1 and 2, we can understand the different temperature dependence of Peak 1 and 2 in their PL spectra, with Peak 1 shifting to the red spectral range and Peak 2 to the blue upon cooling. Peak 1, resulting from $PL_{\text{direct}}(E)$, is modified by reabsorption only from the point where it was created, to the front surface. Reabsorption thus occurs over a typical lengthscale of about 50 nm, depending on the wavelength of excitation. A significant attenuation, say, to a level of 10% of transmitted intensity, would be then obtained for absorption coefficients above about $5 \times 10^5 \text{ cm}^{-1}$. If diffusion of charge carriers is considered, the lengthscale increases to the μm range, and the relevant absorption coefficient decreases to about 10^4 cm^{-1} . In contrast, reabsorption for Peak 2 occurs over a length scale exceeding the crystal thickness of 1 mm, thus becoming relevant for absorption coefficients as low as a few 10 cm^{-1} . Fig. 3d, taken from Ledinsky *et al.*, shows the evolution of the Urbach tail with temperature.⁷⁴ The two arrows indicate the typical absorption coefficients associated with self-absorption for $PL_{\text{direct}}(E)$, which causes Peak 1, and for $PL_{\text{filtered}}(E)$ that gives rise to Peak 2. One can see that the two ranges for the absorption are on different sides of the Urbach focus point. As a result, cooling causes a blue-shift for Peak 2 due to filter effects, despite Peak 1 shifting to the red due to the decreasing bandgap of the perovskite.

In the framework of filtered PL which we present here, also the dependence of the relative intensity of Peak 2 from the

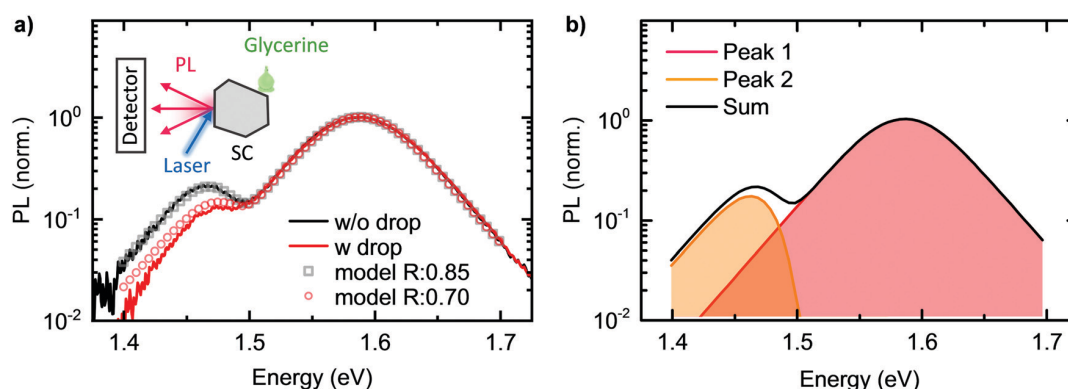


Fig. 5 (a) PL spectrum of a MAPbI₃ single crystal in air at room temperature (black solid line) together with the modelled PL with an internal reflection probability of 0.85 (black open squares). The PL spectrum of the same crystal with a drop of glycerin at the back is displayed as red solid line, together with the modelled PL with an internal reflection probability at the back interface of 0.7 (red open circles). (b) Decomposition of the modelled PL into the contribution of the PL coming directly from the excitation spot (PL_{direct} , Peak 1, red) and the PL after internal reflections and self-absorption (PL_{filtered} , Peak 2, orange).

excitation spot and/or the detection angle can be understood easily. Due to the high refractive index of the perovskite, the direct PL is limited to its escape cone at the spot where the PL is generated. In contrast, the filtered PL can travel large distances and thus can also leave the crystal far away from the excitation spot or at the side surfaces of the crystal. This is in agreement with a very recent study by Kojima *et al.*, where the authors demonstrate by angle dependent PL of a MAPbBr₃ crystal, that direct PL is limited to a small escape cone, whereas filtered PL is also detected from the side and the backside of the crystal.⁸⁰

If we apply our model to fit the PL of the MAPbI₃ thin film from Fig. 1a, it turns out that we need to set the sample thickness to 3.5 μm to model the experimental data satisfyingly. However, the actual thickness of the sample is 0.7 μm, indicating that our model is over-simplified for the application for thin films. This points towards the importance to also consider the lateral component of the propagation direction of the light.

We finally note that the long optical pathways in halide perovskites can also impact their photocurrent measurements. For excitation in the spectral range of the Urbach tail, penetration lengths can be on the length scale of mm, so that the entire sample volume is excited and contributes to charge carrier generation. This can overcompensate the higher density of generated charges for excitation at higher photon energies, where the absorption coefficient is bigger, but the penetration length is limited to tens of nanometers. A peak of the photocurrent in the spectral region of the Urbach tail would be the consequence, bearing danger of misinterpretation if optical effects are not considered.

3. Conclusion

In summary, we have shown that the often observed double peak PL spectra of halide perovskites result from a significant self-absorption effect, which is amplified by the high internal reflection probability of PL in the sample, with Peak 1 being the emission directly outcoupled, and Peak 2 being emission that suffered multiple internal reflections and pronounced self-absorption. This effect not only impacts on the spectra of single crystals but also occurs in thin film spectra, and it is not limited to a specific perovskite composition, thus rendering it a general phenomenon. We found absorption from the Urbach-tail of the perovskite to be highly relevant for the self-absorption-effect, because optical paths in the sample can easily be on the length scale of millimeters. By controlled reduction of the reflection probability at the back side of a single crystal we could experimentally alter the intensity of the additional PL peak, thus providing compelling evidence for our conclusion. Using a relatively simple quantitative model, we were also able to simulate the PL spectra including the additional peaks and the spectral shifts that were observed in the experiment upon changing the reflectivity. Our results will help to interpret photoluminescence spectra of lead halide perovskites correctly by delivering a better understanding of the effects and importance of self-absorption and internal reflections in this material class.

4. Experimental section

4.1 Sample preparation

MAPbI₃ single crystals were prepared following the inverse temperature crystallization technique.⁸¹ In brief, the synthesis started with a 1–1.3 M solution of MAI (from Dyesol-Limited, Now GreatCell Solar) and PbI₂ (Sigma-Aldrich) in gamma-butyrolactone (GBL, Sigma-Aldrich). The precursors dissolved in GBL after 30 minutes of vigorous stirring at 60 °C. Upon filtering the solution using 0.22 μm PVDF filters, the stock solution was then distributed into small vials with 3–4 ml of solution each. The vials were kept undisturbed in an oil bath for 3–4 hours at 110 °C. Once the desired size of the crystals was achieved, the crystals were removed from the synthesis solution, washed quickly with fresh GBL, dried with a N₂ flow.

EA_{0.17}MA_{0.83}PbI₃ single crystals were grown using the antisolvent-vapor diffusion assisted crystallization method, as reported elsewhere.^{82,83} In brief, the precursor solutions were prepared by dissolving proper amount of methylammonium iodide, ethylammonium iodide and PbI₂ in γ-butyrolactone in a ratio of 0.15 M:0.15 M:0.1 M. The precursor solutions were then loaded in a small crystallizing dish with aluminum foil cover, which was then placed in a bigger dish with antisolvent, namely dichloromethane, loaded. The whole setup was sealed with an aluminum foil cover. The inner cover was left with a ~0.5 mm hole to let the antisolvent vapor diffuse inside the precursor solution. The growth process usually takes 4–6 days.

For the Synthesis of the MAPbBr₃ single crystals, a 1 M solution of MAPbBr₃ in DMF was prepared by mixing equimolar amounts of MABr and PbBr₂ in DMF over a period of 1 h. 5–10 ml of the solution were filtered over a 200 nm PTFE filter and placed in a glass Petri dish. The Petri dish was placed on a hotplate and set to 47.5 °C. The heat was increased slowly until the first nuclei were forming outside the mould. Then the temperature was increased to 75 °C with a rate of 5 °C per hour. The crystals were removed from the hot solution and washed with ether.

For fabrication of the MAPbI₃ thin films, the substrates were cleaned with detergent followed by sonication in deionized water, acetone and ethanol for 10 min each, and dried with clean dry air. After ozone treatment (at 50° for 15 min with 2 l per min O₃ flow), the substrates were transferred in a glovebox under N₂ atmosphere. For MAPbI₃ formation, we adapted a published procedure^{84,85} and optimized it as follows. PbI₂ (1 M) was dissolved in *N,N*-dimethyl formamide overnight under stirring conditions at 100 °C and 80 μl solution was spin coated on the quartz substrates at 2000 rpm for 50 s, and dried at 100 °C for 5 min. 100 mg MAI powder (see ESI† for details) was spread out around the PbI₂ coated substrates with a Petri dish covering on the top and heated at 165 °C for 13 h for full conversion.

4.2 Photoluminescence and absorption measurements

The temperature-dependent 1PI-PL of all samples and the fluence-dependent PL were performed using a home-build setup. The samples were put in a continuous flow cryostat (Oxford Instruments, Optistat CF) connected to a temperature

controller (Oxford Instruments ITC503S). The sample is excited with a 337 nm nitrogen laser (LTB MNL 100). The signal is collected via a charge-coupled device (CCD) camera (Andor iDus DU420a-OE) coupled to a spectrograph (Andor Shamrock SR303i).

The passivation experiments and the experiments with the glycerin drop at the back of the crystal were performed on air at room temperature. The crystals were excited using the nitrogen laser (LTB MNL 100) and the emitted PL was collected with an optical fiber and detected by a CCD camera (Andor iDus DU420A-OE) coupled to a spectrograph (LOT Oriel MS125). For both measurements, the sample was not moved between initial and final measurement. For the passivation measurement, it was ensured that all liquid evaporated before the final PL measurement by waiting for five minutes.

For temperature-dependent 2PI-PL measurements, the perovskite crystals used for this experiment were placed in a continuous flow cryostat, connected to a temperature controller (Oxford Instruments MercuryITC). For excitation, we used a mode-locked titanium-sapphire laser (Coherent Chameleon Ultra), with its emission center wavelength adjusted to 1000 nm. The laser power was reduced to 26 mW at 4.73 MHz and focused to a spot with a beam waist of 0.01 mm at the position of the sample. For the transmission measurements of the single crystal, a broadly fluorescent material was placed in the cryostat and its PL was measured once without and once with crystal in front of it. This technique has the advantage against conventional transmission measurements that diffraction effects that deflect the transmitted light from the optical axis play only a little role.

For each set of experiments, a new crystal was used to exclude any influence of degradation effects by previous measurements on the results of the experiment. All PL data were corrected by the corresponding setup efficiency.

Author contributions

FP initiated, and planned the project. KoS performed all optical characterizations and derived the optical model. FP, AK and KoS discussed the project. AMA synthesized the MAPbI₃ single crystals under supervision of KaS. WP synthesized the EAMAPbI₃ single crystals under supervision of OMB. DS synthesized the MAPbBr₃ single crystals under supervision of SH. TG produced the MAPbI₃ thin films under the supervision of MT. FP and KoS wrote the manuscript which was revised by all authors. FP supervised the project.

Conflicts of interest

There are no conflicts to declare.

Acknowledgements

KoS acknowledges financial support from the German National Science Foundation (Project KO 3973/2-1 and GRK 1640). AK, SH and MT acknowledges support by the Bavarian State Ministry of Science, Research, and the Arts for the Collaborative

Research Network "Solar Technologies go Hybrid". KaS acknowledges financial support from NSERC (grant number 06630) and NRC (grant number A1-014009). WP and OMB acknowledge the financial support of KAUST. Furthermore, we thank Daniel Niesner and Laura Herz for fruitful discussions, and Yu Zhong for the help with film characterizations.

References

- 1 L. M. Herz, Charge-Carrier Dynamics in Organic-Inorganic Metal Halide Perovskites, *Annu. Rev. Phys. Chem.*, 2016, **67**, 65–89.
- 2 Y. Kanemitsu, Luminescence Spectroscopy of Lead-Halide Perovskites: Materials Properties and Application as Photovoltaic Devices, *J. Mater. Chem. C*, 2017, **5**(14), 3427–3437.
- 3 T. Meier, T. P. Gujar, A. Schönleber, S. Olthof, K. Meerholz, S. van Smaalen, F. Panzer, M. Thelakkat and A. Köhler, Impact of Excess PbI₂ on the Structure and the Temperature Dependent Optical Properties of Methylammonium Lead Iodide Perovskites, *J. Mater. Chem. C*, 2018, **6**(28), 7512–7519.
- 4 F. Panzer, C. Li, T. Meier, A. Köhler and S. Huettner, Impact of Structural Dynamics on the Optical Properties of Methylammonium Lead Iodide Perovskites, *Adv. Energy Mater.*, 2017, **7**(16), 1700286.
- 5 A. D. Wright, C. Verdi, R. L. Milot, G. E. Eperon, M. A. Perez-Osorio, H. J. Snaith, F. Giustino, M. B. Johnston and L. M. Herz, Electron-Phonon Coupling in Hybrid Lead Halide Perovskites, *Nat. Commun.*, 2016, **7**, 11755.
- 6 R. L. Milot, G. E. Eperon, H. J. Snaith, M. B. Johnston and L. M. Herz, Temperature-Dependent Charge-Carrier Dynamics in CH₃NH₃PbI₃ Perovskite Thin Films, *Adv. Funct. Mater.*, 2015, **25**(39), 6218–6227.
- 7 C. Wehrenfennig, M. Z. Liu, H. J. Snaith, M. B. Johnston and L. M. Herz, Homogeneous Emission Line Broadening in the Organo Lead Halide Perovskite CH₃NH₃PbI_{3-x}Cl_x, *J. Phys. Chem. Lett.*, 2014, **5**(8), 1300–1306.
- 8 F. Panzer, S. Baderschneider, T. P. Gujar, T. Unger, S. Bagnich, M. Jakoby, H. Bäessler, S. Huettner, J. Köhler, R. Moos, M. Thelakkat, R. Hildner and A. Köhler, Reversible Laser Induced Amplified Spontaneous Emission from Coexisting Tetragonal and Orthorhombic Phases in Hybrid Lead Halide Perovskites, *Adv. Opt. Mater.*, 2016, **4**(6), 917–928.
- 9 X. X. Wu, M. T. Trinh, D. Niesner, H. M. Zhu, Z. Norman, J. S. Owen, O. Yaffe, B. J. Kudisch and X. Y. Zhu, Trap States in Lead Iodide Perovskites, *J. Am. Chem. Soc.*, 2015, **137**(5), 2089–2096.
- 10 C. Wehrenfennig, M. Z. Liu, H. J. Snaith, M. B. Johnston and L. M. Herz, Charge Carrier Recombination Channels in the Low-Temperature Phase of Organic-Inorganic Lead Halide Perovskite Thin Films, *APL Mater.*, 2014, **2**(8), 081513.
- 11 J. Li, A. Dobrovolsky, A. Merdasa, E. L. Unger and I. G. Scheblykin, Luminescent Intermediates and Humidity-Dependent Room-Temperature Conversion of the MAPbI₃ Perovskite Precursor, *ACS Omega*, 2018, **3**(10), 14494–14502.
- 12 Y. Tian, M. Peter, E. Unger, M. Abdallah, K. Zheng, T. Pullerits, A. Yartsev, V. Sundstrom and I. G. Scheblykin,

- Mechanistic Insights into Perovskite Photoluminescence Enhancement: Light Curing with Oxygen can Boost Yield Thousandfold, *Phys. Chem. Chem. Phys.*, 2015, **17**(38), 24978–24987.
- 13 G. Grancini, V. D'Innocenzo, E. R. Dohner, N. Martino, A. R. S. Kandada, E. Mosconi, F. De Angelis, H. I. Karunadasa, E. T. Hoke and A. Petrozza, $\text{CH}_3\text{NH}_3\text{PbI}_3$ Perovskite Single Crystals: Surface Photophysics and their Interaction with the Environment, *Chem. Sci.*, 2015, **6**(12), 7305–7310.
 - 14 D. W. deQuilettes, S. M. Vorpahl, S. D. Stranks, H. Nagaoka, G. E. Eperon, M. E. Ziffer, H. J. Snaith and D. S. Ginger, Impact of Microstructure on Local Carrier Lifetime in Perovskite Solar Cells, *Science*, 2015, **348**(6235), 683–686.
 - 15 Q. Jiang, Y. Zhao, X. Zhang, X. Yang, Y. Chen, Z. Chu, Q. Ye, X. Li, Z. Yin and J. You, Surface Passivation of Perovskite Film for Efficient Solar Cells, *Nat. Photonics*, 2019, **13**(7), 460–466.
 - 16 N. K. Noel, A. Abate, S. D. Stranks, E. S. Parrott, V. M. Burlakov, A. Goriely and H. J. Snaith, Enhanced Photoluminescence and Solar Cell Performance via Lewis Base Passivation of Organic Inorganic Lead Halide Perovskites, *ACS Nano*, 2014, **8**(10), 9815–9821.
 - 17 M. Abdi-Jalebi, Z. Andaji-Garmaroudi, S. Cacovich, C. Stavrakas, B. Philippe, J. M. Richter, M. Alsari, E. P. Booker, E. M. Hutter, A. J. Pearson, S. Lilliu, T. J. Savenije, H. Rensmo, G. Divitini, C. Ducati, R. H. Friend and S. D. Stranks, Maximizing and Stabilizing Luminescence from Halide Perovskites with Potassium Passivation, *Nature*, 2018, **555**(7697), 497–501.
 - 18 E. M. Hutter, M. C. Gélvez-Rueda, A. Osherov, V. Bulović, F. C. Grozema, S. D. Stranks and T. J. Savenije, Direct-Indirect Character of the Bandgap in Methylammonium Lead Iodide Perovskite, *Nat. Mater.*, 2017, **16**(1), 115–120.
 - 19 T. Wang, B. Daiber, J. M. Frost, S. A. Mann, E. C. Garnett, A. Walsh and B. Ehrler, Indirect to Direct Bandgap Transition in Methylammonium Lead Halide Perovskite, *Energy Environ. Sci.*, 2017, **10**(2), 509–515.
 - 20 B. Wu, H. F. Yuan, Q. Xu, J. A. Steele, D. Giovanni, P. Puech, J. H. Fu, Y. F. Ng, N. F. Jamaludin, A. Solanki, S. Mhaisalkar, N. Mathews, M. B. J. Roeffaers, M. Grätzel, J. Hofkens and T. C. Sum, Indirect Tail States Formation by Thermal-Induced Polar Fluctuations in Halide Perovskites, *Nat. Commun.*, 2019, **10**, 484.
 - 21 J. H. Fu, N. F. Jamaludin, B. Wu, M. J. Li, A. Solanki, Y. F. Ng, S. Mhaisalkar, C. H. A. Huan and T. C. Sum, Localized Traps Limited Recombination in Lead Bromide Perovskites, *Adv. Energy Mater.*, 2019, **9**(12), 1803119.
 - 22 J. A. Steele, P. Puech, B. Monserrat, B. Wu, R. X. Yang, T. Kirchartz, H. Yuan, G. Fleury, D. Giovanni, E. Fron, M. Keshavarz, E. Debroye, G. Zhou, T. C. Sum, A. Walsh, J. Hofkens and M. B. J. Roeffaers, Role of Electron-Phonon Coupling in the Thermal Evolution of Bulk Rashba-Like Spin-Split Lead Halide Perovskites Exhibiting Dual-Band Photoluminescence, *ACS Energy Lett.*, 2019, 2205–2212.
 - 23 X. Chi, K. Leng, B. Wu, D. Shi, Y. Choy, Z. Chen, Z. Chen, X. Yu, P. Yang, Q.-H. Xu, T. C. Sum, A. Ruydy and K. P. Loh, Elucidating Surface and Bulk Emission in 3D Hybrid Organic-Inorganic Lead Bromide Perovskites, *Adv. Opt. Mater.*, 2018, **6**(15), 1800470.
 - 24 J. Shi, H. Zhang, Y. Li, J. J. Jasieniak, Y. Li, H. Wu, Y. Luo, D. Li and Q. Meng, Identification of High-Temperature Exciton States and their Phase-Dependent Trapping Behaviour in Lead Halide Perovskites, *Energy Environ. Sci.*, 2018, **11**(6), 1460–1469.
 - 25 D. Niesner, O. Schuster, M. Wilhelm, I. Levchuk, A. Osvet, S. Shrestha, M. Batentschuk, C. Brabec and T. Fauster, Temperature-Dependent Optical Spectra of Single-Crystal $(\text{CH}_3\text{NH}_3)_2\text{PbBr}_3$ Cleaved in Ultrahigh Vacuum, *Phys. Rev. B*, 2017, **95**(7), 075207.
 - 26 B. Murali, S. Dey, A. L. Abdelhady, W. Peng, E. Alarousu, A. R. Kirmani, N. C. Cho, S. P. Sarmah, M. R. Parida, M. I. Saidaminov, A. A. Zhumekenov, J. Y. Sun, M. S. Alias, E. Yengel, B. S. Ooi, A. Amassian, O. M. Bakr and O. F. Mohammed, Surface Restructuring of Hybrid Perovskite Crystals, *ACS Energy Lett.*, 2016, **1**(6), 1119–1126.
 - 27 B. Murali, E. Yengel, C. Yang, W. Peng, E. Alarousu, O. M. Bakr and O. F. Mohammed, The Surface of Hybrid Perovskite Crystals: A Boon or Bane, *ACS Energy Lett.*, 2017, **2**(4), 846–856.
 - 28 S. T. Birkhold, E. Zimmermann, T. Kollek, D. Wurmbbrand, S. Polarz and L. Schmidt-Mende, Impact of Crystal Surface on Photoexcited States in Organic-Inorganic Perovskites, *Adv. Funct. Mater.*, 2017, **27**(6), 1604995.
 - 29 F. Chen, C. Zhu, C. X. Xu, P. Fan, F. F. Qin, A. G. Manohari, J. F. Lu, Z. L. Shi, Q. Y. Xu and A. L. Pan, Crystal Structure and Electron Transition Underlying Photoluminescence of Methylammonium Lead Bromide Perovskites, *J. Mater. Chem. C*, 2017, **5**(31), 7739–7745.
 - 30 L. M. Pazos-Outón, M. Szumilo, R. Lamboll, J. M. Richter, M. Crespo-Quesada, M. Abdi-Jalebi, H. J. Beeson, M. Vrucinic, M. Alsari, H. J. Snaith, B. Ehrler, R. H. Friend and F. Deschler, Photon Recycling in Lead Iodide Perovskite Solar Cells, *Science*, 2016, **351**(6280), 1430–1433.
 - 31 Y. Fang, H. Wei, Q. Dong and J. Huang, Quantification of Re-Absorption and Re-Emission Processes to Determine Photon Recycling Efficiency in Perovskite Single Crystals, *Nat. Commun.*, 2017, **8**, 14417.
 - 32 Y. Yamada, T. Yamada, L. Q. Phuong, N. Maruyama, H. Nishimura, A. Wakamiya, Y. Murata and Y. Kanemitsu, Dynamic Optical Properties of $\text{CH}_3\text{NH}_3\text{PbI}_3$ Single Crystals as Revealed by One- and Two-Photon Excited Photoluminescence Measurements, *J. Am. Chem. Soc.*, 2015, **137**(33), 10456–10459.
 - 33 T. Yamada, Y. Yamada, H. Nishimura, Y. Nakaike, A. Wakamiya, Y. Murata and Y. Kanemitsu, Fast Free-Carrier Diffusion in $\text{CH}_3\text{NH}_3\text{PbBr}_3$ Single Crystals Revealed by Time-Resolved One- and Two-Photon Excitation Photoluminescence Spectroscopy, *Adv. Electron. Mater.*, 2016, **2**(3), 1500290.
 - 34 A. Poglitsch and D. Weber, Dynamic Disorder in Methylammoniumtrihalogenoplumbates(II) Observed by Millimeter-Wave Spectroscopy, *J. Chem. Phys.*, 1987, **87**(11), 6373–6378.
 - 35 T. Ishihara, Optical-Properties of PbI-Based Perovskite Structures, *J. Lumin.*, 1994, **60–61**, 269–274.

- 36 W. G. Kong, Z. Y. Ye, Z. Qi, B. P. Zhang, M. Wang, A. Rahimi-Iman and H. Z. Wu, Characterization of an Abnormal Photo-luminescence Behavior upon Crystal-Phase Transition of Perovskite $\text{CH}_3\text{NH}_3\text{PbI}_3$, *Phys. Chem. Chem. Phys.*, 2015, **17**(25), 16405–16411.
- 37 E. S. Parrott, R. L. Milot, T. Stergiopoulos, H. J. Snaith, M. B. Johnston and L. M. Herz, Effect of Structural Phase Transition on Charge-Carrier Lifetimes and Defects in $\text{CH}_3\text{NH}_3\text{SnI}_3$ Perovskite, *J. Phys. Chem. Lett.*, 2016, **7**(7), 1321–1326.
- 38 D. Niesner, M. Wilhelm, I. Levchuk, A. Osvet, S. Shrestha, M. Batenschuk, C. Brabec and T. Fauster, Giant Rashba Splitting in $\text{CH}_3\text{NH}_3\text{PbBr}_3$ Organic-Inorganic Perovskite, *Phys. Rev. Lett.*, 2016, **117**(12), 126401.
- 39 D. Niesner, M. Hauck, S. Shrestha, I. Levchuk, G. J. Matt, A. Osvet, M. Batenschuk, C. Brabec, H. B. Weber and T. Fauster, Structural Fluctuations Cause Spin-Split States in Tetragonal $\text{CH}_3\text{NH}_3\text{PbI}_3$ as Evidenced by the Circular Photogalvanic Effect, *Proc. Natl. Acad. Sci. U. S. A.*, 2018, **115**(38), 9509–9514.
- 40 S. D. Stranks and P. Plochocka, The Influence of the Rashba Effect, *Nat. Mater.*, 2018, **17**(5), 381–382.
- 41 L. Leppert, S. E. Reyes-Lillo and J. B. Neaton, Electric Field- and Strain-Induced Rashba Effect in Hybrid Halide Perovskites, *J. Phys. Chem. Lett.*, 2016, **7**(18), 3683–3689.
- 42 J. M. Richter, K. Chen, A. Sadhanala, J. Butkus, J. P. H. Rivett, R. H. Friend, B. Monserrat, J. M. Hodgkiss and F. Deschler, Direct Bandgap Behavior in Rashba-Type Metal Halide Perovskites, *Adv. Mater.*, 2018, **30**(52), e1803379.
- 43 F. Zheng, L. Z. Tan, S. Liu and A. M. Rappe, Rashba Spin-Orbit Coupling Enhanced Carrier Lifetime in $\text{CH}_3\text{NH}_3\text{PbI}_3$, *Nano Lett.*, 2015, **15**(12), 7794–7800.
- 44 T. Etienne, E. Mosconi and F. De Angelis, Dynamical Origin of the Rashba Effect in Organohalide Lead Perovskites: A Key to Suppressed Carrier Recombination in Perovskite Solar Cells?, *J. Phys. Chem. Lett.*, 2016, **7**(9), 1638–1645.
- 45 M. Kepenekian and J. Even, Rashba and Dresselhaus Couplings in Halide Perovskites: Accomplishments and Opportunities for Spintronics and Spin-Orbitronics, *J. Phys. Chem. Lett.*, 2017, **8**(14), 3362–3370.
- 46 T. Kirchartz and U. Rau, Decreasing Radiative Recombination Coefficients via an Indirect Band Gap in Lead Halide Perovskites, *J. Phys. Chem. Lett.*, 2017, **8**(6), 1265–1271.
- 47 D. A. Egger, A. Bera, D. Cahen, G. Hodes, T. Kirchartz, L. Kronik, R. Lovrincic, A. M. Rappe, D. R. Reichman and O. Yaffe, What Remains Unexplained about the Properties of Halide Perovskites?, *Adv. Mater.*, 2018, **30**(20), e1800691.
- 48 K. Frohna, T. Deshpande, J. Harter, W. Peng, B. A. Barker, J. B. Neaton, S. G. Louie, O. M. Bakr, D. Hsieh and M. Bernardi, Inversion Symmetry and Bulk Rashba Effect in Methylammonium Lead Iodide Perovskite Single Crystals, *Nat. Commun.*, 2018, **9**, 1829.
- 49 C. L. Davies, M. R. Filip, J. B. Patel, T. W. Crothers, C. Verdi, A. D. Wright, R. L. Milot, F. Giustino, M. B. Johnston and L. M. Herz, Bimolecular Recombination in Methylammonium Lead Triiodide Perovskite is an Inverse Absorption Process, *Nat. Commun.*, 2018, **9**(1), 293.
- 50 P. Azarhoosh, S. McKechnie, J. M. Frost, A. Walsh and M. van Schilfhaarde, Research Update: Relativistic Origin of Slow Electron-Hole Recombination in Hybrid Halide Perovskite Solar Cells, *APL Mater.*, 2016, **4**(9), 091501.
- 51 W. Du, S. A. Ghetmiri, B. R. Conley, A. Mosleh, A. Nazzal, R. A. Soref, G. Sun, J. Tolle, J. Margetis, H. A. Naseem and S.-Q. Yu, Competition of Optical Transitions Between Direct and Indirect Bandgaps in $\text{Ge}_{1-x}\text{Sn}_x$, *Appl. Phys. Lett.*, 2014, **105**(5), 051104.
- 52 S. Al-Kabi, S. Ghetmiri, J. Margetis, W. Du, A. Mosleh, M. Alher, W. Dou, J. Grant, G. Sun, R. Soref, J. Tolle, B. Li, M. Mortazavi, H. Naseem and S. Q. Yu, Optical Characterization of Si-Based $\text{Ge}_{1-x}\text{Sn}_x$ Alloys with Sn Compositions up to 12%, *J. Electron. Mater.*, 2016, **45**(4), 2133–2141.
- 53 D. Stange, S. Wirths, N. von den Driesch, G. Mussler, T. Stoica, Z. Ikonik, J. M. Hartmann, S. Mantl, D. Grützmacher and D. Buca, Optical Transitions in Direct-Bandgap $\text{Ge}_{1-x}\text{Sn}_x$ Alloys, *ACS Photonics*, 2015, **2**(11), 1539–1545.
- 54 S. Wirths, R. Geiger, N. von den Driesch, G. Mussler, T. Stoica, S. Mantl, Z. Ikonik, M. Luysberg, S. Chiussi, J. M. Hartmann, H. Sigg, J. Faist, D. Buca and D. Grützmacher, Lasing in Direct-Bandgap GeSn Alloy Grown on Si, *Nat. Photonics*, 2015, **9**(2), 88–92.
- 55 T. W. Jones, A. Osherov, M. Alsari, M. Sponseller, B. C. Duck, Y. K. Jung, C. Settens, F. Niroui, R. Brenes, C. V. Stan, Y. Li, M. Abdi-Jalebi, N. Tamura, J. E. Macdonald, M. Burghammer, R. H. Friend, V. Bulovic, A. Walsh, G. J. Wilson, S. Lilliu and S. D. Stranks, Lattice Strain Causes Non-Radiative Losses in Halide Perovskites, *Energy Environ. Sci.*, 2019, **12**(2), 596–606.
- 56 X. Y. Li, Y. Q. Luo, M. V. Holt, Z. H. Cai and D. P. Fenning, Residual Nanoscale Strain in Cesium Lead Bromide Perovskite Reduces Stability and Shifts Local Luminescence, *Chem. Mater.*, 2019, **31**(8), 2778–2785.
- 57 Goodfellow GmbH, Datasheet polyethylene terephthalate (Polyester, PET, PETP); available from goodfellow.com/E/Polyethylene-terephthalate.html, last accessed September 3, 2019.
- 58 Polymerdatabase, Datasheet poly(ethylene terephthalate) (PET), available from polymerdatabase.com/Commercial%20Polymers/PET.html, last accessed September 3, 2019.
- 59 H. A. Schaeffer and R. Langfeld, *Werkstoff Glas*, Springer Vieweg, Berlin, Heidelberg, Germany, 2014, p. 46.
- 60 S. Singh, C. Li, F. Panzer, K. L. Narasimhan, A. Graeser, T. P. Gujar, A. Köhler, M. Thelakkat, S. Huettner and D. Kabra, Effect of Thermal and Structural Disorder on the Electronic Structure of Hybrid Perovskite Semiconductor $\text{CH}_3\text{NH}_3\text{PbI}_3$, *J. Phys. Chem. Lett.*, 2016, **7**(15), 3014–3021.
- 61 T. J. Jacobsson, L. J. Schwan, M. Ottosson, A. Hagfeldt and T. Edvinsson, Determination of Thermal Expansion Coefficients and Locating the Temperature-Induced Phase Transition in Methylammonium Lead Perovskites Using X-ray Diffraction, *Inorg. Chem.*, 2015, **54**(22), 10678–10685.
- 62 J. Zhao, Y. Deng, H. Wei, X. Zheng, Z. Yu, Y. Shao, J. E. Shield and J. Huang, Strained Hybrid Perovskite Thin Films and Their Impact on the Intrinsic Stability of Perovskite Solar Cells, *Sci. Adv.*, 2017, **3**(11), eaao5616.

- 63 A. Oshero, E. M. Hutter, K. Galkowski, R. Brenes, D. K. Maude, R. J. Nicholas, P. Plochocka, V. Bulovic, T. J. Savenije and S. D. Stranks, The Impact of Phase Retention on the Structural and Optoelectronic Properties of Metal Halide Perovskites, *Adv. Mater.*, 2016, **28**(48), 10757–10763.
- 64 F. Panzer, H. Bässler and A. Köhler, Temperature Induced Order-Disorder Transition in Solutions of Conjugated Polymers Probed by Optical Spectroscopy, *J. Phys. Chem. Lett.*, 2017, **8**(1), 114–125.
- 65 X. P. Zheng, B. Chen, J. Dai, Y. J. Fang, Y. Bai, Y. Z. Lin, H. T. Wei, X. C. Zeng and J. S. Huang, Defect Passivation in Hybrid Perovskite Solar Cells Using Quaternary Ammonium Halide Anions and Cations, *Nat. Energy*, 2017, **2**(7), 17102.
- 66 S. P. Sarmah, V. M. Burlakov, E. Yengel, B. Murali, E. Alarousu, A. M. El-Zohry, C. Yang, M. S. Alias, A. A. Zhumekenov, M. I. Saidaminov, N. Cho, N. Wehbe, S. Mitra, I. Ajia, S. Dey, A. E. Mansour, M. Abdelsamie, A. Amassian, I. S. Roqan, B. S. Ooi, A. Goriely, O. M. Bakr and O. F. Mohammed, Double Charged Surface Layers in Lead Halide Perovskite Crystals, *Nano Lett.*, 2017, **17**(3), 2021–2027.
- 67 R. W. Boyd, *Nonlinear Optics*, Academic Press, Burlington, USA, 3rd edn, 2008, pp. 549–559.
- 68 M. Göppert-Mayer, Über Elementarakte mit zwei Quantensprünge, *Ann. Phys.*, 1931, **401**(3), 273–294.
- 69 G. Nagamine, J. O. Rocha, L. G. Bonato, A. F. Nogueira, Z. Zaharieva, A. A. R. Watt, C. H. de Brito Cruz and L. A. Padilha, Two-Photon Absorption and Two-Photon-Induced Gain in Perovskite Quantum Dots, *J. Phys. Chem. Lett.*, 2018, **9**(12), 3478–3484.
- 70 T. W. Crothers, R. L. Milot, J. B. Patel, E. S. Parrott, J. Schlipf, P. Müller-Buschbaum, M. B. Johnston and L. M. Herz, Photon Reabsorption Masks Intrinsic Bimolecular Charge-Carrier Recombination in $\text{CH}_3\text{NH}_3\text{PbI}_3$ Perovskite, *Nano Lett.*, 2017, **17**(9), 5782–5789.
- 71 S. De Wolf, J. Holovsky, S. J. Moon, P. Loper, B. Niesen, M. Ledinsky, F. J. Haug, J. H. Yum and C. Ballif, Organometallic Halide Perovskites: Sharp Optical Absorption Edge and Its Relation to Photovoltaic Performance, *J. Phys. Chem. Lett.*, 2014, **5**(6), 1035–1039.
- 72 A. Sadhanala, F. Deschler, T. H. Thomas, S. E. Dutton, K. C. Goedel, F. C. Hanusch, M. L. Lai, U. Steiner, T. Bein, P. Docampo, D. Cahen and R. H. Friend, Preparation of Single-Phase Films of $\text{CH}_3\text{NH}_3\text{Pb}(\text{I}_{1-x}\text{Br}_x)_3$ with Sharp Optical Band Edges, *J. Phys. Chem. Lett.*, 2014, **5**(15), 2501–2505.
- 73 V. D'Innocenzo, G. Grancini, M. J. Alcocer, A. R. Kandada, S. D. Stranks, M. M. Lee, G. Lanzani, H. J. Snaith and A. Petrozza, Excitons Versus Free Charges in Organo-Lead Tri-Halide Perovskites, *Nat. Commun.*, 2014, **5**, 3586.
- 74 M. Ledinsky, T. Schönfeldová, J. Holovský, E. Aydin, Z. Hájková, L. Landová, N. Neyková, A. Fejfar and S. De Wolf, Temperature Dependence of the Urbach Energy in Lead Iodide Perovskites, *J. Phys. Chem. Lett.*, 2019, **10**(6), 1368–1373.
- 75 L. J. Phillips, A. M. Rashed, R. E. Treharne, J. Kay, P. Yates, I. Z. Mitrovic, A. Weerakkody, S. Hall and K. Durose, Dispersion Relation Data for Methylammonium Lead Triiodide Perovskite Deposited on a (100) Silicon Wafer Using a Two-Step Vapour-Phase Reaction Process, *Data Brief*, 2015, **5**, 926–928.
- 76 R. Brenes, M. Laitz, J. Jean, D. W. de Quillettes and V. Bulovic, Benefit from Photon Recycling at the Maximum-Power Point of State-of-the-Art Perovskite Solar Cells, *Phys. Rev. Appl.*, 2019, **12**(1), 014017.
- 77 I. Dursun, Y. Z. Zheng, T. L. Guo, M. De Bastiani, B. Tureddi, L. Sinatra, M. A. Hague, B. Sun, A. A. Zhumekenov, M. I. Saidaminov, F. P. G. de Arquer, E. H. Sargent, T. Wu, Y. N. Gartstein, O. M. Bakr, O. F. Mohammed and A. V. Malko, Efficient Photon Recycling and Radiation Trapping in Cesium Lead Halide Perovskite Waveguides, *ACS Energy Lett.*, 2018, **3**(7), 1492–1498.
- 78 J. Rheims, J. Koser and T. Wriedt, Refractive-Index Measurements in the Near-IR Using an Abbe Refractometer, *Meas. Sci. Technol.*, 1997, **8**(6), 601–605.
- 79 L. Q. Phuong, Y. Nakaike, A. Wakamiya and Y. Kanemitsu, Free Excitons and Exciton-Phonon Coupling in $\text{CH}_3\text{NH}_3\text{PbI}_3$ Single Crystals Revealed by Photocurrent and Photoluminescence Measurements at Low Temperatures, *J. Phys. Chem. Lett.*, 2016, **7**(23), 4905–4910.
- 80 K. Kojima, K. Ikemura, K. Matsumori, Y. Yamada, Y. Kanemitsu and S. F. Chichibu, Internal Quantum Efficiency of Radiation in a Bulk $\text{CH}_3\text{NH}_3\text{PbBr}_3$ Perovskite Crystal Quantified by Using the Omnidirectional Photoluminescence Spectroscopy, *APL Mater.*, 2019, **7**(7), 071116.
- 81 M. I. Saidaminov, A. L. Abdelhady, B. Murali, E. Alarousu, V. M. Burlakov, W. Peng, I. Dursun, L. F. Wang, Y. He, G. Maculan, A. Goriely, T. Wu, O. F. Mohammed and O. M. Bakr, High-Quality Bulk Hybrid Perovskite Single Crystals Within Minutes by Inverse Temperature Crystallization, *Nat. Commun.*, 2015, **6**, 7586.
- 82 W. Peng, X. H. Miao, V. Adinolfi, E. Alarousu, O. El Tall, A. H. Emwas, C. Zhao, G. Walters, J. K. Liu, O. Ouellette, J. Pan, B. Murali, E. H. Sargent, O. F. Mohammed and O. M. Bakr, Engineering of $\text{CH}_3\text{NH}_3\text{PbI}_3$ Perovskite Crystals by Alloying Large Organic Cations for Enhanced Thermal Stability and Transport Properties, *Angew. Chem., Int. Ed.*, 2016, **55**(36), 10686–10690.
- 83 D. Shi, V. Adinolfi, R. Comin, M. J. Yuan, E. Alarousu, A. Buin, Y. Chen, S. Hoogland, A. Rothenberger, K. Katsiev, Y. Losovyj, X. Zhang, P. A. Dowben, O. F. Mohammed, E. H. Sargent and O. M. Bakr, Low Trap-State Density and Long Carrier Diffusion in Organolead Trihalide Perovskite Single Crystals, *Science*, 2015, **347**(6221), 519–522.
- 84 T. P. Gujar and M. Thelakkat, Highly Reproducible and Efficient Perovskite Solar Cells with Extraordinary Stability from Robust $\text{CH}_3\text{NH}_3\text{PbI}_3$: Towards Large-Area Devices, *Energy Technol.*, 2016, **4**(3), 449–457.
- 85 F. Panzer, S. Baderschneider, T. P. Gujar, T. Unger, S. Bagnich, M. Jakoby, H. Bässler, S. Huettner, J. Köhler, R. Moos, M. Thelakkat, R. Hildner and A. Köhler, Reversible Laser-Induced Amplified Spontaneous Emission from Coexisting Tetragonal and Orthorhombic Phases in Hybrid Lead Halide Perovskites, *Adv. Opt. Mater.*, 2016, **4**(6), 917–928.

Supporting Information for

Double Peak Emission in Lead Halide Perovskites by Self-Absorption

Konstantin Schötz¹, Abdelrahman Askar², Wei Peng³, Dominik Seeberger⁴, Tanaji P. Guijar⁴, Mukundan Thelakkat⁴, Anna Köhler^{1,5}, Sven Hüttner⁴, Osman M. Bakr³, Karthik Shankar², Fabian Panzer^{1*}

¹: Soft Matter Optoelectronics, University of Bayreuth, 95440 Bayreuth, Germany

²: Department of Electrical and Computer Engineering, University of Alberta, Edmonton, AB T6G 1H9, Canada

³: King Abdullah University of Science and Technology (KAUST), Division of Physical Sciences and Engineering, Thuwal23955-6900, Kingdom of Saudi Arabia

⁴: Department of Chemistry, University of Bayreuth, 95440 Bayreuth, Germany

⁵: Bayreuth Institute of Macromolecular Research (BIMF) and Bavarian Polymer Institute (BPI), University of Bayreuth, 95440 Bayreuth, Germany.

Corresponding Author: fabian.panzer@uni-bayreuth.de

1. Logarithmic version of Figure 1a

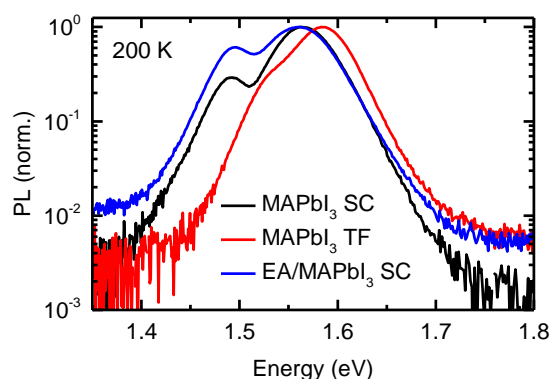


Figure S1: Logarithmic plot of the PL of the iodine samples at 200 K from Figure 1 in the main text. In the logarithmic depiction of the PL of the MAPbI₃ thin film, the additional shoulder at 1.53 eV becomes more obvious.

2. PL Peak 2 intensity dependence on excitation laser spot

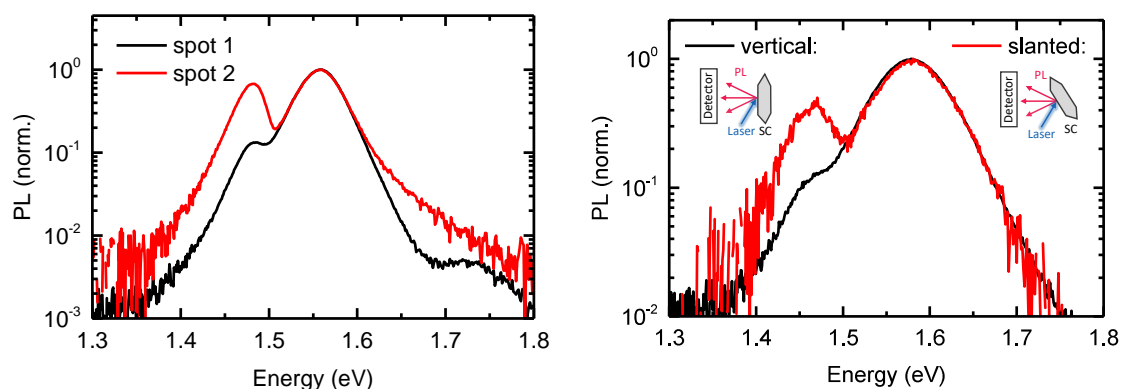


Figure S2: Left: Normalized PL of a MAPbI₃ single crystal at 170 K. Between both measurements the spot of the excitation laser was moved in such a way that at the first position, Peak 2 was less pronounced (spot 1, black curve), while for the second position, Peak 2 was strongly pronounced (spot 2, red curve). Right: Normalized PL of a MAPbI₃ single crystal at 300 K under vertical detection (black) and slanted detection (red) as illustrated in the inset.

3. Temperature-dependent PL of other perovskite samples

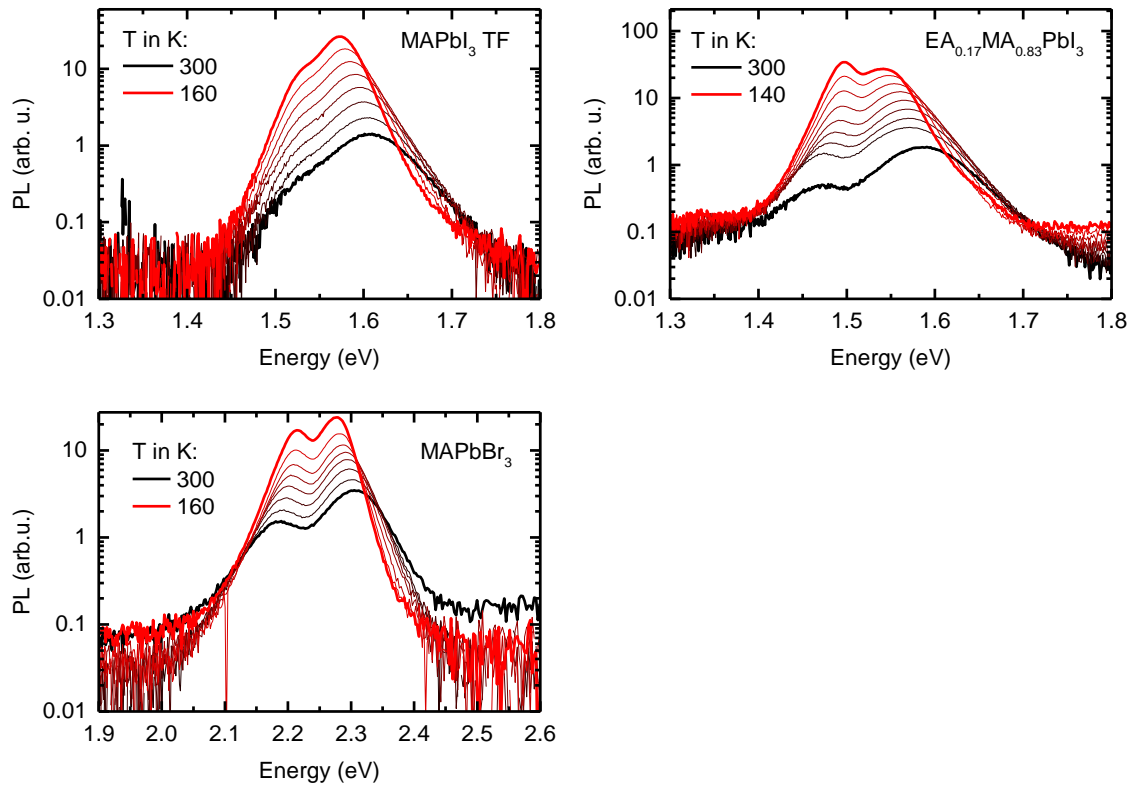


Figure S3: Temperature-dependent PL of the MAPbI₃ thin film (TF), the EA_{0.17}MA_{0.83}PbI₃ single crystal and the MAPbBr₃ single crystal. The temperature difference between each line is 20 K.

4. Spectral decomposition of measured PL spectrum

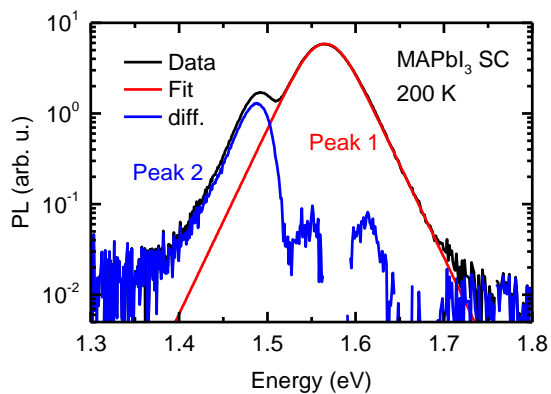


Figure S4: Decomposition of the PL spectrum of the MAPbI₃ single crystal at 200 K. The experimental data is shown in black. The red curve presents an empiric fit to Peak 1 using two hyperbolic secants with equal intensity and width, but shifted by 14 meV to obtain a better fit. The difference between fit and data is plotted in blue and presents the shape of Peak 2.

5. PL of the MAPbI₃ single crystal between 160 – 120 K

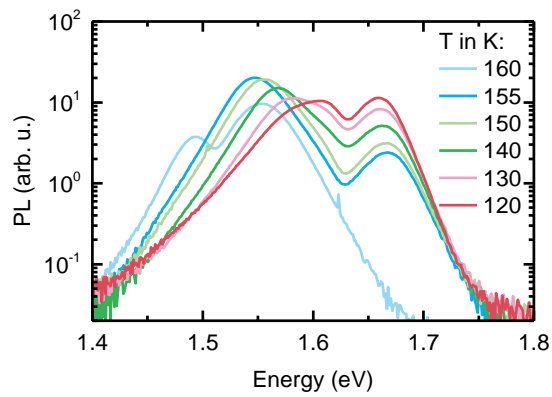


Figure S5: PL spectra of the MAPbI₃ single crystal in the phase transition region between 160 K and 120 K.

6. Low-temperature PL of the MAPbI₃ single crystal

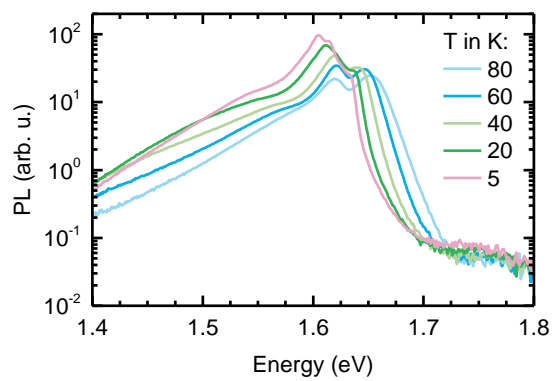


Figure S6: Temperature-dependent PL of the MAPbI₃ single crystal in the range between 80 K to 5 K.

7. Verification of different extend of strain in the MAPbI₃ films on PET- and glass substrate

As mentioned in the main text, strain in the sample has influence on the phase transition of the perovskite. The quantification of the tetragonal to orthorhombic phase transition of the MAPbI₃ thin films on PET and glass substrate via their absorption spectra (see Figure S7a,b) was performed identical to the method described in in the work by Meier et al. and Panzer et al.¹⁻² We extracted the optical density (OD) of the films at 1.62 eV from 170 K to 100 K (Figure S7c). As only the tetragonal phase absorbs at this energy in this temperature range, the OD value is representative of the amount of tetragonal phase in the system. We then calculated the derivative of the temperature dependent OD and fitted this with a Gaussian function (Figure S7d), where its center is the critical temperature T_c and its full width at half maximum (FWHM) describes the width of the phase transition. By doing so, we obtain for the film on the glass substrate $T_{c,Glass} = 145.9 \pm 0.3$ K, $FWHM_{Glass} = 10.1 \pm 0.7$ K and for the PET substrate $T_{c,PET} = 147.2 \pm 0.2$ K, $FWHM_{PET} = 8.8 \pm 0.6$ K.

Additionally, strain in the sample should have influence on the lattice constants and thus on the PL peak position. We therefore analyzed the temperature-dependence of the PL peak position of the MAPbI₃ films on PET and glass substrate (see Figure S7e), where we find a shift of 0.25 meV/K for the sample on glass, and 0.28 meV/K for the sample on PET. The reduced shift for the sample on glass is consistent with more strain being present that counteracts the decrease of the lattice constant of MAPbI₃ upon cooling. This leads to a decreased temperature depend band gap shift, which is reflected in the PL position.

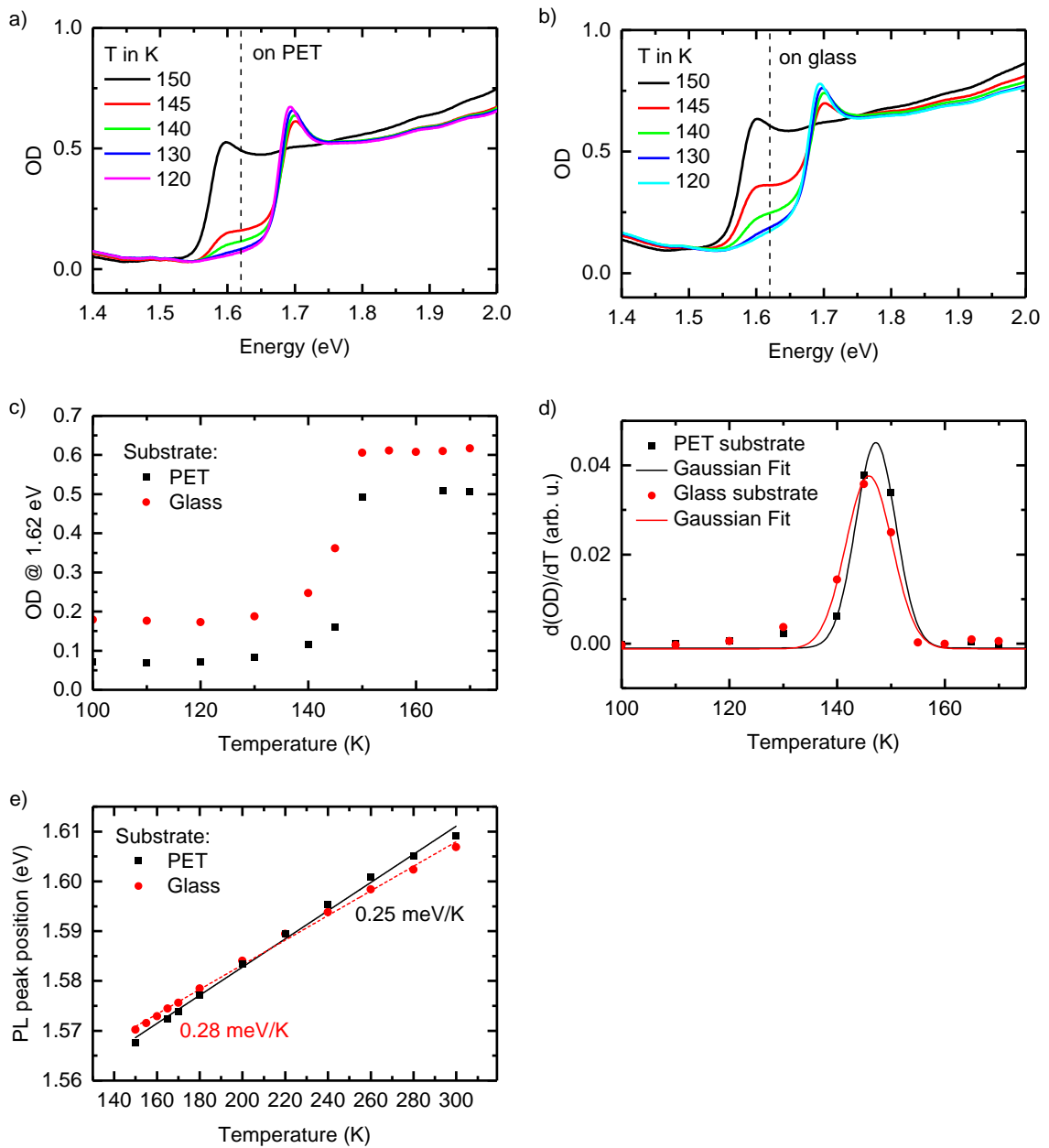


Figure S7: Temperature-dependent absorption of a MAPbI₃ thin film on (a) PET and (b) glass substrate. (c) Optical density of both films at 1.62 eV in the temperature range of the tetragonal to orthorhombic phase transition, i.e. 170 K to 100 K. (d) Derivative of the OD at 1.62 eV together with Gaussian fits (solid lines). (e) Temperature-dependence of the PL peak position of the MAPbI₃ films on PET (black squares) and glass substrate (red circles), together with linear fits to the data points.

8. Spectral decomposition of the PL of MAPbI₃ film on glass and PET substrate

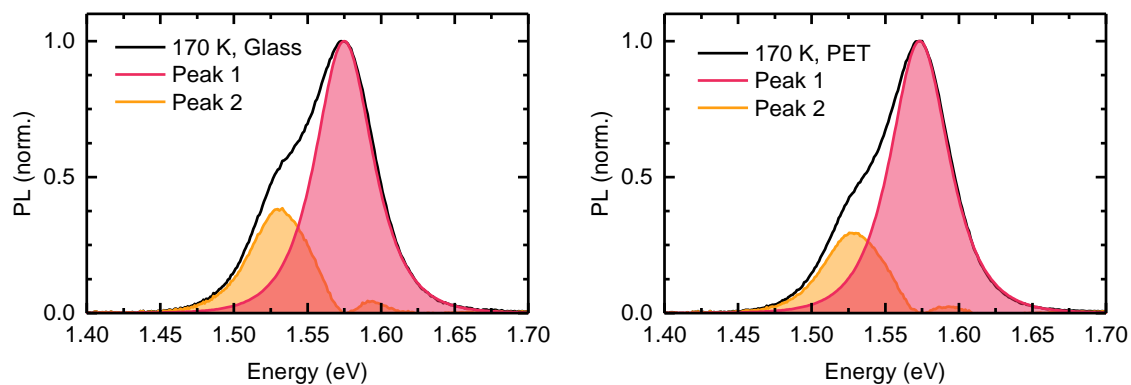


Figure S8: Spectral decomposition of the MAPbI₃ film on glass (left) and PET substrate (right) by fitting a hyperbolic secant to Peak 2

9. Discussion of the spectral blue shift upon passivation

A schematic illustration of the influence of surface passivation on the PL is shown in Figure S9. Before passivation, there is an increased defect density and consequently an increased non-radiative recombination rate near the surface of the perovskite (blue shaded area). Consequently, the PL intensity is reduced in the surface region and most of the detected PL comes from the inside of the material and thus is to a certain extent self-absorbed and therefore red-shifted compared to the intrinsic PL. Surface passivation reduces the defect density at the surface and consequently increases the PL intensity in this area. Hence, the detectable PL after passivation is on average less self-absorbed and less red-shifted than before passivation. Therefore, the PL after surface passivation occurs blue-shifted compared to the PL before passivation.

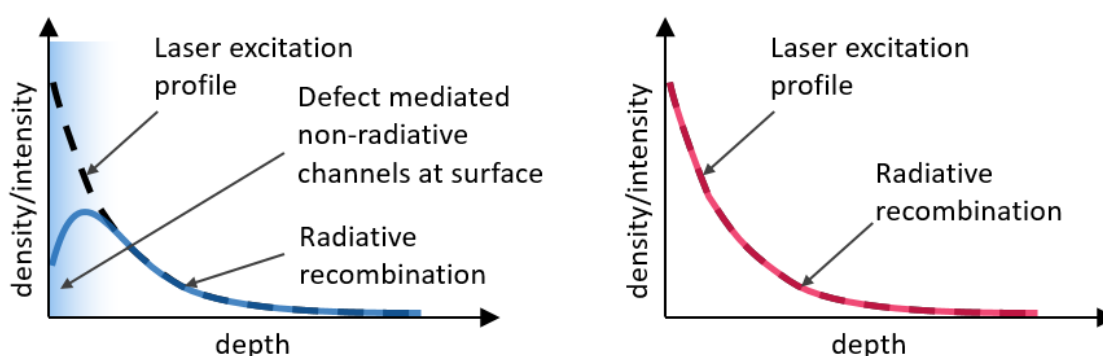


Figure S9: Schematic illustration of the PL intensity (solid line) as a function of depth after laser excitation (dashed line), before (left) and after surface passivation (right).

10. Estimation of charge carrier density after excitation

The initial charge carrier density $n_{initial}$ near the surface of the sample after laser excitation for very short laser pulses, can be estimated by the laser fluence H_e divided by the photon energy E_{photon} , times the absorption coefficient α :

$$n_{initial} = \frac{H_e}{E_{photon}} \alpha$$

With $E_{photon} = 3.67$ eV, $\alpha = 5 \cdot 10^5$ cm⁻¹,³ the lowest fluence $H_e = 10 \frac{\mu J}{cm^2}$ used in this study corresponds to an initial charge carrier density $n_{initial} \left(10 \frac{\mu J}{cm^2}\right) = 8.5 \cdot 10^{18}$ cm⁻³ and the highest fluence $H_e = 420 \frac{\mu J}{cm^2}$ corresponds to an initial charge carrier density $n_{initial} \left(400 \frac{\mu J}{cm^2}\right) = 3.6 \cdot 10^{20}$ cm⁻³. However, the sample is excited in a finite time, that is the pulse width $T_{pulse} = 3$ ns of the excitation laser. On this time scale also recombination processes need to be considered. Thus, the change of charge carrier density near the surface during excitation is given by

$$\frac{dn}{dt} = \frac{H_e}{E_{photon} T_{pulse}} \alpha - (k_1 n + k_2 n^2 + k_3 n^3)$$

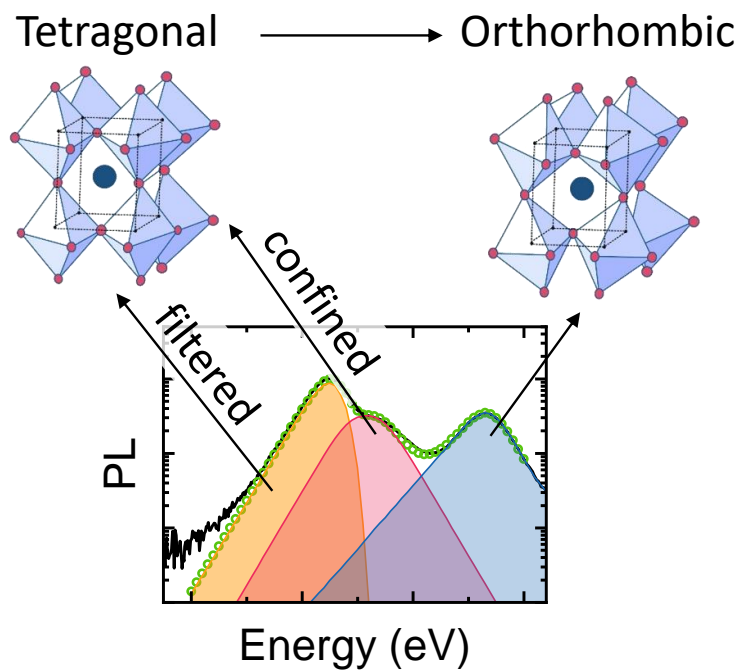
With typical values for the rate constants, $k_1 = 10^6$, $k_2 = 6.8 \cdot 10^{-10}$ and $k_3 = 10^{-29}$,³ we obtain for the lowest fluence $n \left(10 \frac{\mu J}{cm^2}\right) = 2 \cdot 10^{18}$ cm⁻³ and for the highest fluence $n \left(400 \frac{\mu J}{cm^2}\right) = 1.2 \cdot 10^{19}$ cm⁻³. We point out that this reflects only the charge carrier density near the surface and directly after laser excitation, so that the calculated values represent an upper limit.

Supporting References:

1. Meier, T.; Gujar, T. P.; Schönleber, A.; Olthof, S.; Meerholz, K.; van Smaalen, S.; Panzer, F.; Thelakkat, M.; Köhler, A., Impact of excess PbI₂ on the structure and the temperature dependent optical properties of methylammonium lead iodide perovskites. *J Mater Chem C* **2018**, *6* (28), 7512-7519.
2. Panzer, F.; Bössler, H.; Köhler, A., Temperature Induced Order-Disorder Transition in Solutions of Conjugated Polymers Probed by Optical Spectroscopy. *J Phys Chem Lett* **2017**, *8* (1), 114-125.
3. Crothers, T. W.; Milot, R. L.; Patel, J. B.; Parrott, E. S.; Schlipf, J.; Müller-Buschbaum, P.; Johnston, M. B.; Herz, L. M., Photon Reabsorption Masks Intrinsic Bimolecular Charge-Carrier Recombination in CH₃NH₃PbI₃ Perovskite. *Nano Lett* **2017**, *17* (9), 5782-5789.

9

Investigating the Tetragonal-to-Orthorhombic Phase Transition of Methylammonium Lead Iodide Single Crystals by Detailed Photoluminescence Analysis



Konstantin Schötz, Abdelrahman M Askar, Anna Köhler, Karthik Shankar, Fabian Panzer.

Published in

Advanced Optical Materials, **2020**, 8, 17, 2000455

(DOI: 10.1002/adom.202000455)

Reprinted from WILEY-VCH Verlag GmbH & Co. KGaA

Copyright (2020) the Authors

Investigating the Tetragonal-to-Orthorhombic Phase Transition of Methylammonium Lead Iodide Single Crystals by Detailed Photoluminescence Analysis

Konstantin Schötz, Abdelrahman M. Askar, Anna Köhler, Karthik Shankar, and Fabian Panzer*

Here, the phase-transition from tetragonal to orthorhombic crystal structure of the halide perovskite methylammonium lead iodide single crystal is investigated. Temperature dependent photoluminescence (PL) measurements in the temperature range between 165 and 100 K show complex PL spectra where in total five different PL peaks can be identified. All observed PL features can be assigned to different optical effects from the two crystal phases using detailed PL analyses. This allows to quantify the fraction of tetragonal phase that still occurs below the phase transition temperature. It is found that at 150 K, 0.015% tetragonal phase remain, and PL signatures are observed from quantum confined tetragonal domains, suggesting their size to be about 7–15 nm down to 120 K. The tetragonal inclusions also exhibit an increased Urbach Energy, implying a high degree of structural disorder. The results first illustrate how a careful analysis of the PL can serve to deduce structural information, and second, how structural deviations in halide perovskites have a significant impact on the optoelectronic properties of this promising class of semiconductors.


1. Introduction

The unique development of optoelectronic components based on halide perovskites has attracted much attention in recent

K. Schötz, Prof. A. Köhler, Dr. F. Panzer
Soft Matter Optoelectronics
University of Bayreuth
Bayreuth 95440, Germany
E-mail: fabian.panzer@uni-bayreuth.de

A. M. Askar, Prof. K. Shankar
Department of Electrical and Computer Engineering
University of Alberta
Edmonton, AB T6G 1H9, Canada

Prof. A. Köhler
Bayreuth Institute of Macromolecular Research (BIMF) and Bavarian
Polymer Institute (BPI)
University of Bayreuth
Bayreuth 95440, Germany

 The ORCID identification number(s) for the author(s) of this article can be found under <https://doi.org/10.1002/adom.202000455>.

© 2020 The Authors. Published by WILEY-VCH Verlag GmbH & Co. KGaA, Weinheim. This is an open access article under the terms of the Creative Commons Attribution License, which permits use, distribution and reproduction in any medium, provided the original work is properly cited.

DOI: 10.1002/adom.202000455

years. In addition to the development of suitable film production methods, progress in understanding the relationship between the perovskite crystal structure and electronic structure, i.e., optical properties, is an important building block for their success.^[1–3] In this context, the prototypical halide perovskite MAPbI₃ has developed as model system, as it also exhibits a temperature induced phase transition between tetragonal and orthorhombic crystal structure at around 160 K, which clearly affects its optical properties.^[4–7] Various parameters have been identified which can influence this phase transition, such as the exact stoichiometry of the perovskite^[8] or external constraints.^[9] Also, the phase transition was found to proceed differently with temperature, depending on whether a single crystal or a thin film is investigated. In the case of thin films, aspects such as strain,

disorder or polycrystallinity were reported to play an important role in inhibiting the phase transition, i.e., it takes place at lower temperatures and/or over a wider temperature range.^[10] Accordingly, the existence of tetragonal phase even far below 160 K was reported, mostly based on temperature-dependent optical investigations.^[4,11,12] In contrast, studies on single crystals, often based on scattering investigations, suggest that the phase transition is complete at higher temperatures, i.e., it proceeds in a small temperature range of a few Kelvin.^[13,14] In contrast to scattering methods, the investigation of the phase transition by temperature-dependent optical spectroscopy is relatively easily accessible. It exploits the fact that tetragonal and orthorhombic phases have different band gaps and thus exhibit distinct optical signatures. However, several additional peaks and/or shoulders are often observed in the photoluminescence (PL) spectra during the transition and at lower temperatures for single crystals.^[4,13,15] The exact origin of these additional PL signatures is still under debate and thus no precise understanding of the phase transition has evolved yet. In general, it has been shown that self-absorption effects can play an important role and need to be considered when analyzing measured PL spectra.^[16–22] We recently demonstrated that self-absorption can even lead to additional peaks in measured PL. With a relatively simple optical model it was possible to reproduce and

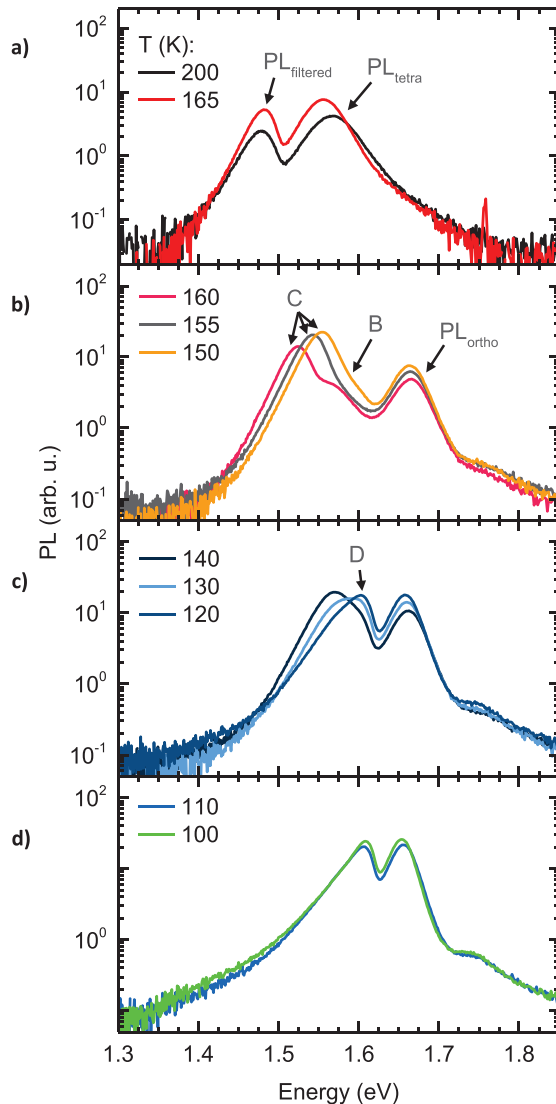


Figure 1. a–d) Temperature-dependent photoluminescence of a MAPbI₃ single crystal from 200 to 100 K, grouped in different temperature regions.

analyze the additional peaks in the case of pure tetragonal or orthorhombic crystal phases.^[23]

Encouraged by these findings, we investigate in detail the tetragonal-orthorhombic phase transition of a MAPbI₃ single crystal using temperature-dependent PL spectroscopy. In the temperature range from 160 to 100 K, we observe complex PL spectra with five different PL peaks. By systematic investigation and detailed modelling of optical effects, it is possible to differentiate the PL signatures of electronic states from those caused by optical effects. This allows quantifying the fraction of tetragonal phase with a high sensitivity, where we find residual tetragonal phase to be present down to 120 K even in the case of a single crystal. Our work thus emphasizes the limited phase purity upon structural changes of hybrid perovskites even in the case of single crystals and sheds further light on how to analyze and interpret PL spectra consisting of multiple peaks.

2. Results

Figure 1 shows the temperature dependent PL spectra of a MAPbI₃ single crystal in the temperature range between 200 and 100 K, grouped into temperature ranges comprising similar spectra. The temperature for the tetragonal to orthorhombic phase transition was identified to be at 163 K in the case of single crystals.^[24,25] Thus, the spectra in Figure 1a at 200 and 165 K are associated with the tetragonal phase. They show two peaks centered at about 1.55 and 1.48 eV. In a previous study we could clarify the origin of the two peaks,^[23] where the higher energy peak (PL_{tetra}) at 1.55 eV is due to PL that leaves the crystal without significant self-absorption, such as PL generated close to the crystal surface. In contrast, the lower energy peak at 1.48 eV (PL_{filtered}) results from an inner filter effect, i.e., it is due to PL that suffered significant self-absorption as it experienced a longer optical path through the perovskite bulk. Here the relatively high probability for reflections at the inner surfaces of the crystal can significantly boost the length of the optical path that the filtered PL experiences (also see Figure S1 in the Supporting Information for details).

Upon further cooling, the PL spectra become more complex. In the range from 160 to 150 K, a new peak appears at 1.67 eV that shifts by about 5 meV to lower energies during cooling to 150 K. Furthermore, there is a shoulder (“peak B”) around 1.57 eV at 160 K that becomes weaker with cooling, and a peak at 1.53 eV (“peak C”) that shifts by 30 meV to higher energies and increases in intensity by about 60%. We can readily assign the peak at 1.67 eV to an optical transition in the orthorhombic phase (PL_{ortho}).^[26–28] In contrast, the origin of peaks B and C is not as straightforward and needs more detailed investigation. Upon further cooling (Figure 1b), peaks B and C seem to merge, and in the temperature range from 140 to 120 K (Figure 1c), a new sharp peak at 1.60 eV appears and gains intensity (peak D). At 110 and 100 K, (lowest temperature we investigated), only PL_{ortho} and peak D remain (Figure 1d). We always observed the above-described PL evolution for different MAPbI₃ single crystals, suggesting that it is a general behavior.

To identify the origin of the various peaks, we take a twofold approach. First, we consider PL spectra collected from a different angle. This allows us to identify self-absorption effects, as we found the relative intensity of PL_{filter} to be sensitive on the measurement geometry.^[23] Second, we model the optical spectra under consideration of optical effects such as reflection and reabsorption.

Figure 2a shows the PL spectra taken at 160 K for two measurement geometries, which slightly differ in the angles between single crystal and the incident laser beam. The difference between the two spectra is also shown (orange shaded area). It is obvious that the spectra differ only in the intensity of peak C, indicating that peak C stems from filtered PL due to self-absorption effects. Likewise, the PL spectra taken under varied geometries at 100 K (Figure 2b) differ in the intensity of peak D, so that we assign peak D to filtered PL of the orthorhombic phase (see Figure S2 in the Supporting Information for all measured spectra between 165 and 100 K).

To underpin the assignment of peak C and peak D to filtered PL, we attempt to reproduce the spectra by optical modelling as

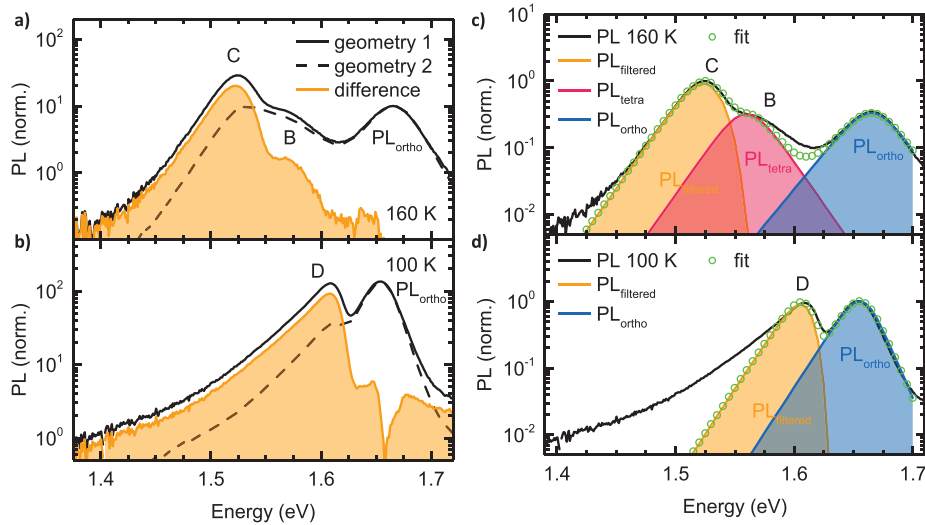


Figure 2. a,b) PL of a MAPbI₃ single crystal in a geometry with strongly (black solid) and weakly pronounced (black dashed) self-absorption effect, as well as the difference (orange) between both spectra at a) 160 K and b) 100 K. c,d) Modelled PL (green circles) considering self-absorption, decomposed in tetragonal (red), orthorhombic (blue), and filtered PL (orange) at c) 160 K and d) 100 K, together with the measured PL spectra (black solid lines).

presented in our earlier work.^[23] In brief, we consider the one dimensional charge carrier distribution generated in the crystal by our 337 nm laser excitation. This charge carrier distribution leads to PL that can travel either to the front or to the back of the crystal, where it is transmitted or reflected at the interface of the perovskite and its surrounding media. The probability for this is determined by the refractive index of the perovskite and the surrounding media, in our case helium. On the way through the crystal, the PL is absorbed by the perovskite. Considering a possible mismatch of excitation and detection spot, the PL leaving the crystal after multiple reflections (filtered PL) can be amplified by a constant factor in our model. The crystal length is set to 1 mm, in accordance with the size of the used crystal. The reflection probability at the perovskite-helium interface is estimated to be 0.85 by using the Fresnel equations and averaging over all incident angles. For the absorption spectra of the tetragonal phase of MAPbI₃, we combine the room temperature absorption coefficient reported by Crothers et al.^[29] with the temperature-dependent absorbance data of the Urbach tail reported by Ledinsky et al.^[30] Since during the phase transition tetragonal and orthorhombic phase coexist, the total absorption spectrum of the crystal is a combination of a certain fraction of tetragonal phase absorption and orthorhombic phase absorption. For the latter, the absorption coefficient is approximated by absorption data from thin films and an extrapolated Urbach tail based on transmission measurements of a single crystal (see Section S3 in the Supporting Information for full details of the modelling approach).^[6,23] In principle, and similar to absorption, the total PL spectrum is the sum of tetragonal and orthorhombic PL. Since energy transfer from the orthorhombic to the energetically lower tetragonal phase can occur easily,^[31,32] the tetragonal PL is expected to appear overproportionally intense in the measured spectra. Furthermore, the different PL features, including filtered PL and the intrinsic PL peaks of tetragonal and orthorhombic phases, typically overlap spectrally. This makes the modeling of the measured

spectra in the phase transition region more complex compared to the analyses of PL spectra of pure phases. A complete modeling of the spectra, including a clear identification of peak C and D, requires first to identify clearly the contributions from neat phases. To access the spectral shape of the intrinsic PL, we recall that the PL lineshape as a function of photon energy E of a classic inorganic semiconductor is described by a generalized Planck law, which reads

$$PL(E) \propto A(E)E^2 \exp\left(-\frac{E}{k_B T}\right) \quad (1)$$

where $A(E)$ is the absorptivity, k_B is the Boltzmann constant and T is the temperature.^[33] For the intrinsic PL line-shape, i.e., the PL without effects of self-absorption, $A(E)$ in Equation (1) can be replaced by the absorption coefficient $\alpha(E)$ (see Section S4 in the Supporting Information).^[34] Below the band gap, MAPbI₃ shows band tail absorption, which decreases exponentially toward lower energies.^[35] It is well described by Urbach tail absorption, expressed by $\alpha(E < E_g) \propto \exp(E/E_u)$, with E_u being the Urbach Energy.^[36] Above the band gap, the absorption is roughly constant in the relevant energy range for the PL, that is the spectral range where PL and absorption overlap (Figure S3, Supporting Information). We thus approximate the shape of the absorption spectrum according to

$$\alpha(E) \approx \frac{\alpha_0}{\exp\left(-\frac{E-E_0}{E_u}\right) + 1} \quad (2)$$

(see Section S4 and Figure S3 in the Supporting Information for details regarding comparison of modelled and experimental spectra). The PL lineshape is then given by

$$PL(E) \approx I_0 \frac{1}{\exp\left(-\frac{E-E_0}{E_u}\right) + 1} E^2 \exp\left(-\frac{E}{k_B T}\right) \quad (3)$$

Using Equation (3), we fitted PL data of MAPbI₃ single crystals and thin film at different temperatures where the material is either in the pure tetragonal or pure orthorhombic phase. We obtained a good agreement between experimental and fitted PL (Figures S3 and S4, Supporting Information), although it was necessary to replace $\exp(-E/k_B T)$ with $\exp(-0.825E/k_B T)$ in Equation (3) in the case of single crystals. While the origin of this factor is not fully clear, there are indications that it occurs from a self-absorption effect as described in more detail in the Supporting Information (Section S5, Supporting Information).

Successfully modelling the intrinsic PL spectra of pure crystal phases builds the basis for modeling and fitting the measured PL at 160 K, where tetragonal and orthorhombic phases coexist. While the temperature is given from the experimental conditions, the relative intensities and energetic positions of the intrinsic PL peaks, the Urbach energies and the fraction of tetragonal inclusions are optimized to obtain best agreement with the measured spectrum. We use the energetic position of the tetragonal PL peak at 165 K, assuming that it does not change significantly within the first 5 K of the phase transition. The modelled PL with its decomposition in the individual contributions is depicted in Figure 2c, showing very good agreement with the experimental data. This underpins that peak C is due to filtered PL, while peak B appears to stem from residual tetragonal inclusions. At 100 K, we model the PL assuming that tetragonal inclusions are absent (Figure 2d). The modelled PL can nicely reproduce peak D, further supporting that it is due to filtered PL from the orthorhombic phase. However, the low energy edge, i.e., the PL below ≈ 1.56 eV, cannot be reproduced assuming only orthorhombic PL.

Having understood the individual features in the PL spectrum at 160 K, we next attempt to extract detailed information about the tetragonal-orthorhombic phase transition by fitting the measured PL spectra between 160 and 100 K using our modelling approach. To do so, it is reasonable to investigate how a variation of parameters such as the content of tetragonal inclusions, the tetragonal PL intensity or tetragonal PL peak position affects the modelled spectra. Figure 3a shows modelled PL spectra differing in the content of tetragonal inclusions, while all other parameters remained unchanged. Upon reducing the content of tetragonal inclusions from 1% to 0.1%, peak C shifts from ≈ 1.52 to ≈ 1.55 eV and its intensity increases. This PL change follows since the reduction of the content of tetragonal phase is accompanied by a corresponding change in the absorption edge, thus influencing the effect of self-absorption on the intrinsic PL. This causes the signature of the filtered PL to shift more and more toward the spectral position of the intrinsic PL of the tetragonal phase. These spectral changes fit nicely to the measured PL changes between 160 and 150 K in Figure 1b. Here we also want to point out that the above-mentioned relationship between the fraction of tetragonal phase and the energetic spacing between $PL_{tet,filter}$ and $PL_{tet,intrinsic}$ allows extracting the fraction of tetragonal phase from fitting our model to the measured PL spectra. Upon cooling, the experimentally observed shift of peak C saturates at 1.57 eV (Figure 1b), where it becomes indistinguishable from PL_{tetra} , similar to the spectral changes in the modelled spectra for a decreasing fraction of tetragonal phase below 0.1% (Figure 3a). Further reducing the fraction of tetragonal phase results in an enhancement

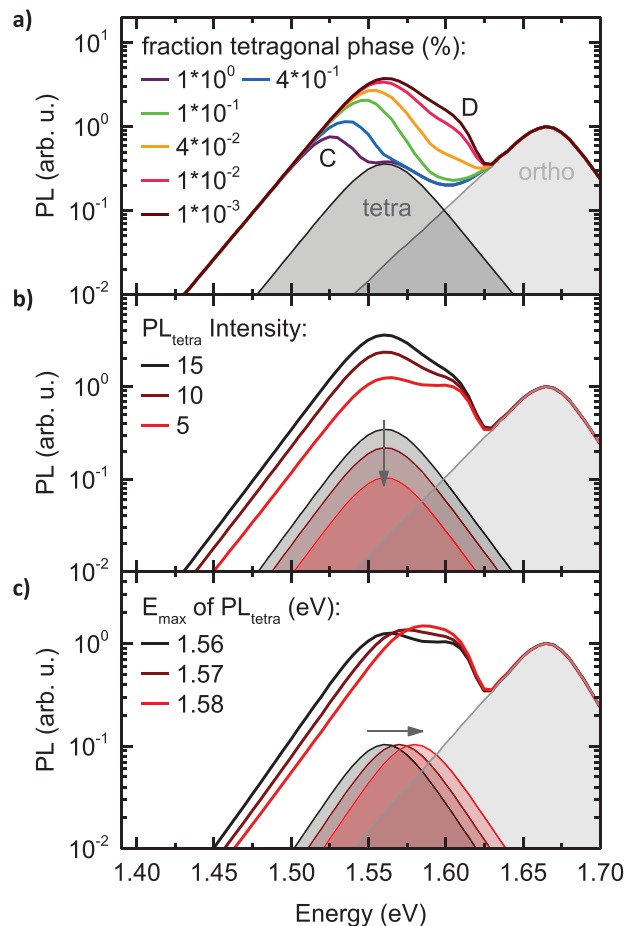


Figure 3. Modeled PL for a) different fractions of tetragonal phase, b) decreasing tetragonal PL intensities, and c) blue-shift of the tetragonal PL peak, using the spectral shapes of tetragonal and orthorhombic PL at 160 K.

of a PL signal at ≈ 1.6 eV. This is caused by the fact that the small fraction of tetragonal phase has only little influence on the absorption edge, which is thus almost exclusively dominated by absorption of the orthorhombic phase. Accordingly, the self-absorption effect is mainly determined by the absorption of the orthorhombic phase, i.e., the feature at 1.6 eV corresponds to filtered PL of the orthorhombic phase. The peak position of this PL feature, as well as its growth, fit very well with the experimentally observed appearance of peak D between 140 and 120 K in Figure 1c. So far, we can conclude that the shift of peak C and the emergence of peak D observed in the measurements upon cooling from 160 to 120 K can be understood qualitatively simply as the result of a reduction in the fraction of tetragonal phase. However, from Figure 1b it becomes clear that upon cooling the low energy edge (<1.5 eV) of the measured PL spectra shifts to higher energies, a spectral dynamic which cannot be captured by just changing the content of tetragonal phase in our model (Figure 3a). This makes it necessary to also allow changing the PL intensity of the tetragonal phase, which is reasonable as the fraction of tetragonal phase decreases. The impact of changing the PL_{tetra} intensity on the overall PL

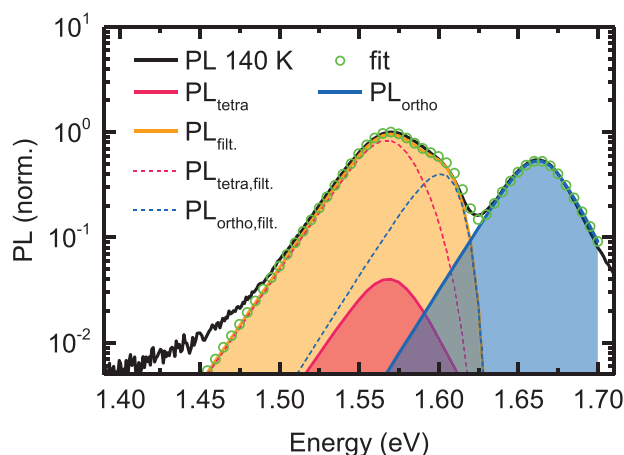


Figure 4. Measured (black solid line) and modelled (green circles) PL at 140 K and spectral decomposition in orthorhombic (blue), tetragonal (red), and filtered PL (orange). The dashed lines indicate individual contributions of orthorhombic and tetragonal phase to the filtered PL.

spectrum is shown in Figure 3b, where exemplarily PL_{tetra} is reduced to a third of its intensity, while the fraction of tetragonal phase is constant at 0.001%. With that, it is possible to account for the experimentally observed shift of the low energy edge, while it is also obvious, that lowering the tetragonal PL intensity always results in a double peak in the spectral region between 1.50 and 1.60 eV, consisting of peak C/B and peak D. This is at variance especially with the measured PL spectrum at 130 K (Figure 1c), where we observed only one broadened peak in the energy range between 1.50–1.63 eV. Allowing PL_{tetra} to shift to higher energies by about 20 meV resolves this deviation between modelled and experimental PL (see Figure 3c).

Using the insights gained from Figure 3, we finally modelled the measured spectra between 160 and 100 K. To fit the measured spectra we varied the fraction of tetragonal phase, PL_{tetra} peak position and PL_{tetra} intensity. Furthermore from modeling the intrinsic PL of tetragonal and orthorhombic phase using Equation (3), also the Urbach energies of the two phases $E_{u,tetra}$ and $E_{u,ortho}$, were derived. **Figure 4** shows an exemplary fit and its spectral decomposition for the PL at 140 K, (see Figure S5 in the Supporting Information for fits to the PL spectra at the other temperatures investigated), from which the good match between measured spectrum and modelled PL is evident. From Figure 4, it also becomes clear how significant the proportion of filtered PL from the tetragonal phase (red dashed line in Figure 4) can be, even though the intensity of the intrinsic PL_{tetra} (solid red line in Figure 4) is relatively low.

Fitting the temperature dependent PL spectra yields the temperature evolution of the fit parameters. **Figure 5a** shows the content of tetragonal inclusions and the integrated intensity of the direct tetragonal PL (normalized to the value at 165 K) between 165 and 100 K. We also extracted the content of tetragonal inclusions based on transmission data of a $MAPbI_3$ single crystal from one of our earlier works.^[23] This crystal was grown via the same synthesis route as the crystal used in this study, so that we expect a similar phase transition behavior. Indeed, we find that the content of tetragonal inclusions extracted from

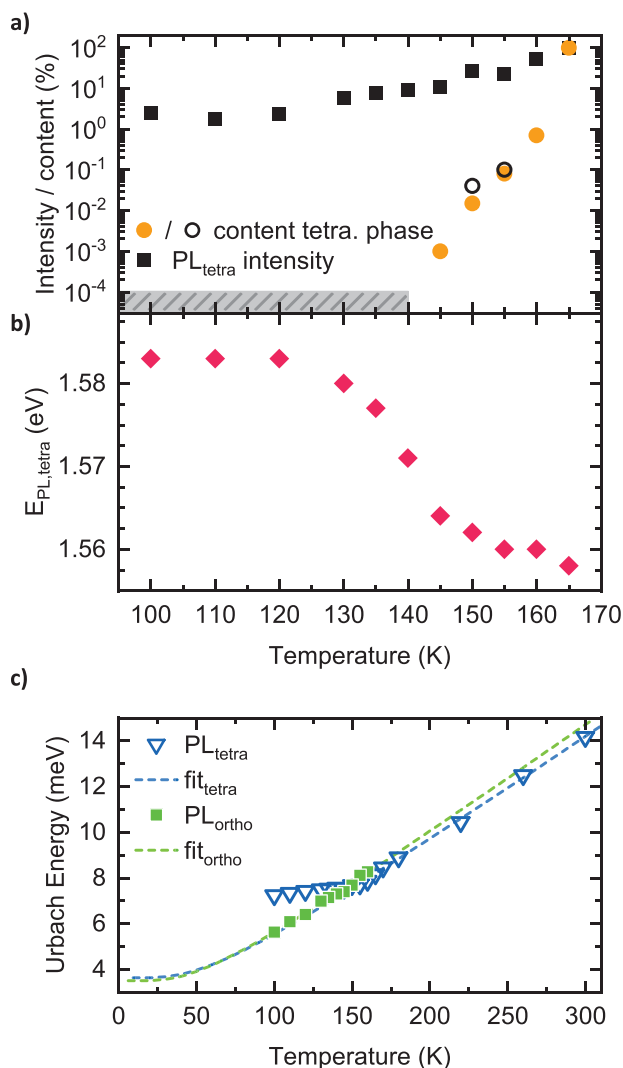


Figure 5. a) Intensity of the tetragonal PL normalized to the value at 165 K (black squares) together with the content of tetragonal phase in the crystal (orange circles) as a function of temperature. The content of tetragonal phase at 155 and 150 K as extracted from transmission measurements on similar $MAPbI_3$ single crystals from an earlier work^[23] is also shown (open black circles). The grey shaded area indicates the upper limit of the content of tetragonal phase below 140 K. b) Temperature-dependence of the tetragonal PL peak position. c) Temperature dependent Urbach energies of the tetragonal (blue triangles) and orthorhombic phase (green squares) together with fits according to Equation (5).

both methods (transmission and PL measurements) agree well, supporting our PL analysis approach. Upon cooling, the content of tetragonal phase drops drastically from 100% at 165 K to 0.7% at 160 K. From there, it further decreases exponentially by about two decades per ten Kelvin to 0.001% at 145 K. At 140 K, the content is so low that no PL filter-effect of tetragonal inclusions occurs, so that a precise quantification of the fraction of tetragonal phase is not possible anymore. Nevertheless, the missing filter effect allows estimating the content of tetragonal inclusions to be below $10^{-4}\%$ (indicated as grey shaded area

in Figure 5a). Similarly, the integrated intensity of the direct tetragonal PL decreases roughly exponentially upon cooling, reaching 2% at 120 K. Thus, it decreases at a rate of about 0.4 decades per ten Kelvin, i.e., less drastic than the decrease of content of tetragonal inclusions. From 120 K, the intensity of the direct tetragonal PL stays roughly constant. However, as mentioned before, below 120 K the spectral signatures of the tetragonal phase is very weak, so that corresponding fit parameters might exhibit a relatively large error. From the temperature dependent fitting of the measured PL spectra, also the peak position of the tetragonal PL was extracted, which is shown in Figure 5b. Starting from 1.558 eV at 165 K, the PL shifts to higher energies, i.e., to 1.562 eV at 150 K. Upon further cooling, this shift becomes more intense, so that the peak position of PL_{tetra} is 1.580 eV at 130 K. After that it reaches its final position at 1.583 eV at 120 K. Figure 5c displays the temperature-dependence of the Urbach energies of the tetragonal and the orthorhombic phase $E_{u,tetra}$ and $E_{u,ortho}$. Here we assume that the factor of 0.825 that we needed to introduced in Equation (3) (*vide supra*) has an artificial origin. We therefore corrected the Urbach energies obtained by fitting Equation (3) to the PL data accordingly (see Section S5 in the Supporting Information). The Urbach energy of the pure tetragonal phase decreases linearly from 14.2 meV at 300 K to 8.2 meV at 165 K. In the temperature range of the phase transition, this trend continues until 155 K, where the Urbach energy of the tetragonal phase is 7.7 meV. Upon further cooling, the decrease in $E_{u,tetra}$ flattens out, changing by only 0.5 meV from 155 to 100 K. At 160 K $E_{u,ortho}$ is 8.2 meV, i.e., similar to the value of $E_{u,tetra}$ at this temperature. However in contrast to the behavior of $E_{u,tetra}$ in the transition region, $E_{u,ortho}$ decreases more rapidly, that is, with a similar slope as $E_{u,tetra}$ between 300 and 165 K, reaching a value of 5.6 meV at 100 K (Figure 5c). The temperature-dependence of the Urbach energy can be expressed as^[37]

$$E_u(T) = \left(\frac{\Theta}{\sigma_0} \right) \left[\frac{1+X}{2} + \left\{ \exp\left(\frac{\Theta}{T} \right) - 1 \right\}^{-1} \right] \quad (4)$$

where T is the absolute temperature, θ is the Einstein characteristic temperature of the phonons that interact with the free charges,^[37,38] and σ_0 is the so-called Urbach Edge parameter.^[37] The parameter $X = \langle U^2 \rangle_x / \langle U^2 \rangle_0$, with $\langle U^2 \rangle_0$ being the zero-point uncertainty of the atomic positions, is related to the structural disorder in the system and would be zero for a perfect crystal.^[37,39] Assuming a perfect crystal ($X = 0$), the term $\theta/(2\sigma_0)$ can be referred to as the static disorder $E_{u,0}$, and Equation (4) becomes^[40]

$$E_u(T) = E_{u,0} + 2E_{u,0} \cdot \left\{ \exp\left(\frac{\Theta}{T} \right) - 1 \right\}^{-1} \quad (5)$$

Fitting Equation (5) to the temperature dependent Urbach energies of the orthorhombic phase from Figure 5c yields $E_{u,0,ortho} = (3.5 \pm 0.3)$ meV and $\theta_{ortho} = (145 \pm 13)$ K. For the pure tetragonal phase, (i.e., considering the Urbach energies between 300 and 165 K), we obtain $E_{u,0,tetra} = (3.6 \pm 0.4)$ meV and $\theta_{tetra} = (156 \pm 19)$ K. Within the accuracy of the approach, these values are identical to the values of the orthorhombic

phase. The fits are indicated as dashed lines in Figure 5d. In case of the tetragonal phase below the phase transition temperature, a clear deviation between the expected Urbach energies from Equation (5) and the values obtained from the measured PL spectra becomes obvious.

3. Discussion

Several studies have so far investigated the tetragonal to orthorhombic phase transition of MAPbI₃ thin films, powder and single crystals. For thin films, typically a large temperature range of 20–40 K can be observed in which both phases coexist.^[4,10,12,41,42] This is argued to be caused by the polycrystalline nature of those films, where every grain can have a slightly different transition temperature, depending, e.g., on the grain size,^[43] or the strain induced by the substrate.^[10,11,44] In powders, the temperature range of the coexistence was reported to be smaller with 5–12 K,^[10,45] which is likely due to the absence of substrate-induced stress on the loose particles.^[10,46] For single crystals, older works suggested that the tetragonal-to-orthorhombic phase transition is abrupt and that there is no coexistence of the two phases.^[13,15] However, more recent works suggest that there is a small temperature window, in which such a coexistence can be observed. Our finding that the fraction of tetragonal phase reduces rapidly by ~99% within the first 5 K of the transition (Figure 5a), thus is in line with the observations found in literature. However, the fact that we observe PL signatures of tetragonal inclusions down to at least 120 K deviates from the expectations from literature. This finding suggests that also in the case of single crystals, certain structural states in halide perovskites persist even if external parameters such as temperature are changed over a wide range. In contrast to the rapid decrease of the fraction of tetragonal phase below the phase transition, the change in PL intensity of the tetragonal inclusions shows a considerably milder decrease (Figure 5a). This implies an efficient energy transfer from orthorhombic phase to the tetragonal inclusions in the temperature range of the phase transition, which is in line with literature reports.^[31,32] It also suggests that the tetragonal inclusions can act as highly efficient traps for the excited states of the predominant orthorhombic perovskite phase.

We also observed and quantified a blue shift of the PL of the tetragonal inclusions by about 20 meV between 155 and 120 K (Figure 5b). One cause of such a shift could be strain on the tetragonal inclusions due to a mismatch between the lattice constants of tetragonal and orthorhombic phase.^[47] Based on temperature-dependent PL measurements and comparison with associated lattice constants, it is possible to estimate the strain that would be necessary to shift the PL by 20 meV to higher energies via the Birch-Murnaghan-equation.^[48] With the assumption that lattice dilation is the dominant factor for the temperature-dependent shift of the PL maximum,^[6,12] we find tensile strain values of 85–165 MPa (see Section S7 in the Supporting Information for details). However, recent studies demonstrated that the unit cell volume of the orthorhombic phase is smaller than the one of the tetragonal phase,^[4,45,49,50] and thus there should be compressive strain instead of tensile strain to affect the tetragonal inclusions. Room temperature measurements showed that

pressure on MAPbI₃ leads to a red shift.^[51–54] Assuming this to also hold true at lower temperatures, strain would not be a satisfying explanation of the observed blue shift.

An alternative interpretation of the blue-shift is via a quantum confinement effect, where the decreasing domain size confines the excited state, leading to a blue-shift of the PL.^[55] The observed blue-shift of 20 meV implies domain sizes of 7–15 nm, based on the correlation between PL peak position and crystal size of MAPbI₃ nanocrystals found in literature,^[56–58] and on the assumption that this correlation also applies to the tetragonal inclusions. We estimate the domain volume to be about (15 nm)³, consider that 0.001% of the crystal is in the tetragonal phase (as it is the case at 145 K) and we assume that the tetragonal inclusions are distributed homogeneously. From this, we obtain a number concentration of $3 \times 10^{12} \text{ cm}^{-3}$ and an average distance of about 0.7 μm between the tetragonal inclusions. This is in the range of the charge carrier diffusion length reported in literature,^[59,60] suggesting that an efficient energy transfer from orthorhombic phase to the tetragonal inclusions is well possible. This also fits well with our observation that the fraction of tetragonal phase decreases more rapidly compared to the corresponding PL intensity (Figure 5a). These results also emphasize that due to the efficient energy transfer, even a low density of domains that deviate regarding their structure from the investigated perovskite can have significant impact on its PL spectra and thus its photophysical properties.

Regarding the extracted temperature dependent Urbach energies of both phases, we find that the values of $E_{u,0,tetra}$ and θ_{tetra} agree well with the results from Ledinsky et al.,^[40] who quantified the temperature dependent Urbach Energies of the tetragonal phase of MAPbI₃ thin films also on the basis of PL measurements. Also, our observation that θ_{tetra} and θ_{ortho} exhibit identical values indicates, that the electronically active phonon modes are the same for orthorhombic and tetragonal phase and that their energy does not change upon the phase transition. Further, we observed that during the coexistence of both phases, the extracted values for $E_{u,tetra}$ deviate from the ones expected according to Equation (5). Since θ appears to be constant, the higher values of $E_{u,tetra}$ indicate a higher static disorder in the tetragonal inclusions, increasing with decreasing domain size. This is reasonable, when considering that the orthorhombic and the tetragonal unit cells have different lattice constants,^[4] implying the build-up of strain in the tetragonal inclusions (see above). The strain leads to a distorted crystal structure, so that X (being a measure for the static disorder) in Equation (4) increases.

Finally, we note that the PL in the temperature range from 160 to 120 K can be modelled with tetragonal, orthorhombic and the corresponding filtered PL and no additional peaks are necessary. This suggests in particular that there is no significant contribution of bound excitons and defects to the PL spectra down to 120 K.

4. Conclusion

In summary, we investigated the tetragonal-to-orthorhombic phase transition of MAPbI₃ single crystals using temperature dependent PL measurements. We carefully considered and modelled optical effects to distinguish between optical features

and intrinsic electronic transitions in measured PL spectra. We quantified the fraction of tetragonal phase during the transition with a high sensitivity, where we find that the tetragonal fraction at 150 K has reduced to 0.001%. Additionally, we can still identify PL signatures of tetragonal phase down to 120 K, where its spectrum shifts to higher energies, being indicative of a confinement effect of the last bit of tetragonal inclusions. Overall, this work demonstrates that the phase transition in MAPbI₃ single crystals is not abrupt, but extends over 40 K, and PL of bound excitons does not play a role above 100 K in our experiments. Furthermore, our results show that even smallest contents of structurally different inclusions in the perovskite can have significant impact on its opto-electronic properties. This aspect will be also relevant for perovskites with mixed stoichiometry, where the structural homogeneity and its influence on the optoelectronic properties is still unclear but crucial for the further development of highly efficient perovskite solar cells.

5. Experimental Section

Sample Preparation: MAPbI₃ single crystals were prepared following the inverse temperature crystallization technique.^[61] In brief, the synthesis started with a 1–1.3 M solution of MAI (from Dyesol-Limited, Now GreatCell Solar) and PbI₂ (Sigma-Aldrich) in gamma-Butyrolactone (GBL, Sigma-Aldrich). The precursors dissolved in GBL after 30 min of vigorous stirring at 60 °C. Upon filtering the solution using 0.22 μm PVDF filters, the stock solution was then distributed into small vials with 3–4 mL of solution each. The vials were kept undisturbed in an oil bath for 34 h at 110 °C. Once the desired size of the crystals was achieved, the crystals were removed from the synthesis solution, washed quickly with fresh GBL, dried with a N₂ flow.

Photoluminescence Measurements: The temperature-dependent PL measurements were performed using a home-built setup. The sample was put in a continuous flow cryostat (Oxford Instruments, Optistat CF) with an automated temperature controller (Oxford Instruments ITC503S). The sample was excited with a 337 nm nitrogen laser (LTB MNL 100). The signal was collected via a charge-coupled device (CCD) camera (Andor iDus DU420a-OE) coupled to a spectrograph (Andor Shamrock SR303i).

Supporting Information

Supporting Information is available from the Wiley Online Library or from the author.

Acknowledgements

Ko.S. acknowledges financial support from the German National Science Foundation (Project KO 3973/2-1 and GRK 1640). F.P. acknowledges support by the German National Science Foundation via the Project PA 3373/3-1. A.K. acknowledges support by the Bayrisches Staatsministerium für Wissenschaft und Kunst for the Collaborative Research Network “Solar Technologies go Hybrid.” Ka.S. acknowledges financial support from NSERC (grant number 06630), Future Energy Systems (grant number T12-P012), and NRC (grant number A1-014009).

Conflict of Interest

The authors declare no conflict of interest.

Keywords

halide perovskites, MAPbI₃, optical spectroscopy, self-absorption

Received: March 16, 2020

Revised: April 24, 2020

Published online: May 26, 2020

- [1] L. M. Herz, *Annu. Rev. Phys. Chem.* **2016**, *67*, 65.
- [2] Y. Kanemitsu, *J. Mater. Chem. C* **2017**, *5*, 3427.
- [3] D. W. deQuilettes, K. Frohna, D. Emin, T. Kirchartz, V. Bulovic, D. S. Ginger, S. D. Stranks, *Chem. Rev.* **2019**, *119*, 11007.
- [4] W. Kong, Z. Ye, Z. Qi, B. Zhang, M. Wang, A. Rahimi-Iman, H. Wu, *Phys. Chem. Chem. Phys.* **2015**, *17*, 16405.
- [5] A. Glushkova, K. Mantulnikovs, G. Giriat, K. Semeniuk, L. Forro, E. Horvath, A. Arakcheeva, *Sol. RRL* **2019**, *3*, 1900044.
- [6] S. Singh, C. Li, F. Panzer, K. L. Narasimhan, A. Graeser, T. P. Gujar, A. Köhler, M. Thelakkat, S. Huettnner, D. Kabra, *J. Phys. Chem. Lett.* **2016**, *7*, 3014.
- [7] E. S. Parrott, R. L. Milot, T. Stergiopoulos, H. J. Snaith, M. B. Johnston, L. M. Herz, *J. Phys. Chem. Lett.* **2016**, *7*, 1321.
- [8] T. Meier, T. P. Gujar, A. Schönleber, S. Olthof, K. Meerholz, S. van Smaalen, F. Panzer, M. Thelakkat, A. Köhler, *J. Mater. Chem. C* **2018**, *6*, 7512.
- [9] N. Arad-Vosk, N. Rozenfeld, R. Gonzalez-Rodriguez, J. L. Coffey, A. Sa'ar, *Phys. Rev. B* **2017**, *95*, 085433.
- [10] A. Oshero, E. M. Hutter, K. Galkowski, R. Brenes, D. K. Maude, R. J. Nicholas, P. Plochocka, V. Bulović, T. J. Savenije, S. D. Stranks, *Adv. Mater.* **2016**, *28*, 10757.
- [11] C. Wehrenfennig, M. Z. Liu, H. J. Snaith, M. B. Johnston, L. M. Herz, *APL Mater.* **2014**, *2*, 081513.
- [12] F. Panzer, C. Li, T. Meier, A. Köhler, S. Huettnner, *Adv. Energy Mater.* **2017**, *7*, 1700286.
- [13] H. H. Fang, R. Raissa, M. Abdu-Aguye, S. Adjokatse, G. R. Blake, J. Even, M. A. Loi, *Adv. Funct. Mater.* **2015**, *25*, 2378.
- [14] G. Schuck, D. M. Tobbens, M. Koch-Muller, I. Efthimiopoulos, S. Schorr, *J. Phys. Chem. C* **2018**, *122*, 5227.
- [15] L. Q. Phuong, Y. Nakaike, A. Wakamiya, Y. Kanemitsu, *J. Phys. Chem. Lett.* **2016**, *7*, 4905.
- [16] M. Chauhan, Y. Zhong, K. Schötz, B. Tripathi, A. Köhler, S. Huettnner, F. Panzer, *J. Mater. Chem. A* **2020**, *8*, 5086.
- [17] L. M. Pazos-Outón, M. Szumilo, R. Lamboll, J. M. Richter, M. Crespo-Quesada, M. Abdi-Jalebi, H. J. Beeson, M. Vrućinić, M. Alsari, H. J. Snaith, B. Ehrler, R. H. Friend, F. Deschler, *Science* **2016**, *351*, 1430.
- [18] Y. J. Fang, H. T. Wei, Q. F. Dong, J. S. Huang, *Nat. Commun.* **2017**, *8*, 14417.
- [19] Y. Yamada, T. Yamada, L. Q. Phuong, N. Maruyama, H. Nishimura, A. Wakamiya, Y. Murata, Y. Kanemitsu, *J. Am. Chem. Soc.* **2015**, *137*, 10456.
- [20] T. Yamada, Y. Yamada, H. Nishimura, Y. Nakaike, A. Wakamiya, Y. Murata, Y. Kanemitsu, *Adv. Electron. Mater.* **2016**, *2*, 1500290.
- [21] F. Staub, I. Anusca, D. C. Lupascu, U. Rau, T. Kirchartz, *J. Phys.: Mater.* **2020**, *3*, 025003.
- [22] D. C. Hong, J. Li, S. S. Wan, I. G. Scheblykin, Y. X. Tian, *J. Phys. Chem. C* **2019**, *123*, 12521.
- [23] K. Schötz, A. M. Askar, W. Peng, D. Seeberger, T. P. Gujar, M. Thelakkat, A. Köhler, S. Huettnner, O. M. Bakr, K. Shankar, F. Panzer, *J. Mater. Chem. C* **2020**, *8*, 2289.
- [24] A. Poglitsch, D. Weber, *J. Chem. Phys.* **1987**, *87*, 6373.
- [25] R. E. Wasylishen, O. Knop, J. B. Macdonald, *Solid State Commun.* **1985**, *56*, 581.
- [26] G. Xing, N. Mathews, S. S. Lim, N. Yantara, X. Liu, D. Sabba, M. Gratzel, S. Mhaisalkar, T. C. Sum, *Nat. Mater.* **2014**, *13*, 476.
- [27] K. Wu, A. Bera, C. Ma, Y. Du, Y. Yang, L. Li, T. Wu, *Phys. Chem. Chem. Phys.* **2014**, *16*, 22476.
- [28] R. L. Milot, G. E. Eperon, H. J. Snaith, M. B. Johnston, L. M. Herz, *Adv. Funct. Mater.* **2015**, *25*, 6218.
- [29] T. W. Crothers, R. L. Milot, J. B. Patel, E. S. Parrott, J. Schlipf, P. Müller-Buschbaum, M. B. Johnston, L. M. Herz, *Nano Lett.* **2017**, *17*, 5782.
- [30] M. Ledinsky, T. Schonfeldova, J. Holovsky, E. Aydin, Z. Hajkova, L. Landova, N. Neykova, A. Fejfar, S. De Wolf, *J. Phys. Chem. Lett.* **2019**, *10*, 1368.
- [31] H. Wang, L. Whittaker-Brooks, G. R. Fleming, *J. Phys. Chem. C* **2015**, *119*, 19590.
- [32] L. Q. Phuong, Y. Yamada, M. Nagai, N. Maruyama, A. Wakamiya, Y. Kanemitsu, *J. Phys. Chem.* **2016**, *7*, 2316.
- [33] P. Würfel, *J. Phys. C: Solid State Phys.* **1982**, *15*, 3967.
- [34] E. Daub, P. Würfel, *Phys. Rev. Lett.* **1995**, *74*, 1020.
- [35] S. Pathak, A. Sepe, A. Sadhanala, F. Deschler, A. Haghighirad, N. Sakai, K. C. Goedel, S. D. Stranks, N. Noel, M. Price, S. Hüttner, N. A. Hawkins, R. H. Friend, U. Steiner, H. J. Snaith, *ACS Nano* **2015**, *9*, 2311.
- [36] F. Urbach, *Phys. Rev.* **1953**, *92*, 1324.
- [37] G. D. Cody, T. Tiedje, B. Abeles, T. D. Moustakas, B. Brooks, Y. Goldstein, *J. Phys. Colloq.* **1981**, *42*, C4.
- [38] S. M. Wasim, C. Rincon, G. Marin, P. Bocaranda, E. Hernandez, I. Bonalde, E. Medina, *Phys. Rev. B* **2001**, *64*, 195101.
- [39] M. Beaudoin, A. J. G. DeVries, S. R. Johnson, H. Laman, T. Tiedje, *Appl. Phys. Lett.* **1997**, *70*, 3540.
- [40] M. Ledinsky, T. Schönfeldová, J. Holovský, E. Aydin, Z. Hájková, L. Landová, N. Neyková, A. Fejfar, S. De Wolf, *J. Phys. Chem. Lett.* **2019**, *10*, 1368.
- [41] H. Tahara, M. Endo, A. Wakamiya, Y. Kanemitsu, *J. Phys. Chem. C* **2016**, *120*, 5347.
- [42] V. D'Innocenzo, G. Grancini, M. J. P. Alcocer, A. R. S. Kandada, S. D. Stranks, M. M. Lee, G. Lanzani, H. J. Snaith, A. Petrozza, *Nat. Commun.* **2014**, *5*, 3586.
- [43] C. Stavrakas, S. J. Zelewski, K. Frohna, E. P. Booker, K. Galkowski, K. Y. Ji, E. Ruggeri, S. Mackowski, R. Kudrawiec, P. Plochocka, S. D. Stranks, *Adv. Energy Mater.* **2019**, *9*, 1901883.
- [44] Z. H. Chen, L. You, C. W. Huang, Y. J. Qi, J. L. Wang, T. Sritharan, L. Chen, *Appl. Phys. Lett.* **2010**, *96*, 252903.
- [45] P. S. Whitfield, N. Herron, W. E. Guise, K. Page, Y. Q. Cheng, I. Milas, M. K. Crawford, *Sci. Rep.* **2016**, *6*, 35685.
- [46] N. Leupold, K. Schötz, S. Cacovich, I. Bauer, M. Schultz, M. Daubinger, L. Kaiser, A. Rebai, J. Rousset, A. Köhler, P. Schulz, R. Moos, F. Panzer, *ACS Appl. Mater. Interfaces* **2019**, *11*, 30259.
- [47] A. Dobrovolsky, A. Merdasa, E. L. Unger, A. Yartsev, I. G. Scheblykin, *Nat. Commun.* **2017**, *8*, 34.
- [48] F. Birch, *Phys. Rev.* **1947**, *71*, 809.
- [49] F. Lehmann, A. Franz, D. M. Tobbens, S. Levchenko, T. Unold, A. Taubert, S. Schorr, *RSC Adv.* **2019**, *9*, 11151.
- [50] A. L. Montero-Alejo, E. Menéndez-Proupin, D. Hidalgo-Rojas, P. Palacios, P. Wahnón, J. C. Conesa, *J. Phys. Chem. C* **2016**, *120*, 7976.
- [51] M. Szafranski, A. Katrusiak, *J. Phys. Chem.* **2016**, *7*, 3458.
- [52] S. Jiang, Y. Fang, R. Li, H. Xiao, J. Crowley, C. Wang, T. J. White, W. A. Goddard 3rd, Z. Wang, T. Baikie, J. Fang, *Angew. Chem., Int. Ed.* **2016**, *55*, 6540.
- [53] A. Jaffe, Y. Lin, C. M. Beavers, J. Voss, W. L. Mao, H. I. Karunadasa, *ACS Cent. Sci.* **2016**, *2*, 201.
- [54] L. Kong, G. Liu, J. Gong, Q. Hu, R. D. Schaller, P. Dera, D. Zhang, Z. Liu, W. Yang, K. Zhu, Y. Tang, C. Wang, S. H. Wei, T. Xu, H. K. Mao, *Proc. Natl. Acad. Sci. USA* **2016**, *113*, 8910.
- [55] D. B. Mitzi, *Prog. Inorg. Chem.* **1999**, *48*, 1.
- [56] E. S. Parrott, J. B. Patel, A. A. Haghighirad, H. J. Snaith, M. B. Johnston, L. M. Herz, *Nanoscale* **2019**, *11*, 14276.

- [57] D. Q. Zhang, L. L. Gu, Q. P. Zhang, Y. J. Lin, D. H. Lien, M. Kam, S. Poddar, E. C. Garnett, A. Javey, Z. Y. Fan, *Nano Lett.* **2019**, *19*, 2850.
- [58] M. Anaya, A. Rubino, T. C. Rojas, J. F. Galisteo-López, M. E. Calvo, H. Miguez, *Adv. Opt. Mater.* **2017**, *5*, 1601087.
- [59] Q. F. Dong, Y. J. Fang, Y. C. Shao, P. Mulligan, J. Qiu, L. Cao, J. S. Huang, *Science* **2015**, *347*, 967.
- [60] D. Shi, V. Adinolfi, R. Comin, M. Yuan, E. Alarousu, A. Buin, Y. Chen, S. Hoogland, A. Rothenberger, K. Katsiev, Y. Losovyj, X. Zhang, P. A. Dowben, O. F. Mohammed, E. H. Sargent, O. M. Bakr, *Science* **2015**, *347*, 519.
- [61] M. I. Saidaminov, A. L. Abdelhady, B. Murali, E. Alarousu, V. M. Burlakov, W. Peng, I. Dursun, L. F. Wang, Y. He, G. Maculan, A. Goriely, T. Wu, O. F. Mohammed, O. M. Bakr, *Nat. Commun.* **2015**, *6*, 7586.

ADVANCED OPTICAL MATERIALS

Supporting Information

for *Adv. Optical Mater.*, DOI: 10.1002/adom.202000455

Investigating the Tetragonal-to-Orthorhombic Phase
Transition of Methylammonium Lead Iodide Single Crystals
by Detailed Photoluminescence Analysis

*Konstantin Schötz, Abdelrahman M. Askar, Anna Köhler,
Karthik Shankar, and Fabian Panzer**

Supporting Information

Investigating the Tetragonal-to-Orthorhombic Phase Transition of Methylammonium Lead Iodide Single Crystals by Detailed Photoluminescence Analysis

Konstantin Schötz¹, Abdelrahman M. Askar², Anna Köhler^{1,3}, Karthik Shankar², Fabian Panzer^{1*}

K. Schötz, Prof. A. Köhler, Dr. F. Panzer: Soft Matter Optoelectronics, University of Bayreuth, 95440 Bayreuth, Germany

E-Mail: fabian.panzer@uni-bayreuth.de

A. M. Askar, Prof. K. Shankar: Department of Electrical and Computer Engineering, University of Alberta, Edmonton, AB T6G 1H9, Canada

Prof. A. Köhler: Bayreuth Institute of Macromolecular Research (BIMF) and Bavarian Polymer Institute (BPI), University of Bayreuth, 95440 Bayreuth, Germany.

Corresponding Author: fabian.panzer@uni-bayreuth.de

1. Alternative description of the result of the filter effect

Often it is possible to associate the occurrence of an optical filter effect with a valley in the PL spectrum at the position where the absorbance sets in. This is valid for phase pure perovskite single crystals.^[1] However, for more complicated spectra, where different phases coexist, this does not necessarily hold true. For example, if we consider the decomposed PL spectrum of the MAPbI₃ single crystal at 160 K (see Figure S6), there is a valley in the spectrum at 1.61 eV, but this valley is not due to the filter effect but due to the coexistence of tetragonal and orthorhombic phase. In contrast, the filter effect is responsible for the small kink at 1.57 eV.

Additionally, since the filtered PL and the direct PL have different optical paths and we can tune their intensity (to a certain degree) independently by varying the measurement geometry, it is preferable to treat the PL features resulting from filtered and direct PL as distinct peaks.

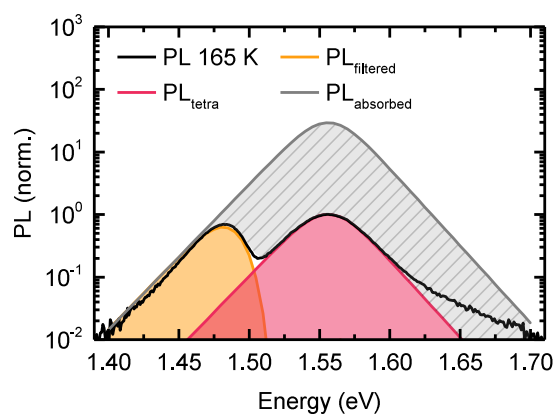


Figure S1: PL of a MAPbI₃ single crystal at 165 K decomposed into direct (red) and filtered PL (orange) and absorbed PL (grey). The absorbed PL was obtained by scaling P_{tetra} to the intensity of the low energetic edge of P_{filtered} . The PL spectrum was recorded under such a geometry that the direct PL was suppressed compared to the filtered PL.

2. PL of the phase transition with different measurement geometries

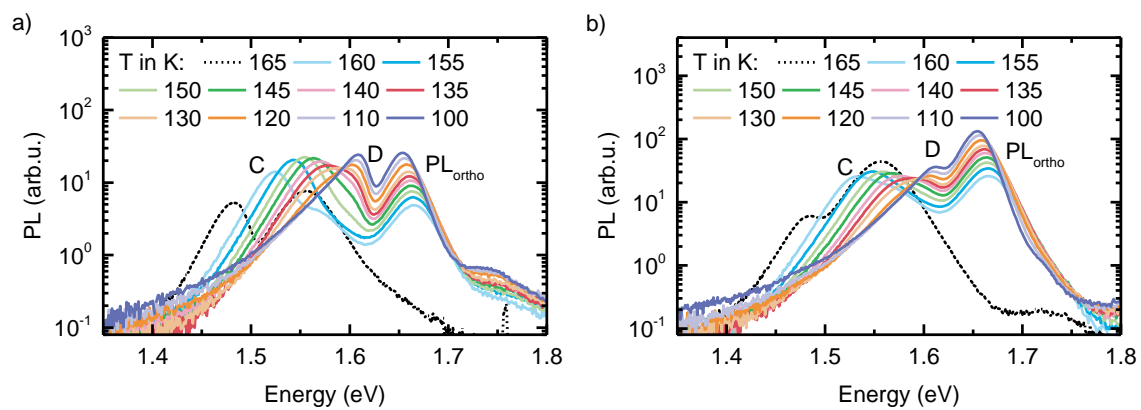


Figure S2: PL from 165 K to 100 K with two different angles between single crystal and impinging laser beam, resulting in (a) strong and (b) decreased relative Intensity of peaks C and D.

3. Details on the modelling approach

To model the PL considering the effect of internal reflections and self-absorption, we calculated the one-dimensional charge carrier distribution after laser excitation following the Beer-Lambert-Law using the absorption coefficient of MAPbI₃ at 337 nm, which can be found e.g. in the work by Crothers et al.^[2]. This charge carrier distribution leads to photoluminescence via bimolecular recombination. The PL can then travel towards either the front or the backside of the crystal, which were set to be 1 mm apart (corresponding to the size of the single crystals used in this study). On the way through the crystal, the perovskite partly absorbs the PL. At the interface between perovskite and surrounding media, the PL is either transmitted or reflected with a certain probability, allowing multiple inner reflections. To consider a possible mismatch between excitation spot and detection spot, we allowed a suppression of the PL coming directly from the crystal without inner reflections via the factor C. The detected PL is then given by:

$$PL_{detected}(E) = C \cdot PL_{direct}(E) + PL_{filtered}(E), \quad (S1)$$

where $PL_{direct}(E)$ and $PL_{filtered}(E)$ are calculated according to the Beer-Lambert law via

$$PL_{direct}(E) = \int_0^L PL_{int}(E) \cdot n(x)^2 \cdot (1 - r_f) \cdot \exp[-\alpha(E) \cdot x] dx \quad (S2)$$

$$PL_{filtered}(E) = \int_0^L \sum_{j=1} PL_{int}(E) \cdot n(x)^2 \cdot (1 - r_f) \cdot \{A_j + B_j\} dx \quad (S3)$$

with

$$A_j = r_f^j \cdot r_b^j \cdot \exp[-\alpha(E) \cdot (2jL + x)] \quad (S4)$$

$$B_j = r_f^{j-1} \cdot r_b^j \cdot \exp[-\alpha(E) \cdot ((2j - 1) \cdot L + (L - x))] \quad (S5)$$

and:

$PL_{int}(E)$: intrinsic PL lineshape

$PL_{direct}(E)$: PL leaving the crystal at the front without internal reflections

$PL_{filtered}(E)$: PL leaving the crystal after (multiple) inner reflections.

C: suppression constant for the direct PL

$n(x)$: charge carrier density as a function of depth x inside the crystal

$\alpha(E)$: absorption coefficient of the material

r_f : reflection probability at the front interface

r_b : reflection probability at the back interface

L : length of the crystal

Since below 165 K both crystal phases coexist, the total intrinsic PL is given by a sum of tetragonal and orthorhombic PL,

$$PL_{int}(E) = D \cdot PL_{int,tetra}(E) + (1 - D) \cdot PL_{int,ortho}(E), \quad (S6)$$

and likewise the absorption spectrum of the crystal with coexisting phases is

$$\alpha(E) = F \cdot \alpha_{tetra}(E) + (1 - F) \cdot \alpha_{ortho}(E). \quad (S7)$$

D is the fraction of tetragonal PL and F is the fraction of tetragonal phase absorption. F is assumed to correspond to the fraction of tetragonal phase in the crystal.

For the absorption spectrum of the tetragonal phase, we took the spectrum, reported by Ledinsky et al.^[3] and normalized it to the absolute values of the absorption coefficient α , as they were reported by Crothers et al.^[2] This approach was necessary as the temperature dependent absorption data from Ledinsky et al. does not yield α , while the data in the work from Crothers et al. does not extend to the spectral range of the Urbach tail. The absorption spectrum of the orthorhombic phase was approximated by combining the absorption of a thin film with an Urbach absorption tail that was based on transmission measurements of the single crystals (see Schötz et al.^[4]).

The intrinsic PL lineshapes of orthorhombic and tetragonal phase are discussed in SI Section 4.

The average reflection probabilities r_f and r_b were calculated via the Fresnel equations assuming a refractive index of 2.5 for MAPbI₃ in the relevant energy range,^[5] and of 1 for helium. Averaging over all angles of incidence, we obtain a reflection probability of 0.85 for the perovskite-helium interface. We note that this approximation does not consider that PL reaching the interface with a larger angle also travelled a longer distance through the material. However a slightly bigger or smaller reflection probability can be compensated easily by a slightly smaller or bigger crystal.

For comparison with measured PL spectra, the calculated spectrum $PL_{detected}(E)$ is normalized to the experimental data.

4. Approximated absorption spectra and resulting PL line shape

As described in the main text, the PL lineshape of inorganic semiconductors in the absence of emission related to defects or bound states, is given by a generalized Planck Law, following

$$PL(E) \propto A(E)E^2 \exp\left(-\frac{E}{k_B T}\right), \quad (S8)$$

where $A(E)$ is the absorptivity, k_B is the Boltzmann constant and T is the temperature of the sample.^[6]

The absorptivity is related to the absorption coefficient $\alpha(E)$ by

$$A(E) = (1 - R(E)) \frac{1 - \exp(-\alpha(E)d)}{1 - R(E)\exp(-\alpha(E)d)}, \quad (S9)$$

where $R(E)$ is the reflectivity at the interfaces.^[7] To obtain the intrinsic PL line shape, which we need for our optical modelling, it is useful to consider that the intrinsic PL is PL of the material without effects of self-absorption or internal reflections, i.e. like PL from a very thin film with perfect light out-coupling. This corresponds to $R(E)$ in Equation (S9) being zero and d being very small. In this case, the relation between the absorptivity and absorption coefficient is given by $A(E) = 1 - \exp(-\alpha(E)d)$. This in turn can be simplified for $\alpha d \ll 1$ using a Taylor series, yielding $A(E) = \alpha(E)d$, i.e. $A(E) \propto \alpha(E)$. Therefore, the intrinsic PL lineshape is obtained by replacing $A(E)$ with $\alpha(E)$ in Equation (S9).

Below the band gap, the absorption of MAPbI₃ is well described by an Urbach tail, which means that $\alpha(E < E_g) \propto \exp\left(\frac{E}{E_u}\right)$, with the Urbach energy E_u .^[8-9] We approximate the absorption spectrum by

$$\alpha(E) \approx \frac{\alpha_0}{\exp\left(\frac{E-E_0}{E_u}\right)+1}, \quad (S10)$$

where α_0 is the absorption coefficient above the band edge and E_0 is a fit parameter and is an energy near the band gap of the material. Equation (S10) fits the measured absorption edge well in the spectral region that is relevant for calculating the PL via Equation (S9). Measured absorption spectra of a MAPbI₃ thin film (presented in an earlier work^[4]) at 300 K and 150 K together with the approximated spectra according to Equation (S10) are depicted in Figure S3, showing good congruence. Inserting Equation (S10) into Equation (S8) leads to

$$PL(E) \approx I_0 \frac{1}{\exp\left(\frac{E-E_0}{E_u}\right)+1} E^2 \exp\left(-\frac{E}{k_B T}\right). \quad (S11)$$

For the special case of $E_u = \frac{k_B T}{2}$ and assuming that the spectral range of the PL is small so that $E^2 \approx \text{const.}$, the PL line shape is a hyperbolic secant, $PL(E) \propto \frac{I_0}{\exp[(E-E_0)/\sigma] + \exp[-(E-E_0)/\sigma]}$, as it was used as the PL line shape in an earlier work.^[4]

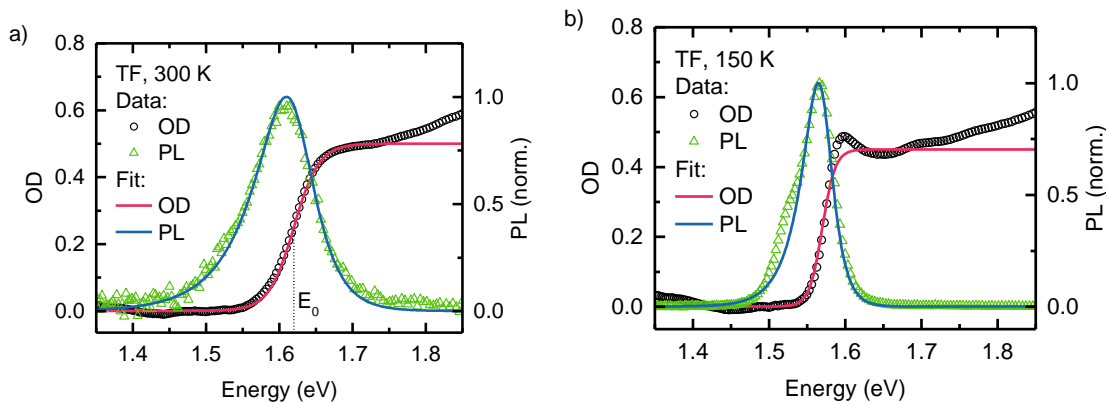


Figure S3: Comparison of experimental absorption spectra (black open circles) of a MAPbI₃ thin film with the fitted absorption spectra according to Equation (S9) (solid red line) at (a) 300 K and (b) 150 K, i.e. in the tetragonal phase. E_0 is indicated as dashed line. Also shown is the experimental PL (green open triangles) together with calculated PL according to Equation (S10) (blue solid line).

To test the applicability of Equation (S11), we plotted the expected PL of the same MAPbI₃ thin film according to Equation (S11), using the values of E_u and E_0 obtained from the fit of the absorption spectra and compared it with measured PL spectra. The result is shown in Figure S3. Apart from a low energy feature around 1.5 eV, which can be associated to filtered PL,^[10] the PL predicted from the absorption spectrum from Equation (S11) and the experimental PL match very well.

To extend this framework also to single crystals, we fitted the PL of a MAPbI₃ single crystal at 165 K and at 100 K (i.e. in its orthorhombic phase) using Equation (S11), also considering self-absorption according to Equation (S1)-(S5). Since we do not have an absorption spectrum of the single crystal, E_u and E_0 are considered to be free parameters. The optimized fits are shown in Figure S4. To achieve an agreement of the high energy edge of modelled and experimental PL, it was necessary to scale the argument of the last exponential function in Equation (S11) by a factor of 0.825. This has the same effect as an increased temperature of the sample. An apparently increased temperature obtained from PL data was already reported earlier.^[11] A more detailed discussion of the flatter high energy edge of the PL and its impact on the extracted Urbach energies can be found in SI Section 5.

For the tetragonal PL, the modelled PL agrees very well with the experimental one (Figure S4a), while the experimental orthorhombic PL shows a flatter tail for energies below 1.57 eV compared to the modelled PL (Figure S4b). This indicates the existence of additional emissive states.

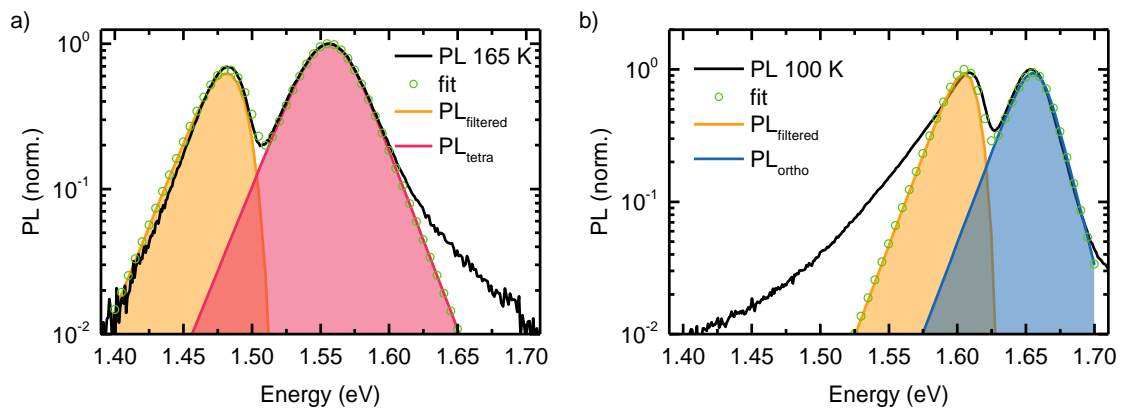


Figure S4: Comparison of modelled PL including self-absorption effects and experimental PL of (a) the tetragonal PL at 165 K and of (b) the orthorhombic phase at 100 K of a MAPbI₃ single crystal.

5. Origin of flatter high energy edge of PL and impact on extracted Urbach energies

A high energy edge of the PL of a perovskite sample that is flatter than one would expect from Equation (S11), i.e. following $\exp\left(-\frac{E}{k_B T}\right)$ was reported earlier, where it was speculated that it originates from hot carriers after non-resonant excitation.^[11] We note that the flatter decrease of the high energy edge could also be caused from a self-absorption effect. We observed in an earlier work that upon surface passivation, the room temperature PL doubled its intensity and shifted to higher energies by about 15 meV, which we associated with more PL coming from the surface region and thus self-absorption has less influence. Additionally, the high energy edge became steeper.^[4] Fitting the high energy edge with $I_0 \exp\left(-\frac{E}{k_B T} \cdot c\right)$ with c being the scaling factor described in SI Section 4, reveals an increase of c from 0.82 before passivation (apparent temperature $T_{app.} = \frac{T}{c} = 365 \text{ K}$) to 0.91 after passivation ($T_{app.} = 330 \text{ K}$) (see Figure S5). This emphasizes that also the flatter high energy edge, resulting in an apparently increased temperature, is a consequence of self-absorption. This is consistent with the finding that the factor c is not necessary for fitting PL of thin films, where self-absorption effects are less pronounced.

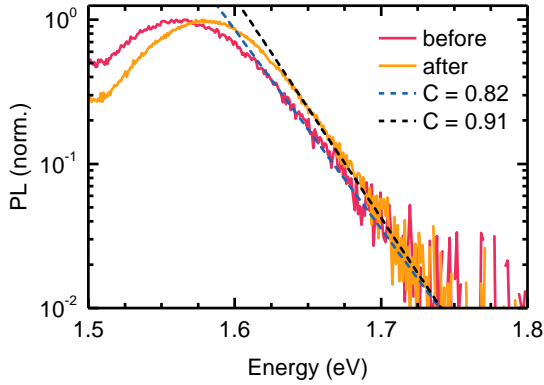


Figure S5: Room temperature PL of a MAPbI₃ single crystal before (red) and after passivation (orange), together with exponential fits to the high energy falling edge according to $I_0 \exp\left(-\frac{E}{k_B T} \cdot c\right)$.

If the flattening of the high energy edge of the PL is due to self-absorption, then also the Urbach energies extracted with Equation (S11) are artificially too big. From Equation (S11) it follows that the low energy edge of the PL is determined by $\exp\left((E - E_0) \cdot \left(\frac{1}{E_u} - \frac{1}{k_B T}\right)\right)$, i.e. by the difference $\frac{1}{E_u} - \frac{1}{k_B T}$. The apparent Urbach energy $E_{u,app.}$ obtained from fitting with the apparent temperature $T_{app.}$

can be related with the actual Urbach energy E_u and actual temperature T by the fact that for both cases, Equation (S11) should result in the experimental low energy falling edge, implying

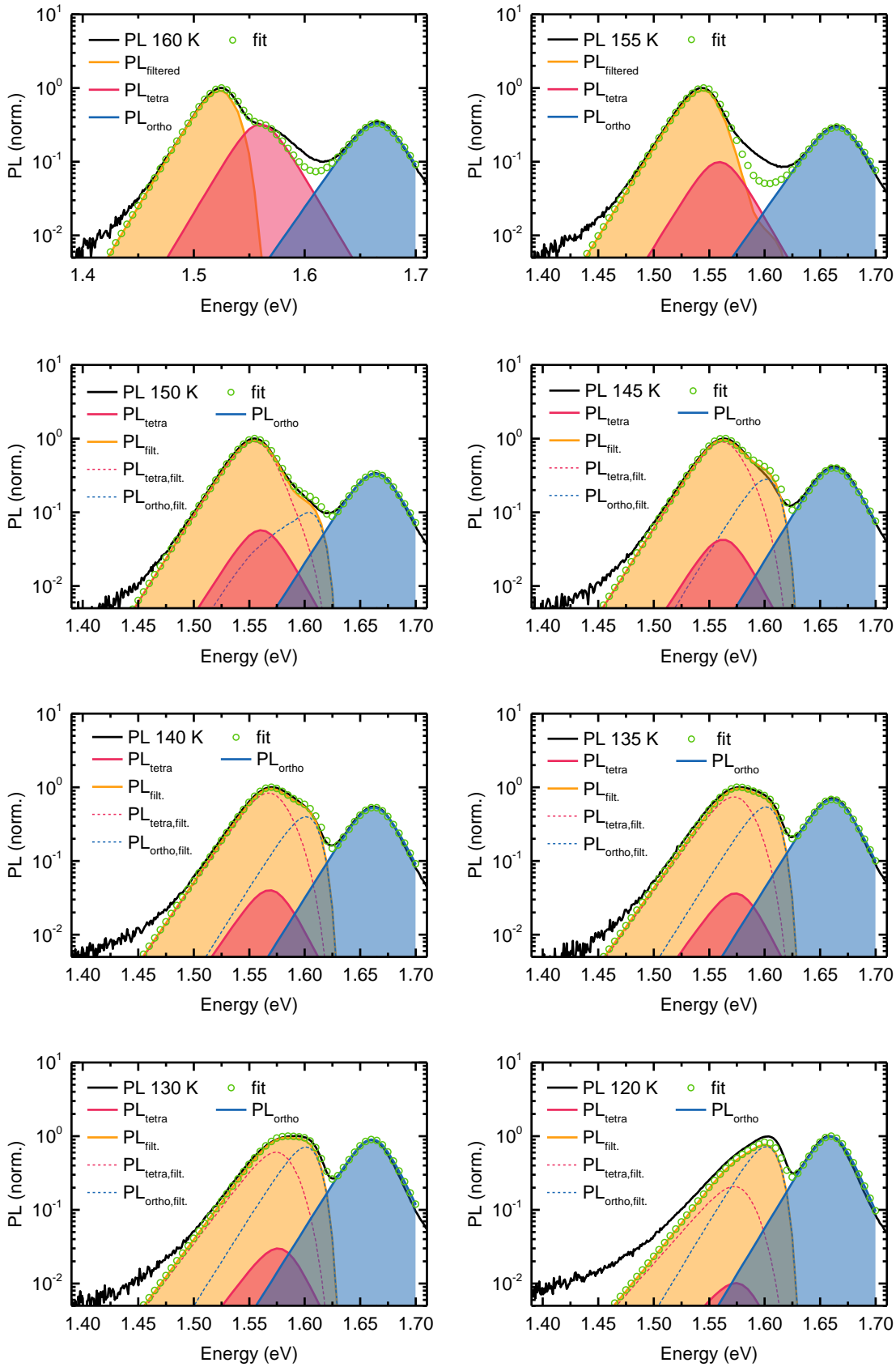
$$\frac{1}{E_{u,app.}} - \frac{1}{k_B T_{app.}} = \frac{1}{E_u} - \frac{1}{k_B T}. \quad (S12)$$

Solving this for the actual Urbach energy and inserting $T_{app.} = \frac{T}{c}$ yields

$$E_u = \left(\frac{1}{E_{u,app.}} + \frac{1-c}{k_B T} \right)^{-1}. \quad (S13)$$

The Urbach energies shown in Figure 5 in the main text are corrected according to Equation (S13) and agree very nicely with the values reported by Ledinsky et al.^[12] This underpins the association of the factor c with a weak self-absorption effect on the direct PL in our single crystal PL spectra.

6. Modelled PL spectra in the temperature range from 160 K to 100 K



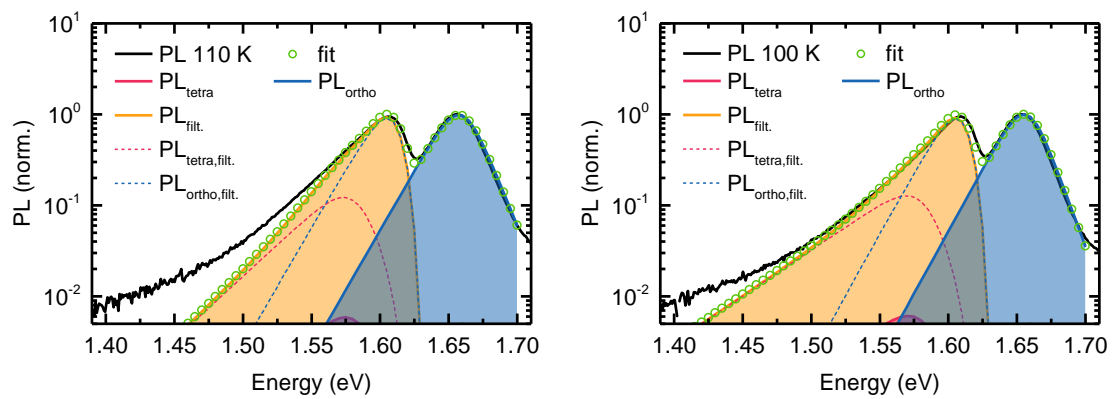


Figure S6: Experimental (black solid line) and modelled (green circles) PL spectra in the temperature range from 160 K to 100 K, together with the decomposition in tetragonal (red), orthorhombic (blue) and filtered (orange) PL. Dashed lines indicate the individual contributions of the two phases to the filtered PL.

7. Estimation of stress on tetragonal inclusions during the phase transition

Assuming that the temperature-dependent shift of the PL is mainly due to the lattice dilation, we can roughly estimate the change in unit cell volume needed to shift the PL by 20 meV to higher energies. To do so, we extract the increase in temperature that would correspond to a certain energy shift from temperature-dependent PL data (see Figure S7). We re-evaluated data reported in an earlier work.^[4] We find that the blue shift of 20 meV happens upon heating to 220 – 230 K. Calculating the initial unit cell volume at 160 K and the one at 220 – 230 K with the help of the temperature-dependent lattice vectors reported by Whitfield et al.^[13] yields an increase of the unit cell volume by 0.74% to 0.87%. Applying Birch's equation of states^[14] and using typical values for the bulk modulus of MAPbI₃ of 14 GPa^[15-17] leads to a tensile stress of 85 – 112 MPa. Extrapolating the tetragonal unit cell volume to 120 K and considering this as initial volume yields a tensile stress of about 165 MPa.

For the temperature-dependence of the PL peak position, the PL of a thin film was preferred in comparison to that of a single crystal, since the former is less affected by self-absorption.

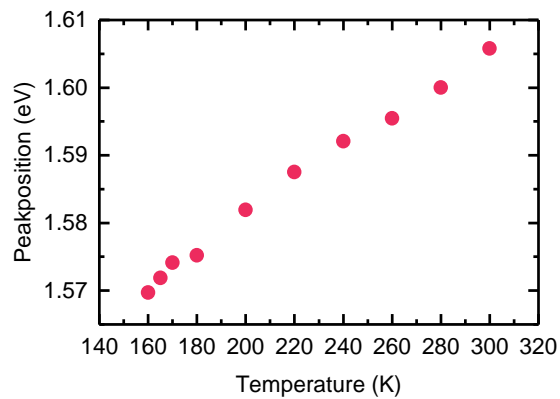


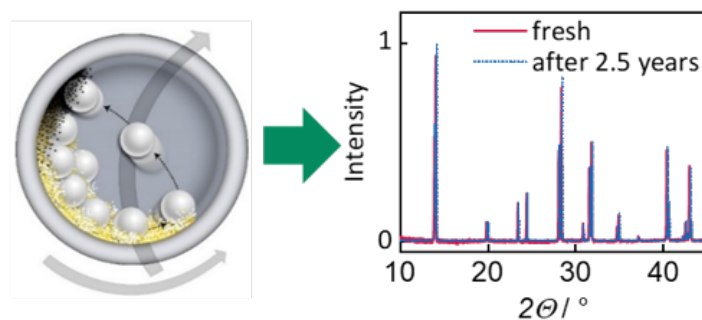
Figure S7: Temperature-dependence of the PL peak position of a MAPbI₃ thin film.

Supporting References

- [1] K. Kojima, K. Ikemura, K. Matsumori, Y. Yamada, Y. Kanemitsu, S. F. Chichibu, *APL Materials* **2019**, 7.
- [2] T. W. Crothers, R. L. Milot, J. B. Patel, E. S. Parrott, J. Schlipf, P. Müller-Buschbaum, M. B. Johnston, L. M. Herz, *Nano Letters* **2017**, 17, 5782.
- [3] M. Ledinsky, T. Schonfeldova, J. Holovsky, E. Aydin, Z. Hajkova, L. Landova, N. Neykova, A. Fejfar, S. De Wolf, *Journal of Physical Chemistry Letters* **2019**, 10, 1368.
- [4] K. Schötz, A. M. Askar, W. Peng, D. Seeberger, T. P. Gujar, M. Thelakkat, A. Köhler, S. Huettner, O. M. Bakr, K. Shankar, F. Panzer, *J. Mater. Chem. C* **2020**, 8, 2289.
- [5] L. J. Phillips, A. M. Rashed, R. E. Treharne, J. Kay, P. Yates, I. Z. Mitrovic, A. Weerakkody, S. Hall, K. Durose, *Data in Brief* **2015**, 5, 926.
- [6] P. Würfel, *J. Phys. C: Solid State Phys.* **1982**, 15, 3967.
- [7] E. Daub, P. Würfel, *Phys. Rev. Lett.* **1995**, 74, 1020.
- [8] F. Urbach, *Phys. Rev.* **1953**, 92, 1324.
- [9] S. Pathak, A. Sepe, A. Sadhanala, F. Deschler, A. Haghghirad, N. Sakai, K. C. Goedel, S. D. Stranks, N. Noel, M. Price, S. Hüttner, N. A. Hawkins, R. H. Friend, U. Steiner, H. J. Snaith, *ACS Nano* **2015**, 9, 2311.
- [10] L. M. Pazos-Outón, M. Szumilo, R. Lamboll, J. M. Richter, M. Crespo-Quesada, M. Abdi-Jalebi, H. J. Beeson, M. Vrućinić, M. Alsari, H. J. Snaith, B. Ehrler, R. H. Friend, F. Deschler, *Science* **2016**, 351, 1430.
- [11] A. D. Wright, C. Verdi, R. L. Milot, G. E. Eperon, M. A. Perez-Osorio, H. J. Snaith, F. Giustino, M. B. Johnston, L. M. Herz, *Nat. Commun.* **2016**, 7, 11755.
- [12] M. Ledinsky, T. Schönfeldová, J. Holovský, E. Aydin, Z. Hájková, L. Landová, N. Neyková, A. Fejfar, S. De Wolf, *J. Phys. Chem. Lett.* **2019**, 10, 1368.
- [13] P. S. Whitfield, N. Herron, W. E. Guise, K. Page, Y. Q. Cheng, I. Milas, M. K. Crawford, *Sci. Rep.* **2016**, 6, 35685.
- [14] F. Birch, *Phys. Rev.* **1947**, 71, 809.
- [15] H. Beck, C. Gehrman, D. A. Egger, *APL Mater.* **2019**, 7, 021108.
- [16] Y. Rakita, S. R. Cohen, N. K. Kedem, G. Hodes, D. Cahen, *MRS Commun.* **2015**, 5, 623.
- [17] A. Jaffe, Y. Lin, C. M. Beavers, J. Voss, W. L. Mao, H. I. Karunadasa, *ACS Cent. Sci.* **2016**, 2, 201.

10 High Versatility and Stability of Mechanochemically Synthesized Halide Perovskite Powders for Optoelectronic Devices

Perovskite Powder



Nico Leupold, Konstantin Schötz, Stefania Cacovich, Irene Bauer, Maximilian Schultz, Monika Daubinger, Leah Kaiser, Amelle Rebai, Jean Rousset, Anna Köhler, Philip Schulz, Ralf Moos, Fabian Panzer.

Published in
ACS Applied Materials & Interfaces, **2019**, 11, 33, 30259-30268
(DOI: 10.1021/acsami.9b09160)

Reprinted with permission from the American Chemical Society
Copyright (2020) American Chemical Society

High Versatility and Stability of Mechanochemically Synthesized Halide Perovskite Powders for Optoelectronic Devices

Nico Leupold,[†] Konstantin Schötz,[‡] Stefania Cacovich,^{||} Irene Bauer,[‡] Maximilian Schultz,[‡] Monika Daubinger,[†] Leah Kaiser,[†] Amelle Rebai,^{||} Jean Rousset,^{||,⊥} Anna Köhler,^{‡,§,||} Philip Schulz,^{||,#} Ralf Moos,[†] and Fabian Panzer^{*,||}

[†]Department of Functional Materials and Zentrum für Energietechnik (ZET), [‡]Soft Matter Optoelectronics, and [§]Bayreuth Institute of Macromolecular Research (BIMF) and Bavarian Polymer Institute (BPI), University of Bayreuth, 95440 Bayreuth, Germany

^{||}IPVF, Institut Photovoltaïque d'Ile de France (IPVF), 30 route départementale 128, 91120 Palaiseau, France

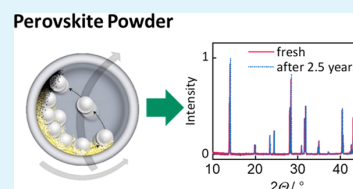
[⊥]EDF R&D, 30 route départementale 128, 91120 Palaiseau, France

[#]CNRS, Institut Photovoltaïque d'Ile de France (IPVF), UMR 9006, 30 route départementale 128, 91120 Palaiseau, France

Supporting Information

ABSTRACT: We show that mechanochemically synthesized halide perovskite powders from a ball milling approach can be employed to fabricate a variety of lead halide perovskites with exceptional intrinsic stability. Our MAPbI₃ powder exhibits higher thermal stability than conventionally processed thin films, without degradation after more than two and a half years of storage and only negligible degradation after heat treatment at 220 °C for 14 h. We further show facile recovery strategies of nonphase-pure powders by simple remilling or mild heat treatment. Moreover, we demonstrate the mechanochemical synthesis of phase-pure mixed perovskite powders, such as (Cs_{0.05}FA_{0.95}PbI₃)_{0.85}(MAPbBr₃)_{0.15}, from either the individual metal and organic halides or from readily prepared ternary perovskites, regardless of the precursor phase purity. Adding potassium iodide (KI) to the milling process successfully passivated the powders. We also succeeded in preparing a precursor solution on the basis of the powders and obtained uniform thin films for integration into efficient perovskite solar cells from spin-coating this solution. We find the KI passivation remains in the devices, leading to improved performance and significantly reduced hysteresis. Our work thus demonstrates the potential of mechanochemically synthesized halide perovskite powders for long-time storage and upscaling, further paving the way toward commercialization of perovskite-based optoelectronic devices.

KEYWORDS: ball milling, MAPbI, passivation, solar cell, strain, hybrid perovskite



1. INTRODUCTION

Optoelectronic devices based on (hybrid organic/inorganic) halide perovskites as active semiconductor materials have undergone a remarkable development within the past few years. The efficiencies of the current flagship applications, perovskite-based solar cells (PSCs), are now at 25.2% and thus on a par with those of classic silicon-based solar cells.¹ This development is accompanied by continuous improvements in device stability, which seem to bring the commercialization of PSCs within reach.^{2–4} While much of the current enthusiasm for halide perovskites is also due to their ability for versatile processing, e.g., from solution or by evaporation, these processing routes are considerably more complex compared to the corresponding processing approaches of, for example, organic semiconductors. This is because the actual crystallization of the target material, namely the perovskite and its film formation, are inevitably coupled to each other. That is, they always take place simultaneously and thus need to be considered and optimized in parallel. This can be seen as one of the reasons for the typically low reproducibility of the film formation and large arbitrary scattering of device performance

even for the same lab,⁵ which is a major obstacle to an industrial uptake.

Both solution processing and co-evaporation typically suffer from a rather limited control of the precursor stoichiometry and, especially on a large scale, from relatively high variations of the surface roughness and the height profile across the module. Furthermore, in the case of co-evaporation, microstructure control is often limited, while for solution-based processing, most of the suitable solvents are considerably toxic, representing a significant safety concern for commercialization.⁶

An alternative synthesis route that is decoupled from the layer formation is the mechanochemical synthesis of halide perovskite powders by simply grinding the reactants into powder form. This can be done, e.g., using a high-energy ball mill,^{7,8} and this procedure was successfully demonstrated for various lead-containing^{9–12} and lead-free^{13,14} halide perovskite compositions. Beneficial aspects of using perovskite powders

Received: May 26, 2019

Accepted: July 26, 2019

Published: July 26, 2019

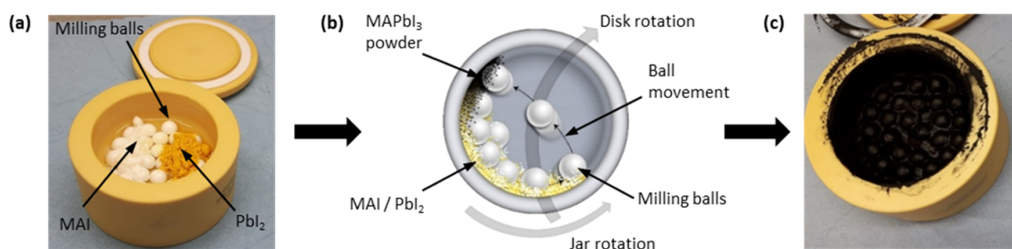


Figure 1. (a) Photograph of a milling jar loaded with milling balls, MAI, and PbI_2 precursor powders. (b) Schematic of the ball milling procedure for the mechanochemical synthesis of perovskite powders. (c) Photograph of the milling jar from (a) after the ball milling process and successful mechanochemical synthesis of black MAPbI_3 powder.

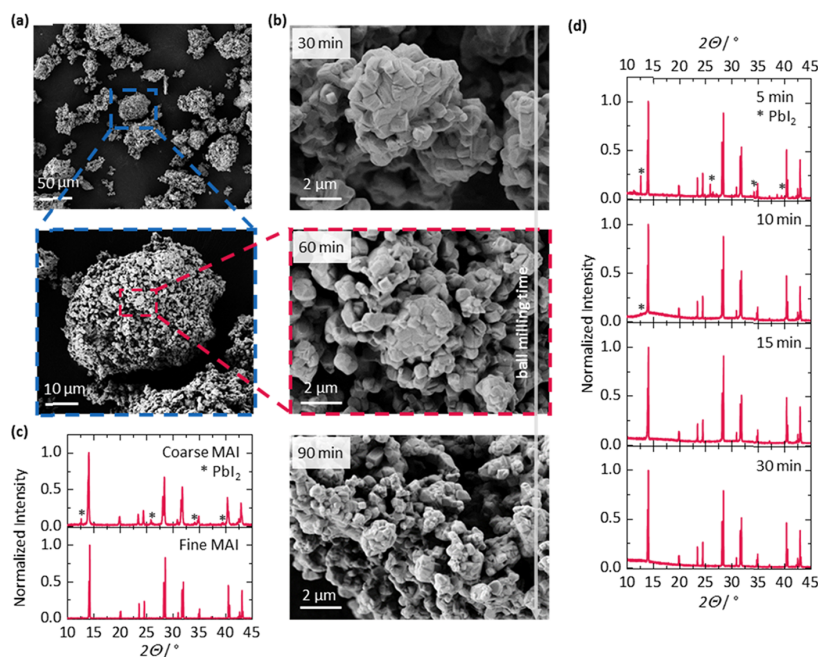


Figure 2. (a) SEM images of mechanochemically synthesized MAPbI_3 powder at different magnifications, as indicated. (b) SEM images of MAPbI_3 powders after 30 min (left), 60 min (center), and 90 min (right) of milling. (c) X-ray diffraction (XRD) patterns of MAPbI_3 powders after 50 min milling time using coarse MAI and after 30 min using fine MAI as shown by photographs. (d) XRD patterns after different milling times of MAPbI_3 powders. Signals from crystalline PbI_2 are indicated with stars.

were shown, including superior storage stability of powders compared to their stock solution counterparts.¹⁵ Furthermore, dry synthesis approaches for perovskite powders allow for an extended range of possible reactants that can be used, as no solubility issues exist.¹⁶ The high level of control of the precursor stoichiometry translates to a high level of control in the overall synthesis, which is also beneficial for improved device properties, when dissolving the thus-prepared perovskite powders for solution-based thin-film processing.^{8,10,11,17} Also, efficient X-ray detectors were demonstrated by directly processing solution-based perovskite powders to form a thick layer without the use of solvents,¹⁸ further emphasizing the versatile potential of halide perovskite powders.

Concerning the mechanochemical synthesis of perovskite powders, the correlation of the reactant properties and synthesis parameters with the structural and optoelectronic properties of the final perovskite powders has, however, not yet been addressed in detail. In this study, we investigate the intrinsic stability of mechanochemically synthesized powders

and their resilience against external stress (e.g., light, oxygen, humidity), which are crucial aspects for commercial deployment.

The paper is structured as follows. In Section 2.1, we demonstrate the impact that milling time and the reactant properties have on the perovskite powder. In Section 2.2, we investigate the exceptional stability of these powders against decomposition, and Section 2.3 shows that phase-pure perovskite powders can be obtained by simple remilling in the case of a prior incomplete conversion or in the case of inadvertent degradation, Section 2.4 demonstrates that the mechanochemical approach offers a high versatility in the synthesis of more complex multinary mixed perovskites as well as for passivation by the addition of potassium iodide (KI). The electrical properties of the powders and thin-film solar cells made from dissolved powder are explored in Section 2.5. A summarizing and evaluating discussion is concluding the paper.

2. RESULTS AND DISCUSSION

2.1. Impact of Processing Parameters on Mechanochemically Synthesized Perovskite Powders. Figure 1 shows the basic principle of the ball milling process for producing perovskite powders. The reactants, e.g., methylammonium iodide (MAI) and lead iodide (PbI_2) powders for the synthesis of the model hybrid perovskite methylammonium lead iodide (MAPbI_3), are weighed to the desired stoichiometry and transferred to a milling jar. The jar also contains milling balls and a sufficient amount of cyclohexane, serving as a milling agent but not taking part in the chemical reaction (Figure 1a). Afterward, the jar is tightly closed and mounted into the ball milling machine. In a planetary ball mill as used in this study, the jar performs two movements: a rotation around its own axis and a rotation around the center of the main disk, on which additional jars can be mounted (Figure 1b).

The combination of these rotational movements leads to a repeated detaching and subsequent tossing of the balls with high energy to the opposing wall. There they collide with the blended reactant-particles and other balls, providing the energy for the reaction to the desired perovskite. In detail, the mechanochemical synthesis of halide perovskites has been explained by the fact that during the milling, MAI can be plastically deformed, while PbI_2 is brittle.¹⁹ The distortion of MAI leads to the formation of voids and cracks in the MAI particles,²⁰ so that PbI_2 particles are pushed into the MAI by the milling balls, being beneficial for the mechanochemical reaction.¹⁹ Additionally, the powders are continuously mixed by the movement of the balls. This ensures a homogenous distribution of all elements in the resulting perovskite. Since cyclohexane has a high vapor pressure, it can be removed within 15 min by evaporation at room temperature. As the last preparation step, the powder is sieved with a $90\ \mu\text{m}$ sieve, where the remaining particles are passed through the sieve using a metal spatula, resulting in a fine, free-flowing powder. For the powders that we produce in this study, typical amounts were in the range of 25–30 g per batch.

Figure 2a shows scanning electron microscopy (SEM) images of mechanochemically synthesized MAPbI_3 powder with a milling time of 60 min at different magnifications. The powder in general consists of porous 20–100 μm sized agglomerates of smaller particles. At higher magnification, it becomes clear that the smaller particles are best characterized as compact aggregates in the range of a few micrometer, which in turn consist of small primary particles in the sub-micrometer range.²¹ To investigate the impact of the milling time on the resulting powder properties, we produced three MAPbI_3 powders differing in their milling time (30, 60, and 90 min). From SEM images (Figure 2b), we can identify a decrease of both aggregate and primary particle size with milling time, where primary particles are well above 1 μm after 30 min of milling, decreasing to below 1 μm after 60 min, and even reducing to less than 300 nm after 90 min of milling.

In the case of MAPbI_3 , we found the minimum milling time for a complete conversion of MAPbI_3 for our synthesis conditions to be 15 min, as is confirmed by X-ray diffraction (XRD) measurements (see Figure 2d). However, we could identify a clear impact of the MAI precursor particle size on the minimum milling time needed for a full perovskite conversion. When coarse-grained MAI with particle sizes in the range of a few mm was used, we find reflexes at $2\theta = 12.6, 25.2, 34.2,$ and 39.5° in the XRD pattern (Figure 2c top panel) after a milling

time of 50 min, which are associated with residual PbI_2 , proofing an incomplete perovskite synthesis.

In contrast, the XRD pattern of the powder on the basis of fine MAI with particle sizes of around 50 μm (Figure 2c bottom) shows only the desired peaks associated with MAPbI_3 already after 30 min of milling. We associate this behavior with the increase of the reactive surface for the fine MAI, leading to a decreased amount of energy that is needed for the initial comminution of coarse-grained MAI.

2.2. Thermal and Temporal Stability of Perovskite Powders. A critical aspect for the development of perovskite applications is the long-term stability of the perovskite powders. In general, the aggregates and primary particles made by the ball milling process appear compact, which is known to be beneficial in terms of stability.^{22–25} To further explore this aspect, we stored mechanochemically synthesized MAPbI_3 powder for more than two and a half years in a glovebox with a dry (dew point $< -50\ ^\circ\text{C}$) and inert atmosphere and measured XRD patterns at the beginning and at the end of the storage time (Figure 3 top panel). Even

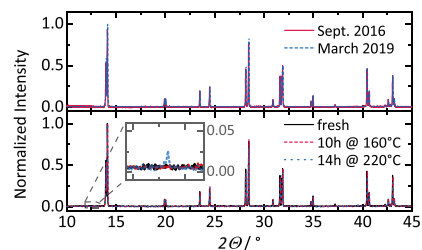


Figure 3. XRD pattern of MAPbI_3 powders before and after more than two and a half years of storage in a dry atmosphere (top panel), and before and after a heat treatment for 10 and 14 h at 160 and 220 $^\circ\text{C}$ in air (bottom panel), with a zoomed region, where the (001) peak of PbI_2 is expected.

though all main processing steps were carried out in air, we find absolutely no sign of any degradation products, such as crystalline PbI_2 , demonstrating the intrinsic long-term stability of MAPbI_3 in powder form at room temperature. This is consistent with a recent report that indicates higher stability of halide perovskites in powder form compared to the corresponding precursor solution.¹⁵ Besides, we also observed an improved temporal stability of mechanochemically synthesized formamidinium lead iodide (FAPbI_3) powders, with a clear deceleration of the typical transformation from its perovskite α -phase toward its nonperovskite hexagonal δ -phase at ambient conditions (for a detailed discussion see the Supporting Information (SI), Figure S1).

To also test their thermal stability, we stored phase-pure MAPbI_3 powders (50 min milling time) at 160 and 220 $^\circ\text{C}$ for 10 and 14 h, respectively. The treatments were conducted in air with a relative humidity of at least 20% at room temperature, corresponding to 0.12% at 160 $^\circ\text{C}$ and 0.03% at 220 $^\circ\text{C}$. Figure 3 bottom panel shows the corresponding XRD patterns, where we find no Bragg peaks corresponding to PbI_2 for the heat treatment at 160 $^\circ\text{C}$ and a nearly negligible intensity of the (001) PbI_2 Bragg peak after the temperature treatment at 220 $^\circ\text{C}$ for 14 h (see Figure S2 for details). This behavior proves the exceptional thermal stability of MAPbI_3 in powder form, especially when considering that typically a

temperature of even less than 160 °C is well sufficient to thermally decompose MAPbI₃ thin films within minutes.²⁶

Analysis of the XRD patterns of the MAPbI₃ powders with different milling times using the Williamson–Hall method (Figure S3) reveals that the microstrain in the powders is nearly negligible (<0.01%). In the literature, macrostrain levels in perovskite thin films were reported to be in the range from 0.2 to 0.6%²⁷ and microstrains to be in the range of 0.1 to 0.2%.²⁸ These recent studies also suggest that strain in perovskite thin films is mainly responsible for defect-assisted nonradiative recombination and accelerated degradation of the thin films.^{27,28} We thus conclude that the nearly negligible strain we find in the perovskite powders ensures their relatively high stability.

2.3. Regeneration of Nonphase-Pure Powders. A further important aspect of technological purposes is the issue of whether nonphase-pure powders can be purified easily. After the heat treatment of MAPbI₃ powder at 220 °C, we observed a small degree of thermal degradation, evident from a visible (001) PbI₂ Bragg peak at $2\theta = 12.6^\circ$. However, simply adding a 20 mol % of MAI precursor powder to the degraded MAPbI₃ and remilling this mixture for 50 min lead to the complete recovery of the MAPbI₃ powder, as indicated by the disappearance of the PbI₂ signatures in the corresponding XRD pattern (Figure 4a). We further exploited this possibility of

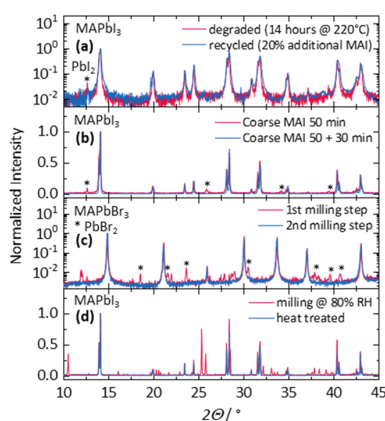


Figure 4. (a) XRD patterns of thermally degraded MAPbI₃ powder from Figure 3a (red), and after a milling step, where 20 mol % MAI was added (blue). (b) XRD pattern of MAPbI₃ powder using coarse MAI as a precursor after 50 min of milling (red, from Figure 2c) and after an additional 30 min of milling (blue). (c) XRD pattern of mechanochemically synthesized MAPbBr₃ powder after the first (50 min) and second milling step (30 min). Signals from crystalline PbBr₂ or PbI₂ are indicated with stars. (d) XRD pattern of MAPbI₃ powder synthesized at a high relative humidity of 80% before and after heat treatment at 120 °C for 30 min.

reprocessing perovskite powders to improve their properties. To this end, we remilled the not yet fully converted MAPbI₃ powder where coarse MAI was used (vide supra) for additional 30 min, which lead to the disappearance of any PbI₂ signal in the XRD pattern (Figure 4b). The same applies to the mechanochemical synthesis of methylammonium lead bromide (MAPbBr₃) powder (Figure 4c), where after the first milling step of 50 min, we find reflexes in the corresponding XRD patterns that are associated with unreacted lead bromide (PbBr₂). When milling this powder for 30 min in a second

milling step, all traces of PbBr₂ are eliminated, indicating a complete conversion of the perovskite.

If the powders are mechanochemically synthesized at a high relative humidity (rh = 80%), we could observe several additional reflexes in the corresponding XRD pattern in the case of MAPbI₃ (Figure 4d), which are typically associated with the formation of hydrates.²⁹ By simple mild heating at 120 °C for about 30 min, it is possible to ensure a complete phase purity of the perovskite, i.e., all additional reflexes have disappeared as evident by XRD.

Overall, our findings demonstrate that ball milling of halide perovskites offers a versatile and easy strategy to recover halide perovskite powders, which can also be beneficial for the development of improved recycling procedures of perovskite-based optoelectronic devices in the future.

2.4. Versatility in the Synthesis of Mixed Perovskites, Including Additives. We also addressed the mechanochemical synthesis of the state-of-the-art multi-cation mixed halide perovskite^{30,31} to achieve optimized stability and charge transport properties. As the first step, we produced systems whereby only cations (FA_{0.5}MA_{0.5}PbI₃) or halides (MAPbBr_{1/2}) were mixed. The successful synthesis of these different compounds could be confirmed by XRD and their optical properties, demonstrating that the chosen ranges of the milling parameters are also suitable for producing mixed perovskites (see Figure S4 and Table S1 in the SI).

We next explored the possibility to synthesize more complicated material compositions via the ball milling technique. Figure 5a shows the XRD patterns of (FAPbI₃)_{0.85}(MAPbBr₃)_{0.15} and (Cs_{0.05}FA_{0.95}PbI₃)_{0.85}(MAPbBr₃)_{0.15} powders, where no signatures of residual phases can be observed after 50 min of milling. Similar to the case of MAPbI₃ powders (Figure 2a), we could not observe any sign of degradation on the basis of XRD characterization of the more complex powders after six months of storage under a continuous flow of dry nitrogen inside a desiccator containing a drying agent (Figure S5). For their synthesis, we used the individual precursors, i.e., powders of formamidinium iodide (FAI), PbI₂, methylammonium bromide (MABr), PbBr₂, or cesium iodide (CsI) in the appropriate stoichiometric ratios. In the case of (FAPbI₃)_{0.85}(MAPbBr₃)_{0.15}, we also explored the possibility to simplify the weighing procedure of the reactants by considering the readily prepared mechanochemically synthesized powders of ternary FAPbI₃ and MAPbBr₃ and use them as starting materials for the mechanochemical synthesis of the mixed perovskite. By doing so, we achieve fully synthesized (FAPbI₃)_{0.85}(MAPbBr₃)_{0.15} already after a milling time of 30 min, even independent of whether the FAPbI₃ used was in its perovskite α -phase or in its degraded, nonperovskite δ -phase, which well emphasizes the versatility of the ball milling approach (Figure 5a).

The elimination of nonradiative recombination pathways by passivation of traps is a known aspect in inorganic semiconductors,^{32,33} and is currently becoming a promising research focus also in the field of halide perovskites.^{34–36} Recently, it was demonstrated that (Cs_{0.05}FA_{0.95}PbI₃)_{0.15}-(MAPbBr₃)_{0.85} can be passivated by adding potassium iodide (KI) to the precursor solution, improving the optoelectronic properties of the perovskite layer and thus device efficiency.³⁷ To explore this possibility in the context of ball milling and perovskite powders, we used (FAPbI₃)_{0.85}(MAPbBr₃)_{0.15} and (Cs_{0.05}FA_{0.95}PbI₃)_{0.85}(MAPbBr₃)_{0.15}, added 5 or 10 mol % solid KI, respectively, and remilled these powders for 50 min.

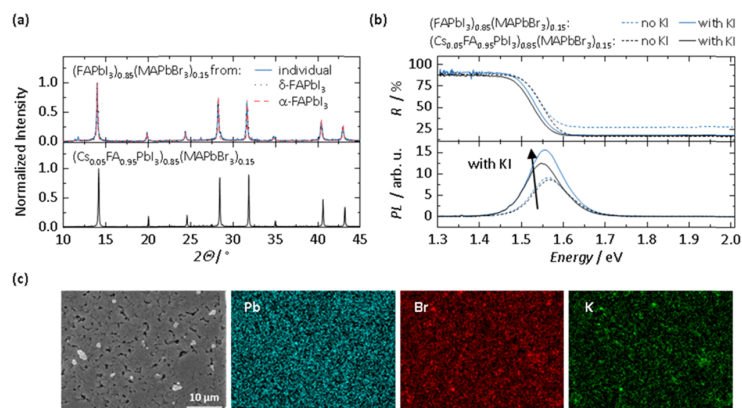


Figure 5. (a) XRD pattern of mechanochemically synthesized $(\text{FAPbI}_3)_{0.85}(\text{MAPbBr}_3)_{0.15}$ and $(\text{Cs}_{0.05}\text{FA}_{0.95}\text{PbI}_3)_{0.85}(\text{MAPbBr}_3)_{0.15}$. (b) Reflectance and photoluminescence (PL) spectra of the pure and KI passivated compounds. (c) SEM image and Pb, Br, and K mapping obtained via energy-dispersive X-ray spectroscopy (EDX) of passivated $(\text{Cs}_{0.05}\text{FA}_{0.95}\text{PbI}_3)_{0.85}(\text{MAPbBr}_3)_{0.15}$.

Figure 5b shows reflectance and photoluminescence (PL) spectra before and after the passivation of the powders. The passivated powders show an increased PL intensity compared to the nonpassivated ones. This behavior was reported as an unambiguous signature of successful passivation, where nonradiative recombination is reduced, resulting in an increased photoluminescence quantum efficiency.^{32,33,38–40} Complementarily, the reflectance measurements show that the band-gap of the passivated powders is slightly shifted to the red with respect to their nonpassivated counterparts. This has been reported as a consequence of the passivation of this compound with KI since the I/Br ratio of the perovskite is slightly increased.³⁷

To probe whether the passivation of the perovskite powders occurred homogeneously, energy-dispersive X-ray spectroscopy (EDX) was performed. This technique allows us to detect the spatial distribution of individual elements such as lead, bromine, and potassium. Exemplary spectra are shown in Figure 5c for passivated $(\text{Cs}_{0.05}\text{FA}_{0.95}\text{PbI}_3)_{0.85}(\text{MAPbBr}_3)_{0.15}$ powder that was pressed as a pellet (also see Figure S6).

The mapping of the elements shows that potassium is in general evenly distributed over the sample, except for some small areas. There, the EDX signal from potassium and bromine characteristic peaks is more intense, indicating a local enrichment of both elements, which is in accordance with the literature.⁴¹ The passivation using KI was suggested to introduce excess iodide into the system, compensating halide vacancies and also attracting and immobilizing additional halide species at grain boundaries and surfaces, facilitating the overall electrical properties of the layer.³⁷

2.5. Electrical Characterization of Test Devices. An appealing aspect of halide perovskites in powder form is that they allow separating their synthesis from the actual film formation process. This makes it possible to optimize the synthesis and the film formation independently of each other. For a proof of principle on the electro-optic suitability of these powders, we used various dry powders and pressed them into the shape of cylindrical pellets with 0.5 mm thickness, using a custom-built press setup (see the SI for details), and measured their photoresponse. Figure 6 shows the baseline-corrected photoresponse of six perovskite pellets with different stoichiometries when a bias voltage of 1 V and a low pressure of 2 MPa are applied. A clear photoresponse for all powders

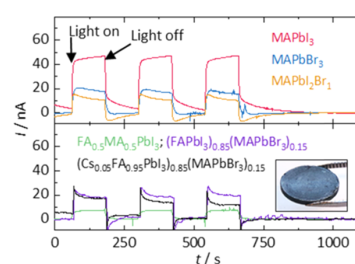


Figure 6. Dark current-corrected temporal photoresponse of different perovskite pellets pressed from their powders upon laser excitation with 405 nm. The top panel shows MAPbI₃, MAPbBr₃, and MAPb₂Br₁, the bottom panel shows multivalent mixed lead halide perovskites. The inset shows a pellet of MAPbBr₃ after the measurement.

can be observed, demonstrating their potential to function as active materials in perovskite-based optoelectronic devices that are processed in a solvent-free manner. A detailed discussion about the electrical characterization can be found in the SI (Figure S7).

However, when it comes to the fabrication of full optoelectronic devices based on perovskite powders, their facile employment in precursors for solution-based thin-film processing of the active layer represents the state-of-the-art.^{8,15} We probe the particular use of such a powder-based precursor for the most ubiquitous device architecture of a halide perovskite solar cell. To pursue this goal, we produced perovskite thin films on top of the $\text{SnO}_2/\text{F}/\text{compact TiO}_2/\text{mesoporous TiO}_2$ (FTO/c-TiO₂/mp-TiO₂) substrates from a 1 M solution of the $(\text{Cs}_{0.05}\text{FA}_{0.95}\text{PbI}_3)_{0.85}(\text{MAPbBr}_3)_{0.15}$ powder in dimethyl sulfoxide/dimethylformamide (DMSO/DMF, 4:1 ratio). The thin films were deposited by spin-coating, following an established protocol as described in our previous work.⁴² Therein, the thin c-TiO₂ layer acts as a hole blocking layer and the mp-TiO₂ layer as an electron transport layer and scaffold for the perovskite film formation. Our perovskite thin films derived in this way from the powder precursor solution showed good uniformity and homogeneity as evidenced by XRD and SEM (Figure S8a,b). The optical properties (PL and UV-Vis absorption) are comparable to the plain powder (Figure S8c,d).

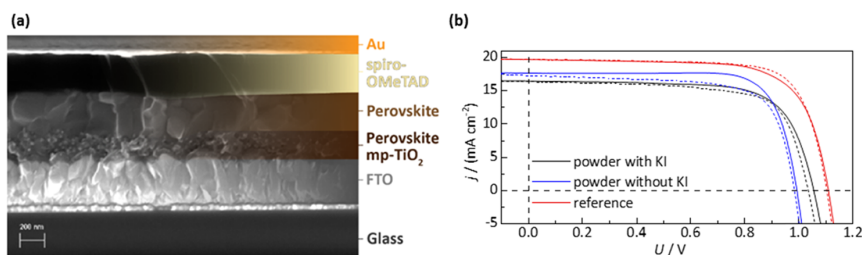


Figure 7. (a) Cross-sectional SEM image of the completed perovskite powder-based solar cell stack with the perovskite thin-film spin-coated of a 1 mol solution of $(\text{Cs}_{0.05}\text{FA}_{0.95}\text{PbI}_3)_{0.85}(\text{MAPbBr}_3)_{0.15}$ powder in DMSO/DMF on top of a mp-TiO₂/c-TiO₂/FTO substrate. (b) J - V characteristic of powder-based (with and without KI) and reference perovskite solar cell in forward (full line) and reverse scan direction (dashed line).

Table 1. Average PSC Device Characteristics for $(\text{Cs}_{0.05}\text{FA}_{0.95}\text{PbI}_3)_{0.85}(\text{MAPbBr}_3)_{0.15}$ Derived from J - V Curves (Figure 7b) with Values for the Champion Device in Brackets^a

sample (champion device)	J_{sc} (mA/cm ²)	V_{oc} (V)	FF (%)	PCE (%)
powder without KI/reverse	16.8 (17.62)	1.000 (0.994)	74 (77)	12.4 (13.5)
powder without KI/forward	16.7 (17.30)	0.970 (0.985)	57 (71)	9.4 (12.1)
powder with KI/reverse	16.5 (16.45)	1.038 (1.056)	70 (71)	12.1 (12.3)
powder with KI/forward	16.7 (16.35)	1.050 (1.036)	67 (71)	11.9 (12.0)
reference/reverse	19.5 (19.70)	1.095 (1.110)	70 (71)	14.8 (15.2)
reference/forward	19.4 (19.70)	1.090 (1.104)	73 (75)	15.4 (16.2)

^aDetailed statistical data are included in the Supporting Information (Figures S9 and S10).

We then deposited a hole transport layer comprised of doped 2,2',7,7'-tetrakis[*N,N*-di(4-methoxyphenyl)amino]-9,9'-spirobifluorene (spiro-OMeTAD) on top of the perovskite film and completed the layer stack by evaporating a gold electrode on top. SEM cross-sectional views of the full photovoltaic device (see Figure 7a) reveal conformal layer growth and a perovskite film thickness of about 350 nm, only marginally thinner than our standard device architecture for solar cells comprising a perovskite layer prepared from a solution of the individual salts (PbI₂, PbBr₂, FAI, MAI, and CsI).

In the following, we refer to the device produced from the perovskite powder-based solution as "powder" and the device produced from a solution of the individual salts in our standard process as the "reference". We note that the perovskite precursor solution for the reference device had been further optimized by a 10% excess of PbI₂, which led to higher efficiencies, less hysteresis, and longer solar cell lifetimes compared to the corresponding cell from a precursor solution without excess PbI₂, whereas the powder precursor solution has not been further optimized for this device application.

The J - V curves of the devices are depicted in Figure 7b and the characteristic solar cell performance parameters sampled over 6 devices for the powder cells and sampled over 3 devices for the reference cells are summarized in Table 1. The powder devices achieved an average power conversion efficiency of 12.4% (9.4% in forward scan direction), with a PCE of 13.5% (12.1% in forward scan direction) for the champion device (13% stabilized after 90 s at the maximum power point). This value is close to the average PCE of a side-by-side fabricated reference device, which amounts to 14.8% (15.4% in forward scan direction) on average and 16.2% for the champion device, respectively.

Notably, the higher PCE of the reference device can be reasoned by the prior optimization of the precursor formulation by excess PbI₂, also leading to a minimal hysteresis effect. While we succeeded in producing stabilized devices

from the perovskite powder solution, these powder devices tend to exhibit a slightly larger hysteresis compared to the reference devices. This manifests in a reduction of the fill factor in the forward scan direction. This effect, together with a lower open-circuit voltage (V_{oc}), in the powder devices, points to nonideal interfaces between the perovskite absorber layer and the charge transport layers that leads to increased interface recombination.^{43,44} The perovskite film morphology as characterized by SEM looks comparable between films derived from the perovskite powder precursor and the reference perovskite films (Figure S8b). XRD measurements reveal a higher concentration of PbI₂ in the reference films compared to the powder films (Figure S8a). We note that unreacted PbI₂ likely plays a critical role in the higher PCE of the reference devices compared to the powder devices, as PbI₂ has been reported to provide a passivation layer at the device interfaces.⁴⁴⁻⁴⁶ In addition, we verified that the onset of optical absorption is similar for the reference films and the powder films with and without KI (Figure S8c), while the PL of the thin films matches to the PL of the powders (Figure S8d).

Furthermore, the lower short-circuit current (J_{sc}) in the powder device compared to the reference device stems from a nonideal thickness of the absorber layer, which amounts to 350 nm for the powder device and 400 nm for the reference device (Figure S11). The measured J_{sc} has been compared to the integrated current density in external quantum efficiency measurements (Figure S9). Here, we observe a larger mismatch between the currents for the powder devices than for the reference device, which could again be attributed to the lack of excess PbI₂ in the powder films leading to an increase in ion migration and hence differences in the static and dynamic measurements.

We further investigated whether the passivation of the powder by adding KI to the powder precursors for the mechanochemical synthesis would translate to the corresponding devices. We compare devices produced from the KI

containing triple-cation perovskite powder, shown in Figure 7 and Table 1, to those from the powder without KI and find a systematic increase in V_{oc} by about 50 mV, indicating passivation of interface defect states. Most remarkably, we achieve a significant reduction of the hysteresis in the devices with KI compared to devices without KI using absorber films from the powder-based solution, which is particularly reflected in the fill factor and in a reduced sensitivity of the device parameters on the scan rate. Again, this behavior is indicative of an improved interface between perovskite and charge transport layers, leading to less recombination and better charge carrier extraction.⁴⁴

3. SUMMARY AND CONCLUSIONS

In summary, we investigated the mechanochemical synthesis of halide perovskite powders at ambient conditions, identifying the impact of milling time and the influence of the reactant properties on the perovskite powder. We find the mechanochemically synthesized powders to exhibit exceptional stability without any sign of degradation after more than two and a half years of storage, consistent with their intrinsic stability at room temperature, which we correlate to the absence of strain in the powder grains. Their exceptional thermal stability manifests in a nearly negligible amount of PbI_2 formed after heat treatment of $MAPbI_3$ powder at 220 °C for 14 h. In the future, it will be an interesting aspect to expand the investigations on the correlation between the lack of strain and improved stability of perovskite powders also to other synthesis approaches such as ultrasonic or precipitation methods. We further demonstrated that we can easily regenerate the perovskites powders in the case of a prior incomplete conversion or in the case of degradation by simple remilling. Similarly, hydrated powders, which form when synthesis is performed at high humidity, can be completely turned to phase-pure powder by soft heat treatment at 120 °C for 30 min. Following the mechanochemical approach, we successfully synthesized phase-pure multinary mixed perovskites including $(FAPbI_3)_{0.85}(MAPbBr_3)_{0.15}$ and $(Cs_{0.05}FA_{0.95}PbI_3)_{0.85}(MAPbBr_3)_{0.15}$, which represent the state-of-the-art compounds used in highly efficient PSCs. For these multinary compounds, we find their successful synthesis to be independent of whether the individual classic precursors (i.e., $MABr$, FAI , CsI , PbI_2 , and $PbBr_2$) or readily prepared perovskite powders of $MAPbBr_3$ and $FAPbI_3$ are used as starting materials. In the latter case, we find that even when using $FAPbI_3$ in its degraded nonperovskite δ -phase, a full synthesis of $(FAPbI_3)_{0.85}(MAPbBr_3)_{0.15}$ remains guaranteed, further proofing the high flexibility of the mechanochemical approach. We also find that these perovskite powders can successfully be passivated by the simple addition of KI in the ball milling process. To assess the functionality in optoelectronic applications, we prepared pellets from the dry powders and demonstrate that all powders show a photoresponse, i.e., a measurable photocurrent. Finally, we dissolved perovskite powder and achieved highly uniform thin films by spin-coating. Thin films from the triple-cation perovskite powder were employed to make solar cells in the conventional PSC device geometry, obtaining reliable device characteristics and decent efficiencies on the order of 13% power conversion efficiency (PCE). Even without further optimization, powders with KI additive led to improved device performance and significantly reduced hysteresis compared to powder without KI additive and reference devices from our baseline fabrication process.

Overall, our work demonstrates that the mechanochemical synthesis is well suited to produce a wide variety of highly stable lead halide perovskite powders that meet the demands for solar cell applications. Ball milling is well known to be suitable for the fabrication of larger quantities. The fact that this approach allows for separate optimization of synthesis and film formation together with the high storage stability and the option to regenerate phase purity by simple remilling is likely to pave the way for their utilization, especially in an industrially relevant context.

4. EXPERIMENTAL SECTION

4.1. Powder Preparation. For ball milling, the reactants (FAI , MAI , PbI_2 , and $PbBr_2$) were weighed to the desired stoichiometry (see the SI for exact amounts) and transferred into an 80 mL ZrO_2 milling jar containing ZrO_2 milling balls with a 10 mm diameter (ball to powder ratio 10:1). Then, 11 mL cyclohexane was added as a milling agent. The powders were milled in a Fritsch "Pulverisette 5/4" planetary ball mill at 400 rpm for 5 min, and then the milling was paused for 20 min to cool down the jar. The procedure was repeated until the desired milling time was reached.

4.2. Powder Characterization. **4.2.1. XRD.** The structural and phase characterization of the perovskite powders was carried out by reflection mode XRD using a Bruker "D8 Discover A25" with $Cu K_{\alpha 1}$ radiation ($\lambda = 0.15406$ nm), whereby the $K_{\alpha 2}$ -rays are removed by a $Ge-K_{\alpha 1}$ -monochromator. The device is operated at 40 kV and 40 mA. The diffractograms were recorded in the 2θ range from 10 to 45° with a 2θ step size of 0.016°.

4.2.2. SEM. The powder morphology was characterized by SEM using a Zeiss Leo 1530 instrument with an accelerating voltage of 3.0 kV. SEM micrographs of perovskite thin films spin-coated from the powder-based solution and the cross-sections of the completed devices were determined on a Zeiss Merlin VP compact microscope using an acceleration voltage of 15 kV.

4.2.3. Optical Characterization. To measure Photoluminescence spectra, we used a home-built setup. The sample was excited using a 337 nm nitrogen laser (LTB MNL 100). The emitted light was focused into a spectrograph (Andor Shamrock 303i) and detected by a charge-coupled device (CCD) camera (Andor iDus DU420a-OE). The recorded data were corrected by the transmission/reflection of optical components and the efficiency of the CCD camera. Reflectance measurements were carried out using a commercial UV/VIS-spectrometer (Varian Cary 5000) with an attached integrating sphere for reflectance measurements (External DRA 2500).

4.3. Device Fabrication. Fluorine-doped tin oxide (FTO)-covered glass substrates (Solems) were cleaned by etching with Zn powder and HCl (4M). The substrates were sonicated for 1 h in an RBS detergent solution (2 vol %), rinsed with deionized water and ethanol, ultrasonicated in ethanol, and dried and annealed to 500 °C. Subsequently, a TiO_2 hole blocking layer was prepared by spray pyrolysis deposition at 450 °C from a precursor solution made of 0.6 mL of titanium diisopropoxide bis(acetylacetonate) (75% in 2-propanol, Sigma Aldrich), 0.4 mL of acetylacetone (Sigma Aldrich) in 9 mL of ethanol as a solvent and O_2 as carrier gas. The mesoporous TiO_2 (mp- TiO_2) layer was prepared by spin-coating a solution of TiO_2 paste (30NR-D from Dyesol) in ethanol (1:7 weight ratio) at 4000 rpm for 30 s. The films were then sintered in a sequential heating process (5 min at 125 °C, 5 min at 325 °C, 5 min at 375 °C, 15 min at 450 °C, and 30 min at 500 °C). The samples were finally transferred into a nitrogen-filled glovebox for the perovskite film processing. Either the reference or powder precursor solution was spin-coated onto the mesoporous TiO_2 layers and, a few seconds later, washed by dripping 0.5 mL of anhydrous diethyl ether to induce the intermediate adduct formation of the films, as reported previously.⁴⁷ For the subsequent hole transport layer deposition, 110 mg of spiro-OMeTAD (2,2',7,7'-tetrakis[N,N-di(4-methoxyphenyl)amino]-9,9'-spirobifluorene) (spiro-OMeTAD) from Merck was dissolved in 1

mL of chlorobenzene along with tris(2-(1H-pyrazol-1-yl)-4-*tert*-butylpyridine) cobalt(III) bis(trifluoromethylsulfonyl)imide (FK209, Dyesol), lithium bis(trifluoromethylsulfonyl)imide (LiTFSI, Sigma Aldrich), and 4-*tert*-butylpyridine (*t*-BP, Sigma Aldrich 96% of purity) as additives in relative molar concentrations of 5%, 50%, and 330%, respectively, with respect to spiro-OMeTAD. Then, 35 μ L of this solution was deposited by spin-coating (3000 rpm for 20 s) on top of the perovskite absorber layer. Finally, 100 nm of gold was thermally evaporated under vacuum as the solar cell top contact.

4.4. Perovskite Film Preparation. In the case of reference devices, the perovskite films were prepared from a $(\text{MA}_{0.17}\text{FA}_{0.83})\text{Pb}(\text{Br}_{0.17}\text{I}_{0.83})_3$ solution made of 1.10 M PbI_2 (TCI Chemicals), 0.20 M PbBr_2 (Alfa Aesar), 1.00 M formamidinium iodide (FAI, Dyesol), and 0.20 M methylammonium bromide (MABr, Dyesol) in a solvent mixture of DMSO/DMF (4:1 in v/v). The stoichiometry of the optimized films was further altered by adding 10% of PbI_2 and 5% CsI to the solution. After vigorous stirring, the precursor solution was deposited by spin-coating (first at 2000 rpm to deposit the precursor solution in the dynamic mode and then at 6000 rpm while 100 μ L of chlorobenzene is applied as the antisolvent). Then, the samples were annealed at 100 $^\circ\text{C}$ for 30 min. In the case of the layer obtained from the powder, a 1 M precursor solution was prepared by dissolving the correct amount of perovskite powder in the solvent mixture of DMSO/DMF (4:1 in v/v). After stirring, the solution is centrifuged and then filtered to extract particles that can eventually remain due to incomplete dissolution. The deposition process is the same as previously described for the reference cell.

4.4.1. X-ray Diffractometry. The structural properties of thin-film absorbers were characterized by X-ray diffraction measurements in the classical Bragg–Brentano θ – 2θ configuration (programmable slit to fix the irradiated area, 0.04° soller slits). The PANalytical Empyrean X-ray diffractometer was operated at 40 kV (40 mA), with Cu K_α (0.15406 nm) radiation, including a Cu–Ni filter to suppress the K_β line.

4.4.2. *J*–*V* Characterization. The photovoltaic properties of the solar cells were measured under a light source with an AM1.5G spectrum and a calibrated intensity of 1 Sun (100 mW/cm^2). A Bio-Logic potentiostat is used to record *J*–*V* curves applying a precise scan rate. The voltage sweeping rate was fixed to 20 mV/s in reverse and forward *J*–*V* scan directions. For steady-state output performance, PCE was plotted as a function of time at maximum power point voltage (V_{MPP}) conditions under continuous illumination using the same light source employed for *J*–*V* measurements. The perovskite-based cells present an active area of 0.16 cm^2 , but the illuminated surface is limited to 0.09 cm^2 with a black metal laser-cut mask during the performance measurements.

■ ASSOCIATED CONTENT

📄 Supporting Information

The Supporting Information is available free of charge on the ACS Publications website at DOI: 10.1021/acsami.9b09160.

Experimental details, figures of stability, photoluminescence measurements, additional device data, discussion on photoresponse behavior (PDF)

■ AUTHOR INFORMATION

Corresponding Author

*E-mail: fabian.panzer@uni-bayreuth.de.

ORCID

Stefania Cacovich: 0000-0002-6402-4816

Anna Köhler: 0000-0001-5029-4420

Philip Schulz: 0000-0002-8177-0108

Fabian Panzer: 0000-0002-2191-9011

Notes

The authors declare no competing financial interest.

■ ACKNOWLEDGMENTS

The authors acknowledge financial support by the German National Science Foundation DFG via the GRK 1640 and via MO 1060/32-1 and by the Bavarian State Ministry of Science, Research, and the Arts for the Collaborative Research Network “Solar Technologies go Hybrid”. We further thank the Department of Metal and Alloys and Dr. Johannes Thiessen from the Department of Chemical Engineering for XRD measurements, and Angelika Mergner and the Keylab Electron and Optical Microscopy of the Bavarian Polymer Institute (BPI) for SEM images. This project has been supported by the French Government in the frame of the program of investment for the future (Program d’Investissement d’Avenir - ANR-IEED-002-01). P.S. acknowledges the French Agence Nationale de la Recherche for funding under contract no. ANR-17-MPGA-0012.

■ REFERENCES

- (1) NREL. *Research Cell Record Efficiency Chart*. <https://www.nrel.gov/pv/cell-efficiency.html> (accessed August 7, 2019).
- (2) Christians, J. A.; Schulz, P.; Tinkham, J. S.; Schloemer, T. H.; Harvey, S. P.; Tremolet de Villers, B. J.; Sellinger, A.; Berry, J. J.; Luther, J. M. Tailored Interfaces of Unencapsulated Perovskite Solar Cells for >1000 h Operational Stability. *Nat. Energy* **2018**, *3*, 68–74.
- (3) Grancini, G.; Roldán-Carmona, C.; Zimmermann, I.; Mosconi, E.; Lee, X.; Martineau, D.; Narbey, S.; Oswald, F.; Angelis, F. de.; Graetzel, M.; Nazeeruddin, M. K. One-Year Stable Perovskite Solar Cells by 2D/3D Interface Engineering. *Nat. Commun.* **2017**, *8*, No. 15684.
- (4) Tsai, H.; Nie, W.; Blancon, J.-C.; Stoumpos, C. C.; Asadpour, R.; Harutyunyan, B.; Neukirch, A. J.; Verduzco, R.; Crochet, J. J.; Tretiak, S.; Pedesseau, L.; Even, J.; Alam, M. A.; Gupta, G.; Lou, J.; Ajayan, P. M.; Bedzyk, M. J.; Kanatzidis, M. G. High-Efficiency Two-Dimensional Ruddlesden-Popper Perovskite Solar Cells. *Nature* **2016**, *536*, 312–316.
- (5) Saliba, M.; Correa-Baena, J.-P.; Wolff, C. M.; Stollerfoht, M.; Phung, N.; Albrecht, S.; Neher, D.; Abate, A. How to Make over 20% Efficient Perovskite Solar Cells in Regular (n–i–p) and Inverted (p–i–n) Architectures. *Chem. Mater.* **2018**, *30*, 4193–4201.
- (6) Holliman, P. J.; Jones, E. W.; Connell, A.; Ghosh, S.; Furnell, L.; Hobbs, R. J. Solvent Issues During Processing and Device Lifetime for Perovskite Solar Cells. *Mater. Res. Innovations* **2015**, *19*, 508–511.
- (7) Jodowski, A. D.; Yépez, A.; Luque, R.; Camacho, L.; de Miguel, G. Benign-by-Design Solventless Mechanochemical Synthesis of Three-, Two-, and One-Dimensional Hybrid Perovskites. *Angew. Chem., Int. Ed.* **2016**, *55*, 14972–14977.
- (8) Prochowicz, D.; Franckevičius, M.; Cieślak, A. M.; Zakeeruddin, S. M.; Grätzel, M.; Lewiński, J. Mechanochemical Synthesis of the Hybrid Perovskite $\text{CH}_3\text{NH}_3\text{PbI}_3$: Characterization and the Corresponding Solar Cell Efficiency. *J. Mater. Chem. A* **2015**, *3*, 20772–20777.
- (9) Elseman, A. M.; Shalan, A. E.; Rashad, M. M.; Hassan, A. M. Experimental and Simulation Study for Impact of Different Halides on the Performance of Planar Perovskite Solar Cells. *Mater. Sci. Semicond. Process.* **2017**, *66*, 176–185.
- (10) Karmakar, A.; Askar, A. M.; Bernard, G. M.; Terskikh, V. V.; Ha, M.; Patel, S.; Shankar, K.; Michaelis, V. K. Mechanochemical Synthesis of Methylammonium Lead Mixed-Halide Perovskites: Unraveling the Solid-Solution Behavior Using Solid-State NMR. *Chem. Mater.* **2018**, *30*, 2309–2321.
- (11) Prochowicz, D.; Yadav, P.; Saliba, M.; Sasaki, M.; Zakeeruddin, S. M.; Lewiński, J.; Grätzel, M. Mechanochemical Synthesis of Pure Phase Mixed-Cation $\text{MA}_x\text{FA}_{1-x}\text{PbI}_3$ Hybrid Perovskites: Photovoltaic Performance and Electrochemical Properties. *Sustainable Energy Fuels* **2017**, *1*, 689–693.
- (12) Sadhukhan, P.; Kundu, S.; Roy, A.; Ray, A.; Maji, P.; Dutta, H.; Pradhan, S. K.; Das, S. Solvent-Free Solid-State Synthesis of High

- Yield Mixed Halide Perovskites for Easily Tunable Composition and Band Gap. *Cryst. Growth Des.* **2018**, *18*, 3428–3432.
- (13) Hong, Z.; Tan, D.; John, R. A.; Tay, Y. K. E.; Ho, Y. K. T.; Zhao, X.; Sum, T. C.; Mathews, N.; Garcia, F.; Soo, H. S. Completely Solvent-free Protocols to Access Phase-Pure, Metastable Metal Halide Perovskites and Functional Photodetectors from the Precursor Salts. *iScience* **2019**, *16*, 312–325.
- (14) Sasaki, M.; Prochowicz, D.; Marynowski, W.; Lewiński, J. Mechanochemical Synthesis, Optical, and Morphological Properties of MA, FA, Cs-SnX₃ (X = I, Br) and Phase-Pure Mixed-Halide MASn_xBr_{3-x} Perovskites. *Eur. J. Inorg. Chem.* **2019**, *2019*, 2680–2684.
- (15) Dou, B.; Wheeler, L. M.; Christians, J. A.; Moore, D. T.; Harvey, S. P.; Berry, J. J.; Barnes, F. S.; Shaheen, S. E.; van Hest, M. F. A. M. Degradation of Highly Alloyed Metal Halide Perovskite Precursor Inks: Mechanism and Storage Solutions. *ACS Energy Lett.* **2018**, *3*, 979–985.
- (16) Prochowicz, D.; Yadav, P.; Saliba, M.; Kubicki, D. J.; Tavakoli, M. M.; Zakeeruddin, S. M.; Lewiński, J.; Emsley, L.; Grätzel, M. One-step Mechanochemical Incorporation of an Insoluble Cesium Additive for High Performance Planar Heterojunction Solar Cells. *Nano Energy* **2018**, *49*, 523–528.
- (17) Prochowicz, D.; Yadav, P.; Saliba, M.; Sasaki, M.; Zakeeruddin, S. M.; Lewiński, J.; Grätzel, M. Reduction in the Interfacial Trap Density of Mechanochemically Synthesized MAPbI₃. *ACS Appl. Mater. Interfaces* **2017**, *9*, 28418–28425.
- (18) Shrestha, S.; Fischer, R.; Matt, G. J.; Feldner, P.; Michel, T.; Osvet, A.; Levchuk, I.; Merle, B.; Golkar, S.; Chen, H.; Tedde, S. F.; Schmidt, O.; Hock, R.; Rühlig, M.; Göken, M.; Heiss, W.; Anton, G.; Brabec, C. J. High-Performance Direct Conversion X-ray Detectors Based on Sintered Hybrid Lead Triiodide Perovskite Wafers. *Nat. Photonics* **2017**, *11*, 436–440.
- (19) Manukyan, K. V.; Yeghishyan, A. V.; Moskovskikh, D. O.; Kapaldo, J.; Mintairov, A.; Mukasyan, A. S. Mechanochemical Synthesis of Methylammonium Lead Iodide Perovskite. *J. Mater. Sci.* **2016**, *51*, 9123–9130.
- (20) Jana, A.; Mittal, M.; Singla, A.; Sapra, S. Solvent-free, Mechanochemical Syntheses of Bulk Trihalide Perovskites and their Nanoparticles. *Chem. Commun.* **2017**, *53*, 3046–3049.
- (21) Walter, D. Primary Particles-Agglomerates-Aggregates. In *Nanomaterials*; Commission for the Investigation of Health Hazards of Chemical Compounds in the Work Area; Wiley-VCH: Weinheim, Germany, 2013; pp 9–24.
- (22) Gujar, T. P.; Thelakkat, M. Highly Reproducible and Efficient Perovskite Solar Cells with Extraordinary Stability from Robust CH₃NH₃PbI₃: Towards Large-Area Devices. *Energy Technol.* **2016**, *4*, 449–457.
- (23) Yen, H.-J.; Liang, P.-W.; Chueh, C.-C.; Yang, Z.; Jen, A. K.-Y.; Wang, H.-L. Large Grained Perovskite Solar Cells Derived from Single-Crystal Perovskite Powders with Enhanced Ambient Stability. *ACS Appl. Mater. Interfaces* **2016**, *8*, 14513–14520.
- (24) Zhang, J.; Zhao, Y.; Yang, D.; Li, C.; Liu, S. Highly Stabilized Perovskite Solar Cell Prepared Using Vacuum Deposition. *RSC Adv.* **2016**, *6*, 93525–93531.
- (25) Wang, B.; Chen, T. Exceptionally Stable CH₃NH₃PbI₃ Films in Moderate Humid Environmental Condition. *Adv. Sci.* **2016**, *3*, No. 1500262.
- (26) Gujar, T. P.; Unger, T.; Schönleber, A.; Fried, M.; Panzer, F.; van Smaalen, S.; Köhler, A.; Thelakkat, M. The Role of PbI₂ in CH₃NH₃PbI₃ Perovskite Stability, Solar Cell Parameters and Device Degradation. *Phys. Chem. Chem. Phys.* **2017**, *20*, 605–614.
- (27) Zhao, J.; Deng, Y.; Wei, H.; Zheng, X.; Yu, Z.; Shao, Y.; Shield, J. E.; Huang, J. Strained Hybrid Perovskite Thin Films and their Impact on the Intrinsic Stability of Perovskite Solar Cells. *Sci. Adv.* **2017**, *3*, No. eaao5616.
- (28) Jones, T. W.; Osherov, A.; Alsari, M.; Sponseller, M.; Duck, B. C.; Jung, Y.-K.; Settens, C.; Niroui, F.; Brenes, R.; Stan, C. V.; Li, Y.; Abdi-Jalebi, M.; Tamura, N.; Macdonald, J. E.; Burghammer, M.; Friend, R. H.; Bulović, V.; Walsh, A.; Wilson, G. J.; Lilliu, S.; Stranks, S. D. Lattice Strain Causes Non-radiative Losses in Halide Perovskites. *Energy Environ. Sci.* **2019**, *12*, 596–606.
- (29) Guo, X.; McCleese, C.; Lin, W.-C.; Burda, C. Curing of Degraded MAPbI₃ Perovskite Films. *RSC Adv.* **2016**, *6*, 60620–60625.
- (30) Saliba, M.; Matsui, T.; Seo, J.-Y.; Domanski, K.; Correa-Baena, J.-P.; Nazeeruddin, M. K.; Zakeeruddin, S. M.; Tress, W.; Abate, A.; Hagfeldt, A.; Grätzel, M. Cesium-Containing Triple Cation Perovskite Solar Cells: Improved Stability, Reproducibility and High Efficiency. *Energy Environ. Sci.* **2016**, *9*, 1989–1997.
- (31) Ono, L. K.; Juarez-Perez, E. J.; Qi, Y. Progress on Perovskite Materials and Solar Cells with Mixed Cations and Halide Anions. *ACS Appl. Mater. Interfaces* **2017**, *9*, 30197–30246.
- (32) Myung, N.; Bae, Y.; Bard, A. J. Enhancement of the Photoluminescence of CdSe Nanocrystals Dispersed in CHCl₃ by Oxygen Passivation of Surface States. *Nano Lett.* **2003**, *3*, 747–749.
- (33) van Vugt, L. K.; Veen, S. J.; Bakkers, E. P. A. M.; Roest, A. L.; Vanmaekelbergh, D. Increase of the Photoluminescence Intensity of InP Nanowires by Photoassisted Surface Passivation. *J. Am. Chem. Soc.* **2005**, *127*, 12357–12362.
- (34) Brenes, R.; Guo, D.; Osherov, A.; Noel, N. K.; Eames, C.; Hutter, E. M.; Pathak, S. K.; Niroui, F.; Friend, R. H.; Islam, M. S.; Snaith, H. J.; Bulović, V.; Savenije, T. J.; Stranks, S. D. Metal Halide Perovskite Polycrystalline Films Exhibiting Properties of Single Crystals. *Joule* **2017**, *1*, 155–167.
- (35) Zheng, X.; Chen, B.; Dai, J.; Fang, Y.; Bai, Y.; Lin, Y.; Wei, H.; Zeng, X. C.; Huang, J. Defect Passivation in Hybrid Perovskite Solar Cells Using Quaternary Ammonium Halide Anions and Cations. *Nat. Energy* **2017**, *2*, No. 17102.
- (36) Niu, T.; Lu, J.; Munir, R.; Li, J.; Barrit, D.; Zhang, X.; Hu, H.; Yang, Z.; Amassian, A.; Zhao, K.; Liu, S. F. Stable High-Performance Perovskite Solar Cells via Grain Boundary Passivation. *Adv. Mater.* **2018**, *30*, No. e1706576.
- (37) Abdi-Jalebi, M.; Andaji-Garmaroudi, Z.; Cacovich, S.; Stavrakas, C.; Philippe, B.; Richter, J. M.; Alsari, M.; Booker, E. P.; Hutter, E. M.; Pearson, A. J.; Lilliu, S.; Savenije, T. J.; Rensmo, H.; Divitini, G.; Ducati, C.; Friend, R. H.; Stranks, S. D. Maximizing and Stabilizing Luminescence from Halide Perovskites with Potassium Passivation. *Nature* **2018**, *555*, 497–501.
- (38) Dänekamp, B.; Droseros, N.; Palazon, F.; Sessolo, M.; Banerji, N.; Bolink, H. J. Efficient Photo- and Electroluminescence by Trap States Passivation in Vacuum-Deposited Hybrid Perovskite Thin Films. *ACS Appl. Mater. Interfaces* **2018**, *10*, 36187–36193.
- (39) Ahmed, G. H.; El-Demellawi, J. K.; Yin, J.; Pan, J.; Velusamy, D. B.; Hedhili, M. N.; Alarousu, E.; Bakr, O. M.; Alshareef, H. N.; Mohammed, O. F. Giant Photoluminescence Enhancement in CsPbCl₃ Perovskite Nanocrystals by Simultaneous Dual-Surface Passivation. *ACS Energy Lett.* **2018**, *3*, 2301–2307.
- (40) Lee, S.; Park, J. H.; Lee, B. R.; Jung, E. D.; Yu, J. C.; Di Nuzzo, D.; Friend, R. H.; Song, M. H. Amine-Based Passivating Materials for Enhanced Optical Properties and Performance of Organic-Inorganic Perovskites in Light-Emitting Diodes. *J. Phys. Chem. Lett.* **2017**, *8*, 1784–1792.
- (41) Kubicki, D. J.; Prochowicz, D.; Hofstetter, A.; Zakeeruddin, S. M.; Grätzel, M.; Emsley, L. Phase Segregation in Potassium-Doped Lead Halide Perovskites from ³⁹K Solid-State NMR at 21.1 T. *J. Am. Chem. Soc.* **2018**, *140*, 7232–7238.
- (42) Bercegol, A.; Ramos, F. J.; Rebai, A.; Guillemot, T.; Ory, D.; Rousset, J.; Lombez, L. Slow Diffusion and Long Lifetime in Metal Halide Perovskites for Photovoltaics. *J. Phys. Chem. C* **2018**, *122*, 24570–24577.
- (43) Fakharuddin, A.; Schmidt-Mende, L.; Garcia-Belmonte, G.; Jose, R.; Mora-Sero, I. Interfaces in Perovskite Solar Cells. *Adv. Energy Mater.* **2017**, *7*, No. 1700623.
- (44) Schulz, P.; Cahen, D.; Kahn, A. Halide Perovskites: Is It All about the Interfaces? *Chem. Rev.* **2019**, *119*, 3349–3417.
- (45) Liu, F.; Dong, Q.; Wong, M. K.; Djurišić, A. B.; Ng, A.; Ren, Z.; Shen, Q.; Surya, C.; Chan, W. K.; Wang, J.; Ng, A. M. C.; Liao, C.; Li, H.; Shih, K.; Wei, C.; Su, H.; Dai, J. Is Excess PbI₂ Beneficial for

Perovskite Solar Cell Performance? *Adv. Energy Mater.* **2016**, *6*, No. 1502206.

(46) Jacobsson, T. J.; Correa-Baena, J.-P.; Halvani Anaraki, E.; Philippe, B.; Stranks, S. D.; Bouduban, M. E. F.; Tress, W.; Schenk, K.; Teuscher, J.; Moser, J.-E.; Rensmo, H.; Hagfeldt, A. Unreacted PbI_2 as a Double-Edged Sword for Enhancing the Performance of Perovskite Solar Cells. *J. Am. Chem. Soc.* **2016**, *138*, 10331–10343.

(47) Ahn, N.; Son, D.-Y.; Jang, I.-H.; Kang, S. M.; Choi, M.; Park, N.-G. Highly Reproducible Perovskite Solar Cells with Average Efficiency of 18.3% and Best Efficiency of 19.7% Fabricated via Lewis Base Adduct of Lead(II) Iodide. *J. Am. Chem. Soc.* **2015**, *137*, 8696–8699.

Supporting Information for:

High Versatility and Stability of Mechanochemically Synthesized Halide Perovskite Powders for Optoelectronic Devices

*Nico Leupold,[†] Konstantin Schötz,[‡] Stefania Cacovich,[‡] Irene Bauer,[‡] Maximilian Schultz,[‡]
Monika Daubinger,[†] Leah Kaiser,[†] Amelle Rebai,[‡] Jean Rousset,^{‡,#} Anna Köhler,^{‡,§} Philip
Schulz,^{‡,◇} Ralf Moos,[†] Fabian Panzer^{‡,†,*}*

[†]Department of Functional Materials and Zentrum für Energietechnik (ZET), University of Bayreuth, 95440 Bayreuth, Germany

[‡]Soft Matter Optoelectronics, University of Bayreuth, 95440 Bayreuth, Germany

[§]Bayreuth Institute of Macromolecular Research (BIMF) and Bavarian Polymer Institute (BPI), University of Bayreuth, 95440 Bayreuth, Germany.

[‡]IPVF, Institut Photovoltaïque d'Ile de France (IPVF), 30 route départementale 128, 91120, Palaiseau, France

[#]EDF R&D, 30 route départementale 128, 91120, Palaiseau, France

[◇]CNRS, Institut Photovoltaïque d'Ile de France (IPVF), UMR 9006, 30 route départementale 128, 91120, Palaiseau, France

*Corresponding author: fabian.panzer@uni-bayreuth.de

1. Stability of mechanochemically synthesized powders

1.1. Temporal stability of FAPbI₃

Figure S1a shows photographs of FAPbI₃ powder at different times after their mechanochemical synthesis. The dark yellow / brownish color indicates a coexistence of a certain fraction of powder which is in its black α -phase and a fraction which is in its yellow δ -phase directly after the synthesis.^{1,2} After two weeks of storage the appearance of the powder remains and only after 17 days it becomes more yellow. The degraded yellow powders could be transformed to their α -phase by simple heat treatment at 120°C for 5 hours, indicated by their purely black appearance, which remained unchanged after a week of storage in a dry atmosphere (Figure S1b). In literature the degradation is reported to typically happen on timescales of minutes to hours in the case of thin films and single crystals,^{3,4} which is significantly shorter compared to the observed timescales in our case.

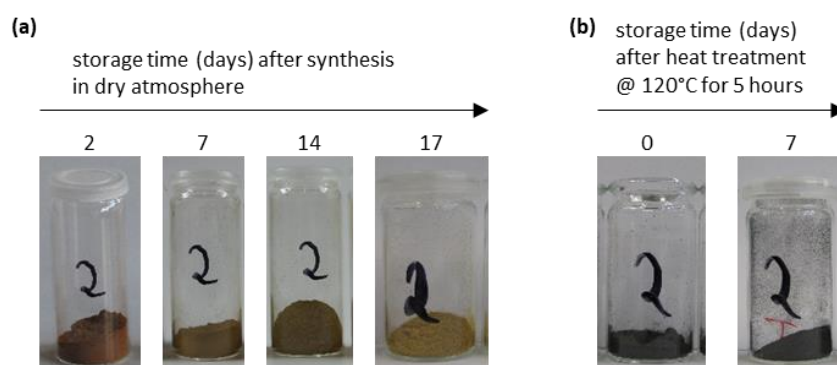


Figure S1. (a) Photographs of FAPbI₃ powder at different times as indicated after the mechanochemical syntheses. (b) FAPbI₃ powder directly after heat treatment at 120°C for 5 hours (left) and after 1 week (right) where no change in color is visible.

1.2. Thermal stability of MAPbI₃

To also explore the thermal stability of the synthesized powders, MAPbI₃ powder was heat treated in an oven for two days at 120 °C. As we could not see any trace of yellow PbI₂ by eye after this treatment, we repeated this for two and a half days at 80 °C. We chose a lower temperature to increase the probability of water adsorption. Before this heat treatment, the powder was stored in a glovebox for seven months. Figure S2 shows the XRD of the powder before (after storage, top) and after (bottom) the heat treatment. As there is no sign of PbI₂ in the XRD spectra, we conclude that the synthesized MAPbI₃ powder is at least on this time scale stable under these conditions.

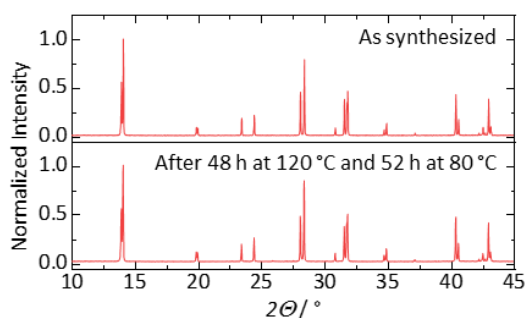


Figure S2. XRD patterns of MAPbI₃ powder before (top) and after (bottom) different heat treatment at 120 °C for 48 hours and 80°C for 52 hours.

2. Williamson Hall analysis on MAPbI₃ powders

From the MAPbI₃ powder XRD-patterns with milling times of 30, 60 and 90 min the full width at half maximum (FWHM) from each reflex is extracted. Together with the corresponding reflex position they are used to generate a Williamson Hall plot,⁵ which is shown in Figure S3. Here it is assumed that reflex broadening is caused by a combination of crystallite size, micro-strain and instrumental resolution of the machine. The broadening caused by small crystallites can be described by the Scherrer equation:

$$B_{\text{size}}(2\theta) = \frac{K \lambda}{L \cos(\theta)} \quad (1)$$

Here $B_{\text{size}}(2\theta)$ is the contribution of the crystallite size to the FWHM of the reflex at position 2θ , K is the Scherrer constant, which is often assumed as 0.94 for spherical crystallites, λ is the wavelength of the x-rays and L is the crystallite size.

The contribution of micro-strain ε is described by

$$B_{\text{strain}}(2\theta) = 4 \varepsilon \tan(\theta) \quad (2)$$

This results in a total reflex broadening of

$$B_{\text{total}} = B_{\text{size}} + B_{\text{strain}} = \frac{K \lambda}{L \cos(\theta)} + 4 \varepsilon \tan(\theta) \quad (3)$$

By multiplying the equation (3) by $\cos(\theta)$ the equation for the Williamson-Hall-plot is obtained:

$$B_{\text{total}} \cos(\theta) = 4 \varepsilon \sin(\theta) + \frac{K \lambda}{L} \quad (4)$$

Therefore, plotting $B \cdot \cos(\theta)$ versus $\sin(\theta)$ leads to a straight line and the crystallite size can be calculated from the intercept with the $B \cdot \cos(\theta)$ -axis and the strain with the aid of the slope. For the three powders shown in Figure S3 a crystallite size of around 150 nm and microstrain $< 0.01 \%$ is obtained. These values are influenced by the instrumental resolution, so we assume the calculated crystallite sizes to be afflicted with a relatively large error. Nonetheless, the calculated strain values indicate the maximum of strain.

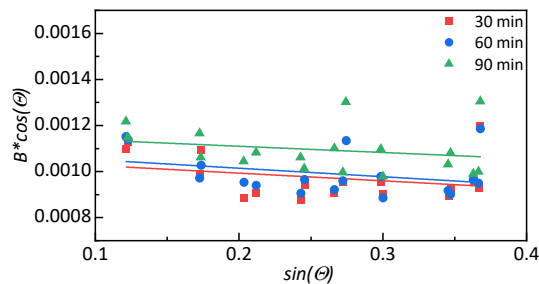


Figure S3. Williamson Hall plot of MAPbI₃-powders with milling times of 30, 60 und 90 min.

3. Synthesis of mixed halide or mixed cation perovskite powders

Besides the standard compositions, as preliminary work for the synthesis of mixed halide or mixed cation perovskites, as described in the main text, we also synthesized mixed halide or mixed cation perovskites. Figure S4 shows the XRD as well as the reflectance and PL spectra of $\text{MAPbI}_2\text{Br}_1$ as mixed halide and $\text{FA}_{0.5}\text{MA}_{0.5}\text{PbI}_3$ as mixed cation perovskites.

Note that the XRD for $\text{FA}_{0.5}\text{MA}_{0.5}\text{PbI}_3$ was taken 4 months after the syntheses, where still no signal from educt phases could be observed, which, similar to the case of MAPbI_3 (Figure 3 in the main text) also demonstrates its good time stability.

An overview of synthesized powders together with their band gap E_g and their PL peak position PL_{max} is given in Table S1. These values agree overall well with those reported in literature. For the estimation of the band gap, we calculated the Kubelka-Munk function $F(R) = (1-R)^2/2R$ from reflectance data and used a Tauc-Plot to extract the band gap energies. Although neglecting excitonic contributions to the absorption / reflectance, this approach has commonly been applied to hybrid perovskites.⁶⁻⁹

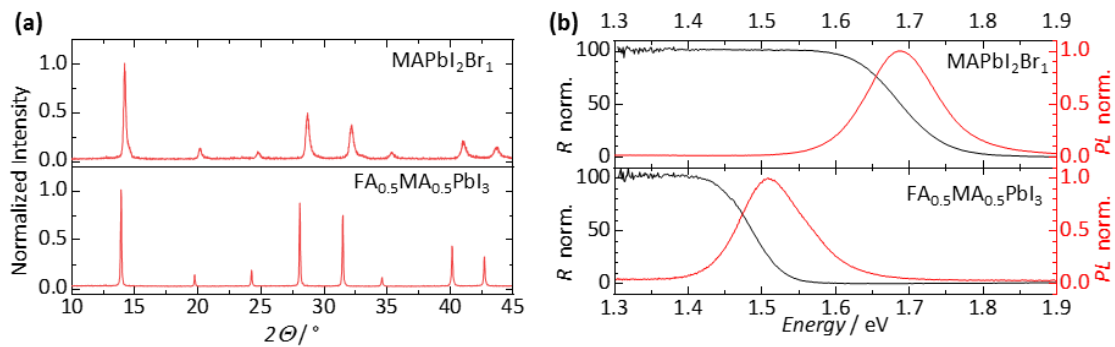


Figure S4. (a) Normalized XRD pattern of the mixed halide perovskite $\text{MAPbI}_2\text{Br}_1$ (top panel) and the mixed cation perovskite $\text{FA}_{0.5}\text{MA}_{0.5}\text{PbI}_3$ (bottom). (b) Reflectance (black) and photoluminescence (red) spectra of $\text{MAPbI}_2\text{Br}_1$ (top) and $\text{FA}_{0.5}\text{MA}_{0.5}\text{PbI}_3$ (bottom).

Table S1. Comparison of PL peak positions and band gaps of powders synthesized within this work and values found in literature (mainly for thin films). The corresponding references are given in superscripts.

Composition	PL _{max,exp} / eV	PL _{max, lit} / eV	E _{g, exp} / eV	E _{g, lit} / eV
MAPbBr ₃	2.24	2.3 ¹⁰	2.24	2.30 ¹¹
MAPbI ₃	1.56	1.604 ¹²	1.55	1.56 - 1.6 ¹¹⁻¹³
MAPbI ₂ Br ₁	1.69	1.75-1.79 ¹⁰	1.70	1.72 ¹¹
FA _{0.5} MA _{0.5} PbI ₃	1.51	-	1.49	1.55-1.57 ^{12,14}
(FAPbI ₃) _{0.85} (MAPbBr ₃) _{0.15}	1.57	1.580 ¹³	1.56	1.56 - 1.60 ¹⁵
(CsFAPbI ₃) _{0.85} (MAPbBr ₃) _{0.15}	1.57	1.62 ¹⁵	1.56	1.59 ¹⁵
K(FAPbI ₃) _{0.85} (MAPbBr ₃) _{0.15}	1.56	-	1.56	-
K(CsFAPbI ₃) _{0.85} (MAPbBr ₃) _{0.15}	1.55	1.55 ¹⁵	1.55	1.56 ¹⁵

4. Time stability and complete synthesis of triple cation mixtures

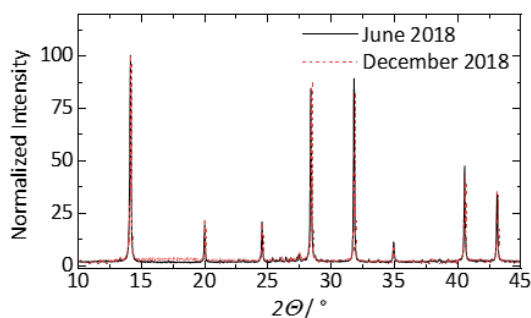


Figure S5. Normalized XRD pattern of triple cation perovskite powder directly after the synthesis (June 2018) and after 6 months of storage in dry atmosphere.

5. Additional EDX Maps

EDX mapping on a pressed pellet sample was performed. Figure S6 shows a homogenous distribution for Cs, I, C, N, and Pb. Solely in the mappings of Br and K some brighter spots can be found as discussed in the main text.

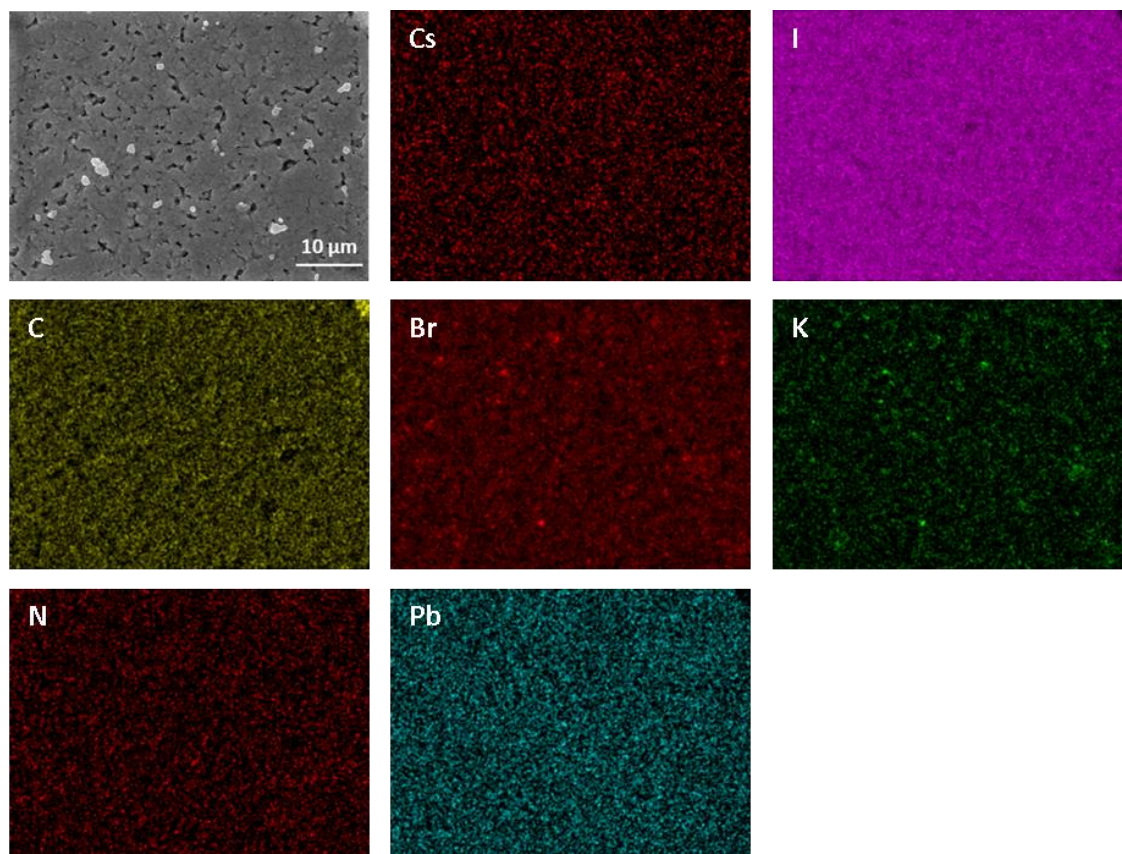


Figure S6. SEM-image and Cs, I, C, Br, K, N and Pb mapping obtained via EDX of $(\text{Cs}_{0.05}\text{FA}_{0.95}\text{PbI}_3)_{0.85}(\text{MAPbBr}_3)_{0.15}$ passivated with 10 mol% KI.

6. Photoresponse of the Pellets

Figure S7 shows the time evolution of current obtained from the electrical measurements for two exemplary samples. While maintaining a constant voltage of 1 V the resulting current changes with time, i.e. after a strong initial decrease within the first 300 s the current slowly increases again. The measurement is conducted in the dark and after about 3600 s a laser diode (Thorlabs) is repeatedly switched on and off for 2 min each to record the photoresponse. For evaluation of the photoresponse, the baseline is fitted by a polynomial function and subtracted.

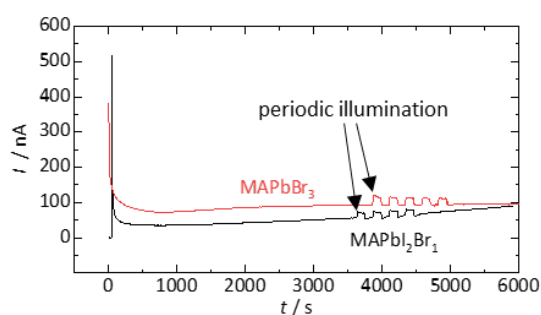


Figure S7. Time dependent behavior of the electrical current as measured shown exemplarily for two hybrid perovskite powders (MAPbBr₃ and MAPbI₂Br₁).

The approach that we follow in the main text to directly press the dry powders and characterize their electrical response, differs from the common strategy to dissolve the powders and re-crystallize them in the course of a conventional solution processing to characterize their electrical properties.^{16–22}

In Figure 6 in the main text, we find the electrical dark conductivity of the MAPbI₃-powder to be in the range of $1 \cdot 10^{-8} \text{ S cm}^{-1}$, in agreement with literature,^{23,24} while the measured values for MAPbBr₃ ($4 \cdot 10^{-9} \text{ S cm}^{-1}$) and FA_{0.5}MA_{0.5}PbI₃ ($3 \cdot 10^{-9} \text{ S cm}^{-1}$) are one or two orders of magnitude lower compared to corresponding literature values respectively.^{24,25} We speculate that the deviations are associated with the differences in the processing approaches and possible slight deviations of stoichiometry in the case of FA_{0.5}MA_{0.5}PbI₃. We also observe drifts of dark currents on a minutes timescale for all investigated samples, which is consistent with reports on comparable thick perovskite layers, and ascribed to ion motion in the layers.^{26,27} In passing we mention that due to the short penetration depth of the illuminating laser (< 50 nm), only a small part of the pellet is excited, explaining the relatively small absolute change in current upon illumination.

In general, all samples show a photoresponse dynamic in the second range and also slow dynamics in the minutes time scale upon laser excitation. We observe different characteristics of the photoresponse for the various samples investigated that can be differentiated into two classes. For MAPbI₃ and FA_{0.5}MA_{0.5}PbI₃, when switching on the illumination we observe a fast rise of the current that is followed by a linear increase and upon switching off the laser, the current shows a fast decay, followed by a slow decrease. Often, this behavior is seen in the literature, too^{28–35} and the rise of the current on the minutes timescale upon excitation is associated with filling of trap states, leading to a better conductivity.^{32,35}

In contrast to this for MAPbBr₃, MAPbI₂Br, (FAPbI₃)_{0.85}(MAPbBr₃)_{0.15} and (Cs_{0.05}FA_{0.95}PbI₃)_{0.85}(MAPbBr₃)_{0.15} we observe an instantaneous increase of the photocurrent upon illumination, which then decreases on a minutes time range. When illumination is switched off, the current initially overshoots into negative currents and then slowly approaches zero again. In the literature this decaying behavior is also reported,^{26,36–39} while to the best of our knowledge no overshooting dynamics into negative currents have been reported yet.

Repeatedly, the rise and decay characteristics of the photoresponse in hybrid perovskites are explained by ion migration and their accumulation at interfaces, which alters the ion movement upon illumination, changes the interface energies and charge extraction speeds and alters the trap density.^{40,41} It is also known that the type of charge extraction layer⁴² together with the corresponding interfaces and band structures,^{30,35,43} the level and direction of the bias voltage,^{30,38–40} the excitation wavelength and intensity,^{26,33,36,38} the environment,⁴⁰ and also the history of devices can influence the photoresponse characteristics, which makes a careful interpretation of this behavior difficult and is beyond the scope of this work. However, it seems that the rise- and decay-times become slower for higher layer thicknesses,^{33,43} which is in accordance with our results when reconsidering a typical thickness of 0.5 mm for the pellets investigated. However, a future systematic study which addresses all these issues in detail would be necessary and highly desirable to shine light on the complex photoresponse dynamics of hybrid perovskites.

7. Characterization of perovskite thin films processed from powder-based solution

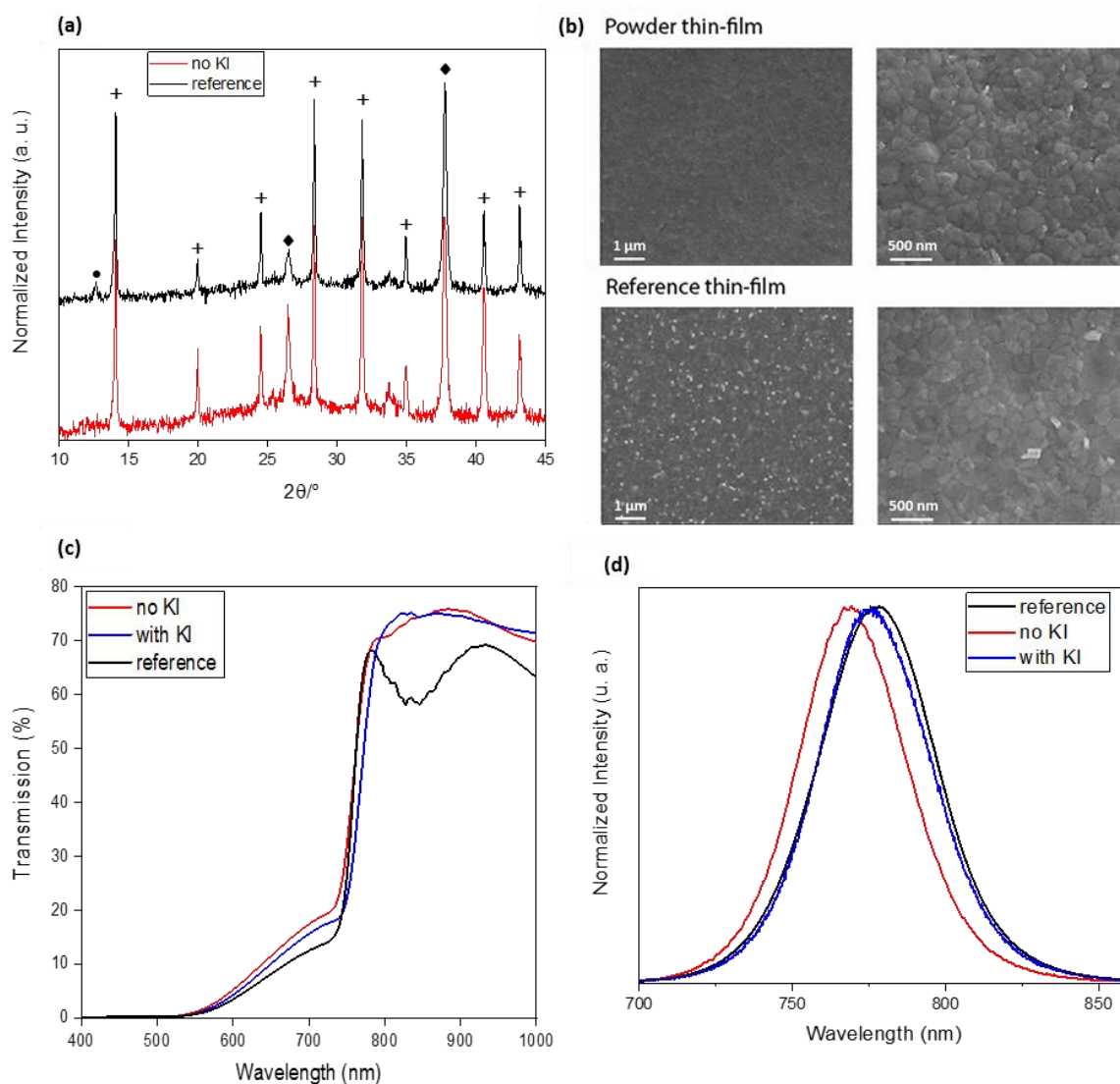


Figure S8. (a) X-ray diffraction pattern of a perovskite thin film from spin-coating of a 1 mol solution of $(\text{Cs}_{0.05}\text{FA}_{0.95}\text{PbI}_3)_{0.85}(\text{MAPbBr}_3)_{0.15}$ powder in DMSO:DMF on top of a mp-TiO₂/c-TiO₂/FTO substrate (red) and corresponding pattern from a reference device (black). Crosses indicate Bragg peaks from the perovskite, while diamonds mark peaks from the FTO substrate. The peak indicated by a circle originates from excess PbI₂ and is only apparent in the reference film. (b) Corresponding SEM images of perovskite thin-films derived from the powder precursor (top row) and of reference perovskite thin-films (bottom row). (c) UV-Vis absorption spectra and (d) photoluminescence spectra of thin-films derived from the perovskite powder without KI additive (red curve), with KI additive (blue curve) and thin-films from the reference solution process.

8. Device statistics and EQE measurements

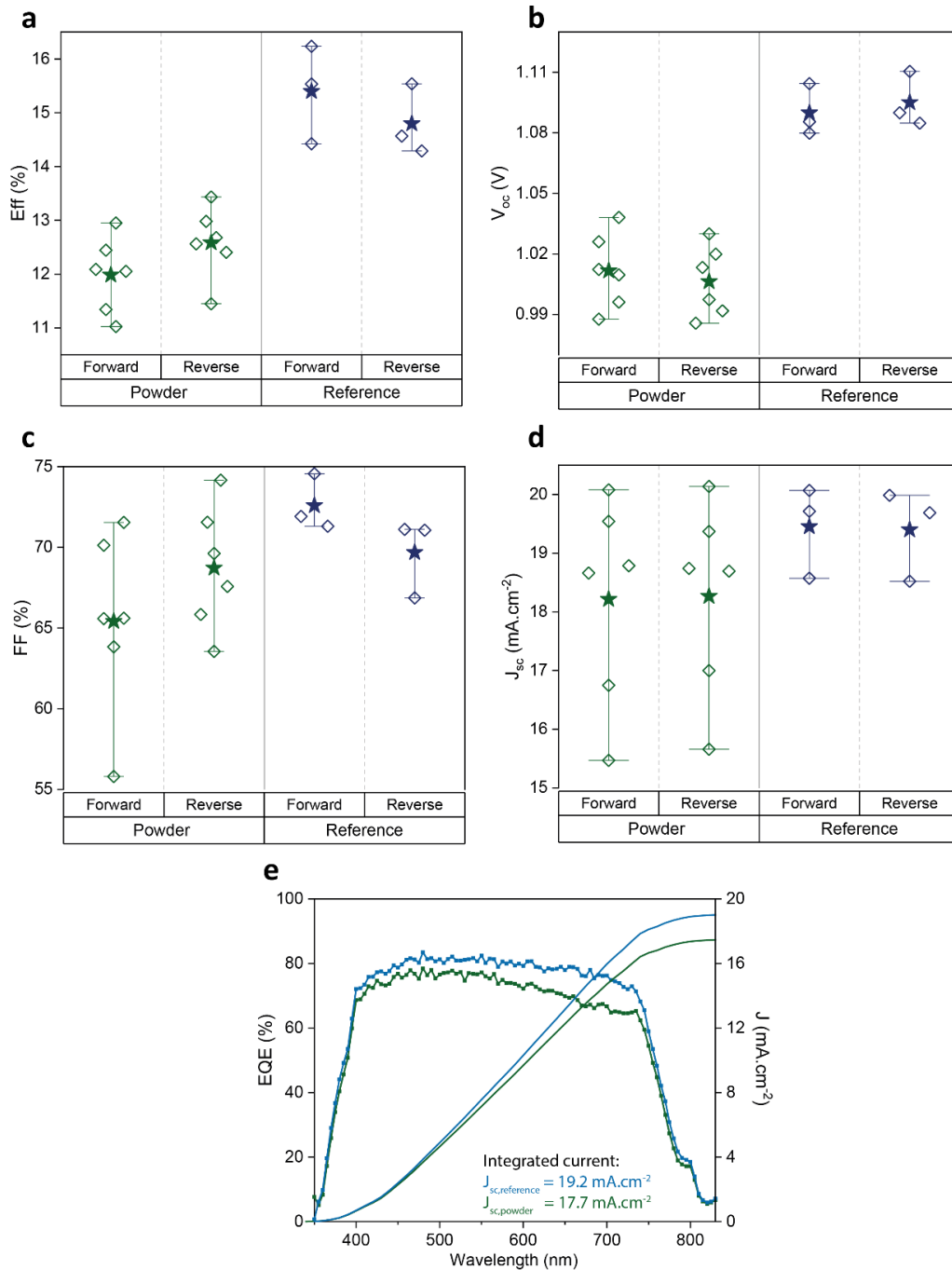


Figure S9. Device statistics of perovskite solar cells with absorber layers from the powder-based (green) and reference (blue) precursor solution. Mean values are represented as stars and whiskers represent the maximum-minimum interval. (a) Power conversion efficiency, (b) open circuit voltage, (c) fill factor, and (d) short circuit current have been extracted from the j-V characteristics of the completed cells. (e) The integrated current from external quantum efficiency measurements (depicted here for the device presented in the main text in Figure 7) matches the reported short circuit current. We refer to the device produced from the

perovskite powder-based solution as “powder” and the device produced from a solution of the individual salts in our standard process as “reference”.

9. Comparison of device statistics for passivated and unpassivated powders

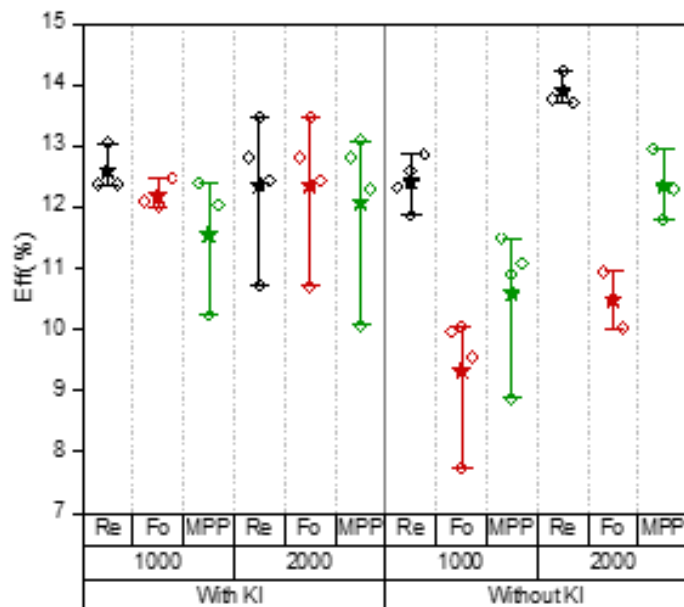


Figure S10. Device statistics for forward (Fo) and reverse (Re) scan direction of perovskite solar cells with absorber layers from the passivated powder-based and unpassivated powder-based precursor solution. MPP: maximum power point

10. Cross-section of the reference device

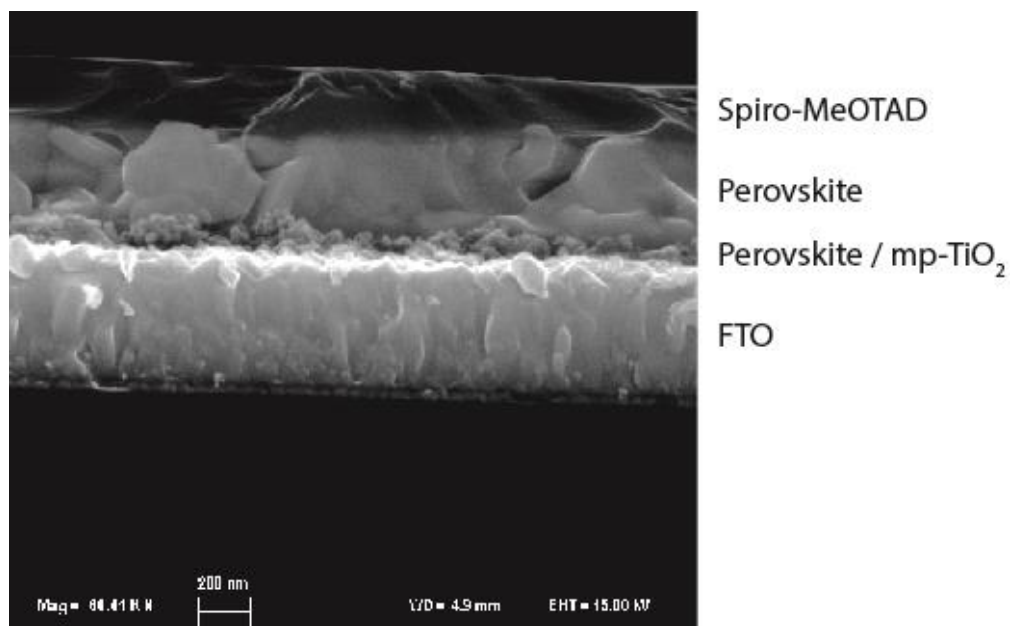


Figure S11. Cross-section SEM image of the PSC reference device.

11. Experimental details

11.1. Synthesis of precursor compounds

MABr: 13.93 ml (112 mmol) methylamine (33 wt.-% in ethanol, Sigma Aldrich) were dissolved in 60 ml of ethanol under an argon atmosphere. At room temperature 22 ml (80.91 mmol) HBr (48 wt.-% in H₂O, Sigma Aldrich) is added dropwise within 30 min and the solution is stirred overnight. The solvent is removed by a rotary evaporator and the powder is recrystallized from ethanol leading to a reaction yield of 14.7 g (58.6 %).

MAI: 28.8 ml (231.1 mmol) methylamine (33 wt.-% in ethanol, Sigma Aldrich) were dissolved in 170 ml of ethanol under an argon atmosphere. 16 ml (121.6 mmol) HI (57 wt.-% in H₂O, Alfa Aesar) is added dropwise within 30 min while being cooled in an ice bath and the solution is stirred overnight. The solvent is removed by a rotary evaporator and the powder is washed with ether and ether/ethanol mixture until the product is white. The reaction yield is 16.2 g (84.4 %).

FAI: 10 g (96.05 mmol) formamidine acetate (abcr) were suspended in 20 ml of methanol under an argon atmosphere. At room temperature 13.1 ml (99.3 mmol) HI (57 wt.-% in H₂O, Alfa Aesar) is added dropwise within 20 min and the solution is stirred overnight. The solvent is removed by a rotary evaporator and the powder is washed with ether multiple times. The suspension is filtrated and the powder is dried. With the aid of acetonitrile non reacted formamidine acetate is removed. The reaction yield is 13.9 g (84 %).

To test the pureness of the synthesized MAI, MABr and FAI, ¹H-NMR (300 MHz, DMSO-d₆) was conducted (Figure S12). Except for the DMSO signal at a chemical shift of 2.5 ppm and a small amount of water stemming from the DMSO at 3.3 ppm only the signals from the protons of MA and FA, respectively, can be seen.

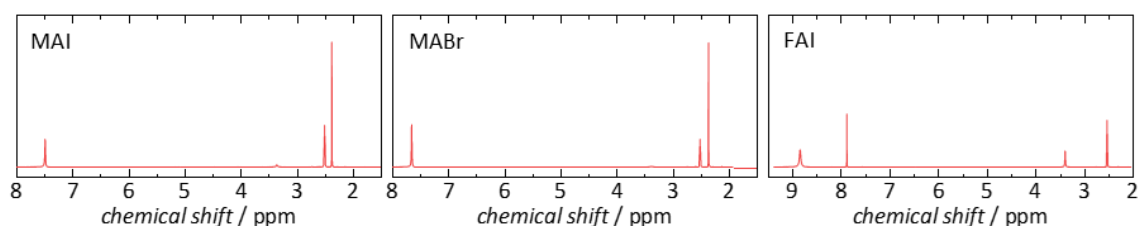


Figure S12. ¹H-NMR (300 MHz, DMSO-d₆) of MAI, MABr and FAI as synthesized

11.2. Exact amounts of precursors for mechanochemical synthesis

MAPbI₃: 1.900 g of MAI (11.95 mmol) and 5.509 g of PbI₂ (11.95 mmol) were milled to prepare the black powder.

MAPbBr₃: 1.525 g of MABr (13.62 mmol) and 5.000 g of PbI₂ (13.62 mmol) were milled to prepare the orange powder.

FAPbI₃: 1.982 g of FAI (11.53 mmol) and 5.312 g of PbI₂ (11.52 mmol) were milled to prepare the dark yellow / brownish powder.

MAPbI₂Br₁: 5.169 g of MAPbI₃ (8.34 mmol) and 2.000 g of MAPbBr₃ (4.18 mmol) were milled to prepare the black powder.

FA_{0.5}MA_{0.5}PbI₃: 3.000 g of FAPbI₃ (4.74 mmol) and 2.934 g of MAPbBr₃ (4.73 mmol) were milled to prepare the black powder.

(FAPbI₃)_{0.85}(MAPbBr₃)_{0.15}: 6.332 g of FAPbI₃ (10.00 mmol) and 0.844 g of MAPbBr₃ (1.76 mmol) were milled to prepare the black powder.

(Cs_{0.05}FA_{0.95}PbI₃)_{0.85}(MAPbBr₃)_{0.15}: 1.448 g of FAI (8.65 mmol), 4.200 g of PbI₂ (9.11 mmol), 0.118 g of CsI (0.45 mmol), 0.180 g of MABr (1.61 mmol) and 0.59 g of PbBr₂ (1.61 mmol) were milled to prepare the black powder.

(FAPbI₃)_{0.85}(MAPbBr₃)_{0.15} + KI: 5.194 g of (FAPbI₃)_{0.85}(MAPbBr₃)_{0.15} (8.52 mmol) and 0.072 g of KI (0.43 mmol) were milled to passivate the powder.

(Cs_{0.05}FA_{0.95}PbI₃)_{0.85}(MAPbBr₃)_{0.15} + KI: 2.500 g of (Cs_{0.05}FA_{0.95}PbI₃)_{0.85}(MAPbBr₃)_{0.15} (4.10 mmol) and 0.075 g of KI (0.45 mmol) were milled to passivate the powder.

11.3. Pressing of powders to pellets and electrical measurements

For the electrical characterization, the powders were pressed into the shape of cylindrical pellets with a custom made press. The press also allows to measure the electrical resistance of the powder under pressure while being able to simultaneously illuminate the pellet. This is achieved by electrically insulating the stainless steel press ram (area 1.27 cm²) from the press and using it to contact the pellet from the top. From the bottom the pellet is contacted by an ITO coated glass. This also allows the pellet to be illuminated from the bottom in a controlled manner. In addition, the press matrix is electrically insulated by a PEEK insert. About 250 mg of hybrid perovskite powder is necessary to obtain pellets with thicknesses in the range of 0.5 mm. The powders were pressed at 30 MPa for 1 h for compacting the powder. Then the pressure was reduced to 1 MPa for the electrical measurement to ensure good contact, but avoid pressure induced effects. A voltage of 1 V is applied between the stainless steel ram and the ITO by a Keithley 2400 Sourcemeter for at least one hour and the current is recorded. To photo excite the pellet a diode laser (Thorlabs) with an excitation wavelength of 405 nm is repeatedly switched on and off for 2 min each by a Rohde and Schwarz HMF2550 arbitrary function generator.

12. References

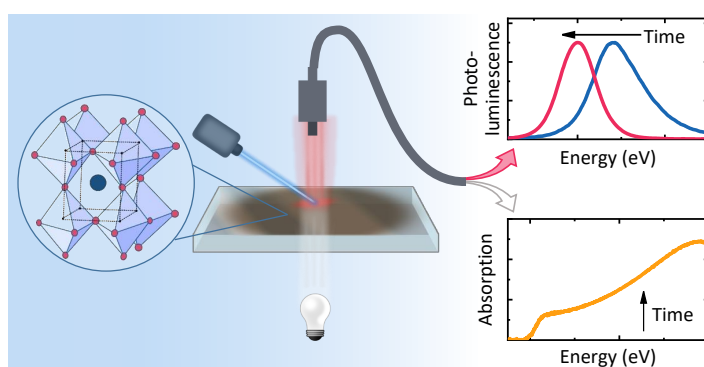
- (1) Pang, S.; Hu, H.; Zhang, J.; Lv, S.; Yu, Y.; Wei, F.; Qin, T.; Xu, H.; Liu, Z.; Cui, G. $\text{NH}_2\text{CH}=\text{NH}_2\text{PbI}_3$: An Alternative Organolead Iodide Perovskite Sensitizer for Mesoscopic Solar Cells. *Chem. Mater.* **2014**, *26*, 1485–1491.
- (2) Li, Y.; Liu, F. Z.; Waqas, M.; Leung, T. L.; Tam, H. W.; Lan, X. Q.; Tu, B.; Chen, W.; Djurišić, A. B.; He, Z. B. Formamidinium-Based Lead Halide Perovskites: Structure, Properties, and Fabrication Methodologies. *Small Methods* **2018**, *2*, 1700387.
- (3) Zhumekenov, A. A.; Saidaminov, M. I.; Haque, M. A.; Alarousu, E.; Sarmah, S. P.; Murali, B.; Dursun, I.; Miao, X.-H.; Abdelhady, A. L.; Wu, T.; Mohammed, O. F.; Bakr, O. M. Formamidinium Lead Halide Perovskite Crystals with Unprecedented Long Carrier Dynamics and Diffusion Length. *ACS Energy Lett.* **2016**, *1*, 32–37.
- (4) Zheng, X.; Wu, C.; Jha, S. K.; Li, Z.; Zhu, K.; Priya, S. Improved Phase Stability of Formamidinium Lead Triiodide Perovskite by Strain Relaxation. *ACS Energy Lett.* **2016**, *1*, 1014–1020.
- (5) Jones, T. W.; Osherov, A.; Alsari, M.; Sponseller, M.; Duck, B. C.; Jung, Y.-K.; Settens, C.; Niroui, F.; Brenes, R.; Stan, C. V.; Li, Y.; Abdi-Jalebi, M.; Tamura, N.; Macdonald, J. E.; Burghammer, M.; Friend, R. H.; Bulović, V.; Walsh, A.; Wilson, G. J.; Lilliu, S.; Stranks, S. D. Lattice strain causes non-radiative losses in halide perovskites. *Energy Environ. Sci.* **2019**, *12*, 596–606.
- (6) Kim, H.-S.; Lee, C.-R.; Im, J.-H.; Lee, K.-B.; Moehl, T.; Marchioro, A.; Moon, S.-J.; Humphry-Baker, R.; Yum, J.-H.; Moser, J. E.; Grätzel, M.; Park, N.-G. Lead iodide perovskite sensitized all-solid-state submicron thin film mesoscopic solar cell with efficiency exceeding 9%. *Sci. Rep.* **2012**, *2*, 591.
- (7) Correa Baena, J. P.; Steier, L.; Tress, W.; Saliba, M.; Neutzner, S.; Matsui, T.; Giordano, F.; Jacobsson, T. J.; Srimath Kandada, A. R.; Zakeeruddin, S. M.; Petrozza, A.; Abate, A.; Nazeeruddin, M. K.; Grätzel, M.; Hagfeldt, A. Highly efficient planar perovskite solar cells through band alignment engineering. *Energy Environ. Sci.* **2015**, *8*, 2928–2934.
- (8) McClure, E. T.; Ball, M. R.; Windl, W.; Woodward, P. M. $\text{Cs}_2\text{AgBiX}_6$ (X = Br, Cl): New Visible Light Absorbing, Lead-Free Halide Perovskite Semiconductors. *Chem. Mater.* **2016**, *28*, 1348–1354.
- (9) Volonakis, G.; Haghighirad, A. A.; Milot, R. L.; Sio, W. H.; Filip, M. R.; Wenger, B.; Johnston, M. B.; Herz, L. M.; Snaith, H. J.; Giustino, F. $\text{Cs}_2\text{InAgCl}_6$: A New Lead-Free Halide Double Perovskite with Direct Band Gap. *J. Phys. Chem. Lett.* **2017**, *8*, 772–778.
- (10) Sutter-Fella, C. M.; Li, Y.; Amani, M.; Ager, J. W.; Toma, F. M.; Yablonovitch, E.; Sharp, I. D.; Javey, A. High Photoluminescence Quantum Yield in Band Gap Tunable Bromide Containing Mixed Halide Perovskites. *Nano Lett.* **2016**, *16*, 800–806.
- (11) Noh, J. H.; Im, S. H.; Heo, J. H.; Mandal, T. N.; Seok, S. I. Chemical management for colorful, efficient, and stable inorganic-organic hybrid nanostructured solar cells. *Nano Lett.* **2013**, *13*, 1764–1769.

- (12) Slimi, B.; Mollar, M.; Assaker, I. B.; Kriaa, I.; Chtourou, R.; Marí, B. Perovskite $FA_{1-x}MA_xPbI_3$ for Solar Cells: Films Formation and Properties. *Energy Procedia* **2016**, *102*, 87–95.
- (13) Eperon, G. E.; Stranks, S. D.; Menelaou, C.; Johnston, M. B.; Herz, L. M.; Snaith, H. J. Formamidinium lead trihalide: a broadly tunable perovskite for efficient planar heterojunction solar cells. *Energy Environ. Sci.* **2014**, *7*, 982–988.
- (14) Salado, M.; Calio, L.; Berger, R.; Kazim, S.; Ahmad, S. Influence of the mixed organic cation ratio in lead iodide based perovskite on the performance of solar cells. *Phys. Chem. Chem. Phys.* **2016**, *18*, 27148–27157.
- (15) Abdi-Jalebi, M.; Andaji-Garmaroudi, Z.; Cacovich, S.; Stavrakas, C.; Philippe, B.; Richter, J. M.; Alsari, M.; Booker, E. P.; Hutter, E. M.; Pearson, A. J.; Lilliu, S.; Savenije, T. J.; Rensmo, H.; Divitini, G.; Ducati, C.; Friend, R. H.; Stranks, S. D. Maximizing and stabilizing luminescence from halide perovskites with potassium passivation. *Nature* **2018**, *555*, 497–501.
- (16) Prochowicz, D.; Franckevičius, M.; Cieślak, A. M.; Zakeeruddin, S. M.; Grätzel, M.; Lewiński, J. Mechanochemical synthesis of the hybrid perovskite $CH_3NH_3PbI_3$: Characterization and the corresponding solar cell efficiency. *J. Mater. Chem. A* **2015**, *3*, 20772–20777.
- (17) Prochowicz, D.; Yadav, P.; Saliba, M.; Sasaki, M.; Zakeeruddin, S. M.; Lewiński, J.; Grätzel, M. Mechanochemical synthesis of pure phase mixed-cation $MA_xFA_{1-x}PbI_3$ hybrid perovskites: Photovoltaic performance and electrochemical properties. *Sustainable Energy Fuels* **2017**, *1*, 689–693.
- (18) Prochowicz, D.; Yadav, P.; Saliba, M.; Sasaki, M.; Zakeeruddin, S. M.; Lewiński, J.; Grätzel, M. Reduction in the Interfacial Trap Density of Mechanochemically Synthesized $MAPbI_3$. *ACS Appl. Mater. Interfaces* **2017**, *9*, 28418–28425.
- (19) Prochowicz, D.; Yadav, P.; Saliba, M.; Kubicki, D. J.; Tavakoli, M. M.; Zakeeruddin, S. M.; Lewiński, J.; Emsley, L.; Grätzel, M. One-step mechanochemical incorporation of an insoluble cesium additive for high performance planar heterojunction solar cells. *Nano Energy* **2018**, *49*, 523–528.
- (20) Elseman, A. M.; Shalan, A. E.; Rashad, M. M.; Hassan, A. M. Experimental and simulation study for impact of different halides on the performance of planar perovskite solar cells. *Mater. Sci. Semicond. Process.* **2017**, *66*, 176–185.
- (21) Rashad, M. M.; Elseman, A. M.; Hassan, A. M. Facile synthesis, characterization and structural evolution of nanorods single-crystalline $(C_4H_9NH_3)_2PbI_2X_2$ mixed halide organometal perovskite for solar cell application. *Optik* **2016**, *127*, 9775–9787.
- (22) Dou, B.; Wheeler, L. M.; Christians, J. A.; Moore, D. T.; Harvey, S. P.; Berry, J. J.; Barnes, F. S.; Shaheen, S. E.; van Hest, M. F.A.M. Degradation of Highly Alloyed Metal Halide Perovskite Precursor Inks: Mechanism and Storage Solutions. *ACS Energy Lett.* **2018**, *3*, 979–985.

- (23) Kim, G. Y.; Senocrate, A.; Yang, T.-Y.; Gregori, G.; Grätzel, M.; Maier, J. Large tunable photoeffect on ion conduction in halide perovskites and implications for photodecomposition. *Nat. Mater.* **2018**, *17*, 445–449.
- (24) Yang, T.-Y.; Gregori, G.; Pellet, N.; Grätzel, M.; Maier, J. The Significance of Ion Conduction in a Hybrid Organic-Inorganic Lead-Iodide-Based Perovskite Photosensitizer. *Angew. Chem. Int. Ed.* **2015**, *54*, 7905–7910.
- (25) Abdelhady, A. L.; Saidaminov, M. I.; Murali, B.; Adinolfi, V.; Voznyy, O.; Katsiev, K.; Alarousu, E.; Comin, R.; Dursun, I.; Sinatra, L.; Sargent, E. H.; Mohammed, O. F.; Bakr, O. M. Heterovalent Dopant Incorporation for Bandgap and Type Engineering of Perovskite Crystals. *J. Phys. Chem. Lett.* **2016**, *7*, 295–301.
- (26) Shrestha, S.; Fischer, R.; Matt, G. J.; Feldner, P.; Michel, T.; Osvet, A.; Levchuk, I.; Merle, B.; Golkar, S.; Chen, H.; Tedde, S. F.; Schmidt, O.; Hock, R.; Rührig, M.; Göken, M.; Heiss, W.; Anton, G.; Brabec, C. J. High-performance direct conversion X-ray detectors based on sintered hybrid lead triiodide perovskite wafers. *Nat. Photonics* **2017**, *11*, 436–440.
- (27) Yakunin, S.; Dirin, D. N.; Shynkarenko, Y.; Morad, V.; Cherniukh, I.; Nazarenko, O.; Kreil, D.; Nauser, T.; Kovalenko, M. V. Detection of gamma photons using solution-grown single crystals of hybrid lead halide perovskites. *Nat. Photonics* **2016**, *10*, 585–589.
- (28) Wei, H.; Fang, Y.; Mulligan, P.; Chuirazzi, W.; Fang, H.-H.; Wang, C.; Ecker, B. R.; Gao, Y.; Loi, M. A.; Cao, L.; Huang, J. Sensitive X-ray detectors made of methylammonium lead tribromide perovskite single crystals. *Nat. Photonics* **2016**, *10*, 333–339.
- (29) Hu, X.; Zhang, X.; Liang, L.; Bao, J.; Li, S.; Yang, W.; Xie, Y. High-Performance Flexible Broadband Photodetector Based on Organolead Halide Perovskite. *Adv. Funct. Mater.* **2014**, *24*, 7373–7380.
- (30) Wang, Y.; Zhang, X.; Jiang, Q.; Liu, H.; Wang, D.; Meng, J.; You, J.; Yin, Z. Interface Engineering of High-Performance Perovskite Photodetectors Based on PVP/SnO₂ Electron Transport Layer. *ACS Appl. Mater. Interfaces* **2018**, *10*, 6505–6512.
- (31) Tang, F.; Chen, Q.; Chen, L.; Ye, F.; Cai, J.; Chen, L. Mixture interlayer for high performance organic-inorganic perovskite photodetectors. *Appl. Phys. Lett.* **2016**, *109*, 123301.
- (32) Shaikh, P. A.; Shi, D.; Retamal, J. R. D.; Sheikh, A. D.; Haque, M. A.; Kang, C.-F.; He, J.-H.; Bakr, O. M.; Wu, T. Schottky junctions on perovskite single crystals: light-modulated dielectric constant and self-biased photodetection. *J. Mater. Chem. C* **2016**, *4*, 8304–8312.
- (33) Fang, Y.; Dong, Q.; Shao, Y.; Yuan, Y.; Huang, J. Highly narrowband perovskite single-crystal photodetectors enabled by surface-charge recombination. *Nat. Photonics* **2015**, *9*, 679–686.
- (34) Dou, L.; Yang, Y. M.; You, J.; Hong, Z.; Chang, W.-H.; Li, G.; Yang, Y. Solution-processed hybrid perovskite photodetectors with high detectivity. *Nat. Commun.* **2014**, *5*, 5404.
- (35) Wang, Y.; Song, Q.; Lin, T.; Fu, Y.; Sun, X.; Chu, B.; Jin, F.; Zhao, H.; Li, W.; Su, Z.; Li, Y. Improved performance of CH₃NH₃PbI₃ based photodetector with a MoO₃ interface layer. *Org. Electron.* **2017**, *49*, 355–359.

- (36) Li, S.; Tong, S.; Meng, J.-Q.; Zhang, C.; Zhang, C.; Shen, J.; Xiao, S.; Sun, J.; He, J.; Gao, Y.; Yang, B.; Yang, J. Fast-response and high-responsivity $\text{FA}_x\text{MA}_{(1-x)}\text{PbI}_3$ photodetectors fabricated via doctor-blading deposition in ambient condition. *Org. Electron.* **2018**, *52*, 190–194.
- (37) Gegevičius, R.; Franckevičius, M.; Pakštas, V.; Augulis, R.; Gulbinas, V. High-Speed, Sensitive Planar Perovskite Photodetector Based on Interdigitated Pt and Au Electrodes. *Phys. Status Solidi A* **2018**, *215*, 1700822.
- (38) Chen, H.-W.; Sakai, N.; Jena, A. K.; Sanehira, Y.; Ikegami, M.; Ho, K.-C.; Miyasaka, T. A Switchable High-Sensitivity Photodetecting and Photovoltaic Device with Perovskite Absorber. *J. Phys. Chem. Lett.* **2015**, *6*, 1773–1779.
- (39) Liu, Y.; Sun, J.; Yang, Z.; Yang, D.; Ren, X.; Xu, H.; Yang, Z.; Liu, S. F. 20-mm-Large Single-Crystalline Formamidinium-Perovskite Wafer for Mass Production of Integrated Photodetectors. *Adv. Opt. Mater.* **2016**, *4*, 1829–1837.
- (40) Lafalce, E.; Zhang, C.; Liu, X.; Vardeny, Z. V. Role of Intrinsic Ion Accumulation in the Photocurrent and Photocapacitive Responses of MAPbBr_3 Photodetectors. *ACS Appl. Mater. Interfaces* **2016**, *8*, 35447–35453.
- (41) Wu, T.; Ahmadi, M.; Hu, B. Giant current amplification induced by ion migration in perovskite single crystal photodetectors. *J. Mater. Chem. C* **2018**, *6*, 8042–8050.
- (42) Perini, C. A. R.; Barker, A. J.; Sala, M.; Petrozza, A.; Caironi, M. High speed solution-processed hybrid perovskite photodetectors with low dark current enabled by a low temperature metal oxide interlayer. *Semicond. Sci. Technol.* **2018**, *33*, 94004.
- (43) Lin, Y.; Lin, G.; Sun, B.; Guo, X. Nanocrystalline Perovskite Hybrid Photodetectors with High Performance in Almost Every Figure of Merit. *Adv. Funct. Mater.* **2018**, *28*, 1705589.

11 Using *In Situ* Optical Spectroscopy to Elucidate Film Formation of Metal Halide Perovskites



Konstantin Schötz, Fabian Panzer.

Published in
The Journal of Physical Chemistry A, **2021**, 125, 11, 2209-2225
(DOI: 10.1021/acs.jpca.0c10765)

Reprinted with permission from the American Chemical Society
Copyright (2020) American Chemical Society

Using In Situ Optical Spectroscopy to Elucidate Film Formation of Metal Halide Perovskites

Konstantin Schötz and Fabian Panzer*



Cite This: *J. Phys. Chem. A* 2021, 125, 2209–2225



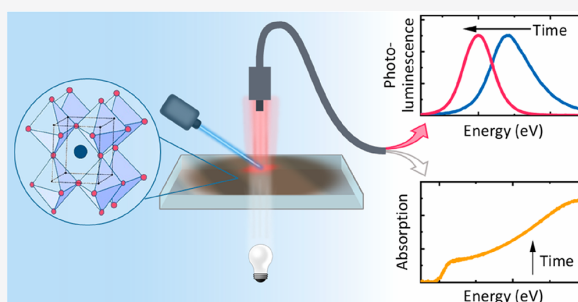
Read Online

ACCESS |

Metrics & More

Article Recommendations

ABSTRACT: The research interest in halide perovskites has gained momentum enormously over the last recent years, also due to the demonstration of high-efficient perovskite-based optoelectronic devices. A prerequisite for such highly efficient devices is to realize high-quality perovskite layers, which requires a deep understanding about the perovskite formation and good process control. In that context, in situ optical spectroscopy during the processing of halide perovskites has become increasingly popular. Even though it is a relatively easily accessible yet powerful tool for studying perovskite formation, there exist some technical and analytical aspects that need to be considered to unfold its full potential. In this Perspective, we give an overview of the latest developments in the field of in situ optical spectroscopy to control and better understand the film processing of halide perovskites. We highlight possibilities and pitfalls regarding the analysis of measured optical data, discuss the development of technical concepts, and address future prospects of optical in situ spectroscopy.



1. INTRODUCTION

Since the first report as an efficient absorber material in solar cells,^{1–3} the interest in halide perovskites has gained enormous momentum. To a large extent, this is because they combine the most desirable properties of inorganic and organic semiconductors. Like organic semiconductors, they can be deposited at room temperature and even from solution, thus allowing for a cost-efficient industrial production on the basis of existing technologies. However, in contrast to organic semiconductors, they order into crystalline morphologies with concomitantly delocalized states and a band structure like classical inorganic semiconductors. This implies that exciton binding energies are low^{4,5} and that diffusion lengths of charges are high.^{6,7} Consequently, halide perovskites are highly valued for next-generation optoelectronic devices such as solar cells,⁸ light-emitting devices (LEDs),⁹ and ionization radiation detectors.^{10–12} Since halide perovskites assemble into a crystalline structure during the formation of a film, the resulting final morphology of the perovskite layer is decisive for their optoelectronic properties and, thus, the efficiency of perovskite-based devices.¹³ Accordingly, it was mainly morphology optimizations, enabling perovskite solar cells to achieve ever-higher record efficiencies so rapidly.¹⁴

Typically, the morphology of a perovskite layer depends decisively on the processing method and, in particular, on the exact timing of each step in the process. The high sensitivity of perovskite's functionality to the timings, during processing, can also be regarded as a reason for the still limited reproducibility of

perovskite solar cell efficiencies.¹⁵ In the past, labor-intensive approaches to optimize the perovskite layer have been pursued, where optimization steps were mostly inferred retrospectively from the characterization of the final thin film.¹⁶ In contrast, during the past few years, investigating and understanding the perovskite formation process during film processing started to attract attention.

Several studies addressed the film formation process with the help of in situ measurements. They mainly were using scattering methods,^{17–25} which allowed to identify the important role of, for example, additives, the exact process conditions, or the morphology of precursor layers.^{19,26–31} In addition to scattering methods, other techniques such as optical spectroscopy are also suitable to study the formation of semiconductor films from solution.^{32,33} This is because the crystallographic structure of the perovskite is very sensitively linked to its electronic structure and thus to its optical properties. Hence, in situ optical spectroscopy has become increasingly popular, often complementing in situ scattering experiments, for example, to identify different crystallization phases and their timing in the film-formation

Received: December 2, 2020

Revised: February 3, 2021

Published: February 17, 2021



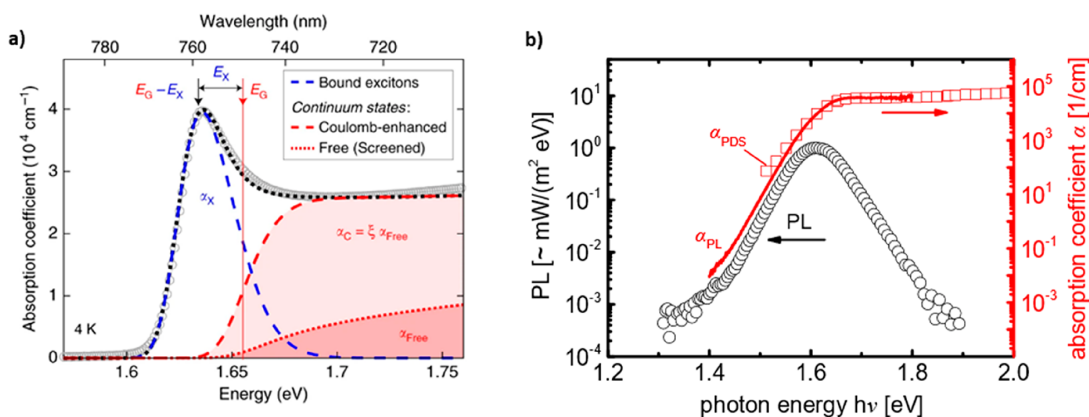


Figure 1. (a) Decomposition of a semiconductor absorption spectrum according to Elliott's theory into band-to-band absorption in the free electron picture (red dotted), absorption of bound states of the exciton (blue), and absorption of the excitonic continuum (red dashed). Reprinted with permission from ref 46. Copyright 2018, the authors. (b) Absorption coefficient α of MAPbI₃ as determined by (red symbols) photothermal deflection (PDS) and (red solid) calculated from the PL (black symbols) according to eq 2. Adapted with permission from ref 55. Copyright 2016, the American Physical Society.

process.^{29,34,35} In addition, driven by in situ optical characterizations, some studies could gain more detailed insights about the nucleation and growth dynamics or about the perovskite growth at the early stage of film formation.^{36,37} Recently, we and others investigated the formation of perovskites in detail by a simultaneous measurement of photoluminescence (PL) and absorption or reflection, further demonstrating the potential of optical in situ spectroscopy during the processing of halide perovskites.^{38,39} Spurred by recent technological and analytical advances,^{38,40} an optical in situ monitoring during film processing has become relatively easily accessible. It thus has significant potential as a versatile and cost-effective investigation method, especially in comparison with time-resolved scattering investigations, which typically can only be performed at suitable beamlines.

In this Perspective, we give an overview of recent developments in the field of optical in situ spectroscopy for investigating perovskite film formation, and we also highlight possible future perspectives. First, we focus on the basic optical properties of halide perovskites and which information can be extracted from them (Section 2). In Section 3, we give an overview of technical developments to measure the optical properties during processing, such as spin coating or slot die coating. We summarize recent developments and studies that use optical in situ spectroscopy either to improve processing control or to better understand the film formation (Section 4) before discussing future prospects in Section 5.

2. OPTICAL PROPERTIES OF HALIDE PEROVSKITES AND THEIR MEASUREMENT-RELATED ARTIFACTS

A simple method to probe the electronic structure of a semiconductor is to measure its absorption spectrum. To do so, typically white light with intensity I_0 is irradiated onto the sample, where the light is either transmitted (T), absorbed (A), scattered (S), or reflected (R).

$$I_0 = T + A + S + R \quad (1)$$

In the absence of scattering, the absorption can be calculated from transmission and reflection data. If the fraction of reflected light is small, for example, upon a perpendicular incidence of the white light, it is possible to calculate the absorption of the sample

by considering only transmission. For lead halide perovskites, the divalent metal and the halide mainly determine the electronic structure of the perovskite band edges,^{41–44} leading to optical properties similar to traditional inorganic semiconductors like GaAs.^{45,46} The absorption spectrum of lead halide perovskites can be decomposed into different contributions, as indicated in Figure 1a.^{46,47}

One contribution is the band-to-band absorption (red dotted line in Figure 1a), which starts at the material-characteristic band gap energy. In addition, excitonic absorption features are present and superimpose the band-to-band absorption. Excitons are electron–hole pairs bound by Coulomb interaction.⁴⁸ This interaction results in bound states below the band gap (blue line in Figure 1a) and also in continuum states above the band gap (red dashed line in Figure 1a).⁴⁹ The absorption spectrum of halide perovskites can be described by Elliott's theory, from which it is possible to extract parameters such as the exciton binding energy and the band gap energy.⁴⁹ The band gap is often also determined using a Tauc plot. There, it is assumed that the absorption is $\sim\sqrt{E}$ for a direct optical transition, so that plotting the square of the absorption versus energy results in a straight line. In such a Tauc plot, the crossing point of a linear fit to the absorption onset with the energy axis determines the band gap. For an indirect transition, the square root of the absorption needs to be taken instead of its square, due to the different spectral dependence of direct and indirect transitions. However, since the excitonic absorption masks the band-to-band transition (Figure 1a), the use of a Tauc plot is inappropriate to determine the absolute band gap energy for typical halide perovskites. It though may be used to quantify changes in absorption onsets.^{46,50}

Apart from band-to-band and excitonic absorptions, there exists a tail-state absorption, which extends far below the band gap of the semiconductor.^{51–53} Here, a typical example is the so-called Urbach tail, with an exponentially decreasing absorption coefficient toward lower energies (Figure 1b).^{54,55} While the exact mechanism causing this exponential decrease is under debate, there is general consensus that electron–phonon interaction as well as static disorder influence the slope of the Urbach tail.^{52,53,56–60} Even though the Urbach tail contains valuable information, it is challenging to access it directly in an

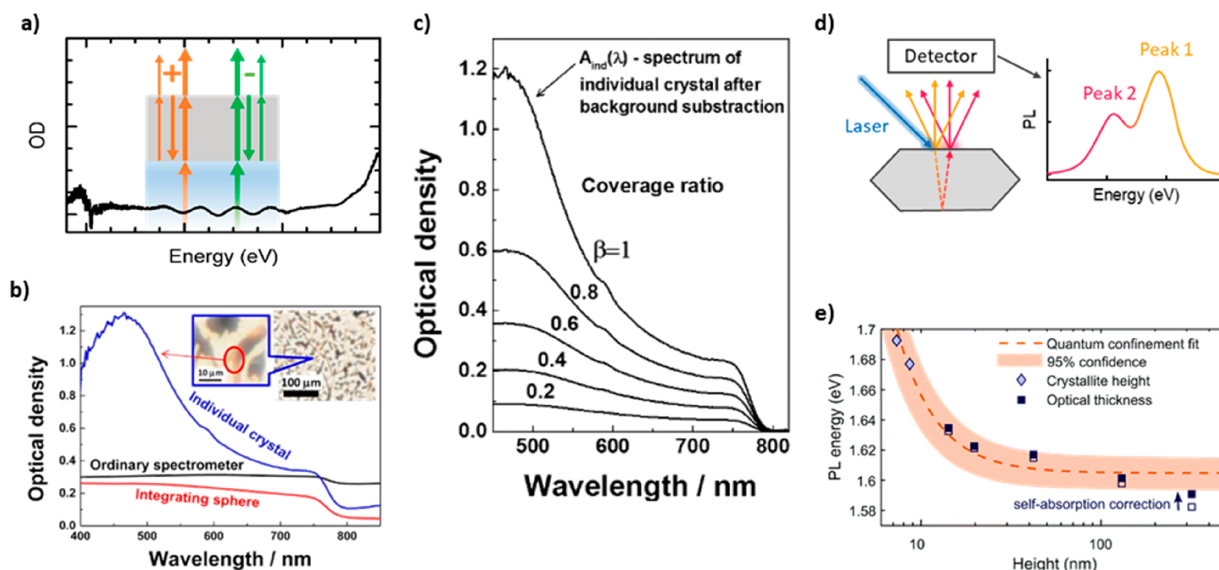


Figure 2. (a) Absorption spectrum with optical density modulations due to interference effects. The inset sketches the interference effect at a thin layer. The arrows in different colors indicate light with different wavelengths, leading either to positive (+) or negative (-) interference caused by reflections at interfaces. (b) Absorption spectra of a perovskite film with incomplete surface coverage for different measurement setups. The blue line shows the absorption of an individual crystal measured with an optical microscope. (inset) Microscopy image of the investigated perovskite film. (c) Calculated absorption spectra for decreasing surface coverage ratio β based on the absorption spectrum of an individual perovskite crystal from (b). (b, c) Reprinted with permission from ref 67. Copyright 2015, American Chemical Society. (d, left) Sketch illustrating prolonged PL paths in a crystal due to internal reflections. (d, right) Resulting PL spectrum, consisting of a contribution due to direct PL (Peak 1) and filtered PL (Peak 2) resulting from self-absorption. Reprinted with permission from ref 68. Copyright 2020, the Royal Society of Chemistry. (e) PL peak position (symbols) as a function of film height for MAPbI₃ thin films with different thicknesses. The dashed line is a fit according to eq 5. Reprinted with permission from ref 69. Published by the Royal Society of Chemistry.

ordinary absorption measurement, due to limited setup sensitivities.

However, the Urbach tail is also reflected in the shape of the PL spectrum, since the latter relates to the absorption of the material. The radiative recombination of free holes and electrons can be described (in a case of spatially homogeneous charge carrier distribution) as^{61,62}

$$PL(E) \propto a(E) \cdot E^2 \cdot \exp\left[-\frac{E}{k_B T}\right] \cdot \exp\left[\frac{\mu}{k_B T}\right] \quad (2)$$

where α is the absorbance, k_B is the Boltzmann constant, and T is the temperature. μ represents the quasi-Fermi level splitting (sometimes also labeled $\Delta\mu$), which is the splitting between the quasi-Fermi levels of the electrons in the conduction and in the valence band. eq 2 implies that the absorption coefficient of a perovskite can be calculated from PL measurements. A comparison of the absorption calculated from PL with an absorption measured by photothermal deflection spectroscopy is shown in Figure 1b.⁵⁵ Furthermore, with the absolute PL intensity or the PL quantum yield (PLQY), it is possible to extract μ by^{63,64}

$$\mu = \mu_{\text{rad}} + k_B T \cdot \ln(\text{PLQY}) \quad (3)$$

where μ_{rad} is the quasi-Fermi-level splitting in the radiative limit. μ reflects the highest achievable open-circuit voltage (V_{OC}) of a device that includes the investigated material as an active layer. Therefore, it is also referred to as implied V_{OC} .

At this point, some brief consideration of the PLQY (or PL intensity) is useful. Charge-carrier recombination in halide perovskites can be described by a rate equation accounting for

monomolecular (defect-assisted, $\sim n$), bimolecular ($\sim n^2$), and Auger ($\sim n^3$) recombination, with only the bimolecular recombination occurring radiatively.⁶⁵ Because of the different dependencies of the individual recombination mechanisms on the charge-carrier density n , also the PLQY is a function of n .⁶⁵ Thus, without the knowledge about the charge-carrier density present in the experiment, a measured PLQY value has only a limited validity to assess the quality of a sample. For example, even under identical experimental conditions (especially laser fluence), a higher n can be present in a polycrystalline sample due to a more limited charge-carrier diffusion as compared to a highly crystalline thin film with large grain sizes.

The models mentioned above describe the intrinsic optical properties of the material. In reality, however, optical effects alter measured spectra. One possible effect is a sinusoidal modulation of the absorption (or transmission) spectra due to white light interference, as illustrated in Figure 2a. Depending on the thickness of the layer and the wavelength of the light (indicated by the color of the arrows in Figure 2a), the directly transmitted light (thick arrow on top) can interfere either positively (indicated by “+” for the orange arrows) or negatively (indicated by “-” for the green arrows) with the internally reflected light (thin arrows on top). Positive interference leads to a decrease in the OD, while negative interference leads to an increase. Interference can be caused, for example, by a wet solvent layer, which becomes thinner upon drying. If the refractive index of the layer causing the interference is known, the layer thickness d can be calculated from the spectral position of two adjacent extrema according to^{24,66}

$$d = \frac{\lambda_1 \lambda_2}{2(\lambda_1 n_2 - \lambda_2 n_1)} \quad (4)$$

where $\lambda_{1,2}$ are the wavelengths at which two neighboring extrema occur, and $n_{1,2}$ are the refractive indices at $\lambda_{1,2}$.

Another aspect affecting the absorption spectra is the surface coverage of the sample, that is, how much of the investigated sample area is covered by perovskite (see Figure 2b,c).⁶⁷ An incomplete surface coverage is likely to be present at the beginning of a film-formation process. This incomplete coverage results in a lower overall absorption intensity, and, notably, it can cause an apparently distorted absorption spectrum where the high-energy region appears flatter (see Figure 2c). This artifact is a direct result from white light passing the uncovered areas of the sample. It can be deduced by a correct application of the Lambert–Beer law by considering that a fraction of the white light is partly absorbed by the perovskite and the rest of the light is transmitted at uncovered areas without being absorbed.⁶⁷ Additionally, an incomplete surface coverage leads to increased light scattering at perovskite crystallites, resulting in an overall lift of the baseline in measured absorption spectra. Measuring the latter in an integrating sphere minimizes the influence of scattering (Figure 2b).

A further optical effect relates to the crystal thickness. When the crystal thickness of the investigated perovskite sample increases, then the measured absorption spectra become more steplike. This is because the fraction of white light passing the sample at the uncovered areas (or the dark current of the detector) determines an upper limit of the detectable absorption. If the absorption of the material exceeds this value, the recorded absorption spectrum is “cut off” at this upper limit. Because of the finite decrease of the absorption coefficient below the band gap, this cutoff happens at lower energies for increasing samples thickness. When such absorption spectra are normalized, the band edge appears shifted to lower energies, due to this optical effect. Thus, a red shift of the absorption edge with increasing perovskite thickness is an optical artifact and not necessarily due to a change of the fundamental band gap. This should be taken into account before associating an absorption shift with a change in band gap energy.

Although it is not meaningful to extract a film thickness from such absorption spectra, it can still be possible to quantify the coverage ratio and average crystal height, as detailed by Tian et al.⁶⁷

Not only absorption but also measured PL can deviate from the intrinsic PL properties. For example, PL spectra of halide perovskites can—depending on the measurement conditions and layer thickness—heavily be influenced by self-absorption. This strong reabsorption of emitted light results from the refractive index difference between the perovskite layer and the air or glass interface. The refractive index of halide perovskites (~ 2.5 for methylammonium lead iodide (MAPbI₃))⁷⁰ typically is significantly higher than the refractive indices of the surrounding media (e.g., for a fused silica substrate ~ 1.45 at the wavelength of the PL of MAPbI₃),⁷¹ which leads to a high probability for internal PL reflections, as can be deduced from the Fresnel equations. This in turn can cause multiple internal reflections of the emitted light and concomitantly a long optical path length. Because of this long optical path, the low absorption at the absorption onset becomes nevertheless relevant, as it reabsorbs the high-energy part of the emitted light, thus apparently shifting the PL peak to lower energies. This effect is accompanied by a reduced PL intensity (i.e., PL quantum

efficiency) and can lead to additional PL features such as shoulders or distinct peaks at lower energies (see Figure 2d).^{68,72–76} Even in perovskite thin films, the effect of self-absorption on measured PL can be surprisingly strong, as the optical path lengths within the perovskite can be significantly longer than the film thickness. Obviously, the surface roughness of the perovskite also influences the reflection probability, changing the light in- and outcoupling.^{73,77} Depending on which parameters should be extracted from the PL, self-absorption needs to be considered quantitatively by optical modeling.^{69,72,78–80} We note that the extent of self-absorption on measured PL typically is sensitive to the specific measurement geometry. This allows to identify self-absorption effects in the PL spectrum by changing the measurement geometry.^{75,78}

In addition to optical effects that alter measured PL spectra, changes of the semiconductor's electronic structure also influence its intrinsic PL properties. A relevant effect in the context of film formation is quantum confinement. It is present if perovskite crystallites are very small, that is, less than approximately 25 nm. Then the PL shifts to higher energies compared to the bulk material (Figure 2e).⁶⁹ The shift can be understood in terms of a quantum mechanical particle in a box model. There, the energy levels (and thus their difference) depend on the square of the size of the box. As illustrated in Figure 2e, the PL peak position E can be related to the crystallite size d according to⁸¹

$$E = E_g + \frac{b}{d^2} \quad (5)$$

where E_g is the bulk PL peak position, and b is a constant, which was reported to be in the range of 1–5 eV/nm² for MAPbI₃.^{69,82} Thus, if b and E_g are known, the size of the crystallites can be estimated from the PL peak position. It is also possible that the PL intensity increases with increasing confinement, which was frequently explained by an increased overlap between electron and hole wave function.^{83–86} If confinement and a size dependence of the PL intensity are present, a distribution of crystal sizes leads to an asymmetric broadening of the measured PL peak.^{85,87} Confinement effects during thin-film processing are most likely to occur at the beginning of the perovskite formation.

Additionally, strain, for example, introduced by a substrate, can alter the electronic structure of the perovskite.^{88–91} In contrast to quantum confinement, the presence of strain can lead to band gap (or PL peak) shifts to higher but also to lower photon energies,^{88–91} as two different effects can occur: a decrease in the Pb–X bond length, which was found to decrease the band gap energy, and a strain-induced decrease of the Pb–X–Pb bond angle causing an increase of the band gap.^{88–90} Even though both changes in strain and quantum confinement can easily occur simultaneously during perovskite processing, it is possible to distinguish the individual effects, as they impact the PL in different ways. While quantum confinement occurs only for crystal sizes below ~ 25 nm, strain is not limited to small crystallites. Furthermore, quantum confinement is often leading to an increased PL intensity and asymmetrically broadened PL peak shape.^{85,87} This is in contrast to strain, which—to the best of our knowledge—does not lead to higher PL intensities, but rather a strain-induced PL decrease was found recently.⁸⁸

Another cause for a spectral shift of the PL peak (and the absorption onset) can be a change of stoichiometry in the perovskite's composition. For example, the band gap of lead halide perovskites can be tuned continuously from 1.55 to 3.15

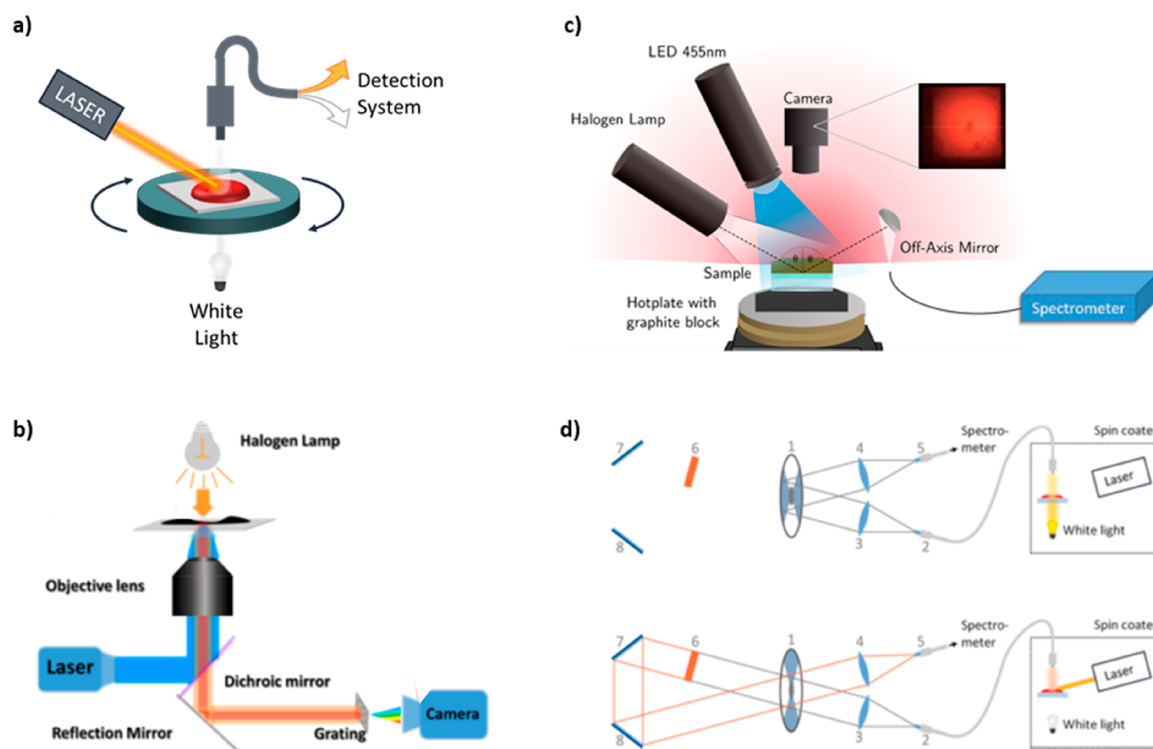


Figure 3. (a) Schematic representation of a spin-coater device, capable of measuring transmission and PL during spinning. Reprinted with permission from ref 40. Copyright 2018, American Chemical Society. (b) Illustration of a wide-field microscope setup, to measure transmission spectra superimposed with PL. Considering reference measurements, individual spectral contributions (absorption and PL) can be extracted. Reprinted with permission from ref 103. Copyright 2019, American Chemical Society. (c) Schematic of the optical monitoring process to simultaneously measure transmittance (by halogen lamp) and PL (excited by 455 nm LED) spectra. Reprinted with permission from ref 38. Published by The Royal Society of Chemistry. (d) Schematic illustration of the main components of a detection system for the quasi-simultaneous measurement of absorption and PL using one spectrometer, with the operation states during absorption (top) and PL (bottom) measurement. Components are chopper wheel (1), optical fiber (2,5), lenses (3,4), optical filter (6), and mirrors (7,8). Reprinted with permission from ref 40. Copyright 2018, American Chemical Society.

eV by changing the halides, that is, by mixing iodine with bromine and bromine with chlorine.^{92–95} Since it is well possible that different halides incorporate into the perovskite crystal with different speed, a change in halide ratio can occur during film formation as well.⁹⁶

When the optical changes that are observed in situ in the course of perovskite formation from a solution are interpreted, it is important to be aware of the above-mentioned optical effects that can impact on absorption and PL spectra.

3. TECHNICAL APPROACHES TO RECORD OPTICAL SIGNALS IN SITU DURING FILM FORMATION

Before one focuses on specific approaches to monitor optical properties during the processing of halide perovskites, it is worthwhile to consider briefly what might technically limit the proper detection of optical spectra. One important aspect is that halide perovskites often exhibit a low PLQY at relevant processing temperatures (e.g., room temperature or higher).⁹⁷ Thus, for excitation intensities that are sufficiently low to avoid perovskite degradation or structural changes, the PL spectra can suffer from a relatively poor signal-to-noise (S/N) ratio. Similarly, in the case of transmission or absorption measurements, a poor S/N ratio can result from a strong absorption of the perovskite or a weak light intensity of the white light source. In steady-state measurements, one can overcome these limitations by using a sufficiently long exposure time for light

detection or by averaging a large number of individual measurements. This, however, is not possible for in situ optical spectroscopy, where spectra are taken several times per second, and thus the exposure or integration time for a spectrum is limited by the rate with which the subsequent spectra are taken. In many cases, depending on the perovskite film-formation route, at least a subsecond time resolution is required. Therefore, most studies in the past used state-of-the-art charge-coupled devices (CCDs) with a subsecond repetition rate for light detection. An obvious way to overcome the limitation on the light accumulation time available for each spectrum during in situ measurements is to increase the intensity of the light source. This works as long as the impinging light intensity does not damage the sample or significantly affect the film-formation dynamics, for example, due to laser heating. This condition is easier to meet for the white light sources employed in transmission measurements than for the laser irradiation required for PL studies. This is one of the reasons why, in the past, in situ measurements to study the film formation of halide perovskites were preferably conducted merely for absorption.^{29,36,98–100}

Generally speaking, the smaller the power density of the incident light (be it white light or laser light), the less light-induced sample degradation occurs. When leaving the power of the incident light constant, it thus can be beneficial to increase the size of the irradiation spot, which decreases the power

density while the overall signal can stay roughly constant. In this context, also the use of optics with high collection efficiency, in combination with large size photodetectors, is beneficial to minimize the necessary excitation power density while maintaining an appropriate S/N ratio.

For in situ transmission measurements, the technical challenge is to place either the white light source or the components for light detection below the sample in the setup used for processing, for example, in a spin coater or slot die coater. In many cases, this makes it necessary to modify existing setups extensively or even to pursue a self-construction. In 2014, Abdelsamie et al. presented a home-built spin coater with a hole in the center of the rotating chuck, with enough space underneath to install an optical fiber. With the help of this fiber, the white light transmitted from above the sample was directed into a spectrograph.¹⁰¹ Using this setup enabled the investigation of the film formation of various solution-processed semiconductors such as organic semiconductors and hybrid perovskites.^{98,101,102}

In 2018, we built a spin coater with a reversed geometry, where the white light is placed below the rotating chuck and the optical fiber for light detection is located above the sample (Figure 3a).⁴⁰ This geometry allows for the quasi-simultaneous detection of absorption and PL as detailed further below. To measure the PL precisely and to minimize self-absorption effects, the sample needs to be excited on the same side from which the PL is detected. One realization for this is that the incident excitation light and the fiber collecting the PL are both above the perovskite/air interface (Figure 3a). If the layer supporting the perovskite film does not cause PL quenching, then it is also possible to invert the measurement geometry as shown in Figure 3b. Such a measurement setup was recently presented by Hong et al.¹⁰³ There, white light shines through the perovskite layer from above for the transmission measurement. The PL is excited from below the sample by a continuous wave (CW) laser beam in the fashion of a confocal PL microscope. The PL that emits into the lower-half space and the transmitted white light are both collected by the microscope objective and directed into a spectrograph. As a result, one detects a transmission spectrum of the halogen lamp through the perovskite layer, superimposed by the perovskite PL. By measuring the transmission also without laser excitation, the spectral contributions of the PL and the transmission can be separated. Since the reference absorption to determine the PL can change over time due to the structural dynamics of the perovskites, it is necessary to record transmission spectra without PL excitation repeatedly. Thus, the measurement of the PL must be interrupted repeatedly for a certain time span. Hence Hong et al. used this method to study changes of optical properties on longer time scales, that is, minutes to hours, and investigated perovskite degradation due to environmental influences.¹⁰³ In his work, the simultaneous monitoring of PL and absorption allowed to differentiate a structural degradation of the perovskite from changes in the electron–hole recombination mechanism. This nicely demonstrates the potential to gain deeper insights when considering both PL and absorption.¹⁰³

Apart from absorption and PL, also PL excitation spectroscopy was recently used to investigate the degradation of lead halide perovskites in a microscope setup.^{104,105} Here, the PL intensity is monitored as a function of excitation wavelength. By also measuring the transmitted excitation light, the absorption of the sample can be calculated, which then enables a calculation of

wavelength-dependent changes in the PLQY. With this approach Merdasa et al. could identify a transition range between MAPbI₃ and PbI₂, at which charge carriers accumulate.¹⁰⁴

The PL and absorbance can be measured simultaneously on shorter time scales and with higher detection rates when using different, dedicated detectors for PL and absorption. This can be implemented in several ways.

In 2016, Engmann et al. presented a setup where a diode laser excites the PL of the sample from above, while white light is directed onto the sample at an angle matching the substrate's Brewster angle.¹⁰⁶ Thus, both the light transmitted through the sample and the light reflected by the sample could be detected separately, using additional polarizers in front of the different spectrographs. This allowed a study of the temporal evolution of PL, absorption (calculated based on transmitted white light), and film thickness (calculated based on reflected white light, see eq 4) during a blade coating of different organic semiconductor blends.¹⁰⁶ To avoid scattered white light disturbing PL spectra, it is necessary to probe PL and transmission or reflection not at the same sample spot but slightly offset from each other. This is sufficient for processing methods such as blade coating or slot coating, where the drying proceeds along one specific direction.

Recently Suchan et al. investigated the perovskite formation of MAPbI_{3-x}Cl_x during annealing, using a homemade setup to measure PL and the reflected white light from the same sample area (Figure 3c).³⁸ Interesting here is that the bottom side of the sample substrate is mirrored. If the white light enters the detector after reflection at this mirrored bottom side, it is transmitted through the perovskite as well. The authors call this transreflectance, which also contains information on the perovskite absorption.³⁸ From a technical viewpoint this is elegant, since all components of the measurement setup can be placed above the sample so that fewer technical modifications of existing processing setups are needed to implement the measurement system. Recently, also Rehermann et al. used this measurement concept to determine transreflectance during a spin coating and subsequent annealing of mixed-halide perovskites of the type MAPb(I_xBr_{1-x})₃.¹⁰⁷

To reduce the technical effort for the measurement of different optical signals, we developed an optical detection system that allows measuring PL spectra and absorption spectra quasi-simultaneously by means of one single detector unit consisting of a spectrograph coupled to a CCD camera.⁴⁰ Figure 3d shows a schematic of the measurement concept. A rotating chopper blade with mirrored segments represents the conceptual centerpiece. With that, it is easily possible to alternate between two different beam paths: During the detection of an absorption spectrum, the laser diode is switched off, and the white light LED is switched on. The light transmitted through the sample is reflected at the mirrored chopper blade segments and directed straight into a spectrograph (Figure 3d, top). In contrast, during PL detection, the laser diode is switched on, the white light LED is switched off, and the chopper blade is in such a position that the PL passes through an empty chopper segment (Figure 3d, bottom). This way, PL enters an extended optical path that includes an optical filter to block any unwanted remaining laser signal. The filtered PL finally is directed into the spectrograph via deflection mirrors. A microcontroller ensures the correct timing between the on and off states of the laser diode, white light, and chopper blade position. The maximum rate for detecting pairs of PL and absorption depends mainly on the maximum detection frequency of the CCD camera used. In

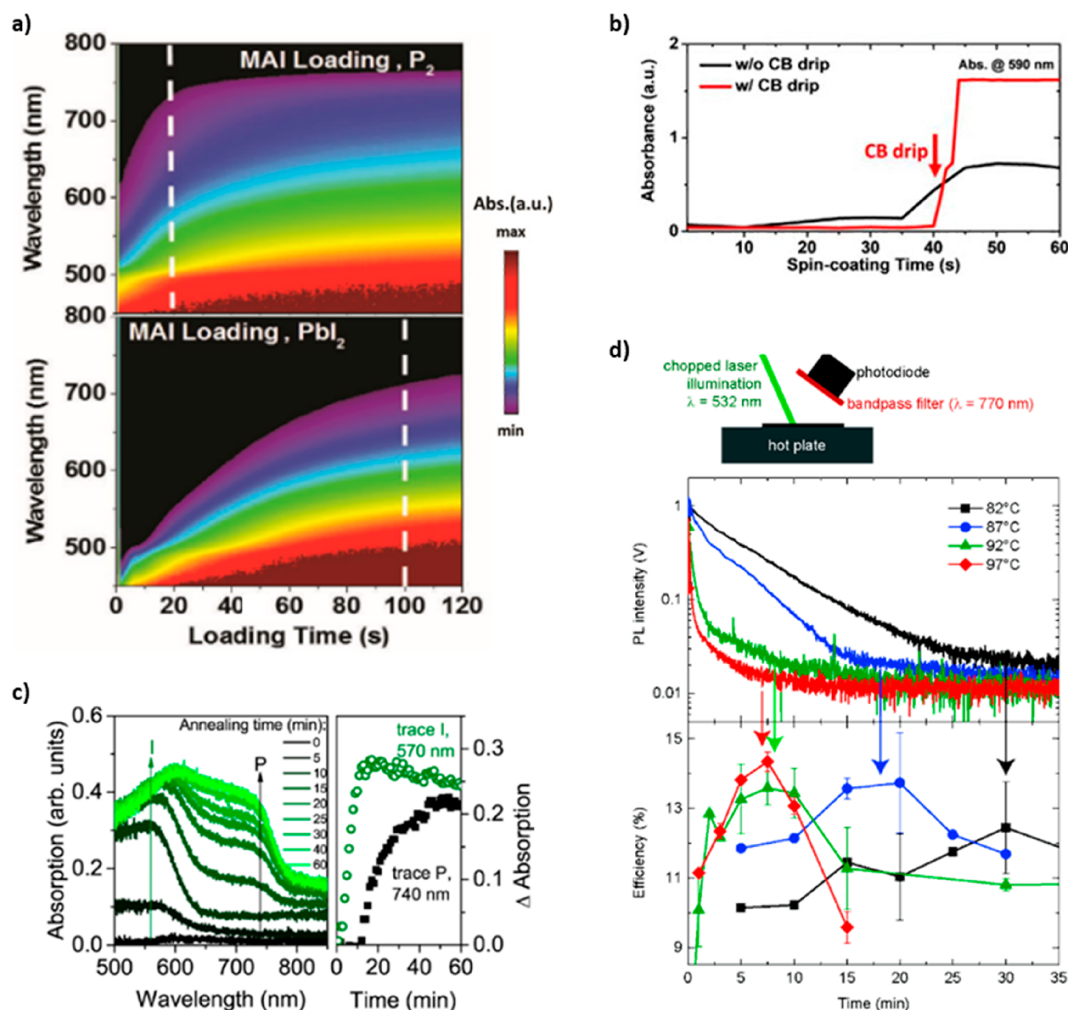


Figure 4. (a) In situ absorption during MAI loading on the P_2 precursor phase (top) and on the dry PbI_2 film (bottom). Reprinted with permission from ref 29. Copyright 2019, Wiley-VCH. (b) Temporal evolution of absorption intensities at 590 nm from in situ absorption measurements during a spin coating of $MA_3Bi_2I_9$ without and with the use of an antisolvent (CB), dripped after 40 s of spin coating. Reprinted with permission from ref 99. Copyright 2019, Wiley-VCH. (c) In situ absorption of $MAPb_{3-x}Cl_x$ during annealing (left). Corresponding temporal slices at a wavelength where the perovskite and the intermediate phase absorb are shown on the right. Reprinted with permission from ref 100. Copyright 2014, American Chemical Society. (d) Temporal evolution of the PL intensity during annealing at different temperatures of a perovskite film deposited on a PEDOT:PSS layer (top). Solar cell efficiencies as a function of annealing time for different temperatures (bottom). The arrows indicate the coincidence of annealing time for maximum device efficiency and time at which the drop in PL intensity saturates. Reprinted with permission from ref 110. Copyright 2016, Wiley-VCH.

our case, it was possible to detect pairs of PL and absorption with a rate of up to 15 Hz, that is, with a minimum acquisition step time of ~ 67 ms, allowing to resolve all typical film-formation dynamics of organic semiconductors and halide perovskites.^{39,40}

This brief, exemplary yet not exhaustive overview may serve to illustrate different concepts that can be employed to monitor optical signals during the processing of halide perovskites. By now, experimental approaches exist that require only a low number of technical components and that are relatively easy to implement in existing processing setups. This is an encouraging development, which facilitates the use of in situ optical monitoring for improving process control, both in the laboratory as well as in the industrial context. Moreover, these technological developments will make it easier to combine in situ monitoring of optical signals with other in situ measurement

techniques, for example, in situ grazing incidence wide-angle X-ray scatter (GIWAXS). The combination of several individual measurements into one time-resolved multimodal measurement allows for a detailed characterization of the sample evolution during processing.^{37,108,109} Following how several properties evolve and correlating them has a high potential to elucidate the film formation of halide perovskites in a level of detail that was previously not possible.

There is, however, a further, only partially resolved, technical aspect that is worth mentioning. The detection of optical spectra taken over a period of time can quickly generate large amounts of data due to high frame rates and/or long investigated time spans. These large collections of data become difficult to deal with, so it becomes necessary to find ways for their efficient processing, display, and analysis. It is evident that this aspect will gain further

importance in the area of in situ monitoring during film processing.

4. RECENT DEVELOPMENTS REGARDING THE CHARACTERIZATION OF THE FILM-FORMATION PROCESS

4.1. In Situ Optical Monitoring to Determine Timings of the Film-Formation Process. In situ spectroscopy of individual optical properties was used repeatedly to monitor the timing of different steps in the perovskite crystallization process and to support the results from corresponding X-ray scattering measurements, for different solution processing methods and during annealing. Already in 2013, Burschka et al. tracked the conversion of PbI_2 to MAPbI_3 in a sequential deposition method by in situ absorption and PL at characteristic wavelengths and observed the perovskite conversion to be complete after ~ 20 s.³⁴ This fast crystallization was enabled by the use of a porous TiO_2 scaffold, leading to perovskite solar cells with, at that time, a record efficiency of 15%. Similarly, Barrit et al. used in situ absorption to investigate the influence of the PbI_2 precursor phase on the perovskite crystallization speed.²⁹ In this work, PbI_2 films were loaded with a methylammonium iodide (MAI) solution, followed by an isopropyl alcohol (IPA) washing step. Using in situ GIWAXS measurements during spin-coating PbI_2 from dimethylformamide (DMF) solution, the authors identified one disordered (P_0) and two ordered (P_1 , P_2) precursor phases before the dry PbI_2 film formed. Ex situ GIWAXS revealed that loading the precursor film with MAI during the P_2 phase already leads to a complete perovskite conversion of the film prior to annealing. To investigate this perovskite formation process, the MAI loading step during P_2 and for a dry PbI_2 film were monitored using in situ absorption measurements (Figure 4a). In the case of MAI loading during the P_2 phase, perovskite absorption appeared quickly and saturated after ~ 20 s, indicating complete conversion. In contrast, when MAI was loaded on the dry PbI_2 film, the perovskite absorption grew significantly slower, implying a slower conversion. This was explained by a decreased uptake of the MAI solution of the dry PbI_2 film. Finally, MAI loading during the P_2 phase led to devices with an improved efficiency and higher reproducibility.

Another example where in situ absorption was used for determining timings during perovskite processing is the work by Lee et al.⁹⁸ The authors built solar cells, where the perovskite layer was deposited by one-step solution processing without and with different additives. On the basis of the device performances and by atomic force microscopy, scanning electron microscopy (SEM), and optical microscope images, *N*-cyclohexyl-2-pyrrolidone (CHP) was identified to be the best additive for improving crystallization and device efficiency. To investigate the perovskite crystallization dynamics, in situ UV–vis absorption was recorded during spin coating without additive and with CHP. With additive, the perovskite formation slowed significantly, as could be concluded from considering the absorption at a perovskite-specific wavelength. Furthermore, there was less contribution of scattering in the spectra, indicating smoother films. Corresponding in situ GIWAXS measurements showed that CHP inhibits the formation of PbI_2 solvate phase, thereby assimilating the crystallization rates of PbI_2 and MAI.

In situ absorption was used also in the case of the solvent engineering method, where an antisolvent is applied during the spin coating to initiate perovskite crystallization. Tang et al. compared the crystallization of MAPbI_3 with that of a bismuth-

based perovskite.⁹⁹ Using in situ GIWAXS measurements, they found that, for natural drying, the bismuth-based perovskite formed directly without an intermediate phase, in contrast to MAPbI_3 . To gain more control over the crystallization process, an antisolvent was dripped onto the wet solution during spin coating. This step was monitored using in situ absorption and analyzed by following the time dependence at a wavelength related to perovskite absorption (Figure 4b). Without antisolvent dripping, the perovskite formation is slow and reduced, whereas it is fast and more complete when the antisolvent is dripped at an appropriate time.

Also, the annealing of perovskite films was monitored by in situ absorption, for example, by Unger et al. for the case of the PbCl_2 -based $\text{MAPbI}_{3-x}\text{Cl}_x$ crystallization (Figure 4c).¹⁰⁰ Directly from the beginning of the annealing process at 100 °C, an absorption feature at wavelengths below 650 nm started to gain intensity (Figure 4c), which they associated with an intermediate phase absorption. For longer times, also absorption at higher wavelengths, indicative for the perovskite absorption, increased. Considering the evolution of absorption intensity at 560 nm (trace I in Figure 4c) and at 740 nm (trace P in Figure 4c) allowed to quantify the delay of the perovskite crystallization to be ~ 10 min. From these measurements it also became clear that the precursors fully converted to perovskite after 40 min. Similarly, van Franeker et al. investigated the annealing of MAPbI_3 films using in situ PL and absorption.¹¹⁰ On the basis of in situ absorption, they found that, when a stock solution and substrates were at room temperature, MAPbI_3 only formed during annealing on a time scale of 1 min, whereas, upon using a hot solution (70 °C) and heated substrate (92 °C), the perovskite formed completely already during spin-coating. Despite a complete perovskite formation during spin coating, the nonannealed hot-casted films exhibited small grains resulting in a low solar-cell performance. Annealing improved the solar cell performance significantly, which was explained by an increased charge carrier mobility, whereas annealing for too long was detrimental. The authors investigated the increase of the mobility during annealing by monitoring in situ the evolution of perovskite PL intensity of samples processed on a quenching layer (here poly(3,4-ethylenedioxythiophene) polystyrene sulfonate (PEDOT:PSS)) (Figure 4d). Upon photoexcitation from the top, carriers are generated near the surface and then diffuse into the bulk. With increasing mobility, more carriers can reach the quenching layer at the bottom, leading to a drop of measured PL intensity. The authors found that the drop of PL intensity saturates after a certain annealing time, depending on the temperature (Figure 4d middle). Since excitation fluence and film thickness were kept constant, this saturation behavior indicates that further annealing does not lead to more carriers reaching the quenching layer. Interestingly this was also the annealing time, which led to the best solar cell performances (Figure 4d bottom). This work thus underlines how powerful in situ optical spectroscopy can be for the inline monitoring of perovskite processing.¹¹⁰

Another example where timings during the annealing step were monitored by in situ spectroscopy, here in addition to the spin coating step, is the work by Rehermann et al.¹⁰⁷ Driven by the question whether stoichiometric inhomogeneities are already introduced during film formation, they investigated the film formation of $\text{MAPb}(\text{I}_x\text{Br}_{1-x})_3$ for different halide ratios x using in situ transmittance and ex situ X-ray diffraction (XRD). From transmittance measurements, they inferred that pure MAPbBr_3 , that is, $x = 0$, crystallizes directly into the perovskite

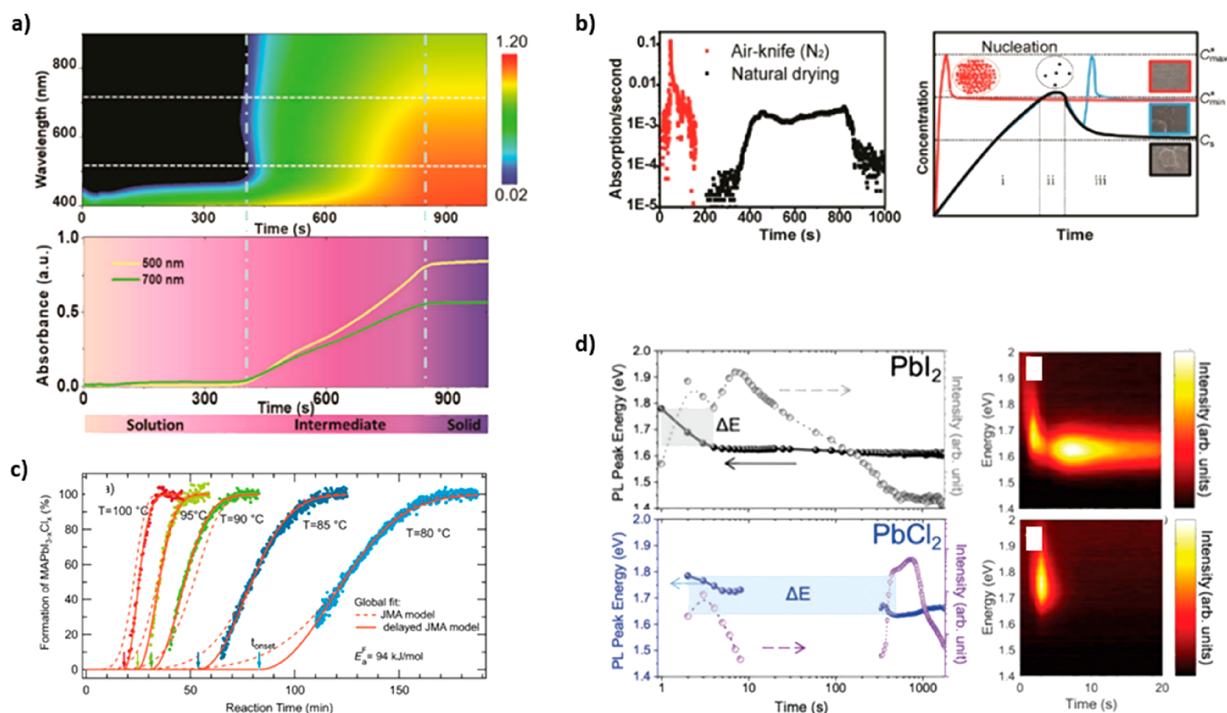


Figure 5. (a) 2D map of the temporal evolution of in situ UV–vis absorption during drying of a blade-coated perovskite film (top), together with a corresponding absorbance evolution at 500 and 700 nm (bottom). On the basis of the optical spectra, the solution, intermediate, and solid states could be identified. (b) First derivative of the evolution of absorbance at 500 nm in the case for natural drying (black) and air knife blowing (red), starting after 40 s of processing (left). Also shown is an illustration of the temporal evolution of perovskite concentration in the framework of a classical LaMer model in the case of nitrogen blowing during a solution state (red line), intermediate state (blue), or in the case of natural drying (black) (right). (a, b) Reprinted with permission from ref 36. Copyright 2019, Wiley-VCH. (c) Temporal evolution of $\text{MAPbI}_{3-x}\text{Cl}_x$ concentration during annealing at different temperatures, together with fits using a JMAK model with (solid lines) and without (dashed lines) considering a delay time t_{onset} (left). Reprinted with permission from ref 38. Published by the Royal Society of Chemistry. (d) Temporal evolution of PL peak position and PL intensity during annealing of MAPbI_3 using PbI_2 (top) or PbCl_2 (bottom) precursors. The shaded areas illustrate ΔE , which is defined as the difference of initial and final PL energy values. Also shown are corresponding 2D maps within the first 20 s of annealing (right). Reprinted with permission from ref 37. Copyright 2019, Wiley-VCH.

phase during spin-coating. However, for nominal halide ratios of $x = 0.3$ and 0.6 , a bromine-rich perovskite phase crystallizes with $x = 0.08$ and $x = 0.38$, respectively, as inferred from the absorption onsets. For higher iodine content, that is, $x = 0.7$ and pure MAPbI_3 , no perovskite phase but only a solvate phase is observed, identified by ex situ XRD. On the basis of the evolution of transmittance intensity associated with perovskite, they could find that the iodine delayed the perovskite formation for $x = 0.3$ and 0.6 , while the bromine delayed the intermediate phase formation for $x = 0.7$ with respect to pure MAPbI_3 . When annealed, also tracked by in situ transmittance and ex situ XRD, the perovskite continues to grow and finally reaches the correct halide ratio as initially introduced in the stock solution.

These examples demonstrate how improved control over the crystallization process can be obtained when monitoring the different steps in the crystal formation process. This also allows to choose the correct time for the addition of an additive, antisolvent, or the correct time for the start of a heating process.

4.2. Probing One Individual Optical Property In Situ to Understand Perovskite Formation. In situ optical spectroscopy is not only suitable to determine the timing of certain film formation dynamics when accompanying in situ scattering investigations. Rather, optical in situ spectroscopic data were also the basis for further analysis and for better understanding

the formation process. For example, Hu et al. monitored the drying behavior of a triple cation perovskite ($\text{Cs}_{0.05}\text{FA}_{0.81}\text{MA}_{0.14}\text{PbI}_{2.55}\text{Br}_{0.45}$) (FA = formamidinium) in a DMF/DMSO (DMSO = dimethyl sulfoxide) mixture at room temperature using in situ absorption measurements.³⁶ In the course of a simple one-step processing, they could identify an intermediate phase occurring between the initial solution phase and the final solid phase (Figure 5a). The intermediate exhibits a wavelength-independent increase in absorption intensity, due to light scattering at structures with sizes in the range of the wavelength of the incident light. In contrast, for perovskite crystallization, the measured absorption intensity increases more strongly in the shorter wavelength range, especially below 700 nm (Figure 5a). On the basis of the timings of the film-formation phases determined by the in situ monitoring, Hu et al. then used a nitrogen air knife and systematically applied it during the different film-formation phases.³⁶ This allowed accelerating the solvent evaporation starting from the moment of nitrogen blowing. The accelerated timings of the film-formation steps and the formation of a stronger perovskite signal were monitored again by in situ absorption measurements. They calculated the first derivative of the measured absorption dA/dt at 500 nm, (i.e., at a wavelength at which the perovskite absorbs) for the natural drying case and for the case when the air knife starts after

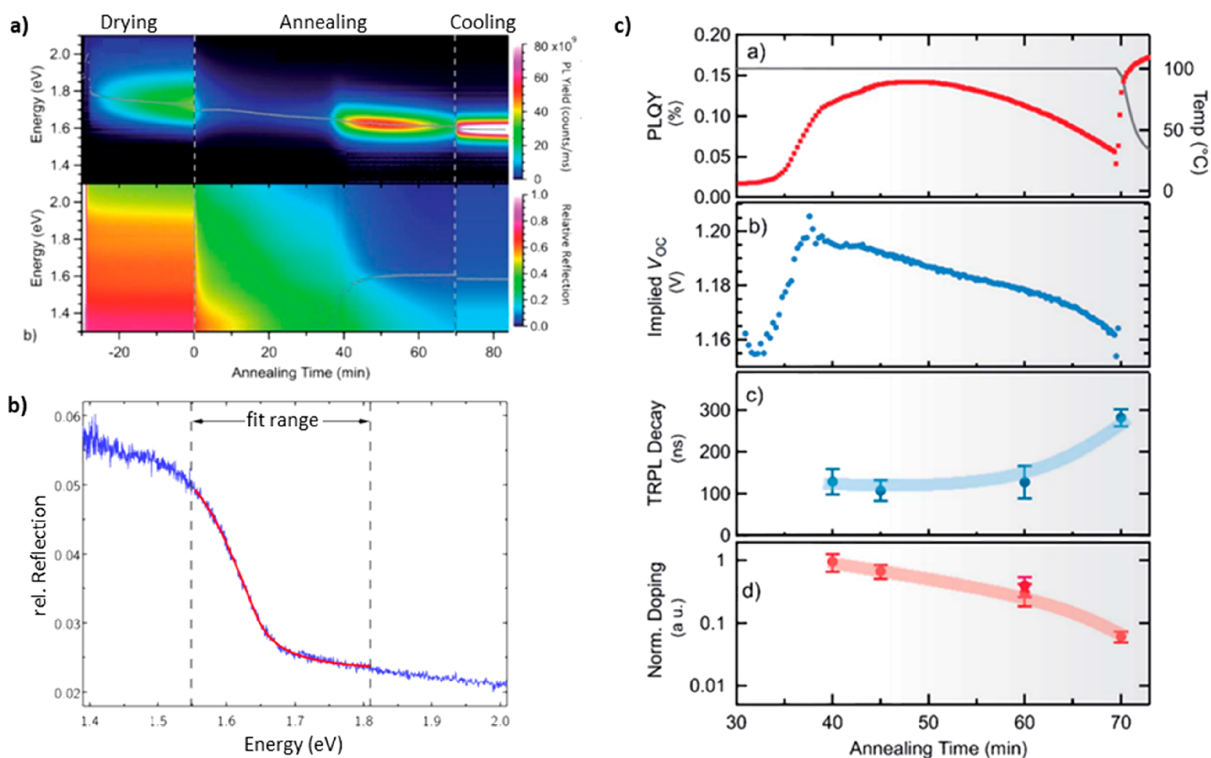


Figure 6. (a) In situ PL and absorption during the processing of an $\text{MAPbI}_{3-x}\text{Cl}_x$ film. (b) Fit of eq 7 to a transmittance spectrum. (c) PLQY (top), calculated implied V_{OC} (top middle), measured PL lifetimes (bottom middle), and calculated relative change in doping density as a function of annealing time. (a–c) Reprinted with permission from ref 38. Published by the Royal Society of Chemistry.

40 s (i.e., during the solution phase) (Figure 5b). This derivative qualitatively reflects the perovskite growth rate, which increased by 2 orders of magnitude upon applying the air knife (Figure 5b). In addition, Hu et al. compared the calculated dA/dt with the expectation of the evolution of perovskite concentration in the framework of a LaMer model to understand the nucleation and growth dynamics with different, growth-rate-dependent supersaturation scenarios (Figure 5b). On the basis of this understanding of the in situ absorption data, it finally was possible to adjust and optimize process parameters to obtain high-quality perovskite thin films, leading to perovskite solar cells with efficiencies above 20%.³⁶

Suchan et al. recently investigated the nucleation and growth of $\text{MAPbI}_{3-x}\text{Cl}_x$ during annealing at different temperatures.³⁸ They considered the temporal evolution of perovskite absorption, which was extracted from in situ transmittance measurements (Section 3) during annealing. For all investigated annealing temperatures, the resulting time-dependent absorption showed a sigmoidal increase (Figure 5c), which they analyzed in the framework of a modified Johnson-Mehl-Avrami-Kolmogorow (JMAK) model for a nucleation and growth process.

In this model the temporal evolution of the perovskite concentration $c(t)$ is described as

$$c(t) = 1 - e^{-(k_0 e^{-(E_a^F/RT)}(t-t_{\text{onset}}))^n} \quad \text{for } t > t_{\text{onset}} \quad (6)$$

with k_0 representing the rate constant, n corresponding to the dimensionality of the growth, E_a^F being the activation energy of the $\text{MAPbI}_{3-x}\text{Cl}_x$ formation, and t_{onset} being a delay time. Only when taking into account t_{onset} in the JMAK model, it was

possible to fit the evolution of perovskite absorption for all investigated temperatures, allowing to quantify $E_a^F = (94 \pm 2) \text{ kJ mol}^{-1}$ as well as an activation energy of the delay time $E_a^O = (84 \pm 7) \text{ kJ mol}^{-1}$ (Figure 5c). Furthermore, an exponent of $n = 2.1 \pm 0.1$ indicated a two-dimensional (2D) growth of the perovskite.³⁸

Recently, Song et al. investigated the crystallization of MAPbI_3 during a spin coating from a solution and during a subsequent annealing for different lead precursors.³⁷ Here in situ PL monitored the film formation, and the measured spectra were analyzed by fitting a Gaussian function to the PL peak. This allowed to extract the PL peak position, full width at half-maximum (fwhm), and PL intensity as a function of annealing time (Figure 5d). For all lead precursors used, the authors observed an initial appearance of PL, located at higher photon energies than typical bulk PL. The peak shifts to lower energies within the first few seconds, accompanied by a reduction of fwhm. As described in Section 2, both optical signatures indicate a confinement effect, so that the initial PL dynamics can be associated with the growth of perovskite nuclei. For the PbCl_2 precursor, that is, in the case of the crystallization of $\text{MAPbI}_{3-x}\text{Cl}_x$, the PL disappears after the fast initial redshift and reappears only after a certain delay time (Figure 5d). A disappearance of optical features of $\text{MAPbI}_{3-x}\text{Cl}_x$ in an intermediate time range is in line with the above-described results from Suchan et al.³⁸

From the works presented in this section it becomes clear that monitoring single optical properties in situ during processing already allows to gain important insights into the perovskite film formation. This includes accessing nucleation and growth

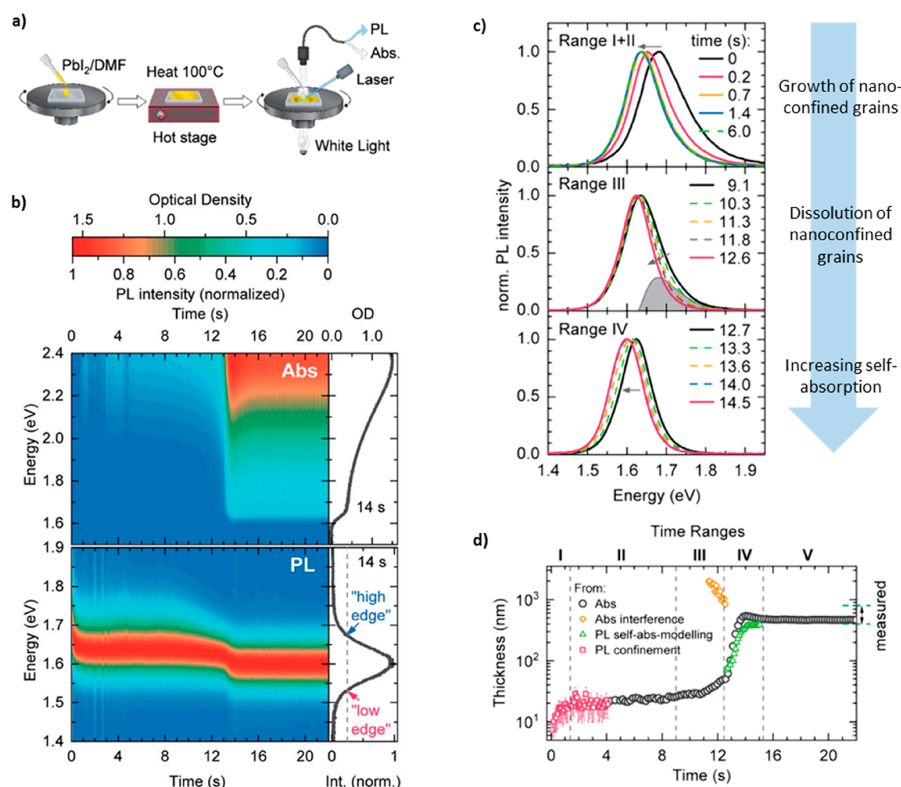


Figure 7. (a) Illustration of the MAPbI₃ two-step processing, with in situ monitoring of PL and absorption during the second processing step. (b) 2D Maps of the evolution of absorption (top) and normalized PL (bottom) during spin coating. (c) Evolution of PL spectra during processing in Time Range I+II (top), Time Range III (middle), and Time Range IV (bottom). Corresponding origins for the different PL shifts are indicated at the right. (d) Evolution of film thickness during spin-coating derived with different approaches, that is, by converting OD into thickness (black), by exploiting thin-film interference (orange diamonds), by association with a confinement effect (red squares), and by associating the PL shift with a self-absorption (green triangles). (a–d) Reprinted with permission from ref 39. Copyright 2020, Royal Society of Chemistry.

dynamics or identifying the initial perovskite growth by exploiting PL quantum confinement effects. However, to gain an even more complete picture of perovskite formation, it is necessary to access additional optoelectronic properties. This, for example, is possible by simultaneous measurements of several optical signals such as PL and absorption/reflection, which is the topic of the following section.

4.3. Understanding Perovskite Film Formation Based on a Simultaneous Monitoring of Multiple Optical Signals. When measuring different optical quantities simultaneously, it is possible to extract considerably more insight about the perovskite formation than when considering only one component. Despite this fact investigations of the film-formation dynamics of halide perovskites by multiple, simultaneously measured optical properties are still rare.

Suchan et al. investigated the spin coating and thermal annealing of the chlorine-derived synthesis of MAPbI_{3-x}Cl_x by in situ transmittance and PL measurements (Figure 6a), which are supported by XRD and X-ray fluorescence (XRF) measurements.³⁸ The absorption was extracted from the transmittance data R , assuming a spectrally constant reflection R_0 at the perovskite–air interface and full reflection at the bottom of the mirrored substrate, that is

$$R(\lambda, t) = R_0(t) + R_1(t)\exp(-\alpha(\lambda, t)2dc(t)) \quad (7)$$

where R_1 is a constant, α is the absorption coefficient of the perovskite, d is the overall film thickness, which is assumed to be constant, and c is the relative concentration of the perovskite. The spectral dependence of the absorption coefficient was approximated by a direct band-to-band absorption with band gap E_g in combination with Urbach tail absorption with the Urbach energy E_u , yielding

$$\alpha(E) = \begin{cases} \alpha_0 \sqrt{E - E_g} & \text{for } E > E_g + E_u/2 \\ \alpha_0 \sqrt{\frac{E_u}{2e}} \exp\left(\frac{E - E_g}{E_u}\right) & \text{for } E < E_g + E_u/2 \end{cases} \quad (8)$$

Here the upper branch describes the band-to-band absorption, while the lower branch represents the exponential Urbach tail absorption. Figure 6b shows a fit of the measured transmittance data using eqs 7 and 8. While the applicability of the model well-below the band gap might be limited as discussed in Section 2, it allows to determine the concentration of perovskite phase $c(t)$, as evidenced by a good agreement of $c(t)$ determined by ex situ XRD and in situ transmittance data. As described before, when analyzing $c(t)$, Suchan et al. observed that the MAPbI_{3-x}Cl_x crystallization during annealing was delayed, that is, starting only after a certain time t_{onset} (Figure 5c), presumably due to the presence of excess chloride.³⁸

In corresponding PL data (Figure 6a), the delayed MAPbI_{3-x}Cl_x crystallization is reflected by a significant increase of PL intensity and PLQY after t_{onset} (here after ~40 s). During spin coating ($t < 0$ s range) and at early annealing times, a clear PL feature was observable, which significantly dropped in intensity upon further annealing until t_{onset} . At the same time, the PL peak shifted to lower energies, which was associated with a halide exchange in MAPbI_{3-x}Cl_x toward a higher iodine concentration. The PL results from Suchan et al. deviate to some extent from the PL results for MAPbI_{3-x}Cl_x by Song et al. (Figure 5d) insofar as Song et al. observed a complete PL quenching until t_{onset} .³⁷ This could be due to differences in the exact processing and measurement conditions, which were attributed in the literature to lead to different MAPbI_{3-x}Cl_x crystallization behaviors.³⁸

Suchan et al. were able to quantify the time-dependent absolute PL intensity, which, together with the transmittance data, allowed calculating the PLQY and, in turn, the implied V_{OC} during annealing, by using an equation similar to eq 3. In the course of annealing, the PLQY as well as implied V_{OC} increased, reached a maximum, and then decreased again (Figure 6c). The implied V_{OC} peaked after 38 min of annealing (i.e., even before the PLQY), when only ~30% of the perovskite had formed. To investigate the decrease of PLQY and implied V_{OC} in more detail, the time-resolved PL at different annealing times was measured. Considering corresponding PLQY values, they could calculate the relative change of doping density according to $\text{PLQY} \propto \tau n_0 a_e$, where τ is the minority carrier lifetime, n_0 is the net doping density, and a_e is the absorptivity at the emission wavelength (Figure 6c). It turned out that the calculated doping density decreased, which they associated with the decrease of the implied V_{OC} .

We recently investigated the two-step processing of MAPbI₃ with spin coating, using the optical detection system and the spin coater described in Section 3 (Figure 3a,e).^{39,40} We monitored in situ the evolution of optical properties during the second processing step, that is, starting when MAI dissolved in isopropyl alcohol is dripped onto a PbI₂ thin film that was produced in a prior, first processing step (Figure 7a). On the basis of the measured PL and absorption within the first 22 s of spin coating (Figure 7b), the film-formation process of MAPbI₃ could be divided into five different time ranges.

While no clear absorption was detected directly after dripping an MAI/IPA solution, a PL signal was already present, appearing at higher photon energies compared to typical MAPbI₃ bulk values (Figure 7c top). This PL shifted rapidly toward lower energies within the first second of spin coating. We associated the blue-shifted PL to stem from a quantum confinement effect, similar to that of Song et al. in Section 4.2. Using the dependency of the PL peak position on the crystal size (see eq 5 and Figure 2e), we quantified the temporal growth of MAPbI₃ crystals in Time Range I (Figure 7d). After 1.5 s the crystal size reached values of ~20 nm, connecting well to the film thicknesses after ~4 s, which were calculated from the absorption measurements using the Beer–Lambert law (Figure 7d). This match suggested that an MAPbI₃ layer, monocrystalline in vertical direction, formed during the Time Range I. In the Time Range II, this compact MAPbI₃ layer prevents further MAI diffusion into the now buried PbI₂ layer, thus acting as a capping layer, which was concluded from the temporally constant PL and absorption spectra.

In Time Range III, a narrowing of the PL on the high-energy edge was observed (Figure 7c middle). To better understand

this PL dynamic, we modeled the spectra using a simple optical model, which considers extended optical paths within the perovskite due to internal reflections at the interface to adjacent media.^{68,78} It turned out that an increase of perovskite layer thickness to ~500 nm during Time Range III would be necessary to model the experimentally observed PL shift, in order to attribute it to self-absorption. This was in clear contradiction to the layer thicknesses extracted by absorption, which were ~1 order of magnitude lower (see Figure 7d between 9.1 and 12.6 s). However, the difference spectrum (gray area in Figure 7c middle) between the PL at the beginning and the end of Time Range III matched well the PL spectrum at 0 s, allowing to associate the difference PL to PL from still nanoconfined grains in the capping layer. A shift of the difference spectrum in the course of Time Range III toward lower energies would indicate a growth of the nanoconfined grains, but this was not observed. Rather, the difference spectrum maintained its spectral shape and position during Time Range III, while its relative intensity decreased. Thus, a detailed PL analysis and simultaneous consideration of absorption allowed to exclude a significant self-absorption effect as well as the growth of nanoconfined grains during Time Range III. In fact, it enabled to identify the beginning of a dissolution process of nanoconfined grains in the capping layer. This is consistent with a dissolution-recrystallization reaction, which was suggested in literature to occur in the course of perovskite two-step processing.^{111,112} Here the dissolution of MAPbI₃ is enabled by an increasing iodine concentration in the MAI/IPA droplet upon solvent evaporation. In Time Range IV the reaction then shifts intensively to the recrystallization process, resulting in a strong increase of perovskite layer thickness, extracted from the absorption data (Figure 7d). In Time Range IV, it was indeed possible to fit the shifting PL using the optical model mentioned above. Here the perovskite layer thicknesses extracted from the PL modeling in Time Range IV matched very well with the thicknesses determined from absorption, which allowed to attribute the PL change in Time Range IV to an increasing self-absorption effect. Thus, it was possible to access the temporal evolution of the layer thickness, during the entire film formation process, by analyzing the different optical quantities in detail (Figure 7d). This finally allowed to quantify the growth rates of the perovskite crystallization steps from the slopes in Figure 7d, where a high rate of 445 nm/s of the recrystallization process in Time Range IV pointed toward its crucial role in the film-formation dynamics.³⁹

Very recently, simultaneous PL and absorption spectroscopy was used to in situ monitor the formation of mixed perovskite (FAPbI₃)_{0.875}(CsPbBr₃)_{0.125} during spin coating.⁹⁶ Together with considering the layer thicknesses of the final films, the evolution of PL peak position, PL peak width, and energetic position of the absorption edge could be extracted as a function of layer thickness. A simultaneous decrease of all three optical parameters indicated the presence of a confinement effect at early processing times. For longer times and subsequently for higher-layer thicknesses, the PL peak position and energetic position of the absorption edge further decreased, while the PL peak width remained constant. Such a behavior was attributed to a change in the stoichiometry, suggesting a more Cs- and Br-rich stoichiometry at early spin coating times followed by a more pronounced incorporation of FA and I at longer times.⁹⁶

From the discussed works in this section, it thus becomes clear that considering two or even more optical signals simultaneously, during the perovskite processing, allows to extract more

information compared to when having only single optical signals so that deep insights about the occurring film formation dynamics can be gained.

5. CONCLUSION AND FUTURE PROSPECTS

This Perspective highlights recent developments in the field of in situ monitoring the film-formation process of halide perovskites using optical spectroscopy. It becomes clear that in situ optical spectroscopy allows investigating the perovskite film formation at different levels of detail, depending on the individual aims and needs. This starts with the direct consideration of the measured data such as PL or absorption intensity, to quantify the timings of film-formation steps, and can extend to access parameters, which are calculated on the basis of a detailed analysis of the measured in situ data. These parameters even allow to access the evolution of the potential optoelectronic functionality of the perovskite during processing such as the implied V_{OC} . Furthermore, in situ optical spectroscopy enables enhanced process control not only for lab-relevant processing methods such as spin coating but also for solution-based methods that allow for easy upscaling such as blade coating. The basis for this is the technical development of the last years, which improved and facilitated the accessibility of in situ optical spectroscopy. This is likely to be beneficial for the entire halide perovskite community, be it for a simple monitoring of timings or for complex multimodal measurements, for example, at beamlines, to gain more in-depth insight about the perovskite film formation.

Regarding the investigated material systems so far, mainly the model halide perovskite MAPbI₃ was the focus of interest. This is fair enough, as the crystallization behavior of such a ternary perovskite appears to be well-suited to investigate basic crystallization concepts or to develop in situ techniques. However, more complex multinary halide perovskites are more relevant for efficient perovskite-based optoelectronic devices, making investigating their film formation process by optical spectroscopy an important future topic. Here we expect that the additional insight provided from a detailed analysis of the data will be increasingly relevant, for example, to clearly differentiate a change of perovskite stoichiometry from other effects such as PL quantum confinement or changes in microstrain of the perovskite.

The latter aspect has to the best of our knowledge not yet been explicitly considered in the analysis of in situ PL data during film formation, even though it is known that changes in microstrain affect the perovskite optical properties. It also has become apparent that microstrain can significantly impact the optoelectronic properties of a perovskite layer,¹¹³ making it feasible that changes in strain also occur during film formation. Because of the possibility to differentiate the optical signatures of changes in strain from other effects such as quantum confinement (Section 2), especially in situ PL spectroscopy could become a valuable method to investigate, e.g., epitaxial growth of perovskites in the future.¹¹⁴ It could also be used to facilitate a targeted stabilization and strain management of perovskite structures and interfaces in optoelectronic devices.^{96,115}

Another future aspect of optical in situ spectroscopy becomes obvious when considering that, so far, only the formation of the perovskite has been investigated, but little attention has been paid to investigate solvent states and intermediate complex states during film formation by optical in situ spectroscopy. It is known that, already in the precursor solution, for example,

depending on the iodine concentration and solvent, different iodoplumbate complexes such as PbI₃⁻ or PbI₄²⁻ can form, which show clear absorption signatures in the UV range.^{116,117} The further perovskite crystallization was found to strongly depend on these precursor states,^{118,119} making it important to study and understand the dynamics of these solution states during a perovskite processing. This is especially important for solvent mixtures, as they are often used in state-of-the-art perovskite solution processing. Here, predominantly in situ absorption with a sufficient time resolution could be an attractive characterization method to directly investigate the transformation from precursor solution to perovskite during solution processing.

Also, when it comes to the perovskite crystallization, there is still potential to gain a more fundamental understanding with the help of optical in situ spectroscopy. In particular, the formation of intermediate phases or the formation of crystalline perovskite solvent complexes often plays an important role for the film formation process, where, for example, needlelike structures can form.^{19,20,120–123} However, these features have so far been studied mainly using scattering techniques,^{19,21,24} while only a few studies used optical in situ spectroscopy.¹²⁴ One reason for this could be that these crystalline structures are often optically inactive and have a rather transparent appearance, preventing the measurement of intense and clear PL or absorption signatures. During the film-formation process, solvent complex structures often exist on length scales comparable to the wavelength range of typical light sources used for the spectroscopic investigations. This circumstance could be used to utilize the optical scattering expected at the solvent complexes, to indirectly characterize the crystallization dynamics and also the transformation of the complex structures to pure perovskites. This could be measured, for example, with the help of in situ reflection spectroscopy, but also when measuring in situ transmission spectra, optical scattering at solvent complex phases would become noticeable by a baseline lift in the optical density.

Finally, it can be noted that the available optical data that are obtained, and possibly even already processed, in the course of film formation may allow for a significant advance, if not even a paradigm shift, in the preparation of halide perovskite-based devices. It allows moving from a rigid processing protocol (that was retrospectively obtained from previous measurements) with set timings for each step, to a process control that relies on the evolution of optical signatures. In combination with high-throughput methods such as automatized and autonomous setups including KI supported data analysis, optical in situ measurements during a perovskite formation could evolve as a substantial building stone to impel the commercialization of perovskite-based optoelectronic devices in the future.

■ AUTHOR INFORMATION

Corresponding Author

Fabian Panzer – *Soft Matter Optoelectronics, University of Bayreuth, Bayreuth 95440, Germany*; orcid.org/0000-0002-2191-9011; Email: fabian.panzer@uni-bayreuth.de

Author

Konstantin Schötz – *Soft Matter Optoelectronics, University of Bayreuth, Bayreuth 95440, Germany*

Complete contact information is available at:
<https://pubs.acs.org/10.1021/acs.jpca.0c10765>

Notes

The authors declare no competing financial interest.

Biographies



Konstantin Schötz received his Master of Science in Physics from the University of Bayreuth, Germany, in 2017. He is currently a Ph.D. student under the supervision of Dr. Fabian Panzer and Prof. Dr. Anna Köhler at the group of Soft Matter Optoelectronics at the University of Bayreuth. His major research interest lies in the optical and optoelectronic properties and their relation to the structure of halide perovskites, organic semiconductors, and spin-crossover complexes.



Fabian Panzer is Habilitation candidate and leads the perovskite subgroup within the Soft Matter Optoelectronics group at the University of Bayreuth. He completed his Diploma in Physics in 2013 at the University of Bayreuth, where he also obtained his Ph.D. in 2016. His research focuses on understanding the processing of emerging semiconductors such as halide perovskites or organic semiconductors, for application in optoelectronic devices like solar cells or X-ray detectors.

ACKNOWLEDGMENTS

K.S. acknowledges financial support by the German National Science Foundation DFG via the project Ko 3973/2-1. We thank the Bavarian State Ministry of Science, Research, and the Arts for support through the Collaborative Research Network "Solar Technologies go Hybrid". We further thank Prof. A. Köhler for proof reading.

REFERENCES

- (1) Kojima, A.; Teshima, K.; Shirai, Y.; Miyasaka, T. Organometal Halide Perovskites as Visible-Light Sensitizers for Photovoltaic Cells. *J. Am. Chem. Soc.* **2009**, *131* (17), 6050–6051.
- (2) Kim, H. S.; Lee, C. R.; Im, J. H.; Lee, K. B.; Moehl, T.; Marchioro, A.; Moon, S. J.; Humphry-Baker, R.; Yum, J. H.; Moser, J. E.; et al. Lead

Iodide Perovskite Sensitized All-Solid-State Submicron Thin Film Mesoscopic Solar Cell with Efficiency Exceeding 9%. *Sci. Rep.* **2012**, *2*, 591.

- (3) Lee, M. M.; Teuscher, J.; Miyasaka, T.; Murakami, T. N.; Snaith, H. J. Efficient Hybrid Solar Cells Based on Meso-Structured Organometal Halide Perovskites. *Science* **2012**, *338* (6107), 643–647.
- (4) Panzer, F.; Li, C.; Meier, T.; Köhler, A.; Huettner, S. Impact of Structural Dynamics on the Optical Properties of Methylammonium Lead Iodide Perovskites. *Adv. Energy Mater.* **2017**, *7* (16), 1700286.
- (5) Baranowski, M.; Plochocka, P. Excitons in Metal-Halide Perovskites. *Adv. Energy Mater.* **2020**, *10* (26), 1903659.
- (6) Stranks, S. D.; Eperon, G. E.; Grancini, G.; Menelaou, C.; Alcocer, M. J. P.; Leijtens, T.; Herz, L. M.; Petrozza, A.; Snaith, H. J. Electron-Hole Diffusion Lengths Exceeding 1 Micrometer in an Organometal Trihalide Perovskite Absorber. *Science* **2013**, *342* (6156), 341–344.
- (7) Zhumekenov, A. A.; Saidaminov, M. I.; Haque, M. A.; Alarousu, E.; Sarmah, S. P.; Murali, B.; Dursun, I.; Miao, X. H.; Abdelhady, A. L.; Wu, T.; et al. Formamidinium Lead Halide Perovskite Crystals with Unprecedented Long Carrier Dynamics and Diffusion Length. *ACS Energy Lett.* **2016**, *1* (1), 32–37.
- (8) Ma, C. Q.; Park, N. G. A Realistic Methodology for 30% Efficient Perovskite Solar Cells. *Chem-Us* **2020**, *6* (6), 1254–1264.
- (9) Park, M. H.; Kim, J. S.; Heo, J. M.; Ahn, S.; Jeong, S. H.; Lee, T. W. Boosting Efficiency in Polycrystalline Metal Halide Perovskite Light-Emitting Diodes. *ACS Energy Lett.* **2019**, *4* (5), 1134–1149.
- (10) Sytnyk, M.; Deumel, S.; Tedde, S. F.; Matt, G. J.; Heiss, W. A Perspective on the Bright Future of Metal Halide Perovskites for X-Ray Detection. *Appl. Phys. Lett.* **2019**, *115* (19), 190501.
- (11) Kakavelakis, G.; Gedda, M.; Panagiotopoulos, A.; Kymakis, E.; Anthopoulos, T. D.; Petridis, K. Metal Halide Perovskites for High-Energy Radiation Detection. *Adv. Sci.* **2020**, *7*, 2002098.
- (12) Basiricò, L.; Ciavatti, A.; Fraboni, B. Solution-Grown Organic and Perovskite X-Ray Detectors: A New Paradigm for the Direct Detection of Ionizing Radiation. *Adv. Mater. Technol-Us* **2020**, 2000475.
- (13) Salim, T.; Sun, S. Y.; Abe, Y.; Krishna, A.; Grimsdale, A. C.; Lam, Y. M. Perovskite-Based Solar Cells: Impact of Morphology and Device Architecture on Device Performance. *J. Mater. Chem. A* **2015**, *3* (17), 8943–8969.
- (14) Tailor, N. K.; Abdi-Jalebi, M.; Gupta, V.; Hu, H. L.; Dar, M. I.; Li, G.; Satapathi, S. Recent Progress in Morphology Optimization in Perovskite Solar Cell. *J. Mater. Chem. A* **2020**, *8* (41), 21356–21386.
- (15) Saliba, M.; Correa-Baena, J. P.; Wolff, C. M.; Stollerfoht, M.; Phung, N.; Albrecht, S.; Neher, D.; Abate, A. How to Make over 20% Efficient Perovskite Solar Cells in Regular (n-i-p) and Inverted (p-i-n) Architectures. *Chem. Mater.* **2018**, *30* (13), 4193–4201.
- (16) Dunlap-Shohl, W. A.; Zhou, Y. Y.; Padture, N. P.; Mitzi, D. B. Synthetic Approaches for Halide Perovskite Thin Films. *Chem. Rev.* **2019**, *119* (5), 3193–3295.
- (17) Zhong, Y. F.; Munir, R.; Li, J. B.; Tang, M. C.; Niazi, M. R.; Smilgies, D. M.; Zhao, K.; Amassian, A. Blade-Coated Hybrid Perovskite Solar Cells with Efficiency > 17%: An In Situ Investigation. *ACS Energy Lett.* **2018**, *3* (5), 1078–1085.
- (18) Barrit, D.; Sheikh, A. D.; Munir, R.; Barbé, J. M.; Li, R. P.; Smilgies, D. M.; Amassian, A. Hybrid Perovskite Solar Cells: In situ Investigation of Solution-Processed PbI₂ Reveals Metastable Precursors and a Pathway to Producing Porous Thin Films. *J. Mater. Res.* **2017**, *32* (10), 1899–1907.
- (19) Bruening, K.; Tassone, C. J. Antisolvent Processing of Lead halide Perovskite Thin Films Studied by In Situ X-Ray Diffraction. *J. Mater. Chem. A* **2018**, *6* (39), 18865–18870.
- (20) Meng, K.; Wu, L. L.; Liu, Z.; Wang, X.; Xu, Q. F.; Hu, Y. D.; He, S. F.; Li, X. L.; Li, T.; Chen, G. In Situ Real-Time Study of the Dynamic Formation and Conversion Processes of Metal Halide Perovskite Films. *Adv. Mater.* **2018**, *30* (11), 1706401.
- (21) Hu, Q.; Zhao, L. C.; Wu, J.; Gao, K.; Luo, D. Y.; Jiang, Y. F.; Zhang, Z. Y.; Zhu, C. H.; Schaible, E.; Hexemer, A.; et al. In Situ Dynamic Observations of Perovskite Crystallisation and Micro-

- structure Evolution Intermediated from $[\text{PbI}_6]^{4-}$ Cage Nanoparticles. *Nat. Commun.* **2017**, *8*, 15688.
- (22) Ternes, S.; Börnhorst, T.; Schwenzer, J. A.; Hossain, I. M.; Abzieher, T.; Mehlmann, W.; Lemmer, U.; Scharfer, P.; Schabel, W.; Richards, B. S.; et al. Drying Dynamics of Solution-Processed Perovskite Thin-Film Photovoltaics: In Situ Characterization, Modeling, and Process Control. *Adv. Energy Mater.* **2019**, *9* (39), 1901581.
- (23) Pistor, P.; Borchert, J.; Fränzel, W.; Csuk, R.; Scheer, R. Monitoring the Phase Formation of Coevaporated Lead Halide Perovskite Thin Films by in Situ X-ray Diffraction. *J. Phys. Chem. Lett.* **2014**, *5* (19), 3308–3312.
- (24) Munir, R.; Sheikh, A. D.; Abdelsamie, M.; Hu, H. L.; Yu, L.; Zhao, K.; Kim, T.; El Tall, O.; Li, R. P.; Smilgies, D. M.; et al. Hybrid Perovskite Thin-Film Photovoltaics: In Situ Diagnostics and Importance of the Precursor Solvate Phases. *Adv. Mater.* **2017**, *29* (2), 1604113.
- (25) Anaya, M.; Galisteo-López, J. F.; Calvo, M. E.; López, C.; Míguez, H. Photophysical Analysis of the Formation of Organic-Inorganic Trihalide Perovskite Films: Identification and Characterization of Crystal Nucleation and Growth. *J. Phys. Chem. C* **2016**, *120* (5), 3071–3076.
- (26) Abdelsamie, M.; Xu, J. W.; Bruening, K.; Tassone, C. J.; Steinrück, H. G.; Toney, M. F. Impact of Processing on Structural and Compositional Evolution in Mixed Metal Halide Perovskites during Film Formation. *Adv. Funct. Mater.* **2020**, *30* (38), 2001752.
- (27) Güldal, N. S.; Kassar, T.; Berlinghof, M.; Ameri, T.; Osvet, A.; Pacios, R.; Li Destri, G.; Unruh, T.; Brabec, C. J. Real-Time Evaluation of Thin Film Drying Kinetics Using an Advanced, Multi-Probe Optical Setup. *J. Mater. Chem. C* **2016**, *4* (11), 2178–2186.
- (28) Chang, C. Y.; Huang, Y. C.; Tsao, C. S.; Su, W. F. Formation Mechanism and Control of Perovskite Films from Solution to Crystalline Phase Studied by in Situ Synchrotron Scattering. *ACS Appl. Mater. Interfaces* **2016**, *8* (40), 26712–26721.
- (29) Barrit, D.; Cheng, P. R.; Tang, M. C.; Wang, K.; Dang, H.; Smilgies, D. M.; Liu, S. Z.; Anthopoulos, T. D.; Zhao, K.; Amassian, A. Impact of the Solvation State of Lead Iodide on Its Two-Step Conversion to MAPbI_3 : An In Situ Investigation. *Adv. Funct. Mater.* **2019**, *29* (47), 1807544.
- (30) Wang, K.; Tang, M. C.; Dang, H. X.; Munir, R.; Barrit, D.; De Bastiani, M.; Aydin, E.; Smilgies, D. M.; De Wolf, S.; Amassian, A. Kinetic Stabilization of the Sol-Gel State in Perovskites Enables Facile Processing of High-Efficiency Solar Cells. *Adv. Mater.* **2019**, *31* (32), 1808357.
- (31) Meng, K.; Wang, X.; Xu, Q. F.; Li, Z. M.; Liu, Z.; Wu, L. L.; Hu, Y. D.; Liu, N.; Chen, G. In Situ Observation of Crystallization Dynamics and Grain Orientation in Sequential Deposition of Metal Halide Perovskites. *Adv. Funct. Mater.* **2019**, *29* (35), 1902319.
- (32) Xie, Y. M.; Yu, B. B.; Ma, C. Q.; Xu, X. W.; Cheng, Y. H.; Yuan, S.; Wang, Z. K.; Chandran, H. T.; Lee, C. S.; Liao, L. S.; et al. Direct Observation of Cation-Exchange in Liquid-to-Solid Phase Transformation in $\text{FA}_{1-x}\text{MA}_x\text{PbI}_3$ based Perovskite Solar Cells. *J. Mater. Chem. A* **2018**, *6* (19), 9081–9088.
- (33) Wilson, K. S.; Wong, C. Y. In Situ Measurement of Exciton Dynamics During Thin-Film Formation Using Single-Shot Transient Absorption. *J. Phys. Chem. A* **2018**, *122* (31), 6438–6444.
- (34) Burschka, J.; Pellet, N.; Moon, S. J.; Humphry-Baker, R.; Gao, P.; Nazeeruddin, M. K.; Grätzel, M. Sequential Deposition as a Route to High-Performance Perovskite-Sensitized Solar Cells. *Nature* **2013**, *499* (7458), 316–319.
- (35) Babbe, F.; Sutter-Fella, C. M. Optical Absorption-Based In Situ Characterization of Halide Perovskites. *Adv. Energy Mater.* **2020**, *10* (26), 1903587.
- (36) Hu, H. L.; Ren, Z. W.; Fong, P. W. K.; Qin, M. C.; Liu, D. J.; Lei, D. Y.; Lu, X. H.; Li, G. Room-Temperature Meniscus Coating of > 20% Perovskite Solar Cells: A Film Formation Mechanism Investigation. *Adv. Funct. Mater.* **2019**, *29* (25), 1900092.
- (37) Song, T. B.; Yuan, Z. H.; Mori, M.; Motiwala, F.; Segev, G.; Masquelier, E.; Stan, C. V.; Slack, J. L.; Tamura, N.; Sutter-Fella, C. M. Revealing the Dynamics of Hybrid Metal Halide Perovskite Formation via Multimodal In Situ Probes. *Adv. Funct. Mater.* **2020**, *30* (6), 1908337.
- (38) Suchan, K.; Just, J.; Becker, P.; Unger, E. L.; Unold, T. Optical In Situ Monitoring during the Synthesis of Halide Perovskite Solar Cells Reveals Formation Kinetics and Evolution of Optoelectronic Properties. *J. Mater. Chem. A* **2020**, *8* (20), 10439–10449.
- (39) Chauhan, M.; Zhong, Y.; Schötz, K.; Tripathi, B.; Köhler, A.; Huettner, S.; Panzer, F. Investigating Two-Step MAPbI_3 Thin Film Formation during Spin Coating by Simultaneous In Situ Absorption and Photoluminescence Spectroscopy. *J. Mater. Chem. A* **2020**, *8* (10), 5086–5094.
- (40) Buchhorn, M.; Wedler, S.; Panzer, F. Setup to Study the in Situ Evolution of Both Photoluminescence and Absorption during the Processing of Organic or Hybrid Semiconductors. *J. Phys. Chem. A* **2018**, *122* (46), 9115–9122.
- (41) Mosconi, E.; Amat, A.; Nazeeruddin, M. K.; Grätzel, M.; De Angelis, F. First-Principles Modeling of Mixed Halide Organometal Perovskites for Photovoltaic Applications. *J. Phys. Chem. C* **2013**, *117* (27), 13902–13913.
- (42) Brivio, F.; Walker, A. B.; Walsh, A. Structural and Electronic Properties of Hybrid Perovskites for High-Efficiency Thin-Film Photovoltaics from First-Principles. *APL Mater.* **2013**, *1* (4), 042111.
- (43) Zhu, X.; Su, H. B.; Marcus, R. A.; Michel-Beyerle, M. E. Computed and Experimental Absorption Spectra of the Perovskite $\text{CH}_3\text{NH}_3\text{PbI}_3$. *J. Phys. Chem. Lett.* **2014**, *5* (17), 3061–3065.
- (44) Lang, L.; Yang, J. H.; Liu, H. R.; Xiang, H. J.; Gong, X. G. First-Principles Study on the Electronic and Optical Properties of Cubic ABX_3 Halide Perovskites. *Phys. Lett. A* **2014**, *378* (3), 290–293.
- (45) Herz, L. M. Charge-Carrier Mobilities in Metal Halide Perovskites: Fundamental Mechanisms and Limits. *ACS Energy Lett.* **2017**, *2* (7), 1539–1548.
- (46) Davies, C. L.; Filip, M. R.; Patel, J. B.; Crothers, T. W.; Verdi, C.; Wright, A. D.; Milot, R. L.; Giustino, F.; Johnston, M. B.; Herz, L. M. Bimolecular Recombination in Methylammonium Lead Triiodide Perovskite is an Inverse Absorption Process. *Nat. Commun.* **2018**, *9*, 293.
- (47) Singh, S.; Li, C.; Panzer, F.; Narasimhan, K. L.; Graeser, A.; Gujar, T. P.; Köhler, A.; Thelakkat, M.; Huettner, S.; Kabra, D. Effect of Thermal and Structural Disorder on the Electronic Structure of Hybrid Perovskite Semiconductor $\text{CH}_3\text{NH}_3\text{PbI}_3$. *J. Phys. Chem. Lett.* **2016**, *7* (15), 3014–3021.
- (48) Pelant, I.; Valenta, J. Luminescence of Excitons. In *Luminescence Spectroscopy of Semiconductors*; Oxford University Press: Oxford, UK, 2012; pp 161–164.
- (49) Elliott, R. J. Intensity of Optical Absorption by Excitons. *Phys. Rev.* **1957**, *108* (6), 1384–1389.
- (50) Green, M. A.; Jiang, Y. J.; Soufiani, A. M.; Ho-Baillie, A. Optical Properties of Photovoltaic Organic-Inorganic Lead Halide Perovskites. *J. Phys. Chem. Lett.* **2015**, *6* (23), 4774–4785.
- (51) Kurik, M. V. Urbach Rule. *Phys. Status Solidi A* **1971**, *8* (1), 9–45.
- (52) Skettrup, T. Urbach Rule Derived from Thermal Fluctuations in Band-Gap Energy. *Phys. Rev. B: Condens. Matter Mater. Phys.* **1978**, *18* (6), 2622–2631.
- (53) Studenyak, I.; Kranjec, M.; Kurik, M. Urbach Rule in Solid State Physics. *Int. J. Opt.* **2014**, *4* (3), 76–83.
- (54) Urbach, F. The Long-Wavelength Edge of Photographic Sensitivity and of the Electronic Absorption of Solids. *Phys. Rev.* **1953**, *92* (5), 1324–1324.
- (55) Staub, F.; Hempel, H.; Hebig, J. C.; Mock, J.; Paetzold, U. W.; Rau, U.; Unold, T.; Kirchartz, T. Beyond Bulk Lifetimes: Insights into Lead Halide Perovskite Films from Time-Resolved Photoluminescence. *Phys. Rev. Appl.* **2016**, *6* (4), 044017.
- (56) Sumi, H.; Toyozawa, Y. Urbach-Martienssen Rule and Exciton Trapped Momentarily by Lattice Vibrations. *J. Phys. Soc. Jpn.* **1971**, *31* (2), 342–358.
- (57) Dow, J. D.; Redfield, D. Toward a Unified Theory of Urbachs Rule and Exponential Absorption Edges. *Phys. Rev. B* **1972**, *5* (2), 594–610.

- (58) Liebler, J. G.; Schmittink, S.; Haug, H. Theory of the Absorption Tail of Wannier Excitons in Polar Semiconductors. *J. Lumin.* **1985**, *34* (1–2), 1–7.
- (59) Grein, C. H.; John, S. Temperature-Dependence of the Urbach Optical-Absorption Edge - a Theory of Multiple Phonon Absorption and Emission Sidebands. *Phys. Rev. B: Condens. Matter Mater. Phys.* **1989**, *39* (2), 1140–1151.
- (60) Cody, G. D.; Tiedje, T.; Abeles, B.; Brooks, B.; Goldstein, Y. Disorder and the Optical-Absorption Edge of Hydrogenated Amorphous-Silicon. *Phys. Rev. Lett.* **1981**, *47* (20), 1480–1483.
- (61) Würfel, P. The Chemical-Potential of Radiation. *J. Phys. C: Solid State Phys.* **1982**, *15* (18), 3967–3985.
- (62) Daub, E.; Würfel, P. Ultralow Values of the Absorption-Coefficient of Si Obtained from Luminescence. *Phys. Rev. Lett.* **1995**, *74* (6), 1020–1023.
- (63) Ross, R. T. Some Thermodynamics of Photochemical Systems. *J. Chem. Phys.* **1967**, *46* (12), 4590–4593.
- (64) Caprioglio, P.; Stolterfoht, M.; Wolff, C. M.; Unold, T.; Rech, B.; Albrecht, S.; Neher, D. On the Relation between the Open-Circuit Voltage and Quasi-Fermi Level Splitting in Efficient Perovskite Solar Cells. *Adv. Energy Mater.* **2019**, *9* (33), 1901631.
- (65) Johnston, M. B.; Herz, L. M. Hybrid Perovskites for Photovoltaics: Charge-Carrier Recombination, Diffusion, and Radiative Efficiencies. *Acc. Chem. Res.* **2016**, *49* (1), 146–154.
- (66) Manificier, J. C.; Gasiot, J.; Fillard, J. P. Simple Method for Determination of Optical-Constants n, k and Thickness of a Weakly Absorbing Thin-Film. *J. Phys. E: Sci. Instrum.* **1976**, *9* (11), 1002–1004.
- (67) Tian, Y. X.; Scheblykin, I. G. Artifacts in Absorption Measurements of Organometal Halide Perovskite Materials: What Are the Real Spectra? *J. Phys. Chem. Lett.* **2015**, *6* (17), 3466–3470.
- (68) Schötz, K.; Askar, A. M.; Peng, W.; Seeberger, D.; Gujar, T. P.; Thelakkat, M.; Köhler, A.; Huettner, S.; Bakr, O. M.; Shankar, K.; et al. Double Peak Emission in Lead Halide Perovskites by Self-Absorption. *J. Mater. Chem. C* **2020**, *8* (7), 2289–2300.
- (69) Parrott, E. S.; Patel, J. B.; Haghighirad, A. A.; Snaith, H. J.; Johnston, M. B.; Herz, L. M. Growth Modes and Quantum Confinement in Ultrathin Vapour-Deposited MAPbI₃ Films. *Nanoscale* **2019**, *11* (30), 14276–14284.
- (70) Ball, J. M.; Stranks, S. D.; Hoerantner, M. T.; Huettner, S.; Zhang, W.; Crossland, E. J. W.; Ramirez, I.; Riede, M.; Johnston, M. B.; Friend, R. H.; et al. Optical properties and limiting photocurrent of thin-film perovskite solar cells. *Energy Environ. Sci.* **2015**, *8* (2), 602–609.
- (71) Malitson, I. H. Interspecimen Comparison of Refractive Index of Fused Silica. *J. Opt. Soc. Am.* **1965**, *55* (10), 1205.
- (72) Staub, F.; Anusca, I.; Lupascu, D. C.; Rau, U.; Kirchartz, T. Effect of Reabsorption and Photon Recycling on Photoluminescence Spectra and Transients in Lead-Halide Perovskite Crystals. *J. Phys-Mater.* **2020**, *3* (2), 025003.
- (73) Richter, J. M.; Abdi-Jalebi, M.; Sadhanala, A.; Tabachnyk, M.; Rivett, J. P. H.; Pazos-Outón, L. M.; Gödel, K. C.; Price, M.; Deschler, F.; Friend, R. H. Enhancing Photoluminescence Yields in Lead Halide Perovskites by Photon Recycling and Light Out-Coupling. *Nat. Commun.* **2016**, *7*, 13941.
- (74) Pazos-Outón, L. M.; Szumilo, M.; Lamboll, R.; Richter, J. M.; Crespo-Quesada, M.; Abdi-Jalebi, M.; Beeson, H. J.; Vručinić, M.; Alsari, M.; Snaith, H. J.; et al. Photon Recycling in Lead Iodide Perovskite Solar Cells. *Science* **2016**, *351* (6280), 1430–1433.
- (75) Patel, J. B.; Wright, A. D.; Lohmann, K. B.; Peng, K.; Xia, C. Q.; Ball, J. M.; Noel, N. K.; Crothers, T. W.; Wong-Leung, J.; Snaith, H. J.; et al. Light Absorption and Recycling in Hybrid Metal Halide Perovskite Photovoltaic Devices. *Adv. Energy Mater.* **2020**, *10* (10), 1903653.
- (76) Yamada, Y.; Yamada, T.; Phuong, L. Q.; Maruyama, N.; Nishimura, H.; Wakamiya, A.; Murata, Y.; Kanemitsu, Y. Dynamic Optical Properties of CH₃NH₃PbI₃ Single Crystals As Revealed by One- and Two-Photon Excited Photoluminescence Measurements. *J. Am. Chem. Soc.* **2015**, *137* (33), 10456–10459.
- (77) Stranks, S. D.; Hoye, R. L. Z.; Di, D. W.; Friend, R. H.; Deschler, F. The Physics of Light Emission in Halide Perovskite Devices. *Adv. Mater.* **2019**, *31* (47), 1803336.
- (78) Schötz, K.; Askar, A. M.; Köhler, A.; Shankar, K.; Panzer, F. Investigating the Tetragonal-to-Orthorhombic Phase Transition of Methylammonium Lead Iodide Single Crystals by Detailed Photoluminescence Analysis. *Adv. Opt. Mater.* **2020**, *8* (17), 2000455.
- (79) Crothers, T. W.; Milot, R. L.; Patel, J. B.; Parrott, E. S.; Schlipf, J.; Müller-Buschbaum, P.; Johnston, M. B.; Herz, L. M. Photon Reabsorption Masks Intrinsic Bimolecular Charge-Carrier Recombination in CH₃NH₃PbI₃ Perovskite. *Nano Lett.* **2017**, *17* (9), 5782–5789.
- (80) Fassl, P.; Lami, V.; Berger, F. J.; Falk, L. M.; Zaumseil, J.; Richards, B. S.; Howard, I. A.; Vaynzof, Y.; Paetzold, U. W. Revealing the internal luminescence quantum efficiency of perovskite films via accurate quantification of photon recycling. Online at <https://arxiv.org/abs/2010.12950>.
- (81) Kayanuma, Y. Quantum-Size Effects of Interacting Electrons and Holes in Semiconductor Microcrystals with Spherical Shape. *Phys. Rev. B: Condens. Matter Mater. Phys.* **1988**, *38* (14), 9797–9805.
- (82) Buin, A.; Comin, R.; Ip, A. H.; Sargent, E. H. Perovskite Quantum Dots Modeled Using ab Initio and Replica Exchange Molecular Dynamics. *J. Phys. Chem. C* **2015**, *119* (24), 13965–13971.
- (83) Neogi, A.; Everitt, H.; Morkoc, H.; Kuroda, T.; Tackeuchi, A. Size Dependence of Carrier Recombination Efficiency in GaN Quantum Dots. *IEEE Trans. Nanotechnol.* **2005**, *4* (2), 297–299.
- (84) Kan, S.; Mokari, T.; Rothenberg, E.; Banin, U. Synthesis and Size-Dependent Properties of Zinc-Blende Semiconductor Quantum Rods. *Nat. Mater.* **2003**, *2* (3), 155–158.
- (85) Meier, C.; Gondorf, A.; Lutjohann, S.; Lorke, A.; Wiggers, H. Silicon Nanoparticles: Absorption, Emission, and the Nature of the Electronic Bandgap. *J. Appl. Phys.* **2007**, *101* (10), 103112.
- (86) Simon, J.; Pelekanos, N. T.; Adelman, C.; Martinez-Guerrero, E.; Andre, R.; Daudin, B.; Dang, L. S.; Mariette, H. Direct Comparison of Recombination Dynamics in Cubic and Hexagonal GaN/AlN Quantum Dots. *Phys. Rev. B: Condens. Matter Mater. Phys.* **2003**, *68* (3), 035312.
- (87) Ravindran, T. R.; Arora, A. K.; Balamurugan, B.; Mehta, B. R. Inhomogeneous Broadening in the Photoluminescence Spectrum of CdS Nanoparticles. *Nanostruct. Mater.* **1999**, *11* (5), 603–609.
- (88) Cao, Y.; Qi, G. Y.; Liu, C.; Wang, L. R.; Ma, Z. W.; Wang, K.; Du, F.; Xiao, G. J.; Zou, B. Pressure-Tailored Band Gap Engineering and Structure Evolution of Cubic Cesium Lead Iodide Perovskite Nanocrystals. *J. Phys. Chem. C* **2018**, *122* (17), 9332–9338.
- (89) Xiao, G. J.; Cao, Y.; Qi, G. Y.; Wang, L. R.; Liu, C.; Ma, Z. W.; Yang, X. Y.; Sui, Y. M.; Zheng, W. T.; Zou, B. Pressure Effects on Structure and Optical Properties in Cesium Lead Bromide Perovskite Nanocrystals. *J. Am. Chem. Soc.* **2017**, *139* (29), 10087–10094.
- (90) Jaffe, A.; Lin, Y.; Karunadasa, H. I. Halide Perovskites under Pressure: Accessing New Properties through Lattice Compression. *ACS Energy Lett.* **2017**, *2* (7), 1549–1555.
- (91) Oksenberg, E.; Merdas, A.; Houben, L.; Kaplan-Ashiri, I.; Rothman, A.; Scheblykin, I. G.; Unger, E. L.; Joselevich, E., Large lattice distortions and size-dependent bandgap modulation in epitaxial halide perovskite nanowires. *Nat. Commun.* **2020**, *11* (1). DOI: 10.1038/s41467-020-14365-2
- (92) Noh, J. H.; Im, S. H.; Heo, J. H.; Mandal, T. N.; Seok, S. I. Chemical Management for Colorful, Efficient, and Stable Inorganic-Organic Hybrid Nanostructured Solar Cells. *Nano Lett.* **2013**, *13* (4), 1764–1769.
- (93) Kumawat, N. K.; Dey, A.; Kumar, A.; Gopinathan, S. P.; Narasimhan, K. L.; Kabra, D. Band Gap Tuning of CH₃NH₃Pb(Br_{1-x}Cl_x)₃ Hybrid Perovskite for Blue Electroluminescence. *ACS Appl. Mater. Interfaces* **2015**, *7* (24), 13119–13124.
- (94) Kitazawa, N.; Watanabe, Y.; Nakamura, Y. Optical Properties of CH₃NH₃PbX₃ (X = halogen) and Their Mixed-Halide Crystals. *J. Mater. Sci.* **2002**, *37* (17), 3585–3587.
- (95) Jang, D. M.; Park, K.; Kim, D. H.; Park, J.; Shojaei, F.; Kang, H. S.; Ahn, J. P.; Lee, J. W.; Song, J. K. Reversible Halide Exchange Reaction

of Organometal Trihalide Perovskite Colloidal Nanocrystals for Full-Range Band Gap Tuning. *Nano Lett.* **2015**, *15* (8), 5191–5199.

(96) Kim, S.-G.; Kim, J.-H.; Rammung, P.; Zhong, Y.; Schötz, K.; Kwon, S. J.; Huettner, S.; Panzer, F.; Park, N. G. How Antisolvent Miscibility Affects Perovskite Film Wrinkling and Photovoltaic Properties. *Nat. Commun.* **2021**, Accepted.

(97) Goetz, K. P.; Taylor, A. D.; Paulus, F.; Vaynzof, Y. Shining Light on the Photoluminescence Properties of Metal Halide Perovskites. *Adv. Funct. Mater.* **2020**, *30* (23), 1910004.

(98) Lee, S.; Tang, M. C.; Munir, R.; Barrit, D.; Kim, Y. J.; Kang, R.; Yun, J. M.; Smilgies, D. M.; Amassian, A.; Kim, D. Y. In Situ Study of the Film Formation Mechanism of Organic-Inorganic Hybrid Perovskite Solar Cells: Controlling the Solvate Phase Using an Additive System. *J. Mater. Chem. A* **2020**, *8* (16), 7695–7703.

(99) Tang, M. C.; Barrit, D.; Munir, R.; Li, R. P.; Barbé, J. M.; Smilgies, D. M.; Del Gobbo, S.; Anthopoulos, T. D.; Amassian, A. Bismuth-Based Perovskite-Inspired Solar Cells: In Situ Diagnostics Reveal Similarities and Differences in the Film Formation of Bismuth- and Lead-Based Films. *Sol RRL* **2019**, *3* (7), 1800305.

(100) Unger, E. L.; Bowring, A. R.; Tassone, C. J.; Pool, V. L.; Gold-Parker, A.; Checharoen, R.; Stone, K. H.; Hoke, E. T.; Toney, M. F.; McGehee, M. D. Chloride in Lead Chloride-Derived Organo-Metal Halides for Perovskite-Absorber Solar Cells. *Chem. Mater.* **2014**, *26* (24), 7158–7165.

(101) Abdelsamie, M.; Zhao, K.; Niazi, M. R.; Chou, K. W.; Amassian, A. In Situ UV-Visible Absorption during Spin-Coating of Organic Semiconductors: A New Probe for Organic Electronics and Photovoltaics. *J. Mater. Chem. C* **2014**, *2* (17), 3373–3381.

(102) Ro, H. W.; Downing, J. M.; Engmann, S.; Herzing, A. A.; DeLongchamp, D. M.; Richter, L. J.; Mukherjee, S.; Ade, H.; Abdelsamie, M.; Jagadamma, L. K.; et al. Morphology Changes upon Scaling a High-Efficiency, Solution-Processed Solar Cell. *Energy Environ. Sci.* **2016**, *9* (9), 2835–2846.

(103) Hong, D. C.; Yang, W. Q.; Tian, Y. X. Distinguish the Quenching and Degradation of $\text{CH}_3\text{NH}_3\text{PbI}_3$ Perovskite by Simultaneous Absorption and Photoluminescence Measurements. *J. Phys. Chem. C* **2020**, *124* (1), 1207–1213.

(104) Merdasa, A.; Kiligaridis, A.; Rehmann, C.; Abdi-Jalebi, M.; Stober, J.; Louis, B.; Gerhard, M.; Stranks, S. D.; Unger, E. L.; Scheblykin, I. G. Impact of Excess Lead Iodide on the Recombination Kinetics in Metal Halide Perovskites. *ACS Energy Lett.* **2019**, *4* (6), 1370–1378.

(105) Kiligaridis, A.; Merdasa, A.; Rehmann, C.; Unger, E. L.; Scheblykin, I. G. Excitation Wavelength Dependence of Photoluminescence Flickering in Degraded MAPbI_3 Perovskite and its Connection to Lead Iodide Formation. *J. Lumin.* **2020**, *222*, 117129.

(106) Engmann, S.; Bokel, F. A.; Ro, H. W.; DeLongchamp, D. M.; Richter, L. J. Real-Time Photoluminescence Studies of Structure Evolution in Organic Solar Cells. *Adv. Energy Mater.* **2016**, *6* (10), 1502011.

(107) Rehmann, C.; Merdasa, A.; Suchan, K.; Schröder, V.; Mathies, F.; Unger, E. L. Origin of Ionic Inhomogeneity in $\text{MAPb}(\text{I}_{1-x}\text{Br}_x)_3$ Perovskite Thin Films Revealed by In-Situ Spectroscopy during Spin Coating and Annealing. *ACS Appl. Mater. Interfaces* **2020**, *12* (27), 30343–30352.

(108) Richter, L. J.; DeLongchamp, D. M.; Bokel, F. A.; Engmann, S.; Chou, K. W.; Amassian, A.; Schaible, E.; Hexemer, A. In Situ Morphology Studies of the Mechanism for Solution Additive Effects on the Formation of Bulk Heterojunction Films. *Adv. Energy Mater.* **2015**, *5* (3), 1400975.

(109) Alsari, M.; Bikondoa, O.; Bishop, J.; Abdi-Jalebi, M.; Ozer, L. Y.; Hampton, M.; Thompson, P.; Hörantner, M. T.; Mahesh, S.; Greenland, C.; et al. In Situ Simultaneous Photovoltaic and Structural Evolution of Perovskite Solar Cells during Film Formation. *Energy Environ. Sci.* **2018**, *11* (2), 383–393.

(110) van Franeker, J. J.; Hendriks, K. H.; Bruijnaers, B. J.; Verhoeven, M. W. G. M.; Wienk, M. M.; Janssen, R. A. J. Monitoring Thermal Annealing of Perovskite Solar Cells with In Situ Photoluminescence. *Adv. Energy Mater.* **2017**, *7* (7), 1601822.

(111) Fu, Y. P.; Meng, F.; Rowley, M. B.; Thompson, B. J.; Shearer, M. J.; Ma, D. W.; Hamers, R. J.; Wright, J. C.; Jin, S. Solution Growth of Single Crystal Methylammonium Lead Halide Perovskite Nanostructures for Optoelectronic and Photovoltaic Applications. *J. Am. Chem. Soc.* **2015**, *137* (17), 5810–5818.

(112) Chen, Q.; Zhou, H. P.; Hong, Z. R.; Luo, S.; Duan, H. S.; Wang, H. H.; Liu, Y. S.; Li, G.; Yang, Y. Planar Heterojunction Perovskite Solar Cells via Vapor-Assisted Solution Process. *J. Am. Chem. Soc.* **2014**, *136* (2), 622–625.

(113) Zhao, J. J.; Deng, Y. H.; Wei, H. T.; Zheng, X. P.; Yu, Z. H.; Shao, Y. C.; Shield, J. E.; Huang, J. S. Strained Hybrid Perovskite Thin Films and Their Impact on the Intrinsic Stability of Perovskite Solar Cells. *Sci. Adv.* **2017**, *3* (11), ea05616.

(114) Chen, Y. M.; Lei, Y. S.; Li, Y. H.; Yu, Y. G.; Cai, J. Z.; Chiu, M. H.; Rao, R.; Gu, Y.; Wang, C. F.; Choi, W. J.; et al. Strain Engineering and Epitaxial Stabilization of Halide Perovskites. *Nature* **2020**, *577* (7789), 209–215.

(115) Moloney, E. G.; Yeddu, V.; Saidaminov, M. I. Strain Engineering in Halide Perovskites. *ACS Mater. Lett.* **2020**, *2* (11), 1495–1508.

(116) Radicchi, E.; Kachmar, A.; Mosconi, E.; Bizzarri, B.; Nunzi, F.; De Angelis, F. Structural and Optical Properties of Solvated PbI_2 in gamma-Butyrolactone: Insight into the Solution Chemistry of Lead Halide Perovskite Precursors. *J. Phys. Chem. Lett.* **2020**, *11* (15), 6139–6145.

(117) Stampelcoskie, K. G.; Manser, J. S.; Kamat, P. V. Dual Nature of the Excited State in Organic-Inorganic Lead Halide Perovskites. *Energy Environ. Sci.* **2015**, *8* (1), 208–215.

(118) Sanchez, S.; Steiner, U.; Hua, X. Phase Evolution During Perovskite Formation-Insight from Pair Distribution Function Analysis. *Chem. Mater.* **2019**, *31* (9), 3498–3506.

(119) Manser, J. S.; Reid, B.; Kamat, P. V. Evolution of Organic-Inorganic Lead Halide Perovskite from Solid-State Iodoplumbate Complexes. *J. Phys. Chem. C* **2015**, *119* (30), 17065–17073.

(120) Petrov, A. A.; Sokolova, I. P.; Belich, N. A.; Peters, G. S.; Dorovatovskii, P. V.; Zubavichus, Y. V.; Khrustalev, V. N.; Petrov, A. V.; Grätzel, M.; Goodilin, E. A.; et al. Crystal Structure of DMF-Intermediate Phases Uncovers the Link Between $\text{CH}_3\text{NH}_3\text{PbI}_3$ Morphology and Precursor Stoichiometry. *J. Phys. Chem. C* **2017**, *121* (38), 20739–20743.

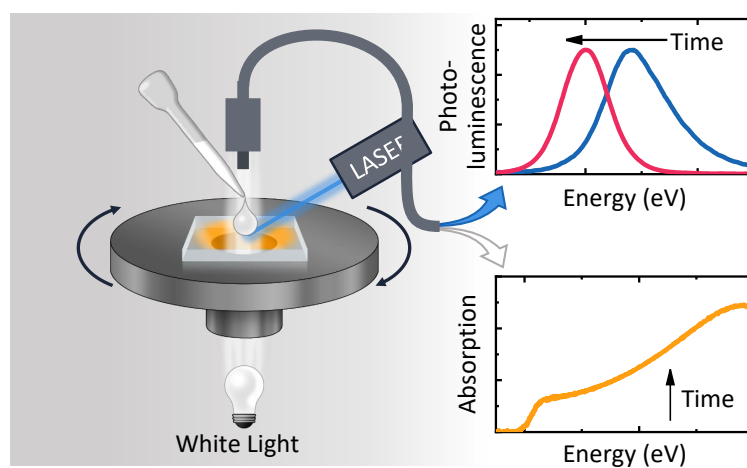
(121) Li, Y. H.; Zhi, L. L.; Ge, G. X.; Zhao, Z. H.; Cao, X. B.; Chen, F. F.; Lin, F.; Ci, L. J.; Sun, J. L.; Zhuang, D. M.; et al. Investigation on Crystallization of $\text{CH}_3\text{NH}_3\text{PbI}_3$ Perovskite and Its Intermediate Phase from Polar Aprotic Solvents. *Cryst. Growth Des.* **2019**, *19* (2), 959–965.

(122) Fateev, S. A.; Petrov, A. A.; Khrustalev, V. N.; Dorovatovskii, P. V.; Zubavichus, Y. V.; Goodilin, E. A.; Tarasov, A. B. Solution Processing of Methylammonium Lead Iodide Perovskite from γ -Butyrolactone: Crystallization Mediated by Solvation Equilibrium. *Chem. Mater.* **2018**, *30* (15), 5237–5244.

(123) Cao, J.; Jing, X. J.; Yan, J. Z.; Hu, C. Y.; Chen, R. H.; Yin, J.; Li, J.; Zheng, N. F. Identifying the Molecular Structures of Intermediates for Optimizing the Fabrication of High-Quality Perovskite Films. *J. Am. Chem. Soc.* **2016**, *138* (31), 9919–9926.

(124) Li, J.; Dobrovolsky, A.; Merdasa, A.; Unger, E. L.; Scheblykin, I. G. Luminescent Intermediates and Humidity-Dependent Room-Temperature Conversion of the MAPbI_3 Perovskite Precursor. *ACS Omega* **2018**, *3* (10), 14494–14502.

12 Investigating Two-Step MAPbI₃ Thin Film Formation During Spin Coating by Simultaneous *In Situ* Absorption and Photoluminescence Spectroscopy



Mihirsinh Chauhan[#], Yu Zhong[#], **Konstantin Schötz**, Brijesh Tripathi, Anna Köhler, Sven Huettner, Fabian Panzer. [#] Authors contributed equally.

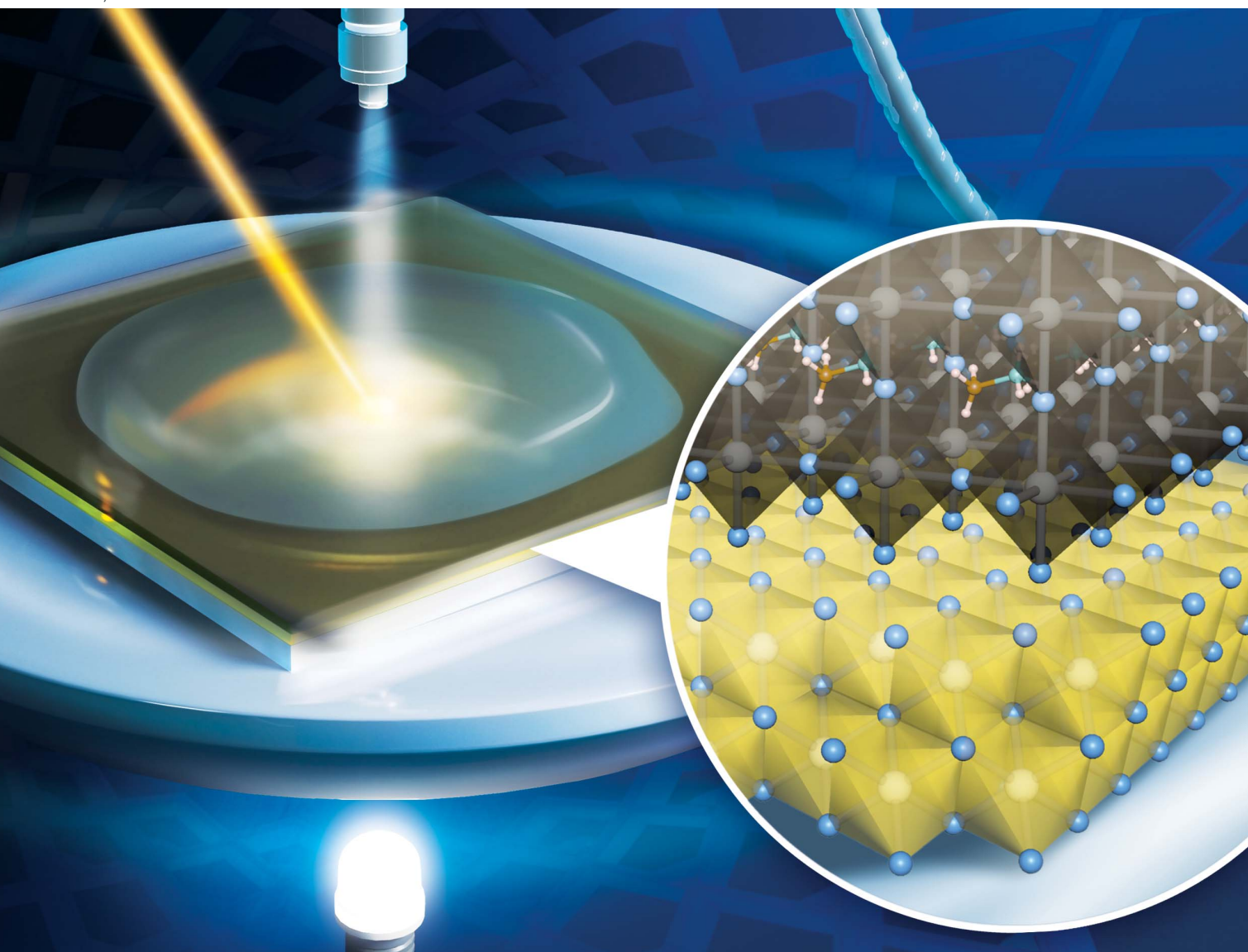
Published in
The Journal of Materials Chemistry A, **2020**, 8, 10, 5086-5094
(DOI: 10.1039/C9TA12409H)

Reprinted with permission from the Royal Society of Chemistry
Copyright (2020) Royal Society of Chemistry

Journal of Materials Chemistry A

Materials for energy and sustainability

rsc.li/materials-a



ISSN 2050-7488

PAPER

Fabian Panzer *et al.*
Investigating two-step MAPbI₃ thin film formation during
spin coating by simultaneous *in situ* absorption and
photoluminescence spectroscopy

Cite this: *J. Mater. Chem. A*, 2020, **8**, 5086

Investigating two-step MAPbI₃ thin film formation during spin coating by simultaneous *in situ* absorption and photoluminescence spectroscopy†

Mihirsinh Chauhan,[‡] Yu Zhong,[‡] Konstantin Schötz,^a Brijesh Tripathi,^b Anna Köhler,^{ad} Sven Huettnert^c and Fabian Panzer^{id}*^a

To date, the two-step processing method represents an attractive route for the thin film formation of halide perovskites. However, a fundamental understanding of the film formation dynamics in the case of spin coating methylammonium iodide (MAI) on PbI₂ has not been established yet. Here we apply *in situ* optical spectroscopy during the two-step film formation of the model halide perovskite MAPbI₃ *via* spin coating. We identify and analyze in detail the optical features that occur in the photoluminescence and the corresponding absorption spectra during processing. We find that the film formation takes place in five consecutive steps, including the formation of a MAPbI₃ capping layer *via* an interface crystallization and the occurrence of an intense dissolution–recrystallization process. Consideration of confinement and self-absorption effects in the PL spectra, together with consideration of the corresponding absorption spectra allows quantification of the growth rate of the initial interface crystallization, which is found to be 11 nm s⁻¹ under our processing conditions. We find that the main dissolution–recrystallization process happens at a rate of 445 nm s⁻¹, emphasizing its importance to the overall processing.

Received 11th November 2019
Accepted 23rd January 2020

DOI: 10.1039/c9ta12409h

rsc.li/materials-a

1. Introduction

The ongoing increase in the efficiencies of perovskite-based optoelectronic devices, in particular solar cells, has been delighting the research community for several years now. Key aspects for this development were various breakthroughs in the thin film processing of the perovskite layer. One of the most important solution-based processing approaches to date is the so-called two-step method, which was first reported in 2013.^{1,2} In this method, a PbI₂ layer is produced in a first processing step, *e.g.* *via* spin coating, and then brought into contact with methylammonium iodide (MAI) dissolved in an alcohol, *e.g.* isopropanol (IPA), in a second processing step, thus initiating the growth of the perovskite MAPbI₃. It is possible to realize the second processing step either by exposing the PbI₂ layer to a MAI gas phase, by dipping the PbI₂ layer into a MAI solution, or by spin coating the latter onto the

PbI₂ substrate. The main advantage of the two-step method is seen in the supposedly higher process control compared to other processing methods.³ However, it became clear in the last few years that, similar to other solution-based film processing methods, the final morphological and thus optoelectronic properties sensitively depend on the precise processing conditions of the two-step method.^{4–8} Some studies have investigated the film formation dynamics during the two-step method⁹ and found that the MAPbI₃ crystallization process depends *e.g.* on the MAI concentration,^{10,11} temperature,^{11,12} and the timing of the processing steps.² Depending on the specific processing conditions it is possible that different types of crystallizations occur, namely *in situ* interface transformation or solid–liquid recrystallization, or both.^{13,14} So far, most of the knowledge about the crystallization behavior of the two-step method was obtained for the case of dipping the PbI₂ layer in MAI solution, where crystallization takes place on relatively long time scales.³ In contrast, faster crystallization takes place when applying MAI/IPA *via* spin-coating, which leads to more homogeneous, compact and smoother films and thus to better solar cells, making it a more technology relevant processing strategy.⁴ Recently we developed a measurement setup that allows the measurement of absorption spectra and, in parallel, photoluminescence (PL) *in situ* during solution-based processing of semiconductor materials, such as spin-coating.¹⁵ By investigating the optical properties of halide perovskites, it is possible to extract detailed information about

^aSoft Matter Optoelectronics, University of Bayreuth, 95440 Bayreuth, Germany. E-mail: fabian.panzer@uni-bayreuth.de

^bSchool of Technology, Pandit Deendayal Petroleum University, 382007 Gandhinagar, India

^cDepartment of Chemistry, University of Bayreuth, 95440 Bayreuth, Germany

^dBayreuth Institute of Macromolecular Research (BIMF), Bavarian Polymer Institute (BPI), University of Bayreuth, 95440 Bayreuth, Germany

† Electronic supplementary information (ESI) available. See DOI: 10.1039/c9ta12409h

‡ These authors contributed equally.

their electronic structure, and concomitantly about their composition.^{16–20} Thus, in this work, we use *in situ* absorption and simultaneous PL spectroscopy to investigate the film formation dynamics of MAPbI₃ for a two-step processing approach using spin coating. We observe changes in both absorption and PL during the spin-coating process. This allows us to categorize the film formation process into five different time ranges. By carefully considering quantum confinement and self-absorption effects, we analyze in detail the spectroscopic changes in the different time ranges. This allows associating the changes in the optical properties with specific morphological states. We find that both interface crystallization and a dissolution–recrystallization process occur. Based on our results it is possible to understand the full sequence of perovskite formation dynamics that occur in the two-step processing *via* spin coating.

2. Results

In the first processing step we spin coat a solution of PbI₂ in dimethylformamide (DMF) (461 mg ml⁻¹) onto a glass substrate (Fig. 1a) and anneal it at 100 °C for 5 minutes (Fig. 1b). This leads to a compact PbI₂ thin film. In the second processing step, we drop 200 μL of MAI dissolved in IPA (40 mg ml⁻¹) onto the PbI₂ film to induce the MAPbI₃ crystallization and immediately start spin coating (corresponding to $t = 0$ s), where the target spin speed of 1000 rpm min⁻¹ is reached after 2 seconds (Fig. 1c). The temperature of the sample and MAI solvent during the spin coating is kept at 26 °C. During this second processing step, we monitor the optical properties, *i.e.* absorption and PL, using a home-built spin coater and optical detection system, both described in detail in ref. 15. In brief, the rotating substrate with the solution is excited with a white-light-source pulsed at 11 Hz from underneath the chuck of the spin-coater, through a hole, and its transmission is recorded with a glass fiber cable connected to a spectrograph.

During the off-periods, a laser beam at 520 nm (2.38 eV) excites the sample and the resulting luminescence is recorded using the same glass fiber cable connected to the spectrograph. In this way, pairs of transmission and PL spectra are measured at a rate of 11 pairs per second. To correct the transmission of

MAPbI₃ $I(t)$ for the transmission of the setup I_0 , we also recorded the transmission signal obtained with a quartz substrate and subtracted it so as to obtain the time dependent optical density using the relation $OD(t) = \log(I_0/I(t))$. The resulting spectrum is shown in the ESI (Fig. S1†). It turns out that a reflection signal from the initially unreacted PbI₂ film obscures the clear identification of the MAPbI₃ absorption in particular in the early stages, when the MAPbI₃ signal is still weak. We therefore also recorded the transmission signal obtained from a quartz substrate covered with a PbI₂ film and used this as reference value I_{ref} to calculate the time dependent optical density as $OD(t) = \log(I_{ref}/I(t))$, shown in Fig. 2a. One may argue that, at later stages, this procedure implies subtracting a no longer existing reflection signal as the PbI₂ layer has been used up. However, once the PbI₂ has been used up, the absorption from the MAPbI₃ is sufficiently strong, so this small subtraction has essentially no effect. All spectra are also set to a common baseline to account for fluctuations in optical scattering. Fig. 2 shows the evolution of the absorption spectra (Fig. 2a) and of the corresponding PL spectra (Fig. 2b), where each PL spectrum is normalized to its maximum value. They are both plotted as 2D color maps, so the color indicates the intensity of PL or optical density (OD). For reference and visualization, the absorption and PL spectra at 14 s are indicated at the side of the maps.

From Fig. 2a it becomes clear that there is little change in the absorption within the first 12 seconds of processing, while the main increase in absorption intensity occurs between 12 and 14 s. From about 14 s onwards, the absorption remains largely unaltered. We point out that the absorption cannot be evaluated quantitatively within the first 4 s, since until then the pipette, used to distribute the MAI solution across the glass substrate at the beginning of spin coating, was in the beam path. In contrast to the absorption, a photoluminescence peak prevails over the entire time range investigated (Fig. 2b). Its energetic position and width changes in the first 14 seconds and remains constant thereafter. It is noteworthy that this PL has a finite intensity even when there is only very little absorption from the MAPbI₃, implying a high quantum yield compared to that in later stages, when there is significant MAPbI₃ absorption. For reference, a plot of the PL spectra with absolute intensities is given in the ESI (Fig. S1†).

To analyze the different spectroscopic signatures and temporal changes in more detail, we display the temporal evolution of different spectral features in Fig. 2c. The optical density at 1.665 eV indicates how the MAPbI₃ absorption develops with time. We also show the evolution of the PL peak position and the two photon energies at which the PL has dropped to 25% of its maximum intensity (essentially following the turquoise line in Fig. 2b). This is referred to as the “high edge” and “low edge”. Furthermore, the temporal evolution of the integrated PL intensity, corrected for the concomitant changes of the absorption at the laser excitation wavelength (2.38 eV) normalized to the value after 10 seconds, is shown. This indicates the relative change of the PL quantum yield (PLQY).

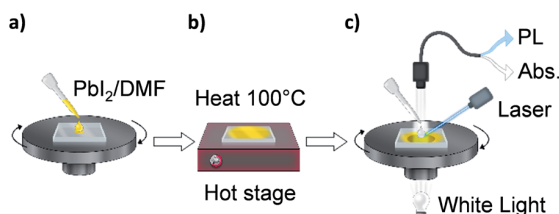


Fig. 1 The preparation of MAPbI₃ film and the *in situ* spectroscopy setup. (a) PbI₂ in DMF is spin coated on a glass substrate. (b) Heat annealing of the PbI₂ layer. (c) MAI in IPA is spin coated on the PbI₂ layer and, during spin coating, PL and absorption of the film are detected.

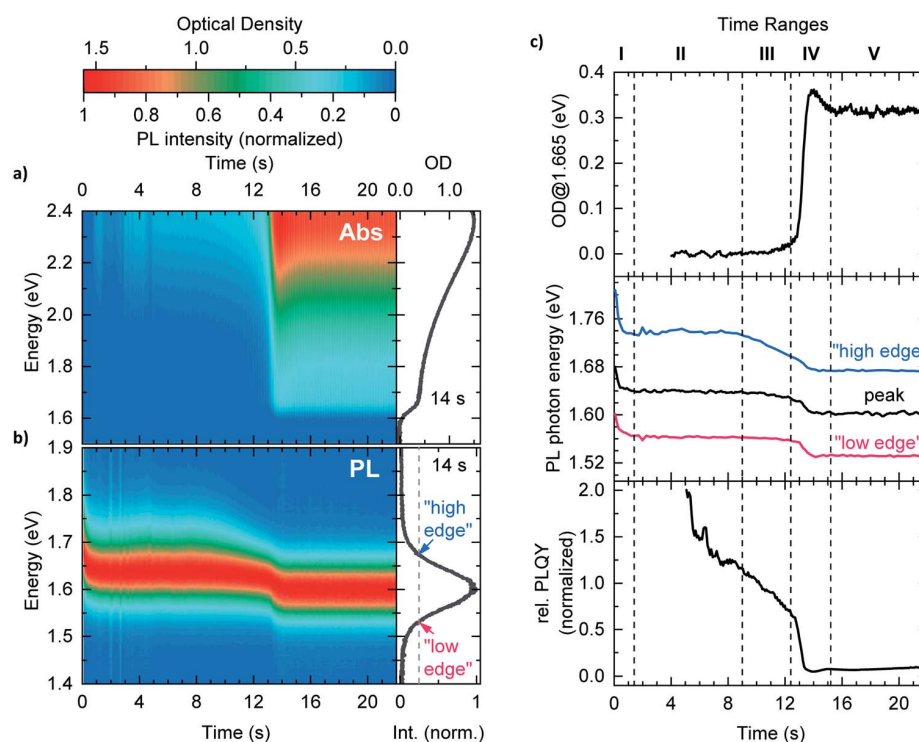


Fig. 2 (a) 2D absorption map. The colour indicates the optical density. (b) PL map, with every spectrum being normalized. (c) Evolution of (top panel) the optical density at 1.665 eV, (middle panel) the PL at the positions of the peak, "high edge" and "low edge", and (bottom panel) the PLQY relative to the value at 10 s.

If we take a closer look at the time evolution of the optical parameters described above (Fig. 2c), we can identify five consecutive time ranges between which specific spectral changes of PL or absorption occur. We briefly describe what characterizes these different regimes, before analyzing each regime in detail. In the first time range, *i.e.* the first 1.4 seconds, indicated as I in Fig. 2c, we observe photoluminescence, and its spectrum shows a fast initial shift towards lower energies. In the subsequent time range II, *i.e.* the next 8 seconds, the PL shape remains constant, while there is no noticeable change in absorption intensity from 4 s onwards. In time range III, the absorption increases slightly, and there are spectral changes in the PL. The high-energy edge of the PL shifts to lower energies, while the position of the low-energy edge remains constant. Range IV can be associated with a steep increase and subsequent decreases in absorption. Simultaneously a further shift of the whole PL spectrum to lower energies occurs, accompanied by a significant reduction of the relative PLQY. After that, in range V, no further change in the absorbance or PL occurs.

Range I

As mentioned above, absorption in range I cannot be evaluated. However, directly after applying the MAI solution to the PbI_2 layer, an initial PL spectrum with a maximum at 1.68 eV occurs, which shifts within the first 1.4 seconds by about 50 meV to lower energies (Fig. 3a top). Fig. 3b shows the temporal evolution of the energetic position of the PL peak, together with a fit

to an exponential decay that gives a time constant of 0.23 ± 0.05 s. We note that the spectral shape of the PL peak is not symmetrical. Rather, it shows a high energy tail that becomes particularly obvious when fitting a hyperbolic secant *e.g.* to the spectrum at 1.4 s (Fig. S2†). Such a line shape was previously found to account well for thermal and inhomogeneous broadening of the PL peak shape of halide perovskites.²¹

To further investigate what may give rise to the high-energy PL tail and the initially blue-shifted position of the maximum, we recall that PL spectra that were blue shifted compared to their bulk PL have been repeatedly associated in the past with a confinement effect of the excited state by a finite crystallite size.^{22–25} For MAPbI_3 , this effect occurs for crystallite or grain sizes below approximately 25–30 nm.^{26–28} We follow the approach outlined by Parrott *et al.* to correlate the measured PL peak position with the crystal size²⁷ using the equation

$$E = E_g + b/d^2 \quad (1)$$

where E_g corresponds to the band gap energy, which we set to 1.63 eV. The parameter b represents a constant, which in the literature is found to be in the range between 1 and 5 eV nm² for MAPbI_3 ,^{27,29} so we assume a value of 3 eV nm² (see the ESI for more details†). With the help of eqn (1), the evolution of peak position with time translates into an evolution of film thickness with time (Fig. 3b and S3†). It appears that the film formation starts at a thickness of about 8 nm, increases to about 20 nm

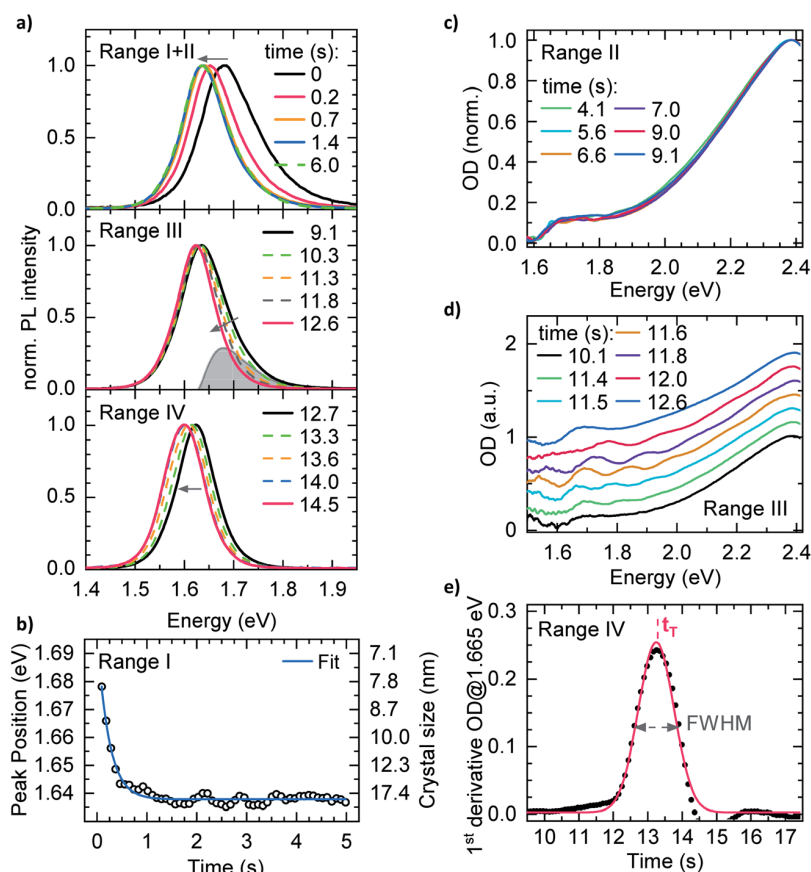


Fig. 3 (a) Evolution of PL during processing. Top: normalized PL within the first 1.4 s (range I) and at 6.0 s (range II). Middle: normalized PL from 9.1 s (black line) to 12.6 s (red line) (range III). The difference between the spectra at 9.1 s and 12.6 s is shown in grey. Bottom: normalized PL from 12.7 s to 14.5 s (range IV). (b) Temporal evolution of the PL peak position together with an exponential decay fit. Also the crystal size that corresponds to a certain PL peak position, as described in the text, is given. (c) Normalized absorption spectra between 4.1 s (red) and 9.1 s of processing (range II). (d) Absorption spectra from 10.1 s to 12.6 s (range III). For clarity each spectrum is offset by 0.15. (e) The 1st derivative of OD at 1.665 eV together with a fit of a Gaussian. The peak position is defined as transition time t_T .

within the first 1.5 s, and then remains constant. A fit to the evolution of crystal size in the range up to 1.0 s gives an initial MAPbI₃ growth rate for the film thickness in the range of 11 ± 2 nm s⁻¹ (Fig. S3†).

Range II

The measured absorption spectra between 4.1 and 9.1 s in range II correspond to the known MAPbI₃ absorption spectrum and its shape remains constant over time (Fig. 3c). After the initial spectral changes in time over time, the shape of the PL spectrum stabilizes from about 1.5 s onwards. This defines the beginning of range II. The PL shape remains nearly constant until a processing time of 9.1 s.

Range III

While the shape of the absorption spectrum does not change over time at the beginning of range III, we observe a modulation of the measured spectra in the time range between 11.4 s and 12.6 s (Fig. 3d). This may be associated with a thin film

interference effect, which is often used to optically determine the thickness of thin films.³⁰ The layer thickness d can be calculated from the spectral position of the extrema using the equation^{31,32}

$$d = \frac{\lambda_1 \lambda_2}{2(\lambda_1 n_2 - \lambda_2 n_1)} \quad (2)$$

where λ_1 and λ_2 correspond to the wavelengths of two adjacent maxima or minima and n_1 and n_2 represent the refractive index of the layer material at λ_1 and λ_2 . While the determination of λ_1 and λ_2 is relatively easily accessible from the measured spectra (see Fig. S7 for details†), it is not so obvious which material causes the thin film interference in range III. If the thicknesses are calculated using the refractive indices for MAPbI₃ (~2.4–2.5) or PbI₂ (~3.1–3.2), the resulting values are clearly too high compared to the thicknesses determined based on the absorption and profilometer data (see the ESI for details†). If the refractive indices of isopropanol (~1.3–1.4) are used, we obtain a thickness of 3.6 μ m at 11.4 s, which rapidly decreases to 1.4 μ m at 12.6 s.

From 9.1 s onward, the spectral shape of the PL evolves. The high-energy edge shifts from 1.74 eV at 9.1 s to 1.70 eV at 12.6 s, *i.e.* by about 40 meV. In the same time range, the spectral position of the low edge shifts merely by 7 meV, starting from 1.56 eV (Fig. 2b and c and 3a middle panel). This spectral dynamic results in an asymmetric narrowing of the measured PL peak from the high-energy edge. At first sight, this might be interpreted as a self-absorption effect in which the PL intensity reduces in the spectral overlap region of PL and absorption.³³ To check the plausibility of the self-absorption scenario in time range III, we used the PL spectrum at the beginning of range III (*i.e.* at 9.1 s) as the reference spectrum to calculate the absorption edge using the subsequent PL spectra (see Fig. S4†). This is a well-known approach, especially for the optical investigation of inorganic semiconductors, where information about the absorption edge can be obtained based on PL data.^{34,35} However, we find that the absorption edges determined by this approach do not match well with the absorption edges determined by the optical density measurements in terms of both shape and energetic position (Fig. S4†). To assess the influence of self-absorption on the PL more precisely, we analyzed the PL spectra in range III using a quantitative model we had already successfully used in the past for this purpose.³⁶ An important feature of this model is that it takes into account extended optical paths in the material due to internal reflections at the layer interfaces. We find that in realistic and exaggerated scenarios with regard to assumed layer thicknesses and/or boundary layer properties, it is virtually impossible to model the experimentally observed narrowing of only one PL edge (Fig. S5†). Rather, a spectral shift of the entire spectrum would result from an increasing amount of self-absorption, which also agrees with other literature reports.^{27,36} From the absorption data in range III we further observe that the absorption is relatively low ($OD < 0.01$ at 1.67 eV), which is further in agreement with the notion that a significant self-absorption effect in time range III is absent.^{27,37}

However, it is noticeable that at the end of range III the PL peak appears more symmetrical, compared to its spectral shape at the beginning of range III. The difference spectrum calculated from the PL spectra at 9.1 s and 12.6 s (shaded area in Fig. 3a middle panel) peaks at 1.68 eV. This matches with the peak position of the first measured PL spectrum at 0 s. If we also calculate the difference spectra between the PL spectrum at 9.1 s and the other spectra in range III, they result in essentially the same spectral shape with the peak position at 1.68 eV (Fig. S6†). It is important to note that this difference spectrum does not shift to the red with increasing time. Rather, exactly the same spectrum prevails at all times, yet its intensity reduces. Thus, the spectral changes in range III can also be understood as decreasing intensity of an additional higher energetic PL feature, which finally disappears at the end of range III.

Given the spectral coincidence of the additional high-energy PL feature with the PL in the early stages, it is reasonable to attribute this feature to small crystallites where the exciton wavefunction is still confined and thus the transition is blue-shifted. Using eqn (1), the peak position of the difference PL at 1.68 eV would correspond to a crystal size of about 15 nm.

Range IV

The significant increase in absorption between 12.6 and 14.0 s is the most noticeable spectral change in range IV (Fig. 2a). To quantify this increase more precisely, it is advantageous to calculate the derivative of the time-dependent OD at 1.665 eV, which leads to a peak shape.³⁸ By fitting a Gaussian to this peak, we can quantify the transition time t_T from the maximum. The full width at half maximum (FWHM) gives information about the width of the transition (Fig. 3e). We find $t_T = 13.3$ s and $FWHM = 1.2$ s.

The increase in absorption can be associated with an increase in film thickness. To this end, we used the absorption coefficient of MAPbI₃ from the literature³⁹ to convert the time-dependent (offset-corrected) optical density from Fig. 2c in the energy range between 1.6 eV and 1.7 eV into a time-dependent layer thickness, shown as black circles in Fig. 4 (see also Fig. S8 for details†). The steep increase in the absorption spectrum then corresponds to an increase of layer thickness from about 50 nm at the beginning to about 500 nm at the end of range IV. If we approximate this evolution by a linear fit in the range between 13 and 14 s, this results in a growth rate of 445 ± 15 nm s⁻¹ (Fig. S9†). Also indicated in Fig. 4 is the film thickness that results from fitting the interference pattern in range III using the refractive index of isopropanol (orange diamonds), and the film thickness that is obtained in the early stages from fitting the shift in the PL spectra using eqn (1) (red squares).

Simultaneously with the steep increase in absorption, the entire PL spectrum shifts from 1.63 eV to 1.60 eV (see Fig. 2c and 3a bottom). If we assume that this shift is due to self-absorption, we can derive the associated film thickness that causes such an absorption. We did this using a modelling approach that considers multiple reflections and that is detailed in ref. 36. As detailed in the ESI (Fig. S10†), we start by using the PL spectrum at 12.7 s, *i.e.* at the beginning of range IV, and consider the intensity of MAPbI₃ absorption present in that moment to

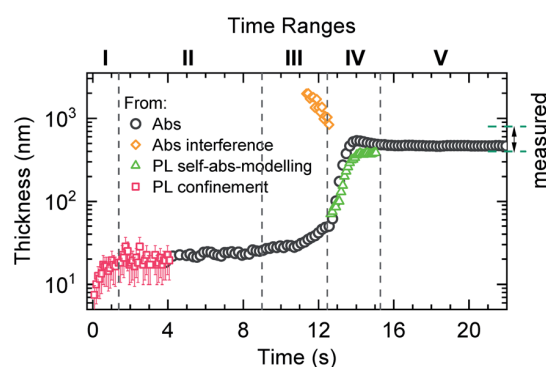


Fig. 4 The film thickness as a function of spin-coating time, derived with different approaches as detailed in the text. Black circles: derived by converting OD into thickness, orange diamonds: derived by fitting the interference pattern, red squares: derived by associating a PL shift with confinement effects, green triangles: derived by associating the PL shift with self-absorption of different thickness films.

calculate the PL spectrum that would result in the absence of self-absorption. The spectrum calculated in this way peaks at 1.63 eV, matching well with the measured PL spectrum after 1.4 s (end of range I), which confirms our approach. As the next step, we calculated the layer thickness necessary to modify this PL spectrum in such a way that it matches the measured PL spectra at each time in range IV (Fig. S11†). The thicknesses that we obtain by this approach are indicated as green triangles in Fig. 4. From the good agreement with the layer thicknesses obtained from considering the OD we conclude that our approach is correct, *i.e.* the shape of the PL spectra in range IV is indeed the result of self-absorption from the increasing amount of MAPbI₃.

Range V

The last time range, starting from 14.0 s, is characterized by the fact that there are no temporal changes in either absorption or PL, *i.e.* the film formation is complete. X-ray scattering results reveal that after time range V no PbI₂ exists in the film, suggesting a full conversion to MAPbI₃ (Fig. S12†). The layer thickness extracted using the absorption data is approximately 500 nm in range V, which matches well with the layer thickness range from 400 to 800 nm determined using a profilometer (Fig. 4). SEM images of a final film show a compact surface coverage and grain sizes in the range from 50 to 300 nm (Fig. S13†). While the relative PLQY has decreased significantly, the PL spectrum appears symmetric, suggesting that no additional PL signatures are present at the end of the processing.

3. Discussion

Having analyzed the spectral features in detail, we can now proceed to derive a possible model for the successive film formation. As before, we shall consider the different temporal regimes one after another. The overall picture we suggest is summarized in Fig. 5.

Range I

The analysis of the PL spectra suggested the initial formation of small MAPbI₃ crystals with crystal sizes that confine the wavefunction below about 25 nm, immediately after applying the MAI solution on the PbI₂ layer. As suggested by the PL shift to

lower energies, these crystallites grow fast with a growth rate of 11 nm s⁻¹ to sizes above about 25 nm in the course of range I. The good match of the calculated crystal sizes from the confinement effect at the end of range I and the thickness extracted from the first reliable absorption spectra in range II of about 20 nm confirm our approach.

Fu *et al.* reported the initial formation of a MAPbI₃ capping layer when dipping PbI₂ layers into MAI/IPA solution, for concentrations above 10 mg ml⁻¹.¹³ The formation of this capping layer was also found to happen faster for higher concentrations, while the average grain size decreases.^{11,13} The MAI concentration of 40 mg ml⁻¹ used in our study is well above 10 mg ml⁻¹, so we associate the initial occurrence of PL and its rapid shift to lower energies with the spectroscopic signatures of the initial formation of MAPbI₃ crystallites that grow within range I so as to form a capping layer. This is also in agreement with the results from Schlipf *et al.* who investigated the MAPbI₃ two-step conversion process with time-resolved scattering methods and found a laterally confined crystal growth at the beginning of the crystallization.⁴⁰ Ko *et al.* reported that the growth rate of the MAPbI₃ nuclei is independent of the MAI concentration, investigating a range between 4 and 8 mg ml⁻¹.¹¹ Their results on the evolution of grain size suggest a growth rate in the range between 10 and 20 nm s⁻¹, which agrees very well with the value of 11 nm s⁻¹ that we find in range I using a concentration of 40 mg ml⁻¹. This suggests that the growth rate of MAPbI₃ nuclei in the two-step process under ambient conditions remains mostly unchanged over at least an order of magnitude of MAI concentration.

The asymmetric shape of the PL spectrum at the end of range I indicates that after the initial MAPbI₃ crystallization, crystallites exist with grain sizes below the confinement limit, *i.e.* below about 25 nm. Ahn *et al.* derived a direct correlation between the MAI concentration and the resulting MAPbI₃ grain size in the case of the two-step method.^{12,41} In this framework, a MAI concentration of 40 mg ml⁻¹ (0.25 M) as used in our study corresponds to an average grain size of approximately 50 nm (Fig. S14†), *i.e.* only slightly higher than the typical confinement limit of MAPbI₃.^{26–28} As the grains in polycrystalline perovskite thin films typically exhibit a size distribution, it appears reasonable that a certain fraction of the grains are below 50 nm, so a confinement effect follows.

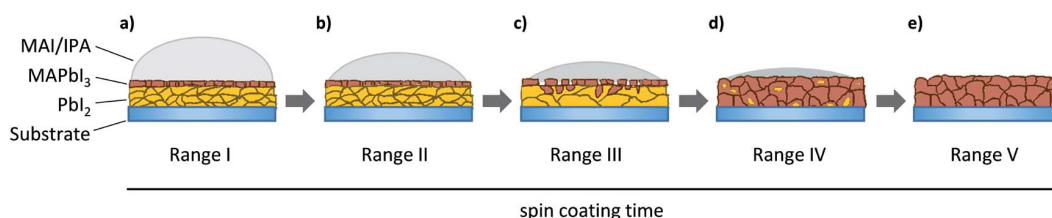


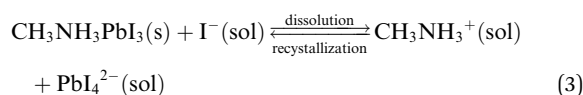
Fig. 5 (a) Range I: the formation of a MAPbI₃ capping layer. (b) Range II: further concentration of the MAI solution above the capping layer through evaporation in the course of several seconds, while the capping layer prevents further MAPbI₃ crystallization. (c) Range III: the iodine concentration increases because of the solvent evaporation and leads to the beginning of the dissolution of the MAPbI₃ capping layer. (d) Range IV: the fast dissolution–recrystallization process, when most of the MAPbI₃ forms. (e) Range V: all of the PbI₂ is transferred into MAPbI₃ and a stable state is reached.

Range II

After the formation of the initial capping layer, the lack of evolution in the spectra suggests that the morphology of the buried PbI_2 and of the MAPbI_3 capping layer formed in the initial period remains highly stable in time range II. This is consistent with reports where the capping layer was found to be very dense due to the higher density of PbI_2 compared to MAPbI_3 .⁴² As a consequence, this has been shown to prevent MAI diffusion to the underlying PbI_2 and thus suppresses further MAPbI_3 crystallization.¹³

Range III

The formation of a dense MAPbI_3 capping layer in time range II obviously raises the question how the MAPbI_3 crystallization is to then proceed eventually. Here a key observation is that in time range III, the high-energy PL tail reduces with time. Importantly, this did not occur by a gradual red-shift of the blue tail, but by a gradual reduction of the PL spectrum that is associated with small crystallites of about 15 nm and below. The disappearance of these smaller crystallites suggests a dissolution process, similar to that observed when dipping PbI_2 layers in MAI solution.^{13,43} Such a so-called “dissolution–recrystallization process” or “solid–liquid recrystallization” is described by the reaction



In this reaction, the balance is shifted to the right side and the formation of PbI_4^{2-} complexes becomes more likely when the MAI concentration is sufficiently high. This explains why the process only sets in after a certain time – in our case after 9 s – when sufficient solvent has evaporated. The generated PbI_4^{2-} complexes are known to dissolve existing MAPbI_3 , *e.g.* the capping layer, so that the underlying PbI_2 becomes accessible for the further MAPbI_3 crystallization.¹³ The dissolution process is considered to start preferably at the grain boundaries and smallest grains,^{6,11,44} and has also been suggested to take place in the case of two-step processing by spin coating.⁴⁴ Consequently, we associate our observed disappearance of the small crystallites with their dissolution in the framework of the dissolution–recrystallization process that sets in during time range III. Even though the smaller MAPbI_3 crystallites dissolve, we do not observe a reduction of absorption, but even a slight increase of the MAPbI_3 thickness from 25 to 50 nm within range III. This suggests that parallel to the dissolution of the smaller crystallites, the underlying PbI_2 reacts with MAI to form more MAPbI_3 which overcompensates for the loss from the dissolution process. Obviously, the newly formed MAPbI_3 does not occupy the space of the just-dissolved MAPbI_3 , but rather the deposits are added to the existing larger MAPbI_3 crystallites, similar to an Ostwald ripening process.

The occurrence of thin film interference in the absorption spectra in range III is consistent with the notion of a dissolution–recrystallization process. It is conceivable that the

interference stems from the MAI/IPA solution layer, possibly influenced by a deterioration of the layer coverage due to the dissolution process. However, it is not clear to what extent the PbI_4^{2-} interacts with the MAI/IPA solution, from which a change in refractive index might occur. In such a case, we expect an increase in the refractive index of the solution layer, as lead halide systems typically exhibit a higher refractive index compared to IPA. Thus, the layer thickness obtained based on the refractive index values of IPA in Fig. 4 represents an upper limit. More detailed investigations are needed to fully address this aspect in the future.

Ranges IV and V

Further solvent evaporation rapidly increases the local MAI concentration and thus further accelerates the solid solution recrystallization process in time range IV. The steep increase of absorption suggests that the equilibrium in eqn (3) shifts significantly towards the recrystallization process. The time scale for the main dissolution–recrystallization process of 1.2 s that we obtained from Fig. 3e is significantly shorter than the typical time scales for this process in the case of dipping PbI_2 in MAI/IPA solution.⁶ Similarly, the growth rate of $445 \pm 15 \text{ nm s}^{-1}$ for the recrystallization process in range IV is much higher than the growth rate of the MAPbI_3 capping layer in range I. This could also explain the significant decrease of the PLQY within range IV, where the fast recrystallization leads to an increased defect density and thus to a more pronounced non-radiative PL decay. The grain sizes of a final film exceed 50 nm as determined by SEM (Fig. S13†). This agrees well with the symmetric shape of the PL spectrum and indicates that no more grains with sizes below 25 nm are present. The spectral position of the PL also matches with the expected bulk spectrum when accounting for self-absorption.

4. Summary and conclusion

Overall, we have monitored the complete two-step film formation process of MAPbI_3 by spin coating using optical spectroscopy. By analyzing the changes in the absorption and photoluminescence spectra, we could identify and quantify different steps in the film formation process. We found that film formation takes place in five consecutive steps, which are as follows: (I) the initial formation of a MAPbI_3 capping layer, (II) further concentration of the MAI solution above the capping layer through evaporation in the course of several seconds, while the capping layer prevents further MAPbI_3 crystallization, (III) the beginning of the dissolution of the MAPbI_3 capping layer due to the increased iodine concentration in the course of progressing solvent evaporation, (IV) a rapid main dissolution–recrystallization process, during which most of the MAPbI_3 crystallizes, and (V) the final, fully converted, temporally stable state. Consideration of confinement and self-absorption effects in the PL spectra, together with consideration of the corresponding absorption spectra made it possible to quantify the growth rate of the initial interface crystallization, which was found to be 11 nm s^{-1} , and the main dissolution–

recrystallization process happens at a rate of 445 nm s^{-1} under our experimental conditions. While the rate for the initial interface crystallization is comparable with results from the two-step method *via* dipping, the growth rate of the dissolution–recrystallization process is significantly higher. This is attributed to the high MAI concentration at the end of the solvent evaporation process. Since most of the MAPbI_3 forms in this short time span (range IV), our results demonstrate the importance of controlling the dissolution–recrystallization process during spin-coating, *e.g.* by controlling the solvent evaporation rate.

We note that the film formation dynamics, *i.e.* extent and timing of the interface crystallization and the dissolution–recrystallization process, depend on the morphology of the PbI_2 layer, which for example can differ significantly when processed on either a mesoscopic or a planar TiO_2 underlying layer.³ Also, for other two-step processing approaches, solvated states can occur which also impact the reaction pathways and crystallization kinetics.^{45,46}

Our work also demonstrates how the film formation process of halide perovskites can be investigated with the help of technically easily accessible *in situ* optical spectroscopy and its analysis. This approach can be easily applied to other, more complex perovskite material systems with mixed halide and/or A-site-cations and processing methods in the future. Our work will therefore help to better understand and optimize the film formation process of halide perovskites in general.

5. Experimental section

Materials and thin film processing

Lead iodide (PbI_2) beads, *N,N*-dimethylformamide (DMF), and isopropanol (IPA) were purchased from Sigma Aldrich company. Methylammonium iodide (MAI) was purchased from Dyesol company. 461 mg ml^{-1} (1 M) PbI_2 was dissolved in dimethylformamide (DMF) and heated at 75°C overnight. $40 \mu\text{L}$ PbI_2 solvent was spin coated on a glass substrate in a N_2 glovebox at $3000 \text{ rpm min}^{-1}$ for 50 s, followed by annealing at 100°C for 5 min. After that, the PbI_2 film was moved to an ambient atmosphere with a humidity of $\sim 50\%$. MAI solvent was prepared in IPA at a concentration of 40 mg ml^{-1} (0.25 M). The PbI_2 film was placed in a homemade spin coater. $200 \mu\text{L}$ MAI solvent was dropped on the PbI_2 film and immediately spin coated at $1200 \text{ rpm min}^{-1}$.

In situ optical spectroscopy

For transmission measurements, a white LED is placed below the rotating chuck, with a bore along the rotation axis of the chuck allowing transmission of white light through the investigated layer and its collection *via* an optical fiber which guides the transmitted light into the detection system. For PL measurements, a diode laser (excitation wavelength: 520 nm) excites the sample area at a shallow angle with a laser power density of $\sim 75 \text{ mW cm}^{-2}$. Use of this laser power density allows estimation of the change in local temperature due to laser heating, which is found to be approximately 0.5°C (see the ESI

for details†). The resulting PL is collected *via* the same optical fiber used for the transmission measurement.

Conflicts of interest

There are no conflicts to declare.

Acknowledgements

S. H., A. K. and Y. Z. acknowledge funding from the Bavarian State Ministry of Science, Research and the Arts for the Collaborative Research Network “Solar Technologies go Hybrid”. Y. Z. acknowledges funding from the China Scholarship Council. K. S. acknowledges financial support from the German National Science Foundation (Project KO 3973/2-1 and GRK 1640). M. C., A. K. and F. P. acknowledge support from the Marie Curie Innovative Training Network (ITN) INFORM. We thank the Bavarian Polymer Institute for SEM characterization.

References

- 1 J. Burschka, N. Pellet, S.-J. Moon, R. Humphry-Baker, P. Gao, M. K. Nazeeruddin and M. Grätzel, *Nature*, 2013, **499**, 316.
- 2 J.-H. Im, I.-H. Jang, N. Pellet, M. Grätzel and N.-G. Park, *Nanotechnol.*, 2014, **9**, 927.
- 3 M. Becker and M. Wark, *Cryst. Growth Des.*, 2018, **18**, 4790–4806.
- 4 Z. Xiao, C. Bi, Y. Shao, Q. Dong, Q. Wang, Y. Yuan, C. Wang, Y. Gao and J. Huang, *Energy Environ. Sci.*, 2014, **7**, 2619–2623.
- 5 H. Chen, *Adv. Funct. Mater.*, 2017, **27**, 1605654.
- 6 T.-Y. Hsieh, C.-K. Huang, T.-S. Su, C.-Y. Hong and T.-C. Wei, *ACS Appl. Mater. Interfaces*, 2017, **9**, 8623–8633.
- 7 J. B. Patel, R. L. Milot, A. D. Wright, L. M. Herz and M. B. Johnston, *J. Phys. Chem. Lett.*, 2015, **7**, 96–102.
- 8 D. Barrit, P. Cheng, M.-C. Tang, K. Wang, H. Dang, D.-M. Smilgies, S. Liu, T. D. Anthopoulos, K. Zhao and A. Amassian, *Adv. Funct. Mater.*, 2019, **29**, 1807544.
- 9 H. Zhang, J. Mao, H. He, D. Zhang, H. L. Zhu, F. Xie, K. S. Wong, M. Grätzel and W. C. Choy, *Adv. Energy Mater.*, 2015, **5**, 1501354.
- 10 S. Mastroianni, F. Heinz, J.-H. Im, W. Veurman, M. Padilla, M. Schubert, U. Würfel, M. Grätzel, N.-G. Park and A. Hinsch, *Nanoscale*, 2015, **7**, 19653–19662.
- 11 H. Ko, D. H. Sin, M. Kim and K. Cho, *Chem. Mater.*, 2017, **29**, 1165–1174.
- 12 N. Ahn, S. M. Kang, J.-W. Lee, M. Choi and N.-G. Park, *J. Mater. Chem. A*, 2015, **3**, 19901–19906.
- 13 Y. Fu, F. Meng, M. B. Rowley, B. J. Thompson, M. J. Shearer, D. Ma, R. J. Hamers, J. C. Wright and S. Jin, *J. Am. Chem. Soc.*, 2015, **137**, 5810–5818.
- 14 S. Yang, Y. C. Zheng, Y. Hou, X. Chen, Y. Chen, Y. Wang, H. Zhao and H. G. Yang, *Chem. Mater.*, 2014, **26**, 6705–6710.
- 15 M. Buchhorn, S. Wedler and F. Panzer, *J. Phys. Chem. A*, 2018, **122**, 9115–9122.
- 16 S. Singh, C. Li, F. Panzer, K. Narasimhan, A. Graeser, T. P. Gujar, A. Köhler, M. Thelakkat, S. Huettner and D. Kabra, *J. Phys. Chem. Lett.*, 2016, **7**, 3014–3021.

- 17 F. Panzer, S. Baderschneider, T. P. Gujar, T. Unger, S. Bagnich, M. Jakoby, H. Bässler, S. Hüttner, J. Köhler and R. Moos, *Adv. Opt. Mater.*, 2016, **4**, 917–928.
- 18 F. Panzer, C. Li, T. Meier, A. Köhler and S. Huettner, *Adv. Energy Mater.*, 2017, **7**, 1700286.
- 19 A. Merdasa, A. Kiligaridis, C. Rehermann, M. Abdi-Jalebi, J. Stöber, B. Louis, M. Gerhard, S. D. Stranks, E. L. Unger and I. G. Scheblykin, *ACS Energy Lett.*, 2019, **4**, 1370–1378.
- 20 J. Li, A. Dobrovolsky, A. Merdasa, E. L. Unger and I. G. Scheblykin, *ACS Omega*, 2018, **3**, 14494–14502.
- 21 M. Cadelano, M. Saba, N. Sestu, V. Sarritzu, D. Marongiu, F. Chen, R. Piras, F. Quochi, A. Mura and G. Bongiovanni, in *Perovskite Materials-Synthesis, Characterisation, Properties, and Applications*, IntechOpen, 2016.
- 22 F. Zhang, S. Huang, P. Wang, X. Chen, S. Zhao, Y. Dong and H. Zhong, *Chem. Mater.*, 2017, **29**, 3793–3799.
- 23 M. E. Kamminga, H.-H. Fang, M. R. Filip, F. Giustino, J. Baas, G. R. Blake, M. A. Loi and T. T. Palstra, *Chem. Mater.*, 2016, **28**, 4554–4562.
- 24 M. Anaya, A. Rubino, T. C. Rojas, J. F. Galisteo-López, M. E. Calvo and H. Míguez, *Adv. Opt. Mater.*, 2017, **5**, 1601087.
- 25 V. Malgras, S. Tominaka, J. W. Ryan, J. Henzie, T. Takei, K. Ohara and Y. Yamauchi, *J. Am. Chem. Soc.*, 2016, **138**, 13874–13881.
- 26 D. N. Dirin, L. Protesescu, D. Trummer, I. V. Kochetygov, S. Yakunin, F. Krumeich, N. P. Stadie and M. V. Kovalenko, *Nano Lett.*, 2016, **16**, 5866–5874.
- 27 E. S. Parrott, J. B. Patel, A.-A. Haghghirad, H. J. Snaith, M. B. Johnston and L. M. Herz, *Nanoscale*, 2019, **11**, 14276–14284.
- 28 L. Polavarapu, B. Nickel, J. Feldmann and A. S. Urban, *Adv. Energy Mater.*, 2017, **7**, 1700267.
- 29 A. Buin, R. Comin, A. H. Ip and E. H. Sargent, *J. Phys. Chem. C*, 2015, **119**, 13965–13971.
- 30 F. A. Jenkins and H. E. White, *Fundamentals of optics*, Tata McGraw-Hill Education, 1937.
- 31 J. Manificier, J. Gasiot and J. Fillard, *J. Phys. E: Sci. Instrum.*, 1976, **9**, 1002.
- 32 R. Munir, A. D. Sheikh, M. Abdelsamie, H. Hu, L. Yu, K. Zhao, T. Kim, O. E. Tall, R. Li and D. M. Smilgies, *Adv. Mater.*, 2017, **29**, 1604113.
- 33 A. Köhler and H. Bässler, *Electronic processes in organic semiconductors: An introduction*, John Wiley & Sons, 2015.
- 34 G. Rey, C. Spindler, F. Babbe, W. Rachad, S. Siebentritt, M. Nuys, R. Carius, S. Li and C. Platzer-Björkman, *Phys. Rev. Appl.*, 2018, **9**, 064008.
- 35 C. Prall, C. Kaspari, A. Knauer, K. Haberland, M. Weyers and D. Rueter, *TM, Tech. Mess.*, 2017, **84**, 747–752.
- 36 K. Schötz, M. A. Askar, W. Peng, D. Seeberger, P. T. Gujjar, M. Thelakkat, A. Köhler, S. Huettner, M. O. Bakr, K. Shankar and F. Panzer, *J. Mater. Chem. C*, 2020, DOI: 10.1039/c9tc06251c.
- 37 T. Yamada, Y. Yamada, Y. Nakaike, A. Wakamiya and Y. Kanemitsu, *Phys. Rev. Appl.*, 2017, **7**, 014001.
- 38 T. Meier, T. P. Gujar, A. Schönleber, S. Olthof, K. Meerholz, S. van Smaalen, F. Panzer, M. Thelakkat and A. Köhler, *J. Mater. Chem. C*, 2018, **6**, 7512–7519.
- 39 T. W. Crothers, R. L. Milot, J. B. Patel, E. S. Parrott, J. Schlipf, P. Müller-Buschbaum, M. B. Johnston and L. M. Herz, *Nano Lett.*, 2017, **17**, 5782–5789.
- 40 J. Schlipf, P. Docampo, C. J. Schaffer, V. Körstgens, L. Biefmann, F. Hanusch, N. Giesbrecht, S. Bernstorff, T. Bein and P. Müller-Buschbaum, *J. Phys. Chem. Lett.*, 2015, **6**, 1265–1269.
- 41 A. E. Lewis, Y. Zhang, P. Gao and M. K. Nazeeruddin, *ACS Appl. Mater. Interfaces*, 2017, **9**, 25063–25066.
- 42 X. Cao, L. Zhi, Y. Jia, Y. Li, K. Zhao, X. Cui, L. Ci, D. Zhuang and J. Wei, *ACS Appl. Mater. Interfaces*, 2019, **11**, 7639–7654.
- 43 Q. Chen, H. Zhou, Z. Hong, S. Luo, H.-S. Duan, H.-H. Wang, Y. Liu, G. Li and Y. Yang, *J. Am. Chem. Soc.*, 2013, **136**, 622–625.
- 44 H. Ko, S. J. Yang, C. Park, D. H. Sin, H. Lee and K. Cho, *ACS Appl. Mater. Interfaces*, 2019, **11**, 7037–7045.
- 45 N. Ahn, D.-Y. Son, I.-H. Jang, S. M. Kang, M. Choi and N.-G. Park, *J. Am. Chem. Soc.*, 2015, **137**, 8696–8699.
- 46 Z.-w. Kwang, C.-W. Chang, T.-Y. Hsieh, T.-C. Wei and S.-Y. Lu, *Electrochim. Acta*, 2018, **266**, 118–129.

Supporting Information for:

Investigating Two-Step MAPbI₃ Thin Film Formation during Spin Coating by Simultaneous in Situ Absorption and Photoluminescence Spectroscopy

Mihirsinh Chauhan,^{1,2,#} Yu Zhong,^{1,3,#} Konstantin Schötz,¹ Brijesh Tripathi,² Anna Köhler,^{1,4} Sven
Huettner³, Fabian Panzer^{1*}

1: Soft Matter Optoelectronics, University of Bayreuth, 95440 Bayreuth, Germany

2: School of Technology, Pandit Deendayal Petroleum University, 382007 Gandhinagar, India

3: Department of Chemistry, University of Bayreuth, 95440 Bayreuth, Germany

4: Bayreuth Institute of Macromolecular Research (BIMF) and Bavarian Polymer Institute (BPI),
University of Bayreuth, 95440 Bayreuth, Germany.

#: Authors contributed equally

Corresponding Author: fabian.panzer@uni-bayreuth.de

S1: Additional OD and PL spectra

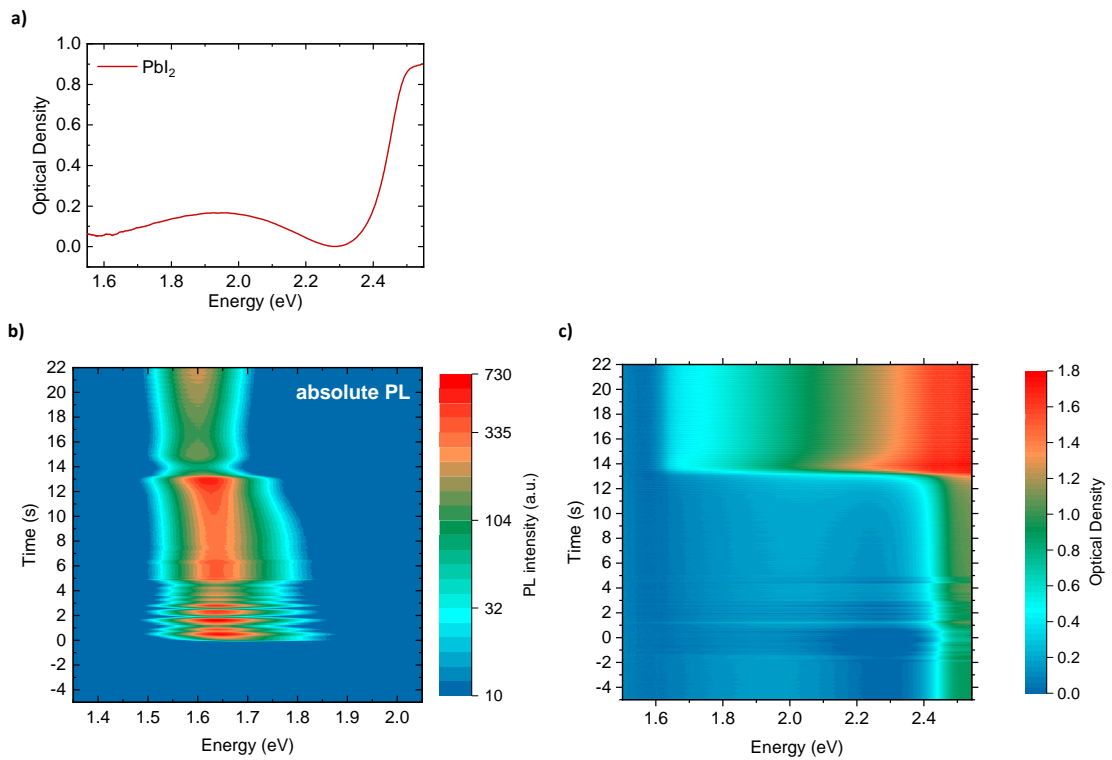


Figure S1: (a) Optical Density of the neat PbI_2 layer. (b) 2D map of the temporal evolution of the PL spectrum with absolute measured intensities as indicated with colors. (c) 2D map of the temporal evolution of the measured Optical Density with intensities as indicated with colors. As a reference spectrum I_0 , the transmission through a blank quartz substrate was used.

S2: Fitting of hyperbolic secant to measured PL in range I

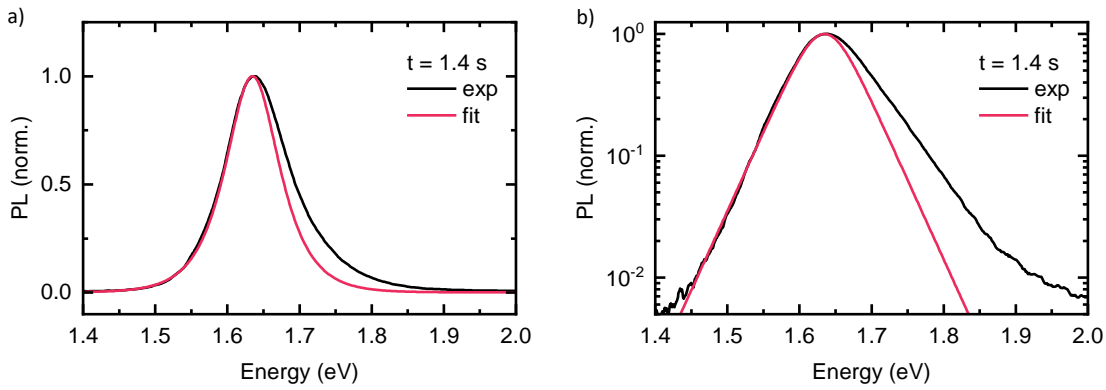


Figure S2: Normalized PL at $t = 1.4$ s (black) and a fit using a hyperbolic secant, demonstrating the asymmetry of the measured PL line shape, plotted on a (a) linear intensity scale and (b) log intensity scale.

S3: Calculation of MAPbI₃ crystal size from the PL spectra in range I using confinement approach:

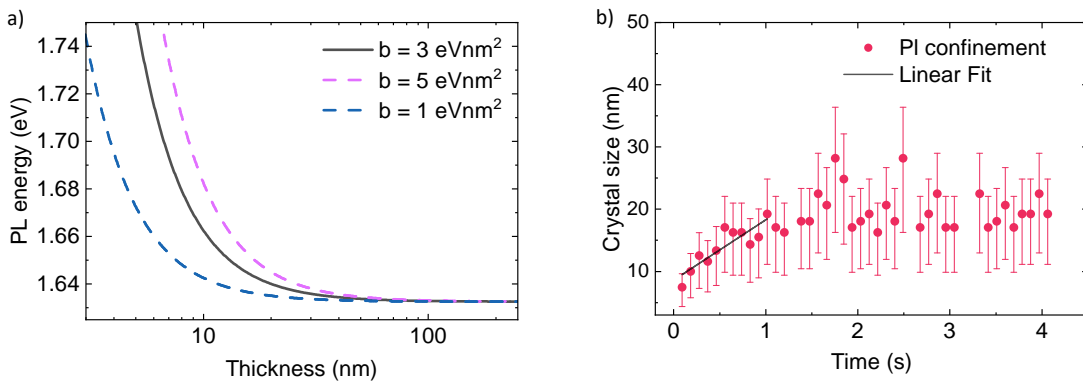


Figure S3: (a) Correlation between PL Peak energy E and crystal size d as proposed by Parrot et al.,¹ $E = E_g + \frac{b}{d^2}$ with $E_g = 1.63$ eV and different b values of 1 eVnm² (dashed blue), 3 eVnm² (solid black) and 5 eVnm² (dashed purple). The curves for $b = 1$ eVnm² and $b = 5$ eVnm² were used to calculate the crystal size error. (b) Evolution of crystal size (red dots) within the first 4 seconds of processing, where the crystal size is calculated on the basis of the black line in (a). The initial growth rate was quantified using a linear fit in the time range up to 1.0 s (black line) where a slope of 11 ± 2 nm/s is obtained.

S4: Extracted absorption edge of PL in range III

The optical density of the absorption edge was extracted by $OD = -\log\left(\frac{PL_{final}}{PL_{initial}}\right)$, where $PL_{initial}$ is the PL at $t = 9.1$ s and PL_{final} is the PL at $t = 12.6$ s scaled to the red falling edge of $PL_{initial}$. Note that this scaling procedure does not alter the spectral shape of the obtained absorption, but only shifts it up in OD to avoid negative ODs.

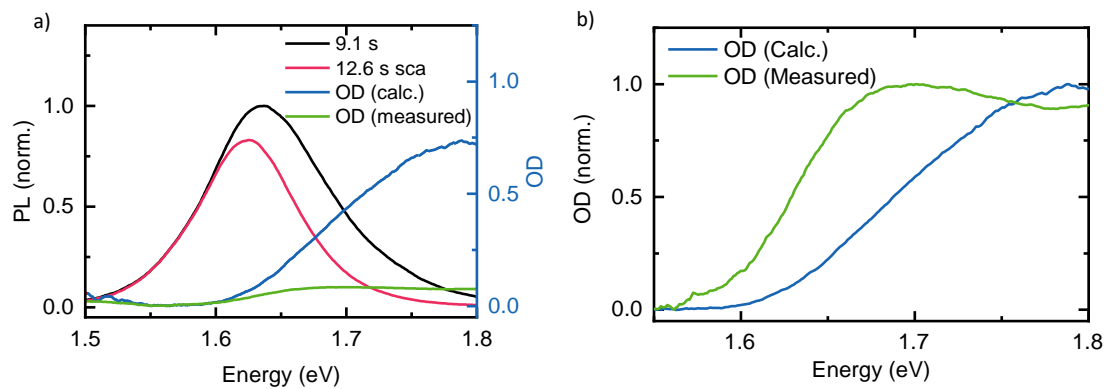


Figure S4: (a) PL at $t = 12.6$ s (red) scaled to the lower energy edge of the PL at $t = 9.1$ s (black) together with the calculated optical density if the spectral change was due to self-absorption (blue line) and the measured absorption edges determined by the measured optical density (green) at $t = 12.6$ s, (b) Normalized calculated (blue) and measured (green) optical density at $t = 12.6$ s, from which the deviations in both shape and energetic position become clear.

S5: Effect of self-absorption in range III

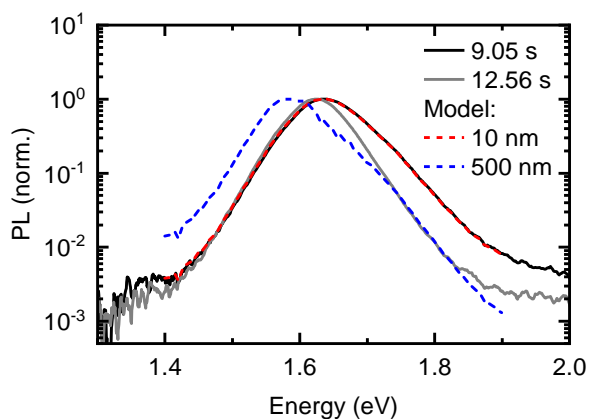


Figure S5: Normalized measured PL at $t = 9.1$ s (black) and $t = 12.6$ s (grey), together with modeled PL considering self-absorption and internal reflections, assuming the PL at $t = 9.1$ s to correspond to the intrinsic PL spectrum. The significant mismatch between the modeled PL and the experimental one at 12.6 s demonstrates that the observed spectral change are not due to self-absorption effects.

S6: Difference PL spectra in range III

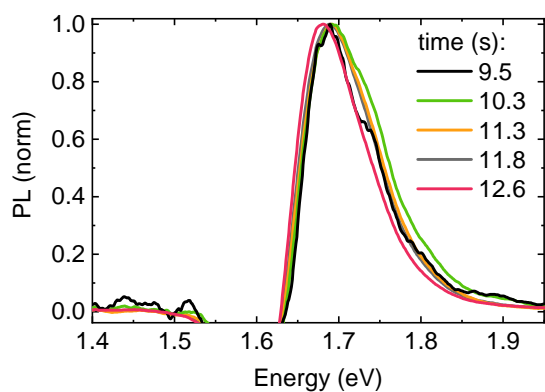


Figure S6: Normalized difference spectra between the PL spectrum at 9.1 s and the later spectra (times as indicated) in range III.

S7: Thickness Calculation from Absorption Interference at range III

Interference fringes in the measured absorption spectra were observed at the end of range III, as shown in Figure S7a $t_2 = 11.6$ s (red curve). Based on the appearance of this interference fringes, we can estimate the thickness of the sample, from the following equation:^{2, 3}

$$d = \frac{\lambda_1 \lambda_2}{2(\lambda_1 n_2 - \lambda_2 n_1)} \quad (S1)$$

d : thickness of the sample;

λ_1 and λ_2 : the wavelength at two adjacent maximum or minimum intensity;

n_1 and n_2 : the sample refractive index at λ_1 and λ_2 .

To quantify the value of λ_1 and λ_2 , we use the normalized absorption e.g. at $t_2 = 11.6$ s and subtract the absorption spectrum at $t_1 = 9.1$ s (without interference) and obtain the blue curve in Figure S7a. The refractive index has been taken from Leguy et al., Sani et al. and Riccardo et al. for $\text{CH}_3\text{NH}_3\text{PbI}_3$, isopropanol and PbI_2 respectively.⁴⁻⁶ In the range between 550 – 750nm, the refractive indexes of these three materials are, 2.4~2.5 ($\text{CH}_3\text{NH}_3\text{PbI}_3$), 1.3~1.4 (isopropanol) and 3.1~3.2 (PbI_2). Depending on the chosen parameters the calculated thicknesses from Equation S1 differ (Figure S7b)

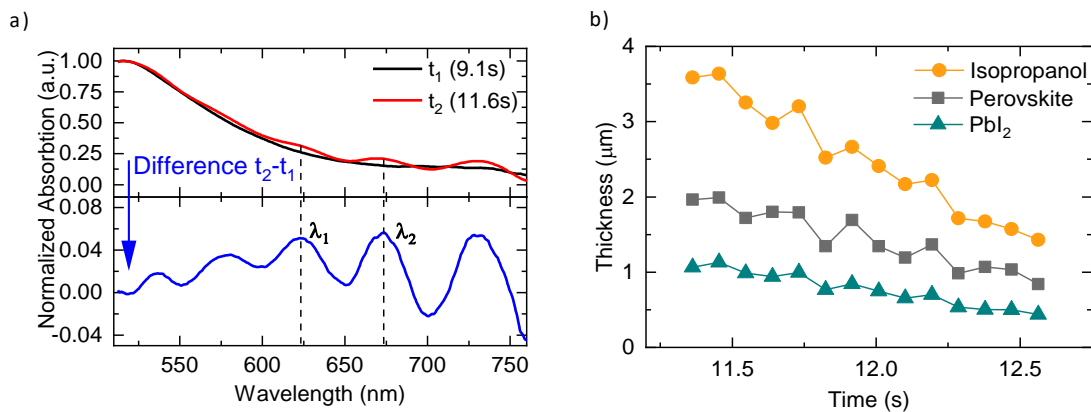


Figure S7: (a) Normalized absorption spectra at 9.1 s (black) and 11.6 s (red). The blue curve indicates the difference of absorption at t_2 and its original absorption at t_1 and was used to extract λ_1 and λ_2 (b) The calculated thickness from the interference fringes using the refractive index of isopropanol (yellow dots), MAPbI_3 (grey squares) and PbI_2 (green triangles).

S8: Estimation of MAPbI₃ thickness from absorption data

From Lambert-Beer law,

$$I = I_0 e^{-a*d} \quad (S2)$$

I_0 : Incident intensity;

I : Transmittance intensity;

a : Absorption coefficient;

d : Film thickness.

Then we can obtain the thickness from the following equation:

$$a = 2.303 \left(\frac{OD}{d} \right) \quad (S3)$$

OD: Optical density.

The absorption coefficient is extracted from literature,⁷ as illustrated in Figure S8a. Figure S8b shows comparison of experimental absorption spectra and calculated absorption with thickness and absorption coefficient plotted in Figure 4 in the main text.

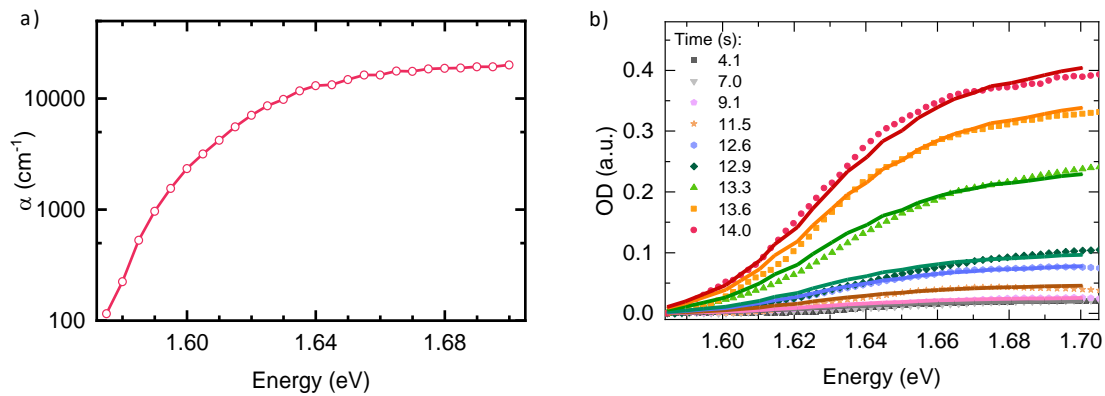


Figure S8: (a) Absorption coefficient of perovskite film used for thickness calculation,⁷ (b) Experimental absorption spectra at different time (Symbol) and the corresponding calculated spectrum from absorption coefficient and thickness (lines).

S9: Calculation of growth rate in range IV

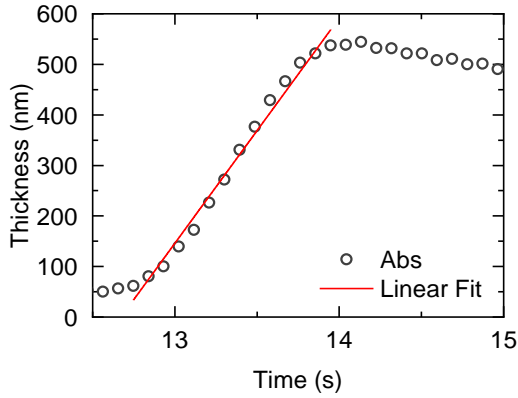


Figure S9: Linear fit to MAPbI₃ layer thickness in range IV to estimate the MAPbI₃ growth rate from resulting slope, where we find a value in the range of 445±15 nm/s.

S10: Estimation of MAPbI₃ thickness from the PL spectra in range IV

As outlined in our previous work,⁸ for a given intrinsic PL, the detectable PL after internal reflections and self-absorption can be expressed as

$$PL_{detected}(E) = C \cdot PL_{direct}(E) + PL_{filtered}(E) \quad (S4)$$

$PL_{direct}(E)$ and $PL_{filtered}(E)$ can be calculated according to the Beer-Lambert law,

$$PL_{direct}(E) = \int_0^L PL_{int}(E) \cdot n(x)^2 \cdot (1 - r_f) \cdot \exp[-\alpha(E) \cdot x] dx \quad (S5)$$

$$PL_{filtered}(E) = \int_0^L \sum_{j=1}^{\infty} PL_{int}(E) \cdot n(x)^2 \cdot (1 - r_f) \cdot \{A_j + B_j\} dx \quad (S6)$$

with $A_j = r_f^j \cdot r_b^j \cdot \exp[-\alpha(E) \cdot (2jL + x)]$ considering the part of the PL that propagates from the site of generation, x_i , towards the front surface, and propagation towards the back surface is considered by $B_j = r_f^{j-1} \cdot r_b^j \cdot \exp[-\alpha(E) \cdot ((2j - 1) \cdot L + (L - x))]$. Here, $\alpha(E)$ denotes the absorption coefficient of the material, r_f and r_b are the reflection probabilities at the front and back interface, respectively, $n(x)$ is the charge carrier density and L denotes the layer

thickness. C is a suppression constant, which accounts for a mismatch of excitation and detection spot, where $C = 1$ means no suppression and $C = 0$ full suppression of the direct PL.

As the PL at the beginning of range IV is already affected by self-absorption, the intrinsic PL must be extracted by solving Equations S4-S6 for the intrinsic PL, $PL_{int}(E)$, which yields

$$\begin{aligned}
 PL_{int}(E) = PL_{detected}(E) & \\
 & \cdot \left\{ C \right. \\
 & \cdot \int_0^L \left[n(x)^2 \cdot (1 - r_f) \cdot \exp[-\alpha(E) \cdot x] \right. \\
 & \left. \left. + \sum_{j=1} n(x)^2 \cdot (1 - r_f) \cdot \{A_j + B_j\} \right] dx \right\}^{-1}
 \end{aligned} \tag{S7}$$

with L being the thickness of the MAPbI₃ layer at the beginning of region IV, as determined by the absorption data. The calculated intrinsic PL is shown in Figure S10. Using this intrinsic PL, the thickness of the MAPbI₃ layer at any time is obtained by a least-squares-fit of Equation S4, normalized, to the normalized experimental PL spectra, for a given parameter set with L being optimized.

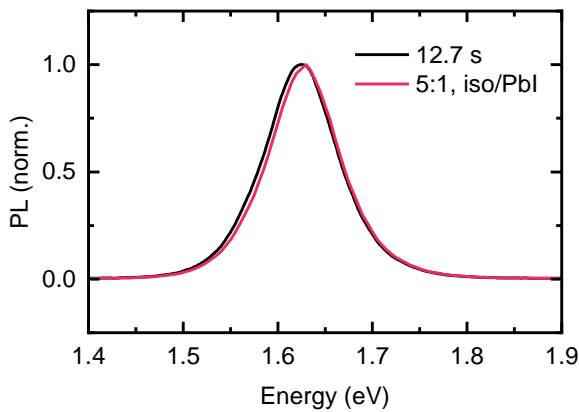


Figure S10: PL at 12.7 s and calculated intrinsic PL for an assumed layer thickness of 50 nm by inversely applying our model for calculating PL affected by self-absorption and internal reflections. The calculated intrinsic PL is then used for the estimation of the layer thickness for the following time steps.

$n(x)$ is approximated identical to the charge carrier density after laser excitation. By this, the model neglects charge carrier diffusion. In the case of thin layers, where the optical path length of the internally reflected light is on a similar length scale as the diffusion length of charge carriers, this is likely to affect the quantitative results of our model.

The reflection probabilities at the interfaces were estimated by calculating the angle-dependent reflection coefficients according to the Fresnel equations and then averaged over all possible incident angles. With refractive indices in the relevant energy range of 2.5 for MAPbI₃^{4,9}, about 1.45 for glass¹⁰, 1.38 for isopropanol⁵, about 2.5 for PbI₂⁶ and 1 for air, one obtains reflection probabilities of 0.85 for the interface MAPbI₃-air, 0.7 for MAPbI₃-glass, 0.71 for MAPbI₃-isopropanol and about 0 for MAPbI₃-PbI₂. Except for the case of MAPbI₃-PbI₂, reflections at other interfaces are neglected for simplicity, but would lead to an increase of the overall “effective” reflection probability. Since MAPbI₃ and PbI₂ are nearly index-matched, we consider instead the PbI₂-glass interface with the same reflection probability as the MAPbI₃-glass interface.

Figure S11a shows the obtained thicknesses for different interfaces (glass-perovskite-air (g-a) and glass-(PbI₂-) perovskite-isopropanol (g-i)) and suppression constants C , together with the one obtained from the absorption measurements. All thicknesses obtained from the modelling agree well with the ones obtained from absorption. Best agreement is obtained for PbI₂ and isopropanol as surrounding media and a suppression constant of 0.3 (g-i, 0.3; blue triangles), while all other parameter sets yield slightly lower thicknesses. However, comparing the resulting modelled PL spectra (Figure S11c-f) with the experimental ones (Figure S11b) reveals that the PL from (g-i, 0.3) (Figure S11e) agrees worst with the experimental data, especially considering the temporal evolution of the high energy falling edge. Second best agreement considering the thicknesses is obtained with (g-i, 0.2), where also the modelled PL spectra (Figure S11f) match the experimental ones nicely. A very similar result is obtained with (g-a, 0.3), and (g-a, 0.2) yields again slightly smaller thicknesses.

To capture the temporal evolution of the thickness more accurately by our model, it would probably be necessary to consider a transition of the interfaces, starting from PbI₂ and isopropanol and ending with glass and air as surrounding media. Since we have no indication on when and how this transition happens, we can not examine this scenario closer.

However, we want to stress that even with the simple model discussed above, good agreement between the thickness from the PL modelling and the one from absorption measurements could be obtained. Further, this clearly demonstrates that the observed red-shift of the PL in range IV is due to self-absorption, and represents a good example of the magnitude of self-absorption, despite excitation and detection being on the same side of the thin film.

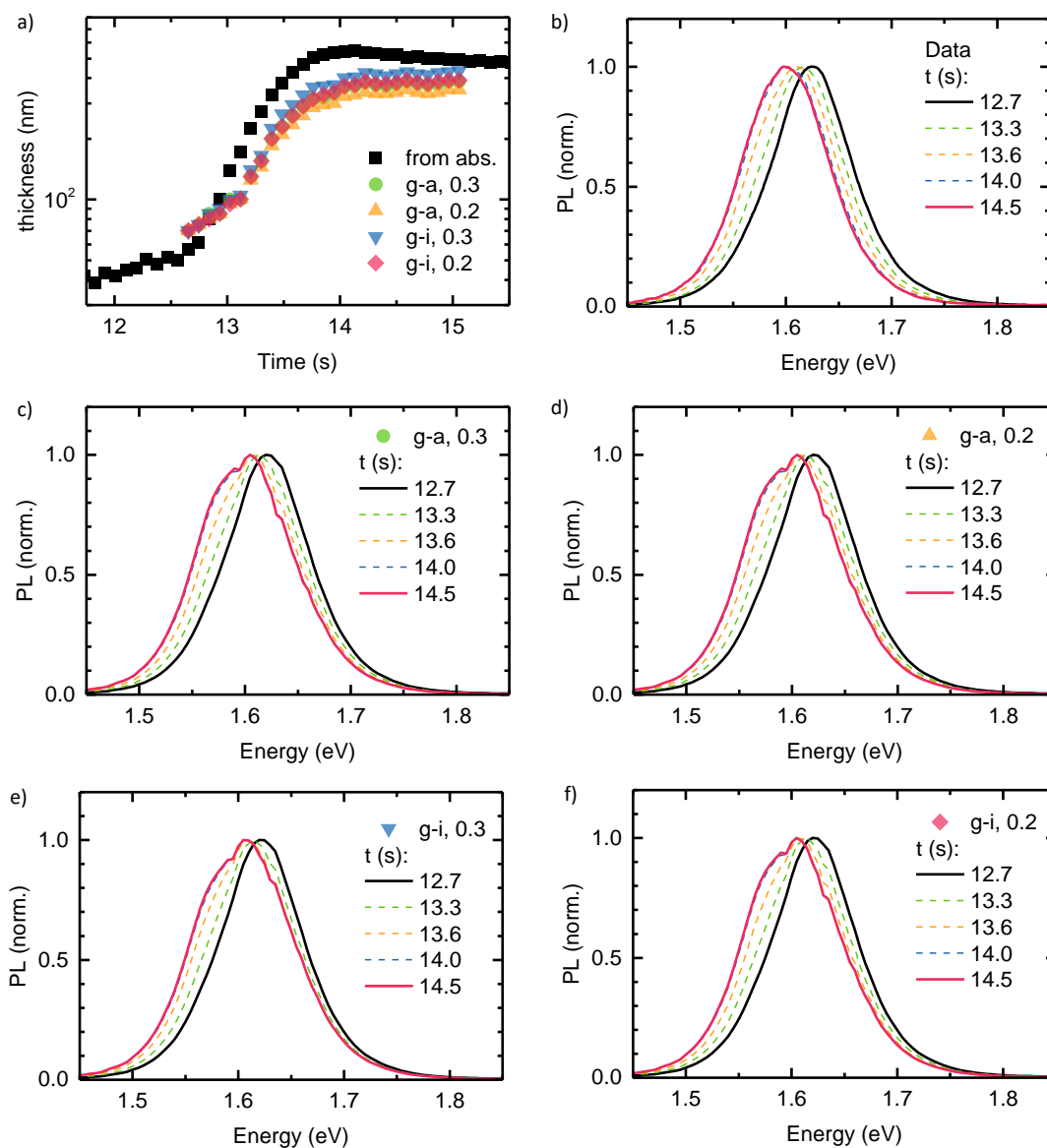


Figure S11: (a) MAPbI₃ layer thickness obtained from absorption measurements (black squares) together with the ones from optical modelling considering internal reflections and self-absorption. (b) Experimental PL spectra in range IV. (c-f) Modelled PL spectra considering internal reflections

and self-absorption for different surrounding media (that is glass and air (g-a), or glass and isopropanol (g-i)) and different suppression constants of 0.3 and 0.2.

S11: XRD measurements of the sample

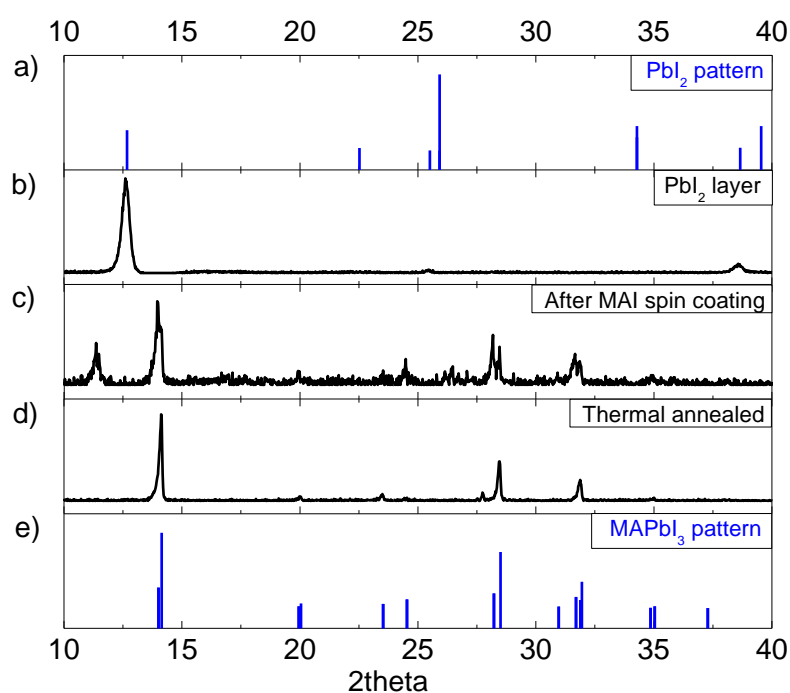


Figure S12: XRD pattern of (a) Pbl₂ and (e) MAPbl₃ obtained from references.^{11, 12} XRD spectra of (b) Pbl₂ layer on glass substrate, (c) with MAI solvent spin coated on the Pbl₂ layer and (d) the MAI + Pbl₂ film after 45min thermal annealing.

Figure S12c shows that the formation of perovskite after the spin coating of MAI solvent. The peak 2θ = 11.4° suggests the existence of dihydrate (MA)₄Pbl₆·2H₂O.^{4, 13} while any sign of remaining educt phase e.g. Pbl₂ is absent. After thermal annealing, the signal from the dihydrate completely vanishes (Figure S12d).

S12: Estimation of average grain size of MAPbI₃ from SEM and theoretical model

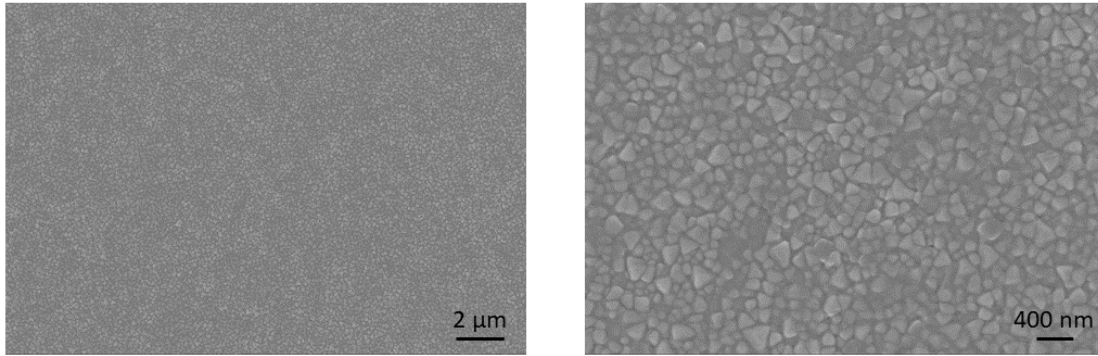


Figure S13: SEM images of the prepared film after spin coating. It yields compacted perovskite crystals. The size of the grains is between 50 nm-300 nm.

Theoretical model:

Ahn et al. derived the interaction formula to correlate grain size (Y) with MAI concentration (X) used in two step processing given as:¹⁴

$$\ln Y = \frac{1.22}{(\ln X - \ln C)^2} + 3.73 \quad (S8)$$

Here, C = 0.02 M MAI solution has been taken as equilibrium concentration by assuming that 0.02 M MAI solution could not react with PbI₂ films at room temperature. Using these conditions, grain size expressed as:

$$Y = \exp(1.22/((\ln(X) - \ln(0.02))^2) + 3.73) \quad (S9)$$

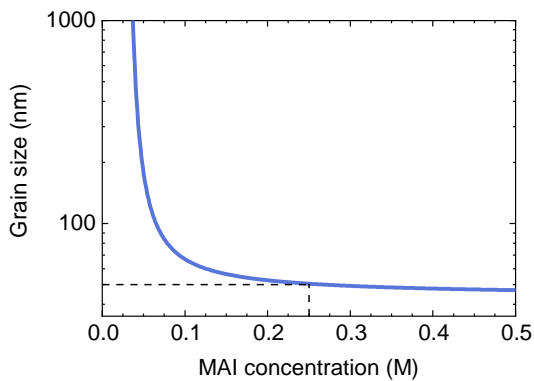


Figure S14: Average grain size of MAPbI₃ as a function of MAI concentration based on the model presented by Ahn et al.¹⁴ The calculated grain size for 0.25 M (40 mg/ml) concentration (used for this study) is about 50 nm.

S13: Estimation of local heating due to laser excitation

The temperature change of the excitation spot during laser light illumination is generally determined by the heat delivered Q , divided by the heat capacity C of the material, thus $\Delta T = Q/C$. The delivered heat by the laser per time $\frac{\Delta Q_{Laser}}{\Delta t}$ is proportional to the laser fluence E_e multiplied by the area of the excitation spot A_{spot} . However, one has to consider that not all the laser light is absorbed. For the excitation wavelength of 520 nm, we observed a maximal optical density of 1 for the perovskite samples, thus 90 % of the laser light is absorbed, neglecting reflection, which would reduce the amount of absorbed light further. Additionally, not all of the absorbed energy is transformed into heat. One part of heat is provided by thermal relaxation of the carriers from their initial energy to the energy of the band gap, which gives a fraction of $\frac{\Delta E}{E_{photon}} = \frac{2.38 \text{ eV} - 1.63 \text{ eV}}{2.38 \text{ eV}} = 0.315$. The relaxed charge carriers can then either recombine radiatively or non-radiatively, producing heat. Assuming a PLQY of 0.1, corresponds to a fraction of non-radiative decay of 90%, so that we get another fraction of $\frac{1.63 \text{ eV} \cdot 0.9}{2.38 \text{ eV}} = 0.616$. Thus in sum, a fraction of $f = 0.931$ of the irradiated energy is transformed to heat.

Since the sample is illuminated continuously during one frame (approx. 0.045 s) and the heat is not delivered instantly, one has to consider the cooling of the heated spot by thermal transport through the substrate to the spin coater. This is given by the heat equation:

$$\frac{\Delta Q}{\Delta t} = \frac{\lambda \Delta T}{l} A \quad (\text{S10})$$

where λ is the thermal conductivity, ΔT is the temperature of the bath minus the temperature of the excitation spot, A is the area normal to the heat flow, and l is the length over which the dissipation takes place. Since the spot size is large compared to the thickness of the perovskite layer, lateral heat transport can be neglected and $A = A_{spot}$.

In thermal equilibrium, the decrease of heat by thermal transport is equal to the increase of heat by laser irradiation,

$$\frac{\Delta Q_{ges}}{\Delta t} = \frac{\lambda \Delta T}{l} A_{spot} + E_e \cdot f \cdot A_{spot} = 0 \quad (\text{S11})$$

Rearranging this equation for ΔT gives

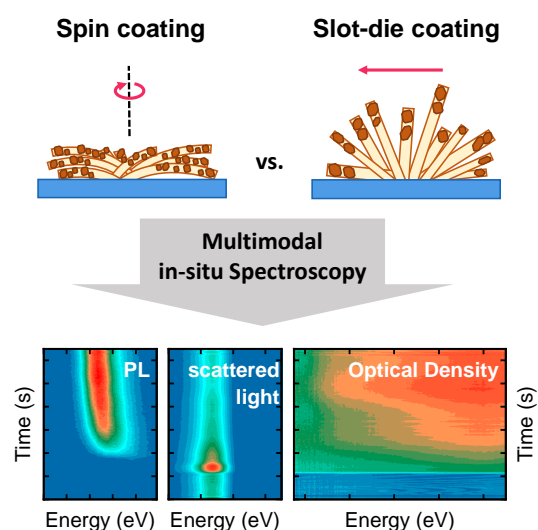
$$-\Delta T = \frac{E_e \cdot f \cdot l}{\lambda} \quad (\text{S12})$$

Considering the spin coater as a thermal bath with a constant temperature of 300 K, the heat transport takes place over the thickness of the substrate, that is $l = 1 \text{ mm}$. The thermal conductivity of fused silica, which transports the heat, is $\lambda = 1.5 \frac{\text{W}}{\text{Km}}$.¹⁵ The fluence of the laser was determined to be $E_e = 75 \text{ mW/cm}^2$. Inserting this into equation S12, gives a heating of the sample of $|\Delta T| \approx 0.5 \text{ K}$ upon laser exposure.

References

1. E. S. Parrott, J. B. Patel, A.-A. Haghighirad, H. J. Snaith, M. B. Johnston and L. M. Herz, *Nanoscale*, 2019, **11**, 14276-14284.
2. J. Manificier, J. Gasiot and J. Fillard, *J. Phys. E: Sci. Instrum.*, 1976, **9**, 1002.
3. R. Munir, A. D. Sheikh, M. Abdelsamie, H. Hu, L. Yu, K. Zhao, T. Kim, O. E. Tall, R. Li and D. M. Smilgies, *Adv. Mater.*, 2017, **29**, 1604113.
4. A. M. Leguy, Y. Hu, M. Campoy-Quiles, M. I. Alonso, O. J. Weber, P. Azarhoosh, M. Van Schilfgaarde, M. T. Weller, T. Bein and J. Nelson, *Chemistry of Materials*, 2015, **27**, 3397-3407.
5. E. Sani and A. Dell'Oro, *Optical Materials*, 2016, **60**, 137-141.
6. R. Frisenda, J. O. Island, J. L. Lado, E. Giovanelli, P. Gant, P. Nagler, S. Bange, J. M. Lupton, C. Schüller and A. J. Molina-Mendoza, *Nanotechnology*, 2017, **28**, 455703.
7. T. W. Crothers, R. L. Milot, J. B. Patel, E. S. Parrott, J. Schlipf, P. Müller-Buschbaum, M. B. Johnston and L. M. Herz, *Nano Lett.*, 2017, **17**, 5782-5789.
8. K. Schötz, M. A. Askar, W. Peng, D. Seeberger, P. T. Guijar, M. Thelakkat, A. Köhler, S. Huettnner, M. O. Bakr and K. Shankar, 2019, submitted.
9. L. J. Phillips, A. M. Rashed, R. E. Treharne, J. Kay, P. Yates, I. Z. Mitrovic, A. Weerakkody, S. Hall and K. Durose, *Data in brief*, 2015, **5**, 926-928.
10. I. Malitson, *Josa*, 1965, **55**, 1205-1209.
11. K. Persson, *Materials Data on Te₂MoWSeS (SG: 156) by Materials Project*, LBNL Materials Project; Lawrence Berkeley National Lab.(LBNL), Berkeley, CA ..., 2017.
12. Y. Dang, Y. Liu, Y. Sun, D. Yuan, X. Liu, W. Lu, G. Liu, H. Xia and X. Tao, *CrystEngComm*, 2015, **17**, 665-670.
13. A. Halder, D. Choudhury, S. Ghosh, A. S. Subbiah and S. K. Sarkar, *The Journal of Physical Chemistry Letters*, 2015, **6**, 3180-3184.
14. N. Ahn, S. M. Kang, J.-W. Lee, M. Choi and N.-G. Park, *Journal of Materials Chemistry A*, 2015, **3**, 19901-19906.
15. B. H. De Jong, R. G. Beerkens, P. A. van Nijnatten and E. Le Bourhis, *Ullmann's Encyclopedia of Industrial Chemistry*, 2000.

13 Understanding Differences in the Crystallization Kinetics between Slot-die Coating and Spin Coating of MAPbI₃ Using Multimodal *In Situ* Optical Spectroscopy



Konstantin Schötz[#], *Christopher Greve*[#], *Arjan Langen*, *Harrie Gorter*, *Ilker Dogan*, *Yulia Galagan*, *Albert JJM van Breemen*, *Gerwin H Gelinck*, *Eva M Herzig*, *Fabian Panzer*.

[#] Authors contributed equally.

Published in

Advanced Optical Materials, **2021**, 9, 2101161

(DOI: 10.1002/adom.202101161)

Reprinted from Wiley-VCH GmbH

Copyright (2021) the Authors

Understanding Differences in the Crystallization Kinetics between One-Step Slot-Die Coating and Spin Coating of MAPbI₃ Using Multimodal In Situ Optical Spectroscopy

Konstantin Schötz, Christopher Greve, Arjan Langen, Harrie Gorter, Ilker Dogan, Yulia Galagan, Albert J. J. M. van Breemen, Gerwin H. Gelinck, Eva M. Herzig, and Fabian Panzer*

To develop a detailed understanding about halide perovskite processing from solution, the crystallization processes are investigated during spin coating and slot-die coating of MAPbI₃ at different evaporation rates by simultaneous in situ photoluminescence, light scattering, and absorption measurements. Based on the time evolution of the optical parameters it is found that for both processing methods initially solvent-complex-structures form, followed by perovskite crystallization. The latter proceeds in two stages for spin coating, while for slot-die coating only one perovskite crystallization phase occurs. For both processing methods, it is found that with increasing evaporation rates, the crystallization kinetics of the solvent-complex structure and the perovskite crystallization remain constant on a relative time scale, whereas the duration of the second perovskite crystallization in spin coating increases. This second perovskite crystallization appears restricted due to differences in solvent-complex phase morphologies from which the perovskite forms. The work emphasizes the importance of the exact precursor state properties on the perovskite formation. It further demonstrates that detailed analyses of multimodal optical in situ spectroscopy allows gaining a fundamental understanding of the crystallization processes that take place during solution processing of halide perovskites, independent from the specific processing method.


1. Introduction

Since the first reports on metal halide perovskites applied as absorber material in perovskite solar cells (PSCs), the efficiency of the latter has increased rapidly and is now at 25.5%.^[1–4] However, most highly efficient PSCs are processed on millimeter lab-scale dimensions using spin coating.^[5–11] To process perovskite layers from solution on a larger scale, methods such as slot-die coating are relevant. With slot-die coating, however, efficiencies of larger-scale PSCs are typically lower than their spin-coated counterparts.^[6,7,11] The main reason for this processing-dependent efficiency gap is seen in differences in the final layer properties that follow from the high complexity of the perovskite film evolution.^[8,11,12]

Thus, numerous works investigated the perovskite formation process using in situ characterization methods.^[6,13–18] Besides scattering techniques,^[19–24] also optical spectroscopy,^[25–28] with, e.g., absorption

K. Schötz, F. Panzer
Soft Matter Optoelectronics
University of Bayreuth
95440 Bayreuth, Germany
E-mail: fabian.panzer@uni-bayreuth.de

C. Greve, E. M. Herzig
Dynamics and Structure Formation - Herzig Group
University of Bayreuth
95440 Bayreuth, Germany

 The ORCID identification number(s) for the author(s) of this article can be found under <https://doi.org/10.1002/adom.202101161>.

© 2021 The Authors. Advanced Optical Materials published by Wiley-VCH GmbH. This is an open access article under the terms of the Creative Commons Attribution License, which permits use, distribution and reproduction in any medium, provided the original work is properly cited.

The copyright line for this article was changed on 1 September 2021 after original online publication.

A. Langen, A. J. J. M. van Breemen, G. H. Gelinck
TNO
Holst Centre
Eindhoven 5656 AE, Netherlands

A. Langen
TNO
Biobased and Circular Technologies
Auvergnedijk 2
Bergen op Zoom 4612 PZ, Netherlands

H. Gorter, I. Dogan, Y. Galagan
TNO
Partner of Solliance
Eindhoven 5656 AE, Netherlands

Y. Galagan
Department of Materials Science and Engineering
National Taiwan University
Taipei 10617, Taiwan

DOI: 10.1002/adom.202101161

and photoluminescence (PL) being measured in parallel during processing of halide perovskites from solution, or even combinations of scattering and optical spectroscopy,^[29,30] allowed to gain insights into the perovskite formation process.

Based on these studies, different structural dynamics, such as the formation of intermediate phases were observed during the early stages of solution processing, i.e., before the actual perovskite crystallization.^[31] In the case of coating the halide perovskite methylammonium lead iodide (MAPbI₃) from dimethylformamide (DMF) solution, the intermediate phase was associated with solvent-complex structures of the form (MA)₂(DMF)₂Pb₂I₆.^[32] These lead to needle-like structures in the final film,^[6,32] since the perovskite crystallization emanates from the complex structures retaining the needle-like morphology.

The needle-like solvent-complex morphology often results in an incomplete film coverage, detrimental for device efficiency.^[6] Thus in the past, strategies were developed to prevent the formation of needle structures during perovskite processing, realized by introducing additional processing steps, such as solution engineering approaches or heating steps.^[33–36] However, the implementation of such additional processing steps are often laborious to realize, especially in industry-relevant approaches such as role-to-role slot-die coating.^[37] Thus, ensuring a successful transfer of one-step solution processing of halide perovskites from spin coating to slot-die coating currently is a highly desired, yet not fully realized goal in the field.^[38]

To better control the crystallization processes and hence the subsequent film morphology across different processing methods, two aspects are crucial to address: First, we need to understand better how the crystallization of the solvent-complex structures is influenced by changes of the drying conditions, and secondly, how the subsequent perovskite crystallization kinetics are affected by differences in the solvent-complex structures.

In this work, we compare the crystallization kinetics that occurs during the processing of MAPbI₃ from DMF precursor solution via spin coating and slot-die coating. To change the crystallization kinetics, we systematically control the solvent drying conditions in both methods by changing the spin speed during spin coating and by changing the airflow above the wet film during slot-die coating using an air knife. To monitor the crystallization processes, we use multimodal in situ spectroscopy measuring in parallel absorption, PL, and light scattering during solvent-complex and subsequent perovskite formation. While absorption and PL give information on the formation of the perovskite, monitoring the evolution of scattered light enables quantifying the crystallization kinetics of optically inactive solvent-complex structures. This allows us to reveal that the crystallization mechanism of the complex structures appears to be independent of the processing method, whereas differences in the kinetics of the subsequent perovskite crystallization exist. In contrast to the case of slot-die coating, during spin coating we observe a second perovskite crystallization process, which is restricted due to higher polycrystallinity of the complex structures.

2. Results and Discussion

To monitor the optical properties in situ during MAPbI₃ processing from solution, we used the setup described by

Buchhorn et al.^[39] In brief, a white light LED is located below the substrate on which the perovskite precursor solution is processed. An optical fiber above the substrate detects the white light transmitted through the substrate and the material during processing. From this transmission spectrum, together with the transmission spectrum through a blank substrate (e.g., measured before the processing), the optical density (OD) is calculated.^[40] However, not only the absorption of the perovskite will contribute to the OD, but also the scattering of the white light at scattering centers in the investigated sample. To differentiate between the two effects, we use an additional LED, emitting at 2.5 eV (490 nm) placed above the substrate.^[39] This allows to better distinguish between absorption and scattering effects, as more scattering leads to an increase, while more absorption leads to a decrease of the detected scattering signal. In the following, we refer to this additional LED as “scatter-LED.” PL is excited with a laser placed above the substrate and detected by the same optical fiber. A detailed description of the setup and optical detection system can be found in Figure S1 in the Supporting Information.

2.1. Spin Coating of MAPbI₃

We processed MAPbI₃ thin films by one-step spin-coating a DMF precursor solution with a concentration of 0.7 M at eight different spin coating rotation speeds between 500 and 2000 rpm at ambient conditions (room temperature (RT), 50%–60% relative humidity). For example, **Figure 1** shows the evolution of PL, scatter-LED signal, and OD within the first 125 s of spin coating at 2000 rpm (see Figure S2, Supporting Information for other spin speeds). For the different optical properties, heat maps (bottom panel) together with spectra at selected times (top panel) after the start of spinning (corresponding to $t = 0$) are shown. While any PL is absent within the first 20 s (Figure 1a), a constant intensity of scattered LED light is present (Figure 1b), which we attribute to (time-invariant) light scattering at the chuck below the substrate and at the interfaces of substrate-solution and solution-air. Within this first time range, the OD spectra (Figure 1c) exhibit a wavelike modulation around zero intensity, where the periodicity of the modulation increases with spin coating time. This modulation is due to thin-film interference.^[40,41] From the periodicity of the modulation, together with the refractive index in which the interference occurs, the layer thickness can be calculated. By doing so, we find that the layer thickness of the solution drops to about 1 μm within the first 20 s of spin-coating (Figure S3, Supporting Information).

Up to 30 s no PL is observed (Figure 1a), whereas the detected intensity of the scatter-LED doubles within 5 s from 22 s onward (Figure 1b). Concomitantly, the OD at 1.55 eV increases from 0.0 to about 0.2, while the OD spectrum is nearly flat (Figure 1c). The increase in OD and I_{scatter} suggests the formation of structures at which the light from the white LED and the light from the scatter-LED are scattered. Due to the absence of any PL signature and absorption edge in the OD spectrum, we exclude the formation of MAPbI₃ to cause the increase in OD and I_{scatter} . Instead, we associate the appearance of the scattering centers with the formation of solvent-complex structures of the form (MA)₂(DMF)₂Pb₂I₆, as they were observed to occur

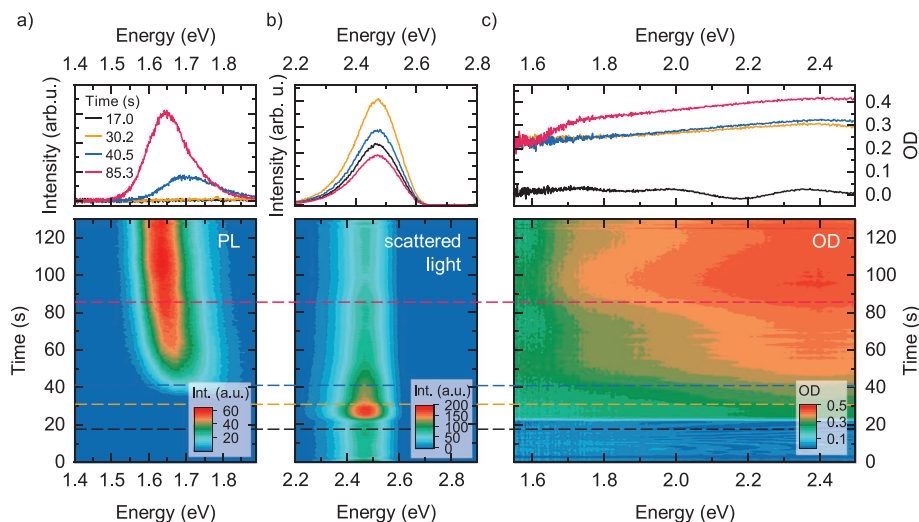


Figure 1. Spectra (top) and heat maps (bottom) of a) photoluminescence (PL), b) light scattering, and c) optical density (OD) measurement during the spin coating of a MAPbI₃ film at 2000 rpm.

during one-step processing of MAPbI₃ from DMF,^[6,32,40,42] and call the time of their onset $t_{0,\text{complex}}$. The light scattering from the solvent-complex structures results in a spectrally constant lift of the OD from $t_{0,\text{complex}}$ onward (Figure S4, Supporting Information), suggesting that at this stage, the solvent-complex structures already exhibit sizes larger than the wavelength λ of the scatter-LED, i.e., $>0.5 \mu\text{m}$.^[43]

After 32 s, a broad, asymmetric PL peak appears at about 1.7 eV, where the high-energy edge is flatter than the low-energy edge (Figure 1a). The PL peak, which is associated with MAPbI₃ nuclei,^[40] then shifts quickly to lower energies and becomes narrower. Almost simultaneously to the rise of the MAPbI₃ PL, the detected intensity of the scattered LED light starts to decrease by about 30% of its maximum value within 5 s (Figure 1b), indicating the reduction of scattering species within the system. Between 30 and 40 s, the OD remains essentially unchanged except for a slight increase in OD above ≈ 2.0 eV (Figure 1c).

For $t > 40$ s, the intensity of the PL increases, the peak width decreases, and the PL peak position shifts to lower energies, reaching ≈ 1.62 eV at the end of the spin-coating process (Figure 1a). In this latter time range, the intensity of the scatter-LED signal continues to decrease, yet more slowly compared to the decrease between 30 and 35 s (Figure 1b). The PL increase and the decrease of the scatter-LED indicate a transition of complex phase to MAPbI₃.

In the OD spectra, the signature of the MAPbI₃ absorption edge appears in the form of an increase above 1.6 eV from about 40 s onward (Figure 1c).^[43,44] The absorption edge becomes more intense toward the end of spin coating. Above the MAPbI₃ absorption edge the OD is flat compared to the expected absorption coefficient of MAPbI₃,^[45] suggesting that the film is not fully covered by perovskites.^[43] In brief, a partial coverage of the substrate allows a certain fraction of the impinging light to pass the sample without being absorbed by the perovskite. Thus, a partial film coverage results in a certain minimum intensity of the transmitted light, which in turn sets an upper limit for the detectable OD. When approaching this

OD limit, the absorption spectrum becomes distorted and softly clipped (i.e., flatter),^[43] similar to an electrical signal in a triode tube gain stage upon grid-current clipping.^[46]

The observed changes of the optical spectra during spin coating are indicative of a nucleation and growth behavior. To access the crystallization kinetics of the complex phase and perovskite phase in a quantitative manner, it is necessary to extract the time evolution of different optical parameters, to analyze them in detail thereafter.

Before explaining which optical parameters we consider and how we extract them, we note that the evolution of the OD and the scatter-LED signal over time extracted from the raw data apparently exhibit a high degree of noise. Actually, the apparently high noise levels result from an aliasing effect due to the different frequencies of data acquisition and the rotating spin coater chuck. Filtering the corresponding beat frequency from the as-measured time traces significantly reduces the noise level (Figure S5, Supporting Information), and we only consider the filtered data for all further analysis.

To extract the time evolution of the PL peak position (Figure 2a, solid line), we fit an asymmetric hyperbolic secant to all detected perovskite PL spectra (see Figure S6, Supporting Information for details). The PL fitting approach also allows extracting the spectral positions where the PL has dropped to $1/e$ of the peak intensity on both sides of the peak-shaped PL spectrum. This spectral region is indicated as shaded area in Figure 2a, and with it, the evolution of peak asymmetry, as well as reduction of the peak width can be accessed. We extract the time evolution of the light scattering by considering the integrated intensity of the scatter-LED signal (referred to as I_{scatter}), shown in Figure 2b. Furthermore, we extract the evolution of the OD_{1.8eV} (Figure 2c), i.e., at a photon energy above the typical MAPbI₃ bandgap energy of ≈ 1.6 eV. Accordingly, the OD_{1.8eV} contains contributions from perovskite absorption and contributions due to the scattering effects within the sample. To extract the contribution from pure perovskite absorption, we calculate the difference between the OD at 1.8 eV and at 1.575 eV, i.e., $\Delta\text{OD} = \text{OD}_{1.8\text{eV}} - \text{OD}_{1.575\text{eV}}$ (Figure 2d). Here we

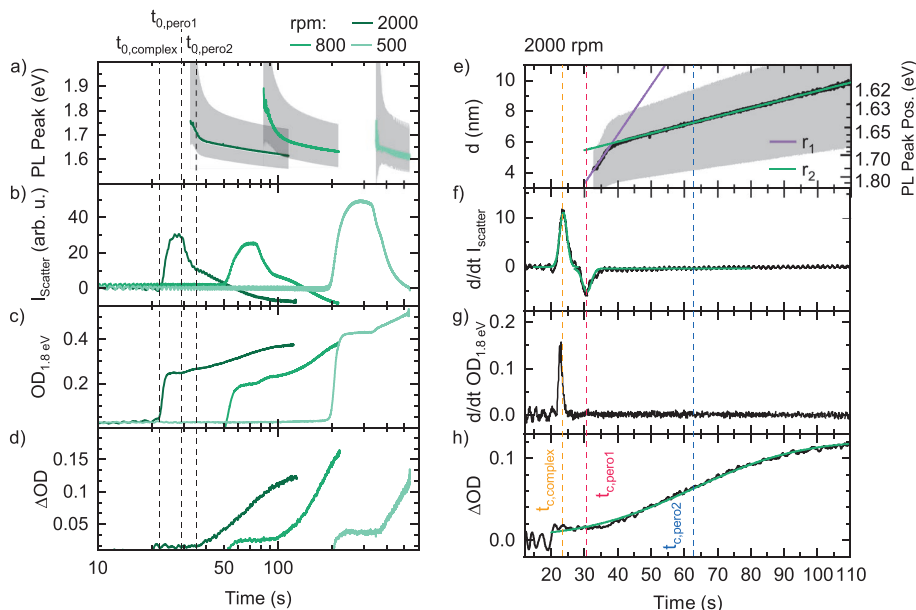


Figure 2. a–d) Time evolution of different optical parameters for spin coating with spin speeds of 2000 rpm (dark green), 800 rpm (green), and 500 rpm (light green). a) PL peak position, with the grey shaded area indicating the spectral range where the PL intensity is above $1/e$ of the peak intensity. b) Integrated intensity of the scatter-LED, I_{scatter} . c) OD at 1.8 eV. d) ΔOD , i.e., the difference of the OD at 1.8 and at 1.575 eV. Vertical dashed lines indicate the onsets t_0 of the different crystallization processes for a spin speed of 2000 rpm. e–h) Analyses of the optical parameters for spin coating at 2000 rpm. e) Average crystallite size determined from the PL peak position using Equation (1). The shaded area indicates the sizes depending on the value of parameter b in Equation (1). f) The derivative of I_{scatter} . g) The derivative of $\text{OD}_{1.8\text{eV}}$ and h) ΔOD together with fits (green lines) as described in the main text. Dashed vertical lines indicate the critical times t_c of the different crystallization processes.

assume that an increase in $\text{OD}_{1.575\text{eV}}$, i.e., at energy below the MAPbI_3 bandgap, is caused exclusively by light scattering. This approach is a valid approximation to the absorption of the perovskite only since the scattering contribution in the OD is only weakly energy dependent. Additionally, the influence of this energy dependence on the ΔOD is minimized by choosing the OD at energies which are close to each other.

From Figure 2a–d it becomes clear that for all spin speeds the different optical parameters proceed in the same qualitative fashion as a function of spin coating time, though they are slower for decreasing spin speeds.

Next, we want to gain a more detailed understanding of the various crystallization processes occurring during spin coating, based on a detailed examination of the evolution of the optical parameters with time. This will be carried out in the following as an example for the case of 2000 rpm.

As already discussed in Figure 1, the formation of solvent-complex phase is reflected in the initial increase of $\text{OD}_{1.8\text{eV}}$ and I_{scatter} starting from $t_{0,\text{complex}}$. After the initial increase, both signals saturate, followed by a rapid decrease of I_{scatter} onward. This point in time we refer to as $t_{0,\text{pero1}}$. A decrease of I_{scatter} can either result from a reduction of scattering structures or result from increasing absorption at the wavelength of the scatter-LED. The fact that $\text{OD}_{1.8\text{eV}}$ increases during the decrease of I_{scatter} , speaks against a reduction in scattering structures. Rather, e.g., after 40.5 s, OD spectra exhibit a slight increase toward higher photon energies, in contrast to the flat OD spectra before $t_{0,\text{pero1}}$ (e.g., $t = 30.2$ s). This additional contribution to the OD spectra could stem from Rayleigh scattering at

structures significantly smaller than the wavelength range of the white light, as it would be the case for perovskite nuclei. The initial perovskite nuclei are likely to exhibit a quantum confinement effect, shifting the corresponding bandgap to higher (e.g., > 1.8 eV) energies.^[47] Hence ΔOD calculated based on $\text{OD}_{1.8\text{eV}}$ might not capture the appearance of absorption from perovskite nuclei that only absorb at higher energies due to a quantum confinement effect. Considering the temporal evolution of ΔOD calculated based on $\text{OD}_{2.2\text{eV}}$ (Figure S7, Supporting Information), indeed shows an increase after $t_{0,\text{pero1}}$, which is similar to the corresponding increase in $\text{OD}_{1.8\text{eV}}$. Thus, we associate the decrease in I_{scatter} to stem from an increase in absorption due to the formation of nanosized perovskite crystals.

A formation of nanosized perovskite crystals is further supported by the fact that the first perovskite PL that could be detected shortly after $t_{0,\text{pero1}}$ is at higher photon energies and exhibits a flatter high-energy edge, compared to bulk PL spectra of MAPbI_3 (Figure S8, Supporting Information). The broadened PL in combination with the PL shift indicates that the PL exhibits a quantum confinement effect due to a perovskite crystal size below the corresponding quantum confinement limit, which was found to be 20–30 nm for MAPbI_3 .^[47–51] This is also in line with the formation of first nanosized perovskite crystals starting from $t_{0,\text{pero1}}$.

Finally, the beginning of a second perovskite formation process is indicated by the significant increase in ΔOD , the slower shift of PL peak position to lower photon energies, and the slowing down of the decrease of I_{scatter} , all starting from

t_{0, pero_2} . Thus, independent from the spin speed, we observe the crystallization processes occurring during spin coating to proceed in the order i) formation of solvent-complexes (in the following referred to as “solvent-complex phase”), ii) formation of nanoconfined perovskite grains (“pero₁ phase”), iii) second perovskite formation process (“pero₂ phase”).

As a next step, we analyze the decrease of the PL peak position (Figure 2a) in more detail. The perovskite PL exhibits a nanoconfinement effect. In such a case, based on quantum mechanical considerations, it was suggested that the PL peak position E_{PL} depends on the average crystallite size d by

$$E_{\text{PL}}(d) = E_{\text{g}} + b/d^2 \quad (1)$$

where E_{g} is the bulk PL position and b is a constant.^[52] We use Equation (1) and calculate the evolution of the average MAPbI₃ crystal size for the different spin speeds over time based on the PL peak positions from Figure 2a. Since the parameter b is reported to be in the range of 1–5 eV nm² for MAPbI₃,^[51,53] we use an average value of 3 eV nm² and $E_{\text{g}} = 1.59$ eV (Figure S8, Supporting Information). Figure 2e exemplarily shows the time evolution of the average crystal size calculated this way for spin coating at 2000 rpm. We consider the average crystal sizes that result when using 1 and 5 eV nm² in Equation (1) as upper and lower error limits, respectively. The resulting error range of average crystal sizes is indicated as the grey shaded area. After about 32 s, the average perovskite crystal size d increases fast from 4 to 6 nm within 6 s and then increases more slowly, reaching 10 nm after 110 s. Using linear fits in the time range of the fast (purple solid line) and slow increase (green solid line) of d allows extraction of perovskite crystal growth rates of 0.32 and 0.06 nm s⁻¹, respectively.

To interpret the average crystallite sizes and thus the growth rates in a substantiated manner, one must also consider that in general, the strongest contribution to the overall confinement effect stems from the shortest length within a crystal.^[51] This means that in crystal structures where only one length is below the confinement limit, a quantum confinement effect still occurs.^[51] Thus the growth of perovskite crystal size during the pero₂ phase is not necessarily inhibited in all spatial directions, but at least in one.

In general, self-absorption effects can have a significant influence on the PL properties,^[40,54–58] where the PL peak is shifted to lower energies and/or even additional PL features at lower energies compared to the intrinsic PL can appear.^[40,54–57] If self-absorption was significant in our data, its impact would become more significant with time, as more perovskite phase is present in the sample. With time, the average crystal size calculated according to Equation (1) would more and more overestimate the actual crystal size and thus the corresponding extracted growth rate. However, since in Figure 2a, the PL peak position is always at significantly higher energies than the bulk PL of MAPbI₃, self-absorption appears to be negligible in our data.

In Figure 2a–d we identified the onset-times of the solvent-complex phase, pero₁ phase, and pero₂ phase. To quantify the kinetics of the different crystallization processes in more detail, we analyze the time evolution of the optical parameters shown in Figure 2b–d.

We follow an analysis approach that we used previously to determine the kinetics of the recrystallization process of MAPbI₃ during solution-based two-step processing.^[40] To this end, we calculate the derivative of I_{scatter} and OD_{1.8 eV} with time from Figure 2b,c. This results in peaks that occur at the times of the different crystallization processes in the corresponding dI_{scatter}/dt and dOD/dt diagrams. Using Gaussians, we fit these peaks and associate the time of a peak maximum with the critical time t_c , and the width $w = 2\sigma$ with the duration of the individual crystallization processes.

This analysis procedure is exemplified in Figure 2f,g for the measurement at 2000 rpm. Due to the clear peak signatures of the solvent-complex formation process in both dI_{scatter}/dt (Figure 2f) and dOD/dt (Figure 2g), we can extract $t_{c, \text{complex}} = 23.2 \pm 0.4$ s and width $w_{\text{complex}} = 1.7 \pm 0.6$ s. The steep decrease of I_{scatter} observed from t_{0, pero_1} onward in Figure 2b, manifests itself as a peak to negative values at t_{c, pero_1} in Figure 2f. This peak is significantly more intense than the corresponding feature of the pero₁ phase in the dOD/dt graph (Figure 2g). Thus a reliable quantification of both $t_{c, \text{pero}_1} = 30.9$ s and the corresponding $w_{\text{pero}_1} = 3.1$ s is possible from dI_{scatter}/dt . However, in both dI_{scatter}/dt and dOD/dt , the noise level obscured any signature of the pero₂ formation phase. To not worsen the signal-to-noise-level by calculating $dOD_{1.8 \text{ eV}}/dt$, we analyze the evolution of ΔOD directly by fitting the error function (that is, the integral of the Gaussian function used above) to the transition (Figure 2h). This allowed to quantify the pero₂ formation process satisfyingly, where we obtain $t_{c, \text{pero}_2} = 62.7$ s and $w_{\text{pero}_2} = 52.2$ s. Overall, it is possible to quantify the critical times t_c and corresponding temporal durations of all three crystallization processes (solvent-complex formation, pero₁ phase and pero₂ phase formation) that appear during spin coating.

The different t_c and widths for the different crystallization processes are shown in Figure 3a as a function of the spin speed. Here, the time sequence of film formation is represented in a columnar form, and the time ranges in which the different

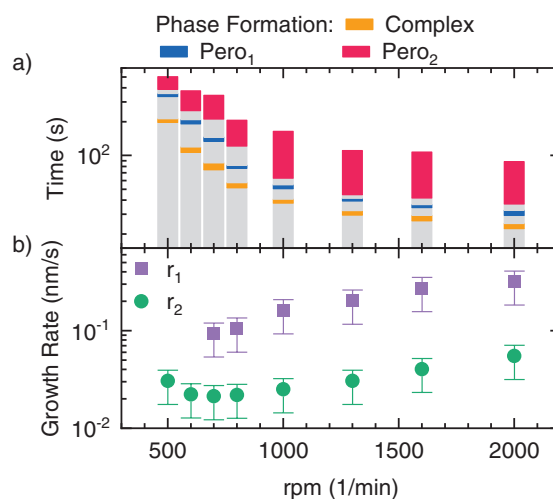


Figure 3. a) Color bar representation of the critical times t_c and widths of the different crystallization phases. b) Perovskite growth rates extracted from the evolution of average crystal size during spin coating (see Figure 2e for 2000 rpm), as a function of spin speed.

crystallization processes occur are colored. The temporal position and width of the colored areas correspond to the t_c and the width w , i.e., each colored area covers the time range $t_c \pm w$ (see also Figure S9 in the Supporting Information for a separated representation of t_c and w). As expected, t_c and corresponding width of all crystallization processes decrease with increasing spin speed due to the accelerated solvent evaporation, i.e., all crystallization processes occur earlier and faster with increasing rpm (also see Figure S9, Supporting Information). It is also evident from Figure 3a that the time duration of the perovskite formation relative to the time durations for the complex phase and perovskite-phase tend to increase with spin speed.

Figure 3b shows the perovskite growth rates extracted following the analysis approach from Figure 2e, as a function of spin speed, where the growth rates at early times (r_1) are about an order of magnitude higher than the growth rates at later times (r_2), with both rates increasing for increasing rpm.

Thus, so far, we could establish all analytical approaches to identify and quantify the different crystallization processes occurring during spin coating. Next, we use these analytical approaches to also investigate the crystallization processes that take place during slot-die coating.

2.2. Slot-Die Coating of MAPbI₃

We processed MAPbI₃ thin films by slot-die coating, using the same precursor solution and ambient conditions as for spin coating, and monitored the film formation by in situ optical spectroscopy. Due to technical reasons, the scatter-LED implementation, as used in the spin coating measurements, was not feasible in the slot-die coater. To still be able to monitor the scattering of solvent-complexes during the processing, we exploit the ambient room light that was available during all slot-die coatings and measured its scattered intensity. However, in contrast to the scatter-LED, the room light is also present during

the OD measurement. Consequently, the background correction recorded before the coating loses its validity upon the formation of scattering centers during slot-die coating. This can lead to distinct spectral features of the room light appearing in the OD spectra. Nevertheless, because of the distinct spectral signatures of the room light, it can be easily distinguished from the optical signatures of solvent-complexes and MAPbI₃.

To control the crystallization kinetics during slot-die coating we use an air knife, mounted just above the carrier parallel to the substrate. With increasing air pressures from 0.5 to 4 bar through the air knife, solvent evaporation can be increased (see Figure S1, Supporting Information for technical details).

Figure 4 shows the evolution of optical properties measured during slot-die coating using an air pressure of 4 bar (see Figure S10, Supporting Information for other air pressures). Analogous to Figure 1, Figure 4 shows the PL, the scattered room light, and the OD as a heat map (bottom panel), together with individual spectra at selected times (top panel). The time axis was chosen so that $t = 0$ coincides with the moment the slot-die head reaches its final position after dispensing the precursor solution on the substrate, which is ≈ 1.5 s (see the Supporting Information for technical details).

Within the first 70 s of slot-die coating, no optical signatures of both perovskite and complex structures were observed and no periodic modulation in the OD spectra was present. A lack of modulation in the OD spectra suggests that the height of the solvent layer that could cause an interference effect is larger than the coherence length of the detected light ($\approx 10 \mu\text{m}$ range). The corresponding analysis in the case of spin coating suggested that the first spectral modulations were linked to a highest detectable layer thickness in the range of $\approx 10 \mu\text{m}$ (Figure S3, Supporting Information). As we used the same white LED also in the slot-die coating experiments, the absence of modulations in the OD spectra in Figure 4c suggests that the solvent level at the moment of the initial complex phase formation was at least $\approx 10 \mu\text{m}$.

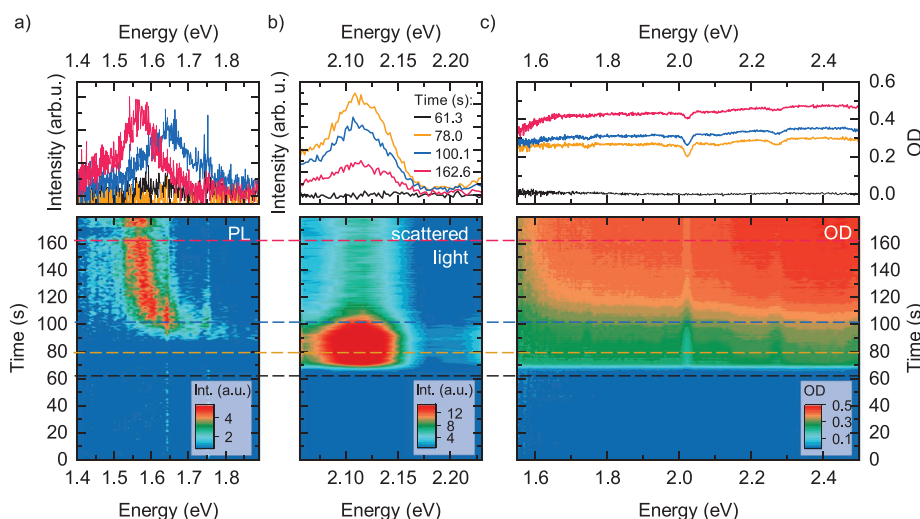


Figure 4. Spectra (top) and heat maps (bottom) of a) photoluminescence (PL), b) light scattering, and c) optical density (OD) during the slot-die coating of a MAPbI₃ film at an air knife pressure of 4 bar. The drop of the PL between 160 and 170 s is due to a fluctuation of the power of the excitation laser.

In the time range from 70 to 90 s, the optical signatures of growing solvent-complex structures become apparent, with the intensity of the scattered light increasing significantly, while concomitantly, the OD increases almost independent from the photon energy. As expected (vide supra), the increase in scattered room light leads to distinct features (e.g., near 2.0 eV) in the OD spectra, while no OD or PL signatures of MAPbI₃ are yet detectable.

After 90 s a PL peak at 1.7 eV appears, which shifts to lower energies for longer times, reaching a final PL peak position of 1.59 eV after 160 s. This final PL peak position matches the PL peak position of bulk MAPbI₃. Compared to the spin coating case the PL intensity is lower, which we associate with a reduced sensitivity for light detection of the measurement setup when implemented at the slot-die coating setup. Simultaneous to the appearance of PL signal, the intensity of the scattered light decreases, reaching a constant intensity after about 120 s, indicating the transition from complex to perovskite phase as was also seen in the spin coating case. Starting from about 100 s, the OD increases more steeply, and concomitantly, an absorption edge of MAPbI₃ at 1.65 eV becomes apparent (see OD at $t = 100$ s), gaining intensity at later times (see OD at $t = 162.6$ s). As in the case of spin coating, the flat shape of the OD above the absorption edge indicates incomplete substrate coverage also in the case of slot-die coating.^[43]

Analogous to the procedure in Figure 3, we extract the evolution of different optical parameters over time for all measured air knife pressures, which is shown for PL peak position and OD at 1.8 eV in Figure 5 (see Figure S11, Supporting Information for the evolution of ΔOD and I_{scatter}). The PL peak position was determined in the same way as in Figure 2a. For the sake of clarity, the decay to $1/e$ is not indicated here (see Figure S12, Supporting Information for a more detailed version of Figure 5a).

For all air knife pressures, the PL peak shifts from 1.7 to 1.59 eV and saturates thereafter (Figure 5a). As in the case of spin coating, we interpret the appearance of a PL signal shifted to higher energies than typically observed for the corresponding bulk value as the signature of perovskite nuclei exhibiting a quantum confinement effect. These nuclei grow continuously

in size, indicated by the shift of the PL peak position to lower energies. The saturation of the PL peak position at the energy of the bulk MAPbI₃ PL (Figure S8, Supporting Information), which occurs for all air pressures used here, suggests that the perovskite crystallites grow to sizes larger than the length scale of the confinement limit (20–30 nm).^[51]

The time evolution of OD_{1.8 eV} exhibits a two-step increase for all air knife pressures (Figure 5b). Further considering the signatures in the evolution of I_{scatter} and ΔOD (Figure S11, Supporting Information), we associate the first OD increase with the formation of complex phase and the second increase with the formation of perovskites. Thus, in contrast to the spin coating, for slot-die coating only one perovskite crystallization process occurs.

We extract t_c and corresponding widths based on the evolution of the optical parameters from Figure 5a,b and Figure S11 in the Supporting Information, analogously to the analysis methods used in Figure 2f–h. Figure 5c shows t_c and widths of the complex (orange) and perovskite formation (blue) on a logarithmic time scale, in the same way the times and durations of the crystallization process occurring during spin coating were presented in Figure 3a (see Figure S13, Supporting Information for alternative version). As expected, as solvent evaporation accelerates with increasing air knife pressures, complex and perovskite formation occur at earlier times and their time widths are reduced. No significant increase in the width of perovskite phase formation relative to the width of complex phase formation seems to occur in Figure 5c for increasing evaporation rate (i.e., for increasing air knife pressures). This constant relative width of perovskite crystallization is reminiscent to the evolution of the pero_1 width, but clearly contrasts the corresponding relative widths for the pero_2 phase in the case of spin coating (Figure 3a).

Analogously to Figure 2e, we estimate the evolution of average perovskite crystallite sizes from the evolution of the PL peak position over time. From the time-dependent increase of the perovskite crystal size, we extract the growth rate of the perovskite crystallites (see Figure S14, Supporting Information), which is plotted as a function of air pressure in Figure 5d. We find the growth rate to increase with air knife pressure,

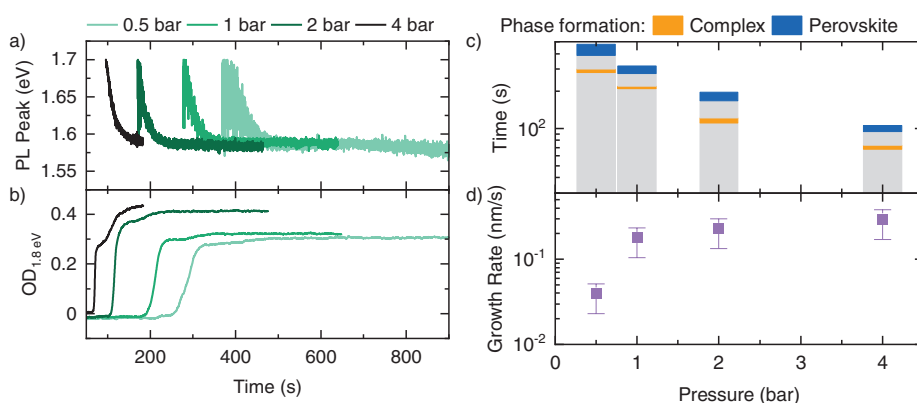


Figure 5. a) PL peak position and b) OD_{1.8 eV} for slot-die coating with different air pressures at the air knife. c) Critical times t_c and widths w of the complex (orange) and perovskite (blue) phase formations and d) perovskite growth rate as extracted from the PL peak position using Equation (1) as a function of the air pressure at the air knife.

exhibiting values in a similar range as those extracted during the early perovskite crystallization for spin coating (compare r_1). We note that since the PL peak position saturates at the value of bulk MAPbI₃ for all air pressures, we conclude that self-absorption again has a negligible or only minor effect on the PL peak position in our measurements.

In summary, analogously to the analysis for spin coating, the different crystallization processes during slot-die coating were quantified and the findings of the spin coating were used to identify qualitative differences and similarities in the crystallization behavior between spin and slot-die coating. In the following, we aim for a systematic and quantitative comparison of the crystallization processes of the two processing methods.

2.3. Comparison of Spin- and Slot-Die Coating

If the crystallization mechanisms do not change, a higher evaporation rate would only result in a corresponding decrease of the crystallization durations and a corresponding reduction of their time differences. Accordingly, one would expect that with suitable normalization, the relative crystallization durations should be independent of the evaporation rate.

We thus aim for considering the durations of the various crystallization processes identified in Figures 3a and 5c relative to each other. We first consider the slot-die coating process, and by using the widths and times of the crystallization processes obtained in Figure 5c, we normalize to the time difference $\Delta t_c = t_{c,perov} - t_{c,complex}$. To do this, we subtract the time $t_{c,complex}$ from all different times, so that $t_{c,complex}$ always is 0. Then we

divide all times (t_c and widths) by the absolute value of Δt_c , so that after normalization $t_{c,perov}$ is 1 (Figure 6a).

From a zoomed-in version of Figure 6a, it becomes clear that the widths of the complex formation and perovskite formation are nearly independent of the air knife pressure (Figure 6b). This supports the hypothesis that an increase of the air knife pressure leads to an acceleration of the film formation, but the mechanisms of the crystallization processes do not change in the case of slot-die coating.

In analogy to Figure 6a, we normalize the t_c and widths of the spin-coating crystallization processes from Figure 3a for all investigated spin speeds (Figure 6c). For the normalization we consider the perov₁ formation, i.e., $t_{c,perov1}$ and corresponding time duration (see Figure S15, Supporting Information for a version normalized to $t_{c,perov2}$). In Figure 6c, the perov₂ formation takes a large fraction of the overall film formation time on this relative time scale, with the width and critical time of the perov₂ formation increasing with increasing spin speed. In contrast, the relative widths of the solvent-complex phase (orange) and the perov₁ phase (blue) are largely independent of spin speed (Figure 6d). Furthermore, the relative widths of complex formation and perov₁ formation for spin coating and slot-die coating are similar (Figure 6c,d). This suggests that the crystallization mechanisms of solvent-complexes and the subsequent perovskite crystallization are comparable in both processing methods, whereas the crystallization of the perov₂ crystallization phase in spin coating differs from the other perovskite crystallization processes.

The independence of the formation mechanism of the solvent-complex structures from the processing method suggests that $t_{c,complex}$ or width $w_{complex}$ are most suitable as independent

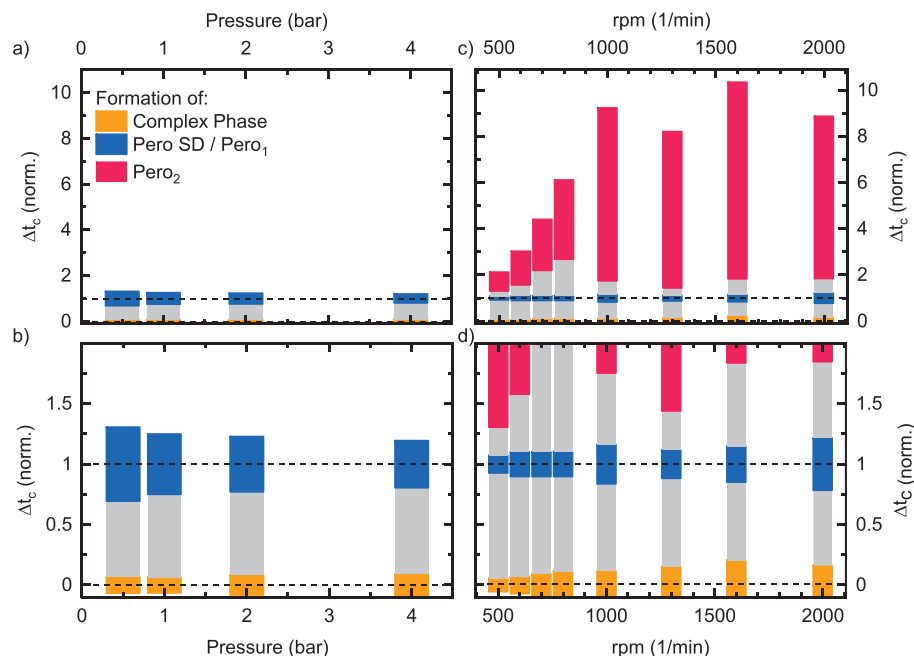


Figure 6. Bar chart of critical time t_c and widths w of the phase formations upon slot-die coating a,b) and spin coating c,d), normalized to $\Delta t_c = t_{c,perov} - t_{c,inter}$, i.e., $t_{c,inter}$ is 0 and $t_{c,perov}$ is 1. b,d) Zoom-in versions of (a,b).

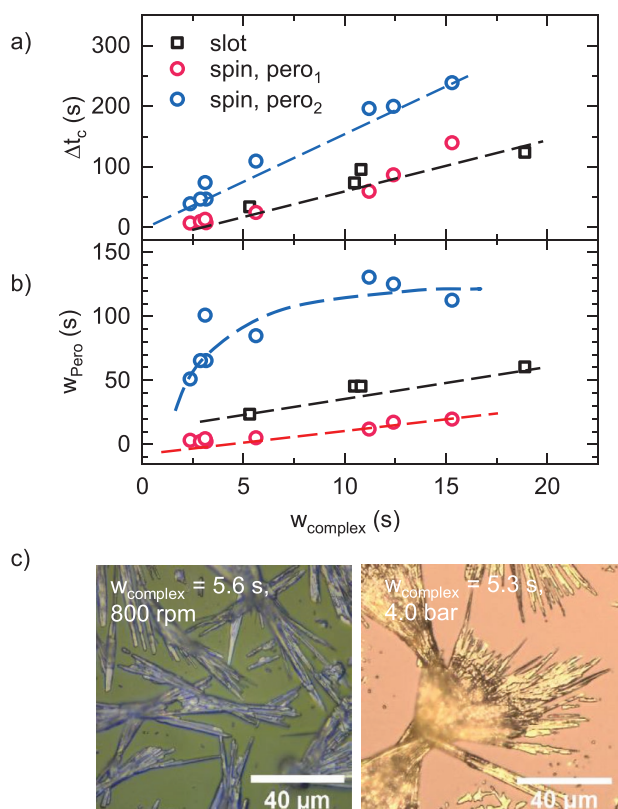


Figure 7. a) $\Delta t_c = t_{c,\text{perov}} - t_{c,\text{complex}}$ and b) width of the perovskite formation w_{perov} as a function of the width of the complex phase formation w_{complex} for slot-die coating (black squares) and first (pero_1 , red circles) and second (pero_2 , blue circles) perovskite crystallization during spin coating. c) Microscopy images of spin coated (left panel) and slot-die coated (right panel) thin films with comparable w_{complex} (for complete list of microscopy images see Figure S17 in the Supporting Information).

parameters to systematically compare the perovskite formation kinetics between spin coating and slot-die coating. As the time zero is often difficult to determine precisely and thus also $t_{c,\text{complex}}$ is, we use w_{complex} as a common parameter and plot both $\Delta t_c = t_{c,\text{perov}} - t_{c,\text{complex}}$ and w_{perov} as a function of w_{complex} for the different perovskite crystallization phases (Figure 7).

In general, Δt_c increases linearly with increasing w_{complex} (i.e., with decreasing air pressure or spin speed), with the values for slot-die coating ($\Delta t_{c,\text{slot}}$, black squares) and for the first perovskite crystallization in spin coating ($\Delta t_{c,\text{perov}_1}$, red circles) exhibit virtually the same increase (Figure 7a). This further indicates that the mechanism of these two perovskite crystallization processes is similar. In contrast, the value for the pero_2 crystallization ($\Delta t_{c,\text{perov}_2}$, blue circles) increases more steeply, i.e., for a certain w_{complex} the pero_2 crystallization in spin coating occurs considerably delayed compared to the perovskite formation in slot-die coating. The different slopes between $\Delta t_{c,\text{perov}_2}$ in spin coating and $\Delta t_{c,\text{slot}}$ (and $\Delta t_{c,\text{perov}_1}$ respectively), suggest that the mechanism of the pero_2 crystallization in spin coating differs from the corresponding mechanism of the one in slot-die coating (and from the first perovskite crystallization in spin coating respectively).

This difference in crystallization behavior is also reflected in the dependence between w_{perov} and w_{complex} (Figure 7b). Here w_{perov} of the slot-die coating and $w_{\text{perov}_1,\text{spin}}$ of the spin coating increase linearly with w_{complex} , exhibiting almost identical slopes. In contrast, $w_{\text{perov}_2,\text{spin}}$ exhibits a non-linear dependence, with a steep increase followed by a flattening out for larger w_{complex} , always at values higher than $w_{\text{perov}_1,\text{spin}}$ and $w_{\text{perov},\text{slot}}$.

Plotting the perovskite growth rates extracted from the PL peak shifts as a function of width w_{complex} , shows that the rates associated with pero_1 during the spin coating are similar to those associated with the perovskite growth during slot-die coating, and both decrease similarly with increasing w_{complex} (Figure S16, Supporting Information). In contrast, the growth rate occurring during the pero_2 formation is significantly diminished by about one order of magnitude. This is in line with the assumption that the mechanism of perovskite crystallization during slot-die coating and the pero_1 crystallization in spin coating is similar, while the pero_2 crystallization in spin coating is more restricted.

To understand the impact of the different crystallization mechanisms on the final film morphology, we took microscopy images of the films processed by spin coating and slot-die coating, where in Figure 7d films with similar w_{complex} are shown. This, for example, was the case for a spin speed of 800 rpm ($w_{\text{complex}} = 5.6$ s) and an air knife pressure of 4 bar ($w_{\text{complex}} = 5.3$ s). As expected, both films show a needle-like morphology determined by the complex structures with an incomplete film coverage. For both processing methods, it can be observed that the film coverage becomes more homogeneous, and the needle structures become smaller with faster drying kinetics (Figure S17, Supporting Information). In general, the needles are arranged in bundles, with a certain preferential direction. However, the degree of orientation of the bundles seems to be somewhat less pronounced in the slot-die coated film than in the spin-coated film. The dark areas inside the needles in both films correspond to perovskite phase,^[59] suggesting that the latter forms within the solvent-complex structures.

Furthermore, in the slot-die coated film, the yellow out-of-focus areas demonstrate that the needles in the center of the bundle are not in the focal plane of the microscope. This suggests that in the center of the bundles, needles grew also into vertical direction. For the film processed by spin coating, growth of the needles out of the focus plane can only be observed, at higher magnification (i.e., smaller focus depth), for the slower spin speeds (Figure S17, Supporting Information). Furthermore, profilometry measurements of the different spin coated films show that with increasing rpm, the mean height of the thin film decreases (Table S1, Supporting Information). In summary, these results suggest that the needle morphology in spin coating is flatter than in slot-die coating.

Thus, despite similar complex phase formation dynamics, the final film morphology between slot-die coated and spin coated films clearly differs. Since the perovskite phase forms and grows within the needles of the complex phase, it stands to reason that differences in solvent-complex phase morphology are responsible for the differences in perovskite growth between spin and slot-die coating.

2.4. Discussion

Based on the previous results, all the necessary knowledge could be derived to develop a complete picture of the differences in crystallization processes during spin- and slot-die coating, which will be discussed in the following. The sequence of crystallization processes, normalized to the duration of complex phase formation, analogously to the procedure in Figure 7, is illustrated in Figure 8.

As inferred from the temporal increase of I_{scatter} and OD, in both processing methods needle-like solvent-complex structures crystallize first (Figure 8a).^[32]

Independent from the specific solution processing method, the formation process of the complex phase follows from a supersaturation-induced heterogeneous nucleation and growth process, as suggested by Fong et al.^[14] Upon their first detection, i.e., from $t_{0,\text{complex}}$ onward, the needles are already μm -sized, as suggested by the scattering contribution of the solvent-complex structures being independent of photon energy. For both processing methods the size of the needles increases to above $\approx 50 \mu\text{m}$ in the final film (Figure S17, Supporting Information).

However, in spin coating, the white light interference in the OD spectra at the beginning of the processing revealed that at the time of the first detection of the complex structures, the solvent level had already dropped to a few μm . Accordingly, in the case of spin coating, we conclude that the growth of needles perpendicular to the substrate is limited by the decreasing solvent level from a certain point during spin coating. Further, for increasing rpm we observed that the solvent level just before $t_{0,\text{complex}}$ decreases (Figure S3c, Supporting Information), while at the same time the complex phase formation accelerates (decreasing w_{complex} Figure 3b; Figure S9, Supporting Information). This indicates that for increasing rpm, the decreasing solvent level influences the growth of the complex phase needles over a longer relative time span. As it is possible to explain the flat needle morphology to be the result of the decreasing solvent levels, shear forces in the needles, induced by centrifugal forces during substrate rotation, might not alter the needle growth direction significantly in case of spin coating.

In contrast, in slot-die coating the solvent level just before $t_{0,\text{complex}}$ could be estimated to be at least $10 \mu\text{m}$. This might suggest that the complex phase formation during slot-die coating is not significantly limited by the solvent level (Figure 8b). This fits with the needle structures observed in Figure 7, some of which protrude considerably upward in the slot-die coated sample, whereas a flat needle morphology is present in the spin-coated sample.

After the complex structure formation, the perovskite crystallizes within the complex structures (Figure 8c), which could be inferred from the time evolution of the optical parameters and from the microscopy images (Figure S17, Supporting Information). Examining the formation kinetics of $\text{pero}_{\text{slot}}$ and $\text{pero}_{1,\text{spin}}$, similar growth rates (Figure S16, Supporting Information) and Δt_c values (Figure 7a) for comparable w_{complex} (Figure 7a) indicate that their crystallization behavior is similar (Figure 8d).

However, in contrast to slot-die coating, a significant reduction of the perovskite growth rate in at least one spatial direction occurs in spin coating after exceeding an average crystal

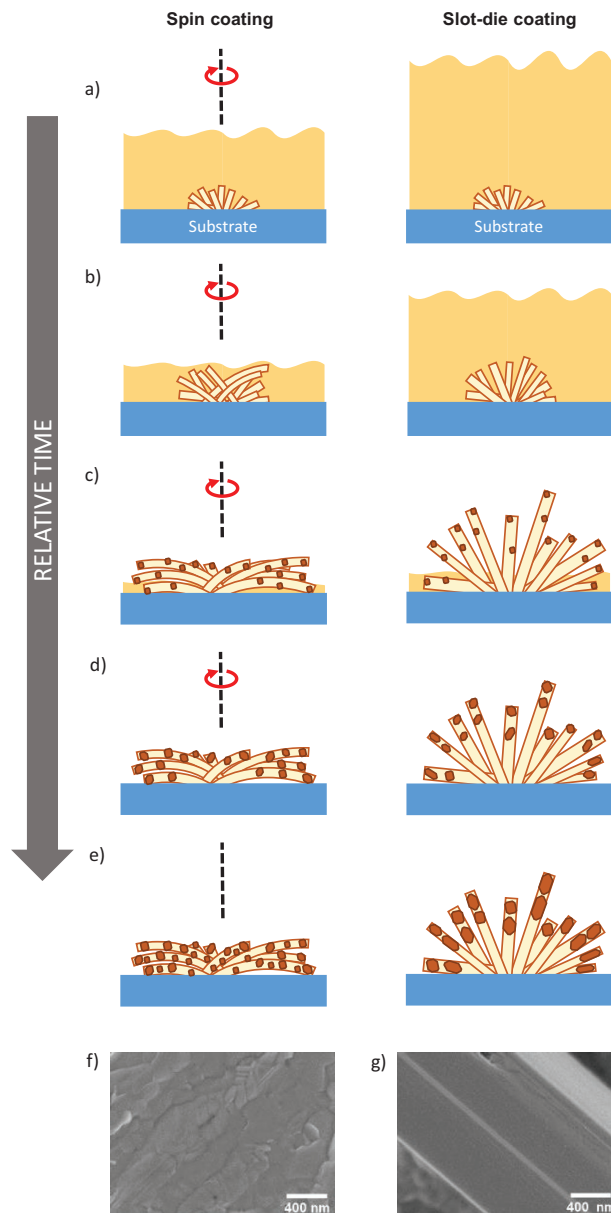


Figure 8. a–e) Illustration of the crystallization processes occurring during spin- (left) and slot-die coating (right) on a relative time axis, which is normalized to the duration of the complex phase formation. Supersaturated precursor solution leading to the initial solvent-complex phase nucleation is depicted in orange, while solvent-complexes are in beige and perovskite nuclei in brown. f,g) SEM images of a spin-coated MAPbI_3 thin film f) and a film obtained by drop casting g). For full list of SEM images see Figure S18 in the Supporting Information.

size of about 5–7 nm (Figure 2e). This suggests a restricted crystallization for $\text{pero}_{2,\text{spin}}$ compared to $\text{pero}_{\text{slot}}$ and $\text{pero}_{1,\text{spin}}$. In addition to the reduced growth rate, the second perovskite formation process during spin coating proceeded over a longer relative time span than the first perovskite formation phase, an effect that intensified with increasing spin speed (Figure 7b). These results suggest that the changed crystallization properties

of $\text{perO}_{2,\text{spin}}$ are related to the flattened needle-like morphology of the complex phase. The growth rates we observe (Figure S16, Supporting Information) are significantly lower compared to values reported for other synthesis approaches where the perovskite forms directly, ranging from about 10 nm s^{-1} to $1 \mu\text{m s}^{-1}$.^[40,60–62] This indicates that perovskite formation from a solvent-complex phase is considerably slower than direct perovskite phase formation from solution. Accordingly, it is reasonable to assume that the morphology of the complex phase has a significant influence on the perovskite crystallization. Hence this further supports that the altered crystallization properties of $\text{perO}_{2,\text{spin}}$ could be the result of a changed morphology of the complex phase.

A possible reason for the restricted perovskite crystallization could be an increased polycrystallinity of the solvent-complex structures. We speculate that an increased bending of the needle during growth, or growth along a non-preferred orientation parallel to the solvent surface could lead to more deficient growth and thus increased polycrystallinity in the complex needle. Consequently, the growth of perovskite nuclei would be restricted when reaching a solvent-complex phase grain boundary, resulting in overall smaller perovskite crystallites. In the wake of less restricted solvent-complex growth, as it appears to be the case for slot-die coating, the perovskite phase can crystallize more unhindered.

A more unhindered perovskite crystallization for slot-die coating is in line with our observations of the perovskite crystal size exceeding the confinement limit (Figure 8e). Furthermore, scanning electron microscopy (SEM) images of the final morphologies demonstrate that in the spin coating case (Figure 8f), the needle morphology is determined by many small grains. In contrast, the needle structures resulting from slot-die coating (Figure 8g) appear significantly less polycrystalline, with grain sizes $>1 \mu\text{m}$.

Thus, it becomes clear that based on the knowledge gained from the detailed analyses applied to the multimodal optical in situ spectroscopy in 2.1–2.3, a complete picture on the different crystallization processes during spin and slot-die coating can be derived.

3. Conclusion

In summary, we investigated in detail the crystallization processes taking place during the one-step solution processing of MAPbI_3 via spin and slot-die coating using multimodal optical in situ spectroscopy. We measured in parallel the time evolution of PL, light scattering and absorption and utilized PL and absorption to monitor the crystallization of MAPbI_3 , while by measuring the scattered light the crystallization process of the optically inactive solvent complex phase was accessed.

From the time evolution of PL peak position, integrated scattered light intensity, and the optical density at different photon energies, we identified the signatures of the different crystallization processes. We find that for both methods, a solvent-complex phase emerges, followed by perovskite crystallization. The latter occurs in two steps, separated in time for spin coating, while for slot-die coating only one perovskite crystallization phase could be observed.

Further analysis of the time evolution of the optical parameters and their derivatives allowed accessing the kinetics of each crystallization process. This in turn allowed investigating the behavior of the crystallization kinetics upon systematically altering the evaporation rate. Furthermore, the time duration of the complex phase formation was found to be a suitable independent parameter to identify differences in perovskite crystallization kinetics between slot-die and spin coating on a relative time scale. For both processing methods, the solvent-complex structure formation and the subsequent perovskite crystallization were independent of the evaporation rate on a relative time scale. In contrast, the second perovskite crystallization during spin coating proceeds restrictedly with a reduced perovskite crystal growth rate, where the average crystal sizes do not exceed $\approx 10 \text{ nm}$ in at least one spatial direction.

Here, the rapid decrease in solvent level at the beginning of spin coating, the spectral signature of the scattered light and microscopy images of the final film revealed that an increased polycrystallinity and flatter orientation of the solvent-complex phase are responsible for the changed perovskite crystallization kinetics.

On the one hand, our work demonstrates that multimodal optical in situ spectroscopy, combined with detailed data analysis represents a powerful tool to gain fundamental insights on the crystallization processes during solution-based halide perovskite processing. By identifying w_{complex} as a suitable independent parameter, we were able to compare the crystallization kinetics for both processing techniques quantitatively. Further, the methodology presented in this work yields potential to also achieve improved process and film control, e.g., in an industrial context. Here, monitoring (besides PL) the optical transmission signal that contains contributions from absorption as well as light scattering during the processing can give important information about the film coverage and film thickness, i.e., about the film quality. In the future, the presented methodology can be applied to state-of-the-art precursor chemistries or solvent mixtures relevant for industrially favorable one-step processing, and combining multimodal optical spectroscopy with, e.g., in situ X-ray scattering measurements would further allow to gain broader insights, e.g., about the perovskite phase purity.

On the other hand, our work also highlights the high sensitivity of perovskite crystallization kinetics on changes of the properties of the precursor phase from which perovskite forms. It thus represents an important step to enhance the general understanding of the crystallization processes occurring during halide perovskite evolution, independent of the specific solution-based coating method.

4. Experimental Section

Thin Film Fabrication: Precursors were used as received. Methylammonium iodide (MAI) was purchased from Dyesol and Lead(II) iodide (PbI_2 , 99%) was purchased from Acros. ITO substrates were cleaned in an ultrasonic bath with isopropanol (IPA, analytical grade (VWR)) followed by O_2 plasma treatment prior to use. For precursor solutions used for spin coating and for slot-die coating, MAI and PbI_2 were dissolved in DMF ($>99.5\%$, Fisher Chemical) with a concentration of 0.7 M .

Spin-coated perovskite films were prepared using a custom-built spin coater on ITO substrates with spin speeds of 500 to 2000 rpm in a one-step processing approach, using 70 μL of precursor solution per substrate at RT. The setup is shown in Figure S1a in the Supporting Information.

Slot-die coated perovskite films were prepared using an nRad slot-die coater system (nTact) on ITO substrates with a coating speed of 40 mm s^{-1} , a gap distance of 60 μm and a solvent dispensing rate of 100 $\mu\text{L s}^{-1}$ at RT. An air knife (Super Air Knife, Exair) was directed parallel to the printed precursor film with air pressure between 0.5 and 4 bar. The setup is shown in Figure S1b in the Supporting Information.

Spin coatings and slot-die coatings were performed at ambient air with a relative humidity in the range of 50%–60%.

In Situ Optical Spectroscopy: In situ optical spectra were recorded with the setup detailed in Section S1 in the Supporting Information. For the spin coating measurements, the scattered light of a LED emitting at 490 nm was measured, whereas for slot-die coating, the scattered room light was detected. PL and scattered light were measured simultaneously in one spectrum. PL/scattered light and absorption were then recorded alternating frame by frame, with a frame rate (for pairs of PL/scattered light and absorption) of 7.5 Hz in the case of slot-die coating and spin coating at 500 rpm, and with a frame rate of 11.6 Hz for spin coating with faster spin speeds (i.e., 600–2000 rpm).

Microscopy: Images of the solution processed films were taken with a Leica DM 2700M using Leica N Plan EPI objectives (20 \times /0.40 BD and 100 \times /0.85 BD).

Scanning Electron Microscopy: The samples were characterized by SEM using a Zeiss Ultra plus, equipped with a field-emission cathode using an in-lens secondary electron detector and an accelerating voltage of 3.0 kV.

Supporting Information

Supporting Information is available from the Wiley Online Library or from the author.

Acknowledgements

K.S. and C.G. contributed equally to this work. F.P. acknowledges funding from the German Academic Exchange Service (DAAD) in the framework of a Postdoc Research Grant (Postdoc-Program, Scholarship ID: 57407594). K.S. acknowledges financial support by the German National Science Foundation DFG via the project Ko 3973/2-1. C.G. and E.M.H. acknowledge financial support by the German National Science Foundation DFG through TUM International Graduate School of Science and Engineering (IGSSE). The Bavarian State Ministry of Science, Research, and the Arts is thanked for the support through the Collaborative Research Network “Solar Technologies go Hybrid.” Martina Heider and the KeyLab Electron and Optical Microscopy of the Bavarian Polymer Institute (BPI) are thanked for SEM images. Santosh Shanmugam is thanked for the help with the slot-die coating setup.

Correction added on 1 September 2021, after first online publication: Projekt Deal funding statement has been added.

Open access funding enabled and organized by Projekt DEAL.

Conflict of Interest

The authors declare no conflict of interest.

Data Availability Statement

Research data are not shared.

Keywords

absorption, halide perovskites, light scattering, photoluminescence, thin film formation

Received: June 8, 2021

Revised: July 13, 2021

Published online: August 29, 2021

- [1] N. R. E. Laboratory Best Research-Cell Efficiency Chart, www.nrel.gov/pv/assets/pdfs/best-research-cell-efficiencies.20200104.pdf (accessed: April 2021).
- [2] M. M. Lee, J. Teuscher, T. Miyasaka, T. N. Murakami, H. J. Snaith, *Science* **2012**, 338, 643.
- [3] H.-S. Kim, C.-R. Lee, J.-H. Im, K.-B. Lee, T. Moehl, A. Marchioro, S.-J. Moon, R. Humphry-Baker, J.-H. Yum, J. E. Moser, M. Graetzel, N.-G. Park, *Sci. Rep.* **2012**, 2, 591.
- [4] A. Kojima, K. Teshima, Y. Shirai, T. Miyasaka, *J. Am. Chem. Soc.* **2009**, 131, 6050.
- [5] Y. Vaynzof, *Adv. Energy Mater.* **2020**, 10, 2003073.
- [6] Y. Zhong, R. Munir, J. Li, M.-C. Tang, M. R. Niazi, D.-M. Smilgies, K. Zhao, A. Amassian, *ACS Energy Lett.* **2018**, 3, 1078.
- [7] S. S. Shin, E. J. Yeom, W. S. Yang, S. Hur, M. G. Kim, J. Im, J. Seo, J. H. Noh, S. I. Seok, *Science* **2017**, 356, 167.
- [8] H. W. Ro, J. M. Downing, S. Engmann, A. A. Herzing, D. M. DeLongchamp, L. J. Richter, S. Mukherjee, H. Ade, M. Abdelsamie, L. K. Jagadamma, A. Amassian, Y. Liu, H. Yan, *Energy Environ. Sci.* **2016**, 9, 2835.
- [9] D.-Y. Son, J.-W. Lee, Y. J. Choi, I.-H. Jang, S. Lee, P. J. Yoo, H. Shin, N. Ahn, M. Choi, D. Kim, N.-G. Park, *Nat. Energy* **2016**, 1, 16081.
- [10] W. S. Yang, J. H. Noh, N. J. Jeon, Y. C. Kim, S. Ryu, J. Seo, S. I. Seok, *Science* **2015**, 348, 1234.
- [11] Y. Deng, E. Peng, Y. Shao, Z. Xiao, Q. Dong, J. Huang, *Energy Environ. Sci.* **2015**, 8, 1544.
- [12] Y. Tidhar, E. Edri, H. Weissman, D. Zohar, G. Hodes, D. Cahen, B. Rybtchinski, S. Kirmayer, *J. Am. Chem. Soc.* **2014**, 136, 13249.
- [13] P. W.-K. Fong, H. Hu, Z. Ren, K. Liu, L. Cui, T. Bi, Q. Liang, Z. Wu, J. Hao, G. Li, *Adv. Sci.* **2021**, 8, 2003359.
- [14] P. W.-K. Fong, G. Li, *Front. Mater.* **2021**, 8, 635224.
- [15] M. Kim, S.-Y. Ham, D. Cheng, T. A. Wynn, H. S. Jung, Y. S. Meng, *Adv. Energy Mater.* **2021**, 11, 2001753.
- [16] K. Meng, L. Wu, Z. Liu, X. Wang, Q. Xu, Y. Hu, S. He, X. Li, T. Li, G. Chen, *Adv. Mater.* **2018**, 30, 1706401.
- [17] Q. Hu, L. Zhao, J. Wu, K. Gao, D. Luo, Y. Jjiang, Z. Zhang, C. Zhu, E. Schaible, A. Hexemer, *Nat. Commun.* **2017**, 8, 15688.
- [18] S. Lee, M.-C. Tang, R. Munir, D. Barrit, Y.-J. Kim, R. Kang, J.-M. Yun, D.-M. Smilgies, A. Amassian, D.-Y. Kim, *J. Mater. Chem. A* **2020**, 8, 7695.
- [19] L. E. Mundt, L. T. Schelhas, *Adv. Energy Mater.* **2020**, 10, 1903074.
- [20] O. Filonik, M. E. Thordardottir, J. Lebert, S. Pröller, S. Weiss, L. J. Haur, A. Priyadarshi, P. Fontaine, P. Mueller-Buschbaum, N. Mathews, E. M. Herzig, *Energy Technol.* **2019**, 7, 1900343.
- [21] D. Barrit, P. Cheng, M.-C. Tang, K. Wang, H. Dang, D.-M. Smilgies, S. (F.) Liu, T. D. Anthopoulos, K. Zhao, A. Amassian, *Adv. Funct. Mater.* **2019**, 29, 1807544.
- [22] K. S. Wilson, C. Y. Wong, *J. Phys. Chem. A* **2018**, 122, 6438.
- [23] Y.-M. Xie, B. Yu, C. Ma, X. Xu, Y. Cheng, S. Yuan, Z.-K. Wang, H. T. Chandran, C.-S. Lee, L.-S. Liao, S.-W. Tsang, *J. Mater. Chem. A* **2018**, 6, 9081.
- [24] K. Bruening, B. Dou, J. Simonaitis, Y.-Y. Lin, M. F. A. M. van Hest, C. J. Tassone, *Joule* **2018**, 2, 2464.
- [25] K. Schötz, F. Panzer, *J. Phys. Chem. A* **2021**, 125, 2209.
- [26] C. M. Sutter-Fella, *Adv. Energy Mater.* **2021**, 11, 2003534.

- [27] K. Suchan, J. Just, P. Becker, E. L. Unger, T. Unold, *J. Phys. Chem. A* **2020**, *8*, 10439.
- [28] S.-G. Kim, J.-H. Kim, P. Ramming, Y. Zhong, K. Schötz, S. J. Kwon, S. Hüttner, F. Panzer, N.-G. Park, *Nat. Commun.* **2021**, *12*, 1554.
- [29] M. Abdelsamie, T. Li, F. Babbe, J. Xu, Q. Han, V. Blum, C. M. Sutter-Fella, D. B. Mitzi, M. F. Toney, *ACS Appl. Mater. Interfaces* **2021**, *13*, 13212.
- [30] T.-B. Song, Z. Yuan, M. Mori, F. Motiwala, G. Segev, E. Masquelier, C. V. Stan, J. L. Slack, N. Tamura, C. M. Sutter-Fella, *Adv. Funct. Mater.* **2020**, *30*, 1908337.
- [31] M. Abdelsamie, J. Xu, K. Bruening, C. J. Tassone, H.-G. Steinrueck, M. F. Toney, *Adv. Funct. Mater.* **2020**, *30*, 2001752.
- [32] A. A. Petrov, I. P. Sokolova, N. A. Belich, G. S. Peters, P. V. Dorovatovskii, Y. V. Zubavichus, V. N. Khrustalev, A. V. Petrov, M. Graetzel, E. A. Goodilin, A. B. Tarasov, *J. Phys. Chem. C* **2017**, *121*, 20739.
- [33] A. D. Taylor, Q. Sun, K. P. Goetz, Q. An, T. Schramm, Y. Hofstetter, M. Litterst, F. Paulus, Y. Vaynzof, *Nat. Commun.* **2021**, *12*, 1878.
- [34] K. Liu, Q. Liang, M. Qin, D. Shen, H. Yin, Z. Ren, Y. Zhang, H. Zhang, P. W. K. Fong, Z. Wu, J. Huang, J. Hao, Z. Zheng, S. K. So, C.-S. Lee, X. Lu, G. Li, *Joule* **2020**, *4*, 2404.
- [35] W. Nie, H. Tsai, R. Asadpour, J.-C. Blancon, A. J. Neukirch, G. Gupta, J. J. Crochet, M. Chhowalla, S. Tretiak, M. A. Alam, H.-L. Wang, A. D. Mohite, *Science* **2015**, *347*, 522.
- [36] N. J. Jeon, J. H. Noh, Y. C. Kim, W. S. Yang, S. Ryu, S. I. Seok, *Nat. Mater.* **2014**, *13*, 897.
- [37] Y. Galagan, *Oxford Open Mater. Sci.* **2021**, *1*, itaa004.
- [38] M.-C. Tang, Y. Fan, D. Barrit, X. Chang, H. X. Dang, R. Li, K. Wang, D.-M. Smilgies, S. (F.) Liu, T. D. Anthopoulos, K. Zhao, A. Amassian, *J. Mater. Chem. A* **2020**, *8*, 1095.
- [39] M. Buchhorn, S. Wedler, F. Panzer, *J. Phys. Chem. A* **2018**, *122*, 9115.
- [40] M. Chauhan, Y. Zhong, K. Schötz, B. Tripathi, A. Köhler, S. Huettner, F. Panzer, *J. Phys. Chem. A* **2020**, *8*, 5086.
- [41] H. E. W. Francis, A. Jenkins, *Fundamentals of Optics*, Tata McGraw-Hill Education, New York **1937**.
- [42] R. Munir, A. D. Sheikh, M. Abdelsamie, H. Hu, L. Yu, K. Zhao, T. Kim, O. E. Tall, R. Li, D.-M. Smilgies, *Adv. Mater.* **2017**, *29*, 1604113.
- [43] Y. Tian, I. G. Scheblykin, *J. Phys. Chem. Lett.* **2015**, *6*, 3455.
- [44] X. Zhu, H. Su, R. A. Marcus, M. E. Michel-Beyerle, *J. Phys. Chem. Lett.* **2014**, *5*, 3061.
- [45] T. W. Crothers, R. L. Milot, J. B. Patel, E. S. Parrott, J. Schlipf, P. Mueller-Buschbaum, M. B. Johnston, L. M. Herz, *Nano Lett.* **2017**, *17*, 5782.
- [46] M. Blencowe, *Designing Valve Preamps for Guitar and Bass, Second Edition*, Wem Publishing, **2013**.
- [47] S. Demchyshyn, J. M. Roemer, H. Groiß, H. Heilbrunner, C. Ulbricht, D. Apaydin, A. BÖhm, U. Rütt, F. Bertram, G. Hesser, *Sci. Adv.* **2017**, *3*, e1700738.
- [48] L. Protesescu, S. Yakunin, M. I. Bodnarchuk, F. Krieg, R. Caputo, C. H. Hendon, R. X. Yang, A. Walsh, M. V. Kovalenko, *Nano Lett.* **2015**, *15*, 3692.
- [49] L. Wang, N. E. Williams, E. W. Malachosky, J. P. Otto, D. Hayes, R. E. Wood, P. Guyot-Sionnest, G. S. Engel, *ACS Nano* **2017**, *11*, 2689.
- [50] V. Malgras, J. Henzie, T. Takei, Y. Yamauchi, *Chem. Commun.* **2017**, *53*, 2359.
- [51] E. S. Parrott, J. B. Patel, A.-A. Haghighirad, H. J. Snaith, M. B. Johnston, L. M. Herz, *Nanoscale* **2019**, *11*, 14276.
- [52] Y. Kayanuma, *Phys. Rev. B* **1988**, *38*, 9797.
- [53] A. Buin, R. Comin, A. H. Ip, E. H. Sargent, *J. Phys. Chem. C* **2015**, *119*, 13965.
- [54] K. Schötz, A. M. Askar, W. Peng, D. Seeberger, T. P. Gujar, M. Thelakkat, A. Köhler, S. Huettner, O. M. Bakr, K. Shankar, *J. Phys. Chem. C* **2020**, *8*, 2289.
- [55] P. Fassel, V. Lami, F. J. Berger, L. M. Falk, J. Zaumseil, B. S. Richards, I. A. Howard, Y. Vaynzof, U. W. Paetzold, *Matter* **2021**, *4*, 1391.
- [56] D. Hong, J. Li, S. Wan, I. G. Scheblykin, Y. Tian, *J. Phys. Chem. C* **2019**, *123*, 12521.
- [57] J. B. Patel, A. D. Wright, K. B. Lohmann, K. Peng, C. Q. Xia, J. M. Ball, N. K. Noel, T. W. Crothers, J. Wong-Leung, H. J. Snaith, *Adv. Energy Mater.* **2020**, *10*, 1903653.
- [58] M. Wang, K. Wang, Y. Gao, J. I. Khan, W. Yang, S. De Wolf, F. Laquai, *Sol. RRL* **2021**, *5*, 2100029.
- [59] Y. Li, Z. Zhao, F. Lin, X. Cao, X. Cui, J. Wei, *Small* **2017**, *13*, 1604125.
- [60] Y. Zhao, H. Tan, H. Yuan, Z. Yang, J. Z. Fan, J. Kim, O. Voznyy, X. Gong, L. N. Quan, C. S. Tan, *Nat. Commun* **2018**, *9*, 1607.
- [61] Y.-H. Deng, Z.-Q. Yang, R.-M. Ma, *Nano Convergence* **2020**, *7*, 25.
- [62] J. Ding, S. Du, Y. Zhao, X. Zhang, Z. Zuo, H. Cui, X. Zhan, Y. Gu, H. Sun, *J. Mater. Sci.* **2017**, *52*, 276.

ADVANCED OPTICAL MATERIALS

Supporting Information

for *Adv. Optical Mater.*, DOI: 10.1002/adom.202101161

Understanding Differences in the Crystallization Kinetics between One-Step Slot-Die Coating and Spin Coating of MAPbI₃ Using Multimodal In Situ Optical Spectroscopy

*Konstantin Schötz, Christopher Greve, Arjan Langen, Harrie Gorter, Ilker Dogan, Yulia Galagan, Albert J. J. M. van Breemen, Gerwin H. Gelinck, Eva M. Herzig, and Fabian Panzer**

Supporting Information to

Understanding Differences in the Crystallization Kinetics between One-Step Slot-die Coating and Spin Coating of MAPbI₃ using multimodal *in-situ* Optical Spectroscopy

*Konstantin Schötz[#], Christopher Greve[#], Arjan Langen, Harrie Gorter, Ilker Dogan, Yulia Galagan, Albert J.J.M. van Breemen, Gerwin H. Gelinck, Eva M. Herzig, and Fabian Panzer**

Konstantin Schötz, Dr. Fabian Panzer
Soft Matter Optoelectronics, University of Bayreuth, 95440 Bayreuth, Germany
E-mail: fabian.panzer@uni-bayreuth.de

Christopher Greve, Prof. Dr. Eva M. Herzig
Dynamics and Structure Formation – Herzig Group, University of Bayreuth, 95440 Bayreuth, Germany

Arjan Langen[§], Dr. Albert J.J.M. van Breemen, Prof. Dr. Gerwin H. Gelinck
TNO, Holst Centre, 5656 AE Eindhoven, The Netherlands

Harry Gorter, Dr. Ilker Dogan, Prof. Dr. Yulia Galagan[§]
TNO, Partner of Solliance, 5656 AE Eindhoven, The Netherlands

[§]Current Address: Department of Materials Science and Engineering, National Taiwan University, Taipei, Taiwan

[§]TNO, Biobased and Circular Technologies, 4612PZ Bergen op Zoom

[#] Authors contributed equally

S1: Detailed description of the measurement setups

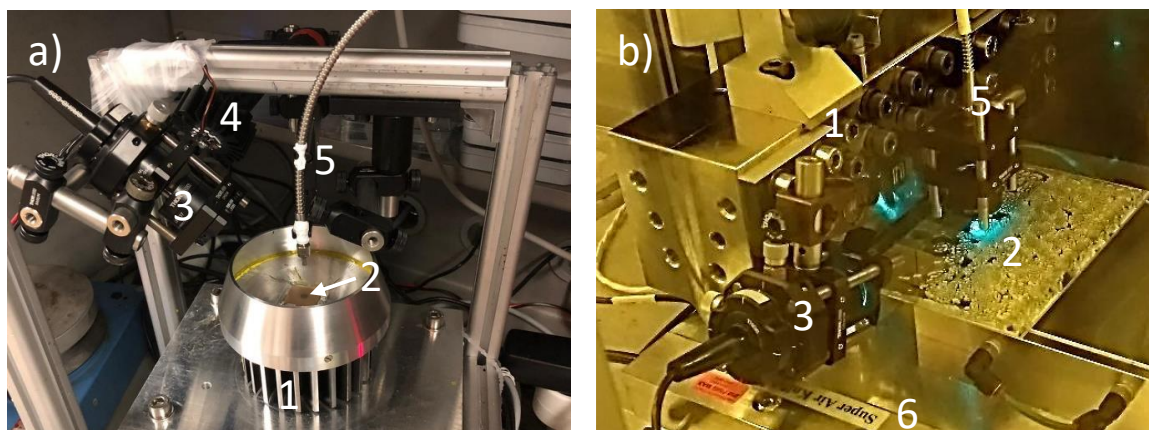
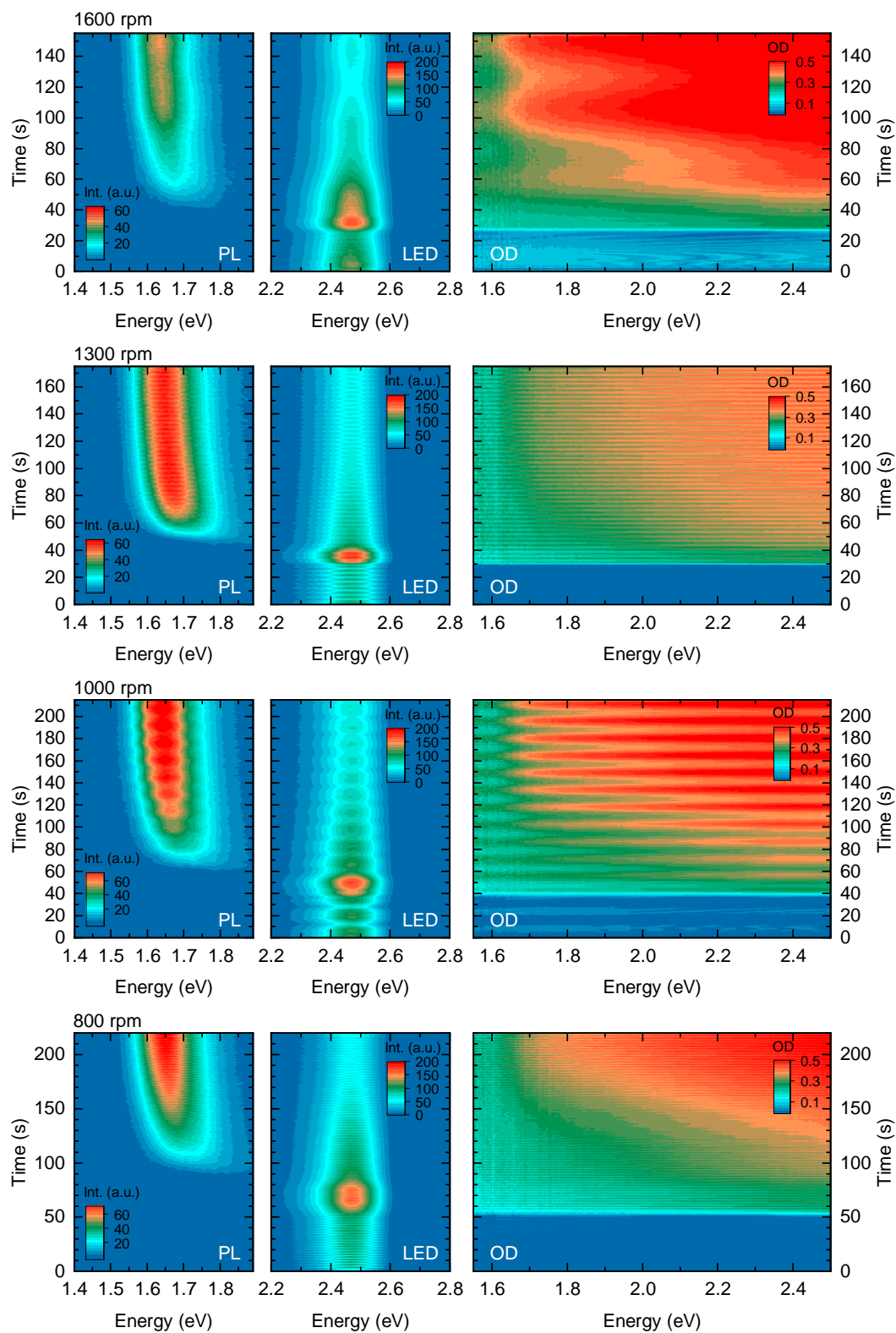


Figure S1: a) Photograph of the setup used for measuring the *in situ* optical data during spin coating. b) Photograph of the setup used for measuring the *in situ* optical data during slot-dye coating.

The setup for measuring the *in situ* optical data during spin-coating is shown in Figure S1a. It consists of a custom-built spin-coater (1) with a hole in the middle (2). Underneath the spin-coater a white-light LED is placed. Its light shines through the hole in the middle of the spin-coater and serves as a white light for transmission measurements. A laser diode (405 nm) in combination with focusing optics and a diaphragm (3) are mounted above the spin-coater for exciting the sample for PL measurements. An LED emitting at 490 nm (4) is placed next to the laser, whose scattered light can be detected (referred to as scatter-LED). White-light and excitation laser are turned on and off alternately, so that either transmission or PL is probed. Transmitted light, PL and scattered LED light are collected with one optical fiber (5), which is coupled to the detection system. The detection system consists of a CCD camera, coupled to a spectrograph, and a home-built detection setup, which is described in detail in Supporting Reference 1. In brief, the detection setup switches the optical path between transmission and PL measurements, so that for PL measurements, the laser wavelength is blocked by a suitable filter (in this case a 420 nm long pass filter). In contrast, for transmission measurements, the transmitted light is coupled into the spectrograph without additional filtering. The detection setup further synchronizes the CCD camera with the white-light LED, the laser and the optical path switching. Using this setup, we can record PL and transmission during spin-coating quasi-simultaneously (i.e., alternating frame by frame) with a rate of more than 10 Hz. From the transmission measurements, the optical density (OD) is calculated based on a reference measurement prior to spin-coating. Scattered LED light is recorded during the PL measurements.

Figure S1b shows the adaption of the setup described above for measuring the optical data *in situ* during slot-dye coating. Here, the optical fiber for signal collection (5) and the laser diode (3) are mounted on the printer head (1). The white-light LED is placed underneath the substrate at a fixed position (2), so that in the final position of the printer head, white-light and optical fiber are well aligned for transmission measurements. For this setup, instead of using an additional scatter-LED, the scattered room light is detected. The optical fiber is connected to the same detection system as described above. For manipulating the drying kinetics, an air knife (6) is placed next to the substrate, generating a controlled nitrogen flow from the side.

S2: Intensity Heat Maps of the *in situ* optical data during spin coating for all other spin speeds



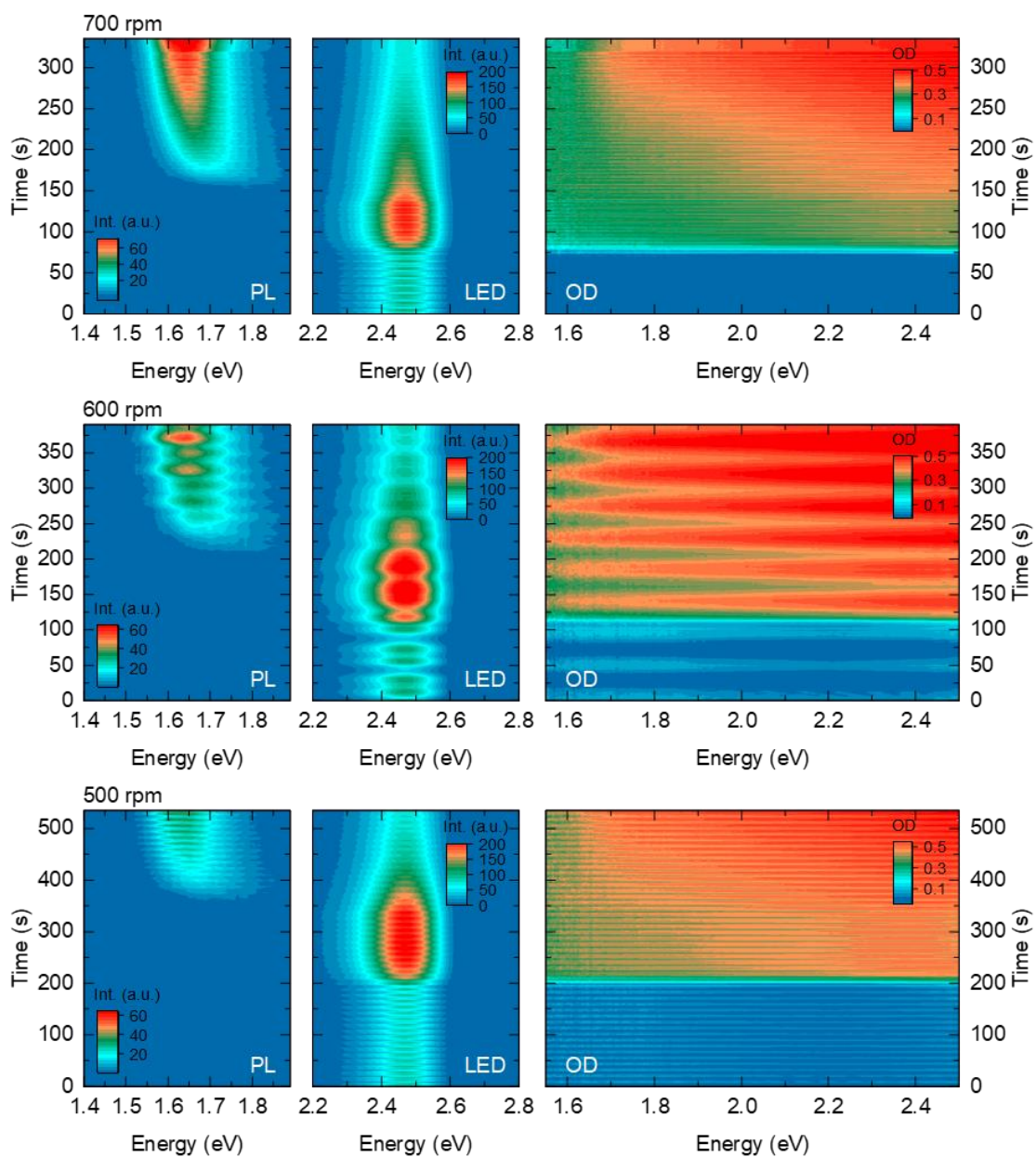


Figure S2: Intensity heat maps of the *in situ* PL (left), of the scattered LED light (middle) and of the optical density (right) for the different spin speeds during spin-coating.

S3: Estimation of layer thickness based on white light interference

Prior to the formation of the intermediate phase, we observe a sinusoidal modulation of the OD spectrum upon spin-coating (see inset in Figure S3). Such a modulation is indicative of positive and negative interference of white light caused by a thin layer and reflection at its interfaces. If the refractive index of the layer causing the interference is known, the thickness of the layer can be calculated from the distance of adjacent extrema in the OD using²⁻³

$$d = \frac{\lambda_1 \lambda_2}{2(\lambda_1 n_2 - \lambda_2 n_1)}, \quad (\text{S1})$$

where λ_i is the wavelength of the extremum i and n_i is the refractive index at wavelength λ_i . Assuming that n is roughly constant in the investigated spectral range, i.e. $n_1 \approx n_2$, and converting the wavelength to energy, Equation S1 can be re-written to

$$d = \frac{hc}{2n\Delta E}, \quad (\text{S2})$$

where ΔE is the energetic difference of two adjacent extrema in the OD.

ΔE was extracted from the frequency of a sine function fitted to the OD (see orange dashed line in the inset in Figure S3a). The thickness of the layer was then calculated using the refractive index of DMF, that is $n = 1.43$. The calculated layer thickness using Equation S2 is shown exemplarily for 2000 rpm in Figure S3a and for all spin speeds in Figure S3b. Figure S3c shows the calculated layer thickness at the time where the interference pattern vanishes. For 2000 rpm to 1000 rpm, this time coincides well with the onset time of the complex phase formation.

Note that if the refractive index of the solution layer is higher than of pure DMF due to the presence of solute Pbl_2 , the resulting layer thickness would be smaller. It follows that the layer thickness calculated with the refractive index of DMF can be seen as an upper limit to the actual layer thickness of the solution layer.

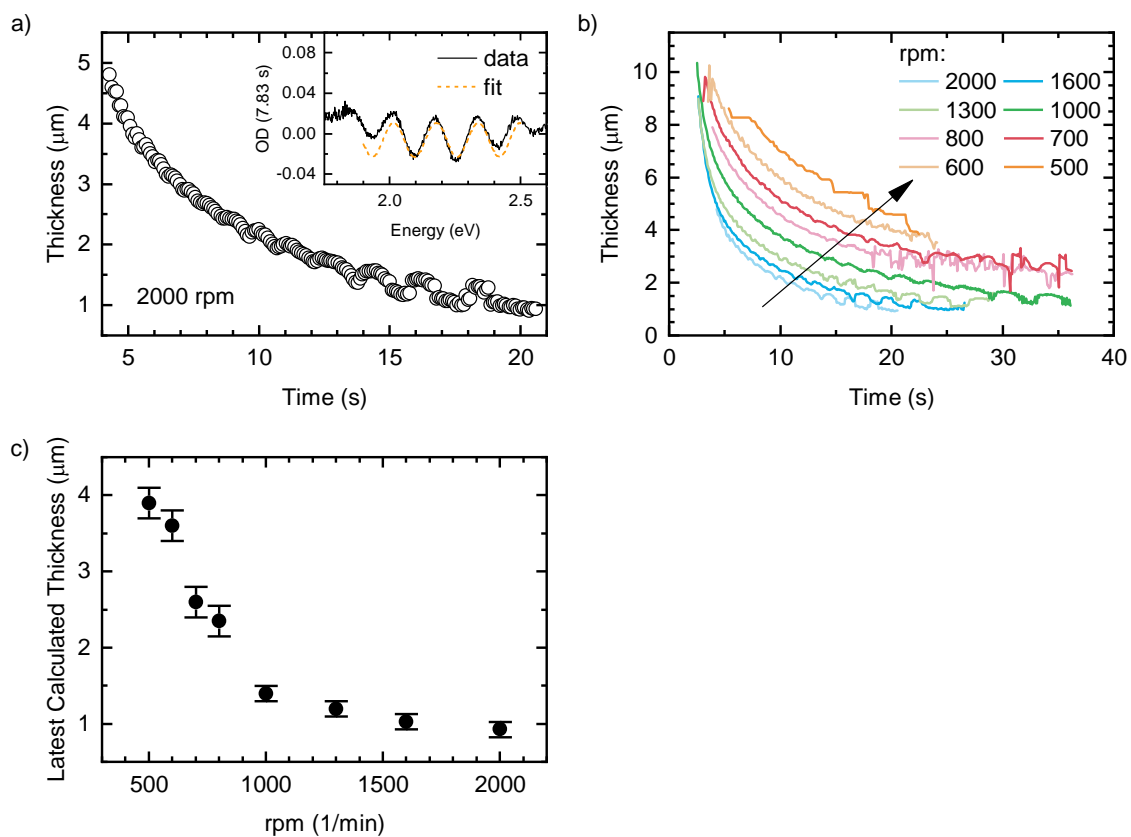


Figure S3: a) Layer thickness as a function of time of the solution layer causing white light interference for the case of the spin speed of 2000 rpm. Inset: sinusoidal modulation of the OD caused by white light interference (black) together with a sine function following equation XXX, fitted to the modulation of the OD (orange dashed). b) Layer thickness as a function of time for all investigated spin speeds. c) Layer thickness extracted at the time when the interference pattern in the OD spectra vanishes. For 2000 rpm to 1000 rpm, this coincides with the onset time of the complex phase formation $t_{0,\text{complex}}$.

S4: Optical density during the complex phase formation upon spin coating

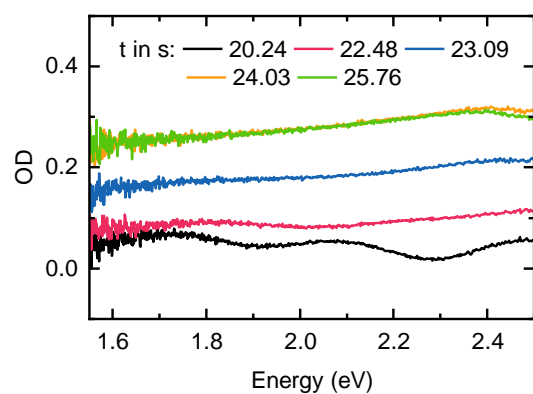


Figure S4: Optical density at selected times during the formation of the intermediate phase upon spin coating with a spin speed of 2000 rpm.

S5: Aliasing effect

All signal intensities (transmitted white light, scattered LED light, PL) depend slightly on the angular position of the spin coater, i.e. the detectable intensities change due to the rotation of the spin coater with the frequency of the spin coater. In combination with the finite frequency of detection, this leads to aliasing if the Nyquist criterium cannot be obeyed. As a result, the recorded signal is modulated with the aliasing frequency. This aliasing frequency can be seen as a sharp peak in the Fourier transform of the signal, as shown in Figure S5a for the case of the $OD_{1.8\text{ eV}}$ for the spin speed of 1600 rpm. By applying a band block filter (notch filter) on the Fourier transform of the signal, the effect of aliasing on the recorded signal can be eliminated, or at least reduced. This is illustrated in Figure S5b. The grey solid line shows the $OD_{1.8\text{ eV}}$ as recorded. By applying a band block filter with cutoff frequencies of 2.3 Hz and 2.5 Hz, the signal quality can be improved significantly. While this demonstrates clearly that the “noise” in the data is caused by an aliasing effect, it can be more convenient to use other types of filter, which do not require the determination of the aliasing frequency. The blue line in Figure S5b shows the $OD_{1.8\text{ eV}}$ after applying a Savitzky-Golay filter with a window size of 25 points (corresponding to 2.2 s) and polynomial order 2, resulting in a curve that is similarly smooth as the one resulting from the application of a notch filter. For the measurements in our setup, the modulation of the signals by the aliasing effect was always significantly faster than the observed dynamics in the film formation, which facilitates the filtering/smoothing of the recorded data without losing temporal resolution or information about the film formation dynamics.

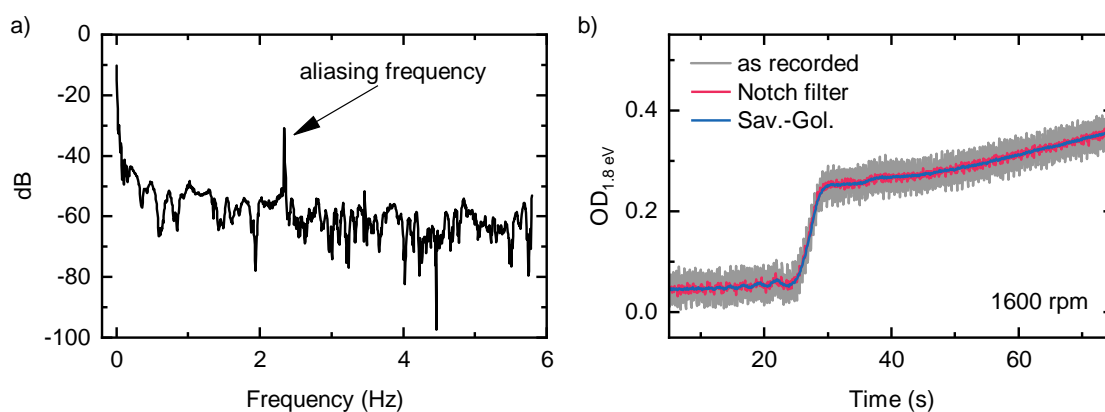


Figure S5: a) Fourier transform of the $OD_{1.8\text{ eV}}$ at the spin speed of 1600 rpm. The peak at 2.34 Hz is the aliasing frequency, determined by the rotation frequency of the spin coater and the detection frequency. b) $OD_{1.8\text{ eV}}$ at the spin speed of 1600 rpm as recorded (grey), with applied Notch filter (band block 2.3 Hz – 2.5 Hz) (red) and with applied Savitzky-Golay filter (window size 25 points, polynomial order 2) (blue).

S6: Details on the PL peak fitting

For fitting the PL spectra, we use an empirical line shape in the form of an asymmetric hyperbolic secant, that is

$$I(E) = I_0 \frac{2}{e^{-\frac{E-E_0}{\sigma_1}} + e^{\frac{E-E_0}{\sigma_2}}} \quad (S3)$$

where I_0 is the PL peak intensity, E_0 is the PL peak position and $\sigma_{1/2}$ are the slopes for the exponentially decreasing high/low energy edge. A symmetric hyperbolic secant (i.e. $\sigma_1 = \sigma_2$) has been used successfully in the past to fit the PL of MAPbI₃.⁴⁻⁵ The usage of this peak shape can be rationalized by considering the reciprocity theorem of PL and absorption and the absorption spectrum of MAPbI₃, as detailed in Supporting Ref. 6.

The asymmetry in Equation S3 accounts for the peak broadening caused by the PL peak shift due to quantum confinement in combination with a particle size distribution.⁷⁻⁸ For illustrating the peak width in Figure 2a in the main text, we calculated the energy where the intensity drops to 1/e based on Equation S3 and the obtained fit parameters.

An exemplary fit of Equation S3 to the PL during the spin-coating is shown in Figure S6.

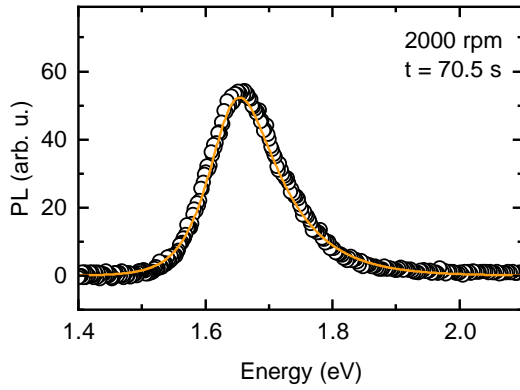


Figure S6: PL of the MAPbI₃ thin film coated at 2000 rpm at 70.5 s after the start of the spin coater (open symbols) together with a fit of Equation S3 (orange line) to the experimental data.

S7: ΔOD as calculated with 2.2 eV for spin coating at 2000 rpm

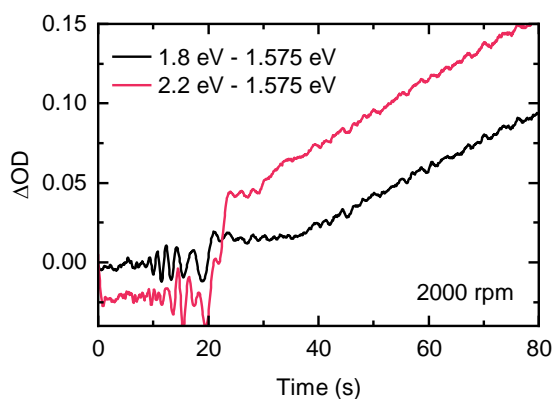


Figure S7: ΔOD as calculated from the OD @ 2.2 eV – OD @ 1.575 eV (red) for the spin speed of 2000 rpm. Calculating the ΔOD with these energies, a rise similar to the one observed in the OD_{1.8 eV} during the pero₁ formation can be observed. For comparison, the ΔOD as calculated with 1.8 eV is also shown (black).

S8: Bulk PL of MAPbI₃

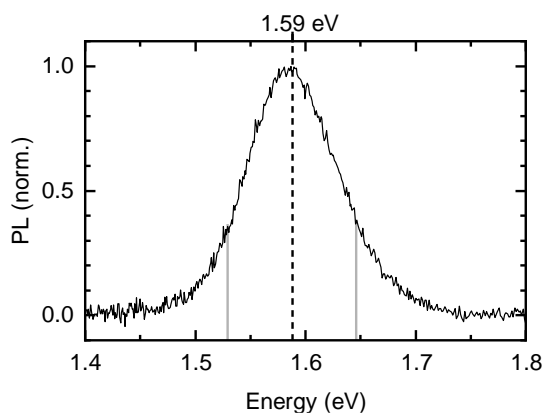


Figure S8: Normalized PL of an annealed MAPbI₃ thin film, measured with the setup described in Section S1. The dashed line indicates the Peak position at 1.59 eV, the grey solid lines indicate the energy where the intensity falls to 1/e of the peak intensity.

S9: Alternative version of Figure 3a from the main text

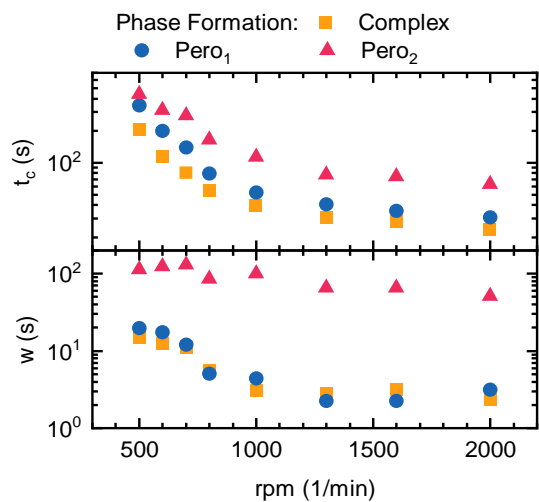


Figure S9: Alternative representation of Figure 3a from the main text. Critical times t_c (top) and widths w (bottom) for the complex (orange), $pero_1$ (blue) and $pero_2$ (red) formation as a function of spin speed.

S10: Intensity heat maps of the *in situ* optical data during slot-die coating for all other air knife pressures

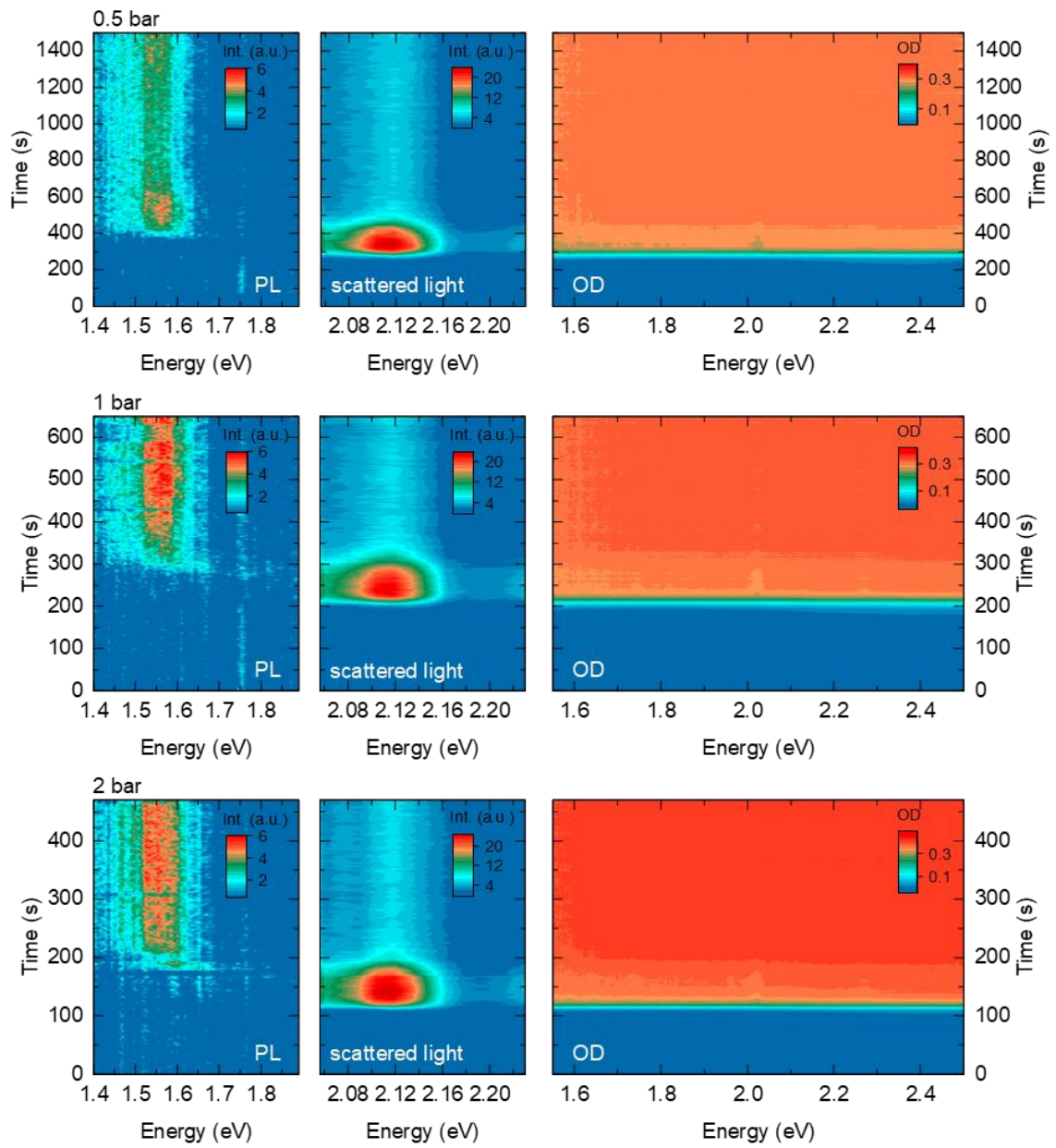


Figure S10: Intensity heat maps of the *in-situ* PL (left), of a selected spectral range of the scattered room light (middle) and of the optical density (right) for the different air pressures at the air knife.

S11: ΔOD and I_{scatter} for the slot-die coatings with different air pressures at the air knife

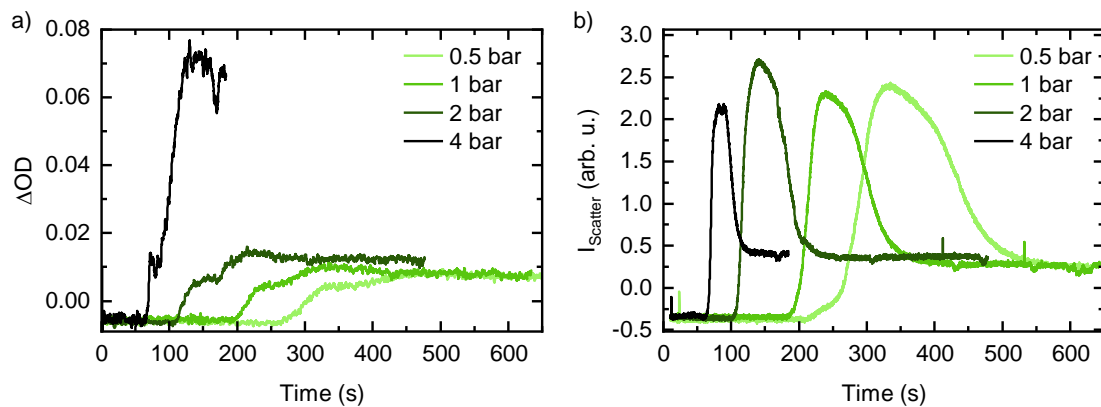


Figure S11: ΔOD ($OD_{1.8\text{ eV}} - OD_{1.575\text{ eV}}$) (a) and I_{scatter} (b) as a function of time for the slot-die coatings with different air pressures at the air knife.

S12: Peak position and width of the perovskite PL during slot-die coatings

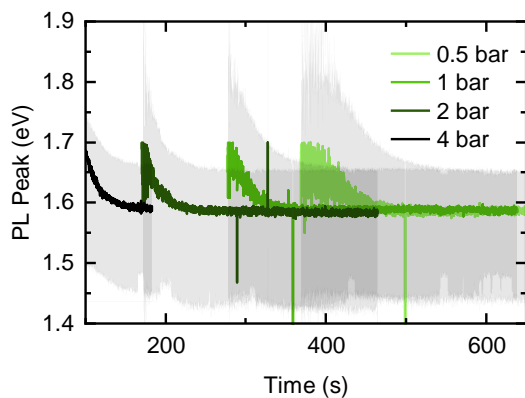


Figure S12: PL peak position as a function of time during the slot-die coatings with different air pressures at the air knife. The shaded areas indicate the spectral range where the PL intensity is more than $1/e$ of the peak intensity.

S13: Alternative version of Figure 5c from the main text

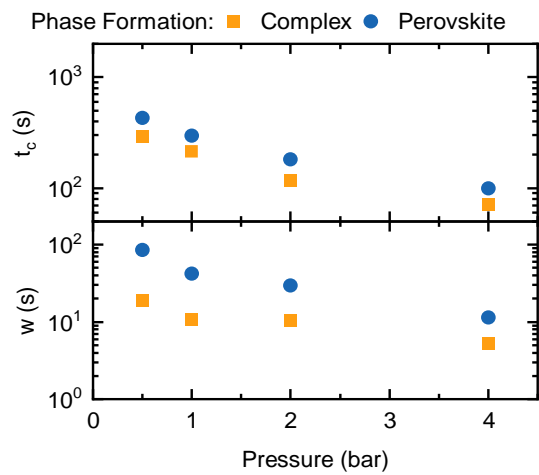


Figure S13: alternative representation of Figure 5c from the main text. Critical times t_c (top) and widths w (bottom) of the complex (orange) and the perovskite (blue) formation as a function of the air pressure at the air knife.

S14: Exemplary estimate of the crystal growth rate from the PL Peak position during slot-die coating

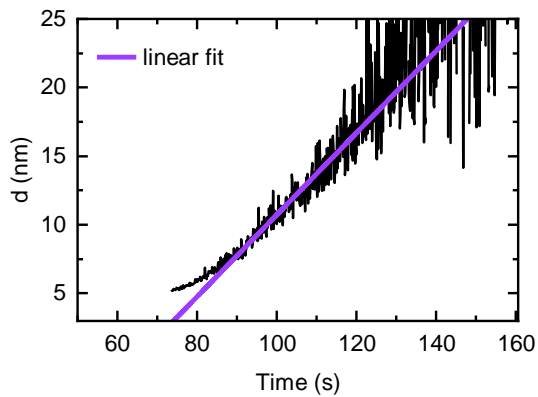


Figure S14: Average crystal size (black) calculated from the PL peak position using eq. 1 from the main text, together with a linear fit (purple) for extracting the crystal growth rate for the air pressure of 4 bar at the air knife.

The deviation of the time evolution of crystal sizes in the earliest time range suggests that the initial perovskite growth is relatively slow. We speculate that this effect might be connected to a distribution of growth rates during the earliest time range, which in turn might be correlated to the fact that the widest distribution of crystal sizes, relative to the average crystal size, is present during this time range. A wide distribution of crystal sizes at the beginning of perovskite crystallization is also supported by the decrease of PL Peak FWHM as a function of time in Figure S12. Nevertheless, the fit in Figure S14 is still satisfying for most of the investigated time span, allowing to extract the average crystal growth rate satisfyingly.

S15: Alternative version of Figure 6d from the main text

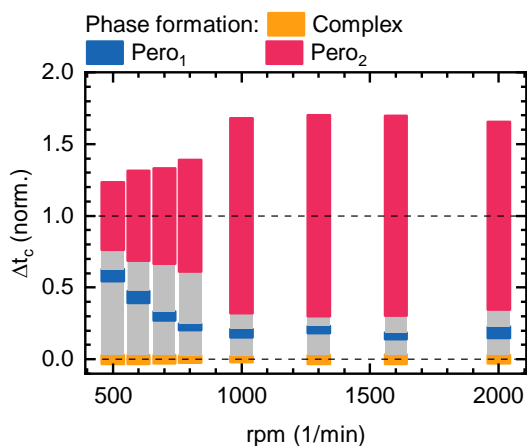


Figure S15: Bar chart of critical time t_c and widths w of the complex (orange), pero₁ (blue) and pero₂ (red) phase formations upon spin coating, normalized to $\Delta t_c = t_{c,pero2} - t_{c,complex}$, i.e. $t_{c,complex}$ is set to 0 and $t_{c,pero2}$ to 1.

S16: Comparison of the calculated growth rates during spin coating and slot-die coating

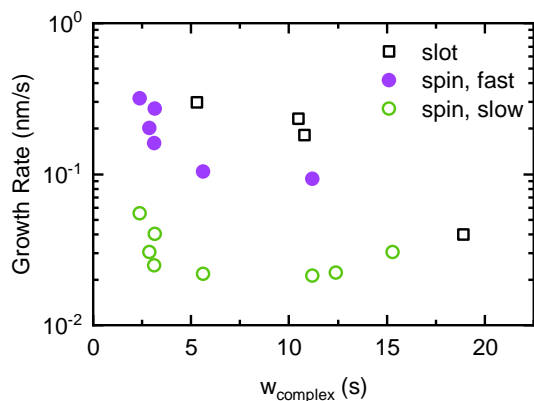
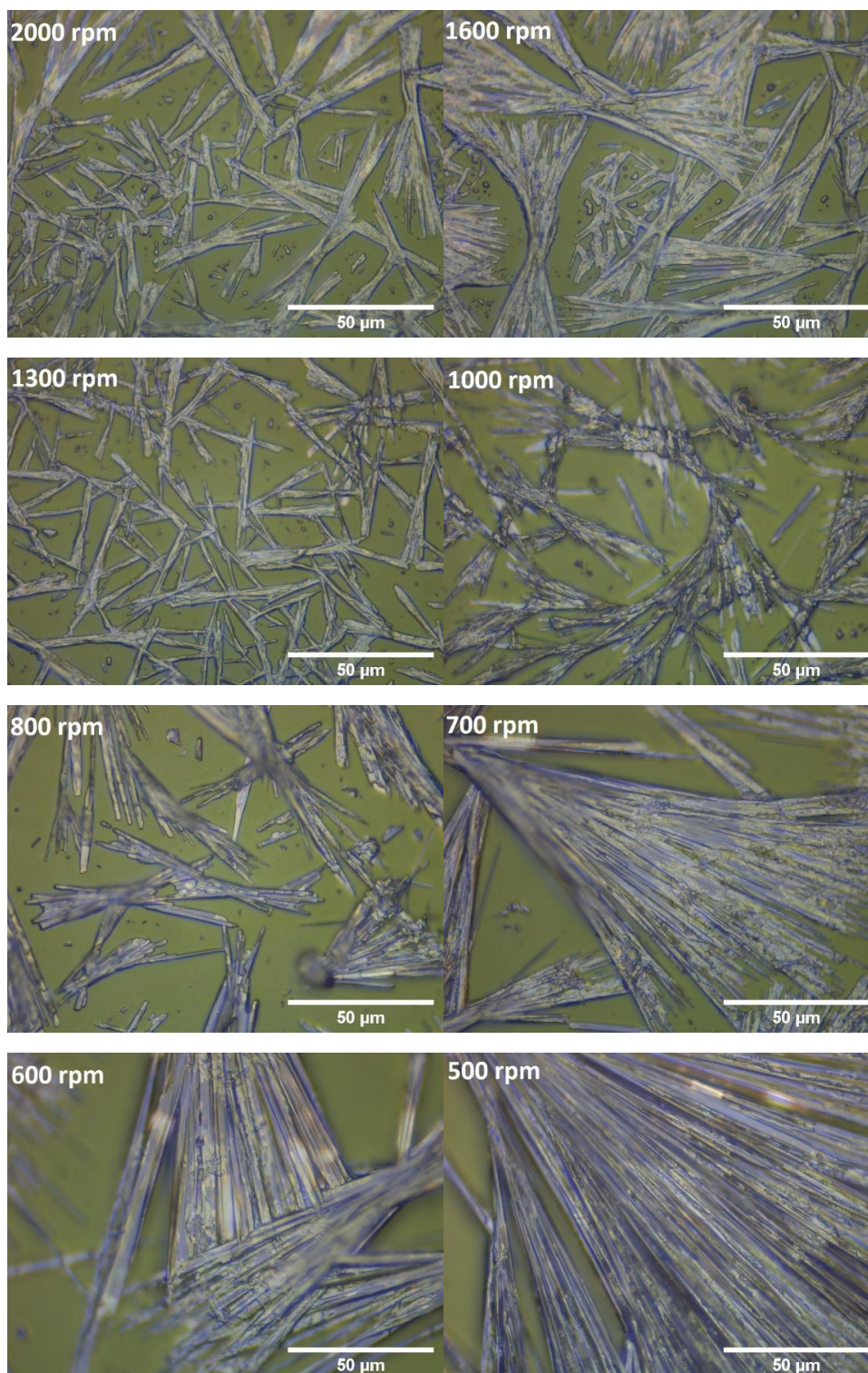


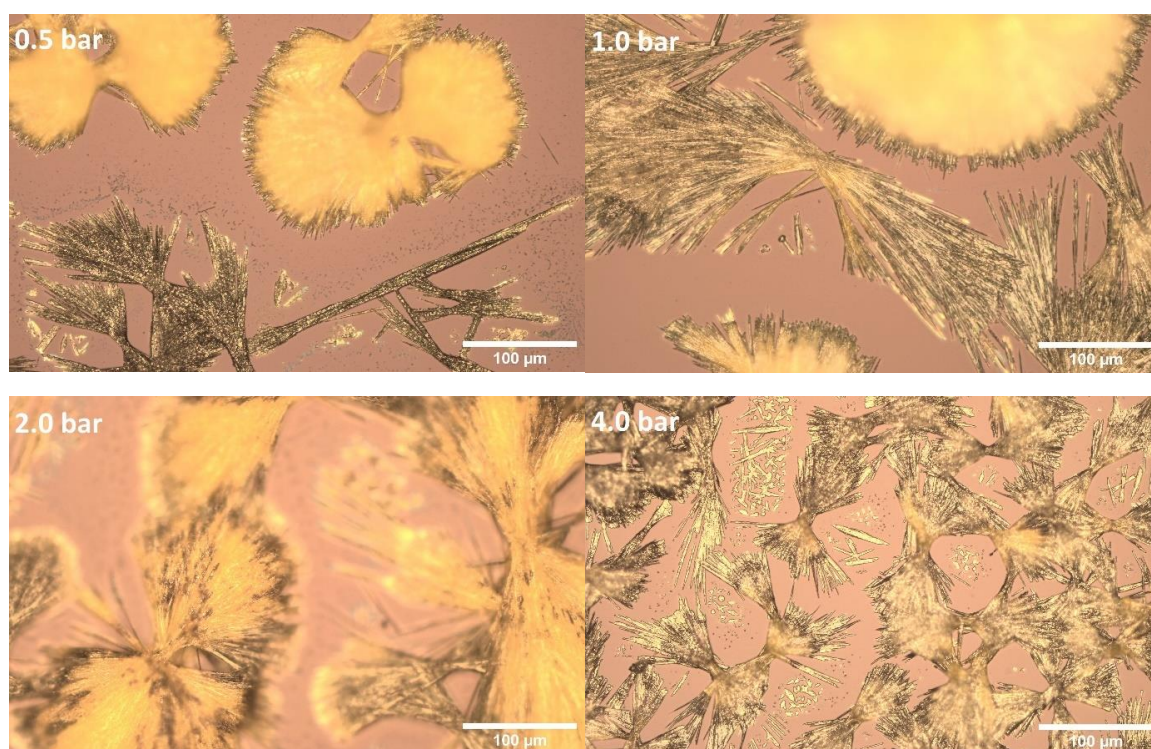
Figure S16: MAPbI₃ growth rate, estimated based on the PL peak shift for slot-die coating and spin coating as a function of $w_{complex}$.

S17: Microscopy images for perovskite phase identification in spin coating

a) Microscopy images of spin coated films:



b) Microscopy images for slot-die coated films



c) Overview Microscopy images of spin coated films:

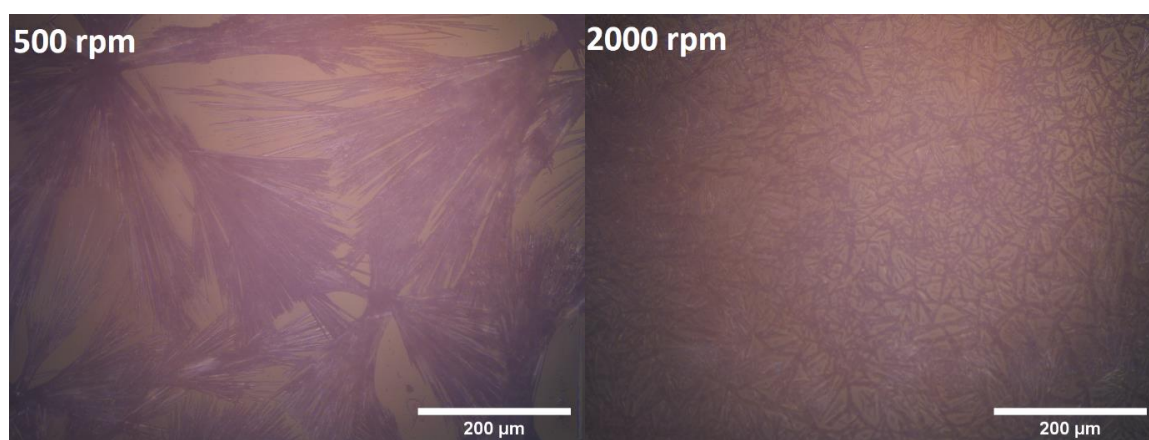


Figure S17: a) Microscopy Image (100x) of MAPbI₃ thin films spin coated with spin speeds 2000 rpm, 1600 rpm, 1300 rpm, 1000 rpm, 800 rpm, 700 rpm, 600 rpm and 500 rpm (from top left to bottom right). From focal plane and off-focus depictions it is evident that with decreasing rpm the height variations of the film increase. b) Microscopy Image (20x) of MAPbI₃ thin films slot-die coated with air pressures at the air-knife of 0.5, 1.0 bar, 2.0 bar and 4.0 bar (from top left to bottom right). c) Microscopy Image (20x) of MAPbI₃ thin films spin coated with spin speeds of 500 rpm and 200 rpm. From the images it becomes evident that faster drying kinetics leads to a more homogenous film coverage with smaller needle structures.

S18: Characterization of final layer morphologies

Measurements of layer thicknesses by profilometry

To estimate the layer thickness Dektak profilometry measurements were performed for spin coated thin films. To estimate the layer thickness within the excitation area, where PL and OD spectra are captured, 3 parallel aligned measurements with a length of 500 μm are carried out with an approximate distance of 250 μm between the measurements. The mean height is calculated by the mean of detected height values and the error, representing the roughness of the layer, is given by the standard deviation of the detected height values. Table S1 shows the minimum and maximum value of detected mean height values with their error. With increasing rpm the mean height and corresponding roughness reduces, as well as the error (approximation of a surface roughness value).

rpm	Maximum mean height (nm)	Minimum mean height (nm)
2000	600 \pm 360	560 \pm 340
1600	640 \pm 400	530 \pm 420
1300	750 \pm 370	540 \pm 370
1000	1100 \pm 520	840 \pm 520
800	1300 \pm 970	1200 \pm 870
700	2200 \pm 1700	1700 \pm 1400
600	3700 \pm 2700	1700 \pm 1100
500	7000 \pm 5900	4600 \pm 4600

Table S1: Maximum and minimum mean height of spin coated MAPb₃ thin films measured by Dektak profilometry. For both the maximum and minimum mean height dependence with rpm an increase in thin film height with increasing rpm is captured.

Scanning Electron Microscopy of a spin coated MAPbI₃ thin film

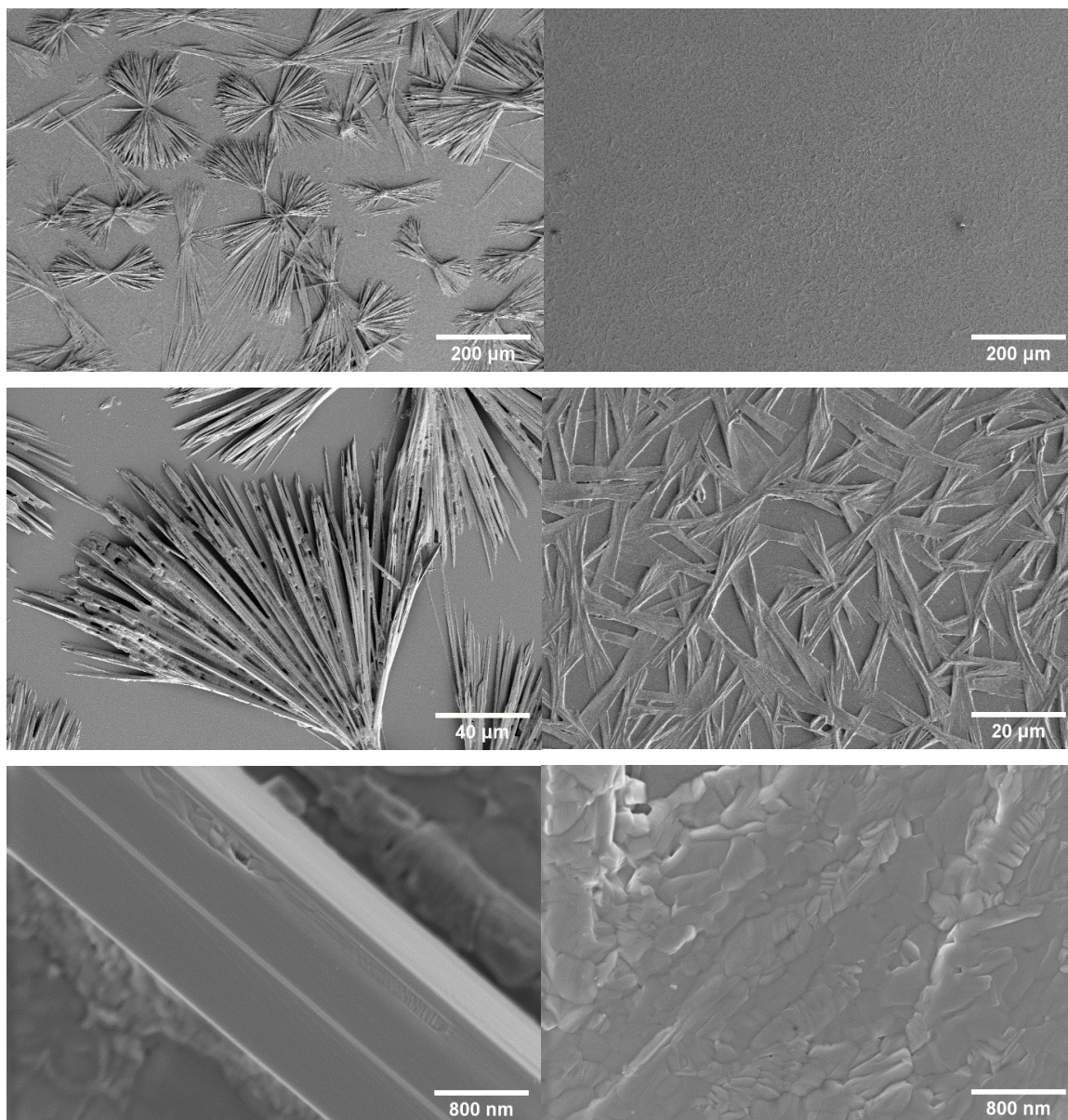


Figure S18: SEM images of MAPbI₃ thin films, from drop-casting with 0 bar air-knife (left column) and spin coating with 2000 rpm (right column). The magnification increases from top to bottom from 100x, 500x and 25.000x. The last row shows, that the solely evaporation dried thin film consists of highly crystalline needles (making up a good portion of the thin film), while one can see for spin coating a high number of small grains with at least one dimension being smaller than 20-30 nm, which is approximately the limit required for quantum confinement to be visible within the PL signal.⁹

Supporting References:

1. Buchhorn, M.; Wedler, S.; Panzer, F., Setup to Study the in Situ Evolution of Both Photoluminescence and Absorption during the Processing of Organic or Hybrid Semiconductors. *J Phys Chem A* **2018**, *122* (46), 9115-9122.
2. Munir, R.; Sheikh, A. D.; Abdelsamie, M.; Hu, H. L.; Yu, L.; Zhao, K.; Kim, T.; El Tall, O.; Li, R. P.; Smilgies, D. M., et al., Hybrid Perovskite Thin-Film Photovoltaics: In Situ Diagnostics and Importance of the Precursor Solvate Phases. *Adv Mater* **2017**, *29* (2), 1604113.
3. Manificier, J. C.; Gasiot, J.; Fillard, J. P., Simple Method for Determination of Optical-Constants n , k and Thickness of a Weakly Absorbing Thin-Film. *J Phys E Sci Instrum* **1976**, *9* (11), 1002-1004.
4. Schötz, K.; Askar, A. M.; Peng, W.; Seeberger, D.; Gujar, T. P.; Thelakkat, M.; Köhler, A.; Huettner, S.; Bakr, O. M.; Shankar, K., et al., Double Peak Emission in Lead Halide Perovskites by Self-Absorption. *J Mater Chem C* **2020**, *8* (7), 2289-2300.
5. Kim, S.-G.; Kim, J.-H.; Ramming, P.; Zhong, Y.; Schötz, K.; Kwon, S. J.; Huettner, S.; Panzer, F.; Park, N. G., How Antisolvent Miscibility Affects Perovskite Film Wrinkling and Photovoltaic Properties. *Nat Commun* **2021**, *12*, 1554.
6. Schötz, K.; Askar, A. M.; Köhler, A.; Shankar, K.; Panzer, F., Investigating the Tetragonal-to-Orthorhombic Phase Transition of Methylammonium Lead Iodide Single Crystals by Detailed Photoluminescence Analysis. *Adv Opt Mater* **2020**, *8* (17), 2000455.
7. Meier, C.; Gondorf, A.; Luttjohann, S.; Lorke, A.; Wiggers, H., Silicon Nanoparticles: Absorption, Emission, and the Nature of the Electronic Bandgap. *J Appl Phys* **2007**, *101* (10), 103112.
8. Ravindran, T. R.; Arora, A. K.; Balamurugan, B.; Mehta, B. R., Inhomogeneous Broadening in the Photoluminescence Spectrum of CdS Nanoparticles. *Nanostruct Mater* **1999**, *11* (5), 603-609.
9. Parrott, E. S.; Patel, J. B.; Haghighirad, A. A.; Snaith, H. J.; Johnston, M. B.; Herz, L. M., Growth Modes and Quantum Confinement in Ultrathin Vapour-Deposited MAPbI₃ Films. *Nanoscale* **2019**, *11* (30), 14276-14284.




14 How Antisolvent Miscibility Affects Perovskite Film Wrinkling and Photovoltaic Properties

*Seul-Gi Kim, Jeong-Hyeon Kim, Philipp Ramming, Yu Zhong, **Konstantin Schötz**, Seok Joon Kwon, Sven Huettnner, Fabian Panzer, Nam-Gyu Park.*

Published in
Nature Communications, **2021**, 12, 1, 1554
(DOI: 10.1038/s41467-021-21803-2)

Reprinted from Springer Nature
Copyright (2021) the Authors

How antisolvent miscibility affects perovskite film wrinkling and photovoltaic properties

Seul-Gi Kim¹, Jeong-Hyeon Kim¹, Philipp Ramming^{2,3}, Yu Zhong^{2,3}, Konstantin Schötz³, Seok Joon Kwon^{1,4}, Sven Huettner ², Fabian Panzer ³ & Nam-Gyu Park ¹✉

Charge carriers' density, their lifetime, mobility, and the existence of trap states are strongly affected by the microscopic morphologies of perovskite films, and have a direct influence on the photovoltaic performance. Here, we report on micro-wrinkled perovskite layers to enhance photocarrier transport performances. By utilizing temperature-dependent miscibility of dimethyl sulfoxide with diethyl ether, the geometry of the microscopic wrinkles of the perovskite films are controlled. Wrinkling is pronounced as temperature of diethyl ether (T_{DE}) decreases due to the compressive stress relaxation of the thin rigid film-capped viscoelastic layer. Time-correlated single-photon counting reveals longer carrier lifetime at the hill sites than at the valley sites. The wrinkled morphology formed at $T_{DE} = 5\text{ }^{\circ}\text{C}$ shows higher power conversion efficiency (PCE) and better stability than the flat one formed at $T_{DE} = 30\text{ }^{\circ}\text{C}$. Interfacial and additive engineering improve further PCE to 23.02%. This study provides important insight into correlation between lattice strain and carrier properties in perovskite photovoltaics.

¹School of Chemical Engineering, Sungkyunkwan University (SKKU), Suwon, Korea. ²Department of Chemistry, University of Bayreuth, Bayreuth, Germany. ³Chair for Soft Matter Optoelectronics, University of Bayreuth, Bayreuth, Germany. ⁴Nanophotonics Research Center, Korea Institute of Science and Technology (KIST), Seoul, Korea. ✉email: npark@skku.edu

Since the pioneering reports on the ~10% efficient solid-state perovskite solar cell (PSC) in 2012^{1,2}, demonstrating long-term stability by resolving the dissolution issue of organic–inorganic lead halide perovskite in photoelectrochemical-type solar cell employing liquid electrolyte^{3,4}, the perovskite photovoltaics has surged swiftly. As a result, the power conversion efficiency (PCE) as high as 25.5% has been achieved in 2020⁵. Although the composition of perovskite started with methylammonium lead iodide, abbreviated to MAPbI₃, the recent excellent performing PSCs are based on formamidinium lead iodide, abbreviated to FAPbI₃^{6–8} or its derivatives with a certain amount of other cations in FA-site and/or bromide in I site^{9–11}. Along with compositional engineering for making progress toward higher PCE, methods for controlling crystal growth have significantly contributed to producing defect-less high-quality perovskite films^{12,13}. Forming Lewis acid–base adduct intermediate via antisolvent engineering was widely adapted to achieve large perovskite crystals with less grain boundaries^{14,15}, instead of a direct conversion of wet film to the perovskite phase. Despite the enlarged perovskite grains, the crystal growth by solvent engineering can hardly manipulate morphology of perovskite layer. Epitaxial growth, for example, could provide crystal growth normal to the substrate, which is expected to be beneficial to carrier transport. In addition, a flat perovskite surface induced by the solvent engineering may not be effective in optimizing light in- and out-coupling. Thus, it is still required to develop a methodology enabling an opto-electronically optimized perovskite layer.

Recently, an approach to control the perovskite morphology has been explored. For example, microscopic wrinkles have been observed for a certain composition of perovskite that suffers buckling of the perovskite thin film^{16,17}. In particular, the buckling was explained as a result of local compressive stress relaxation¹⁷. However, detailed and comprehensive studies for effects of the microscopic wrinkles on the photovoltaic performances, as well as wrinkling mechanism have not been reported yet. Here, we report a simple and yet effective experimental approach to control and optimize the microscopic geometry of the wrinkles of perovskite thin films to maximize the photovoltaic performances, as well as long-time durability. We also suggest a theoretical model elucidating the wrinkling mechanism based on the detailed experimental data. To control the wrinkled morphology, we have designed an experimental method based on temperature-dependent miscibility of dimethyl sulfoxide (DMSO) with diethyl ether (DE) and composition optimization of perovskite materials (i.e., FA_{1-x}MA_xPb(Br_yI_{1-y})₃, FA_{1-z}Cs_zPb(Br_yI_{1-y})₃ and MA_{1-w}Cs_wPb(Br_yI_{1-y})₃). To study the detailed mechanism of the wrinkling, we suggest a bilayer wrinkling model with a theoretical analysis supported by numerical simulations and experimental measurement of optical diffraction. We extend a scope of the study to the investigation of the effects of the microscopic wrinkles on the charge carrier dynamics with time-correlated single-photon counting (TCSPC) coupled with fluorescence lifetime imaging microscopy (FLIM) and photoconductive atomic force microscope (pc-AFM). From the combined experimental data, we have found that the wrinkled morphology notably facilitates the charge carriers transport inside the perovskite films.

Results and discussion

Formation of wrinkled morphologies depending on perovskite composition. Experimental procedure to control microscopic wrinkles in PSC is schematically illustrated in Fig. 1a. The perovskite precursor solution is first spin-coated on a solid substrate for 20 s, followed by dripping DE 10 s right after spinning. The cross-sectional profile of the microscopic wrinkles can be

represented as a sinusoidal curve with a wavelength (λ) and an amplitude (A). λ is estimated by calculating the governing characteristic periodic length scales from the 2D Fourier transform of optical microscope images (Supplementary Fig. 1) and A by calculating the average height difference between the hill (h_{hill}) and the valley (h_{valley}) such that $A = (h_{\text{hill}} - h_{\text{valley}})/2$. From the experiments, we found that the wrinkling geometry is affected by substrate temperature (T_{sub}) and the temperature of diethyl ether (T_{DE}), as well as the perovskite composition. For example, the wrinkle geometry exhibited a dependence on the compositions of FAPbI₃ perovskite. Hereby MA (or Cs) and Br are used as a substitute for FA and I in FAPbI₃ to form nominal compositions of FA_{1-x}MA_xPb(Br_yI_{1-y})₃ and FA_{1-z}Cs_zPb(Br_yI_{1-y})₃, and MA and I are partially substituted with Cs and Br in MAPbI₃, leading to MA_{1-w}Cs_wPb(Br_yI_{1-y})₃. Figure 1b, c show detailed phase diagram of the wrinkle geometries as a function of the composition parameters (i.e., x and y for Fig. 1b and z and y for Fig. 1c, respectively) (see Supplementary Fig. 1a, b for entire experimental data for the wrinkled morphologies). We observed that the wrinkling occurs in selective range of the compositions (i.e., $0 \leq x \leq 0.4$ and $0.2 \leq y \leq 0.8$) or ($0.6 \leq x \leq 0.8$ and $0.4 \leq y \leq 0.6$) in FA_{1-x}MA_xPb(Br_yI_{1-y})₃ and ($z = 0.1$ and $0 \leq y \leq 0.8$), ($z = 0.2$ and $0 \leq y \leq 0.6$), ($z = 0.3$ and $0.2 \leq y \leq 0.4$) or ($z = 0.4$ and $y = 0.2$) in FA_{1-z}Cs_zPb(Br_yI_{1-y})₃. Notably, we also observe that there is no wrinkling in MAPbI₃ or its derivatives (see Supplementary Fig. 1c, d). In addition, hundred percent Br (FA_{1-x}MA_xPbBr₃) would not lead to wrinkling (i.e., for the FA_{1-x}MA_xPb(Br_yI_{1-y})₃ perovskite, λ tends to increase with decreasing x (Fig. 1b)). From these experimental observations, it is obvious that the presence of limited amount of Br plays an important role in introducing the wrinkled morphology. With a composition of Br in the range of $0.2 \leq y \leq 0.8$, λ decreases with increasing the composition of MA (i.e., $\lambda \sim 20 \mu\text{m}$ for $0 \leq x \leq 0.2$, $\lambda \sim 15 \mu\text{m}$ for $0.2 \leq x \leq 0.4$, and $\lambda \sim 8 \mu\text{m}$ for $x \approx 0.6$). It is also notable that wrinkling hardly occurs for higher composition of x and y such that being >0.8 . We also observe that A is relatively shallow (~65 nm) for the composition range with $0 \leq x \leq 0.4$ and $0.2 \leq y \leq 0.8$, while is deep (~100 nm) for the composition range with $0.1 \leq x \leq 0.3$ and $0.3 \leq y \leq 0.6$. As shown in Fig. 1c, substitution of FA with Cs, the wrinkled morphology is accompanied by further amplified value of A ($> 100 \text{ nm}$) in the range of $0.05 \leq z \leq 0.4$ and $0.2 \leq y \leq 0.6$. The sampled composition can be expressed as (FAPbI₃)_{1-z}(CsPbBr₃)_z in case of $z = y$ and more detailed phase diagram and images of the wrinkled morphology are provided in Supplementary Fig. 2a, b, and d. Interestingly, the as-spun films prior to the annealing also show a wrinkled morphology in the range of $0.1 \leq z \leq 0.2$ (Supplementary Fig. 2a), which is sustained even after the annealing (Supplementary Fig. 2b), with slightly decrease in λ (Supplementary Fig. 2d). This indicates that the solvent evaporation during the annealing process hardly affects the wrinkle framework, as is the context in the case of (FAPbI₃)_{1-x}(MAPbBr₃)_x in Supplementary Fig. 2c, e. The annealed films show a decrease in the value of λ from 19.7 to 13.9 μm when increasing z from 0.1 to 0.2, while an increase in the value of A from 46.5 nm ($z = 0.1$) to 112.5 nm ($z = 0.2$).

Effect of T_{DE} on wrinkled morphologies. Next, with a representative sample with the maximum amplitude (i.e., (FAPbI₃)_{0.875}(CsPbBr₃)_{0.125} ($z = 0.125$)), we have examined the effects of T_{sub} and T_{DE} on the wrinkling morphology as shown in Fig. 1d. With fixed T_{sub} , λ decreases and A increases with decreasing T_{DE} . The effects of T_{DE} on the wrinkled morphology can be explained by the microscopic phase separation of solvent and antisolvent mixture in which the lower the mixture temperature the less molar fraction of the solvent, which in turn shorter wavelength and greater amplitude. Detailed theoretical

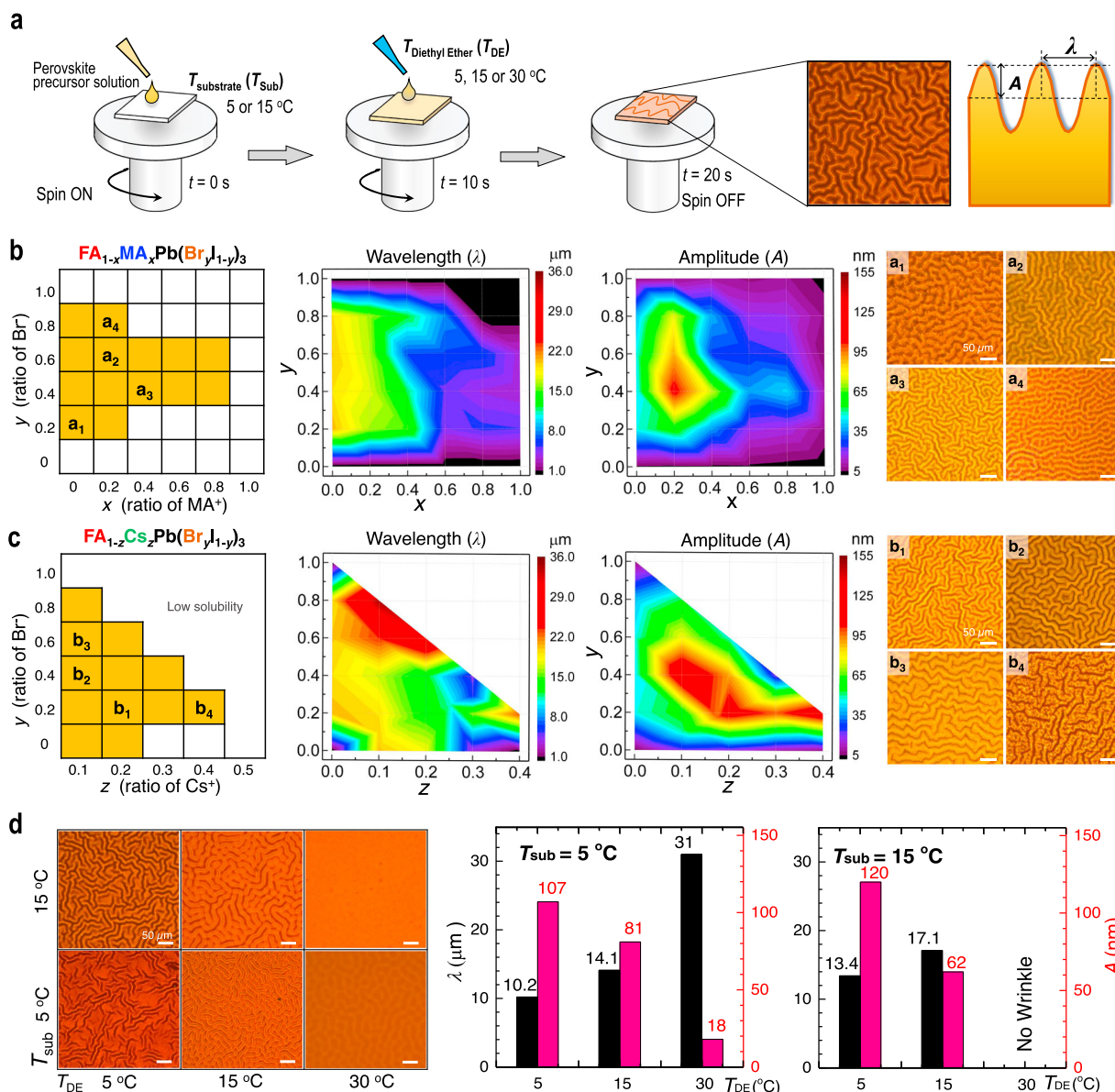


Fig. 1 Wrinkled morphologies of perovskite thin film. **a** A schematic illustration of the experimental procedure to control wrinkled morphology in the perovskite film, together with an optical microscope image of the wrinkled morphology having amplitude (A) and wavelength (λ). Phase diagrams of the wrinkled morphology for **(b)** $\text{FA}_{1-x}\text{MA}_x\text{Pb}(\text{Br}_{y1-y})_3$ (annealed at 145°C for 10 min) and **(c)** $\text{FA}_{1-z}\text{Cs}_z\text{Pb}(\text{Br}_{y1-y})_3$ (annealed at 145°C for 10 min) perovskite thin films with different compositions. Color maps of wavelength (λ) and amplitude (A) are presented in the middle panels for each composition. Selected optical microscope images of a_1 – a_4 and b_1 – b_4 are presented in the right panels for each composition. **d** Optical microscope images for the $\text{FA}_{0.875}\text{Cs}_{0.125}\text{Pb}(\text{Br}_{0.125}\text{I}_{0.875})_3$ perovskite films with different temperatures of T_{DE} and T_{Sub} . Scale bar is $50\ \mu\text{m}$. Dependence of A and λ values on T_{DE} s at a given T_{Sub} is illustrated with bar graph on the right panels.

analysis on the effects of T_{DE} can be found in Supplementary note 1. In addition, there are no wrinkles at sufficiently high T_{DE} such as 30°C at a given $T_{\text{Sub}} = 15^\circ\text{C}$.

Bilayer model for wrinkling mechanism. The formation of wrinkling can be explained with a simple thin film mechanics model. In particular, we can employ a bilayer model in which wrinkles form in the course of relaxation of a compressive stress developed in the perovskite film. It was reported that the compressive stress is due mainly to the differences in the thermal expansion coefficients between the perovskite precursor solution

and the substrate¹⁸. Previous study on the wrinkling of perovskite thin films suggested that the compressive stress can be developed by the volume change during a fast perovskite formation by using wafer curvature stress measurements¹⁷. This mechanism requires relatively long-time wrinkle formation dynamics up to several minutes to hours^{19,20}. However, we observe that the wrinkles form within 10 s. Therefore, we have developed a more detailed model by which the overall morphology of wrinkles can be elucidated, as well as the wrinkling mechanism based on previous reports^{17,18}. Using a model based on the thin film mechanics, the wrinkle geometry can be described as a function of the thickness and mechanical constants of the materials. We also derive

relationships of λ and A of the wrinkles with the compositions and T_{DE} (see detailed analysis in Supplementary note 1).

To confirm the wrinkling mechanism, in situ photoluminescence (PL) and simultaneous absorption are examined within the first 24 s of spinning (see ref. 21 for details of the setup). PL and absorption signals commonly emerge immediately after the contact with DE with duration of spinning of 10 s, indicating that perovskite phase forms. As shown in Fig. 2a, the PL peak initially occurs at 712 nm and then shifts to longer wavelengths from 10 s to 24 s. A faster change in PL from 712 nm to over 760 nm is observed for $T_{DE} = 5$ and 15 °C, whereas a more gradual change is observed for $T_{DE} = 30$ °C (Fig. 2b). Extracting the band edge evolution from the in situ absorption data (Fig. 2c), and comparing it to the corresponding evolution of PL peak position show, that early after dripping diethyl ether, the PL peak position is at a lower wavelength than the band edge (Supplementary Fig. 3). We interpret this as the optical signature of a confinement effect, while the subsequent continuous red-shift of PL and band edge indicates a more Cs and Br rich stoichiometry at early times followed by more pronounced incorporation of FA and I at longer times (see Supplementary note 2 for details). We also observe that absorbance becomes stronger at later stage and with increased T_{DE} . This indicates that the growth rate of the thin film thickness (h_f) is faster for higher T_{DE} . The absorbance variation dynamics is translated into the thin film growth dynamics using the absorption coefficient of the perovskite thin films and reference data at equilibrium as shown in Fig. 2d demonstrating that the thickness of the perovskite layer becomes thinner as T_{DE} decreases. (see Supplementary Fig. 3d and Supplementary note 2 for detailed procedure). It is also notable that the PL red-shift is faster for lower T_{DE} (Fig. 2b).

From the in situ PL and absorbance spectra, we can propose that the spin-coated perovskite thin film suffers morphological evolution from viscoelastic layer to elastic layer-capped viscoelastic bilayer. The formation of the elastic capping layer is due mainly to the antisolvent, which drives solvents out of the top part of the coated thin film. In particular, solution of precursor materials of perovskite in DMSO suffers rapid phase separation by introducing the antisolvent DE at the top surface of the film. This leads to the fast crystallization of the top region of the spin-coated layer, which turns into the thin capping layer. The phase separation at lower temperature also gives rise to higher concentration of the perovskite in the top capping layer, which can explain the dependences of the wrinkle geometry on T_{DE} (see Figs. 1d and 2f, and details in Supplementary note 1 with mixing behavior test in Supplementary Fig. 4). In particular, as shown in Supplementary Fig. 4, we observe higher miscibility at relatively higher temperatures (i.e., >25.4 °C), while phase separation of DMSO and DE mixture at relatively low temperature (i.e., <15.2 °C) indicating less miscibility, whereas dimethylformamide (DMF), the main solvent of precursor solution, is fully miscible with DE regardless of the mixing temperature. In contrast, the underlying bottom layer is different from the top capping layer. In particular, as shown in PL and absorbance spectra at earlier stage, the underlying layer exhibited no distinct peaks or band edges signals, and therefore, can be considered as amorphous layer. In addition, the bottom layer is expected to be viscous as demonstrated in the supporting experiment, where DE is poured into the $(\text{FAPbI}_3)_{1-z}(\text{CsPbBr}_3)_z$ and $(\text{FAPbI}_3)_{1-x}(\text{MAPbBr}_3)_x$ precursor solution (Supplementary Fig. 5). The viscous precipitate (Supplementary Fig. 5a, b) is maintained for 2–5 min and then converted to the solid phase (Supplementary Fig. 5c, d), while precipitates in $z \geq 0.25$, $x \geq 0.8$ and MAPbI₃ are immediately transferred to solid phase with high viscosity (η) of about 10^{5-7} Pa·s (Supplementary Fig. 6). As shown in Fig. 2e for the case of relatively low dynamic viscosity of the viscous precipitate

(samples shown in Supplementary Fig. 5a, b), the viscosity in the bottom layer indicates that the layer is assuredly different from the top capping layer. Based on the in situ absorption and emission studies, combined with dynamic viscosity measurements, we conclude, that the wrinkled structure is likely formed via a bilayer intermediate with a perovskite top layer on a viscous amorphous bottom layer (case 2 in Fig. 2f), while a flat surface results when not undergoing the bilayer intermediate (case 1 in Fig. 2f). Interestingly, too high viscosity (solid precipitate) with the composition of $z \geq 0.3$ also leads to no wrinkle formation as shown in the Case 3 in Fig. 2f. This indicates that the compressive stress of the underlying layer is not dissipated in a local manner, which results in disordered morphological deformation as shown in the optical microscope image in the Case 3. These findings are clearly different from the previous study, suggesting that the crystallization (or nucleation) occurs from the bottom¹⁷.

Experimental evidence and numerical simulation for bilayer model. To further confirm the bilayer model for the wrinkling mechanism, we have numerically simulated the morphological evolution of the thin film wrinkling based on temporal evolution of the wrinkle geometry (see details in Supplementary note 3)²². As shown in Supplementary Figs. 7 and 8, we can find that the bilayer model provides qualitatively similar wrinkling morphologies accompanied by two-dimensional (2D) fast Fourier transform (FFT) images to the experimentally observed images. We have also tested again the bilayer model by examining the optical diffraction patterns of the wrinkled thin films (Fig. 2g). As shown in Fig. 2h, the optical diffraction patterns would exhibit different patterns (i.e., concentric ring patterns for the wrinkled bilayer, while dot or single ring pattern for the wrinkled monolayer) with different configurations as denoted in Fig. 2g. Indeed, we observe concentric ring patterns at glass side (bottom) of film just after contacted with diethyl ether (10 s after spin started), and the patterns disappears with time, whereas the transmitted concentric ring patterns was sustained for long time as shown in Fig. 2i. This can be compared to the diffraction patterns of the wrinkled perovskite films obtained from reflected side and transmitted side, which are commonly sustained over long time (Supplementary Fig. 9a, b). With the theoretical analysis supported by numerical calculations and experimental observations of the diffraction patterns, we can suggest that the wrinkling of the perovskite thin films can be elucidated by a bilayer model.

Comparison of photovoltaic property between wrinkled and flat morphology. To study the effect of bilayer-engineered wrinkled perovskite layer to photovoltaic property, current density(J)–voltage(V) characteristics and external quantum efficiency (EQE) of PSCs are measured as shown in Fig. 3a, b. It is evident that the wrinkled morphology affects mainly the open-circuit voltage (V_{oc}) and fill factor (FF), while J_{sc} remains nearly unchanged. This is due mainly to a fact that the wrinkled texture is formed at the back-contact side, and therefore, does provide negligible effects on the light absorption or anti-reflection. Indeed, the integrated J_{sc} based on the EQE spectrum in Fig. 3b is calculated to be 22.318 mA/cm² ($T_{DE} = 30$ °C) and 22.567 mA/cm² ($T_{DE} = 5$ °C), which is well consistent with the measured J_{sc} values indicating overall change in the light absorption of solar spectrum induced by the wrinkled morphology is nearly negligible. More specifically, the amplitude of the wrinkles (~100 nm) is sufficiently smaller than the quarter of the wavelength of visible and near infrared light. In addition, the spatial periodicity such as wavelength of the wrinkles is sufficiently greater than the wavelength of visible and near infrared incident light, which limits the grating effects of the micro-structures. As listed in Supplementary

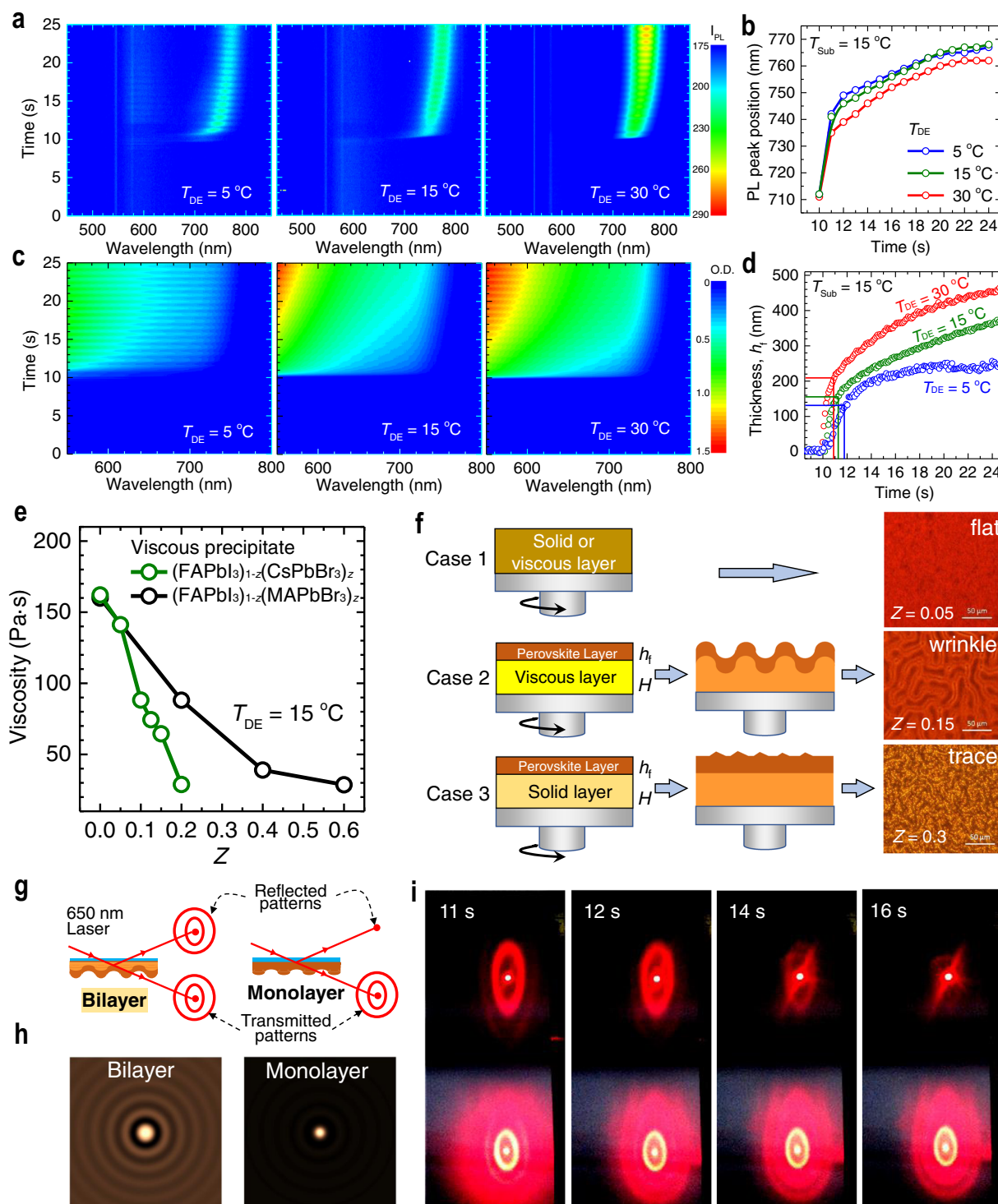


Fig. 2 Bilayer-induced wrinkling mechanism. **a** In situ photoluminescence (PL) measured in the course of spinning from 0 s to 24 s at $T_{\text{Sub}} = 15\text{ }^{\circ}\text{C}$ and $T_{\text{DE}} = 5, 15,$ and $30\text{ }^{\circ}\text{C}$. **b** Plot of PL peak positions as a function of spinning time. Spin-coating duration was 20 s (dashed line). **c** In situ UV-Vis absorption spectra measured during spinning from 0 s to 24 s at $T_{\text{Sub}} = 15\text{ }^{\circ}\text{C}$ and $T_{\text{DE}} = 5, 15\text{ }^{\circ}\text{C}$ and $30\text{ }^{\circ}\text{C}$. **d** The evolution of the thin solid upper perovskite layer thickness (h_t) calculated from the measured absorption data. Spin-coating duration was 20 s. **e** Viscosity of an amorphous viscous precipitates obtained by pouring diethyl ether to the perovskite precursor solution for $(\text{FAPbI}_3)_{1-z}(\text{CsPbBr}_3)_z$ with $z = 0-0.2$ and $(\text{FAPbI}_3)_{1-x}(\text{MAPbBr}_3)_x$ with $x = 0-0.6$ (Supplementary Fig. 5). **f** An intermediate layer structure for the flat surface (case 1), the wrinkled structure (case 2) and the coarse surface with trace of wrinkle (case 3). A bilayer model with a solid upper layer with thickness of h_t was proposed to explain the wrinkling process. **g** Schematic representation of setup for measuring optical diffraction pattern at bottom surface of bilayer film. **h** Reflected optical diffraction patterns for bilayer and monolayer films. **i** Photographs of reflected (up), transmitted (down) optical diffraction patterns as function of spin-coating time (11, 12, 14, and 16 s) after perovskite precursor is contacted with diethyl ether at 10 s ($T_{\text{Sub}} = 15\text{ }^{\circ}\text{C}$ and $T_{\text{DE}} = 5\text{ }^{\circ}\text{C}$).

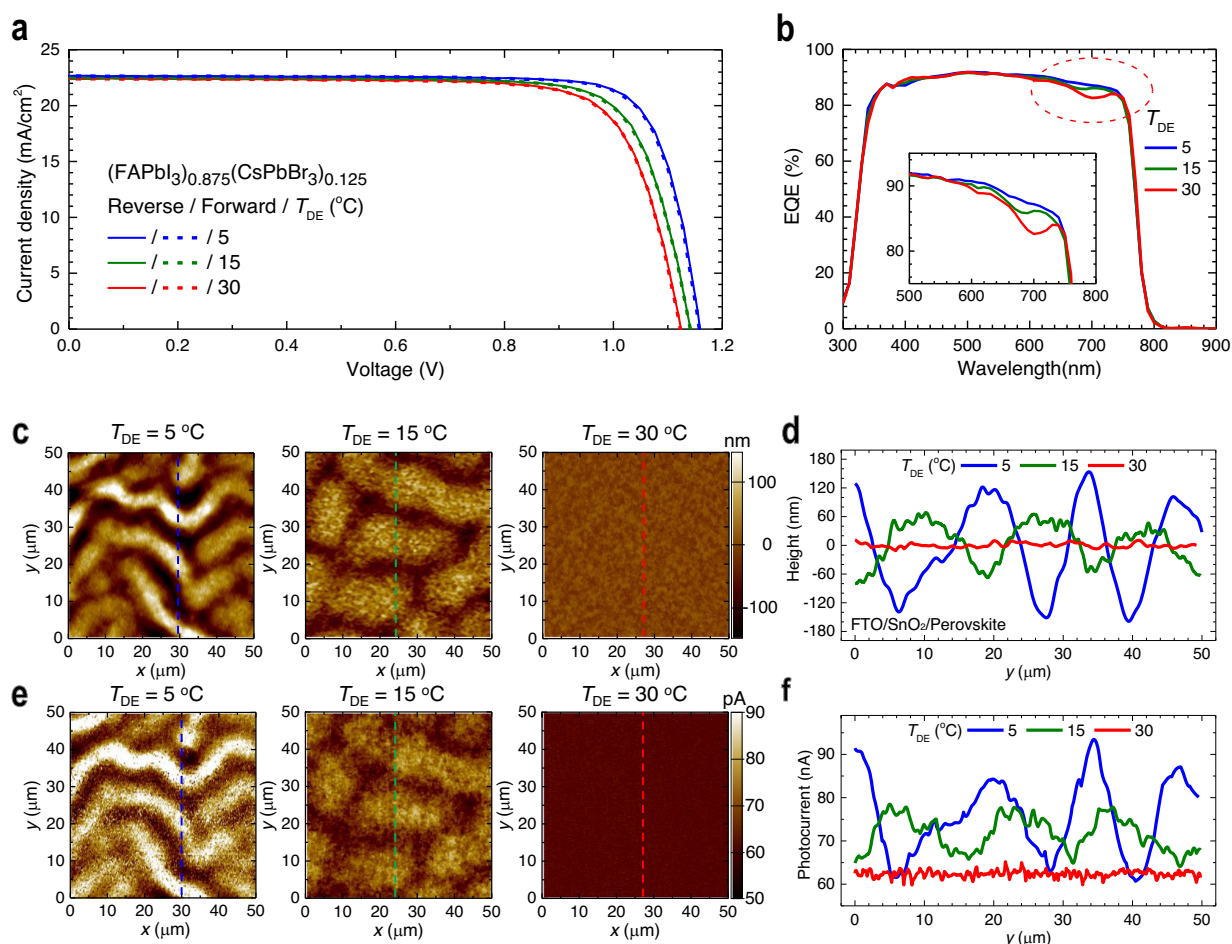


Fig. 3 Dependence of current-voltage curves on T_{DE} and photocurrent depending on the hills and the valleys. **a** Current density (J) – voltage (V) curves of PSCs employing $(\text{FAPbI}_3)_{0.875}(\text{CsPbBr}_3)_{0.125}$ films formed from different T_{DE} . Solid and dashed lines represent reverse and forward scanned data, respectively. **b** External quantum efficiency (EQE) for each condition. Inset shows EQE from 500 to 800 nm. **c** Atomic force microscopy (AFM) topographies of the annealed $(\text{FAPbI}_3)_{0.875}(\text{CsPbBr}_3)_{0.125}$ films deposited on the SnO_2 -coated FTO substrate at $T_{\text{Sub}} = 15^\circ\text{C}$ and at different T_{DE} of 5, 15, and 30°C . λ and A are estimated to be $13.4\ \mu\text{m}$ and $120\ \text{nm}$ for $T_{DE} = 5^\circ\text{C}$, $17.1\ \mu\text{m}$, and $62\ \text{nm}$ for $T_{DE} = 15^\circ\text{C}$. **d** Height profile with respect to the contour lines in **c**. **e** Photoconductive AFM (pc-AFM) images of the annealed $(\text{FAPbI}_3)_{0.875}(\text{CsPbBr}_3)_{0.125}$ films deposited on the SnO_2 -coated FTO substrate at $T_{\text{Sub}} = 15^\circ\text{C}$ and at different T_{DE} of 5, 15, and 30°C on the same areas in **c**. **f** pc-AFM data-based photocurrent profile with respect to the contour lines in **c** or **e**.

Table 1 and Supplementary Fig. 10, the forward- and reverse-scanned photovoltaic measurements exhibited improvement of the overall average PCE from 19.46% ($J_{\text{sc}}: 22.365\ \text{mA}/\text{cm}^2$, $V_{\text{oc}}: 1.123\ \text{V}$, FF: 0.7729) to 21.00%. ($J_{\text{sc}}: 22.662\ \text{mA}/\text{cm}^2$, $V_{\text{oc}}: 1.158\ \text{V}$, FF: 0.8004) upon decreasing T_{DE} from 30 to 5°C . In Fig. 3b, we can identify the possible contributions made by the wrinkled morphology. For example, in the spectral range between 600 and 750 nm, EQE shows enhancement for the wrinkled morphology ($T_{DE} = 5^\circ\text{C}$) compared to the flat reference ($T_{DE} = 30^\circ\text{C}$). This enhancement can be attributed by extended collection length (L_C) of carriers responsible for the longer wavelength incident photons. The extended charge carrier collection length corresponds to the longer carrier diffusion length (L_D)²³. This implies that the enhanced photovoltaic performances of the wrinkled morphology is due mainly to the facilitated transport property of photo-carriers. To verify the facilitated transport, microscopic pc-AFM images are measured for the wrinkled sample. As shown in Fig. 3c–f, pc-AFM images clearly exhibit the strong correlation between the wrinkle morphology and the photocurrent. In a device configuration with FTO/ SnO_2 /Perovskite/spiro-MeOTAD

layers, the spiro-MeOTAD layer also exhibits a wrinkle morphology (Supplementary Fig. 11), which indicates that spiro-MeOTAD layer forms conformal contact with the wrinkled perovskite thin film without delamination (A is reduced to 70 nm for $T_{DE} = 5^\circ\text{C}$ and 25 nm for $T_{DE} = 15^\circ\text{C}$). As shown in Fig. 3f, it is remarkable that the photocurrent is higher for the hill sites with lower T_{DE} , while photocurrent for the valley sites is nearly constant regardless of T_{DE} . The average photocurrent (over the area of $50 \times 50\ \mu\text{m}^2$) increases from 62.1 to 69.6 pA and to 76.0 pA as T_{DE} decreases from 30 to 15°C and to 5°C . To study the dependence of perovskite thickness on the measured photocurrent, J - V curves and pc-AFM are measured for the flat $(\text{FAPbI}_3)_{0.875}(\text{CsPbBr}_3)_{0.125}$ films with different film thickness of 477 and 693 nm. As shown in Supplementary Fig. 12, the difference in the measured J_{sc} and in the pc-AFM photocurrent is negligible, i.e., $\Delta J_{\text{sc}} = 0.5\ \text{mA}/\text{cm}^2$ and $\Delta\text{photocurrent} = \sim 2.9\ \text{pA}$, respectively. This indicates that the photocurrent difference at the hill and valley sites is not due to the thickness difference. In addition, it was reported that the concentration of photo-generated carriers is reduced to about 1/10 at a depth of

412 nm under the film surface and to 1/100 at 709 nm as compared to the carrier concentration at near surface (~ 67 nm)²⁴. Therefore, it is expected that difference in photocurrent between 477 nm- and 693 nm-thick perovskite layers is <4%. These findings allow us to explore another mechanism for the photocurrent enhancement given by the micro wrinkle morphology (i.e., ~ 470 nm (Valley, $T_{DE} = 5$ °C) and ~ 700 nm (Hill, $T_{DE} = 5$ °C)).

Carrier lifetime of wrinkled perovskite film. One of the possible contributions of the wrinkled morphology to the photocurrent enhancement can be found in better crystallinity of the film. Indeed, although the wrinkling process seems to be hardly changes the grain size, an enhanced intensity of the ($h00$) planes with decreasing T_{DE} , as could be found from X-ray diffraction measurements (Supplementary Fig. 13), is indicative of a more preferred orientation of the grains, which could be advantageous to charge extraction²⁵. To find the underlying mechanism of the enhanced photocurrent and overall photovoltaic performances of the wrinkled morphology perovskite films, we have attempted to analyze microscopic dynamics of the photocarriers inside the films at the hill and valley sites. Using fluorescence lifetime imaging microscopy (FLIM) coupled with time-correlated single-photon counting (TCSPC), we measure position-specific lifetime map of the photocarriers in the wrinkled perovskite films. For better comparison, FLIM images are measured from top and from the bottom side of each perovskite film. As shown in Fig. 4a, b, it is evident that the wrinkle morphology (T_{DE} of 5 and 15 °C) is distinctively and consistently reflected in the microscopic PL lifetimes maps, where valleys appear brighter than hills (hill and valley sites in FLIM are identified from the optical microscope images of the same areas (Supplementary Fig. 14)). No compositional changes between hill and valley on top and bottom sides are confirmed by steady-state photoluminescence (PL) (Supplementary Fig. 15), which is consistent with previous report²⁶. We associate this to the differences in the local layer thickness of hill and valley, so that the laser induced charge carriers distribute within a larger volume in case of the hills, leading to a lower charge carrier density and thus lower PL intensity. In particular, when comparing the average lifetime of the photocarriers between top and bottom, it is also evident that the higher the amplitude of the wrinkles, the greater the difference between the lifetimes of the carriers at the hill and valley sites. This can also be confirmed by the nearly constant lifetime maps of the flat sample (i.e., film with $T_{DE} = 30$ °C in Fig. 4a, b). In detail, we analyze the average lifetime of the photocarriers at the hill and valley sites with time-resolved PL (TRPL) as shown in Fig. 4c, d. In general, the measured PL decay at earlier times after excitation is dominated by bimolecular recombination, while for longer times, it is dominated by monomolecular recombination at defects²⁷. The latter process is strongly correlated with the defect concentration²⁸. From the exponential fitting of the PL decay curve, we can deduce the decaying rate k_1 such that $PL(t) \propto \exp(-2 \cdot k_1 t)$ (see Supplementary note 4 for details and Supplementary Table 2). From the exponential fitting, we found that k_1 is lower at the hill sites, while higher at the valley sites. Also, it decreases as T_{DE} is lowered (i.e., 3.6×10^6 s⁻¹ or 4.4×10^6 s⁻¹ for the spots T-a or T-c (hill sites) vs. 5.7×10^6 s⁻¹ or 7.4×10^6 s⁻¹ for the spots T-b or T-d (valley sites)). The difference in the recombination rate at the hill and valley sites can be attributed by the difference of the local defect densities at the hill and the valley sites. It was reported that both tensile, as well as compressive strain in halide perovskite thin films lead to an increase in the defect density²⁹. Areas with higher local strain can result in faster PL decay³⁰. Atomistic calculations based on the first-principle models, the defect density is indeed proportional to the degree of the local strain. Indeed, k_1 is observed to

decrease with higher amplitude wrinkle morphology (with lower T_{DE}), which indicates that defects densities at the hill sites decrease with amplitude. This can be attributed to the reduced structural defects such as grain boundary defects at the hill sites because local strain is additionally alleviated at structural defects³¹. The reduced grain boundary defects should be accompanied by the enhanced uniformity of the grain sizes, which can be checked by the narrower distribution of the grain areas (Supplementary Fig. 16). Therefore, it is possible to suggest that the wrinkle morphology provides additional virtue for the hill sites with less defects, which in turn is responsible for the extended lifetime of the photocarriers, which results in the higher photocurrent at pc-AFM measurement. This can be confirmed again by the comparison of the photocurrent and average carrier lifetime as shown in Fig. 4e. As compared in the plot, the average diffusion length of the photocarriers, which is proportional to the square root of the lifetime of top and bottom surface, $\tau_{av}^{1/2}$, is strongly correlated with photocurrent. Considering a fact that the lifetime is inversely proportional to defect density (N_d), we can deduce that the hill sites with higher amplitude is clearly associated with lower defects than flat or valley sites. Moreover, it is also notable that k_1 is lower at the bottom than at the top (i.e., $k_1 = 3.6 \times 10^6$ s⁻¹ in spot T-a at the top vs. $k_1 = 2.6 \times 10^6$ s⁻¹ in spot B-f at the bottom). This indicates the bottom side of the films has the lower defect concentration. This would confirm again that that the crystal grows from the top surface (initially crystallized part with more defects) to the bottom (retarded crystallization in relatively DMSO-rich environment), which can further allow lower defects. Based on these observations, we can suggest that the microscopic wrinkle morphology genuinely gives rise to reduced defects, which considerably extends photocarrier lifetimes, and therefore, increase the V_{oc} and FF. The decreased defect densities facilitate charge extraction at the perovskite/electron transport layer (ETL) interface and results in a gain in voltage.

Light soaking stability. Based on the analysis of wrinkling mechanism and the wrinkle-morphology effects on the optoelectronic properties, we can proceed to the morphology tailoring to maximize the photovoltaic performances. We have found the optimized composition for the best wrinkle morphology such as $FA_{0.92}Cs_{0.08}PbBr_{0.15}I_{2.85}$ including a K-doping approach to passivate halide ion interstitials due to Frenkel defects^{32,33}, where the K-doped $FA_{0.92}Cs_{0.08}PbBr_{0.15}I_{2.85}$ results in $\lambda = 14$ μ m and $A = 115$ nm at $T_{DE} = 5$ °C. With this tailored perovskite thin films, we obtain a PCE as high as 23.02% along with $J_{sc} = 23.536$ mA/cm², $V_{oc} = 1.1948$ V and FF = 0.8188 (Supplementary Fig. 17). This optimized morphology also exhibit satisfactory performances of long-term stability. As shown in Supplementary Fig. 18, from the long-term light soaking test for over 1000 h conducted from maximum power point tracking (MPPT) under continuous light illumination (97 mW/cm²), stable performance as high as 83.4% of the initial PCE (22.09% (0 h) to 18.42% (1008 h)) is maintained. The decrease in PCE by 11.6% until 432 h (from 22.09 to 19.74% (432 h)) is due mainly to a lowered V_{oc} without alternation in J_{sc} (see inset in Supplementary Fig. 18), which might be attributed to interfacial defect generated during illumination^{34,35}, after which the photovoltaic parameters remain almost unchanged as confirmed by J - V curves.

In this study, we found the substantial effects of the microscopic wrinkles on the photovoltaic performances of the perovskite solar cells. The wrinkling mechanism hinges on the compressive stress relaxation of the bilayer in the course of spin-coating intervened by the antisolvent-driven microscopic phase separation of the film. The wrinkle geometry such as wavelength and amplitude were systematically controlled by changing the composition, antisolvent

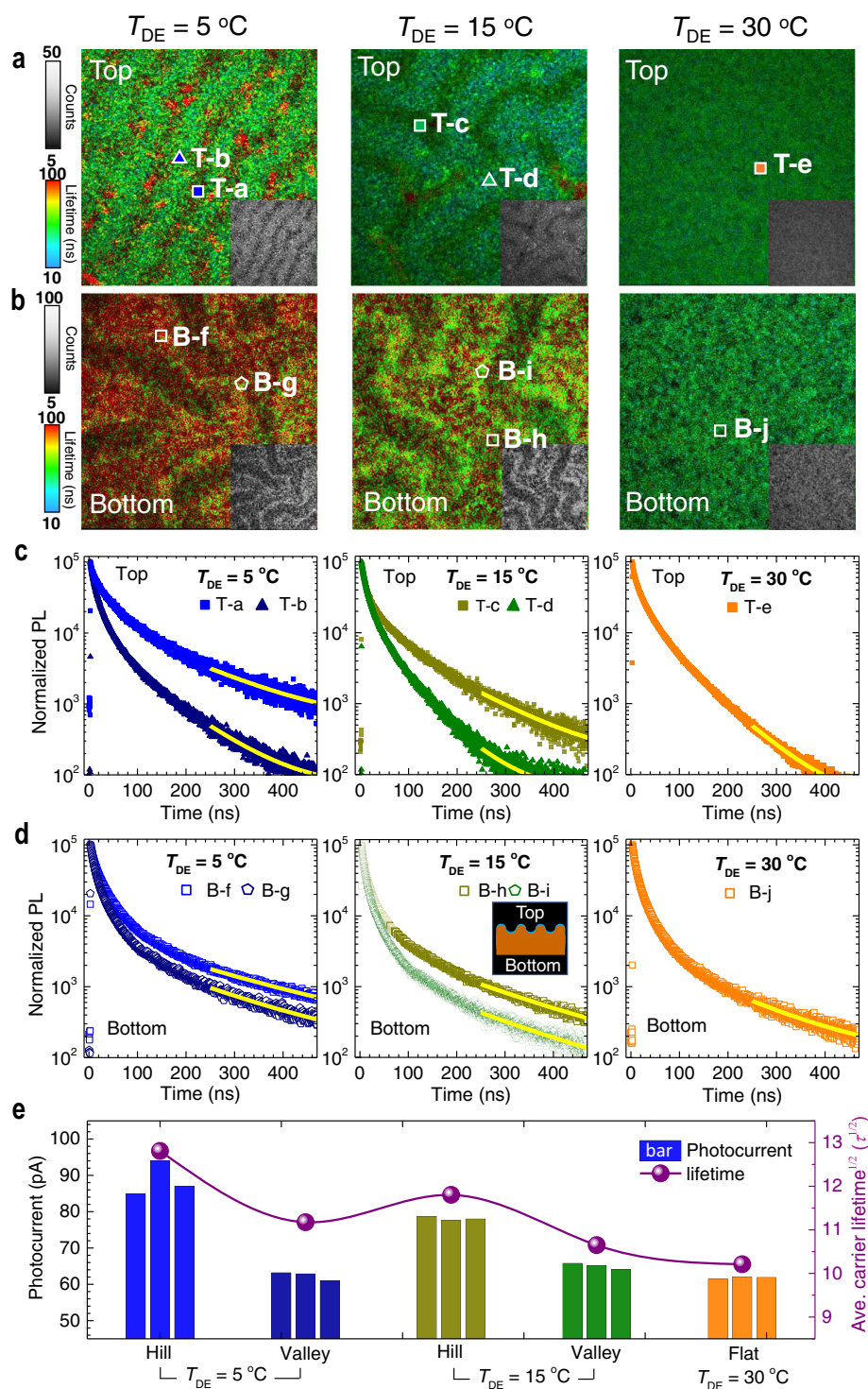


Fig. 4 Carrier lifetime on the hills and the valleys on top and bottom of the sinusoidal wrinkled structures. Fluorescence lifetime imaging microscopy (FLIM) images on (a) the top and (b) the bottom of the PMMA/(FAPbI₃)_{0.875}(CsPbBr₃)_{0.125}/Glass device, where the perovskite layers were prepared at $T_{DE} = 5, 15,$ and 30 °C at the given $T_{Sub} = 15$ °C. PMMA (poly(methyl methacrylate)) and glass are top and bottom side, respectively. Insets are gray scale images. Plots of time-correlated single-photon counting (TCSPC) measured on the selected areas (hill (T-a, B-f, T-c, and B-h), valley (T-b, B-g, T-d, and B-i) and flat (T-e and B-j)) on (c) the top and (d) the bottom surface, where top and bottom sites are illustrated in inset. Imaging area was $50 \times 50 \mu\text{m}^2$ and each pixel was about ~ 97 nm in diameter (excitation/PL collection spot: 512×512 pixels). **e** Plot of $\tau_{av}^{1/2}$ ($\tau_{av} = (\tau_{hill} + \tau_{valley})/2$) and photocurrent values from pc-AFM at hill and valley (three positions of each area) in Fig. 3e of the PMMA/(FAPbI₃)_{0.875}(CsPbBr₃)_{0.125}/Glass device.

temperature and substrate temperature. We provided a fundamental analysis based on the theoretical model supported by experiments to elucidate the wrinkling mechanism. In addition, we also provided the detailed mechanism underlying the microscopic wrinkle-driven enhancement of photocurrents. From the experimental observations, we found that the hill sites with higher amplitude of the wrinkles suffer less defects, which in turn extended photocarrier lifetime, which results in enhanced photo-response and V_{oc} . The wrinkling process was also found to be beneficial to both ETL and hole transport layer (HTL) interfaces because of a decreased defect concentration in the perovskite. Based on the understanding the fundamental mechanism of the wrinkling and its effects on the photovoltaic performances, we tailored the morphology to maximize the photovoltaic properties, and could obtain a PCE as high as 23% with satisfactory long-term stability. We expect the present study delivers a substantial benefit in further exploring the possibility of enhancement of photovoltaic performance and stability by tailoring photocarriers via wrinkling the perovskite films.

Methods

Materials synthesis. Formamidinium iodide (FAI, $FA = HC(NH_2)_2^+$) or methylammonium iodide (MAI, $MA = CH_3NH_3^+$) was synthesized by reacting 20 mL hydroiodic acid (57 wt% in water, Sigma Aldrich) with 10 g of formamidinium acetate (99%, Sigma Aldrich) or 18.2 mL of methylamine (40 wt% in methanol, TCI) in an ice bath. After stirring for 30 min, brown precipitate was formed, which was collected by evaporating the solvent at 60 °C using a rotary evaporator. The solid precipitate was washed with diethyl ether (99.0%, Samchun) several times, followed by recrystallization in anhydrous ethanol. The white precipitate was dried under vacuum for 24 h and then stored in a glove box filled with Ar.

Device fabrication. The patterned FTO glass (Pilkington, TEC-8, 8 Ω /sq) was ultrasonically cleaned with detergent, DI water, ethanol and acetone, successively, which was treated with Ultraviolet–Ozone (UVO) for 40 min to remove organic contaminants. The 15 wt% SnO_2 aqueous colloidal solution (Alfa Aesar) was diluted to 4 wt%, which was spin-coated on the FTO-coated glass substrates at 3000 rpm for 30 s and then annealed on a hot plate in ambient air atmosphere at 185 °C for 30 min. After cooling down to room temperature, the film was exposed again to UVO for 40 min prior to coating the perovskite layer. Perovskite films with different compositions were spin-coated using precursor solutions. For example, the $(FAPbI_3)_{0.875}(CsPbBr_3)_{0.125}$ perovskite was deposited using a precursor solution prepared by mixing 0.1505 g of FAI, 0.4034 g of PbI_2 (99.9985%, Alfa Aesar), 0.0459 g of $PbBr_2$ (99.999%, Sigma Aldrich) and 0.0266 g of CsBr (99.999%, Sigma Aldrich) in 75 μ L dimethyl sulfoxide (DMSO, > 99.5%, Sigma Aldrich), 0.525 mL of N,N' -dimethylformamide (99.8% anhydrous, Sigma Aldrich). The solutions were filtered with 0.20 μ m-pore-sized PTFE-H filter (Hyundai MICRO). Prior to coating, the precursor solutions were mildly stirred at 50 °C for 10 min in ambient condition to remove unwanted gas molecules dissolved in the solutions. The precursor solutions (solution temperature was 15 °C) were spin-coated on the substrate (substrate temperature was 5 °C or 15 °C) at 4000 rpm for 20 s, where 0.35 mL of diethyl ether with different temperature (5, 15, or 30 °C) was dripped in 10 s after spinning. The brownish adduct films were formed right after deposition, which was heated at 145 °C for 10 min. The 20 μ L of spiro-MeOTAD solution, which was prepared by dissolving 72.3 mg spiro-MeOTAD, 28.8 μ L of 4-*tert*-butyl pyridine and 17.5 μ L of lithium bis(trifluoromethanesulfonyl)imide (Li-TFSI) solution (520 mg Li-TFSI in 1 mL acetonitrile (99.8%, Sigma Aldrich)) in 1 mL of chlorobenzene, was spin-coated on the perovskite layer at 3000 rpm for 20 s. Whole coating process was carried out in dry room (RH < 0.3%, 18–20 °C). Finally, 90 nm of Au electrode was deposited by using a thermal evaporator at an evaporation rate of 0.05 nm/s. For K-doped $FA_{0.92}Cs_{0.08}PbBr_{0.15}I_{2.85}$ perovskite, a precursor solution was prepared by mixing 0.1592 g of FAI, 0.4449 g of PbI_2 (99.9985%, Alfa Aesar), 0.0128 g of $PbBr_2$ (99.999%, Sigma Aldrich) and 0.0170 g of CsBr (99.999%, Sigma Aldrich) in 75 μ L dimethyl sulfoxide (DMSO, > 99.5%, Sigma Aldrich), 0.465 mL of N,N' -dimethylformamide (99.8% anhydrous, Sigma Aldrich) and 60 μ L KI solution (0.166 g of KI (99.999%, Sigma Aldrich) in 10 mL of DMF). The precursor solution kept at temperature of 15 °C was spin-coated on the substrate (substrate temperature was 15 °C) at 4000 rpm for 20 s, where 0.35 mL of diethyl ether ($T_{DE} = 5$ °C) was dripped in 10 s after spinning. The brownish adduct film formed right after deposition was heated at 145 °C for 10 min. After the perovskite film was cooled down to room temperature, 30 μ L of 4-fluoro phenylethylammonium iodide (4F-PEAI) solution (10 mM in IPA) was spin-coated at 6,000 rpm for 20 s.

Characterizations. Optical images were obtained by using an inverted optical microscope (Primo Vert, Carl Zeiss) with objective lens (Primo Plan-ACHROMAT 20x/0.30). Current density–voltage (J – V) curves were measured under AM 1.5 G one

sun (100 mW/cm²) illumination using a solar simulator (Oriol Sol 3A, class AAA) equipped with 450 W Xenon lamp (Newport 6280NS) and a Kiethley 2400 source meter. The light intensity was adjusted by NREL-calibrated Si solar cell having KG-5 filter. The device was covered with a metal mask with aperture area of 0.125 cm². The External Quantum Efficiency (EQE) spectra were collected by using a QEX-7 series system (PV measurements Inc.) in which a monochromatic beam was generated from a 75 W Xenon source lamp (USHIO, Japan) under DC mode. Steady-state photoluminescence (PL) were measured by a Quantaurus-Tau compact fluorescence lifetime spectrometer (Quantaurus-Tau C11367-12, Hamamatsu). The film samples were excited with 464 nm laser (PLP-10, model M12488-33, peak power of 231 mW and pulse duration of 53 ps, Hamamatsu) pulsed at repetition frequency of 10 MHz for steady-state PL. All measurements were done at room temperature (~298 K). Viscosity was measured by using rheometer (25 mm aluminum parallel plate, TA Instruments, New Castle, DE, USA) at different temperature with 0.6 rad/s for solid (Zero shear-rate viscosity) and 120 rad/s for liquid of angular frequency and oscillation strain 1%. The atomic force microscopy (AFM) and photoconductive AFM (pc-AFM) were measured with a perovskite/SnO₂/FTO and spiro-MeOTAD/perovskite/SnO₂/FTO structured samples, respectively, by using white LED (light intensity: 0.228 mW/cm²) and 1 V of sample bias (NX10 system, AD-2.8-AS ($k = 2.8$ N/m, conductive diamond coating, radius = 10 nm) or CDT-CONTR ($k = 0.5$ N/m, conductive diamond coating, Park Systems)). All images were obtained under the ambient condition. Ellipsometry measurements were carried out with the perovskite/c-Si, the SnO₂/c-Si and the spiro-MeOTAD/c-Si samples by using Elli-SE Ellipsometer from 240 to 1000 nm (1.2–5.2 eV) wavelength. In situ photoluminescence (PL) and UV–Vis absorption were measured while spinning the samples by custom-built setup. In detail, brushless DC motor (Trinamic BLDC4208) was connected with the rotatable chuck that was connected with Peltier element located on a heat diffuser via a cogged V-belt. RPM was controlled with a motor driver (Trinamic TMC1640). To allow quasi-simultaneous detection of both absorption and PL during processing, a diode laser (520 nm) was supplied on the substrate and white light (generic cold white LED) was incident above the substrate. The optical fiber was used for gathering the signals. By using a mechanical chopper with blade and mirror, light path was separated and gathered spectrometers for absorption and for PL. The fluorescence lifetime imaging microscopy (FLIM) measurement was carried out on a PicoQuant MicroTime 200. The FLIM system is based on an inverted optical microscope (Olympus IX71). A pulsed laser source with 561 nm (PicoQuant) was operated at 2.5 MHz and a fluence of about 0.5 μ J/cm². The laser was focused on the sample through a high numerical aperture objective lens (Olympus PlanApo 60x/1.20 water immersion and 100x/0.9 air). The emission from the sample was passed through a long-pass filter and a 100 μ m pinhole before being detected by a single-photon avalanche diode (SPCM-AQRH SPAD, Excelitas Technologies) and processed by time-correlated single-photon counting (TCSPC) electronics (Time harp 260 Pico, PicoQuant). The FLIM images were analyzed by PicoQuant SynPhoTime 64 (v. 2.4.4874).

Long-term stability test. Long-term light soaking test for over 1000 h was conducted by exposing the unsealed device to a white LED light with intensity of 97 mW/cm² (0.97 sun) in N₂ glove box at temperature ranging between 25 and 31 °C, where UV filter (Schott, GG-400) was applied to the device and pre-conditioning was performed before light soaking experiment by aging the fresh device for 96 h under 0.6 mW/cm². The J – V curves and the steady-state PCE at maximum power point tracking (MPPT) were measured every 12 h or 24 h in dry room with relative humidity of <5% using a solar simulator (VeraSol-2 LED Class AAA Solar Simulator (Newport), 100 mW/cm²). After each measurement, the devices were stored under 0.97 sun illumination in N₂ globe box again. The metal mask with aperture area of 0.10 cm² was placed on top of the cell.

Reporting summary. Further information on research design is available in the Nature Research Reporting Summary linked to this article.

Data availability

The authors declare that the main data supporting the findings of this study are available within the article and its Supplementary Information files. Extra data are available from the corresponding author upon reasonable request.

Received: 7 September 2020; Accepted: 5 February 2021;

Published online: 10 March 2021

References

1. Kim, H.-S. et al. Lead iodide perovskite sensitized all-solid-state submicron thin film mesoscopic solar cell with efficiency exceeding 9%. *Sci. Rep.* **2**, 591 (2012).
2. Lee, M. M., Teuscher, J., Miyasaka, T., Murakami, T. N. & Snaith, H. J. Efficient hybrid solar cells based on meso-superstructured organometal halide perovskites. *Science* **338**, 643–647 (2012).

3. Kojima, A., Teshima, K., Shirai, Y. & Miyasaka, T. Organometal halide perovskites as visible-light sensitizers for photovoltaic cells. *J. Am. Chem. Soc.* **131**, 6050–6051 (2009).
4. Im, J.-H., Lee, C.-R., Lee, J.-W., Park, S.-W. & Park, N.-G. 6.5% efficient perovskite quantum-dot-sensitized solar cell. *Nanoscale* **3**, 4088–4093 (2011).
5. Green, M. A. et al. Solar cell efficiency tables (version 55). *Prog. Photovolt. Res. Appl.* **28**, 3–15 (2020).
6. Lee, J.-W., Seol, D.-J., Cho, A.-N. & Park, N.-G. High-efficiency perovskite solar cells based on the black polymorph of $\text{HC}(\text{NH}_2)_2\text{PbI}_3$. *Adv. Mater.* **26**, 4991–4998 (2014).
7. Koh, T. M. et al. Formamidinium-containing metal-halide: an alternative material for near-IR absorption perovskite solar cell. *J. Phys. Chem. C* **118**, 16458–16462 (2014).
8. Pang, S. et al. $\text{NH}_2\text{CH}=\text{NH}_2\text{PbI}_3$: an alternative organolead iodide perovskite sensitizer for mesoscopic solar cells. *Chem. Mater.* **26**, 1485–1491 (2014).
9. Lee, J.-W. et al. Formamidinium and cesium hybridization for photo- and moisture-stable perovskite solar cell. *Adv. Energy Mater.* **5**, 1501310 (2015).
10. Saliba, M. et al. Cesium-containing triple cation perovskite solar cells: improved stability, reproducibility and high efficiency. *Energy Environ. Sci.* **9**, 1989–1997 (2016).
11. Jeon, N. J. et al. Compositional engineering of perovskite materials for high-performance solar cells. *Nature* **517**, 476–480 (2015).
12. Seok, S. I., Grätzel, M. & Park, N.-G. Methodologies toward highly efficient perovskite solar cells. *Small* **14**, 1704177 (2018).
13. Park, N.-G. & Zhu, K. Scalable fabrication and coating methods for perovskite solar cells and solar modules. *Nat. Rev. Mater.* **5**, 333–350 (2020).
14. Jeon, N. J. et al. Solvent engineering for high performance inorganic-organic hybrid perovskite solar cells. *Nat. Mater.* **13**, 897–903 (2014).
15. Ahn, N. et al. Highly reproducible perovskite solar cells with average efficiency of 18.3% and best efficiency of 19.7% fabricated via Lewis base adduct of lead (II) iodide. *J. Am. Chem. Soc.* **137**, 8696–8699 (2015).
16. Bercegol, A. et al. Spatial inhomogeneity analysis of cesium-rich wrinkles in triple-cation perovskite. *J. Phys. Chem. C* **122**, 23345–23351 (2018).
17. Bush, K. A. et al. Controlling thin-film stress and wrinkling during perovskite film formation. *ACS Energy Lett.* **3**, 1225–1232 (2018).
18. Sveinbjörnsson, K. et al. Ambient air-processed mixed-ion perovskites for high-efficiency solar cells. *J. Mater. Chem. A* **4**, 16536–16545 (2016).
19. Yoo, P. J. & Lee, H. H. Morphological diagram for metal/polymer bilayer wrinkling: influence of thermomechanical properties of polymer layer. *Macromolecules* **38**, 2820–2831 (2005).
20. Shugurov, A. R., Kozelskaya, A. I. & Panin, A. V. Wrinkling of the metal-polymer bilayer: the effect of periodical distribution of stresses and strains. *RSC Adv.* **4**, 7389–7395 (2014).
21. Buchhorn, M., Wedler, S. & Panzer, F. Setup to study the in situ evolution of both photoluminescence and absorption during the processing of organic or hybrid semiconductors. *J. Phys. Chem. A* **122**, 9115–9122 (2018).
22. Im, S. H. & Huang, R. Evolution of wrinkles in elastic-viscoelastic bilayer thin films. *J. Appl. Mech.* **72**, 955–961 (2005).
23. Nakane, A. et al. Quantitative determination of optical and recombination losses in thin-film photovoltaic devices based on external quantum efficiency analysis. *J. Appl. Phys.* **120**, 064505 (2016).
24. Patel, J. B. et al. Light absorption and recycling in hybrid metal halide perovskite photovoltaic devices. *Adv. Energy Mater.* **10**, 1903653 (2020).
25. Wiegold, S. et al. Precursor concentration affects grain size, crystal orientation, and local performance in mixed-ion lead perovskite solar cells. *ACS Appl. Energy Mater.* **1**, 6801–6808 (2018).
26. Braunger, S. et al. $\text{Cs}_x\text{FA}_{1-x}\text{Pb}(\text{I}_{1-y}\text{Br}_y)_3$ perovskite compositions: the appearance of wrinkled morphology and its impact on solar cell performance. *J. Phys. Chem. C* **122**, 17123–17135 (2018).
27. Herz, L. M. Charge-carrier dynamics in organic-inorganic metal halide perovskites. *Annu. Rev. Phys. Chem.* **67**, 65–89 (2016).
28. Stranks, S. D. et al. Recombination kinetics in organic-inorganic perovskites: excitons, free charge, and subgap states. *Phys. Rev. Appl.* **2**, 034007 (2014).
29. Jiao, Y. et al. Strain Engineering of metal halide perovskites on coupling anisotropic behaviors. *Adv. Funct. Mater.* **2020**, 2006243 (2020).
30. Jones, T. W. et al. Lattice strain causes non-radiative losses in halide perovskites. *Energy Environ. Sci.* **12**, 596–606 (2019).
31. Jariwala, S. et al. Local crystal misorientation influences non-radiative recombination in halide perovskites. *Joule* **3**, 1–13 (2019).
32. Son, D.-Y. et al. Universal approach toward hysteresis-free perovskite solar cell via defect engineering. *J. Am. Chem. Soc.* **140**, 1358–1364 (2018).
33. Kim, S.-G. et al. Potassium ions as a kinetic controller in ionic double layers for hysteresis-free perovskite solar cells. *J. Mater. Chem. A* **7**, 18807–18815 (2019).
34. Kim, J. Y., Lee, J.-W., Jung, H. S., Shin, H. & Park, N.-G. High-efficiency perovskite solar cells. *Chem. Rev.* **120**, 7867–7918 (2020).
35. Chen, J. & Park, N.-G. Materials and methods for interface engineering toward stable and efficient perovskite solar cells. *ACS Energy Lett.* **5**, 2742–2786 (2020).

Acknowledgements

This work was supported by the National Research Foundation of Korea (NRF) grants funded by the Ministry of Science, ICT Future Planning (MSIP) of Korea under contracts NRF-2012M3A6A7054861 (Global Frontier R&D Program on Center for Multiscale Energy System) and NRF-2016M3D1A1027663 and NRF-2016M3D1A1027664 (Future Materials Discovery Program). This work was supported in part by Basic Science Research Program through the NRF under contract NRF-2018K2A9A2A15075785 (Germany-Korea Partnership Program). S.-G.K. acknowledges financial support from NRF under contract 2016R1A2B3008845, NRF-2017H1A2A1046990 (NRF-2017-Fostering Core Leaders of the Future Basic Science Program/Global Ph.D. Fellowship Program). Corresponding support was provided by the German Academic Exchange Service (DAAD project-ID 57449733). S.H. and P.R. thank the German Science Foundation (DFG) for financial support and the BPI KeyLab Electron and Optical Microscopy. S.H. thanks the Bavarian framework program Soltech for funding. K.S. acknowledges financial support from the German National Science Foundation (Project KO 3973/2-1 and GRK 1640). P.P. acknowledges support by the German National Science Foundation via the Project PA 3373/3-1. Y.Z. acknowledges funding from China Scholarship Council. The authors thank PicoQuant Inc for providing SynPhoTime 64(v. 2.4.4874) Program.

Author contributions

N.-G.P., F.P., and S.H. supervised the research; S.-G.K. designed and conducted experiments and measurements; J.-H.K. conducted experiments and measurements; Y.Z., S.-G.K., and K.S. measured and analyzed in situ PL and absorbance measurements. P.R. and S.-G.K. measured and analyzed FLIM and TCSPC. S.J.K. conducted simulation study of bilayer wrinkle system. S.-G.K. and N.-G.P. wrote manuscript; and all authors discussed the results and revised the manuscript.

Competing interests

The authors declare no competing interests.

Additional information


Supplementary information The online version contains supplementary material available at <https://doi.org/10.1038/s41467-021-21803-2>.

Correspondence and requests for materials should be addressed to N.-G.P.

Peer review information *Nature Communications* thanks the anonymous reviewer(s) for their contribution to the peer review of this work. Peer reviewer reports are available.

Reprints and permission information is available at <http://www.nature.com/reprints>

Publisher's note Springer Nature remains neutral with regard to jurisdictional claims in published maps and institutional affiliations.

 **Open Access** This article is licensed under a Creative Commons Attribution 4.0 International License, which permits use, sharing, adaptation, distribution and reproduction in any medium or format, as long as you give appropriate credit to the original author(s) and the source, provide a link to the Creative Commons license, and indicate if changes were made. The images or other third party material in this article are included in the article's Creative Commons license, unless indicated otherwise in a credit line to the material. If material is not included in the article's Creative Commons license and your intended use is not permitted by statutory regulation or exceeds the permitted use, you will need to obtain permission directly from the copyright holder. To view a copy of this license, visit <http://creativecommons.org/licenses/by/4.0/>.

© The Author(s) 2021

Supplementary Information

How antisolvent miscibility affects perovskite film wrinkling and photovoltaic properties

Seul-Gi Kim¹, Jeong-Hyeon Kim¹, Philipp Ramming^{2,3}, Yu Zhong^{2,3}, Konstantin Schötz³, Seok Joon Kwon^{1,4}, Sven Huettner², Fabian Panzer³, Nam-Gyu Park^{1*}

¹School of Chemical Engineering, Sungkyunkwan University (SKKU), Suwon 440-746, Republic of Korea.

²Department of Chemistry, University of Bayreuth, Universitätsstrasse 30, 95447 Bayreuth, Germany.

³Chair for Soft Matter Optoelectronics, University of Bayreuth, Universitätsstrasse 30, 95447 Bayreuth, Germany

⁴Nanophotonics Research Center, Korea Institute of Science and Technology (KIST), Seoul 02792, Korea.

*Corresponding author

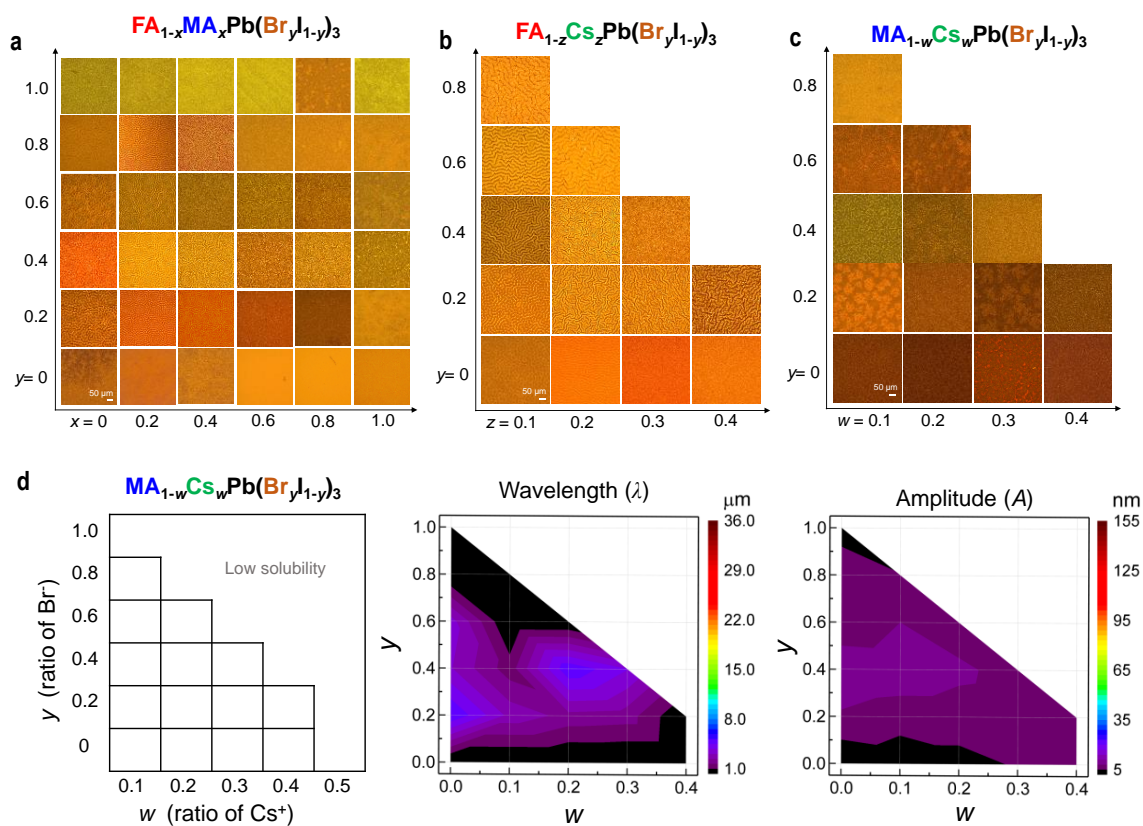
E-mail: npark@skku.edu, Tel: +82-31-290-7241

Supplementary Fig. 1-18 : pages s1-s16

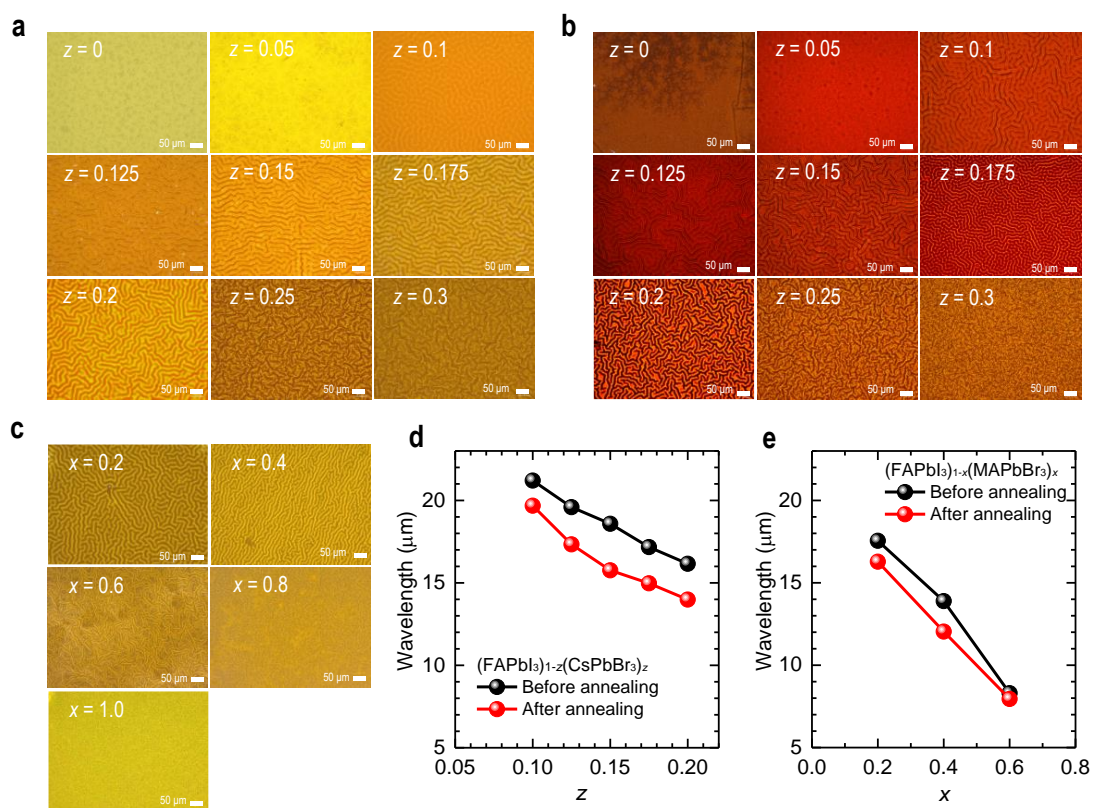
Supplementary Table 1-2: pages s17-s18

Supplementary Note 1-4: pages s19-s25

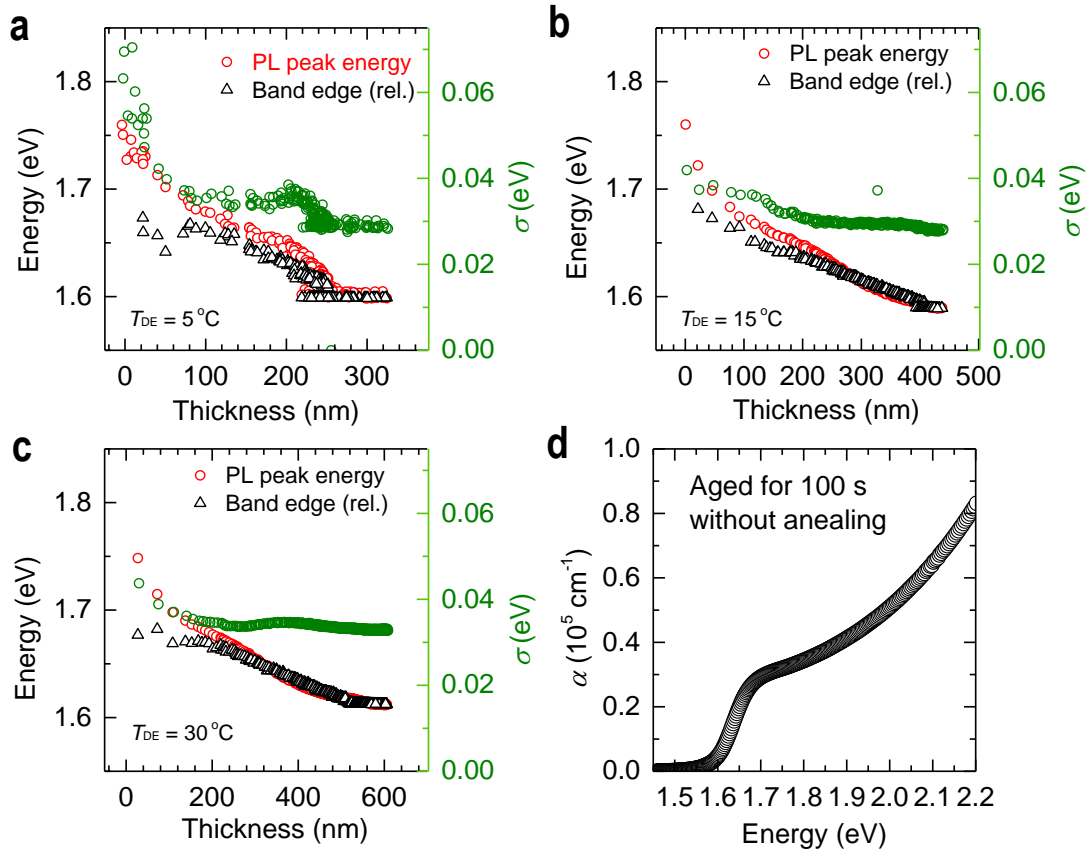
Supplementary References: page s26-s27



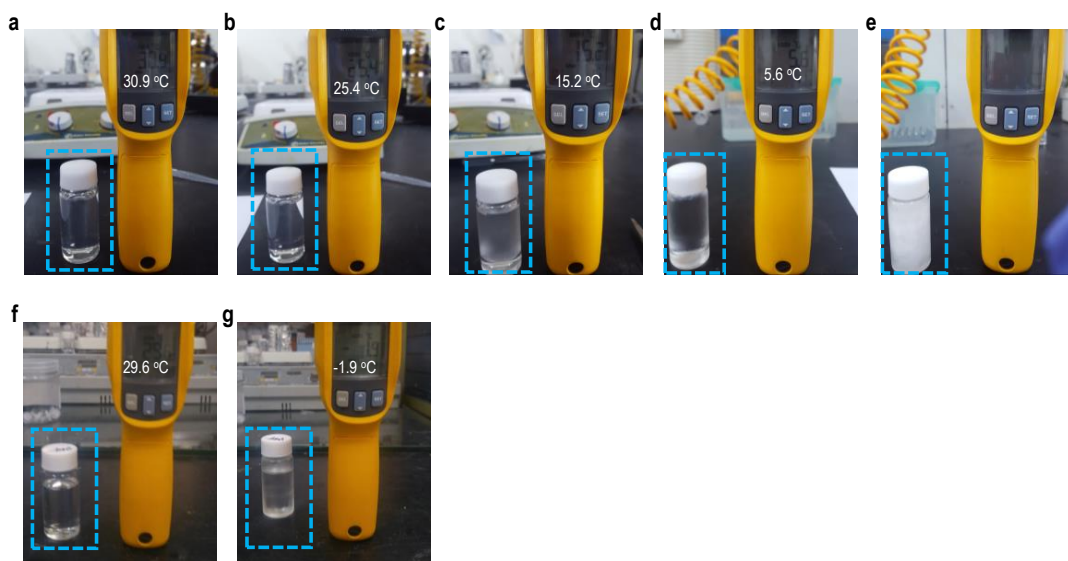
Supplementary Fig. 1. Optical microscope images of the surface morphology of perovskite films with different compositions for (a) $\text{FA}_{1-x}\text{MA}_x\text{Pb}(\text{Br}_y\text{I}_{1-y})_3$, (annealed at 145 °C for 10 min) (b) $\text{FA}_{1-z}\text{Cs}_z\text{Pb}(\text{Br}_y\text{I}_{1-y})_3$ (annealed at 145 °C for 10 min) and (c) $\text{MA}_{1-w}\text{Cs}_w\text{Pb}(\text{Br}_y\text{I}_{1-y})_3$ (annealed at 100 °C for 10 min). (d) Wrinkled phase diagrams of $\text{MA}_{1-w}\text{Cs}_w\text{Pb}(\text{Br}_y\text{I}_{1-y})_3$ perovskite thin films with different compositions, together with color maps showing almost no wrinkled morphologies.



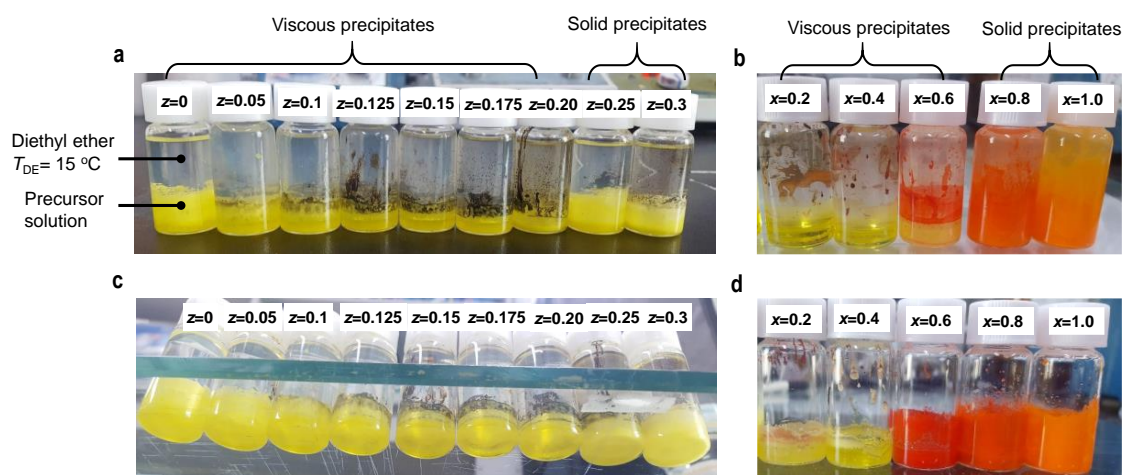
Supplementary Fig. 2. Optical microscope images of the surface morphology of perovskite films with the composition of $(\text{FAPbI}_3)_{1-z}(\text{CsPbBr}_3)_z$ (a) before and (b) after annealing at 145 °C for 10 min. (c) Optical microscope images of the surface morphology of the non-annealed $(\text{FAPbI}_3)_{1-x}(\text{MAPbBr}_3)_x$ perovskite film. Effect of the composition on wavelength (λ) of the wrinkled films for (d) $(\text{FAPbI}_3)_{1-z}(\text{CsPbBr}_3)_z$ and (e) $(\text{FAPbI}_3)_{1-x}(\text{MAPbBr}_3)_x$ perovskite film before and after annealing. All the images were obtained with temperature conditions of $T_{\text{Sub}} = 15$ °C and $T_{\text{DE}} = 15$ °C.



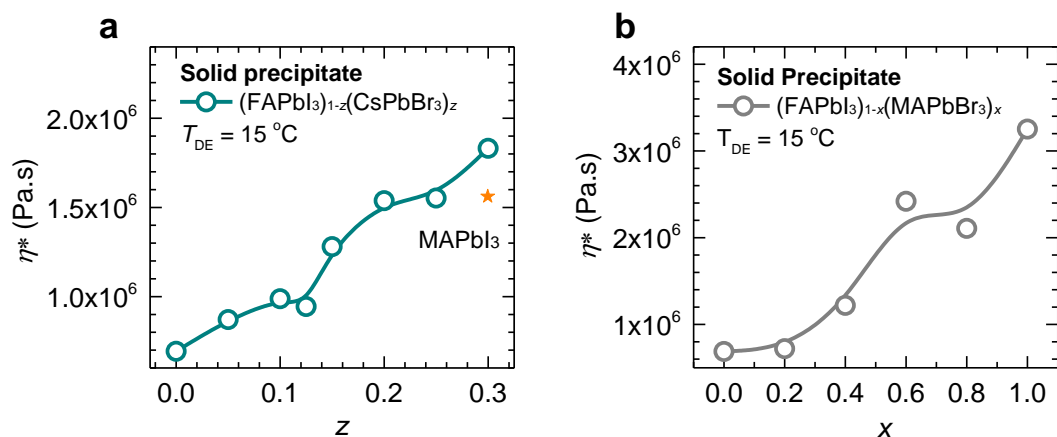
Supplementary Fig. 3. (a-c) PL peak position (red circles), PL peak width σ (green circles), and band edge energy (black triangles) as a function of perovskite layer thickness during spin coating for three different temperatures of diethyl ether. The band edge energy was determined by fitting the band edge of the spectrum at the end of each measurement, to all prior spectra, where the fitted spectrum was allowed to be shifted in energy and scaled in intensity. (d) Absorption coefficient as a function of wavelength for the as-spun film aged for 100 s without annealing. Perovskite composition was $(\text{FAPbI}_3)_{0.875}(\text{CsPbBr}_3)_{0.125}$.



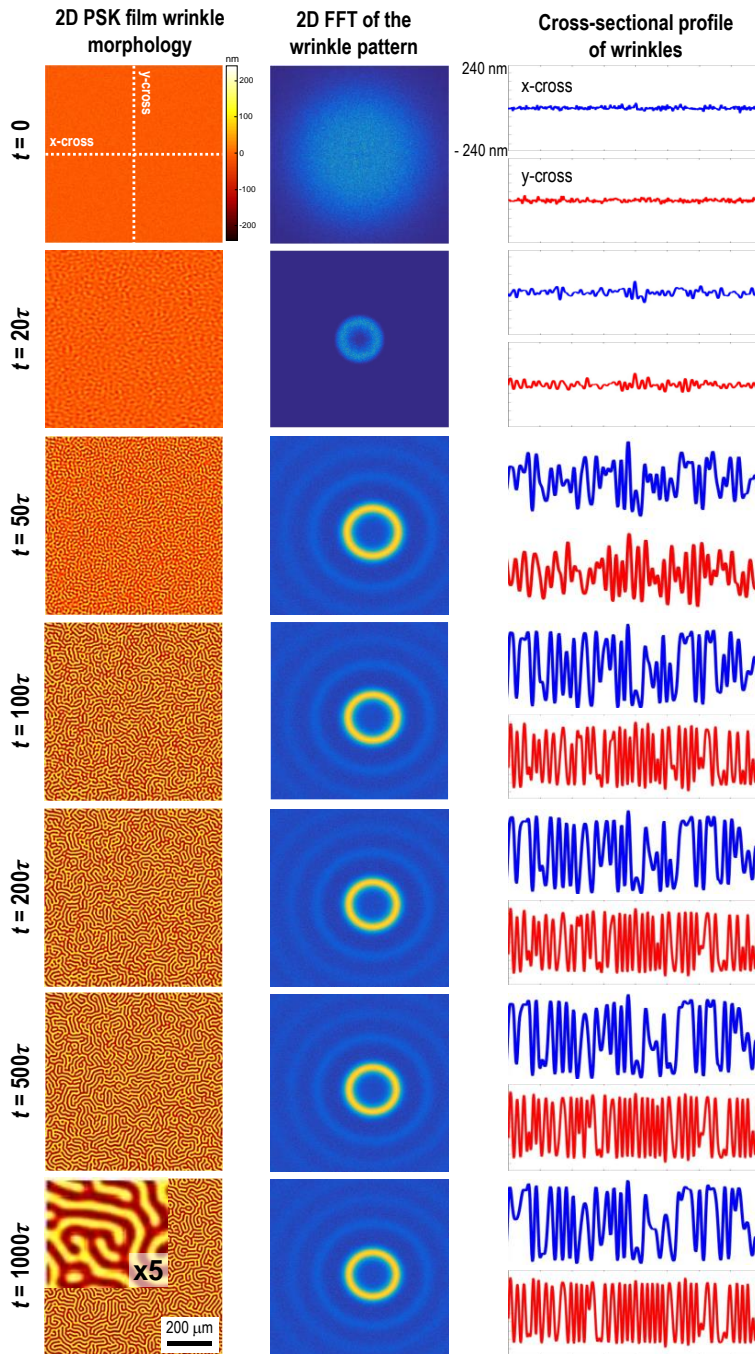
Supplementary Fig. 4. Digital photographs of the mixture of DMSO and diethyl ether (1:8 v/v) at different solution temperatures of (a) 30.9 °C, (b) 25.4 °C, (c) 15.2 °C, and (d) 5.6 °C. (e) Photograph of the solution prepared at 5.6 °C showing that the solution was spontaneously frozen. Photographs of the mixture of DMF and diethyl ether (1:8 v/v) at different solution temperatures of (f) 29.6 °C and (g) -1.9 °C.



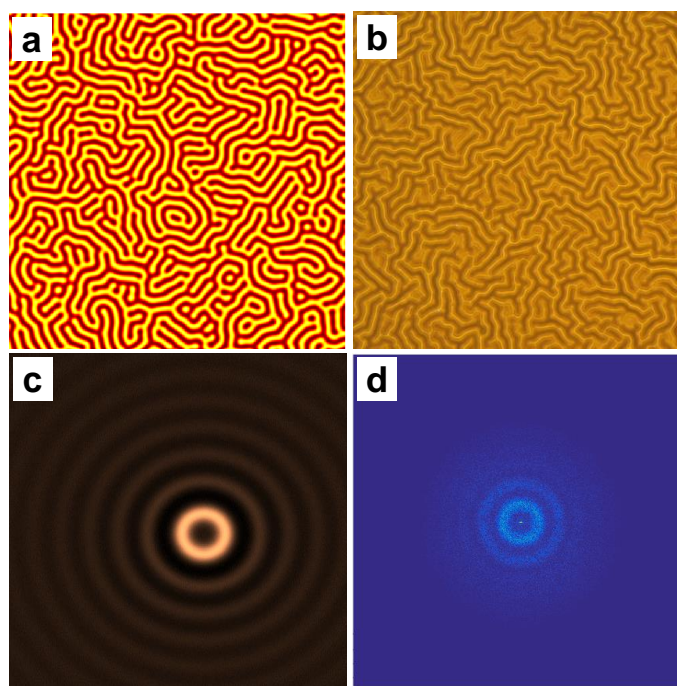
Supplementary Fig. 5. Photographs of the solution formed by pouring diethyl ether ($T_{DE} = 15$ °C) into a vial containing (a) $(\text{FAPbI}_3)_{1-z}(\text{CsPbBr}_3)_z$ and (b) $(\text{FAPbI}_3)_{1-x}(\text{MAPbBr}_3)_x$ precursor solution. The solution was prepared by mixing 1 mL of the precursor solution and 15 mL of diethyl ether, which was followed by extracting the supernatant and then pouring diethyl ether, which was repeated four times to remove DMSO and DMF. The viscous precipitates were formed with range of $0 \leq z \leq 0.2$ for $(\text{FAPbI}_3)_{1-z}(\text{CsPbBr}_3)_z$ and $0 \leq x \leq 0.6$ for $(\text{FAPbI}_3)_{1-x}(\text{MAPbBr}_3)_x$ while the precipitates were immediately formed as solid phase for $z = 0.25$ and 0.3 in $(\text{FAPbI}_3)_{1-z}(\text{CsPbBr}_3)_z$, $x = 0.8$ and 1 for $(\text{FAPbI}_3)_{1-x}(\text{MAPbBr}_3)_x$. In about 5 min, the solutions (a) and (b) were solidified, which was shown in (c) and (d), respectively.



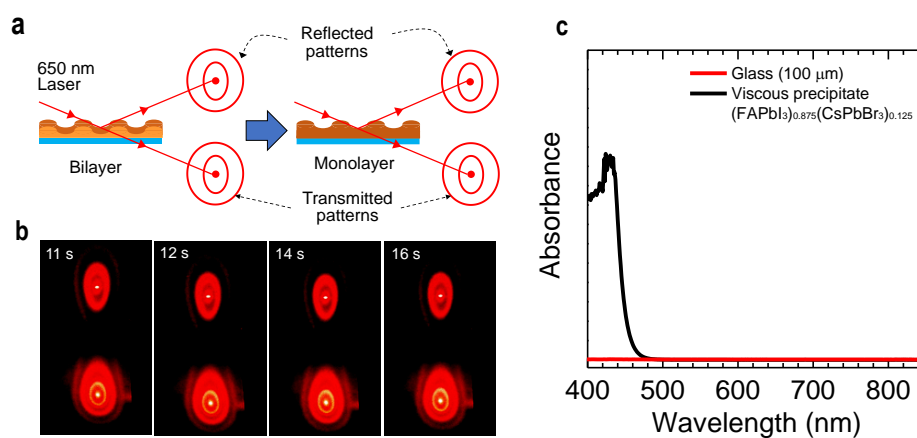
Supplementary Fig. 6. Viscosity of solid precipitates in (a) $(\text{FAPbI}_3)_{1-z}(\text{CsPbBr}_3)_z$ and (b) $(\text{FAPbI}_3)_{1-x}(\text{MAPbBr}_3)_x$. The viscosity of solid precipitate of MAPbI_3 (star symbol in (a)) was also measured.



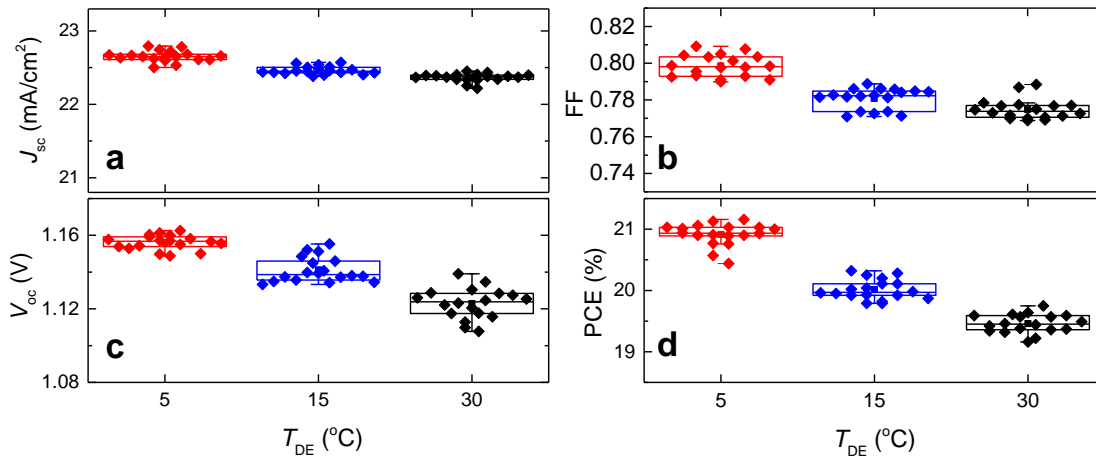
Supplementary Fig. 7. Numerical simulation results of the morphological evolution of perovskite (PSK) wrinkles of elastic-viscoelastic bilayer. τ denotes dimensionless time scale. The left column is for the time-dependent surface wrinkle morphology. The inset for 1000τ shows a 5 times magnified image. The middle column is the 2D FFT patterns of the wrinkles. The right column is the cross-sectional profiles of the wrinkles along the horizontal (namely x-cross) and vertical directions (namely y-cross).



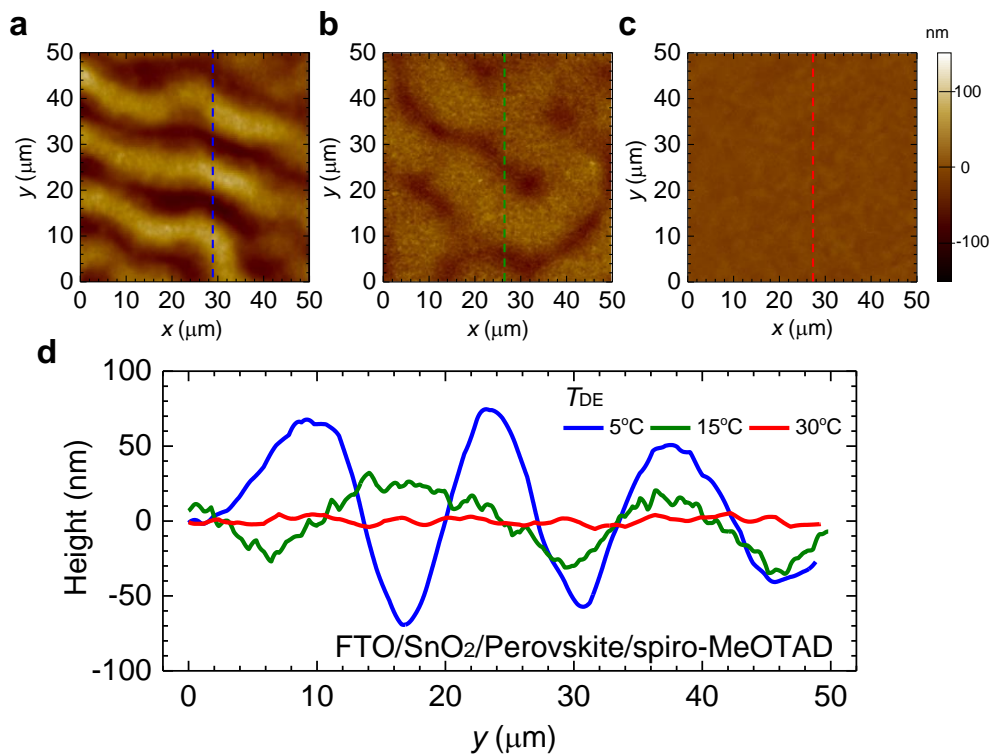
Supplementary Fig. 8. Comparison of the morphologies of the wrinkle pattern obtained from (a) numerical calculation and (b) experimental observation. 2D FFT patterns for (c) numerically calculated wrinkles and (d) experimentally observed wrinkles (c for a and d for b).



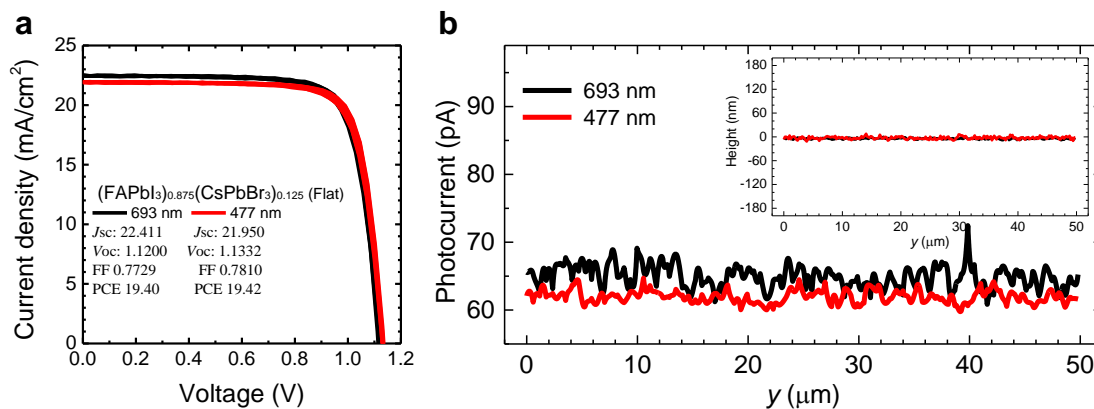
Supplementary Fig. 9. (a) Schematic representation of setup for measuring optical diffraction pattern at top surface of bilayer perovskite film. (b) Photographs of the reflected (up) and the transmitted (down) optical diffraction patterns at top surface as function of spin coating time (11 s, 12 s, 14 s and 16 s) after perovskite precursor was contacted with diethyl ether at 10 s. $T_{\text{Sub}} = 15 \text{ }^{\circ}\text{C}$ and $T_{\text{DE}} = 5 \text{ }^{\circ}\text{C}$. (c) UV-Vis spectrum of glass substrate and viscous precipitate obtained by pouring diethyl ether to the $(\text{FAPbI}_3)_{0.875}(\text{CsPbBr}_3)_{0.125}$ perovskite precursor solution.



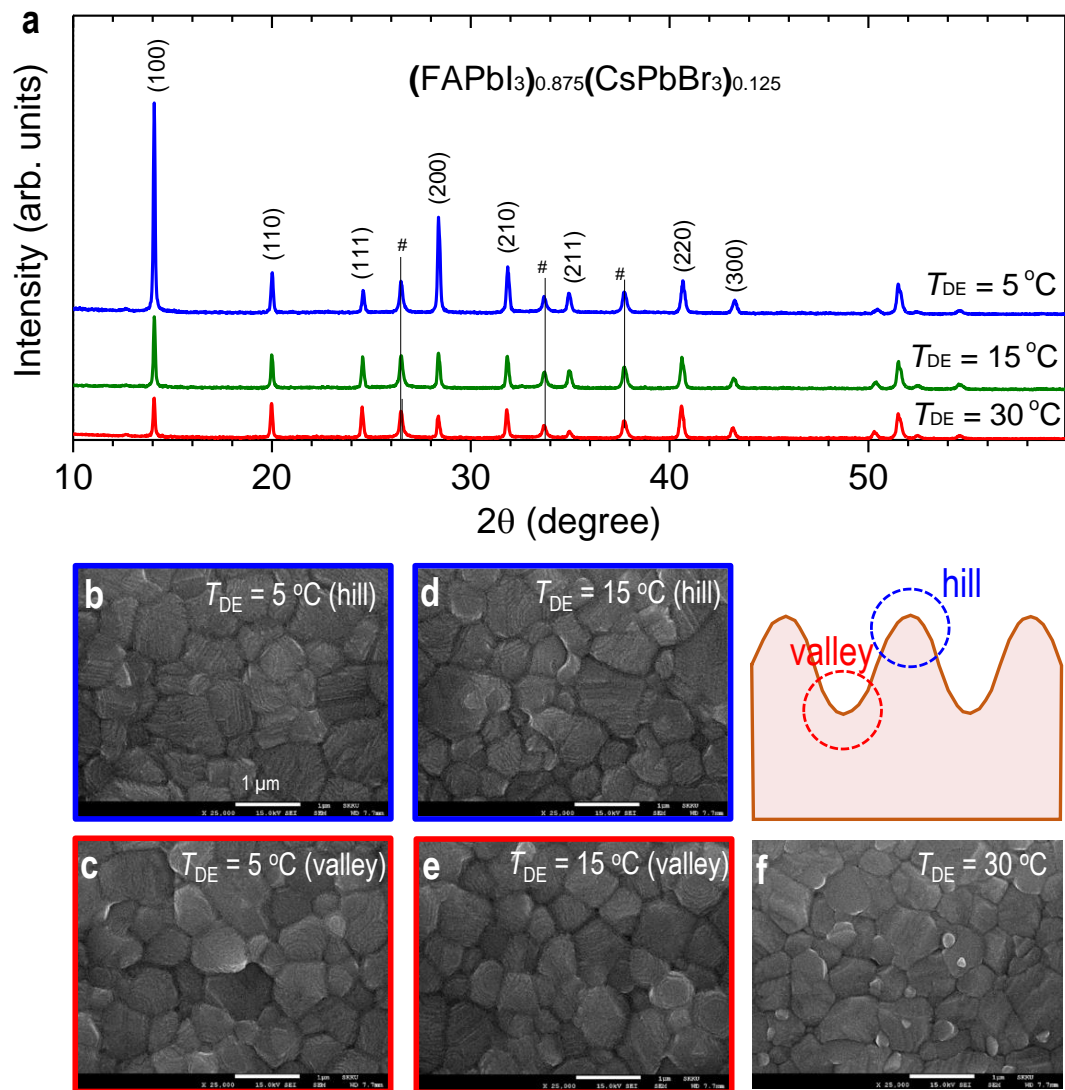
Supplementary Fig. 10. Statistical photovoltaic parameters of (a) J_{sc} , (b) FF, (c) V_{oc} and (d) PCE for the $(\text{FAPbI}_3)_{0.875}(\text{CsPbBr}_3)_{0.125}$ PSCs as function of T_{DE} (5 °C, 15 °C and 30 °C), measured at a scan rate of 130 mV/s under A.M. 1.5G one sun illumination (100 mW/cm²). Aperture mask area was 0.125 cm².



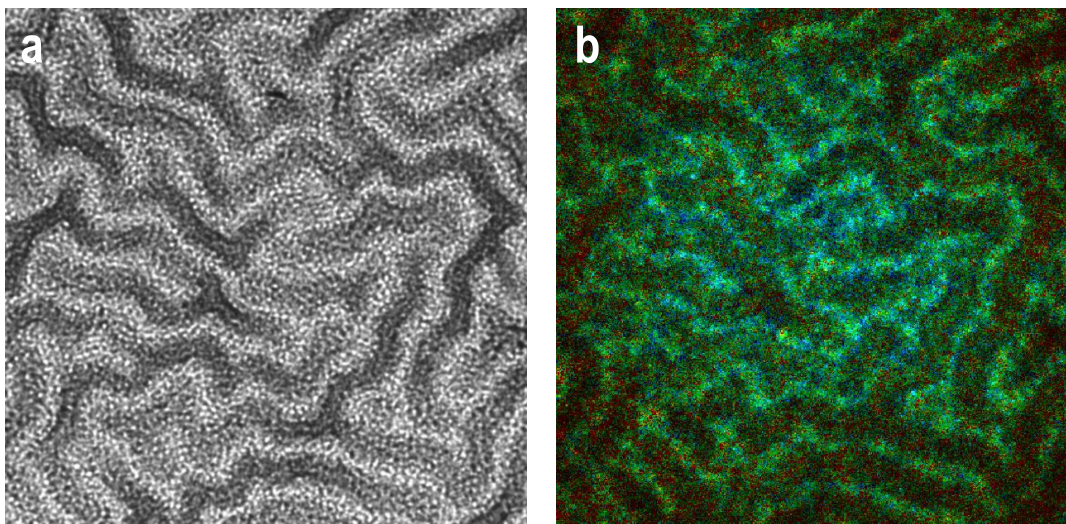
Supplementary Fig. 11. AFM image showing the spiro-MeOTAD surface in the glass/FTO/SnO₂/(FAPbI₃)_{0.875}(CsPbBr₃)_{0.125}/spiro-MeOTAD device, where the perovskite layer was formed from $T_{DE} =$ (a) 5 °C, (b) 15 °C and (c) 30 °C. (d) Height profile along the y -direction.



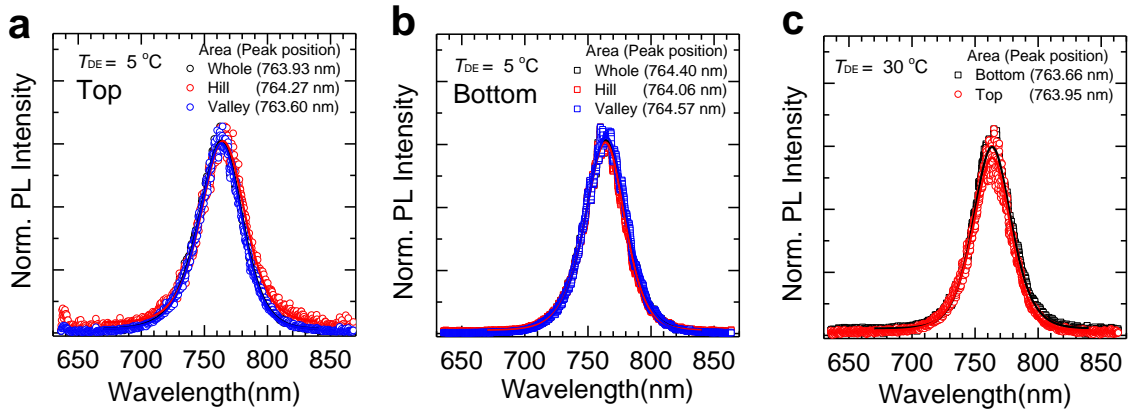
Supplementary Fig. 12. (a) J - V curves of PSCs (FTO/SnO₂/Perovskite/Spiro-MeOTAD/Au) employing the flat (FAPbI₃)_{0.875}(CsPbBr₃)_{0.125} films, formed at $T_{DE} = 30$ °C, with different thickness of 693 nm and 477 nm. (b) Photocurrent profiles of the flat (FAPbI₃)_{0.875}(CsPbBr₃)_{0.125} films (FTO/SnO₂/Perovskite) depending on film thickness. Inset is height profile of (FAPbI₃)_{0.875}(CsPbBr₃)_{0.125} films.



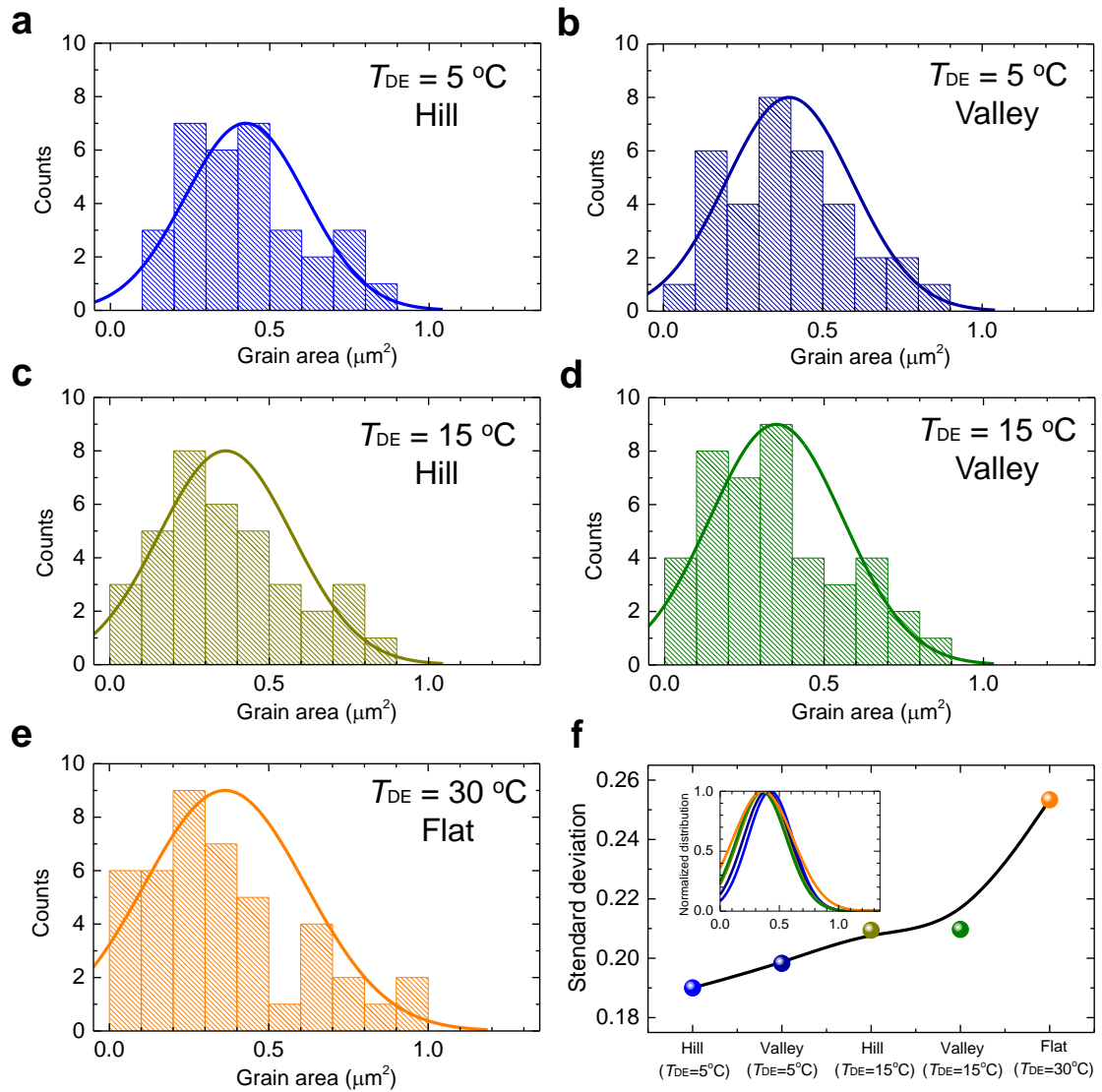
Supplementary Fig. 13. (a) XRD pattern of the (FAPbI₃)_{0.875}(CsPbBr₃)_{0.125} perovskite films formed from $T_{DE} = 5\text{ }^{\circ}\text{C}$, $15\text{ }^{\circ}\text{C}$ and $30\text{ }^{\circ}\text{C}$. Peaks with # are corresponding to FTO. SEM images of perovskite surface measured at hill and valley region (see cartoon) for $T_{DE} =$ (b, c) $5\text{ }^{\circ}\text{C}$ and (d, e) $15\text{ }^{\circ}\text{C}$. (f) SEM image of the flat surface formed from $T_{DE} = 30\text{ }^{\circ}\text{C}$.



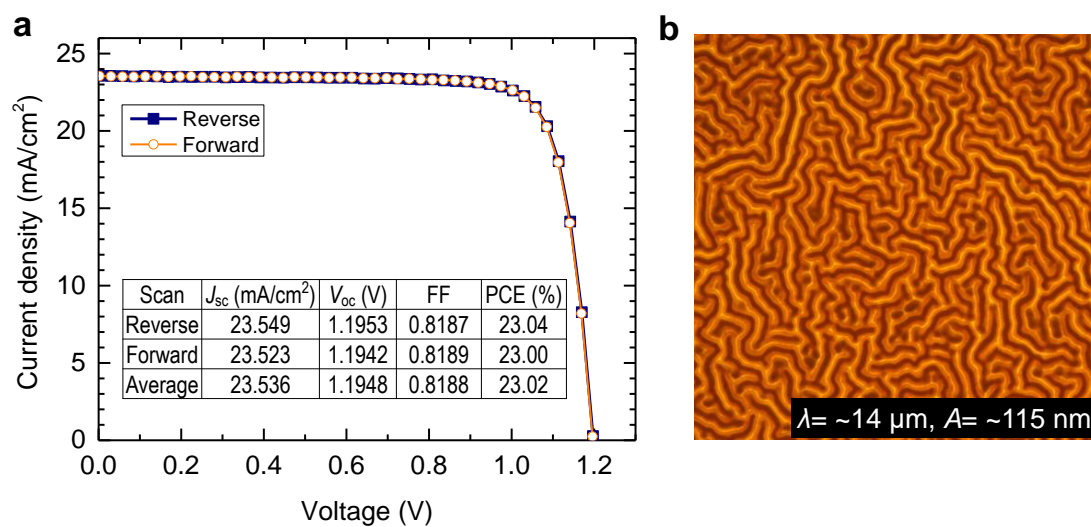
Supplementary Fig. 14. (a) An optical microscope image and (b) the corresponding FLIM image of the $(\text{FAPbI}_3)_{0.875}(\text{CsPbBr}_3)_{0.125}$ film, taken over the same region (dimension = $100\ \mu\text{m} \times 100\ \mu\text{m}$) to identify hills and valleys of the wrinkled morphology.



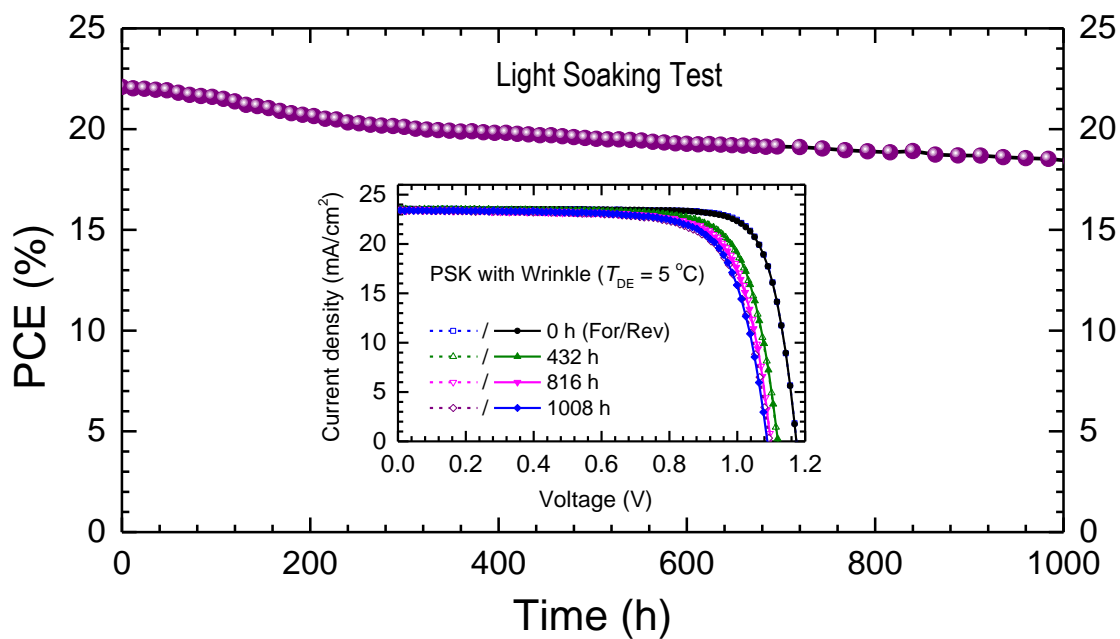
Supplementary Fig. 15. Steady-state PL spectra of (a) the top surface and (b) the bottom surface of the annealed $(\text{FAPbI}_3)_{0.875}(\text{CsPbBr}_3)_{0.125}$ perovskite film with temperature conditions of $T_{\text{Sub}} = 15\text{ }^{\circ}\text{C}$ and $T_{\text{DE}} = 5\text{ }^{\circ}\text{C}$. (c) PL spectra of top and bottom surface of the annealed $(\text{FAPbI}_3)_{0.875}(\text{CsPbBr}_3)_{0.125}$ perovskite film with temperature conditions of $T_{\text{Sub}} = 15\text{ }^{\circ}\text{C}$ and $T_{\text{DE}} = 30\text{ }^{\circ}\text{C}$. The surface area for PL measurement was $50 \times 50\text{ }\mu\text{m}^2$. Since the films formed at $T_{\text{Sub}} = 15\text{ }^{\circ}\text{C}$ and $T_{\text{DE}} = 5\text{ }^{\circ}\text{C}$ showed the wrinkled morphology, PL for hill and valley was measured together with the whole film surface area.



Supplementary Fig. 16. Distributions of grain area (μm^2) extracted from the images in Supplementary Fig. 13, of (a) hill and (b) valley for $T_{DE} = 5\text{ }^\circ\text{C}$, (c) hill and (d) valley for $T_{DE} = 15\text{ }^\circ\text{C}$ and (e) flat for $T_{DE} = 30\text{ }^\circ\text{C}$. T_{Sub} was $30\text{ }^\circ\text{C}$. (f) Standard deviation and normalized distribution (inset) of grain size depending on T_{DE} .



Supplementary Fig. 17. (a) J - V curve of PSC employing the K-doped $\text{FA}_{0.92}\text{Cs}_{0.08}\text{PbBr}_{0.15}\text{I}_{2.85}$ perovskite ($T_{\text{Sub}} = 15 \text{ }^\circ\text{C}$ and $T_{\text{DE}} = 5 \text{ }^\circ\text{C}$). The ratio of $[\text{Pb}^{2+}]$ to $[\text{K}^+] = 0.006$. Data were collected under A.M. 1.5G one sun illumination at scan rate of 260 mV/s. Aperture area was 0.1 cm^2 . (b) Optical microscope image of the K-doped perovskite film.



Supplementary Fig. 18. Light soaking test under continuous illumination with an intensity of $97 \text{ mW}/\text{cm}^2$ at temperature ranging $25\text{-}31^\circ\text{C}$. Perovskite composition of $\text{FA}_{0.92}\text{Cs}_{0.08}\text{PbBr}_{0.15}\text{I}_{2.85}$ with KI additive formed from $T_{DE} = 5^\circ\text{C}$ was employed for long-term stability measurement. The aperture area was 0.10 cm^2 . Inset shows J - V curves measured at different light soaking time.

Supplementary Table 1. Photovoltaic parameters of short-circuit current density (J_{sc}), open-circuit voltage (V_{oc}), fill factor (FF) and power conversion efficiency (PCE) for the PSCs employing $(\text{FAPbI}_3)_{0.875}(\text{CsPbBr}_3)_{0.125}$ perovskite films formed by different T_{DES} . T_{Sub} was 15 °C.

T_{DE} (°C)	Scan direction	J_{sc} (mA/cm ²)	V_{oc} (V)	FF	PCE (%)
5	Forward	22.663	1.157	0.7997	20.97
	Reverse	22.661	1.159	0.8010	21.04
	Average	22.662	1.158	0.8004	21.00
15	Forward	22.484	1.139	0.7811	20.00
	Reverse	22.447	1.142	0.7848	20.12
	Average	22.466	1.141	0.7830	20.07
30	Forward	22.353	1.121	0.7721	19.35
	Reverse	22.377	1.124	0.7736	19.46
	Average	22.365	1.123	0.7729	19.41

Supplementary Table 2. Fitted parameters of fluorescence decay curves for the top surface (Top) and the bottom area (Bottom) of $(\text{FAPbI}_3)_{0.875}(\text{CsPbBr}_3)_{0.125}$ films depending on T_{DES} .

T_{DE}	Spot*	τ (ns)	k_1 ($\times 10^6 \text{ s}^{-1}$)
5 °C (Top)	T-a	136.5	3.6
	T-b	87.4	5.7
15 °C (Top)	T-c	112.2	4.4
	T-d	67.5	7.4
30 °C (Top)	T-e	72.4	6.9
5 °C (Bottom)	B-f	191.7	2.6
	B-g	162.3	3.1
15 °C (Bottom)	B-h	166.4	3.0
	B-i	159.3	3.1
30 °C (Bottom)	B-j	136.1	3.7

*Spots are marked in Fig. 4a-f in the main text.

Supplementary Note 1

Theoretical Analysis of Wrinkling of a Bilayer System

1. Calculation of the governing wavelength of the wrinkle

To describe the wrinkling of a perovskite thin film observed in experiments, we can employ a simple elastic-viscoelastic bilayer model as suggested by Im and Huang [1]. In the model, the system is modeled as an elastic layer (hereafter denoted as a subscript f)-capped viscoelastic substrate (hereafter denoted as a subscript S). Using a linear perturbation analysis, the wrinkling morphology can be approximated as a sinusoidal function with amplitude of A and period (wavelength) of λ . The development of the wrinkled morphology follows a dynamics governed by the fastest growing mode, which can be expressed with a growing constant α such that

$$\alpha \propto - \left[k^2 h_f^2 - \frac{12(1 - \nu_f^2)\sigma_0}{E_f} \right], k = \frac{2\pi}{\lambda} \quad (S1)$$

where h_f is the thickness, ν_f is Poisson's ratio, and E_f is elastic modulus of the elastic capping layer, respectively. The wrinkling results from the relaxation of the in-plane compressive stress denoted as σ_0 . The origin of the in-plane stress comes from the difference of mechanical responses of the elastic capping film and the underlying viscoelastic substrate. For example, we can suggest that the difference is due mainly to the thermal expansion coefficient of the two layers [2]. The absolute value of the compressive stress developed by discrepancy of the thermal expansion coefficients can be expressed as follows.

$$|\sigma_0| = \frac{(\Delta\alpha\Delta T)E_S}{\frac{h_f}{H}(1 - \nu_S) + \frac{E_S}{E_f}(1 - \nu_f)} \quad (S2)$$

where $\Delta\alpha$ denotes the difference of thermal expansion coefficients of the two layers, ν_S , E_S and H are Poisson's ratio, elastic modulus, and the thickness of the underlying viscoelastic substrate, respectively. The strain developed by the thermal expansion discrepancy is assuredly proportional to the temperature change ΔT . For most of the elastic-viscoelastic bilayer system, $\frac{E_S}{E_f} \ll 1$, and therefore, we can simplify eq (S2) as follows.

$$|\sigma_0| \approx \frac{(\Delta\alpha\Delta T)E_S H}{(1 - \nu_S) h_f}. \quad (S3)$$

With the information on σ_0 in eq (S3), we can proceed to calculation of the fastest growing mode for the wrinkling amplitude from a relationship of $\left. \frac{\partial\alpha}{\partial k} \right|_{k=k_C} = 0$, $k_C = \frac{2\pi}{\lambda_C}$, where λ_C denotes the characteristic wavelength of the wrinkle corresponding to the fastest growing amplitude, which results in

$$\lambda_C = \pi\beta h_f, \beta \equiv \left(\frac{-2E_f}{3(1 - \nu_f^2)\sigma_0} \right)^{1/2} \quad (S4)$$

The critical compressive stress corresponding to can be calculated as follows [1],

$$\sigma_C = \left(\frac{-2h_f E_f \mu_R}{3(1 - 2\nu_S)(1 + \nu_S)H} \right)^{1/2} \quad (S5)$$

where μ_R denotes the rubbery modulus of the underlying viscoelastic layer. In the case in which $|\sigma_0|$ is greater than $|\sigma_C|$, the bilayer system suffers morphological instability which is initiated by small fluctuation of thickness. The small fluctuation is spontaneously evolved into the wrinkle patterns with growing amplitude. From eq (S2) and (S4), we can obtain the dependence of on the thickness of the bilayer as follows.

$$\lambda_C \propto h_f \left(\frac{h_f}{H} \right)^{1/2} \quad (S6)$$

At equilibrium, typical wrinkle morphology exhibits amplitude which is considerably smaller than period (i.e., $A/\lambda \ll 1$). For example, in our experiments, $A/\lambda \sim 10^{-2}$. Considering this fact, we can further calculate in-plane strain of the wrinkled bilayer, ε , by calculating expanded areas of the wrinkled surface relative to the flat surface such that

$$\varepsilon = \frac{\Delta l}{\lambda} = \frac{\int_0^\lambda (1 + A^2 \sin^2 kx)^{1/2} dx - \lambda}{\lambda} \approx \frac{(4A + \lambda) - \lambda}{\lambda} = \frac{4A}{\lambda} \quad (S7)$$

From eq (S3) and (S7), we can deduce an additional relationship between and thickness of the bilayer such that

$$\frac{A}{\lambda} \propto \frac{H}{h_f} \quad (S8)$$

s20

Using eq (S6) and (S8), it is also possible to obtain a relationship of A as a function of the bilayer thickness as follows.

$$A \propto H \left(\frac{h_f}{H} \right)^{1/2} \quad (S9)$$

2. Effects of antisolvent temperature on the wrinkle morphology

As shown in Fig. 1d, the major factor governing the wrinkle morphology of a perovskite thin film is the temperature of antisolvent diethyl ether (T_{DE}). At fixed temperature of the substrate (T_{Sub}), we observed that λ increases while A decreases with increasing T_{DE} . Using the bilayer model suggested in the previous part, we can explain these dependences on T_{DE} . The role of the antisolvent is to drive solvent (i.e., DMSO) out of the spin-coated perovskite precursor film by inducing phase separation. For the sake of simplicity, let us assume that the spin-coated layer form bilayer mixture such that DMSO solution containing perovskite precursors and DE. Due to the limited miscibility of DMSO and DE, the mixture suffers phase separation, and the separation can be modeled as spinodal decomposition. For a simple binary mixture which suffers thermodynamic instability, the free energy density of the mixture, ΔF , can be modeled as a function of the composition of one of the components, ϕ [3],

$$\Delta F = \gamma\phi(1 - \phi) + k_B T(\phi \log \phi + (1 - \phi) \log(1 - \phi))$$

where γ denotes a constant concerning the interaction energy of two components and k_B is the Boltzmann constant. In a typical temperature (T)-composition (ϕ) phase diagram of a binary mixture, spinodal decomposition results in two phases containing high and low compositions. In the case of DMSO solution and DE binary mixture, the molar fraction of DMSO solution in the DMSO-rich phase and the DE-rich phase can be expressed as $1 - \phi_d$ and ϕ_d , respectively. Considering a fact that DMSO-solution has higher density, the separated phases form bilayer composed of upper layer containing dilute DMSO-solution and lower layer containing higher concentration of DMSO-solution. Without losing generality, for DMSO-dilute phase, the (upper) elastic film thickness would be proportional to ϕ_d , while the (lower) viscoelastic layer thickness would be proportional to $1 - \phi_d$. Therefore, using eq (S6) and (S9), we can proceed to expression of λ and A as a function of ϕ_d as follows

$$\lambda_C \propto h_f \left(\frac{h_f}{1 - \phi_d} \right)^{1/2} \propto (1 - \phi_d)^{-1/2}, A \propto (1 - \phi_d) \left(\frac{h_f}{1 - \phi_d} \right)^{1/2} \propto (1 - \phi_d)^{1/2} \quad (S10)$$

In eq (S10), we assumed that the thickness of the initially formed elastic layer is not dependent of ϕ_d .

Based on a typical phase diagram of spinodal decomposition, we can find that ϕ_d increases as the temperature of the binary mixture increases approaching the critical temperature. Therefore, ϕ_d for the case in which DE temperature is relatively low (i.e., $T_{DE} = 5$ °C) is smaller than ϕ_d for the cases of relatively high DE temperature (i.e., $T_{DE} = 15$ °C). Then, from eq (S10), we can find that the lower the value of T_{DE} , the lower the value of ϕ_d , and therefore, λ_C increases while A decreases. This can explain the experimental observation of the changes of λ_C and A with different T_{DE} , as reported in Fig. 1d.

3. Effect of the composition of perovskite materials on the wrinkling

We observed that the substitution of FA with Cs or MA and I with Br resulted in the decrease in λ and the increase in A at a certain substitution ratio. The smaller size of the substituents can increase σ_0 , which increase λ according to eq (S3) and (S4). Regarding the increased A , η is decreased with increasing the amount of Cs and Br or MA and Br (see Fig. 1b and c). According to ref S12, amplitude (A) is derived function of dimensionless growth rate (s), characteristic time scale (τ) and formation time (t) ($A = A_0 e^{\frac{st}{\tau}}$, $s = \alpha - \mu_R/E_f$ and $\tau = \eta/E_f$). The A is exponentially anti-proportional to η . Therefore, when η is decreased, A is enlarged. Except for the specific ratio, however, the compositions with $z \geq 0.25$ or $x \geq 0.8$ formed a solid bottom layer, which leads to a very large η (see Supplementary Fig. 6) and thereby a significant increase of characteristic time scale (τ) to about $10^4 \sim 10^5$ times, resulting in less formation of wrinkled texture.

4. Effect of the annealing condition on the wavelength of the wrinkles

Given a condition of $\sigma_0 > \sigma_c$, wrinkling starts with long wavelength (λ_0) which will be eventually narrowed and saturated as the stress is being relaxed until $\sigma_0 = \sigma_c$ [4]. However, in perovskite film formation process, λ_0 cannot be saturated because the bottom layer is solidified before it is saturated, which may lead to a residual compressed stress after spin-coating [5]. The slight decrement of λ after annealing is evidence of the presence of residual stress because the

relaxation of residual stress will further decrease λ as shown in Supplementary Fig. 2d-e.

5. Null contribution of E_f and ν_f

E_f and ν_f can be also assumed to be constant due to a small difference in E_f between 10.2~11.8 GPa for FAPbI₃ and 9.7~12.3 GPa for FAPbBr₃ even upon replacing iodide with bromide [6] and small ν_f of perovskite (0.28~0.33) [7].

6. Effect of T_{Sub}

At fixed temperature such as $T_{\text{DE}} = 15$ °C, λ increases, while A decreases with increasing T_{Sub} from 5 °C to 15 °C (see Fig. 1d). Upon increasing T_{Sub} , h_f is expected to increase because the miscibility between DMSO and diethyl ether is enhanced by elevating T_{Sub} . This can lead to an increase in h_f but decreases in A .

Supplementary Note 2

The PL peak position E_0 and width σ were extracted by fitting each frame of the PL data with a hyperbolic secant, according to $\text{PL}(E) = I_0 \left[\exp\left(-\frac{E-E_0}{\sigma}\right) + \exp\left(\frac{E-E_0}{\sigma}\right) \right]^{-1}$. The band edge energy was determined by fitting the band edge of the spectrum at the end of each measurement, to all prior spectra, where the fitted spectrum was allowed to be shifted in energy and scaled in intensity. For comparison with PL, the band edge was shifted in energy to match the final PL peak position.

The PL peak position as well as the band edge energy continuously shift to lower energies upon increasing perovskite layer thickness. Above approx. 100 nm (longer times), the shift of the PL peak position and band edge are nearly identical, and the PL peak width is constant. Below approx. 100 nm (shorter times), the shift of the PL peak is steeper and accompanied by a pronounced decrease of the PL peak width. A shift of the band gap / PL peak to higher energies, together with an increased PL peak width are characteristic for a quantum confinement effect, which decreases with increasing layer thickness [8-12]. We note that the thickness of 100 nm, which is where the decrease of σ stops, is far above the confinement limit reported for halide perovskites (~ 25-30 nm) [13-15]. This suggests that even though the average layer thickness is above the confinement limit, individual grains can still be very small and can have limited electronic interaction with adjacent grains. The PL quantum efficiency of such grains is

s23

enhanced by the quantum confinement effect [16], so that they contribute overproportionally strong in the PL spectra. The slower shift for longer time could either stem from a change in stoichiometry or a decreasing confinement effect. Since the PL peak width remains constant during this shift, we can exclude a decreasing confinement effect as cause for this spectral shift, so we associate it with a change in stoichiometry during spin coating (not annealed film). This indicates a preferential formation of a bromine-rich phase, possibly e.g. due to differences in the enthalpy of formation, as reported for MAPbI₃ and MAPbBr₃ [17], or different diffusivity in solution of the different compounds. By comparison with another mixed halide perovskite, MAPbI_{3-y}Br_y [18], we are able to estimate the change in stoichiometry during spin coating. The observed shift of the band edge and PL peak position by about 50 meV corresponds to a change from $y = 0.5$ to $y = 0.375$, which would correspond to a change of material composition from (FAPbI₃)_{0.833}(CsPbBr₃)_{0.167} to (FAPbI₃)_{0.875}(CsPbBr₃)_{0.125} in our case, (based on the assumption that the latter is the final film stoichiometry).

Supplementary Note 3

Evolution of the wrinkle pattern of the bilayer

To confirm the wrinkling mechanism of a bilayer structure observed in our experiments, we provide a computer simulation of the temporal morphological evolution of the surface wrinkles of the bilayer. For this simulation, we employed a typical finite-difference method for 2D simulation box (800×800) with periodic boundary condition. According to the theoretical and numerical scheme suggested by Im and Huang [1], we modeled the morphological evolution of the bilayer wrinkles as shown in Supplementary Fig. 7. As shown in Supplementary Fig. 8, one can find that the simulated wrinkle morphology is similar to the experimentally observed morphology. The similarity is confirmed again by comparing the 2D fast Fourier transform (2D FFT) signals obtained from the simulated and experimentally observed morphologies, in which isotropic wrinkles pattern with notable concentric ring patterns which correspond to the characteristic length scale (i.e., λ_C) of the wrinkles. The computer simulated bilayer wrinkle morphology strongly supports that the wrinkling mechanism of the perovskite thin film hinges on the relaxation of the in-plane compressive stress developed in the elastic-viscoelastic bilayer.

Supplementary Note 4

Analysis of charge carrier density from PL intensity

The charge carrier recombination in halide perovskites is given by

$$\frac{dn(t)}{dt} = -k_1n(t) - k_2n(t)^2 - k_3n(t)^3, \quad (\text{S11})$$

where k_1 is associated with mono-molecular, trap-assisted recombination, k_2 is the rate constant for bimolecular and in this case radiative recombination, and k_3 is the rate constant for Auger-recombination. In general, this leads to a non-exponential decrease of the charge carrier density and accordingly of the PL intensity, which is proportional to

$$\text{PL}(t) \propto k_2n(t)^2. \quad (\text{S12})$$

However, for low charge densities, i.e. for low excitation densities or long delay times, the mono-molecular recombination becomes dominant and the change of charge carrier density is given by

$$\frac{dn(t)}{dt} \approx -k_1n(t). \quad (\text{S13})$$

Thus, the temporal evolution of the charge carrier density is given by

$$n(t) \approx n_0 \exp(-k_1t). \quad (\text{S14})$$

Inserting this into eq. S12 yields a mono-exponential decay of the PL intensity according to

$$\text{PL}(t) \propto k_2n(t)^2 \approx k_2n_0^2 \exp(-2k_1t). \quad (\text{S15})$$

The PL decay for low charge carrier densities thus depends on the mono-molecular recombination constant and contains information about the trap density in the material.

Supplementary References

1. S. H. Im, R. Huang, Evolution of Wrinkles in Elastic-Viscoelastic Bilayer Thin Films. *J. Appl. Mech.* **2005**, 72, 955–961.
2. W. -J. Chang, T. -H. Fang, C. -M. Lin, Thermally induced viscoelastic stresses in multilayer thin films, *J. Appl. Phys.* **2005**, 97, 103521.
3. Hill, T. L. *An Introduction to Statistical Thermodynamics*; Dover Publications, Inc.: New York, 1986.
4. S. Chatterjee, C. McDonald, J. Niu, S. S. Velankar, P. Wang, R. Huang, Wrinkling and folding of thin films by viscous stress. *Soft Matter*, **2015**, 11, 1814–1827.
5. K. A. Bush, N. Rolston, A. Gold-Parker, S. Manzoor, J. Hausele, Z. J. Yu, J. A. Raiford, R. Cheacharoen, Z. C. Holman, M. F. Toney, R. H. Dauskardt, M. D. McGehee. Controlling Thin-Film Stress and Wrinkling during Perovskite Film Formation. *ACS Energy Lett.* **2018**, 3, 1225–1232
6. S. Sun, F. H. Isikgor, Z. Deng, F. Wei, G. Kieslich, P. D. Bristowe, J. Ouyang, A. K. Cheetham, Factors Influencing the Mechanical Properties of Formamidinium Lead Halides and Related Hybrid Perovskites. *ChemSusChem*, **2017**, 10, 3740–3745.
7. J. Feng, Mechanical properties of hybrid organic inorganic $\text{CH}_3\text{NH}_3\text{BX}_3$ (B = Sn, Pb; X = Br, I) perovskites for solar cell absorbers. *APL Mater.* **2014**, 2, 081801.
8. V. Malgras, S. Tominaka, J. W. Ryan, J. Henzie, T. Takei, K. Ohara, Y. Yamauchi, Observation of Quantum Confinement in Monodisperse Methylammonium Lead Halide Perovskite Nanocrystals Embedded in Mesoporous Silica. *J. Am. Chem. Soc.* **2016**, 138, 13874–13881.
9. M. Anaya, A. Rubino, T. C. Rojas, J. F. Galisteo-López, M. E. Calvo, H. Míguez, Strong Quantum Confinement and Fast Photoemission Activation in $\text{CH}_3\text{NH}_3\text{PbI}_3$ Perovskite Nanocrystals Grown within Periodically Mesoporous Films. *Adv. Optical Mater.* **2017**, 5, 1601087.
10. M. E. Kamminga, H.-H. Fang, M. R. Filip, F. Giustino, J. Baas, G. R. Blake, M. A. Loi, T. T. M. Palstra, Confinement Effects in Low-Dimensional Lead Iodide Perovskite Hybrids.

Chem. Mater. **2016**, *28*, 4554–4562.

11. F. Zhang, S. Huang, P. Wang, X. Chen, S. Zhao, Y. Dong, H. Zhong, Colloidal Synthesis of Air-Stable CH₃NH₃PbI₃ Quantum Dots by Gaining Chemical Insight into the Solvent Effects. *Chem. Mater.* **2017**, *29*, 3793–3799.

12. M. Chauhan, Y. Zhong, K. Schötz, B. Tripathi, A. Köhler, S. Huettnner, F. Panzer, Investigating two-step MAPbI₃ thin film formation during spin coating by simultaneous in situ absorption and photoluminescence spectroscopy. *J. Mater. Chem. A* **2020**, *8*, 5086–5094.

13. D. N. Dirin, L. Protesescu, D. Trummer, I. V. Kochetygov, S. Yakunin, F. Krumeich, N. P. Stadie, M. V. Kovalenko, Harnessing Defect-Tolerance at the Nanoscale: Highly Luminescent Lead Halide Perovskite Nanocrystals in Mesoporous Silica Matrixes. *Nano Lett.* **2016**, *16*, 5866–5874.

14. E. S. Parrott, J. B. Patel, A.-A. Haghighirad, H. J. Snaith, M. B. Johnston, L. M. Herz, Growth modes and quantum confinement in ultrathin vapour-deposited MAPbI₃ films. *Nanoscale* **2019**, *11*, 14276–14284.

15. L. Polavarapu, B. Nickel, J. Feldmann, A. S. Urban, Advances in Quantum-Confined Perovskite Nanocrystals for Optoelectronics. *Adv. Energy Mater.* **2017**, *7*, 1700267.

16. S. Kan, T. Mokari, E. Rothenberg, U. Banin, Synthesis and size-dependent properties of zinc-blende semiconductor quantum rods. *Nat. Mater.* **2003**, *2*, 155–158.

17. C. Rehermann, A. Merdasa, K. Suchan, V. Schröder, F. Mathies, E. L. Unger, Origin of Ionic Inhomogeneity in MAPb(IxBr_{1-x})₃ Perovskite Thin Films Revealed by In-Situ Spectroscopy during Spin Coating and Annealing, *ACS Appl. Mater. Interfaces* **2020**, *12*, 30343–30352.

18. C. M. Sutter-Fella, Y. Li, M. Amani, J. W. Ager, F. M. Toma, E. Yablonovitch, I. D. Sharp, A. Javey, High Photoluminescence Quantum Yield in Band Gap Tunable Bromide Containing Mixed Halide Perovskites. *Nano Lett.* **2016**, *16*, 800–806.

15 Full list of Publications

Peer-reviewed publications:

1. Charles Lochenie, **Konstantin Schötz**, Fabian Panzer, Hannah Kurz, Bernadette Maier, Florian Puchtler, Seema Agarwal, Anna Köhler, Birgit Weber, *Spin-crossover iron (II) coordination polymer with fluorescent properties: correlation between emission properties and spin state*
Journal of the American Chemical Society, **2018**, 140 (2), 700-709.
2. Dominic Raithel, Lena Simine, Sebastian Pickel, **Konstantin Schötz**, Fabian Panzer, Sebastian Baderschneider, Daniel Schiefer, Ruth Lohwasser, Jürgen Köhler, Mukundan Thelakkat, Michael Sommer, Anna Köhler, Peter J. Rossky, Richard Hildner, *Direct observation of backbone planarization via side-chain alignment in single bulky-substituted polythiophenes*
Proceedings of the National Academy of Sciences, **2018**, 115 (11), 2699-2704.
3. Markus Reichenberger, Daniel Kroh, Giovanni M. Matrone, **Konstantin Schötz**, Stephan Pröllner, Oliver Filonik, Margret E. Thordardottir, Eva M. Herzig, Heinz Bässler, Natalie Stingelin, Anna Köhler, *Controlling aggregate formation in conjugated polymers by spin-coating below the critical temperature of the disorder–order transition*
Journal of Polymer Science Part B: Polymer Physics, **2018**, 56 (6), 532-542.
4. Nico Leupold, **Konstantin Schötz**, Stefania Cacovich, Irene Bauer, Maximilian Schultz, Monika Daubigner, Leah Kaiser, Amelle Rebai, Jean Rousset, Anna Köhler, Philip Schulz, Ralf Moos, Fabian Panzer, *High Versatility and Stability of Mechanochemically Synthesized Halide Perovskite Powders for Optoelectronic Devices*
ACS applied materials & interfaces, **2019**, 11 (33), 30259-30268.
5. **Konstantin Schötz**, Abdelrahman M. Askar, Wei Peng, Dominik Seeberger, Tanaji P. Gujar, Mukundan Thelakkat, Anna Köhler, Sven Huettner, Osman M. Bakr, Karthik Shankar, Fabian Panzer, *Double peak emission in lead halide perovskites by self-absorption*
Journal of Materials Chemistry C, **2020**, 8 (7), 2289-2300

6. Mihirsingh Chauhan, Yu Zhong, **Konstantin Schötz**, Brijesh Tripathi, Anna Köhler, Sven Hüttner, Fabian Panzer,
Investigating two-step MAPbI₃ thin film formation during spin coating by simultaneous in situ absorption and photoluminescence spectroscopy
Journal of Materials Chemistry A, **2020**, 8 (10), 5086-5094.
7. Philip Schmode, **Konstantin Schötz**, Oleksandr Dolynchuk, Fabian Panzer, Anna Köhler, Thomas Thurn-Albrecht, Mukundan Thelakkat,
Influence of ω -Bromo Substitution on Structure and Optoelectronic Properties of Homopolymers and Gradient Copolymers of 3-Hexylthiophene
Macromolecules, **2020**, 53 (7), 2474-2484.
8. **Konstantin Schötz**, Abdelrahman M. Askar, Anna Köhler, Karthik Shankar, Fabian Panzer,
Investigating the Tetragonal-to-Orthorhombic Phase Transition of Methylammonium Lead Iodide Single Crystals by Detailed Photoluminescence Analysis
Advanced Optical Materials, *2020*, 8 (17), 2000455.
9. Sophie Schönfeld, Katja Dankhoff, Dirk Baabe, Marc-Kevin Zaretzke, Martin Bröring, **Konstantin Schötz**, Anna Köhler, Gerald Hörner, Birgit Weber,
Iron (II) Spin Crossover Complexes Based on a Redox Active Equatorial Schiff-Base-Like Ligand
Inorganic Chemistry, **2020**, 59 (12), 8320-8333.
10. Yuan-Yuan Guo, Lin-Jie Yang, Simon Biberger, Jason A. McNulty, Teng Li, **Konstantin Schötz**, Fabian Panzer, Philip Lightfoot,
Structural Diversity in Layered Hybrid Perovskites, A₂PbBr₄ or AAPbBr₄, Templated by Small Disc-Shaped Amines
Inorganic Chemistry, **2020**, 59 (17), 12858-12866.
11. **Konstantin Schötz**, Fabian Panzer,
Using In Situ Optical Spectroscopy to Elucidate Film Formation of Metal Halide Perovskites
Journal of Physical Chemistry A, **2021**, 125 (11), 2209-2225.
12. Hannah Kurz, **Konstantin Schötz**, Ilias Papadopoulos, Frank W. Heinemann, Harald Maid, Dirk M. Guldi, Anna Köhler, Gerald Hörner, Birgit Weber,
A Fluorescence-Detected Coordination-Induced Spin State Switch
Journal of the American Chemical Society, **2021**, 143 (9), 3466-3480.
13. Seul-Gi Kim, Jeong-Hyeon Kim, Philipp Ramming, Yu Zhong, **Konstantin Schötz**, Seok Joon Kwon, Sven Huettner, Fabian Panzer, Nam-Gyu Park,

How Antisolvent Miscibility Affects Perovskite Film Wrinkling and Photovoltaic Properties

Nature Communications, **2021**, 12 (1), 1554.

14. Philipp Ramming, Nico Leupold, **Konstantin Schötz**, Anna Köhler, Ralf Moos, Helen Grüninger, Fabian Panzer,
Suppressed ion migration in powder-based perovskite thick films using an ionic liquid
Journal of Materials Chemistry C, 2021, 9 (35), 11827-11837.
15. **Konstantin Schötz**, Christopher Greve, Arjan Langen, Harrie Gorter, Ilker Dogan, Yulia Galagan, Albert JJM van Breemen, Gerwin H Gelinck, Eva M Herzig, Fabian Panzer,
Understanding Differences in the Crystallization Kinetics between One-Step Slot-Die Coating and Spin Coating of MAPbI₃ Using Multimodal In Situ Optical Spectroscopy
Advanced Optical Materials, 2021, 9, 2101161.
16. Patrick Beer, Paul M. Reichstein, **Konstantin Schötz**, Dominic Raithel, Mukundan Thelakkat, Jürgen Köhler, Fabian Panzer, Richard Hildner,
Disorder in P3HT nanoparticles probed by optical spectroscopy on P3HT-b-PEG micelles
accepted in The Journal of Physical Chemistry (2021).

Prepared for submission:

1. **Konstantin Schötz**, Hazem Bakr, Giovanni Maria Matrone, Natalie Stingelin, Anna Köhler, Fabian Panzer,
Conformational changes of PffBT₄T-2OD (PCE11) aggregates upon blending with HDPE probed by optical spectroscopy
2. Matthew J. Dyson, Hazem Bakr, Stefan Wedler, **Konstantin Schötz**, Mihirsinh Chauhan, Paul N. Stavrinou, Natalie Stingelin, Anna Köhler, Fabian Panzer,
Processing condition dependent aggregation pathways in conjugated polymers

Patents:

1. Fabian Panzer, **Konstantin Schötz**, Michael Buchhorn, Dominik Hanft,
Vorrichtung zur schnellen aufeinanderfolgenden Detektion von Emissions- und Absorptionsspektren von organischen oder perowskitischen Halbleitern
2. Ralf Moos, **Konstantin Schötz**, Fabian Panzer, Anna Köhler, Nico Leupold,
Verfahren zur Aufarbeitung von hybriden Perowskiten

Appendix

Acknowledgements

The four years in which I made the work for this thesis went by incredibly fast. Together with the overall two years of Bachelor and Master-studies, the work at the university in the group of Anna Köhler has been a constant feature in my life for over six years. This constant accompanied me through very good times, and gave me some stability in very difficult times. I want to thank Anna Köhler for the opportunity to work in her group for such a long time. Thank you for all your support and interest in my work, and for making it possible to visit several international conferences, both scientifically stimulating and located in very nice places. I will probably remember these times at the conferences for my whole life! Also, thank you for appreciating social breaks as an important part of everyday work. Thank you for all your trust and all the opportunities.

Special thanks to Fabian Panzer, who took care of me during my whole time in the workgroup. Thank you for sharing your technical, scientific and musical knowledge with me, for the inspiring discussions and for your realistic optimism. I am very grateful for both, your scientific and your mental support. Thank you for all the social events that you initiated. And even thank you for pushing me out of my comfort zone by making me a contributed speaker at conferences ;)

I want to thank Irene Bauer and Frank Schirmer for their steady support and their will to help me with my - sometimes slightly spontaneous - problems. Thank you very much for keeping everything running and functioning, for your overall very positive attitude and for your care for the whole group! I want to thank Michaela Fischer and Laura Schwarze for keeping everything organized and for compensating our organizational mess. Additionally, I want to thank Thomas Dabisch for letting me use his tools and workshop, and of course for the positivity that you spread.

I also want to thank my collaborators for the nice collaborations (not for the not-so-nice-ones), for the scientific exchange and for the mostly beautiful works that resulted from these collaborations. Never underestimate the importance of honest scientific exchange and good, respectful communication.

And now a very important part: I want to thank all my colleagues and the nice colleagues of the group of Eva Herzig for the very pleasant, funny and relaxed atmosphere at our hallways, offices and laboratories. I am very happy that I had the possibility to share so much time with so many great people, and I am hoping that I will be able to continue sharing time

with you in the future. It is a pity that Corona did steel quite a lot of social time from us, canceling conferences, barbecues and forcing us to work at home. However, even in this difficult times, we managed to have social exchange, GeoGuesser-Christmas-events and so on. I want to thank you all, present and former members, for all the joy and inspiration that you brought into my life. I hope the SMØ Party Crew + Guests will continue to accompany me. I would like to thank all people for forgiving my moderately strong organizational skills, my reluctant decisiveness, and my occasional spontaneity. I think that this might not have always been easy for other people. At least it has not been always easy for me.

I want to thank my friends for all the fun time, for deep talks, for nonsense, for making Bayreuth a great place to be for me. I hope I can stay in touch with you when your or my time in Bayreuth will end.

Finally, I want to thank my whole family. I want to thank my parents for the great education, all the opportunities and all the impressions that I could gather with their help. Thanks to my whole family (including partners. You belong to the family.) for all the support, the trust, the respect, the patience and for tolerating and compensating my above-mentioned organizational skills, decisiveness and spontaneity. Thank you for all the love, and all the great time that we had, have and will have together! I am very grateful for you and I am proud of you!

I also want to thank caffeine and Stack Overflow, without whom this work would hardly have been possible.

So long!

Erklärung und eidesstattliche Versicherung

Hiermit versichere ich an Eides statt, dass ich die vorliegende Arbeit selbstständig verfasst und keine anderen als die von mir angegebenen Quellen und Hilfsmittel verwendet habe.

Weiterhin erkläre ich, dass ich die Hilfe von gewerblichen Promotionsberatern bzw. -vermittlern oder ähnlichen Dienstleistern weder bisher in Anspruch genommen habe, noch künftig in Anspruch nehmen werde.

Zusätzlich erkläre ich hiermit, dass ich keinerlei frühere Promotionsversuche unternommen habe.

Bayreuth, den

Konstantin Schötz

